Taira, A., Hill, I., Firth, J., et al., 1991
Proceedings of the Ocean Drilling Program, Initial Reports, Vol. 131

6. SITE 808[1]

Shipboard Scientific Party[2]

HOLE 808A

Date occupied: 4 April 1990

Date departed: 6 April 1990

Time on hole: 2 days, 10 hr

Position: 32° 21.12′N, 134° 56.67′E

Bottom felt (rig floor; m; drill-pipe measurement): 4686.7

Distance between rig floor and sea level (m): 10.70

Water depth (drill-pipe measurement from sea level, m): 4676.0

Total depth (rig floor; m): 4798.10

Penetration (m): 111.40

Number of cores (including cores with no recovery): 13

Total length of cored section (m): 111.40

Total core recovered (m): 88.68

Core recovery (%): 79

Oldest sediment cored:
Depth sub-bottom (m): 111.40
Nature: clastic turbidite
Earliest age: Pleistocene
Drill below core (m): 0.00

HOLE 808B

Date occupied: 6 April 1990

Date departed: 15 April 1990

Time on hole: 8 days, 19 hr

Position: 32° 21.09′N, 134° 56.61′E

Bottom felt (rig floor; m; drill-pipe measurement): 4685.0

Distance between rig floor and sea level (m): 10.80

Water depth (drill-pipe measurement from sea level, m): 4674.2

Total depth (rig floor; m): 5043.80

Penetration (m): 358.80

Number of cores (including cores with no recovery): 28

Total length of cored section (m): 247.80

Total core recovered (m): 59.71

Core recovery (%): 24

Oldest sediment cored:
Depth sub-bottom (m): 358.80
Nature: silty turbidite
Earliest age: Pleistocene
Drill below core (m): 0.00

[1] Taira, A. Hill, I., Firth, J., et al., 1991. *Proc. ODP, Init. Repts.*, 131: College Station, TX (Ocean Drilling Program).

[2] Shipboard Scientific Party is as given in the list of participants preceding the contents.

HOLE 808C

Date occupied: 15 April 1990

Date departed: 1 May 1990

Time on hole: 16 days, 11 hr

Position: 32° 21.17′N, 134° 56.66′E

Bottom felt (rig floor; m; drill-pipe measurement): 4685.5

Distance between rig floor and sea level (m): 10.90

Water depth (drill-pipe measurement from sea level, m): 4674.6

Total depth (rig floor; m): 6012.50

Penetration (m): 1327.00

Number of cores (including cores with no recovery): 108

Total length of cored section (m): 1028.50

Total core recovered (m): 572.43

Core recovery (%): 55

Oldest sediment cored:
Depth sub-bottom (m): 1300.00
Nature: red shale
Earliest age: middle Miocene
Basement:
Depth sub-bottom (m): 1289.90
Drill below core (m): 0.00

HOLE 808D

Date occupied: 1 May 1990

Date departed: 8 May 1990

Time on hole: 6 days, 10 hr

Position: 32° 21.14′N, 134° 56.58′E

Bottom felt (rig floor; m; drill-pipe measurement): 4684.0

Distance between rig floor and sea level (m): 11.30

Water depth (drill-pipe measurement from sea level, m): 4672.7

Total depth (rig floor; m): 5464.00

Penetration (m): 780.00

Number of cores (including cores with no recovery): 0

Total length of cored section (m): 0.00

Total core recovered (m): 0.00

Core recovery (%): 0

Drill below core (m): 780.00

HOLE 808E

Date occupied: 8 May 1990

Date departed: 27 May 1990

Time on hole: 18 days, 16 hr, 30 min

Position: 32° 21.11′N, 134° 56.61′E

Bottom felt (rig floor; m; drill-pipe measurement): 4684.5

Distance between rig floor and sea level (m): 11.60

Water depth (drill-pipe measurement from sea level, m): 4672.9

Total depth (rig floor; m): 5884.5

Penetration (m): 1200.00

Number of cores (including cores with no recovery): 0

Total length of cored section (m): 0.00

Total core recovered (m): 0.00

Core recovery (%): 0

Drill below core (m): 1200.00

HOLE 808F

Date occupied: 27 May 1990

Date departed: 28 May 1990

Time on hole: 1 day, 7 hr, 30 min

Position: 32° 21.15′N, 134° 56.76′E

Bottom felt (rig floor; m; drill-pipe measurement): 4696.0

Distance between rig floor and sea level (m): 11.70

Water depth (drill-pipe measurement from sea level, m): 4684.3

Total depth (rig floor; m): 4836.00

Penetration (m): 140.00

Number of cores (including cores with no recovery): 4

Total length of cored section (m): 61.00

Total core recovered (m): 2.37

Core recovery (%): 0.0

Drill below core (m): 0.00

HOLE 808G

Date occupied: 28 May 1990

Date departed: 30 May 1990

Time on hole: 2 days, 2 hr, 30 min

Position: 32° 21.15′N, 134° 56.76′E

Bottom felt (rig floor; m; drill-pipe measurement): 4696.0

Distance between rig floor and sea level (m): 11.70

Water depth (drill-pipe measurement from sea level, m): 4684.3

Total depth (rig floor; m): 4919

Penetration (m): 213.00

Number of cores (including cores with no recovery): 12

Total length of cored section (m): 99.60

Total core recovered (m): 12.80

Core recovery (%): 17.5

Oldest sediment cored:
Depth sub-bottom (m): 203.00
Nature: clastic turbidite
Earliest age: Pleistocene

Drill below core (m): 0.00

Principal results: Site 808 produced a continuously cored section through 1290 m of middle Miocene to Holocene (15 Ma to present) sediments at the toe of the accretionary prism. The upper 560 m of sediments are dominantly turbidites that have traveled along the Nankai Trough from the Izu collision zone to the east and have been deposited at the high rate of more than 1 km/m.y. The lower sediments are mainly hemipelagic muds that accumulated away from the trench in the Shikoku Basin.

The major thrust fault at 366 m below sea floor (mbsf) is marked by folding of the sediments, with overturned beds just below the fault plane. At 960 mbsf there is a zone, about 20 m wide, containing brecciated and sheared rock. Below it, the rocks are virtually undeformed. This zone was identified as the decollement. The complete interval between the thrust and the decollement shows pervasively deformed sediments, with abundant minor faulting at depth while complex shear bands predominate near the thrust fault. There is evidence that shear bands pre-date the faulting. This demonstrates that the style of sediment deformation changes with time and/or position within the accretionary prism.

Physical properties of the recovered sediments were measured at about 1-m intervals throughout the cored section. The most remarkable discovery here was the large contrast in properties occurring across the décollement. One example is the considerable increase in porosity below the décollement, violating the normal pattern of decreasing porosity with depth due to compaction. This may indicate that the sediments contain fluid at higher than normal (hydrostatic) pressures. Chemical analysis of the interstitial water showed gradients in composition related to changing lithology, and to the two major faults. A large-amplitude smooth decrease in chlorinity toward the décollement can be interpreted either as evidence for fossil fluid flow or a result of *in-situ* reaction. There is, however, no direct evidence for the major localized fluid flow that has been implied in other accretionary prisms. The complete absence of mineralized veins supports this view.

Wireline logs to determine *in-situ* values of physical properties were only obtained over limited sections of the holes drilled, due to unstable hole conditions, but allow comparison with shipboard measurements on recovered cores. Thermal measurements have shown a steep thermal gradient of some 120°C/km, and measured values of thermal conductivity allow calculation of a heat flow value of 130 mW/m^2. Preliminary analysis of hydrocarbon gases suggests that the thermal gradient may have been even higher in the past. A vertical seismic profile (VSP) was recorded to allow closer correlation of the core samples to the seismic section. Attempts to directly measure the permeability of the sediments by packer experiments were frustrated by instrumental problems, probably related to the difficult hole condition.

BACKGROUND AND OBJECTIVES

Site 808 (planning designation NKT-2) is situated at the toe of the Nankai accretionary prism. The sediment within the upper part of this prism is dominated by clastic material transported by turbidity currents that flowed southwestward along the Nankai Trough from the collision zone between Japan and the Izu-Bonin Arc. The lower part of the prism is formed from hemipelagic sediments deposited on the oceanic crust of the Shikoku Basin, formed by backarc spreading during the period 25 to 15 Ma. These lithologies are interdigitated, the proportion of turbidite material increasing upward.

The objective in drilling this site was to investigate the relationships between lithology, physical properties, mechanical state, and hydrogeology in a clastic accretionary prism undergoing the initial phases of deformation. The location of Site 808 was determined by several different requirements. A position was chosen so that drilling could intersect a major thrust in the prism and the décollement. The site was chosen near to the toe of the prism so that the structures would be relatively simple and well imaged by multichannel seismic profiles. The thrust fault should be intersected at a depth where sediment would be well consolidated, so that core recovery would be optimum and borehole measurements could be made in relatively stable hole conditions. The position along the length of the Nankai Trough was determined by the desire to make the site as shallow as possible, avoiding excessive sedimentary thicknesses. The actual site is located near the extinct spreading center of the Shikoku Basin, where the relatively young oceanic crust lies at shallower depth as it reaches the trench.

The area was extensively surveyed using multichannel seismic reflection, ESP seismic profiles, Sea Beam and IZANAGI sidescan sonar (Moore et al, 1990, Moore et al., this volume, and Background and Objectives chapter, this volume). The site was chosen to lie on the multichannel line NT 62-8, at about CDP 950, where the other surveys, principally Sea Beam and IZANAGI, showed the structure to be relatively uniform in the strike direction. The chosen location is shown on Figure 1 and the geological structure is shown in the small section of the seismic line NT 62-8 shown in Figure 2.

The seismic data were processed with a nominal 60 fold at a CMP bin diameter of 16.7 m. A comprehensive processing sequence has been carried out, including depth migration, to produce the section as seen in Figure 2. The full section is shown in the backpocket fold-out (Fig. 2, Chapter 2) and described by Moore et al., Chapter 2 (this volume). The primary features of this section are the oceanic basement, shown as a rather planar reflector at 1260 mbsf, and the frontal thrust of the accretionary prism. This thrust is imaged as a reflector with an average dip of about 30° (the vertical exaggeration of the figure is about 1.5×). It shows a sinuous trace, shallowing toward the surface and between 700 to about 850 mbsf, at which depth it becomes indistinct. Bright reflectors such as those in the thrust footwall at 550 to 650 mbsf can be correlated across the thrust giving an estimate of vertical offset of about 150 m. A primary division between the strongly

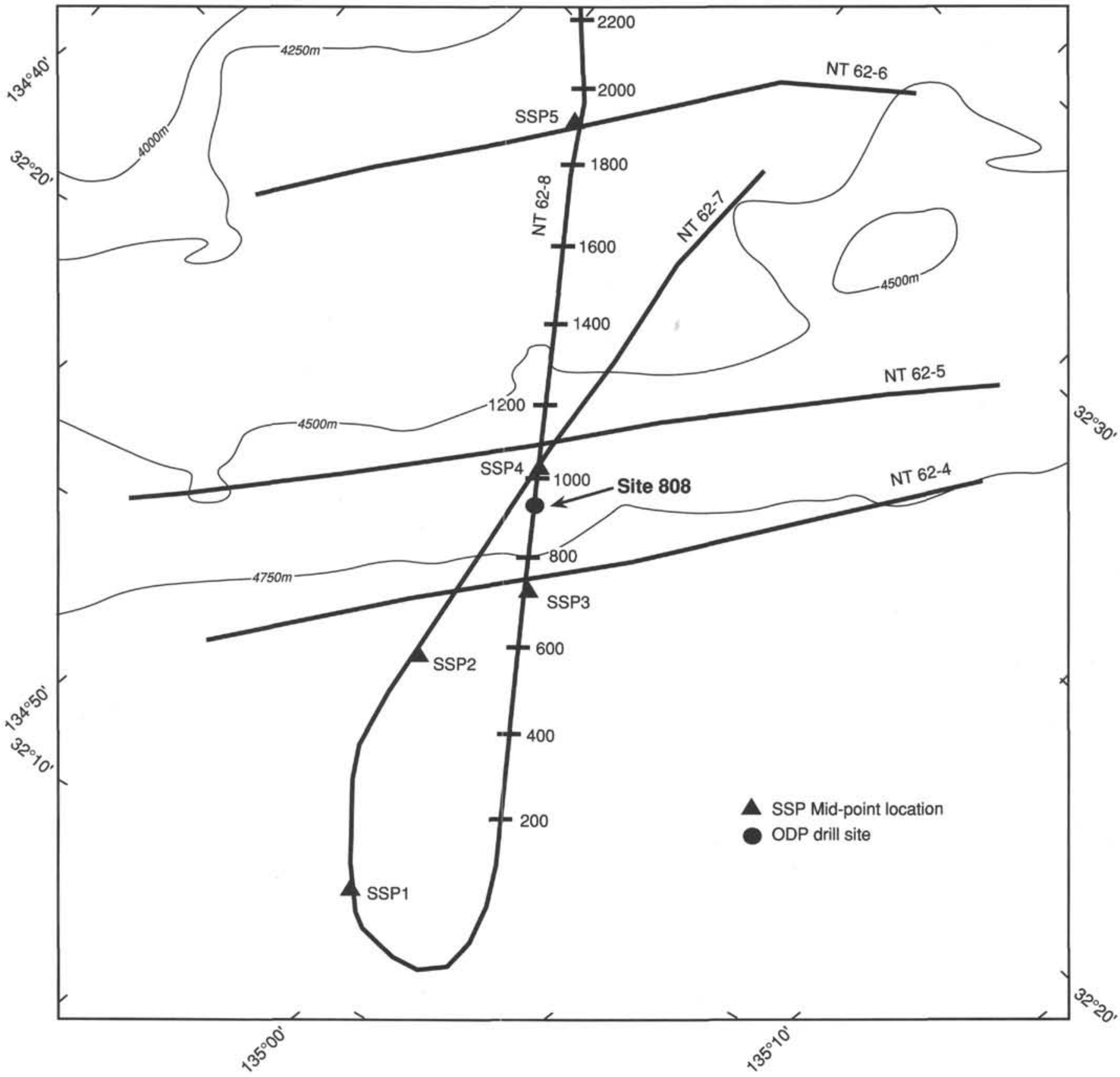

Figure 1. Map showing the location of Site 808 with respect to the morphology of the Nankai prism toe, and multichannel seismic profile NT 62-8.

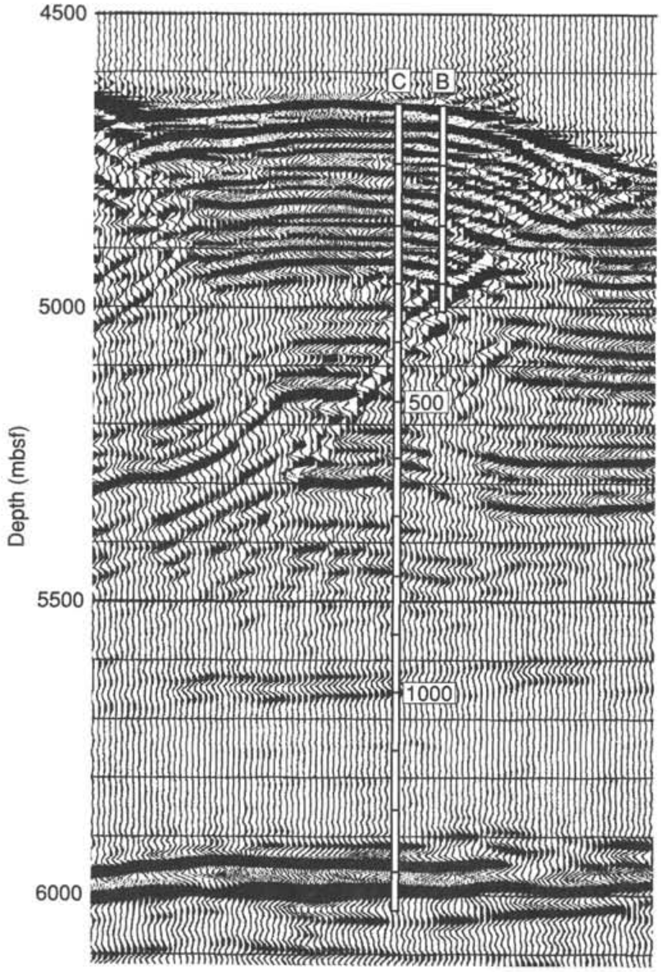

Figure 2. Part of multichannel seismic section from line NT 62-8. These data have been fully processed, including depth migration. The locations of Holes 808B and 808C are shown. Holes 808A and 808D lie along strike from Holes 808B and 808C, respectively. Numbers beside the line of the Hole 808C represent estimates of depth in mbsf for that hole.

layered upper, predominantly turbidite, sedimentary sequence and the lower hemipelagic material is clear, but the boundary between the two is not sharp. Indeed, the hemipelagic sequence in the Shikoku Basin is typically divisible into two (or more) units, one comprising an acoustically transparent base and the other, developing higher in the sequence, having a reflective character. From the character of the seismic section, the base of the turbidite-influenced sedimentation could be placed at about 650 mbsf, at the position of the deepest bright reflector.

One of the most interesting reflectors in the section occurs at about 960 mbsf. Because the illustrated section attempts to preserve true amplitudes, it can be seen that this is not a bright reflector, but it is nevertheless distinct. It is continuous landward under the prism and extends further seaward, dying out beyond the protothrust zone. Although no thrusts are clearly imaged splaying from this feature, the reflector is interpreted as marking the décollement surface. The nature of the physical change that generates the acoustic impedance contrast at this zone is obviously of primary interest. Within the depth range 700 to 850 mbsf there are reflectors with a weak, sinuous character. Similar reflectors can be seen within the upper hemipelagic sequence of the Shikoku Basin sediments, and it is not clear whether these reflectors represent primary sedimentation features or are of more complex origin.

The operational plan for Site 808 was designed to satisfy the overall objectives by achieving the following specific aims:

1. Determine the sediment lithology and structures.
2. Investigate the physics of the deformation by measuring rock physical properties throughout the sedimentary column.
3. Investigate the presence and driving mechanism of fluid flow by measuring porosity, pore-pressure, permeability, and fluid chemistry.

These data can then be compared with those from other sites within the prism to show the horizontal gradients of these properties as the deformation process in the prism progresses. In this way the specific structures and properties observed in recovered core can be related to the large-scale features of the prism as revealed by seismic reflection sections. For this approach to be possible, properties must be related on all geologically significant scales, i.e., from lab measurement on individual samples (cm), through borehole logging (m), to the seismic section (tens of m to km). Measurement of core physical properties, downhole measurements, and wireline logging are all essential to achieve the aims above (Figure 7, Chapter 1, this volume). Indeed, downhole measurements have a much higher priority than is usual for an ocean drilling leg, with about 14 days allocated at this site.

Some of the measurements required cannot be obtained with conventional equipment, and this site was the first deployment of a number of new tools, notably the lateral stress tool (LAST), wireline packer (WP), pressure core sampler (PCS) and long-term thermal measurement string (ONDO). The details of these devices are given in the Explanatory Notes chapter, this volume.

From previous drilling legs in the Nankai Trough it was anticipated that hole stability would be a problem, due to the presence of a combination of unconsolidated sands in the upper sedimentary sequence and swelling clays in the lower. In addition to this, the objective of drilling through the active thrust and décollement further increased the chances of hole instability. For this reason a composite site plan was developed using four complementary holes drilled for different purposes (Fig. 3).

The objectives for each hole are as follows:

1. Core to below thrust, log with the wireline log, and make downhole measurements with FMS, WSTP, and LAST.
2. Drill to 550 m, core to below décollement, log with wireline log and make downhole measurements with FMS and WP.
3. Drill to below décollement to provide fresh hole for downhole measurements, Drill-string packer experiments, and FMS.
4. Drill and case to below décollement, core to basement, use log, FMS, and install ONDO. VSP experiment to be conducted in Holes 808C or D as appropriate.

Such a complex program is unusual for ODP sites, but was designed to try to cope with the expected drilling conditions and incorporate necessary flexibility of action.

OPERATIONS

Guam to Site 808

The *JOIDES Resolution* departed Guam at 1930 UTC on 30 March 1990 (0430 hr, 31 March, local). The transit to Site 808 (proposed site NKT-2) covered 1230 nmi in just over 4 days at

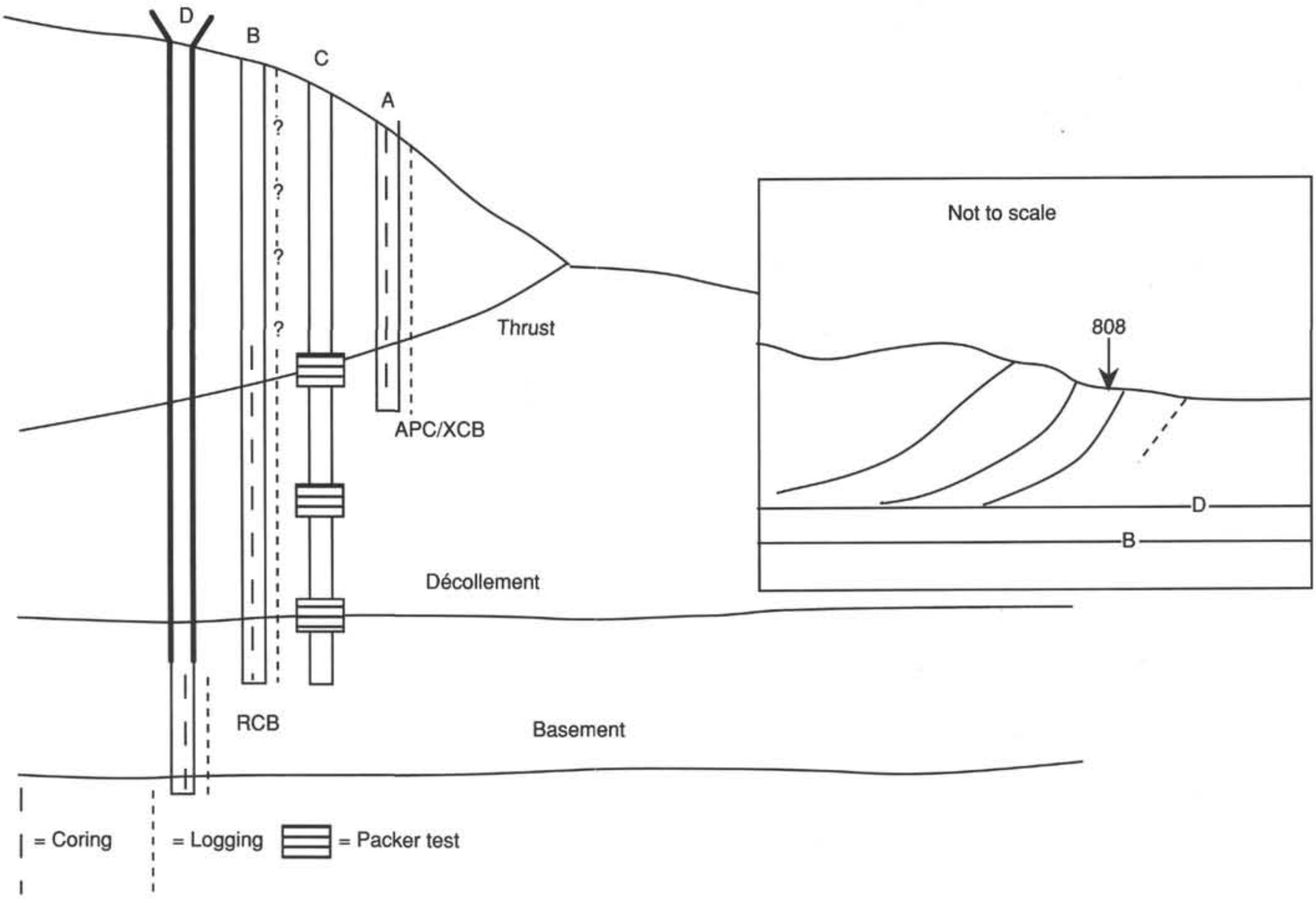

Figure 3. Sketch showing a four-hole strategy for achieving coring and downhole measurement objectives at Site 808. For detailed explanation see text.

an average speed of 12.4 kt. Relatively calm seas and excellent weather prevailed through most of the transit. About 16 nmi southeast of the proposed drill site, speed was reduced and the pre-site survey began. Ship speed was kept at about 7 kt to compensate for winds up to 30 kt and a strong Kuroshio Current coming from varying directions. The seismic survey used two 3.3-L (200-in.^{3}) water guns and the standard eel, with 3.5- and 12-kHz echosounders operating. Owing to the sea conditions and the need for the ship to travel 7 kt to maintain steerage way, the seismic data were very noisy. The survey proceeded northwestward to about 5 nmi past the site, at which point the ship then turned to a reciprocal course and recrossed the site, at times allowing 50° set for the effect of current and sea.

Site 808

The site location was identified from comparison of the 3.5-kHz profile record with the reference seismic reflection profile, and an acoustic positioning beacon was dropped on the second crossing at 0240 hr, 4 April 1990, at 32°21.111'N and 134°56.671'E (Fig. 4). GPS satellite positioning was available during the site survey. *JOIDES Resolution* continued about 2 nmi southeastward before retrieving the seismic gear and returning to the beacon to take station.

The original operations plan for Site 808 is summarized in Background and Objectives, this chapter (Fig. 3). It was recognized that poor drilling conditions could significantly alter this plan.

Hole 808A

The ship was positioned about 14 m northwest of the beacon, and Hole 808A was spudded in at 2145 hr, 4 April 1990, at 32°21.116'N and 134°56.666'E in 4687 m (precision depth recorder, PDR) of water. In Core 131-808A-1H we recovered 6.27 m of sediment (Table 1) and the mudline was estimated by drill-pipe measurement (DPM) to be 4686.7 m below rig floor (mbrf). Cores 131-808A-1H through -13H were taken from 0.0–111.4 mbsf with 111.4 m of sediment cored and 88.68 m recovered (79.6% recovery; see Table 1). Core orientation surveys were taken on Cores 131-808A-2H through -6H. The cored sediments throughout this hole were highly expanded due to considerable gas. After Core 131-808A-11H, at 96.9 mbsf, the WSTP tool was run for temperature and water sampling, but encountered 1.5 m of fill in the bottom of the hole. The tool retrieval mechanism failed during the sampling cycle, making it necessary to retrieve the WSTP with a wireline run. Core 131-808A-12H was attempted at the same depth as the WSTP run, but had no recovery. The hole collapsed after Core 131-808A-13H. The coring line and APC were removed, but attempts to free the drill string were unsuccessful. The bottom hole assembly (BHA) was severed with a back-off charge at the bottom of the top (7-1/4-in.) drill collar at 0545 hr, 6 April 1990. The drill string cleared the rig floor at 1445, 6 April 1990, ending Hole 808A.

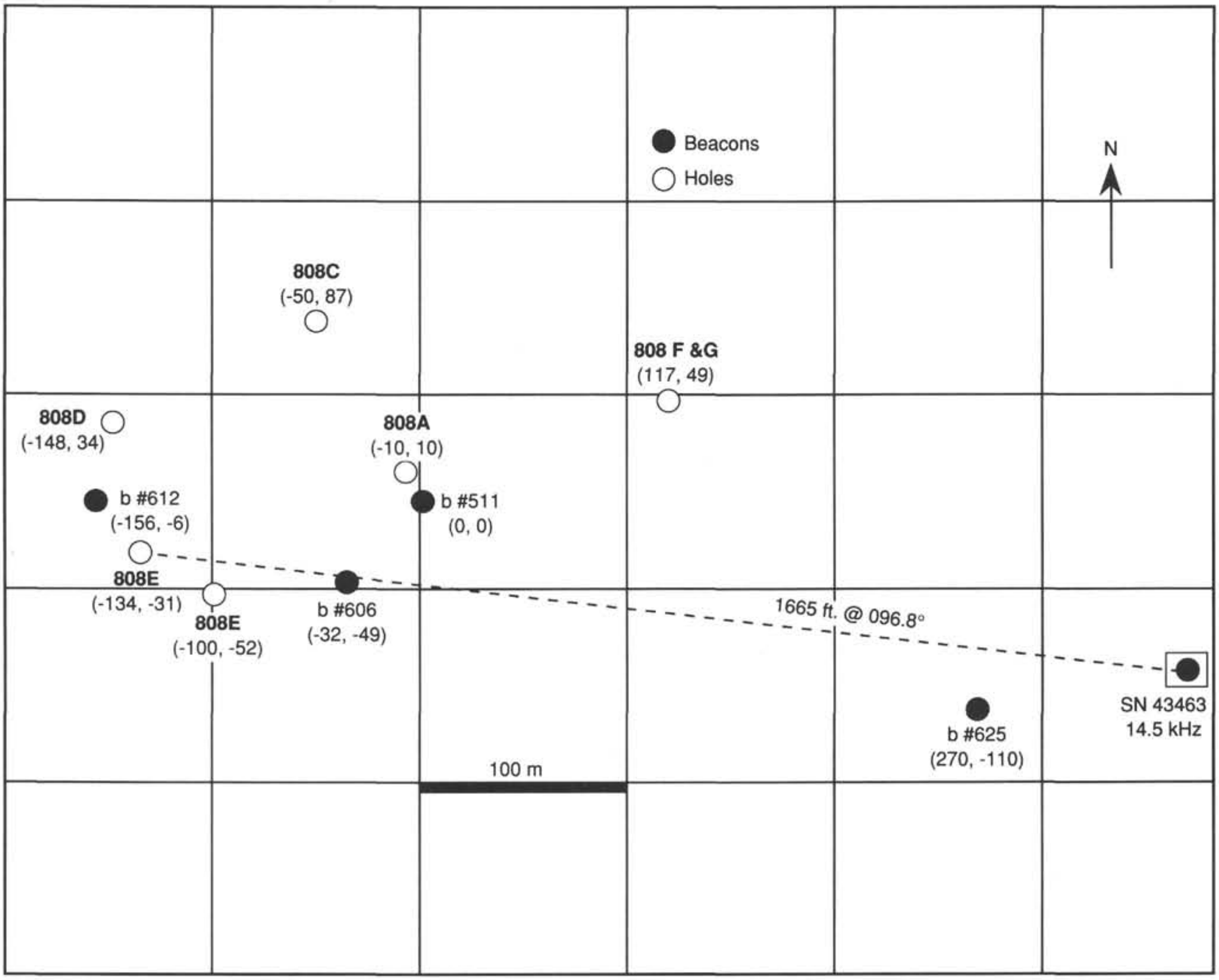

	Positions of Holes				Method	Water depth	Depth mbsf
Hole 808A	32°	21.116′N	134°	56.666′E	Mean GPS	4676.0	111.4
Hole 808B	32°	21.085′N	134°	56.613′E	Mean GPS	4674.2	358.8
Hole 808C	32°	21.170′N	134°	56.657′E	Mean GPS	4674.6	1327.0
Hole 808D	32°	21.143′N	134°	56.578′E	Mean GPS	4672.7	780.0
Hole 808E	32°	21.108′N	134°	56.610′E	Mean GPS	4672.9	1200.0
Hole 808F	32°	21.146′N	134°	56.762′E	Mean GPS	4684.3	140.0
Hole 808G	32°	21.146′N	134°	56.762′E	Mean GPS	4684.3	213.0

Beacon b # 511 lies at 32° 21.111′N, 134° 56.671′E

(Showing location of beacon SN 43463, dropped to aid re-entry on Leg 132)

Figure 4. Location, water depth, and total depth of holes at Site 808.

Hole 808B

The ship was offset about 100 m southwest of the beacon, where the precision depth recorder estimated depth was 4685.0 m. Because of a planned re-entry cone at this site, a jet-in test was conducted to determine the conductor casing point. The bit could be jetted only to 24 mbsf without rotation. After the jet-in test, the bit was pulled clear of the seafloor and offset 10 m farther southwestward. Hole 808B was spudded at 0400 hr, 7 April 1990, at 32°21.085'N and 134°56.613'E, at a depth of 4685 mbrf (DPM), and was drilled without coring to the total depth of Hole 808A at 111 mbsf. Continuous XCB coring began while weather conditions deteriorated. After Core 131-808B-7X was taken (178.5 mbsf), the combination of strong winds and strong current from different directions caused the ship to take positioning excursions up to 185 m. The current was too strong to permit turning the ship into the wind. It was decided to plug the hole with mud, pull clear of

Table 1. Summary of coring operations at Site 808.

Core no.	Date (1990)	Time (local)	Depth (mbsf)	Cored (m)	Recovered (m)	Percent Recovery
131-808A-						
1H	April 4	2225	0.0–6.3	6.3	6.27	99.5
2H	5	0000	6.3–15.8	9.5	10.64	112.0
3H	5	0110	15.8–25.3	9.5	9.07	95.5
4H	5	0250	25.3–34.8	9.5	10.18	107.1
5H	5	0410	34.8–44.3	9.5	7.52	79.1
6H	5	0530	44.3–53.8	9.5	6.39	67.2
7H	5	0645	53.8–63.3	9.5	8.27	87.0
8H	5	0800	63.3–68.3	5.0	1.91	38.2
9H	5	0930	68.3–77.8	9.5	10.09	106.2
10H	5	1030	77.8–87.4	9.6	10.18	106.0
11H	5	1145	87.4–96.9	9.5	3.19	33.6
12H	5	1720	96.9–106.4	9.5	0.00	0.0
13H	5	1820	106.4–111.4	5.0	4.97	99.4
	Coring Totals			111.4	88.68	79.6
131-808B-						
1X	7	1135	111.0–120.6	9.6	0.00	0.0
2X	7	1315	120.6–130.3	9.7	1.11	11.4
3X	7	1510	130.3–139.9	9.6	0.00	0.0
4X	7	1700	139.9–149.5	9.6	1.31	13.6
5X	7	1920	149.5–159.1	9.6	1.96	20.4
6X	7	2155	159.1–168.8	9.7	0.00	0.0
7X	8	0045	168.8–178.5	9.7	5.19	53.5
8X	8	0450	178.5–188.2	9.7	0.91	9.4
9X	8	0650	188.2–197.4	9.2	5.53	60.1
10X	8	1030	197.4–206.8	9.4	6.31	67.1
11X	8	1240	206.8–216.3	9.5	3.57	37.6
12X	8	1625	216.3–225.8	9.5	0.42	4.4
13X	8	1830	225.8–235.1	9.3	2.80	30.1
14X	8	2245	235.1–244.5	9.4	1.04	11.0
15X	9	0140	244.5–254.2	9.7	0.75	7.7
16X	9	0530	254.2–263.4	9.2	1.71	18.6
17X	9	0945	263.4–273.0	9.6	6.02	62.7
18X	9	1205	273.0–282.5	9.5	0.00	0.0
19X	9	1430	282.5–287.9	5.4	3.81	70.5
20X	9	1630	287.9–297.5	9.6	2.33	24.3
21X	9	2020	297.5–307.1	9.6	0.48	5.0
22X	9	2230	307.1–316.8	9.7	1.98	20.4
23X	10	0120	316.8–326.4	9.6	0.87	9.1
24X	10	0400	326.4–336.0	9.6	4.65	48.4
25X	10	0630	336.0–340.6	4.6	6.27	136.0
26X	10	0915	340.6–345.6	5.0	0.14	2.8
27X	10	1315	345.6–355.2	9.6	0.22	2.3
28X	10	1620	355.2–358.8	3.6	0.33	9.2
	Coring Totals			247.8	59.71	24.1
131-808C-						
1R	17	0900	298.5–308.0	9.5	2.34	24.6
2R	17	1145	308.0–317.6	9.6	0.89	9.3
3R	17	1330	317.6–327.2	9.6	1.25	13.0
4R	17	1525	327.2–336.9	9.7	2.29	23.6
5R	17	1715	336.9–346.6	9.7	0.55	5.7
6R	17	1915	346.6–356.2	9.6	4.31	44.9
7R	17	2110	356.2–365.9	9.7	0.65	6.7
8R	17	2310	365.9–375.6	9.7	2.94	30.3
9R	18	0105	375.6–385.2	9.6	1.35	14.0
10R	18	0330	385.2–394.8	9.6	4.21	43.8
11R	18	0525	394.8–404.6	9.8	2.16	22.0
12R	18	0745	404.6–414.3	9.7	4.96	51.1
13R	18	0540	414.3–424.0	9.7	5.20	53.6
14R	18	1130	424.0–433.7	9.7	5.83	60.1
15R	18	1330	433.7–443.0	9.3	6.74	72.5
16R	18	1520	443.0–452.7	9.7	6.86	70.7
17R	18	1730	452.7–462.4	9.7	7.10	73.2
18R	18	1935	462.4–472.0	9.6	7.88	82.1
19R	18	2140	472.0–481.7	9.7	6.61	68.1
20R	18	2350	481.7–491.3	9.6	7.32	76.2
21R	18	0155	491.3–501.0	9.7	7.23	74.5
22R	18	0355	501.0–510.7	9.7	6.88	70.9
23R	18	0550	510.7–520.3	9.6	7.17	74.7
24R	18	0800	520.3–530.0	9.7	6.54	67.4
25R	18	0945	530.0–539.7	9.7	4.16	42.9

Table 1 (continued).

Core no.	Date (1990)	Time (local)	Depth (mbsf)	Cored (m)	Recovered (m)	Percent Recovery
26R	18	1200	539.7–549.3	9.6	7.74	80.6
27R	18	1400	549.3–558.9	9.6	9.46	98.5
28R	18	1605	558.9–568.6	9.7	7.93	81.7
29R	18	1800	568.6–578.3	9.7	9.42	97.1
30R	18	2000	578.3–587.6	9.3	9.23	99.2
31R	18	2250	587.6–597.3	9.7	2.81	28.9
32R	20	0050	597.3–606.9	9.6	8.23	85.7
33R	20	0300	606.9–616.5	9.6	7.37	76.8
34R	20	0450	616.5–626.2	9.7	6.98	71.9
35R	20	0640	626.2–635.9	9.7	8.24	84.9
36R	20	0830	635.9–645.5	9.6	6.91	72.0
37R	20	1000	645.5–654.9	9.4	2.38	25.3
38R	20	1150	654.9–664.5	9.6	9.82	102.0
39R	20	1320	664.5–674.2	9.7	6.72	69.3
40R	20	1615	674.2–683.8	9.6	3.42	35.6
41R	20	1830	683.8–693.5	9.7	2.48	25.5
42R	20	2105	693.5–703.2	9.7	8.46	87.2
43R	20	2310	703.2–712.4	9.2	8.76	95.2
44R	21	0125	712.4–722.0	9.6	9.10	94.8
45R	21	0330	722.0–731.7	9.7	8.05	83.0
46R	21	0530	731.7–741.4	9.7	7.58	78.1
47R	21	0710	741.4–751.1	9.7	9.23	95.1
48R	21	0930	751.1–760.7	9.6	9.80	102.0
49R	21	1145	760.7–770.4	9.7	6.83	70.4
50R	21	1345	770.4–780.1	9.7	9.27	95.5
51R	21	1545	780.1–789.8	9.7	9.73	100.0
52R	21	1745	789.8–799.4	9.6	8.14	84.8
53R	21	1950	799.4–809.1	9.7	8.64	89.1
54R	21	2155	809.1–818.7	9.6	9.52	99.1
55R	22	0000	818.7–828.4	9.7	8.02	82.7
56R	22	0230	828.4–838.1	9.7	7.14	73.6
57R	22	0445	838.1–847.4	9.3	7.08	76.1
58R	22	0645	847.4–857.1	9.7	6.68	68.8
59R	22	0845	857.1–866.8	9.7	7.05	72.7
60R	22	1030	866.8–876.5	9.7	7.72	79.6
61R	22	1220	876.6–886.1	9.6	8.33	86.8
62R	22	1415	886.1–895.8	9.7	7.80	80.4
63R	22	1625	895.8–905.5	9.7	5.79	59.7
64R	22	1845	905.5–915.1	9.6	6.88	71.6
65R	22	2050	915.1–924.8	9.7	2.86	29.5
66R	22	2300	924.8–934.5	9.7	6.30	64.9
67R	23	0115	934.5–944.2	9.7	1.96	20.2
68R	23	0415	944.2–953.8	9.6	2.03	21.1
69R	23	0635	953.8–963.4	9.6	6.86	71.4
70R	23	0835	963.4–973.1	9.7	6.57	67.7
71R	23	1055	973.1–982.8	9.7	6.15	63.4
72R	23	1300	982.8–992.1	9.3	6.41	70.0
73R	23	1510	992.1–1001.8	9.7	8.97	92.5
74R	23	1715	1001.8–1011.3	9.5	3.22	33.9
75R	23	1920	1011.3–1020.5	9.2	2.83	30.7
76R	23	2110	1020.5–1029.9	9.4	8.20	87.2
77R	23	2305	1029.9–1039.1	9.2	7.83	85.1
78R	24	0100	1039.1–1048.3	9.2	7.78	84.5
79R	24	0300	1048.3–1057.8	9.5	6.88	72.4
80R	24	0500	1057.8–1067.1	9.3	5.11	54.9
81R	24	0705	1067.1–1076.5	9.4	2.43	25.8
82R	24	0920	1076.5–1085.8	9.3	2.81	30.2
83R	25	1150	1085.8–1092.0	6.2	3.79	61.1
84R	25	1350	1092.0–1098.3	6.3	3.96	62.8
85R	25	1610	1098.3–1108.0	9.7	4.44	45.8
86R	25	1915	1108.0–1117.6	9.6	3.55	37.0
87R	25	2125	1117.6–1126.9	9.3	2.20	23.6
88R	25	2350	1126.9–1136.6	9.7	1.95	20.1
89R	25	0225	1136.6–1146.3	9.7	2.68	27.6
90R	26	0440	1146.3–1155.9	9.6	2.83	29.5
91R	26	0650	1155.9–1165.6	9.7	3.17	32.7
92R	26	0910	1165.6–1175.3	9.7	2.03	20.9
93R	26	1130	1175.3–1184.9	9.6	1.55	16.1
94R	26	1415	1184.9–1194.6	9.7	2.37	24.4
95R	26	1650	1194.6–1204.3	9.7	1.65	17.0
96R	26	1925	1204.3–1214.0	9.7	1.92	19.8
97R	26	2150	1214.0–1223.7	9.7	1.72	17.7
98R	27	0015	1223.7–1233.4	9.7	0.97	10.0
99R	27	0300	1233.4–1243.0	9.6	1.06	11.0
100R	27	0545	1243.0–1252.2	9.2	2.43	26.4
101R	27	0830	1252.2–1261.5	9.3	6.51	70.0
102R	27	1100	1261.5–1270.9	9.4	4.70	50.0

Table 1 (continued).

Core no.	Date (1990)	Time (local)	Depth (mbsf)	Cored (m)	Recovered (m)	Percent Recovery
103R	27	1515	1270.9–1280.4	9.5	4.72	49.7
104R	27	2100	1280.4–1289.9	9.5	3.01	31.7
105R	28	0000	1289.9–1299.1	9.2	1.19	12.9
106R	28	0340	1299.1–1308.3	9.2	2.40	26.1
107R	28	0700	1308.3–1317.5	1.18	12.8	
108R	28	1205	1317.5–1327.0	9.5	0.99	10.4
	Coring Totals			1028.5	572.43	55.7
131-808F-						
1M	27	1700	50.0–55.0	5.0	0.00	0.0
2P	27	2035	55.0–56.0	1.0	0.00	0.0
3M	28	0230	85.0–90.0	5.0	0.00	0.0
4W	28	0830	90.0–140.0	50.0	2.37	(wash core)
	Coring Totals			11.0	0.00	0.0
	Washing Totals			50.0	2.37	
	Combined Totals			61.0	2.37	
131-808G-						
1W	May 28	1420	85.0–120.0	35.0	1.50	(wash core)
2X	28	1545	120.0–129.6	9.6	0.00	0.0
3X	28	1715	129.6–139.2	9.6	0.00	0.0
4X	28	1855	139.2–148.9	9.7	0.00	0.0
5X	28	2235	148.9–158.6	9.7	0.00	0.0
6P	29	0515	185.0–186.0	1.0	0.49	49.0
7M	29	0845	186.0–191.0	5.0	0.84	16.8
8X	29	1435	193.0–203.0	10.0	9.97	99.7
9M	29	1850	203.0–208.0	5.0	0.00	0.0
10X	29	2100	208.0–212.0	4.0	0.00	0.0
11M	29	2255	212.0–213.0	1.0	0.00	0.0
12M	30	0100	213.0–213.0	0.0	0.00	0.0
	Coring Totals			64.6	11.30	17.5
	Washing Totals			35.0	1.50	
	Combined Totals			99.6	12.80	

the hole, and respud in after the weather improved. After the hole had been filled and before the drill string had been tripped out, the weather improved and it was decided to recommence coring. Coring continued to 358.8 mbsf (Core 131-808B-28X), with WSTP measurements taken following Cores 131-808B-9X, -11X, -13X, -15X, -17X, -20X, -26X, and -28X. Five successful temperature measurements were made, down to depths of 345.6 mbsf. Coring operations were terminated because the rate of penetration (ROP) slowed to less than 5 m/hr, and because of consistently low core recovery (24.1% recovery overall; see Table 1). The operating plan was changed to include an RCB penetration as deep as possible after the logging of Hole 808B.

In preparation for logging, the hole was flushed with 30 bbl of high viscosity mud. A final WSTP measurement was attempted at the total depth (TD) of the hole, but was unsuccessful due to excessive hole fill. A wiper trip to 65 mbsf and back to TD was made to condition the hole, with high drag (up to 35,000 lb) noted at several levels within the hole. A second mud sweep was followed by displacement water and enough lime-enhanced viscous mud to fill the hole. The bit was pulled to 102 mbsf for logging.

The first run for the seismic stratigraphy string was cut short when the threaded bullnose of the LDGO temperature logging tool unscrewed and an electrical problem occurred. The second run could not pass an obstruction in the hole at 181 mbsf; therefore the hole was logged from 181 to 80 mbsf. A second wiper trip was successfully made without rotation to test the feasibility of using the side entry subassembly (SES) to aid the logging. The SES was installed with the bit at 102 mbsf. Two attempts at running the lithoporosity string were short-circuited because current-induced vibrations of the drill string caused loosening of a tool connection. On the third attempt, after the tool was lowered out of the pipe at the bottom of the hole, the drill string was accidentally lowered down over the tool due to a combination of ship heave (during high winds and strong current) and to clear rigging problems with a circulating hose and support cable for the SES logging sheave. The lithoporosity tool was jammed into the bit and broken, causing a loss of power to the tool and slackening of the logging cable. The cable and drill string were raised together until the SES reentered the moonpool. The logging cable was crimped and cut downhole to free the cable and hold the tool in the pipe. Before raising the pipe out of the hole, a free-fall funnel (FFF) was dropped to the seafloor in case the tool became freed and remained in the hole. The BHA was brought up, and the tool was not in the bit. A fishing attempt for the tool in the hole was unsuccessful, and was further hampered by rough weather conditions and problems with a stripped outer strand of the VIT-camera cable. The hole was filled with barite-weighted mud and cemented in the upper part. The drill string reached the rig floor at 1000 hr, 15 April 1990, ending Hole 808B.

Hole 808C

Hole 808C was spudded at 1530 hr, 16 April 1990, about 90 m northwest of Hole 808A, at 32°21.170'N and 134°56.657'E, and at a depth of 4685.5 mbrf (DPM). An 86-m string of

11-3/4-in. casing was drilled into place from 19–105 mbsf using the drill-in casing system (DIC), the first successful deployment of this system. Drilling then proceeded with the RCB bit and an inner core barrel in place, to 298.5 mbsf. Continuous RCB coring then began. A fault zone was penetrated on the very first core and initiated a sequence of hole-cleaning problems. Several faults, including a major thrust zone, were cored in the next 100 m as indicated by fractured and sheared core and reduced core recovery. Hole fill of 4–9 m on connections persisted, despite repeated mud pills and extra circulation, to about 480 mbsf. Good recovery and relative hole stability then were encountered through a siltstone/claystone section to the décollement at about 960 mbsf.

The associated fracture zones of the décollement extended over a 30–40 m interval. The fractured and sheared sediments caused reduced recovery and some hole instability. Below the décollement, hole conditions again stabilized. Core recovery was reduced somewhat by vertical fractures in the claystone that caused the core to jam in the liner and/or catcher. The success in reaching and penetrating the décollement prompted the decision to extend the hole through the lower pelagic sediment section and into basement. Coring continued nonstop to a TD of 1327 mbsf in basement at 1205 hr, 28 April. Overall recovery in Hole 808C was 55.7%. The pipe became stuck several times, requiring greater than 100,000 lb overpull to free it. Most of the problems occurred at the several fault zones, including the décollement, that were identified in the coring. Excessive torque while coring indicated possible swelling in the lowermost portion of the hole.

The hole was then prepared for logging operations with mud sweeps and two wiper trips. The bit was released and the hole was displaced with logging mud. The pipe was then pulled to 747 mbsf for logging. The seismic stratigraphy string was run in the hole until it encountered a bridge at 756 mbsf. While we attempted to spud the bridge with the logging tools, we lost communication with the tools and they had to be retrieved. With the logging tools out of the hole, the pipe was lowered back to TD (1312 mbsf) in an attempt to clear the bridges. The pipe was then raised to 891 mbsf (just above the décollement) for the next logging attempt. The lithoporosity string would not come out of the pipe so the hole was logged through the pipe from 891 mbsf to the mudline. The geochemical string would come only 3 m out of the pipe so the hole was once again logged up to the mudline through the drill pipe. Owing to the instability of the entire borehole, it was not prudent to deploy the SES. The logging equipment was rigged down and the hole was filled with heavy mud from 891 mbsf to the mudline. The drill string was pulled from the hole, and the BHA reached the rig floor at 2045 hr, 1 May 1990.

Hole 808D

Hole 808D was planned as a re-entry hole for the ONDO tool. The hole was spudded at 1530 hr, 2 May 1990 (31°21.143'N, 134°56.578'E, 4684 mbrf), when jetting-in of the 16-in. casing and re-entry cone assembly began. The jet-in procedure went smoothly and the re-entry cone mud skirt was landed on the sea floor in 1 1/2 hrs. The drill string was released from the running tool and the hole was drilled ahead to 780 mbsf.

Hole-conditioning procedures required 36 hr due to swelling clays and a troublesome fracture zone at approximately 400 mbsf. Drilling operations had to be suspended for 12 hr during the hole cleaning process due to weather. Strong north winds gusting to 58 kt coupled with the ever-present Kuroshio Current from the west caused the ship to roll a maximum of 12 degrees. Although hole conditions were not ideal for running casing, further hole conditioning would not have improved them. Therefore, the hole was displaced with casing mud and a round trip was made for the 11 3/4-in. casing string.

The ship was moved up current 25 nmi and allowed to drift back while we deployed the 11 3/4-in. casing string, to avoid excessive stress on the casing due to the current. The drift of the ship over the 25 nmi was calculated at 1.9 kt. The backward drift of the ship during drilling operations flustered the crew of an oil tanker passing nearby. While lowering the 741-m casing string into the hole, it became apparent that weight of the casing string had been lost. The drill string was lowered to just below the point at which the 11 3/4-in. casing hanger should have landed in the re-entry cone without setting down. The drill pipe was then pulled from the hole for inspection.

Once on deck, only the hex-kelly running tool with VIT guide sleeve, cementing swivel, and cross-over subassembly with 2.45 m of 5-in. drill pipe attached, remained of the casing/cementing assembly. There was no clear evidence of what had caused the failure. Hole 808D officially ended at 0630 hr, 8 May 1990, when the 11 3/4-in. casing running tool was pulled through the drill floor.

Hole 808E

Hole 808E was a retry of Hole 808D. Hole 808E (32°21.108'N and 134°56.610'E, 4684.5 mbrf) was spudded at 1740 hr, 9 May 1990, with jetting-in of a re-entry cone. After jetting-in, the hole was drilled ahead to 554 mbsf. The hole was conditioned to receive the 11 3/4-in. casing string. Then the drill pipe was retrieved.

While rigging up the casing running equipment, the ship was moved 18 nmi. up current and allowed to drift back to location as 521 m of 11 3/4-in. casing and cementing stringer were made up and deployed. Hole 808E was re-entered at 1930 hr, 11 May. The casing was lowered into the hole, latched into the re-entry cone, cemented in place, and then the drill pipe was retrieved.

Hole 808E was re-entered at 1230 hr, 13 May with an RCB BHA. The cementing shoe was drilled out and the hole was drilled to a TD of 1200 mbsf. After several wiper trips, the bit was released, the hole was displaced with weighted KCL mud, and the BHA was pulled to 35.7 mbsf for logging operations. The first logging suite consisted of the seismic stratigraphy string. The hole was logged from the mudline down to 576 mbsf where an impenetrable bridge was encountered. The hole was then logged back to the mudline and the logging tools retrieved. The drill pipe was lowered to 850 mbsf to clear any existing bridges. The seismic stratigraphy string was redeployed, encountering a bridge at 621 mbsf. The open hole was logged and the logging tools retrieved. The drill pipe was lowered to 850 mbsf and then retrieved.

Hole 808E was re-entered at 1047 hr, 19 May, for vertical seismic profile (VSP) and TAM drill string packer experiments. The well seismic tool (WST) was deployed and VSP data gathered from 600 mbsf to the mudline. The WST was retrieved and the packer was positioned at 511 mbsf. The first attempt to inflate the packer resulted in a partial set. The packer was deflated and the go-devil retrieved. The go-devil and Kuster recorders were redressed and redeployed on wireline. Again a partial set of the packer was indicated. With allotted packer experiment time expiring, flow tests were carried out in the hope that the downhole recorders would gather some useful information. The packer was deflated and with the go-devil left in place for inspection, the drill pipe was retrieved. The Kuster recorders were lost in the hole.

Hole 808E was re-entered at 0930 hr, 22 May for deployment of the ONDO thermistor array. The array was deployed twice, both times stopping at 3830 mbrf. The array was recovered and a core barrel deployed without encountering any obstructions in the drill pipe. The array was redeployed two more times, stopping inside the BHA at 4660 mbrf. The array was retrieved and a modified set of landing pads installed. The array was redeployed again, stopping inside the BHA at 4660 mbrf. With expiration of deployment time, the array was pulled from the hole. The ONDO array was successfully deployed at the beginning of Leg 132 (see ONDO section, this chapter, and the Operations chapter, Leg 132). The drill pipe was retrieved and Hole 808E officially ended at 0055 hr, 26 May, with the bit back on deck.

Hole 808F

A standard APC/XCB BHA was made up for the next hole, which was to be dedicated to special tool measurements. Hole 808F (32°21.146'N and 134°56.762' E; 4684.3 mbrf DPM) was spudded at 1320 hr, 27 May, 1990, and then washed to 50 mbsf. The LAST tool was deployed at 50 and 85 mbsf with incomplete data gathered, due to power and software problems. The WSTP temperature probe was deployed at 55 and 90 mbsf, with a good temperature reading only from the second run. The pressure core sampler (PCS) was unsuccessfully deployed at 55 mbsf owing to its being sanded up. A broken XCB cutting shoe lost in the bottom of the hole stopped the drilling. The BHA was pulled from the hole and the bit cleared the seafloor at 0825 hr, 28 May, 1990, officially ending Hole 808F.

Hole 808G

Hole 808G was spudded immediately after we pulled out of Hole 808F at 0825 hr, 28 May, and was washed to 120 mbsf. The XCB was deployed at 120.0, 129.6, 139.2, 148.9, 193.0, and 208.0 mbsf. Core 131-808G-8X at 193.0–203.0 mbsf recovered 9.97 m of sandy and silty clay. The other cores did not recover any sediment. The WSTP temperature probe was deployed at 148.9 and 192.0 mbsf, and the WSTP pressure probe was deployed at 192.0 mbsf. In all cases, the tools flooded with water. The PCS was deployed at 185.0 mbsf, recovering 0.49 m of pressurized core. While it was in cold storage, the PCS pressure chamber lost most of its trapped pressure. Once the pressure chamber had reached *in-situ* temperature the core was removed and immediately immersed in liquid nitrogen. The LAST was deployed at 186.0, 203.0, 212.0, and 213.0 mbsf, with only the first run recovering 0.84 m of core, and *in-situ* stress and pore-pressure data collected from the first, third, and fourth runs. The 'GS' overshot prematurely sheared twice causing minor delays in the down-hole measurements.

With the allotted leg time expiring, the hole had to be abandoned. While the drill pipe was being retrieved, another beacon was dropped for easier location of Hole 808E by the Leg 132 crew for their attempt to deploy the ONDO tool. The bit was back on deck at 1110 hr, 30 May, officially ending Hole 808G and Site 808.

Owing to the long duration of Site 808, five beacons were dropped, at 0240 hr, 4 April; 2230 hr, 11 April; 2230 hr, 1 May; 0000 hr, 9 May, and 1000 hr, 30 May 1990.

Site 808 to Pusan

The voyage to Pusan covered 520 nm in 57 hr at an average speed of 9.1 kt. The *JOIDES Resolution* arrived outside Pusan at 2030 hr, 1 June. The leg officially ended with the dropping of the anchor at 2100 UTC, 1 June (0600, 2 June, local).

SEDIMENTOLOGY

The principal objectives of this section are to: (1) document the main lithostratigraphic units at Site 808 (Holes A, B, and C); (2) interpret the depositional processes and overall plate-tectonic environment of deposition; (3) present the initial shipboard analyses of the sediment composition from carbonate measurements, smear slides, thin sections, and bulk-powder X-ray diffraction studies, together with preliminary interpretations of sediment provenance and diagenesis. For the purposes of clarity, this section is divided into two parts: in the first part we discuss the lithostratigraphy, sedimentary processes, and environments of deposition, and in the second part we discuss the petrology, provenance, and diagenesis of the sediments.

Lithostratigraphy

Lithostratigraphic Units

The lithologies recovered in Holes 808A, 808B, and 808C comprise six discrete lithologic units, two of which contain subunits (Table 2; Fig. 5). The units/subunits were differentiated on the basis of visual core descriptions, grain size, bed/layer thickness, and mineralogy. The following lithologic units define the stratigraphy from top to bottom of Site 808:

1. Unit I: Lower-slope apron (0–20.55 mbsf);
2. Unit II: Trench-fill deposits (20.55–556.80 mbsf), further subdivided as:
   Subunit IIa: Upper axial-trench sandy deposits (20.55–120.60 mbsf);
   Subunit IIb: Lower axial-trench silty deposits (120.60–264.90 mbsf in Hole 808B; 365.90–409.54 mbsf in Hole 808C);
   Subunit IIc: Outer marginal trench silty deposits (264.90–355.50 mbsf in Hole 808B; 298.50–365.90 mbsf and 409.54–556.80 mbsf in Hole 808C);
3. Unit III: Trench to basin transitional deposits (556.80–618.47 mbsf);
4. Unit IV: Shikoku Basin deposits (618.47–1243.00 mbsf), further subdivided as:
   Subunit IVa: Upper Shikoku Basin deposits (618.47–823.74 mbsf);
   Subunit IVb: Lower Shikoku Basin deposits (823.74–1243.00 mbsf);
5. Unit V: Acidic volcaniclastic deposits (1243.00–1289.90 mbsf);
6. Unit VI: Basaltic basement (1289.90–1327.00 mbsf).

Stratigraphic analysis shows that a distinct matrix-supported mudstone-pebble conglomerate is duplicated across the frontal thrust; the base of this important marker bed occurs at 264.90 mbsf (Section 131-808B-17X-1, 150 cm) and 409.54 mbsf (Section 131-808C-12R-4, 37 cm), giving a vertical offset of 144.64 m. The similar repetition of a distinct, yellowish carbonate (altered nannofossil ooze) below the conglomerate at 289.70 mbsf (Section 131-808B-20X-2, 30 cm) and at 437.33 mbsf (Section 131-808C-15R-3, 63 cm), gives a vertical offset of 147.63 m. Based on these occurrences, a value of 145 m of stratigraphic duplication is used in this section as an approximation of the vertical displacement along the frontal thrust.

In Hole 808B, the frontal thrust zone appears to occur in Core 131-808B-25X (336.0–340.6 mbsf), whereas in Hole 808C, sited landward of Hole 808B, the thrust zone encompasses Cores 131-808C-8R to -10R (365.9–394.8 mbsf). The most highly fractured lithologies, showing a scaly fabric, occur in Interval 131-808C-8R-1, 20–60 cm (366.1–366.5 mbsf). Based on the geometry of overturned beds within Core 131-808C-8R, and vertical to subvertical bedding in the lower part of Core 131-808C-8R and throughout Core 131-808C-9R, the zone of maximum displacement of the frontal thrust appears to be at approximately 366 mbsf (see Structural

Table 2. Summary table of lithologic units in Holes 808A, 808B, and 808C. Clayey silt and silty clay (or the lithified equivalents) are referred to as muds.

Unit, subunit		Depth (mbsf)		Age (Ma)	Lithologies	Sedimentation accumulation rate m/m.y.	Characteristic processes	Plate environment
I		0–20		<0.09	Thin sand, silt, mud	902	Downslope Sediment slides, Hemipelagic sed. Turbidity currents	Lower forearc slope-apron
II	IIa	20–557	20–121	0.09–0.28	Sand, mud	787		Axial trench channels
	IIb		121–265*	0.09–0.46	thin sand, silt, mud	787	Turbidity currents	& interchannel
	IIc		410–557**	0.28–0.46	silt and mud	1381	Hemipelagic settling	Outer marginal trench
III		557–618		0.28–0.46	Silt, mud, ash/tuff	1381	Turbidity currents, settling of ashes Hemipelagic sed.	Trench-basin transition, incl. outer trench high
IV	IVa	618–1243	618–824	0.46–<2.65	Mud/ash/tuff	107	Hemipelagic sed.,	Shikoku Basin near trench
	IVb		824–1243	<2.65–13.6	Mud, disseminated ash	46	settling of ashes	Shikoku Basin away from trench
V		1243–1290		13.6–?15	Mud, acidic volcaniclastic deposits	approx. 33	Acidic volcanism	?Honshu Arc volcanism associated with ridge subduction
VI		1290–1327		13.6–?15	Basalt, minor mud	??	Formation of oceanic crust	Opening of Shikoku Basin

*depths valid for Hole 808B only
**depths valid for Hole 808C only

Geology section, this chapter). The inorganic geochemistry, moreover, shows clearly defined anomalies in elements such as Ca, Mg, and Li at about the same level (see Inorganic Geochemistry section, this chapter). Here a depth of about 366 mbsf is taken as the position of the frontal thrust in Hole 808C. Thus, the frontal thrust repeats about 145 m of stratigraphy at Site 808, from approximately 365 to 220 mbsf (Fig. 5).

The abundances of the turbidites and ashes/tuffs were used as the main criteria to help define the lithostratigraphic units at Site 808. Figures 6 and 7 show the thickness vs. depth (meters below seafloor) for all the discrete sand or silt (turbidite) beds/layers, and the ashes, tuffs, and pure volcanic sandstone layers, respectively. These diagrams must be viewed within the context of core-recovery percentages (e.g., Fig. 49).

Figure 8 shows the variation in bulk mean grain size with depth (mbsf) for representative, disaggregated, clayey silts and silty clays in Holes 808A and 808B. The bulk mean grain size of the muds (=clayey silts/silty clays) appears to be less in the upper 40 m of the succession. The reasons for this are somewhat unclear, but it may suggest a fining-upward trend in the uppermost 40 m from axial-trench channel to slope apron, recording a reduction in energy level of the turbidity currents. This change in sedimentation may correspond with the Holocene rise in sea level. It is also noteworthy that the bulk mean grain size shows that the finer grained, background, sediments are mainly silts *sensu stricto*, and that there are very few clay-sized particles in the succession. It seems likely, however, that the Lasentec particle size analyzer employed during shipboard analyses underestimates the amount of clay-sized fragments (see Explanatory Notes, this chapter).

Unit I (0–20.55 mbsf)

Sections 131-808A-1H-1, 0 cm, through 131-808A-3H-4, 35 cm; age, Pleistocene (Zone NN21).

Unit I extends from the seafloor to the top of the first thick sand bed. Unit I consists of interlayered clayey silt and fine-grained sand; homogeneous, bioturbated, clayey silt; sandy clayey silt (Fig. 9); and very thin ash layers. Gas expansion has affected much of this unit (Fig. 9). Bioturbation and trace amounts of redeposited shell material are common in the finer grained lithologies. The very thin to medium-bedded, normally graded, fine-grained sands have sharp bases and show typical Bouma T_{abde} sequences. An authigenic carbonate crystal aggregate or concretion occurs in Section 131-808A-2H-1, 131 cm.

The lower part of Unit I is characterized by layers of deformed sediments in discrete intervals up to at least 4.5 m thick. Layers of wet-sediment deformation are particularly well developed in Intervals 131-808A-2H-5, 38 cm, through 131-808A-2H-CC, 62 cm (12.68–16.80 mbsf), and 131-808C-3H-1, 0 cm, through 131-808C-3H-3, 150 cm (16.80–20.20 mbsf). It is possible that both of these intervals represent the upper and lower parts of a single- slide mass of deformed sediments, that is from 12.68–20.20 mbsf (Fig. 10). The deformed sediments show small-scale open to isoclinal folds, attenuated beds, and sheared beds, many of which are overturned (Figs. 11 and 12).

The stratigraphic and bathymetric position of Unit I, the fine bulk mean grain size, and the occurrence of deformed unlithified, un-drained, and semi-lithified sediments, suggest that this unit represents the lower-slope apron, with large-scale downslope sliding of semiconsolidated sediments. The sands may represent uplifted (accreted) trench deposits, originally derived from axially-flowing turbidity currents. Alternatively, the sands may have accumulated directly on the lower slope as thicker axial flows lapped onto the landward wall of the trench. A sediment plume measuring only 150 m in thickness would reach the bathymetric position of Site 808. IZANAGI sidescan sonar images of the seafloor in the vicinity of Site 808 support the interpretation of mass wasting; the occurrences of large lobate and irregular, hummocky, masses represent relatively recent sediment slides and debris flow deposits (Fig. 6, Geological Background and Objectives chapter).

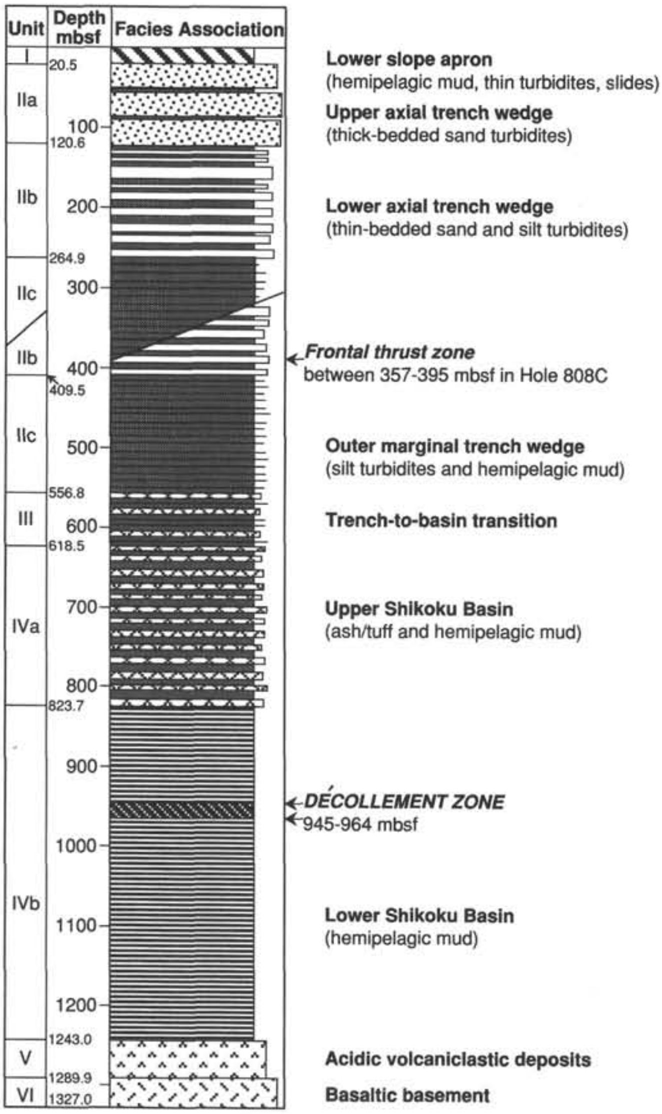

Figure 5. Schematic composite lithostratigraphy from Holes 808A, 808B, and 808C, with interpreted depositional environments.

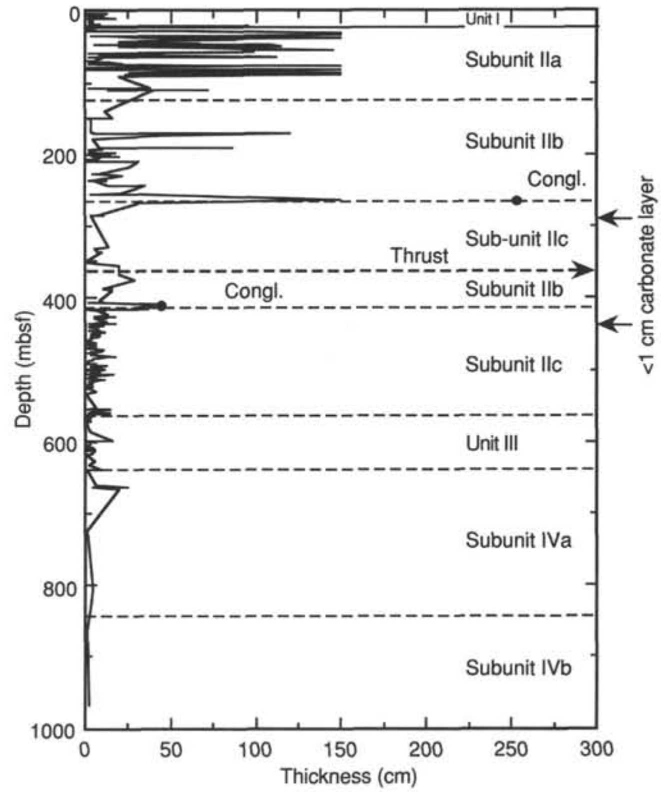

Figure 6. Graph of turbidite thickness (cm) vs. depth (mbsf) for all recovered gravel-, sand-, and silt-graded beds or layers. The lithostratigraphic unit boundaries are shown. The matrix-supported mudstone-pebble conglomerates in Sections 131-808B-17X-1 (top = 264.11 mbsf) and 131-808C-12R-4 (top = 409.10 mbsf) are probably the same deposit, as are the two yellowish <1-cm-thick carbonate layers in Sections 131-808-20X-2, 30 cm (289.70 mbsf), and 131-808C-15R-3, 63 cm (437.33 mbsf). These deposits suggest a vertical offset of the stratigraphy across the frontal thrust of 145 m and 147.63 m, respectively. Allowing for a dip on the thrust of 30° and Holes 808B and 808C being 100 m apart downslope, the original environments of deposition would have been approximately 350 m apart.

Unit II (20.55–556.8 mbsf)

Sections 131-808A-3H-4, 35 cm, through 131-808C-27R-5, 150 cm; age, Pleistocene (Zones NN20-21).

Subunit IIa (20.55–120.60 mbsf)

Sections 131-808A-3H-4, 35 cm through 131-808B-2X-1, 0 cm; age, Pleistocene (Zone NN21).

Subunit IIa begins at the top of the first thick sand and extends to the inferred base of the last thick/medium-bedded sand and top of a finer grained unit. The subunit is characterized by silty to very coarse-grained sands in beds/units showing considerable variation in bed thickness (very thin to very thick-bedded) and internal structure (normally graded to structureless). The beds have sharp, smooth to loaded bases and show typical Bouma T_{abe} and rare T_{cde} sequences (Fig. 13).

The thicker bedded, coarser grained sands that appear structureless show diffuse, irregular, subvertical concentrations of fine silt to clay, caused by coring-induced fluidization and elutriation of the fines (Fig. 14). A few well-preserved examples, however, show erosional scours at the base with concentrations of granule pebbles, graded bedding from coarse to fine sand, and plant debris, commonly concentrated towards the top. Disseminated plant material is common in some intervals. These silts and sands are interbedded with bioturbated (mottled) clayey silts. A few very thin ash layers also occur (<1 cm thick). Intervals of deformed sediments, interpreted as sediment slide deposits (perhaps associated with levee failure), occur in Intervals 131-808A-9H-3, 48–68 cm (Fig. 15), and 131-808A-10H-1, 75–114 cm.

The sand-rich nature of Subunit IIa, together with its seismostratigraphic position, suggests that it represents axial-trench sandy channel and nonchannel (overbank and sheet) deposits. Thin-section point-counting of sands from Subunit IIa supports the axial-flow interpretation, with a provenance from the Izu Collision Zone (see summary below, and sedimentary petrology section, this chapter).

Subunit IIb

Sections 131-808B-2X-1, 0 cm through 131-808B-17X-1, 150 cm (120.6–264.90 mbsf); Sections 131-808C-8R-1, 0 cm through 131-808C-12R-4, 44 cm (365.90–409.54 mbsf); age, Pleistocene (Zones NN20–NN21). The interval in Hole 808B

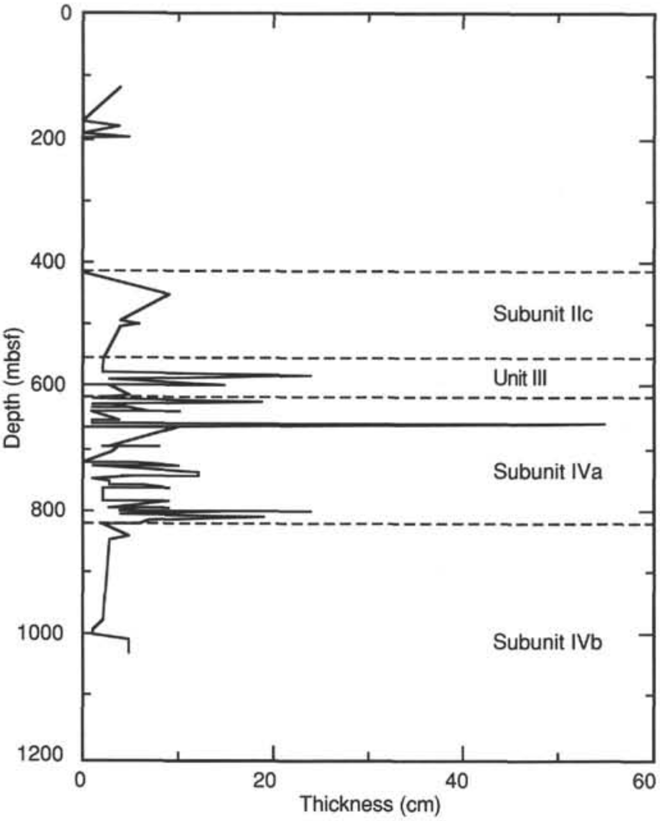

Figure 7. Layer thickness (cm) of discrete ash/tuff and pure volcanic sandstone vs. depth (mbsf) for Holes 808A, 808B, and 808C. The lithostratigraphic unit boundaries are also shown, but only for the units in which preserved ashes/tuffs are important. Subunit IVa is clearly picked out on this graph, between 556.8–823.74 mbsf as an ash/tuff-rich unit.

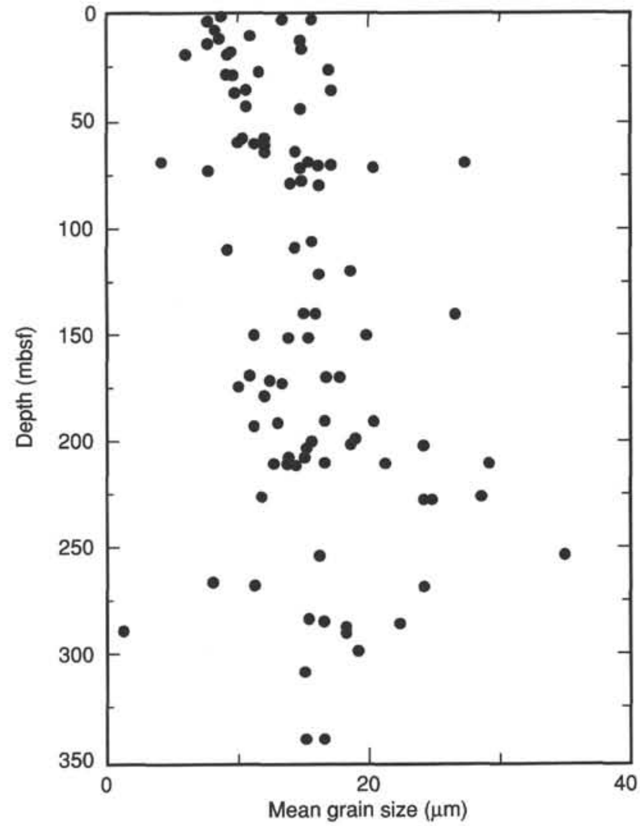

Figure 8. Graph of bulk mean grain size for representative samples of disaggregated clayey siltstone/silty claystone at Site 131-808, measured on the shipboard grain-size analyzer. The data show that the background sedimentation throughout Hole 808A and the unlithified part of Hole 808B comprises essentially silts rather than clays, although this result is probably in error due to limitations of the analyzer.

from about 220–264.9 mbsf is duplicated below the frontal thrust in Hole 808C from about 365–409.5 mbsf.

Subunit IIb has a finer overall bulk mean grain size and thinner mean bed thickness compared with the overlying Subunit IIa. Subunit IIb is defined from the base of the last major sand to the base of a unique matrix-supported mudstone-pebble conglomerate. There is a gradational contact between Subunits IIa and IIb, and we stress here that recovery rates within Subunit IIb were rather poor.

Subunit IIb comprises very thin to thin-bedded, very fine-grained sandstones, the mudstone-pebble conglomerate used as a marker bed, very thin to thin-bedded siltstones, and mud (= clayey siltstone/silty claystone). Ashes constitute a minor lithology (Fig. 7). The sandstones (Fig. 16) and siltstones (Fig. 17) show sharp and smooth to loaded bases, normal grading, and partial Bouma T_{bcde} sequences. The ratio of sandstone + siltstone to mud is estimated at 1:9 to 1:4.

At the base of Subunit IIb, there is a matrix-supported mudstone-pebble conglomerate, at least 40–50 cm thick, but possibly up to the order of 3 m thick, that is unique to the entire lithostratigraphy at Holes 808A, 808B, and 808C. As mentioned previously, the conglomerate provides an important correlative deposit that is duplicated across the frontal thrust. The large mudstone clasts are well rounded to subrounded, Pleistocene in age, and up to more than 9 cm in maximum dimension, i.e., greater than the core width (Fig. 18). The largest mudstone clasts in Section 131-808C-12R-4 show incipient brecciation by fracturing and the invasion of matrix along the dislocations (Fig. 19). The matrix comprises about 40% silt/clay, 40% medium to very fine sand, and 20% coarse sand to granules, including pumice grains. Granule-grade, well-rounded, quartz grains and woody plant material are common; the organic fragments constitute up to 5% of the matrix and reach 2 mm in length (Figs. 19 and 20).

The stratigraphic position of Subunit IIb, the relatively fine bulk mean grain size, and thin beds, compared to the overlying Subunit IIa, suggest that it represents axial-trench deposits, probably deposited in the outer part of the trench floor. The basal conglomerate may be a debris-flow deposit (debrite), within or outside of the axial channel. This inferred debrite appears to correspond to the position of a prominent seismic reflector, above which reflectors onlap to the seaward side of the trench (Backpocket Fig. 2, Chapter 2, this volume).

Subunit IIc

Sections 131-808B-17X-2, 0 cm, through 131-808B-28X-CC, 30 cm; depth 264.90–355.50 mbsf;

Sections 131-808C-1R-1, 0 cm, through 131-808C-8R-1, 0 cm; depth 298.50–365.90 mbsf;

Sections 131-808C-13R-1, 0 cm, through 131-808C-27R-5, 150 cm; depth, 409.54–556.80 mbsf; age, Pleistocene (Zone NN20). The interval from 409.54 to about 511 mbsf in Hole 808C

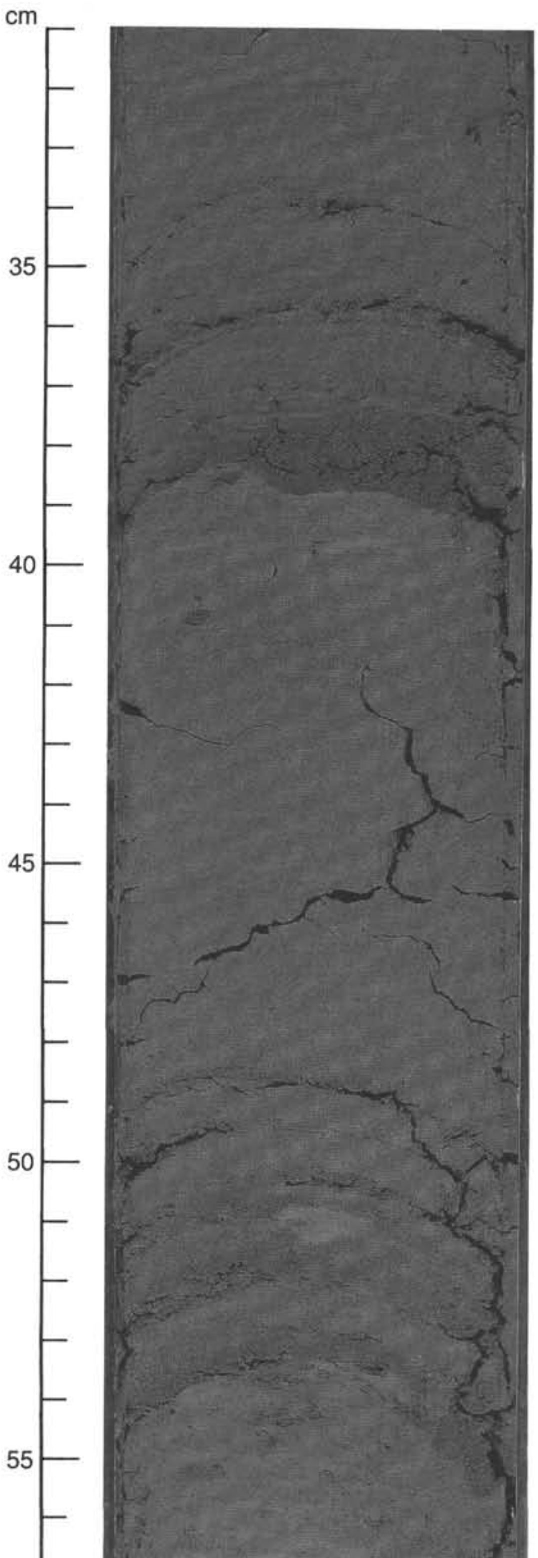

Figure 9. Core photograph showing representative sediments in Unit I, showing interlayered clayey silt, fine-grained sand, homogeneous, bioturbated clayey silt, and sandy clayey silt, interval 131-808A-1H, 31–57 cm. Gas expansion caused the fracturing of the core during recovery.

is stratigraphically equivalent to the interval from 264.90–365.90 mbsf above the frontal thrust in Holes 808B and 808C.

Subunit IIc is defined from immediately below the matrix-supported, mudstone-pebble conglomerate, to the first occurrence of a thick tuff in Hole 808C. Subunit IIc contrasts with the overlying Subunit IIb in containing little sand. There are very few ash/tuff layers relative to the underlying Unit III (Fig. 7). The major lithology is mottled (thoroughly bioturbated) clayey siltstone and silty claystone, with interbeds of normally graded, very thin to medium-bedded, very fine-grained sandstone and coarse siltstone showing Bouma T_{cde} sequences.

The very fine-grained sandstone and coarse siltstone beds (Fig. 21A) are a particularly distinctive feature of Subunit IIb (and Unit III below). Bouma T_c, ripple-laminated divisions appear common within Subunit IIc (Fig. 21B). The medium-bedded siltstone turbidites typically display a complex vertical architecture. The beds are essentially bipartite, with a lower thoroughly laminated part, overlain by a diffusely-laminated to apparently structureless clayey siltstone cap up to decimeters in thickness. Bioturbation, if present within these beds, is generally weak to moderate and commonly as *Chondrites*. In contrast, the surrounding clayey siltstone/silty claystone lithology appears thoroughly bioturbated.

The thoroughly laminated siltstones show no obvious overall vertical grading. They tend to show repeated current-ripple divisions, rarely as climbing-ripple lamination (Fig. 21B); the rippled zones are separated by divisions of parallel lamination. The current ripples invariably show stoss-side erosion and only lee-side preservation. Convolute laminae and over-steepened lee faces to ripples occur in some beds. Grain-size breaks are represented by clayey siltstone divisions up to 1 cm thick, but generally on a millimeter scale. Very low-angle to wavy lamination is common within some of these beds (Fig. 22). The bases of beds appear sharp and planar, and the bases are overlain either by parallel lamination (Fig. 21A) or current ripples (Fig. 21B). The lowest layer of current ripples, if present, may be slightly coarser grained than the overlying thoroughly laminated part of the bed. The avalanche faces of the ripples dip in various directions, even within a single turbidite bed.

Unusual aspects of the turbidites include the vertical repetition of current-ripple lamination between parallel lamination, the occurrence of distinct grain-size breaks, the lack of well-developed normal grading throughout the beds (within what is interpreted as a genetically-linked depositional event), the variation in observed flow directions, and the weakly bioturbated clayey siltstone caps. Collectively, these features suggest deposition from unsteady flows that may have been reflected and/or deflected from the inner and outer trench slopes. The turbidity currents may have originated somewhere on the inner trench slope (accretionary prism); alternatively, they may have traveled as axial currents along the Nankai Trough from the Izu Collision Zone, as suggested for the majority of the sand turbidites of Subunit IIa (Taira and Niitsuma, 1986). Whatever the angle of upslope flow on the seaward trench slope (i.e., orthogonal to oblique), the reflected flows then were directed down-gradient perpendicular to isobaths.

A large variety of ichnogenera, including abundant *Chondrites* (Fig. 23), occur within the clayey siltstone/silty claystone lithology. The proportion of silty turbidites to the clayey siltstone/silty claystone lithologies is estimated at 30%–40%.

The stratigraphic position of Subunit IIc, between deposits interpreted as trench-fill (Subunits IIa and IIb) and trench-to-

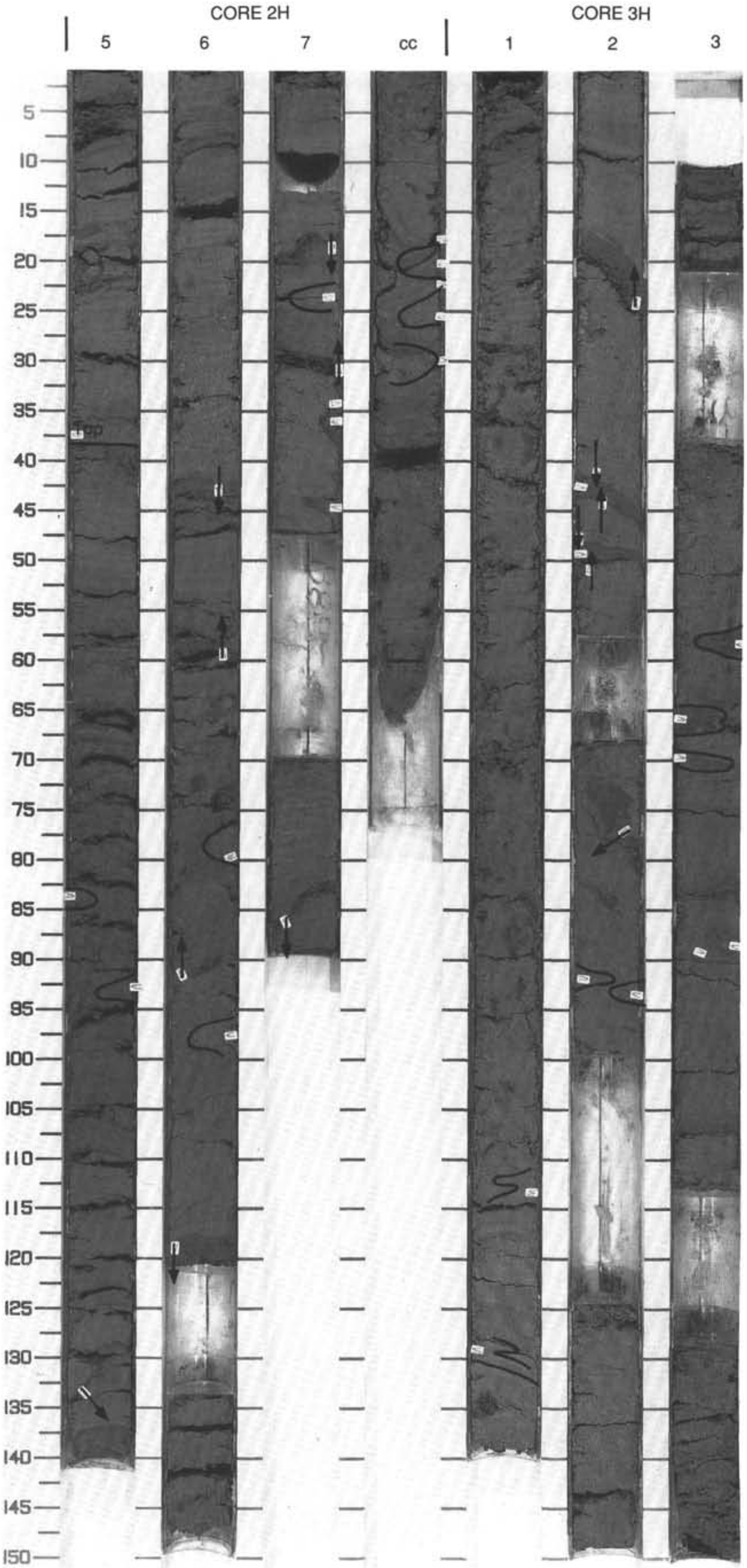

Figure 10. Core photographs showing sediment slide deposit in interval 131-808A-2H-5, 38 cm, through 131-808A-3H-3, 150 cm (12.68–20.20 mbsf), with line-drawing interpretation of fold closures and facing directions of bedding. Arrows point toward stratigraphic tops.

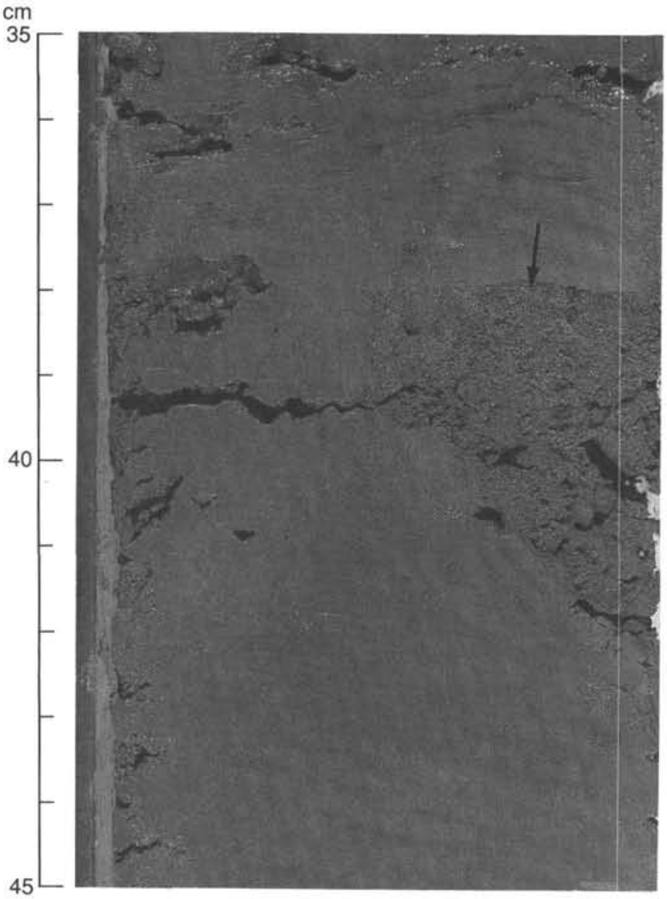

Figure 11. Core photograph showing detail of top of a sediment slide deposit in Figure 10. The top is a sharp surface (arrowed) that truncates the underlying folded very fine-grained sands, silts and clayey silts. Interval 131-808A-2H-5, 35–45 cm.

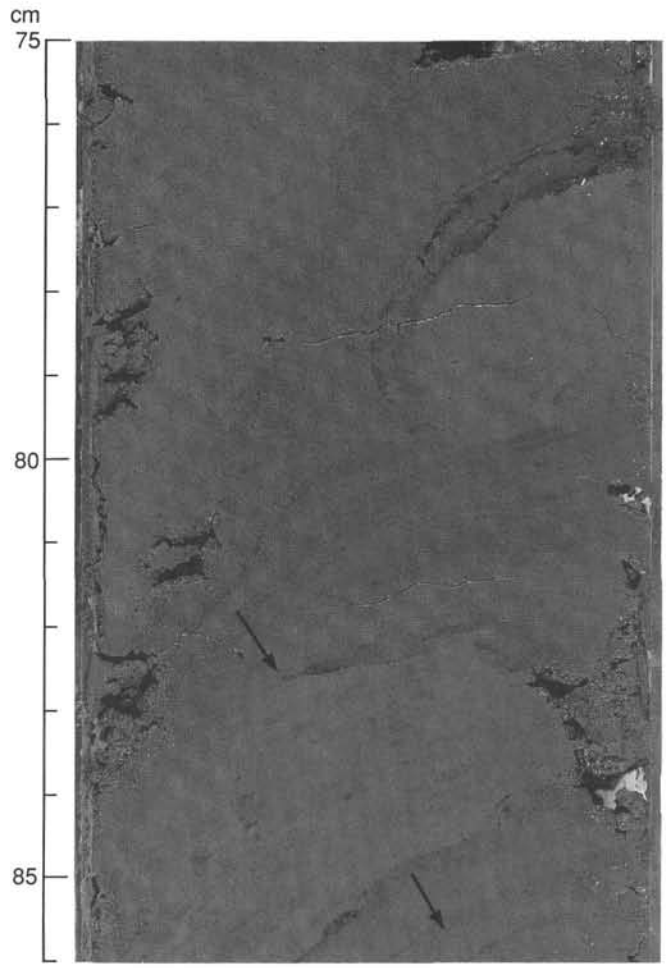

Figure 12. Core photograph showing folded and truncated bedding within sediment slide deposit; interval 131-808A-2H-6, 75–86 cm. The lower graded beds/laminae are inverted as seen by the sharp basal surfaces overlain by normally graded, laminated layers (arrowed).

basin transitional deposits (Unit III), is consistent with deposition in an outer, marginal, trench environment.

Unit III (556.80–618.47 mbsf)

Sections 131-808C-27R-6, 0 cm, through 131-808C-34R-2, 47 cm; age, Pleistocene (Zone NN20).

Unit III is defined from the first occurrence of a thick tuff unit to the last ripple-laminated siltstone turbidite in Hole 808C. Essentially, Unit III contains elements of both the overlying Subunit IIc and the underlying Subunit IVa.

Unit III is dominated by thoroughly bioturbated (mottled) clayey siltstone/silty claystone (Fig. 24), with ash/tuff layers up to 25 cm thick. Very thin/thin-bedded, normally-graded, Bouma T_{cde} and T_{de} siltstone turbidites also occur sporadically within the unit.

The stratigraphic position of Unit III, between trench-fill deposits and the predominantly hemipelagic Shikoku Basin deposits, suggests that this unit represents trench-to-basin transitional deposits, perhaps including sediments that were deposited on the outer trench high.

Unit IV (618.47–1243.0 mbsf)

Sections 131-808C-34R-2, 47 cm, through 131-808C-99R-CC; age, middle Miocene-Pleistocene (Zones NN20–NN5).

Subunit IVa (618.47–823.74 mbsf)

Sections 131-808C-34R-2, 47 cm, through 131-808C-55R-4, 54 cm; age, Pliocene-Pleistocene (Zones NN20–NN18).

Subunit IVa is defined from the base of the last very thin-bedded Bouma T_{cde} turbidite, through an ash/tuff-rich interval, to the last occurrence of abundant ash/tuff layers (Fig. 7). The overlying Subunit IIc and underlying Subunit VIa are relatively free of discrete volcanic layers. Thus, the characteristic feature of Subunit IVa is the abundance of preserved, very thin to thin layers of tuff and vitric sandstone (Figs. 25 and 26), intercalated within a thoroughly bioturbated (mottled) mud succession rich in foraminifer tests (Fig. 27). Volcaniclastic beds reach thicknesses up to 20–50 cm (Fig. 7). Subunit IVa contains thoroughly bioturbated mudstone intervals with abundant zeolites (see Sedimentary Petrology, this chapter) which are an indication of the amount of disseminated ash.

The ash/tuff layers occur either as widely separated and thin layers, commonly showing moderate bioturbation, or in closely-spaced layers (Fig. 25), suggesting punctuated phases of multiple volcanic eruptions. The tuffs tend to have sharp, smooth bases, but in some cases load structures are preserved

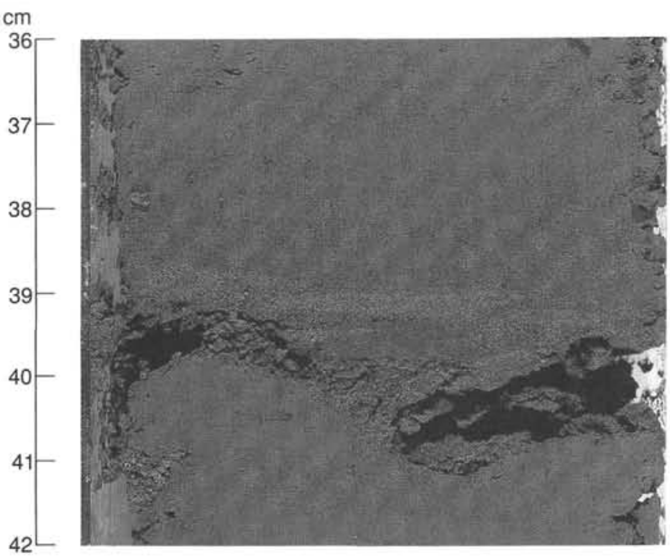

Figure 13. Core photograph showing normally graded, thin-bedded T_{cd} turbidite, showing an erosional base overlain by fine/very fine-grained current ripples (flow sense to left), capped by parallel-laminated silt/clayey silt; interval 131-808A-4H-2, 36–42 cm.

(Fig. 25). The coarser tuffs generally show normal, or rarely inverse, grading. A diffuse low-angle or parallel lamination is present in some tuffs (Fig. 25), suggesting that at least some of these layers were probably deposited from turbidity currents, rather than vertical grain-by-grain settling through the water column. Some tuff layers also show convolute laminae and dish-like structures, suggesting liquefaction and fluidization during, or shortly after, deposition.

In Interval 131-808C-39R-1, 48–53 cm, there is a small-scale synsedimentary normal fault, truncated by a graded tuff layer (Fig. 26). Interval 131-808C-54-4, 18–28 cm, contains an enigmatic clastic dike of very coarse-grained volcanic-terrigenous sandstone (Fig. 28). There were no likely donor beds recovered in nearby layers, either above or below this dike. Furthermore, the anomalously coarse grain size and polymictic composition of this sediment, compared to the other volcanic lithologies in this unit is difficult to explain (see comparison with DSDP Site 297 below).

The seismostratigraphic position of Subunit IVa, together with the absence of terrigenous sandy or silty turbidites, suggests that Subunit IVa represents the upper Shikoku Basin deposits, dominated by hemipelagic sedimentation and the accumulation of volcanic layers. Sediment accumulation rates show a substantial decrease from Unit III into Subunit IVa (see Sediment Accumulation Rates section, this chapter); this decrease is consistent with a change in depositional environment from the trench area where turbidity currents were relatively important in contributing sediment, to an open ocean basinal setting dominated by hemipelagic and, possibly, pelagic sedimentation.

Subunit IVb (823.74–1243.0 mbsf)

Sections 131-808C-55R-4, 54 cm, through 131-808C-99R-CC; age, middle Miocene-Pliocene (Zones NN5–NN18).

The top of Subunit IVb corresponds to the disappearance of the abundant, intact, ash/tuff layers, and the base corresponds to the appearance of predominantly acidic volcaniclastic deposits. Subunit IVb comprises an essentially monotonous succession of thoroughly bioturbated clayey siltstones and silty claystones (Fig. 29) with traces of disseminated volcanic glass. The intense bioturbation, including common well-developed *Zoophycos* ichnogenera, has destroyed any primary depositional layering to give a mottled appearance to the lithologies. There are local concentrations of foraminifers and pyrite in pockets of bioturbated sediment. Siliceous worm

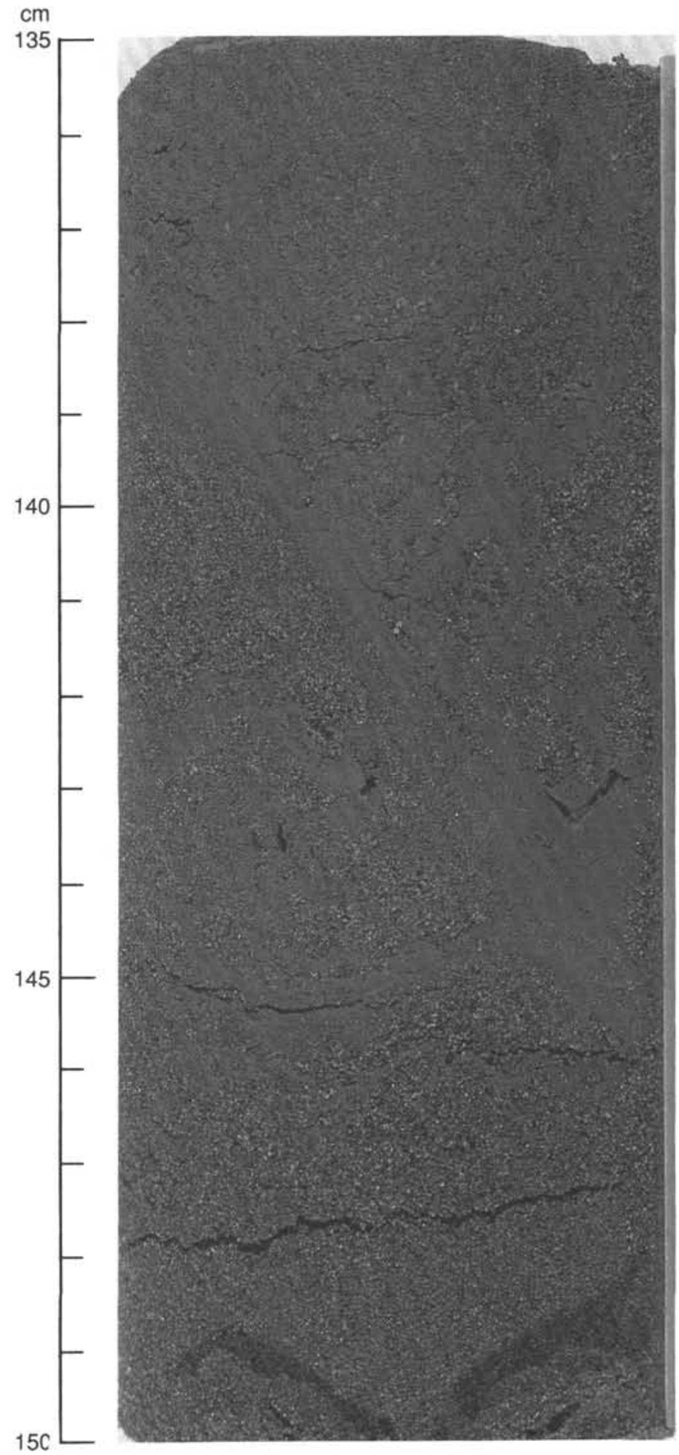

Figure 14. Core photograph showing coarse-grained structureless sand, interval 131-808A-5H-6, 135–150 cm. Coring-induced fluidization and elutriation of the fines has destroyed any primary sedimentary structures.

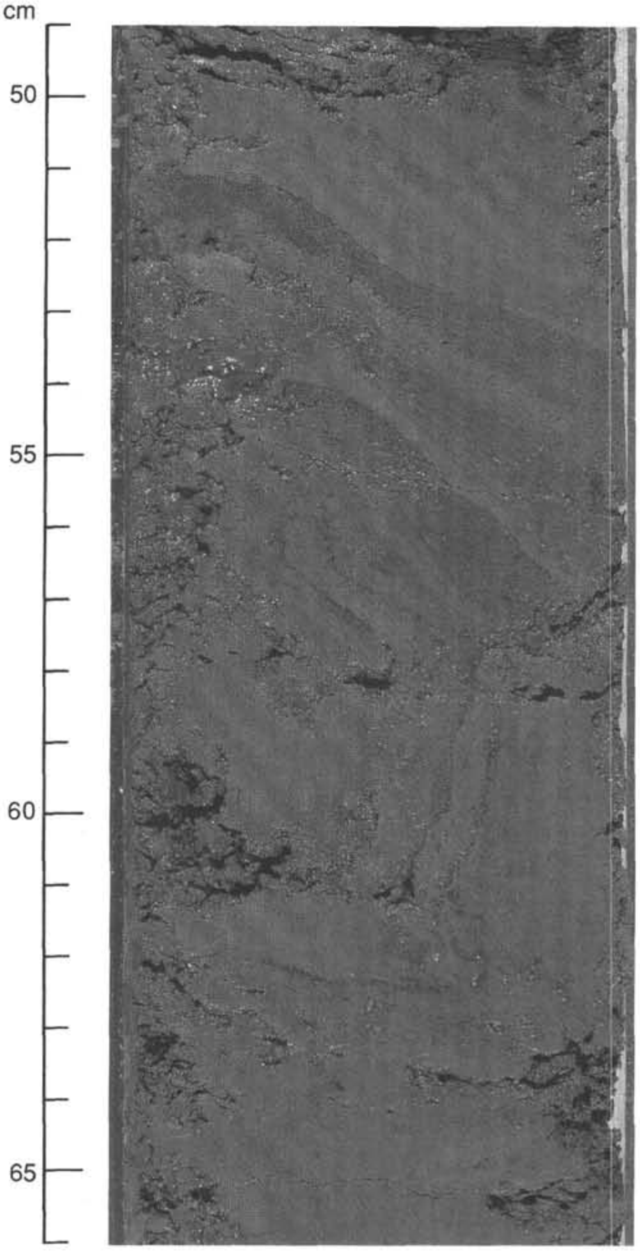

Figure 15. Core photograph showing part of sediment slide showing folded bedding; interval 131-808A-9H-3, 49–66 cm.

tubes occur disseminated throughout the unit. In contrast to Subunit IVa, Subunit IVb contains virtually no preserved ash/tuff layers (Fig. 7).

The seismostratigraphic position of Subunit IVb, between upper Shikoku Basin deposits and the acidic volcaniclastic unit that rests on basaltic basement, suggests that Subunit IVb represents hemipelagites of the lower Shikoku Basin.

Unit V (1243.0–1289.9 mbsf)

Sections 131-808C-100R-1, 0 cm, through 131-808C-104R-CC; age, middle Miocene (Zone NN5).

Unit V is defined by the development of an acidic volcaniclastic unit lying directly upon basaltic basement. The principal lithology in Unit V is varicolored tuff. The tuffs include: (1)

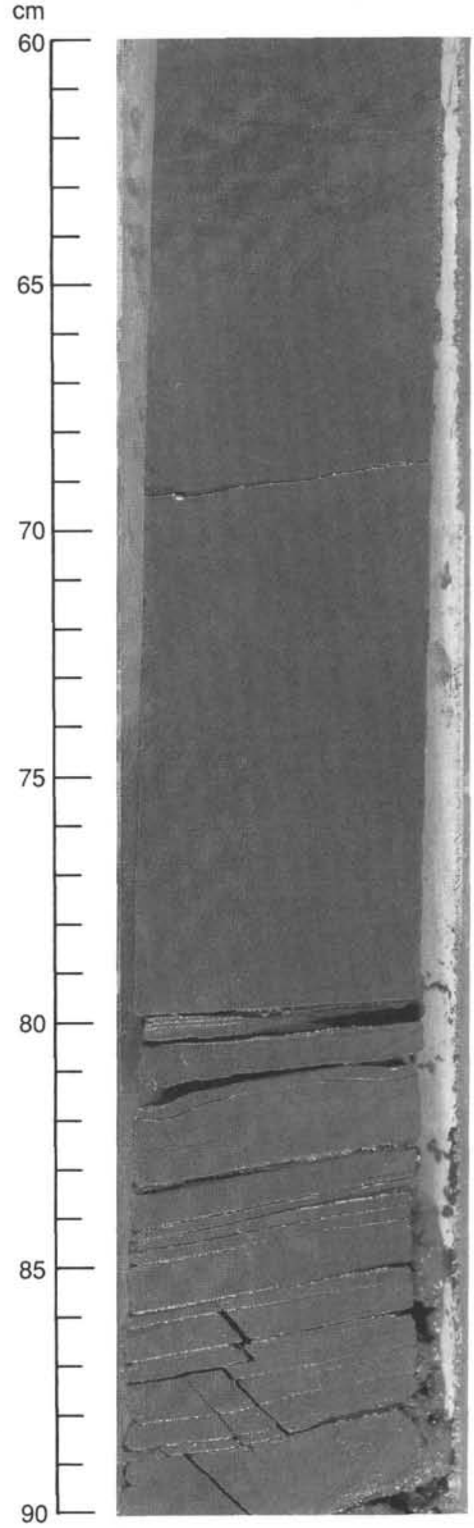

Figure 16. Core photograph showing normally graded, parallel-laminated, very fine-grained turbidite overlain by structureless clayey siltstone with mottled (bioturbated) upper part; interval 131-808C-4R-1, 60–90 cm. Note the well-developed shear bands in the structureless clayey siltstone.

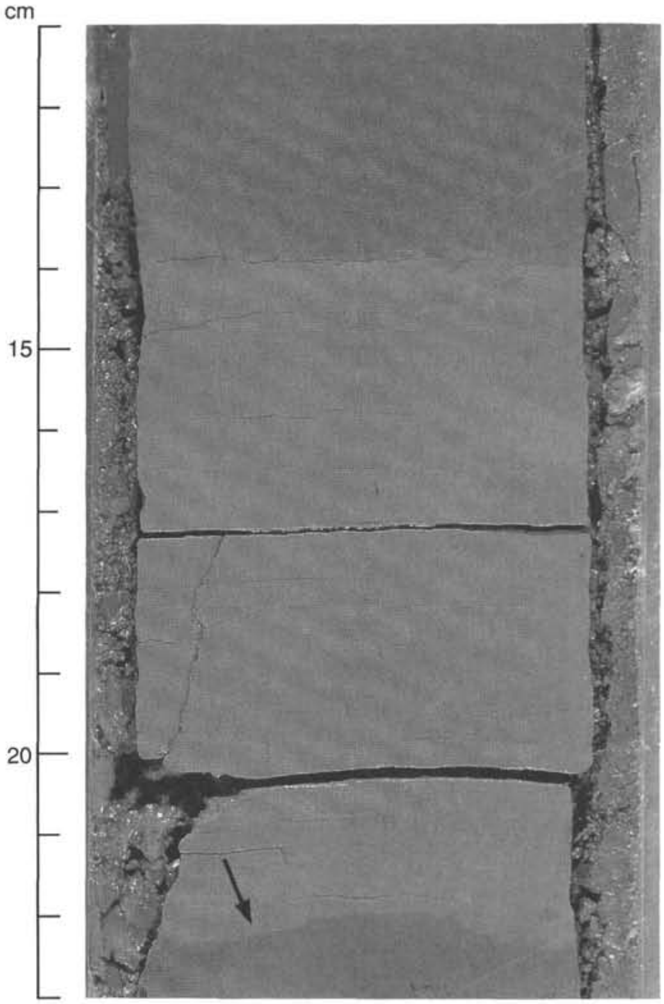

Figure 17. Core photograph showing normally graded, parallel-laminated siltstone turbidite with irregular, loaded base (arrow); interval 131-808C-1R-2, 11–23 cm. Note the clayey siltstone (11–14 cm) is mottled due to intense bioturbation.

a very thick, white-gray, acidic tuff; (2) gray-greenish gray altered tuff; (3) varicolored tuffaceous mudstone (containing foraminifers and calcareous nannofossils); and (4) thin, dark, olive-gray mudstones. The thickness of the tuffs changes from very thin and graded, to very thick-bedded and structureless. Dewatering structures occur below some tuffs, as anastomosing, submillimeter, dark veins (Fig. 30).

The stratigraphic position of Unit V, together with its acidic composition, suggest that it represents an extra-basinal volcanic episode, with volcanic centers situated in an unspecified part of the Honshu Arc (mainland Japan). The terrigenous-free nature of some of the tuffs suggests emplacement directly through the water column from air-fall rather than by turbidity currents or some other type of sediment gravity flow. The tuffs that contain terrigenous material may have been deposited from subaerial pyroclastic surges that were transformed into subaqueous turbidity currents. Whatever their origin, the acidic tuffs do not represent epiclastic deposits. Contemporaneous volcanic activity is known from various parts of the Honshu Arc, for example the approximately 14-Ma volcanic rocks in Kyushu and the Kumano/Ohmine acidic volcanic units of Kii Peninsula (Chijiwa, 1988, Nishi, 1988).

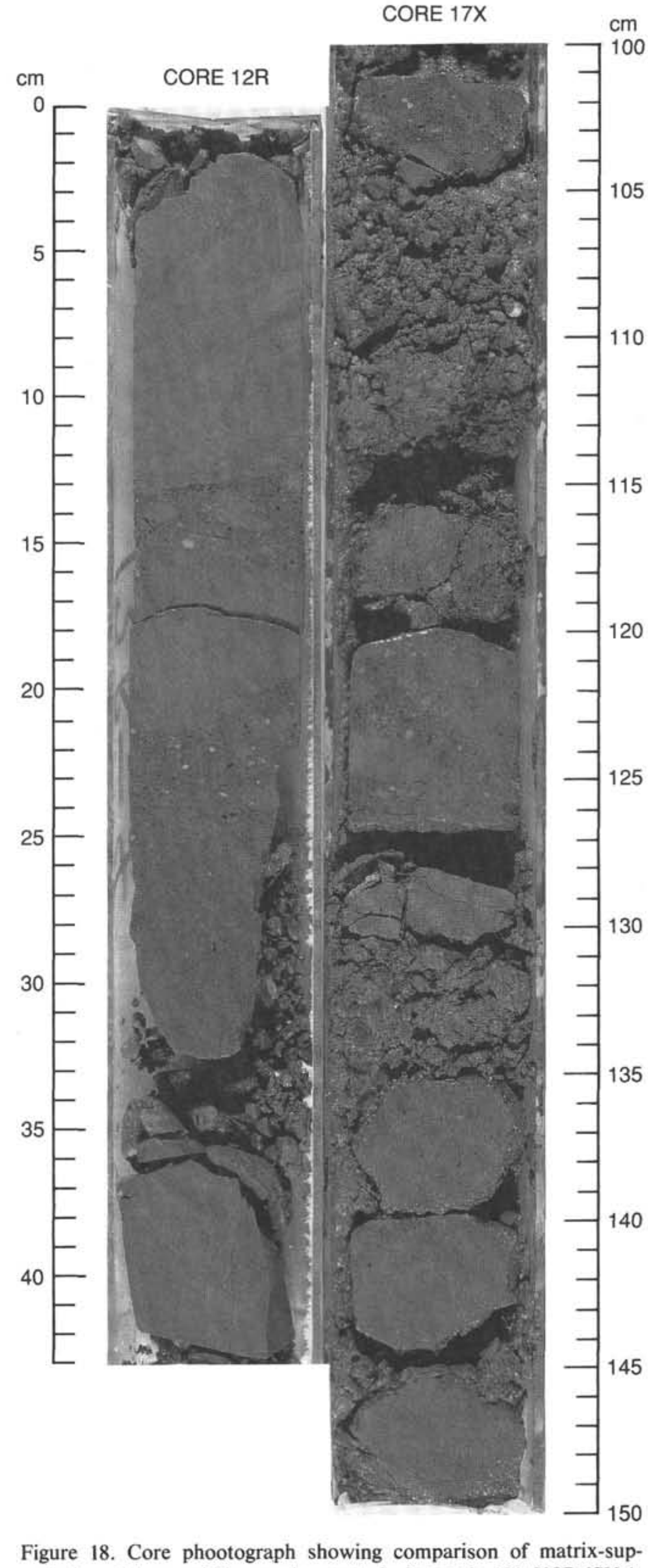

Figure 18. Core phootograph showing comparison of matrix-supported mudstone-pebble conglomerate in intervals 131-808B-17X-1, 100–150 cm, and 131-808C-12R-4, 0–43 cm. The two conglomerates are probably the same deposit, duplicated across the frontal thrust to give a vertical offset of about 145 m.

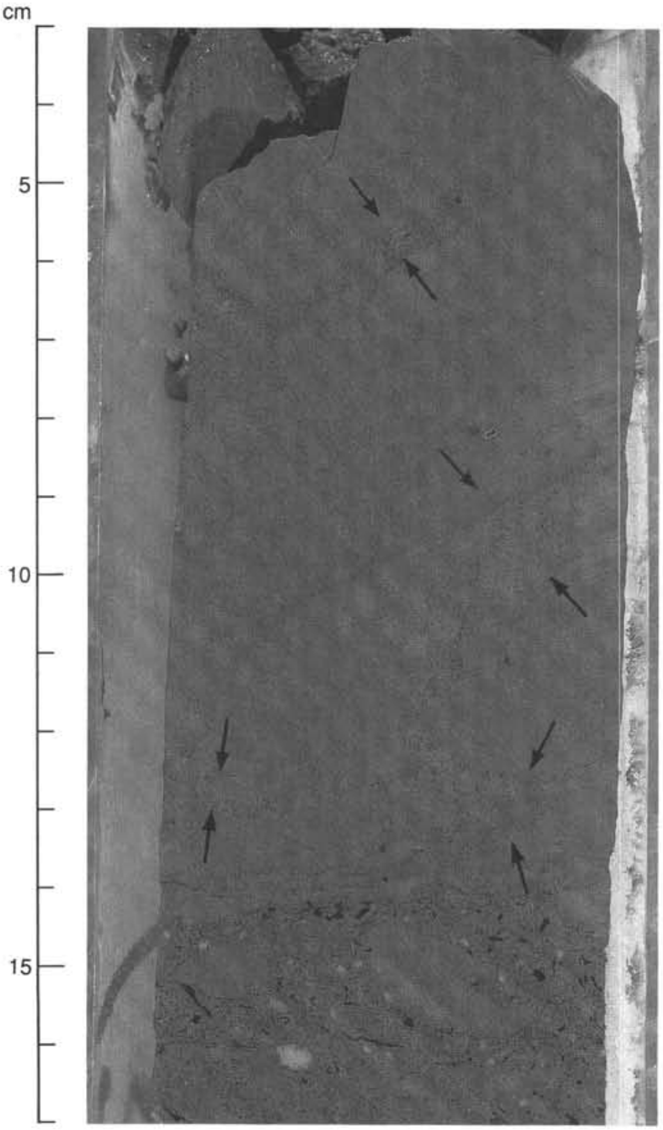

Figure 19. Close-up core photograph of partially brecciated mudstone clast (2–14 cm) in the matrix-supported mudstone-pebble conglomerate, interval 131-808C-12R-4, 3–17 cm. Arrows show boundaries of matrix injections along fracture in the clast. Note the well-rounded mudstone, quartz, and volcanic rock clasts in the matrix, together with abundant black woody material (14–17 cm).

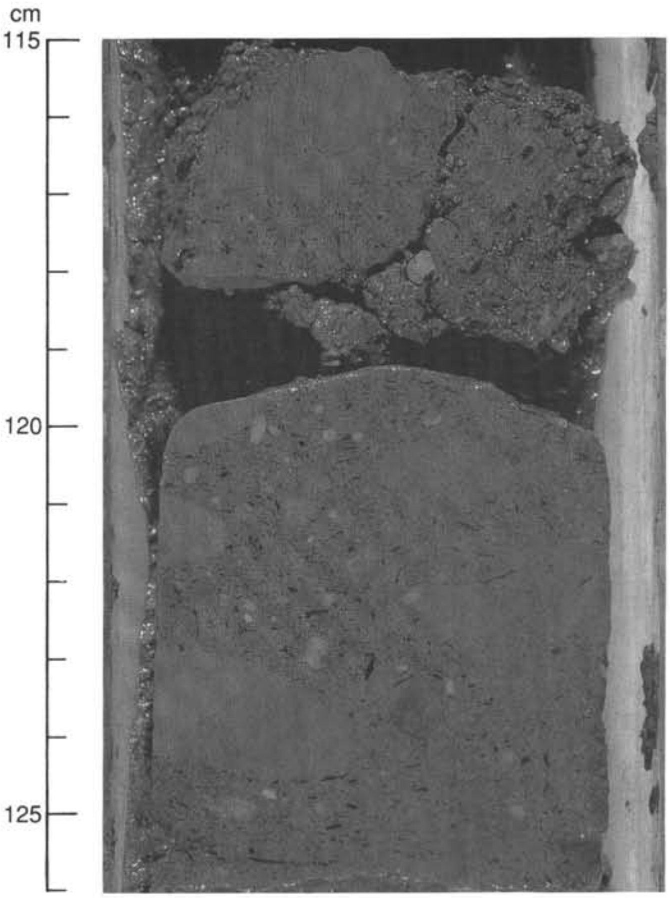

Figure 20. Close-up core photograph of part of matrix-supported mudstone-pebble conglomerate, interval 131-808B-17X-1, 115–126 cm. The matrix contains abundant plant material (black elongate clasts) and prominent well-rounded quartz and volcanic rock fragments (lighter color).

Unit VI (1289.9–1318.82 mbsf)

Sections 131-808C-105R-1, 0 cm, through 131-808C-108R-1, 132 cm; age, middle Miocene-? (Zone NN5).

Unit VI is defined by the first occurrence of basalt. The basalt contains small intervals of reddened, baked sediment, in Section 131-808C-106R-1, Piece 1, and Section 131-808C-106R-2, Pieces 9 and 10. Detailed descriptions of the lithologies within Unit VI are dealt with in the Basement Lithology and Geochemistry section, this chapter.

The seismostratigraphic position of Unit VI suggests that it represents the uppermost parts of the Shikoku Basin oceanic crust.

Synthesis and Summary

The stratigraphy at Site 808 shows a classic overall coarsening-upward sequence above the basaltic basement (Unit VI) and acidic volcaniclastic rocks (Unit V), from the hemipelagic and pelagic Shikoku Basin sediments (Unit IV), through transitional basin-to-trench (Unit III), to the coarse-grained, turbiditic, trench-fill sediments (Unit II). Site 808 was drilled within the toe of the accretionary prism, just landward of the surface expression of the main frontal thrust; consequently, this stratigraphy is presently capped by about 20 m of lower slope sediments. The slope sediments are characterized by sediment slides, as seen in the cores and from sidescan sonar images of the present seafloor in the vicinity of Site 808. These slope sediments may represent mainly remobilized accreted trench-fill deposits, and at least some sediment derived from the Shikoku shelf/forearc slope. It is even conceivable that at least some of the fine-grained sediment veneer on the lowermost inner-trench slope, in the vicinity of Site 808, was deposited from the uppermost parts of axially-flowing, very thick turbidity currents.

It has not been possible yet, to recognize a provenance for deposits other than the thick sand, the turbidites; shipboard point-counts support the hypothesis of axial-trench transport of volcanic-rich and sedimentary-rich material from much farther east in the Izu Collision Zone (Taira and Niitsuma, 1986).

Previous drilling in the area of Site 808 involved Site 582 within the Nankai Trough (DSDP Leg 87, Kagami, Karig, Coulbourn, et al., 1986), Site 298 on the lower inner slope of the Nankai Trough (DSDP Leg 31, Karig, Ingle, et al., 1975),

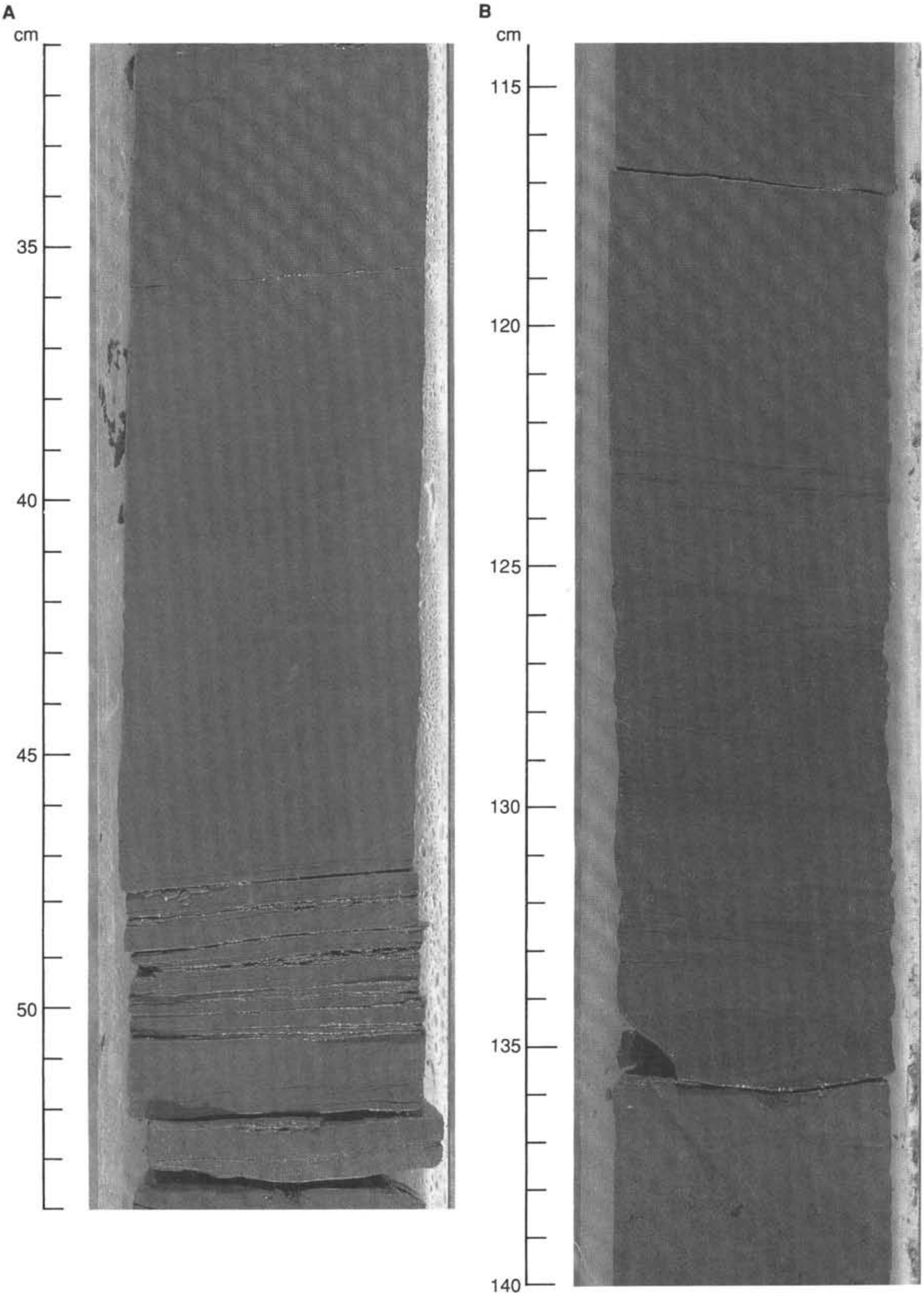

Figure 21. Core photgraphs of **A.** Siltstone turbidite showing thoroughly laminated lower part (47–53.5 cm), overlain by structureless, moderately bioturbated, siltstone/clayey siltstone (31–47 cm), interval 131-808C-13R-3, 31–53.5 cm). **B.** Siltstone turbidite, showing thoroughly laminated, including current-rippled, lower part (122–136 cm), overlain by virtually nonbioturbated, diffusely-laminated to structureless, clayey siltstone cap (above 114–122 cm); interval 131-808C-27R-4, 114–140 cm.

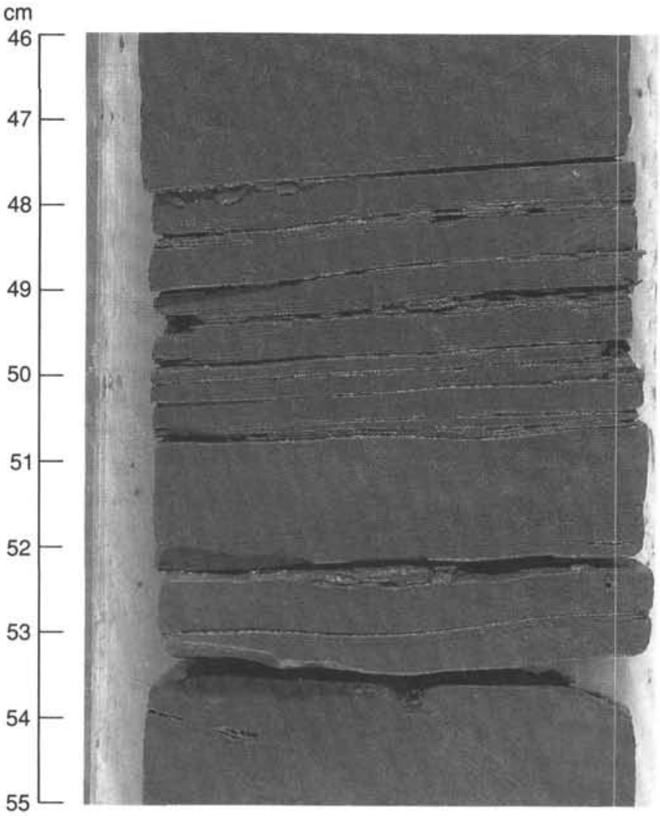

Figure 22. Close-up core photograph of lower part of the thoroughly laminated siltstone turbidite shown in Figure 21A. Above the sharp base, there are divisions of low-amplitude wavy lamination, low-angle microcurrent ripples, diffuse wavy lamination, low-angle micro-current ripples, low-amplitude wavy, then parallel, lamination, all overlain by structureless fine siltstone/clayey siltstone.

and within the Shikoku Basin Sites 297, 296 (DSDP Leg 31, Karig, Ingle et al., 1975), 442, 443, and 444 (DSDP Leg 58, Klein, Kobayashi, et al. 1980). The Shikoku Basin sites comprise typical hemipelagites/pelagites, similar to those encountered in Subunits IVa and IVb at Site 808.

Site 808 appears to have been near the lysocline and/or below the CCD during at least part of its history, based on the paucity of preserved foraminifers and calcareous nannofossils in certain intervals in the Miocene-Pliocene sections (see Biostratigraphy section, this chapter). Site 808, however, contains very thin diagenetic carbonate layers in the Shikoku Basin Subunits IVa and IVb, which may have been sourced as dilute turbidity currents from the relatively shallower water chalks along the flanks of the paleo-Kyushu-Palau Ridge.

Sedimentary Petrology

In addition to routine smear-slide descriptions, three analytical methods were used to document accurately the composition of sedimentary units at ODP Site 808: bulk mineralogy was measured by X-ray diffraction (XRD); absolute weight percentages of $CaCO_3$ were recorded using a coulometric analyzer (see Geochemistry section, Explanatory Notes chapter, this volume); and thin-section petrography was utilized to quantify relative abundances of all major detrital modes in the turbidite sands. Measurements of carbonate content were completed on all Physical Properties (PP) and headspace-gas sediment specimens. X-ray diffraction was employed on the trimmings from interstitial water sediment specimens; in addition, at least one PP sample was analyzed per core. The density of sample spacing for XRD analyses was increased in the vicinity of major structural features, such as the frontal thrust and the décollement zone, and where changes had been detected in the gradients of physical properties and/or interstitial-water geochemistry. At least one representative sample of sand per core was taken for petrographic study of the upper axial trench wedge facies (Subunit IIa).

The objectives of these petrologic analyses were as follows: (1) to provide a compositional base level for interpretations of sediment provenance and pathways of sediment dispersal; (2) to test whether lithofacies units can be discriminated further on the basis of mineralogic changes; (3) to establish the bulk mud composition to serve as a frame of reference for more detailed analyses of clay mineralogy and clay-mineral diagenesis; (4) to test for possible mineralogic influences on sediment physical properties, including bulk density, thermal conductivity, and down-hole log response; and (5) to investigate whether changes in mineralogy coincide with the locations of major structural features such as the décollement zone.

Carbonate Content

Figure 31 illustrates the variability in calcium-carbonate content at Site 808 (see Table 3, backpocket microfiche, for a listing of all data). As a general trend, the weight-percent of calcium carbonate increases as a function of sub-bottom depth (Table 4). With the exception of rare layers enriched in remobilized nannofossils, the slope apron (Unit I) contains less than 5 wt% $CaCO_3$. The mean value for Unit I is 2.2 wt%, and the greatest value is 17.9 wt% $CaCO_3$. The sandy portion of the trench turbidite wedge (Subunit IIa) contains uniformly small amounts of carbonate, with a mean value of 1.8 wt% and a standard deviation of 0.9 wt%. Subunits IIb and IIc display increases in mean, median, and maximum carbonate values, as well as the respective standard deviations (Table 4). The transition from the trench-wedge facies to the hemipelagites of the Shikoku Basin (Unit III) is accompanied by a slight decrease in carbonate content (Fig. 31).

Values greater than 10 wt% $CaCO_3$ are common only below a depth of about 625 mbsf, within the ash/hemipelagite facies of the Shikoku Basin (Subunit IVa). The mean value for Subunit IVa increases to 4.9 wt%; this is the highest mean value among the facies units and subunits, and the corresponding standard deviation increases to 4.1 wt%. The ash-free hemipelagites of the Shikoku Basin (Subunit IVb) display an even higher scatter in carbonate content, with a standard deviation of 7.0 wt% and maximum values as high as 57.7 wt% $CaCO_3$. This increased scatter is probably due to marked fluctuations in the terrigenous and pelagic components of the hemipelagic sediment.

It is worth noting that the carbonate content does not change significantly across the décollement zone; instead, carbonate increases within the zone of intense deformation (beginning at about 953 mbsf) to a depth approximately 25 m below the décollement. At approximately 1000 mbsf, the values drop again over a 50-m-thick interval, with data consistently below 5 wt% $CaCO_3$ (Fig. 31). Irregular fluctuations in carbonate then occur throughout the remainder of Subunit IVb. Unit V shows very low carbonate values in its

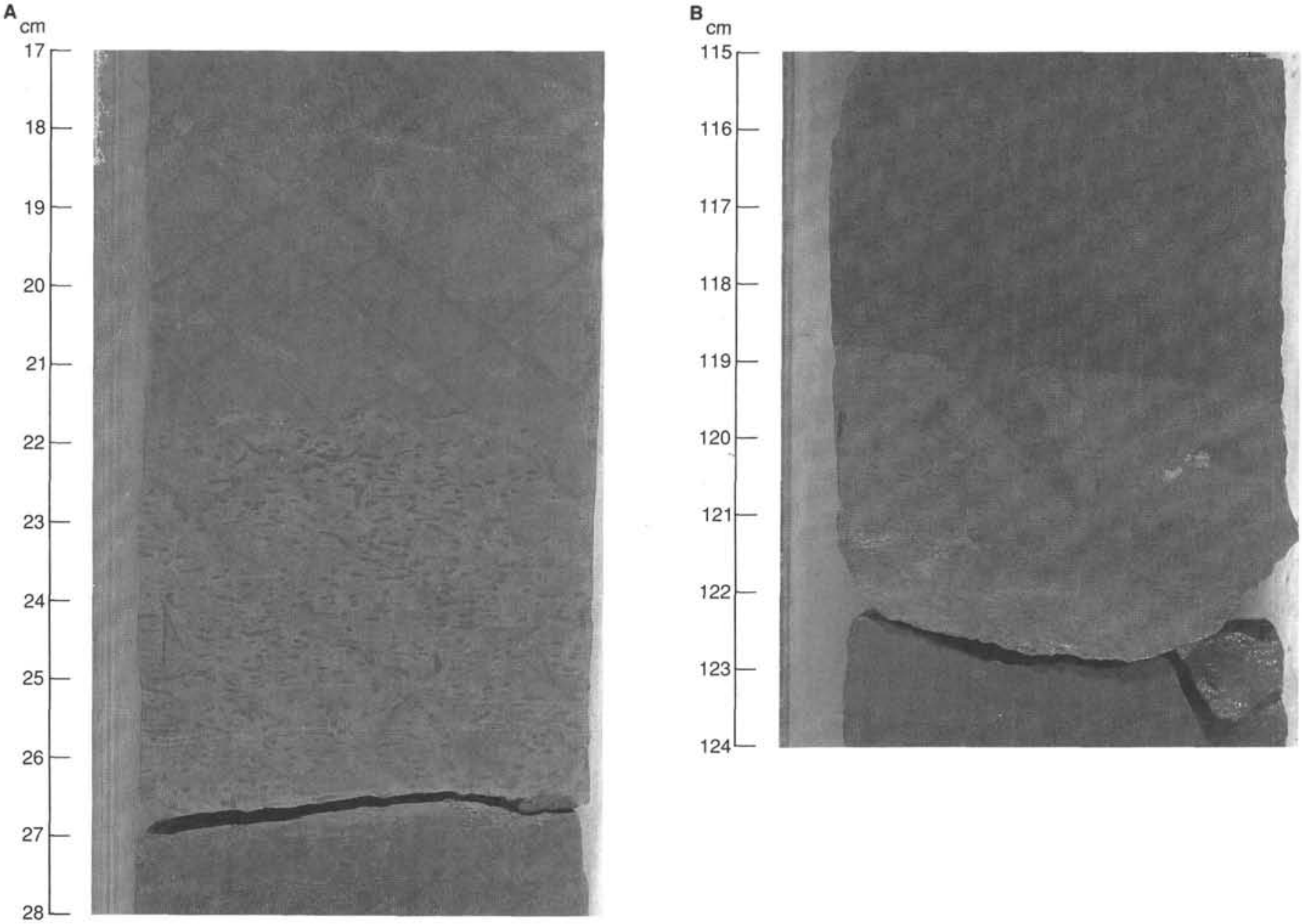

Figure 23. Core photographs of A. Thoroughly bioturbated clayey siltstone/silty claystone showing ichnogenera; the darker and smaller burrows are *Chondrites*, Note the conjugate shear bands throughout the core interval, 131-808C-16R-2, 17–28 cm. B. Bioturbated ash (lighter color) with large V-shaped mud-filled burrow; interval 131-808C-22R-3, 115–124 cm.

upper part and irregular fluctuations in its lower part; the mean carbonate content for Unit V is 4.4 wt%, and the standard deviation is 6.7 wt% (Table 4).

Bulk Mineralogy

Based on uncorrected peak intensities from X-ray diffraction analyses of bulk sediment powders, it is clear that four principal components dominate the sediments at Site 808; these components include the clay-mineral group (illite, smectite, chlorite, and kaolinite), quartz, plagioclase, and calcite (see Tables 5, 6, and 7 for data compilations from each hole). Overall trends in the relative proportions of the major mineral constituents are illustrated in Figure 32. Bulk XRD analyses were also run as a pilot study on representative volcanic-ash deposits throughout the sedimentary column, and on vitric mudstones within Unit V; these data are included in a separate compilation (Table 8).

One measure of the accuracy of our estimates of relative bulk mineralogy is provided by a comparison between values of percent-calcite from XRD and the wt% carbonate values derived from coulometrics measurements. Figure 33 shows that there is excellent statistical agreement between the two data sets, particularly for samples containing less than 10% calcite. At higher calcite contents, the XRD estimates are slightly larger; this discrepancy is to be expected because the XRD data only represent abundances with respect to quartz, plagioclase, and total clay minerals, rather than weight-percentages of the total solids. We caution, however, that similar calibration tests were not completed for the other mineral components, so the errors for their estimates remain unknown. In particular, the error associated with percent total clay minerals propagates with the summation of error for each individual clay species. The XRD data, therefore, should be viewed only as a semi-quantitative measure of the relative proportions of common minerals rather than absolute percentages.

Tests of internal reproducibility were made using fourteen separate samples; these duplicate runs included both repeated scans of the same powder mount and separate mounts of the same sample. The average variations in the relative mineral percentages are as follows: total clay minerals = 3.2%; quartz = 2.6%; plagioclase = 3.6%; calcite = 0.6%.

Minor minerals, such as pyroxene, amphibole, pyrite, and siderite were recognized in the XRD data for some samples, but these observations were not quantified because of generally low peak intensities and inconsistent occurrences. The most significant of the minor mineral constitu-

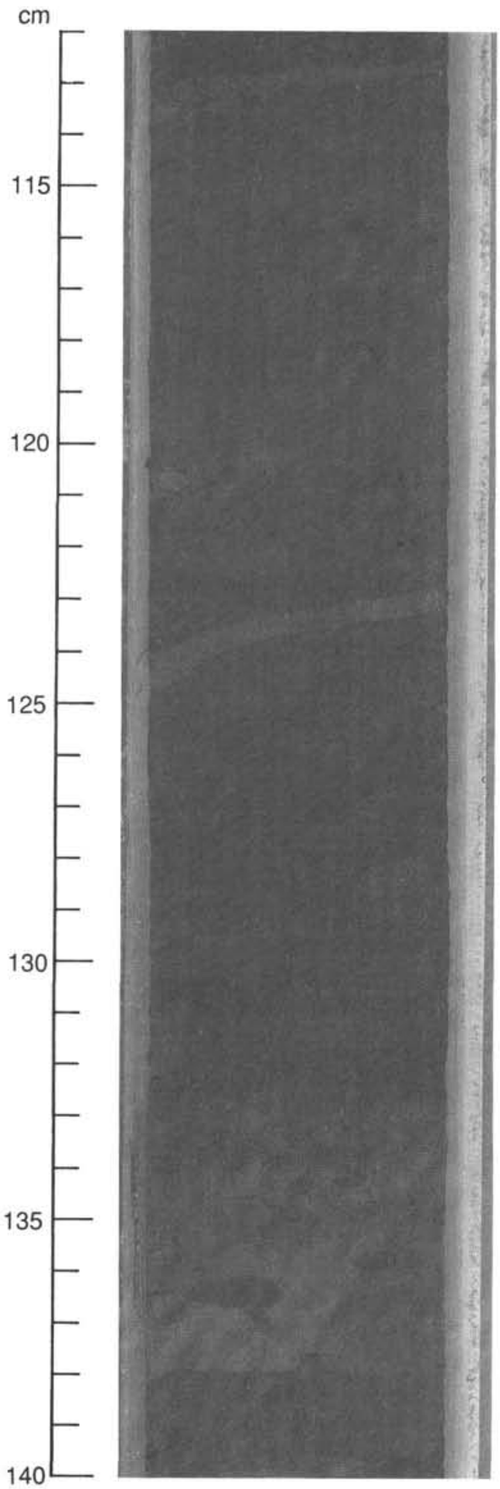

Figure 24. Core photograph showing characteristic deposits in Unit III of thoroughly bioturbated (mottled) clayey siltstone/silty claystone, with *Zoophycos* burrows, and light-colored, bioturbated, volcanic ash/tuff (133–138 cm); interval 131-808C-30R-2, 112–140 cm.

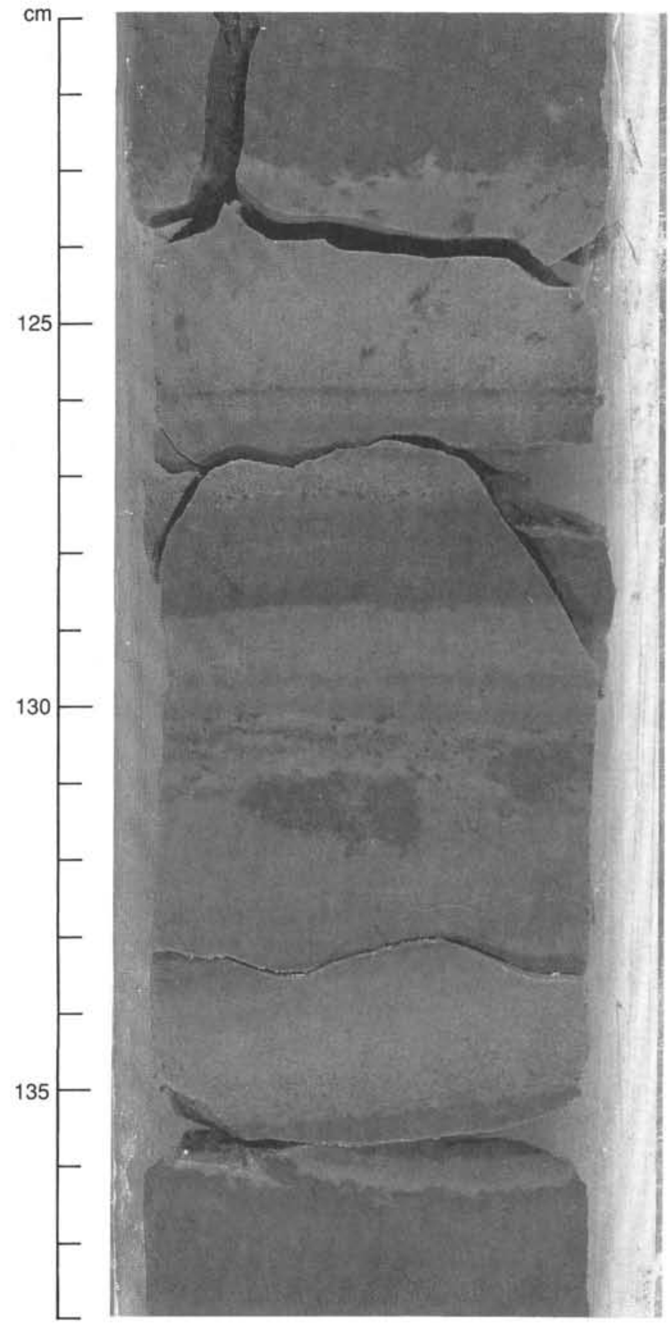

Figure 25. Core photograph showing normally-graded, partially bioturbated, ash/tuff layers; interval 131-808C-46R-5, 121–138 cm. The lowest tuff shown has a loaded base, and the overlying thicker tuff shows normal grading and diffuse, low-angle lamination. These tuffs represent a phase of intense volcanic activity.

ents are the zeolites. Two closely related zeolites, clinoptilolite and heulandite, both produce a principal XRD peak within the scanning range of 9.70°–9.99°2θ and cannot be differentiated using untreated bulk powders. Undifferentiated clinoptilolite/heulandite is particularly common in cores 808C-31R through 808C-53R, which correspond to facies Unit III and Subunit IVa and a sub-bottom depth range of approximately 590-820 mbsf (Fig. 34). The zeolites

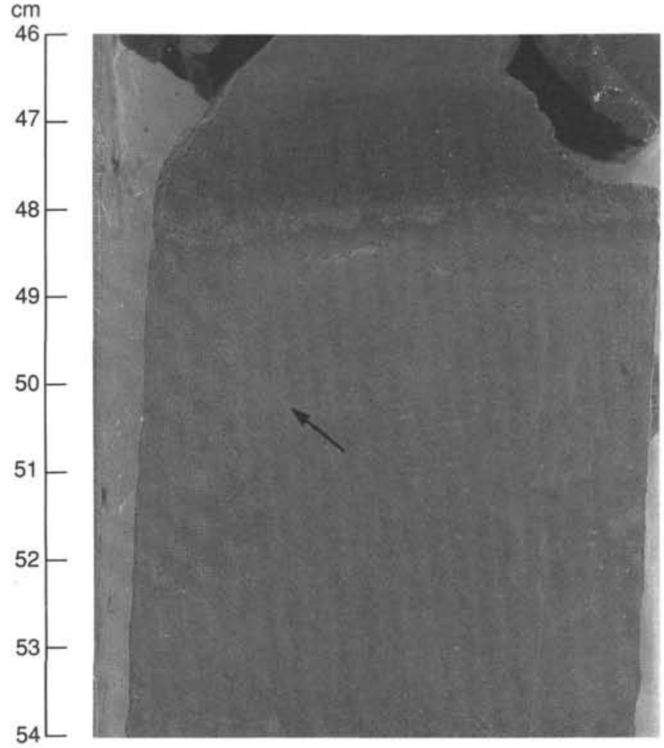

Figure 26. Core photograph showing sedimentary small-scale normal fault (arrowed), truncated by a normally graded ash/tuff layer with loaded base; interval 131-808C-39R-1, 46–54 cm.

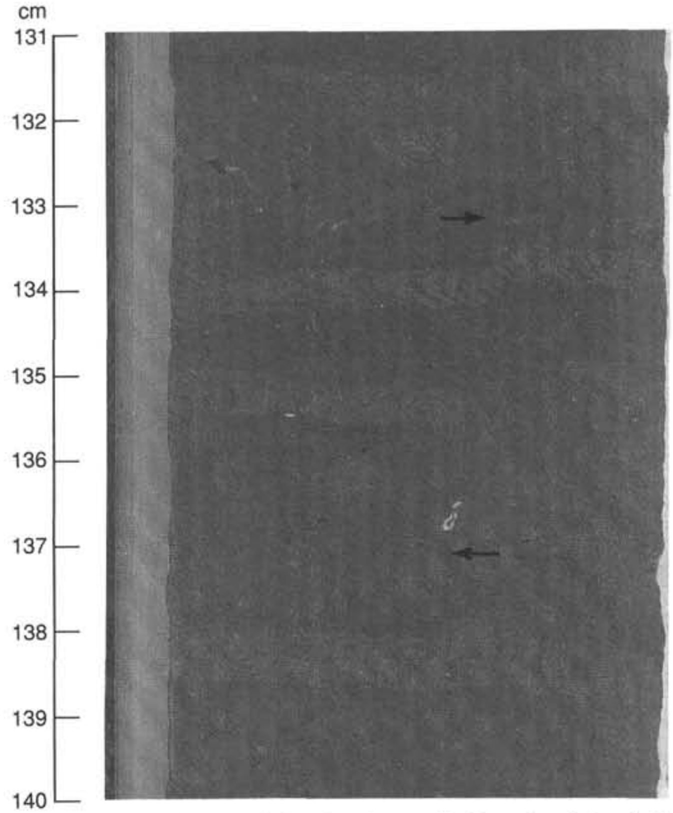

Figure 27. Core photograph showing thoroughly bioturbated (mottled) clayey siltstone/silty claystone, with abundant *Zoophycos* burrows, siliceous worm tubes, and a steep normal fault offsetting the burrows. This lithology is the main constituent in Subunit IVa; interval 131-808C-50R-4, 131–140 cm.

reach maxima of intensity and frequency between 780 and 810 mbsf and then disappear abruptly at a sub-bottom depth somewhere between 816.5 and 817.5 m; this depth is approximately 6.5 m above the defined base of facies Subunit IVa (Fig. 34). The presence of clinoptilolite/heulandite is related to the influx of volcanic ash in Subunit IVa and is a meaningful measure of the amount of ash disseminated in the hemipelagic mud.

Another type of zeolite, analcite, produces a diagnostic X-ray diffraction peak at 15.6°–16.2°2θ. This mineral occurs only in the acidic volcaniclastic deposits of Unit V (Table 8). In deep-marine sediments, analcite is associated most commonly with basaltic volcanic material, but the mineral also coexists with clinoptilolite, which is the silica-rich end member of the heulandite series (Kastner, 1979). Table 8 shows that a clinoptilolite/heulandite precursor coexists with analcite in some of the coarse-grained gray tuff deposits of Unit V. Whether these minerals coexist under equilibrium conditions remains uncertain.

There are several significant differences in bulk mineralogy between the slope apron (Unit I) and the underlying succession of thick-bedded, sandy turbidites (Subunit IIa). The slope deposits contain higher percentages of total clay minerals than the trench turbidites, and values of quartz and plagioclase are relatively uniform in the uppermost 20 m (Fig. 35; Table 5). In contrast, samples extracted from the sandy turbidites and interlayered hemipelagic muds display extreme variations in the relative proportions of detrital quartz and feldspar. The sand layers typically are enriched in plagioclase relative to the muddy inter-turbidite deposits (Fig. 35; Table 5). Thin-section petrography shows that plagioclase is abundant both in a monocrystalline form and as phenocrysts within volcanic rock fragments (see following section). Thin-sections also show that most of the clay minerals in the turbidite sands actually reside in fine-grained sedimentary rock fragments and altered volcanic rock fragments.

There are no clear trends in the abundances of individual clay minerals within Unit I and Subunit IIa (Fig. 36; Table 5). The two most-abundant clay minerals are illite and chlorite, with smectite and kaolinite occurring in lesser amounts (see Explanatory Notes chapter for methods of mineral identification). These four clay minerals (plus mixed-layer clays) were also detected in similar and relatively constant proportions by Chamley et al. (1986) during DSDP Leg 87A. According to these previous workers, the clay mineralogy can be accounted for by the erosion of rock types and soils presently seen in Japan.

As the trench wedge gradually changes with increasing depth from thick-bedded sandy turbidites to the thin silty turbidites and hemipelagites of Subunits IIb and IIc, the bulk mineralogy becomes more uniform (Fig. 37). The weighted XRD intensities for the clay mineral peaks show no significant change through this facies transition (Fig. 38). The relative abundance of detrital quartz, however, increases slightly from Subunit IIb to Subunit IIc, and there is a concomitant decrease in plagioclase over the same range of sub-bottom depths (Fig. 37; Table 6). It is important to note that the quartz/plagioclase ratio throughout the sedimentary column at Site 808 is affected by a downsection decrease in mean grain

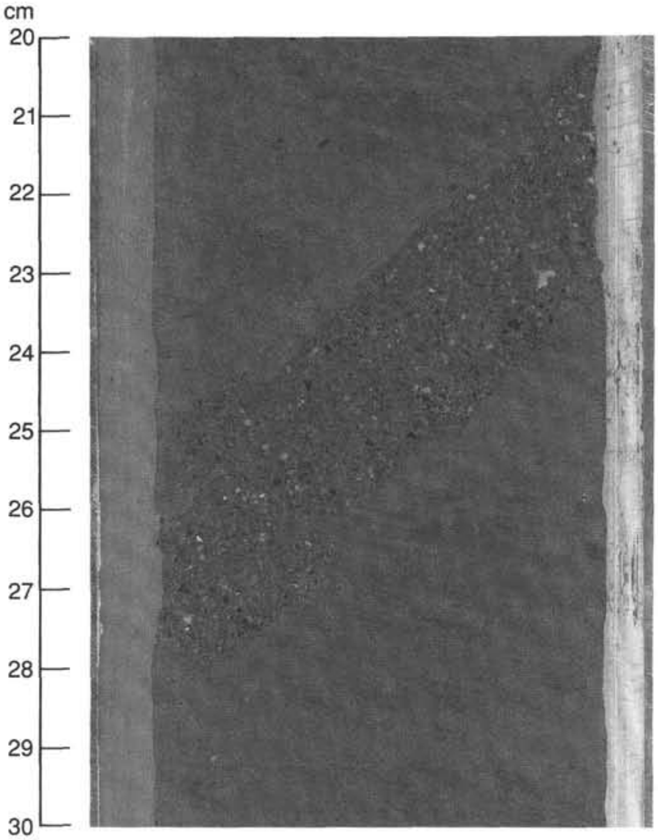

Figure 28. Core photograph showing clastic dike of volcanic/terrigenous coarse-grained sandstone; interval 131-808C-54R-4, 20–30 cm. The large white grains are diagenetic carbonate concretions.

size (Fig. 32e). The reduction of detrital feldspar in Hole 808B, in particular, is consistent with the downhole decrease in turbidite sand (Fig. 39).

The results of XRD analyses from Hole 808C are illustrated in Figures 40 through 47 and tabulated in Table 7. The overall scatter in both quartz and plagioclase content decreases downsection in response to a decrease in the amount and frequency of sediment influx via turbidity currents. There is also a marked increase in quartz content within Subunit IVb (Fig. 41) and a corresponding decrease in detrital plagioclase from the silt and ash-rich units into the finer-grained hemipelagic facies of Subunit IVb (Fig. 42). Calcite content increases significantly near the base of Unit III and maintains consistently high values throughout Subunit IVa (Fig. 43). The décollement zone within Subunit IVb also displays relatively high calcite percentages, beginning at the top of the deformation zone and extending to a depth of roughly 1000 mbsf (Fig. 43).

There is a very slight reduction down Hole 808C in the relative abundance of total clay minerals (Fig. 40); in addition, there are some subtle changes in some of the individual clay species. For example, the weighted intensities of discrete smectite (i.e., the 6.2°2θ peak intensity, air-dried, with a weighting factor of 3.00) decrease from typical values of 6%–7% within the frontal thrust zone and facies Subunit IIc to lesser values of 4%–5% in Subunit IVb (Fig. 44). Illite weighted intensities (from the 8.9°2θ peak) vary between 15%–30% down to a depth of approximately 850 mbsf. At greater depths, illite then decreases slightly to a range of about 10%–20% through the remainder of Subunit IVb (Fig. 45). There is also a slight reduction in the amount of

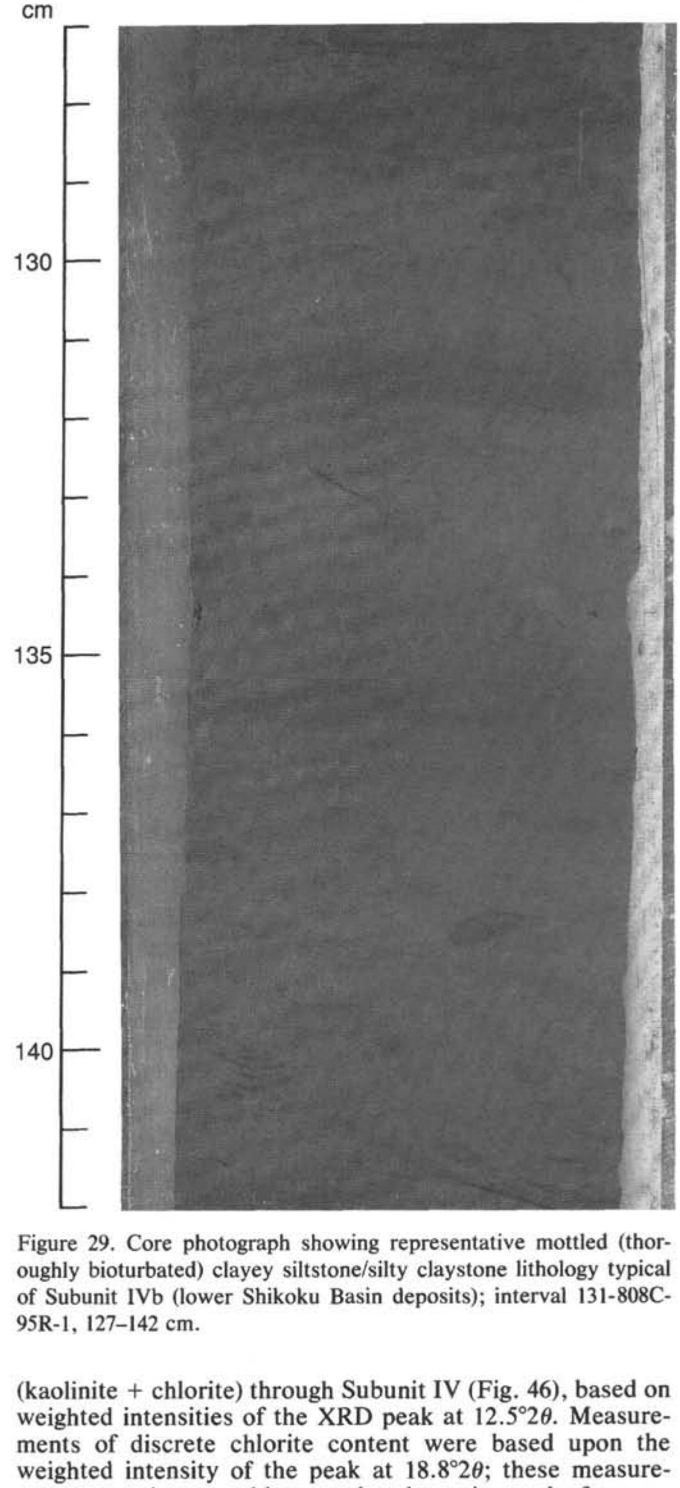

Figure 29. Core photograph showing representative mottled (thoroughly bioturbated) clayey siltstone/silty claystone lithology typical of Subunit IVb (lower Shikoku Basin deposits); interval 131-808C-95R-1, 127–142 cm.

(kaolinite + chlorite) through Subunit IV (Fig. 46), based on weighted intensities of the XRD peak at 12.5°2θ. Measurements of discrete chlorite content were based upon the weighted intensity of the peak at 18.8°2θ; these measurements were hampered by very low-intensity peaks for samples cored below the frontal thrust. The sporadic chlorite-intensity values of zero (Fig. 47) show that the 18.8°2θ peak is not high enough above background to allow detection; chlorite probably still contributes to the [kaolinite + chlorite] peak at approximately 12.5°2θ, and may also interfere somewhat with the smectite peak at approximately 6.2°2θ.

Overall, the clay-mineral data indicate that the outer marginal trench wedge and the hemipelagic deposits of the Shikoku Basin were supplied by diverse detrital sources, as suggested previously by Chamley et al. (1986), based on

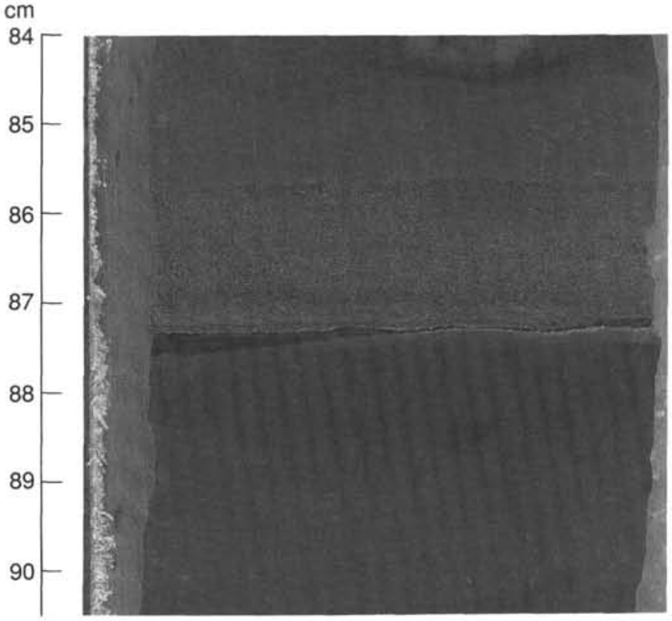

Figure 30. Core photograph showing dewatering structures below graded ash/tuff layer, Unit V; interval 131-808C-102R-1, 84–90.5 cm.

their results from DSDP Leg 87A. However, our data show a small downhole decrease in smectite content, rather than the increase in detrital smectite indicated by Chamley et al. (1986) for roughly equivalent facies units. This result is somewhat surprising considering the influx of volcanic ash within Unit III and Subunit IVa and the occurrence of abundant zeolite as an authigenic byproduct of the ash. We suggest that the reduction in the amount of discrete smectite at Site 808 is a manifestation of early diagenetic illitization of detrital and/or authigenic smectite. It is noteworthy that the peak associated with the (001) illite reflection (at approximately 8.9°2θ) becomes increasingly broad and asymmetric beginning at a depth of roughly 530 mbsf. The geometric change in the illite peak is undoubtedly a response to the formation of an illite:smectite mixed-layer phase (Moore and Reynolds, 1989). Additional detailed work must be completed, however, using oriented aggregates and proper sample treatments, before this important diagenetic trend can be defined with proper accuracy and precision.

Bulk powders of volcanic ash deposits were also analyzed by XRD to test for possible mineralogic effects of diagenetic alteration. Because of the high content of amorphous volcanic glass in these samples, semiquantitative estimates of mineral abundances were not made. Some of the volcanic deposits within the uppermost 600 meters of the sedimentary column generated broad humps in the XRD tracing; this response is typical of unaltered ash. Primary crystalline constituents include plagioclase, quartz, rare amphibole, and pyroxene (Table 8). Important authigenic and diagenetic phases include cristobalite, calcite, siderite, clinoptilolite/heulandite, analcite, and clay minerals, particularly smectite and mixed-layer illite:smectite (Table 8). The occurrences of these secondary minerals are irregular.

Sand Petrography

Sandy turbidites from Subunit IIa of the Site 808 sedimentary succession (20.55–120.60 mbsf) contain a remarkably diverse assemblage of detrital constituents. The results of modal analyses are listed in Table 9 and displayed on

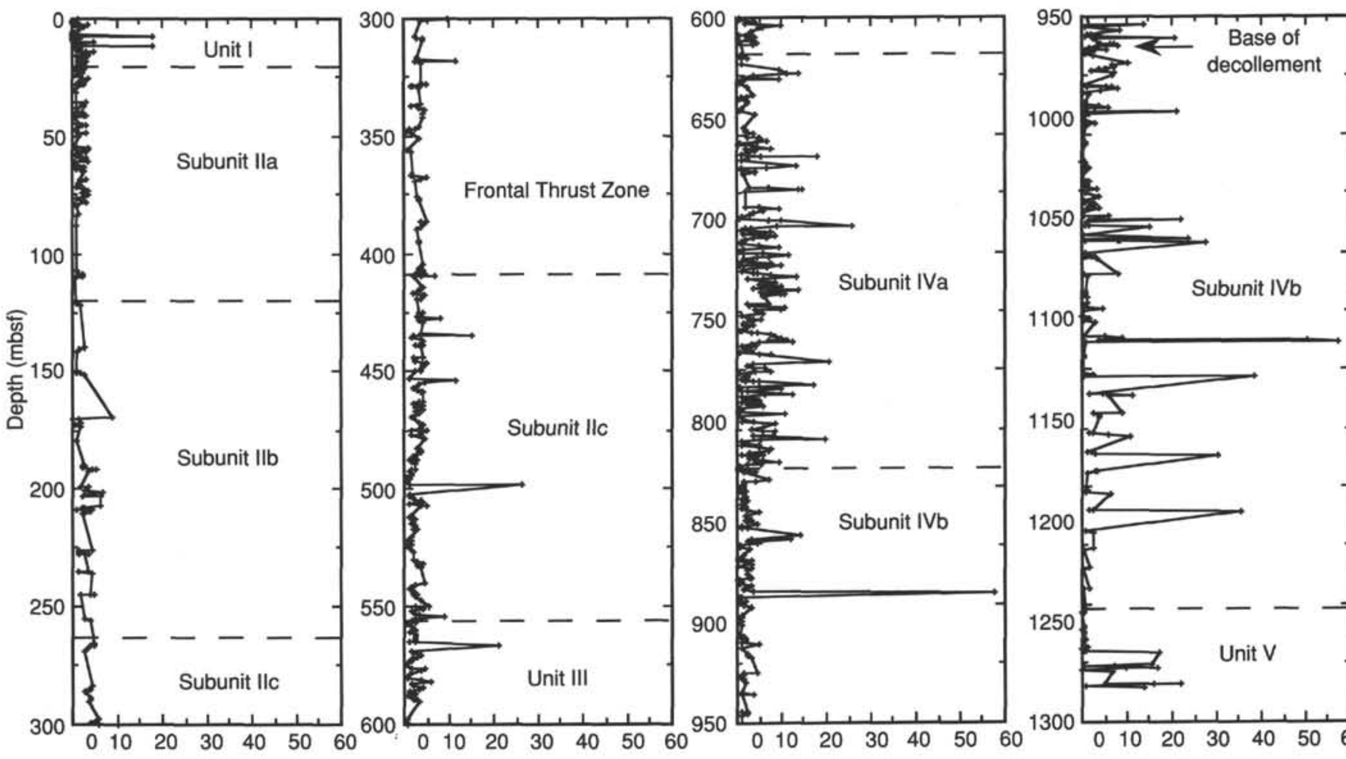

Figure 31. Absolute weight-percentages of $CaCO_3$ vs. depth for Site 808. Carbonate contents were measured using a coulometric analyzer. The frontal thrust zone includes strata assigned to both Subunit IIb and Subunit IIc.

Table 4. Statistical comparison of calcium-carbonate contents (in absolute wt%) for each facies unit and subunit cored at ODP Site 808.

Unit/ Subunit	No.	Maximum	Minimum	Mean	Median	Std. deviation
I	57	17.9	0.2	2.16	1.3	3.33
IIa	97	3.5	0.3	1.77	1.5	0.96
IIb	83	8.7	0.2	3.01	2.6	1.59
IIc	197	26.7	0.6	3.37	2.9	2.49
III	70	21.2	0.3	2.75	2.2	2.78
IVa	227	26.1	0.3	4.88	3.8	4.08
IVb	312	57.7	0.2	3.59	1.8	7.00
V	32	22.3	0.2	4.39	0.4	6.68

standard ternary diagrams (Fig. 48). The average Q-F-L values for the trench turbidites are: Q-22.5, F-19.7, L-57.8; the average Q_p-L_v-L_{sm} polycrystalline modes are: Q_p-9.6, L_v-44.0, L_{sm}-46.4 (see Explanatory Notes chapter for definition of detrital modes). The occurrence of neovolcanic pumice fragments, which are typically stained by iron-oxide coatings, is noteworthy; these conspicuous lithic grains occur together with a wide variety of basaltic, microlitic, and felsitic volcanic rock fragments. The abundance of both volcanic debris and recycled sedimentary rock fragments, together with appreciable quantities of chert and low-grade metasedimentary rock fragments, provides unequivocal evidence for a polymictic or mixed tectonic provenance.

Our data agree fairly well with the results obtained by Taira and Niitsuma (1986) during DSDP Leg 87A; Site 582 penetrated the Nankai Trough turbidite wedge farther to the southwest. The content of feldspar is slightly higher at Site 808 than at Site 582 (Fig. 48), although this apparent increase may be an artifact caused by different methods used to classify plagioclase phenocrysts. The relative abundance of volcanic rock fragments is also somewhat higher, on average, at Site 808 (Fig. 48). In contrast, the data of DeRosa et al. (1986), which include results from both Site 582 and 583, show much lower percentages of sedimentary rock fragments (typically less than 5%) in both the trough axis and the lower accretionary prism. The reasons for the large discrepancy between the data sets of Taira and Niitsuma (1986) and DeRosa et al. (1986) remain unclear but could be due to inadvertent disaggregation of fragile rock fragments during sample preparation.

We concur with the interpretations of Taira and Niitsuma (1986), who attributed the majority of sandy deposits in the axial part of Nankai Trough to southwest-directed turbidity currents; their interpretations are based upon analyses of magnetic grain fabric and petrologic comparisons with all possible detrital sources, as represented by the major fluvial drainage basins of Japan. Most of the axial sediment gravity flows were initially funneled through Suruga Trough from a source region that included the Fuji River drainage basin. This turbidite source terrane was created by uplift and volcanism associated with the collision between the Izu-Bonin Arc and the Honshu Arc.

BIOSTRATIGRAPHY

Introduction

Of the 1289.9 meters of sediments that were cored at Site 808, the upper 780 m were assigned to the Pleistocene. The remaining 500-m range in age from Pliocene to middle Miocene. Of the two microfossil groups studied, only the calcareous nannofossils were found in sufficient amounts for age estimates, the majority of the samples being barren of radiolarians. Table 10 summarizes the nannofossil events used for the biostratigraphic zonation of Site 808.

Calcareous Nannofossils

Hole 808A

Hole 808A was APC-cored to 111.4 mbsf. The sediments recovered contain nannofossil assemblages that are mostly well preserved. The estimated abundances of nannofossil specimens in the samples observed range from barren to abundant. In addition to the core catcher samples, some additional samples were examined from undisturbed or little disturbed muds within the cores. This was done because of the risk of sand caving in, reaching the core catcher and giving a seemingly younger age for the assemblages observed.

All samples in Hole 808A were assigned to Zone NN21 of the Pleistocene (Fig. 49). The major components of the assemblages are gephyrocapsids and *Emiliania huxleyi* down to Sample 131-808A-9H-5, 5 cm, below which *E. huxleyi* is rare and occurs sporadically. The relative abundance of *E. huxleyi* out of 300 specimens per sample was counted in selected samples, which made it possible to determine the onset of the *E. huxleyi* acme (0.09 Ma) between Samples 131-808A-9H-5, 5 cm and -10H-CC (81.17 ± 6.82 mbsf). *Helicosphaera carteri*, *Coccolithus pelagicus* and *Calcidiscus leptoporus* are rare to few in Hole 808A. Other Pleistocene species rarely observed are *Ceratolithus cristatus*, *Umbilicosphaera mirabilis*, *Umbilicosphaera sibogae* and *Pontosphaera japonica*. Traces of reworked older nannofossils were observed in most samples from Hole 808A, e.g. discoasters, sphenoliths and reticulofenestrids.

Hole 808B

Hole 808B was washed to 111.0 mbsf and XCB-cored from 111.0 to 358.8 mbsf. The nannofossil assemblages observed are mostly well preserved. The upper part of Hole 808B was assigned to Zone NN21 (Fig. 49) of the Pleistocene with the same nannofossil species as in Hole 808A, except *E. huxleyi* is rare. The NN21/NN20 boundary (0.28 Ma) was determined by the first occurrence of *E. huxleyi*, observed between Samples 131-808B-13X-1, 42 cm, and -13X-CC (230.66 ± 4.40 mbsf). Traces of reworked older species were also observed throughout Hole 808B.

Hole 808C

Hole 808C was washed to 298.5 mbsf and RCB-cored from 298.5 to 1327 mbsf; basalt was reached at 1289.9 mbsf. The sediments recovered range in age from the upper part of Zone NN20 of the Pleistocene to Zone NN5 of the middle Miocene (Fig. 49).

Pleistocene

Pleistocene sediments recovered from Hole 808C contain moderately to well-preserved nannofossil assemblages. The last occurrence of *Pseudoemiliania lacunosa* (0.46 Ma) was observed between Samples 131-808C-34R-4, 134 cm, and -34R-CC (624.27 ± 1.93 mbsf), marking the top of Zone NN19 (Fig. 49). The last occurrence of *Reticulofenestra asanoi* (0.83 Ma, between Samples 131-808C-37R-CC and -38R-CC), together with the last and first occurrences of large *Gephyrocapsa* (1.10 Ma between Samples 131-808C-41R-CC, and -42R-CC, and 1.36 Ma between Samples 131-808C-46R-CC, and 47R-CC, respectively) provided further datum levels that could be used for subdividing the Pleistocene. Sample 131-808C-50R-4, 59–60 cm, is the deepest that contains *Gephyrocapsa caribbeanica*, therefore

Table 5. X-ray mineralogy data for randomly oriented bulk powders, Hole 808A. The designation next to some of the sample numbers indicates that the specimen is a sand. I-values (from left to right) represent uncorrected peak intensities for the following: smectite (6.2°2θ); illite (8.9°2θ); undifferentiated kaolinite + chlorite (12.5°2θ); chlorite (18.8°2θ); quartz (26.65°2θ); plagioclase (27.9°2θ); calcite (29.4°2θ); and ratio of quartz to plagioclase. Estimates of relative percentages are based on weighted intensities (using factors listed in Explanatory Notes) and normalized to 100%.

Core, section interval (cm)	Depth (mbsf)	I-Smec	I-Illite	I-(K + C)	I-Chlorite	I-Quartz	I-Plag	I-Calcite	%-Clay	%-Quartz	%-Plag	%-Calcite	Qtz/Plag
131-808A-													
1-1-58	0.60	1.72	4.85	5.28	2.39	100.00	20.53	0.00	22.66	49.11	28.23	0.00	1.74
1-2-19	1.70	0.93	2.95	3.98	1.58	100.00	19.24	0.00	16.06	54.55	29.39	0.00	1.86
1-3-0	3.00	2.45	3.91	6.01	2.07	100.00	22.83	2.66	20.85	47.03	30.06	2.06	1.56
1-3-51	3.51	2.35	4.40	7.26	2.87	100.00	19.39	4.67	23.51	47.22	25.64	3.64	1.84
1-4-29	4.80	2.11	3.27	5.79	1.89	100.00	20.32	2.36	19.51	50.06	28.48	1.95	1.76
1-4-140	5.90	2.21	4.41	5.84	1.93	100.00	22.91	1.12	21.78	47.12	30.23	0.87	1.56
2-1-86	7.16	2.53	5.35	5.54	1.93	100.00	20.31	27.79	20.46	39.23	22.31	17.99	1.76
2-2-23 S	8.03	1.90	5.49	5.49	1.94	100.00	22.54	3.49	23.19	45.48	28.71	2.62	1.58
2-3-0	9.30	2.28	5.46	7.39	2.63	100.00	18.29	3.11	26.45	47.04	24.09	2.41	1.95
2-3-39	9.69	1.59	3.07	3.76	1.32	100.00	39.33	1.84	12.93	40.85	44.98	1.24	0.91
2-4-39	11.21	2.30	5.06	6.43	2.01	100.00	21.25	0.71	24.35	47.08	28.01	0.55	1.68
2-5-33	12.65	2.19	4.55	6.41	2.34	100.00	22.22	3.07	22.40	46.39	28.86	2.35	1.61
2-5-140	13.70	2.03	3.73	6.69	2.07	100.00	31.33	7.74	17.84	40.98	35.95	5.23	1.14
2-6-50	14.32	2.21	4.86	5.33	2.21	100.00	27.72	7.89	20.04	41.94	32.55	5.46	1.29
2-7-45 S	15.76	2.26	5.29	6.51	1.98	100.00	21.31	0.25	24.93	46.89	27.98	0.19	1.68
3-1-61	16.41	3.18	7.26	8.68	3.28	100.00	25.97	3.18	28.98	39.91	29.02	2.09	1.38
3-2-75	18.04	1.32	3.80	4.61	1.48	100.00	24.53	1.48	17.83	48.02	32.98	1.17	1.46
3-3-0	18.78	2.18	4.26	6.33	2.13	100.00	18.81	3.72	22.59	48.75	25.67	2.99	1.90
3-3-52	19.30	2.24	5.24	8.56	2.45	100.00	23.23	5.08	24.87	43.32	28.18	3.63	1.54
3-4-3 S	20.34	1.18	3.37	3.27	1.01	100.00	37.20	2.17	13.03	41.87	43.61	1.50	0.96
3-5-108	22.89	1.92	4.08	6.60	1.78	100.00	22.01	23.65	18.35	40.69	25.08	15.88	1.62
3-5-140	23.21	2.60	6.05	7.46	2.92	100.00	26.13	5.59	25.03	41.11	30.07	3.79	1.37
3-6-89 S	24.20	2.14	3.65	5.81	2.64	100.00	21.56	0.33	20.46	49.43	29.84	0.27	1.66
4-1-11 S	25.40	1.80	3.72	4.80	2.29	100.00	20.17	3.37	19.42	49.73	28.08	2.77	1.77
4-1-135	26.64	1.70	3.45	5.28	2.33	100.00	38.15	6.72	14.74	39.13	41.79	4.34	0.94
4-2-88	27.68	2.55	5.11	10.34	3.80	100.00	24.18	3.80	26.14	42.45	28.74	2.66	1.48
4-2-96	27.75	2.76	4.93	7.26	2.43	100.00	22.36	3.93	24.27	44.79	28.04	2.90	1.60
4-3-111 S	29.40	1.48	3.73	5.30	1.83	100.00	72.24	3.73	11.16	28.80	58.26	1.77	0.49
4-4-78 S	30.60	0.57	0.90	1.82	0.75	100.00	81.92	2.33	3.25	29.03	66.60	1.12	0.44
4-5-71 S	32.00	1.18	3.17	3.11	2.25	97.38	100.00	0.00	8.20	23.69	68.11	0.00	0.35
5-1-29 S	35.10	0.75	1.86	2.82	1.65	100.00	24.74	2.05	11.11	51.48	35.66	1.74	1.44
5-2-19 S	36.50	2.23	4.54	6.78	2.99	100.00	82.61	2.63	12.78	25.99	60.11	1.13	0.43
5-2-26	36.56	1.65	1.42	1.94	0.00	100.00	45.35	0.00	7.29	40.85	51.87	0.00	0.79
5-4-39 S	39.70	1.23	2.37	4.29	1.50	100.00	30.85	2.74	12.62	45.77	39.54	2.07	1.16
5-5-99 S	41.80	0.56	1.70	3.16	1.54	100.00	78.47	0.00	5.75	29.38	64.77	0.00	0.46
5-6-110 S	43.40	1.73	3.73	6.06	2.26	100.00	20.21	1.60	20.46	49.89	28.23	1.32	1.77
5-6-120	43.50	2.40	4.48	6.76	2.20	100.00	24.50	3.18	22.09	44.82	30.74	2.35	1.46
5-7-49 S	44.30	0.90	2.22	3.41	1.32	100.00	61.25	1.58	7.96	33.58	57.59	0.88	0.58
6-1-0	44.31	2.52	4.50	5.83	2.35	100.00	57.81	3.60	15.11	31.70	51.31	1.88	0.62
6-1-58	44.89	1.69	4.30	7.04	2.79	100.00	24.39	4.30	21.03	45.03	30.75	3.19	1.46
6-2-39 S	46.20	0.60	1.43	2.19	1.02	100.00	21.15	1.58	8.70	56.42	33.41	1.47	1.69
6-3-35 S	47.65	1.18	3.23	3.83	1.76	100.00	34.06	4.67	13.48	42.61	40.63	3.28	1.05
6-4-50 S	49.30	1.02	3.16	3.66	1.42	100.00	96.12	2.74	7.49	24.76	66.63	1.12	0.37
6-5-59 S	50.90	1.11	2.63	2.84	1.28	86.28	100.00	5.32	6.37	21.54	69.90	2.19	0.31
6-6-60 S	52.42	1.07	3.16	3.45	1.02	100.00	31.77	5.51	13.13	43.86	39.02	3.99	1.12
7-1-60 S	54.40	0.96	2.10	2.90	2.21	100.00	55.71	4.27	9.13	34.55	53.89	2.43	0.64
7-2-30	55.60	1.59	3.39	5.77	2.30	100.00	27.00	4.18	17.27	45.33	34.27	3.13	1.32
7-2-130	56.60	0.98	3.07	3.77	1.15	100.00	68.02	1.33	9.30	31.00	59.10	0.70	0.53
7-3-50 S	57.30	1.41	3.86	4.24	1.57	100.00	71.62	9.85	10.44	28.27	56.69	4.59	0.50
7-4-20	58.50	1.64	3.81	5.50	1.85	100.00	20.47	0.00	20.33	50.64	29.03	0.00	1.74
7-4-135	59.65	2.86	4.47	7.30	2.62	100.00	26.30	4.95	22.18	42.80	31.52	3.50	1.36
7-5-20 S	60.00	1.80	3.27	4.94	2.13	100.00	20.80	3.70	18.02	49.88	29.05	3.05	1.72
8-1-49 S	63.80	1.72	5.35	4.99	2.49	100.00	37.32	3.17	19.12	38.56	40.30	2.02	0.96
8-1-135	64.66	2.71	5.23	6.84	2.39	100.00	24.35	2.39	24.18	44.05	30.03	1.74	1.47
8-2-6	64.85	1.39	3.00	4.84	1.56	100.00	22.88	1.51	16.56	50.10	32.09	1.25	1.56
9-1-29	68.60	2.34	4.98	7.42	2.79	100.00	22.52	3.74	24.05	44.88	28.30	2.77	1.59
9-2-124	71.05	2.14	5.47	6.70	2.88	100.00	22.22	0.00	25.08	46.18	28.73	0.00	1.61
9-3-50	71.80	2.94	8.07	11.01	4.06	100.00	40.92	2.27	27.31	33.30	38.15	1.25	0.87
9-3-140	72.70	1.79	2.86	4.46	1.84	100.00	20.79	2.26	16.74	51.41	29.93	1.92	1.72
9-5-49	74.80	1.94	4.16	6.42	2.19	100.00	21.08	2.19	21.76	48.11	28.40	1.74	1.69
9-6-99 S	76.80	0.00	1.62	2.38	1.66	100.00	78.28	4.78	5.20	28.98	63.53	2.29	0.46
10-1-19	78.00	2.00	4.79	6.67	2.24	100.00	28.40	2.98	21.24	42.70	33.96	2.10	1.26
10-2-14	79.45	1.22	3.89	3.95	1.84	100.00	22.24	1.25	18.01	49.89	31.07	1.03	1.61
10-3-0	80.81	2.99	5.29	7.29	2.61	100.00	23.50	3.69	24.94	43.67	28.73	2.66	1.52
10-4-39 S	82.70	0.88	2.39	2.26	0.96	100.00	57.80	1.89	7.69	34.84	56.39	1.09	0.62
11-1-49 S	87.90	1.18	3.68	3.56	1.62	100.00	52.77	4.71	11.63	34.58	51.10	2.69	0.68
13-1-49	106.90	1.81	4.51	6.35	1.90	100.00	16.98	0.00	24.07	51.46	24.47	0.00	2.10
13-2-99	108.90	1.80	4.48	6.71	1.89	100.00	18.46	1.37	23.53	49.67	25.67	1.12	1.93
13-2-122	109.13	2.87	3.08	5.74	1.86	100.00	32.75	4.89	16.68	41.71	38.24	3.37	1.09
13-3-69	110.10	1.30	3.10	5.37	1.50	100.00	17.44	3.77	18.24	52.73	25.75	3.28	2.05

Table 6. X-ray mineralogy data for randomly oriented bulk powders, Hole 808B. See Table 5 for complete explanation of column headings.

Core, section interval (cm)	Depth (mbsf)	I-Smec	I-Illite	I-(K + C)	I-Chlorite	I-Quartz	I-Plag	I-Calcite	%-Clay	%-Quartz	%-Plag	%-Calcite	Qtz/Plag
131-808B-													
2-1-25	120.85	1.93	4.87	5.86	1.98	100.00	40.35	1.64	18.26	37.90	42.81	1.03	0.89
4-1-76	140.65	1.98	4.76	5.54	2.10	100.00	41.13	1.86	17.71	37.71	43.43	1.16	0.87
4-2-19	141.58	2.25	3.52	6.70	2.30	100.00	22.22	5.14	20.10	46.81	29.12	3.97	1.61
5-1-25	149.75	2.06	4.08	5.70	2.16	100.00	25.08	1.25	20.15	46.35	32.55	0.96	1.42
5-1-88	150.38	2.21	3.77	6.43	2.21	100.00	21.79	1.29	21.13	48.34	29.49	1.03	1.64
5-2-25	151.25	1.98	4.06	6.50	2.19	100.00	24.91	1.88	20.63	45.92	32.03	1.42	1.43
7-1-18	168.97	2.37	3.43	5.20	1.86	100.00	18.73	25.69	16.82	42.69	22.39	18.10	1.91
7-1-130	170.09	1.35	2.58	3.68	1.72	100.00	25.49	2.96	13.73	48.95	34.93	2.39	1.40
7-2-20	170.50	0.86	2.29	2.52	0.77	100.00	21.75	2.26	11.78	53.59	32.63	2.00	1.64
7-3-29	172.08	1.55	3.07	4.05	1.98	100.00	23.79	2.12	16.19	49.27	32.82	1.72	1.50
7-4-60	173.90	2.35	3.29	5.82	2.35	100.00	20.63	5.32	19.32	48.44	27.98	4.25	1.73
8-1-68	179.20	2.23	5.36	5.99	1.95	100.00	47.34	0.00	18.37	35.10	46.53	0.00	0.75
9-1-147	189.67	2.61	4.66	6.64	2.27	100.00	36.74	7.21	19.11	37.66	38.75	4.48	0.97
9-2-28	190.00	1.84	3.20	5.22	1.80	100.00	19.07	2.88	18.74	51.38	27.44	2.44	1.87
9-2-135	191.07	1.94	4.00	6.23	2.49	100.00	21.21	7.78	20.29	46.28	27.49	5.94	1.68
9-3-16	191.37	1.63	4.05	5.44	2.03	100.00	19.47	6.68	20.02	48.32	26.34	5.33	1.83
10-1-134	198.75	1.91	4.34	5.54	1.96	100.00	23.82	2.09	20.63	46.65	31.11	1.61	1.50
10-2-129	200.20	2.06	4.53	5.92	2.06	100.00	24.33	4.25	21.04	45.08	30.71	3.16	1.47
10-3-59	201.00	2.00	4.05	5.50	2.45	100.00	18.72	12.92	19.72	46.21	24.22	9.85	1.91
10-4-59	202.50	2.12	3.90	6.06	2.41	100.00	16.74	5.38	21.79	50.21	23.54	4.46	2.13
10-4-130	203.21	1.78	4.20	4.76	1.37	100.00	29.98	4.82	17.69	42.89	36.00	3.41	1.19
11-1-27	207.08	1.78	4.58	3.61	1.88	100.00	16.75	9.61	20.56	48.81	22.89	7.74	2.13
11-2-26	208.58	2.02	4.62	6.88	2.16	100.00	21.72	2.21	23.05	46.79	28.46	1.71	1.64
11-2-130	209.62	2.01	2.96	5.73	2.01	100.00	25.42	4.95	16.98	46.29	32.95	3.78	1.40
11-3-33	210.12	1.87	3.72	6.19	1.61	100.00	18.49	2.35	21.19	50.63	26.21	1.96	1.93
11-4-9	211.40	2.17	3.40	4.89	2.13	100.00	31.64	4.75	16.18	42.67	37.80	3.34	1.13
13-1-32	226.12	1.48	3.16	5.55	1.60	100.00	17.76	4.61	18.57	51.75	25.74	3.94	2.01
13-1-125	227.05	1.26	2.52	3.86	1.22	100.00	17.45	2.43	15.29	55.42	27.08	2.22	2.05
13-2-40	227.70	1.16	2.77	3.42	0.92	100.00	19.10	1.74	15.09	54.30	29.04	1.56	1.87
14-1-54	235.66	2.35	3.80	6.60	1.67	100.00	17.84	5.74	21.90	48.99	24.47	4.64	2.00
15-1-9	244.60	1.66	3.37	5.84	1.58	100.00	19.88	6.00	18.80	49.04	27.30	4.86	1.80
16-1-48	254.69	1.62	4.25	5.49	1.90	100.00	24.92	5.35	19.30	45.18	31.53	3.99	1.43
16-1-126	255.47	1.49	2.60	4.63	1.35	100.00	32.13	5.48	13.28	43.57	39.20	3.94	1.11
17-2-48	265.38	2.82	2.76	6.99	2.49	100.00	22.21	11.71	18.33	44.99	27.98	8.69	1.61
17-2-130	266.20	4.10	2.70	7.10	2.49	100.00	24.47	10.78	19.27	43.33	29.69	7.71	1.46
17-3-74	267.13	2.97	2.59	6.06	2.59	100.00	33.31	10.52	15.31	40.21	37.50	6.98	1.07
17-4-83	268.74	1.81	2.64	4.30	2.24	100.00	28.18	6.18	14.61	45.16	35.63	4.60	1.27
19-1-98	283.49	1.85	3.16	5.21	1.94	100.00	35.28	3.47	15.05	41.54	41.03	2.38	1.01
19-1-135	283.86	2.26	2.88	6.29	2.15	100.00	19.04	2.26	19.57	51.22	27.30	1.91	1.88
19-2-49	284.50	1.19	3.61	3.73	2.14	100.00	16.53	4.04	18.98	52.97	24.52	3.53	2.16
19-3-9	285.59	1.97	3.86	6.21	2.11	100.00	21.04	4.46	20.56	47.78	28.15	3.52	1.70
20-1-62	288.52	1.73	3.89	5.88	1.65	100.00	17.85	4.20	21.02	50.33	25.16	3.49	2.00
20-1-130	289.20	1.73	3.13	4.22	1.28	100.00	25.59	1.62	16.11	48.13	34.48	1.29	1.40
20-2-45	289.87	2.15	3.16	5.33	1.93	100.00	16.45	3.50	19.76	52.84	24.34	3.05	2.17
21-CC-25	297.76	1.72	3.96	5.32	1.72	100.00	20.41	6.39	19.60	47.94	27.40	5.05	1.75
22-1-81	307.92	2.17	4.51	5.10	1.93	100.00	21.92	3.89	21.16	46.98	28.84	3.02	1.63
22-1-140	308.51	2.22	3.26	4.49	1.50	100.00	20.30	10.46	17.26	47.52	27.01	8.20	1.76
23-1-4	316.85	2.21	4.60	5.54	1.77	100.00	19.92	2.27	22.64	48.49	27.05	1.82	1.79
23-CC-5	317.37	1.85	2.67	4.77	1.55	100.00	20.24	2.07	16.79	51.98	29.46	1.78	1.76
24-1-143	327.84	1.24	4.26	5.32	1.66	100.00	15.36	7.79	20.93	50.73	21.82	6.52	2.33
24-2-22	328.13	1.14	2.97	4.35	1.54	100.00	23.47	4.00	15.26	49.18	32.32	3.25	1.52
24-2-70	328.61	2.22	4.58	6.69	2.12	100.00	27.10	4.73	21.12	42.94	32.58	3.35	1.32
24-3-29	329.70	1.60	4.06	5.29	2.03	100.00	20.02	4.65	20.05	48.83	27.37	3.75	1.78
24-3-114	330.55	2.30	2.34	4.77	1.67	100.00	18.68	2.49	16.84	53.17	27.81	2.18	1.91
25-1-27	336.27	1.92	3.79	5.73	1.92	100.00	25.17	3.66	19.00	45.89	32.34	2.77	1.42
25-1-34	336.34	2.05	4.70	6.12	1.82	100.00	20.14	1.68	23.21	48.24	27.21	1.34	1.77
25-2-16	337.67	1.59	3.51	5.18	1.63	100.00	24.39	5.03	17.51	46.71	31.90	3.88	1.46
25-2-108	338.58	2.70	4.09	6.30	2.30	100.00	17.84	3.94	23.03	49.20	24.57	3.20	2.00
25-3-114	340.15	1.34	3.82	4.69	1.78	100.00	22.15	7.40	17.71	47.23	29.29	5.77	1.61
25-3-135	340.36	2.07	3.82	6.77	2.07	100.00	20.60	6.48	20.85	47.01	27.11	5.03	1.73
25-4-113	341.63	2.80	5.70	7.87	2.63	100.00	28.23	7.87	23.90	39.63	31.32	5.15	1.27
25-4-124	341.75	1.29	2.50	5.00	1.40	100.00	23.27	5.59	14.73	48.90	31.86	4.51	1.53
27-CC-2	345.65	1.08	3.13	5.05	1.84	100.00	21.88	4.83	16.48	49.35	30.24	3.93	1.63

the Pliocene/Pleistocene boundary (1.66 Ma), defined by the first occurrence of *G. caribbeanica*, was placed between Samples 131-808C-50R-4, 59–60 cm, and -50R-6, 72–73 cm (Fig. 49, 777.06 ± 1.56 mbsf).

Pliocene

The sediments recovered from the Pliocene in Hole 808C contain poorly to moderately preserved nannofossil assemblages.

The last occurrence of *Discoaster brouweri* (1.89 Ma) between Samples 131-808C-51R-3, 85–86 cm, and -51R-5, 77–78 cm, marks the top of Zone NN18 of the Pliocene (Fig. 49, 785.42 ± 1.46 mbsf). Sample 131-808C-52R-5, 25–26 cm contained *D. brouweri* and Sample 131-808C-52R-CC, was barren of nannofossils. The nannofossil assemblage in Sample 131-808C-53R-CC, contained *D. brouweri*, *Discoaster pentaradiatus*, *Discoaster surculus*, and *Discoaster asymmetricus* and was thus assigned to Zones NN17-NN16 (Fig.

Table 7. X-ray mineralogy data for randomly oriented bulk powders, Hole 808C. Volcaniclastic samples from Unit V are included in Table 8. See Table 6 for complete explanation of column headings.

Core, section interval (cm)	Depth (mbsf)	I-Smec	I-Illite	I-(K + C)	I-Chlorite	I-Quartz	I-Plag	I-Calcite	%-Clay	%-Quartz	%-Plag	%-Calcite	Qtz/Plag
131-808C-													
1-1-98	299.48	1.71	3.09	5.27	1.58	100.00	18.97	3.03	18.3	51.6	27.4	2.6	1.88
1-1-133	299.83	2.90	4.51	8.06	3.09	100.00	21.98	8.69	23.5	43.5	26.8	6.2	1.62
1-2-15	300.15	0.00	3.86	7.68	0.00	100.00	18.93	80.06	12.4	30.7	16.3	40.6	1.89
2-1-38	308.38	2.40	4.38	6.08	1.99	100.00	25.00	3.96	21.1	44.7	31.3	2.9	1.43
2-1-66	308.66	2.07	3.73	5.55	1.63	100.00	22.06	3.12	19.7	48.1	29.7	2.5	1.62
3-1-15	317.75	2.43	2.96	5.02	1.30	100.00	19.89	8.53	17.6	48.5	27.0	6.8	1.80
3-1-109	318.69	2.20	4.48	6.37	1.53	100.00	19.05	2.98	23.2	48.5	25.9	2.4	1.87
4-1-130	328.50	1.60	3.04	4.62	1.31	100.00	21.45	0.23	17.2	51.6	31.0	0.2	1.67
4-2-43	329.13	1.73	2.79	3.98	1.38	100.00	16.27	2.34	17.1	55.5	25.3	2.1	2.20
5-CC-0	336.90	1.96	2.49	4.83	1.45	100.00	16.92	2.01	17.4	54.8	26.0	1.8	2.11
5-CC-36	337.26	1.92	3.28	5.07	1.62	100.00	19.26	1.27	19.1	51.8	28.0	1.1	1.85
6-1-84	347.44	2.23	3.95	4.91	1.68	100.00	18.79	0.00	21.4	51.5	27.1	0.0	1.90
6-2-40	348.50	2.42	3.27	5.96	2.42	100.00	24.19	0.00	19.4	48.1	32.6	0.0	1.48
6-3-20	349.80	3.10	6.25	7.40	2.52	100.00	26.76	0.00	26.6	42.0	31.4	0.0	1.33
6-3-100	360.60	1.00	2.03	3.18	1.58	100.00	18.89	1.66	12.9	56.0	29.6	1.5	1.89
6-3-108	350.68	2.40	3.75	5.62	1.71	100.00	37.96	2.45	16.8	39.6	42.1	1.6	0.94
7-1-8	356.28	1.53	3.51	5.05	1.78	100.00	27.16	0.00	17.4	46.9	35.7	0.0	1.31
7-1-55	356.75	2.36	4.46	5.19	1.83	100.00	20.74	0.00	22.4	49.1	28.5	0.0	1.72
8-1-93	366.83	1.28	2.02	3.83	1.12	100.00	28.29	0.00	12.1	49.1	38.9	0.0	1.26
8-2-114	368.54	2.15	2.96	4.90	1.42	100.00	25.09	4.11	16.6	47.1	33.1	3.2	1.42
8-2-126	368.66	1.90	2.26	5.01	1.45	100.00	17.85	3.83	16.3	53.5	26.8	3.4	2.00
8-2-127	368.67	2.08	3.05	5.62	2.14	100.00	19.07	4.42	18.8	50.5	27.0	3.7	1.87
9-1-58	376.18	3.49	1.25	4.33	2.52	100.00	33.82	4.16	13.1	43.1	40.8	3.0	1.06
9-1-120	376.80	3.20	1.83	6.43	2.43	100.00	30.35	8.59	15.0	42.7	36.3	6.1	1.18
10-1-72	385.92	1.38	2.47	3.74	1.58	100.00	23.45	5.28	13.6	49.6	32.5	4.3	1.52
10-1-103	386.23	1.89	2.66	5.38	1.56	100.00	18.52	3.94	17.6	52.1	27.0	3.4	1.93
10-2-108	387.78	1.62	2.99	4.18	0.00	100.00	22.40	5.49	15.8	49.0	30.7	4.4	1.59
10-2-130	388.00	2.39	3.45	4.75	1.64	100.00	20.48	5.05	18.9	49.0	28.1	4.1	1.74
10-3-91	389.12	2.11	3.00	5.19	2.01	100.00	22.37	3.92	17.6	48.8	30.5	3.2	1.60
11-1-13	394.93	1.94	3.76	6.19	1.76	100.00	16.37	3.39	21.8	51.6	23.7	2.9	2.18
11-2-50	396.80	2.21	2.72	5.60	2.54	100.00	31.26	3.47	15.5	43.7	38.3	2.5	1.14
11-2-51	396.81	2.37	3.63	5.96	2.02	100.00	24.34	4.58	19.4	45.9	31.3	3.5	1.47
12-1-19	404.79	1.94	3.18	5.22	0.00	100.00	17.22	4.04	19.1	52.2	25.2	3.5	2.07
12-1-130	405.90	2.00	4.11	5.22	2.16	100.00	18.25	4.00	21.2	50.0	25.5	3.3	1.96
12-2-43	406.53	1.77	2.62	3.84	1.81	100.00	17.56	4.39	16.1	53.6	26.4	3.9	2.03
12-3-131	408.91	2.68	4.65	7.06	2.99	100.00	21.25	3.32	23.9	46.1	27.4	2.5	1.68
12-4-26	409.36	1.99	2.27	5.19	2.39	100.00	36.28	6.49	12.9	41.0	41.7	4.4	0.98
13-1-97	415.27	2.15	2.31	3.29	1.51	100.00	32.86	6.20	12.1	43.5	40.0	4.4	1.09
13-2-135	417.15	2.34	2.65	5.45	1.31	100.00	20.33	4.45	17.6	50.1	28.5	3.7	1.76
13-3-2	417.32	2.20	3.18	5.86	2.37	100.00	21.65	4.98	18.7	48.1	29.2	4.0	1.65
14-1-70	424.70	1.96	3.28	5.46	1.61	100.00	21.01	2.63	18.8	49.7	29.3	2.2	1.70
14-1-101	425.01	2.50	4.85	6.01	2.97	100.00	21.33	4.47	23.5	45.8	27.3	3.4	1.67
14-3-131	429.36	2.50	4.89	6.51	2.29	100.00	21.24	4.16	23.6	45.9	27.3	3.2	1.68
15-1-47	434.17	2.38	4.03	5.47	1.99	100.00	24.59	3.21	20.0	45.9	31.6	2.4	1.45
15-1-130	435.00	2.68	4.93	6.92	2.19	100.00	21.29	2.84	24.5	46.0	27.4	2.2	1.68
15-3-62	437.32	1.66	2.34	3.86	0.00	100.00	16.49	0.00	15.9	57.5	26.6	0.0	2.17
15-4-115	439.35	1.74	3.08	4.31	1.52	100.00	31.06	3.14	14.8	44.3	38.6	2.3	1.15
15-4-116	439.36	1.84	2.76	4.72	1.84	100.00	26.29	2.35	15.6	47.6	35.0	1.8	1.36
16-2-130	445.80	2.23	3.96	6.11	2.13	100.00	21.10	3.45	21.2	47.9	28.3	2.7	1.69
16-4-127	448.77	1.41	2.77	5.18	1.71	100.00	16.68	2.77	17.7	54.4	25.4	2.5	2.14
17-1-77	453.47	2.84	3.08	6.48	0.00	100.00	21.71	62.74	13.6	32.7	19.9	33.8	1.65
17-4-130	458.46	2.15	3.25	5.45	2.10	100.00	18.21	3.73	19.6	51.2	26.1	3.2	1.96
17-5-10	458.80	1.53	3.14	5.11	1.45	100.00	20.84	3.19	17.6	50.4	29.4	2.7	1.71
18-2-41	464.31	2.35	4.59	6.60	2.35	100.00	20.98	3.11	23.2	46.9	27.5	2.4	1.70
18-3-130	466.70	2.73	3.44	5.39	1.92	100.00	19.71	6.77	19.8	48.2	26.6	5.4	1.81
19-2-127	474.77	2.64	3.50	5.57	2.06	100.00	19.41	2.21	20.8	50.1	27.2	1.8	1.84
19-3-89	475.89	2.04	3.52	5.32	1.85	100.00	20.03	1.62	19.8	50.5	28.3	1.4	1.78
19-3-133	476.33	1.43	1.43	4.15	0.00	100.00	19.46	0.49	12.5	56.3	30.7	0.5	1.84
20-4-120	487.40	1.44	3.35	4.40	1.44	100.00	20.45	0.00	17.9	52.2	29.9	0.0	1.75
20-4-132	487.52	2.51	3.64	5.91	1.96	100.00	18.69	1.92	21.5	50.5	26.4	1.6	1.91
21-1-82	492.12	1.51	2.96	4.40	0.41	100.00	20.32	0.00	17.0	52.9	30.1	0.0	1.76
21-1-120	492.50	2.85	5.67	7.36	2.15	100.00	46.00	0.93	20.4	34.5	44.5	0.5	0.78
22-1-65	501.65	1.44	3.39	4.43	1.86	100.00	20.31	0.00	18.1	52.2	29.7	0.0	1.76
22-3-130	505.30	2.31	3.11	4.99	1.71	100.00	20.27	2.15	18.7	50.7	28.8	1.8	1.76
23-1-22	510.92	1.64	3.11	4.98	1.96	100.00	18.71	2.06	18.3	52.5	27.5	1.8	1.91
23-1-130	512.00	1.64	2.51	3.84	1.57	100.00	19.93	1.49	15.3	53.5	29.9	1.3	1.79
23-2-143	513.63	2.66	3.34	5.02	1.53	100.00	26.64	3.15	17.9	45.6	34.0	2.4	1.34
24-2-145	523.25	1.34	2.90	4.48	1.38	100.00	20.81	0.00	16.6	52.7	30.7	0.0	1.72
24-3-107	524.37	1.56	2.93	4.29	0.00	100.00	16.75	0.00	17.8	55.9	26.2	0.0	2.13
24-4-0	524.80	1.61	2.70	4.40	1.49	100.00	18.99	0.00	16.8	54.3	28.9	0.0	1.88
24-4-100	525.80	1.51	3.02	4.19	1.71	100.00	20.32	1.96	16.7	52.0	29.6	1.7	1.76
25-1-50	530.50	1.34	2.91	3.12	1.52	100.00	14.95	0.24	16.9	58.4	24.4	0.2	2.39
25-2-0	531.50	2.96	5.62	7.68	2.73	100.00	20.47	4.64	26.6	44.5	25.5	3.4	1.74
25-2-49	531.99	1.70	3.45	4.95	1.75	100.00	23.68	2.97	17.7	48.0	31.9	2.4	1.51

Table 7 (continued).

Core, section interval (cm)	Depth (mbsf)	I-Smec	I-Illite	I-(K + C)	I-Chlorite	I-Quartz	I-Plag	I-Calcite	%-Clay	%-Quartz	%-Plag	%-Calcite	Qtz/Plag
25-2-88	532.38	1.69	2.89	5.68	2.01	100.00	19.65	2.72	18.1	51.4	28.3	2.3	1.82
25-3-79	533.79	1.54	2.74	4.02	1.15	100.00	13.96	4.21	17.1	56.8	22.2	3.9	2.56
26-1-11	539.81	1.95	4.16	6.01	2.31	100.00	27.85	6.82	19.0	42.8	33.4	4.8	1.28
26-2-108	542.28	1.06	2.23	3.43	1.39	100.00	20.32	1.69	13.2	54.4	30.9	1.5	1.76
26-3-92	543.62	1.65	3.31	4.75	1.61	100.00	17.65	0.66	19.1	53.8	26.6	0.6	2.02
26-3-130	543.90	2.05	2.63	4.13	1.43	100.00	15.25	2.53	17.5	56.1	24.0	2.3	2.34
26-4-115	545.35	1.60	3.80	4.42	1.87	100.00	19.15	4.00	19.0	50.6	27.1	3.3	1.86
26-5-140	547.10	1.79	4.32	5.76	1.62	100.00	16.08	4.25	22.5	50.9	22.9	3.6	2.22
27-1-94	550.24	1.63	4.34	5.38	1.74	100.00	16.22	1.67	22.5	52.3	23.8	1.4	2.20
27-2-107	551.87	1.65	3.86	5.54	1.65	100.00	18.12	1.17	21.0	51.7	26.3	1.0	1.97
27-3-90	553.20	1.40	3.85	4.82	1.21	100.00	21.86	0.00	19.1	50.2	30.7	0.0	1.63
27-4-114	554.94	2.29	4.27	5.72	1.76	100.00	20.34	2.73	21.9	48.4	27.5	2.2	1.76
27.5-112	556.42	1.89	4.56	5.07	1.38	100.00	20.43	0.00	22.0	49.6	28.4	0.0	1.75
27-5-123	556.53	2.08	2.08	4.67	0.00	100.00	29.02	0.00	13.9	47.5	38.6	0.0	1.23
27-5-124	556.54	3.94	2.44	6.16	0.00	100.00	24.88	0.00	19.2	47.6	33.2	0.0	1.44
28-1-50	559.40	1.95	4.22	5.53	2.26	100.00	14.87	0.00	23.5	54.0	22.5	0.0	2.40
28-2-18	560.58	1.83	3.76	4.81	1.78	100.00	17.62	0.00	20.7	53.1	26.2	0.0	2.03
28-2-124	561.64	2.21	3.73	5.41	1.60	100.00	15.15	0.26	22.4	54.3	23.1	0.2	2.36
28-3-143	563.33	1.66	3.48	4.35	1.41	100.00	17.67	0.00	19.3	54.0	26.7	0.0	2.02
28-4-106	564.46	1.59	2.96	4.33	1.07	100.00	17.34	2.13	17.5	54.2	26.3	1.9	2.06
28-4-110	565.50	1.85	3.31	4.96	1.40	100.00	20.30	6.38	17.9	49.0	27.9	5.2	1.76
28-4-111	565.51	1.75	2.63	5.10	0.00	100.00	26.16	5.59	15.1	46.5	34.1	4.3	1.37
28-5-141	566.31	1.66	3.50	4.77	1.45	100.00	17.99	50.55	13.6	37.0	18.6	30.8	1.99
29-2-59	570.69	1.34	2.53	3.88	1.34	100.00	17.68	3.38	15.3	54.6	27.0	3.0	2.02
29-3-31	571.91	1.86	3.10	4.66	1.57	100.00	30.51	3.87	15.3	44.2	37.7	2.8	1.17
29-4-41	573.51	2.40	4.20	6.09	1.84	100.00	16.78	2.30	23.4	50.8	23.9	1.9	2.13
29-5-131	575.91	1.75	3.29	4.94	1.54	100.00	18.89	0.00	19.1	52.9	28.0	0.0	1.89
29-6-118	577.28	1.59	3.63	4.89	0.00	100.00	18.79	0.00	19.7	52.6	27.7	0.0	1.90
29-6-125	575.88	2.23	3.39	5.01	1.76	100.00	17.88	2.59	19.9	51.9	26.0	2.2	2.00
29-7-109	578.69	1.56	3.63	5.57	1.60	100.00	23.26	5.42	18.3	46.9	30.6	4.2	1.54
30-1-115	579.45	1.81	3.35	4.80	1.41	100.00	17.33	0.00	19.7	54.1	26.2	0.0	2.06
30-2-104	580.84	1.15	3.07	3.76	0.00	100.00	20.76	9.06	14.9	49.2	28.6	7.3	1.72
30-3-113	582.43	1.75	2.86	4.39	0.00	100.00	17.72	9.88	16.3	50.5	25.0	8.2	2.02
30-3-125	582.55	1.70	1.94	3.11	1.32	100.00	20.30	3.70	12.7	53.6	30.4	3.3	1.76
30-4-50	583.30	1.28	2.37	3.45	1.18	100.00	14.84	3.86	14.9	57.6	23.9	3.7	2.41
30-5-101	585.31	1.27	3.42	4.30	1.53	100.00	20.85	6.21	16.8	49.4	28.8	5.1	1.71
30-6-104	586.84	1.65	4.46	4.97	1.56	100.00	15.49	3.58	22.3	52.0	22.6	3.1	2.31
31-1-25	587.85	1.79	4.64	5.57	1.47	100.00	19.10	0.00	23.0	50.2	26.8	0.0	1.87
31-2-0	589.10	2.31	3.65	5.23	1.55	100.00	18.20	1.12	21.0	51.7	26.3	1.0	1.96
31-2-34	589.44	1.48	3.70	4.34	1.26	100.00	16.18	3.34	19.4	53.4	24.2	2.9	2.21
32-2-71	599.51	1.96	3.67	4.00	1.87	100.00	18.12	0.00	19.8	53.2	27.0	0.0	1.97
32-3-125	601.55	1.72	2.45	4.57	1.39	100.00	19.90	10.78	14.8	49.1	27.4	8.7	1.79
33-2-18	608.58	1.95	3.67	5.62	1.77	100.00	19.21	4.32	20.1	49.6	26.7	3.5	1.86
33-4-0	611.40	4.03	4.97	6.80	2.49	100.00	27.01	15.70	22.1	38.6	29.2	10.0	1.32
34-1-56	617.06	0.93	2.74	3.64	1.57	100.00	18.41	20.83	12.9	46.9	24.2	16.1	1.94
34-2-125	619.25	2.32	3.57	4.91	2.20	100.00	28.49	2.75	17.6	44.7	35.7	2.0	1.25
35-1-10	626.30	2.26	2.40	4.42	0.00	100.00	19.97	37.02	12.5	40.3	22.5	24.6	1.79
35-4-132	632.02	2.36	2.42	3.57	0.00	100.00	20.78	2.64	15.4	52.0	30.3	2.3	1.72
35-5-84	633.05	2.09	2.58	3.05	0.00	100.00	18.99	0.00	15.7	55.0	29.3	0.0	1.88
36-2-103	638.43	1.99	4.63	5.10	1.61	100.00	24.56	7.86	19.9	44.1	30.3	5.7	1.45
36-2-125	638.65	1.69	3.86	4.05	1.64	100.00	32.65	5.02	15.8	42.2	38.6	3.5	1.09
37-1-45	645.95	1.79	5.55	4.63	2.28	100.00	18.83	0.00	24.6	49.3	26.0	0.0	1.90
37-2-0	647.00	2.34	2.29	4.36	1.13	100.00	16.14	13.34	15.5	50.6	22.9	11.1	2.21
38-2-93	657.33	1.75	4.40	5.06	1.59	100.00	15.49	6.29	21.9	50.8	22.0	5.3	2.31
38-4-125	660.65	1.73	2.96	4.21	0.00	100.00	17.29	0.32	17.9	55.1	26.7	0.3	2.07
39-1-40	664.90	1.51	4.06	3.91	0.00	100.00	32.03	20.80	14.4	38.2	34.3	13.1	1.12
39-3-130	668.80	1.93	4.63	5.15	0.00	100.00	17.37	40.20	17.4	38.4	18.7	25.5	2.06
40-2-10	675.80	1.54	3.92	4.93	1.80	100.00	17.64	0.00	20.8	53.0	26.2	0.0	2.02
40-2-125	676.95	2.34	3.50	5.48	1.41	100.00	28.97	1.96	18.0	44.5	36.1	1.4	1.23
41-1-97	684.77	1.70	4.97	4.10	0.00	100.00	20.66	18.24	19.0	43.1	24.9	13.0	1.73
41-1-123	685.03	2.03	4.12	5.65	1.73	100.00	15.88	46.25	16.5	37.8	16.8	28.9	2.25
42-3-55	697.05	2.06	3.44	3.58	0.00	100.00	16.44	9.67	17.7	50.8	23.4	8.1	2.17
42-3-125	697.75	2.39	3.82	4.03	0.00	100.00	16.69	23.69	17.4	44.4	20.8	17.4	2.14
42-5-108	700.58	1.93	2.24	3.10	0.00	100.00	20.31	23.27	11.8	45.2	25.7	17.3	1.76
43-2-69	705.39	1.0	3.18	3.57	0.00	100.00	13.14	0.42	18.1	59.6	21.9	0.4	2.72
43-5-0	709.20	1.31	2.47	3.65	1.52	100.00	14.20	14.88	14.1	52.3	20.8	12.8	2.52
44-4-23	717.13	1.18	2.90	3.65	1.10	100.00	15.94	14.60	14.7	50.5	22.6	12.2	2.24
44-4-123	718.13	3.48	7.73	8.12	2.31	100.00	20.01	27.93	27.1	36.1	20.2	16.6	1.78
45-3-115	726.15	1.87	3.05	3.82	0.00	100.00	14.23	7.86	17.5	54.0	21.5	7.0	2.51
45-4-125	727.75	1.45	2.26	2.97	1.12	100.00	14.30	15.90	12.9	52.4	21.0	13.7	2.50
46-2-32	733.52	1.66	4.09	4.16	0.00	100.00	19.79	30.21	15.9	41.0	22.7	20.4	1.80
46-2-125	734.45	2.12	2.80	4.92	1.40	100.00	16.88	34.06	14.4	42.1	19.9	23.6	2.12
47-1-24	741.64	1.61	3.06	4.00	0.00	100.00	16.58	20.57	15.1	47.0	21.8	16.0	2.15
47-3-99	745.39	1.41	3.62	3.55	0.00	100.00	15.42	12.31	17.2	50.7	21.9	10.3	2.32
47-3-125	745.75	1.28	5.12	3.79	1.28	100.00	16.21	19.66	19.5	45.3	20.5	14.7	2.20
48-1-93	752.03	2.07	4.83	4.27	1.38	100.00	16.13	0.28	23.5	52.5	23.7	0.2	2.21
48-3-125	755.35	2.64	2.70	3.94	0.00	100.00	17.39	0.00	18.2	55.0	26.8	0.0	2.05

Table 7 (continued).

Core, section interval (cm)	Depth (mbsf)	I-Smec	I-Illite	I-(K + C)	I-Chlorite	I-Quartz	I-Plag	I-Calcite	%-Clay	%-Quartz	%-Plag	%-Calcite	Qtz/Plag
49-1-75	761.45	1.42	4.19	3.75	1.42	100.00	17.16	11.97	18.4	48.6	23.4	9.6	2.08
49-2-125	763.45	2.28	4.35	5.44	1.73	100.00	17.95	0.28	23.1	51.0	25.7	0.2	1.99
50-3-53	773.93	2.12	4.42	4.42	1.39	100.00	17.85	10.07	20.4	47.8	23.9	7.9	2.00
50-5-125	776.87	1.34	1.94	3.41	0.00	100.00	16.35	4.61	13.2	56.6	25.9	4.3	2.18
51-1-50	780.60	1.49	3.36	3.85	1.32	100.00	19.10	14.98	15.7	47.3	25.3	11.7	1.87
51-2-119	782.79	1.66	3.57	3.70	1.33	100.00	24.01	4.23	16.6	47.9	32.2	3.3	1.49
51-3-114	784.24	1.30	4.02	2.92	0.00	100.00	18.34	43.94	13.4	38.7	19.9	28.1	1.95
51-4-91	785.51	1.65	5.00	3.96	0.00	100.00	19.53	1.89	21.7	49.6	27.1	1.5	1.83
51-4-120	785.80	1.74	5.28	3.56	1.09	100.00	54.91	16.95	13.7	30.6	47.1	8.6	0.65
51-5-105	787.15	1.65	3.52	3.39	0.00	100.00	13.93	15.23	17.0	50.5	19.7	12.7	2.56
51-6-122	788.82	1.21	3.30	3.57	0.00	100.00	15.85	10.55	16.3	51.7	23.0	9.0	2.25
52-1-61	790.41	0.00	3.76	2.84	0.00	100.00	21.98	0.00	15.2	52.5	32.3	0.0	1.62
52-2-3	791.33	0.65	3.49	2.83	0.00	100.00	18.97	19.13	13.7	46.7	24.8	14.8	1.88
52-3-18	792.98	1.61	4.96	4.22	1.52	100.00	15.38	15.24	20.8	47.1	20.3	11.8	2.32
52-4-137	795.67	1.75	4.91	4.13	0.00	100.00	14.83	0.00	23.7	53.9	22.4	0.0	2.41
52-5-25	796.05	1.98	3.94	4.01	0.00	100.00	23.40	0.33	18.9	48.9	32.0	0.3	1.53
52-5-120	797.00	1.75	2.76	3.38	0.00	100.00	15.00	34.31	12.7	43.3	19.4	24.5	2.23
52-6-36	797.66	1.09	4.35	3.57	0.00	100.00	14.66	0.00	21.1	56.0	23.0	0.0	2.44
51-1-17	799.57	1.42	4.79	4.10	0.00	100.00	22.45	2.36	20.2	47.9	30.1	1.9	1.59
53-2-32	801.22	1.43	5.18	3.91	0.00	100.00	15.94	23.71	19.4	43.9	19.6	17.2	2.24
53-3-114	803.54	1.15	3.95	3.72	0.00	100.00	17.89	17.24	16.6	46.7	23.4	13.3	2.00
53-4-115	805.05	1.64	4.40	3.97	0.00	100.00	15.34	17.01	19.1	47.3	20.3	13.3	2.33
53-4-120	805.10	1.81	4.94	4.62	1.57	100.00	14.30	21.38	20.6	45.3	18.1	16.0	2.50
53-5-125	806.65	1.91	4.49	3.96	0.00	100.00	16.87	24.72	18.1	43.6	20.6	17.8	2.12
53-6-26	807.16	1.59	3.69	2.76	0.00	100.00	19.54	8.64	16.4	49.5	27.1	7.1	1.83
54-1-135	810.45	1.33	3.85	2.91	0.00	100.00	32.41	1.43	14.8	44.1	40.0	1.0	1.10
54-2-31	810.91	1.84	4.11	4.48	0.00	100.00	25.98	3.49	18.4	45.7	33.3	2.6	1.37
54-2-120	811.80	2.38	3.59	2.85	1.72	100.00	21.58	5.35	18.0	48.4	29.3	4.3	1.65
54-3-87	812.97	0.78	2.73	2.73	0.00	100.00	17.35	15.23	12.5	50.4	24.5	12.7	2.06
54-4-79	814.39	1.35	2.98	3.29	0.00	100.00	15.83	23.44	13.8	47.1	20.9	18.2	2.26
54-4-100	814.60	1.81	2.75	4.10	0.00	100.00	19.34	12.92	15.1	48.4	26.2	10.3	1.85
54-4-101	814.61	1.91	2.33	3.35	0.00	100.00	29.40	16.90	11.5	42.1	34.7	11.7	1.21
54-5-122	816.32	1.40	3.39	3.64	1.28	100.00	12.95	15.76	16.8	51.3	18.6	13.3	2.76
54-6-121	817.81	1.47	3.25	3.65	1.27	100.00	23.25	11.51	14.9	46.3	30.1	8.8	1.54
55-1-100	819.70	1.80	3.54	4.23	1.36	100.00	14.03	13.51	18.3	50.5	19.9	11.3	2.55
55-2-114	821.34	1.07	5.65	3.72	1.11	100.00	13.11	13.81	22.2	48.8	17.9	11.1	2.72
55-2-120	821.40	2.17	4.81	5.87	1.63	100.00	16.61	12.50	22.5	46.4	21.6	9.6	2.15
55-3-115	822.85	1.05	3.32	2.95	0.00	100.00	15.94	0.31	17.0	57.2	25.5	0.3	2.24
55-4-124	824.44	0.86	2.38	3.22	0.94	100.00	27.72	0.00	11.9	49.6	38.5	0.0	1.29
55-5-93	825.63	1.12	2.99	3.04	0.00	100.00	14.21	3.32	16.2	57.7	22.9	3.2	2.51
56-1-55	828.95	1.83	3.52	3.71	0.00	100.00	16.65	15.94	16.8	48.1	22.4	12.7	2.15
56-2-13	830.03	1.23	3.01	2.89	0.00	100.00	13.16	3.12	16.6	58.7	21.6	3.0	2.71
56-3-113	832.56	1.46	2.41	3.01	0.00	100.00	13.59	1.15	15.5	60.4	23.0	1.1	2.63
56-4-50	833.40	1.90	4.10	4.30	1.18	100.00	18.37	1.90	20.5	51.4	26.4	1.6	1.94
56-4-120	834.10	0.93	2.49	3.59	1.17	100.00	12.87	4.88	15.2	58.9	21.2	4.7	2.78
57-1-34	838.44	1.45	4.68	4.96	1.45	100.00	17.19	0.00	22.7	52.2	25.1	0.0	2.08
57-2-108	840.68	1.16	3.57	3.57	1.06	100.00	12.37	0.24	19.6	59.5	20.6	0.2	2.89
57-2-120	840.80	2.10	5.06	5.27	2.01	100.00	22.0	2.67	22.6	46.6	28.8	2.1	1.62
57-3-109	842.19	1.49	3.86	3.66	1.22	100.00	18.98	0.00	19.0	52.9	28.1	0.0	1.88
57-4-80	843.40	1.64	2.97	3.75	0.00	100.00	20.39	0.88	16.4	52.7	30.1	0.8	1.75
57-5-103	845.13	1.58	2.45	3.52	1.06	100.00	14.45	11.40	14.7	53.6	21.7	10.1	2.47
58-1-149	848.89	1.55	3.47	3.64	1.34	100.00	13.09	5.99	18.7	55.5	20.3	5.5	2.73
58-2-72	849.62	1.78	3.97	3.91	1.69	100.00	27.60	1.87	17.4	45.8	35.4	1.4	1.29
58-3-109	851.49	1.49	2.85	3.30	0.00	100.00	21.14	10.34	14.1	48.7	28.8	8.3	1.69
58-3-115	851.55	1.59	2.33	3.64	1.27	94.76	100.00	8.14	6.5	22.8	67.4	3.2	0.34
58-4-99	852.89	0.78	1.94	3.17	0.95	100.00	17.86	1.69	12.1	57.5	28.8	1.6	2.00
58-5-11	853.51	1.76	3.66	3.99	1.30	100.00	17.18	4.83	18.8	52.0	25.0	4.1	2.08
59-2-63	859.23	1.44	3.85	4.10	1.36	100.00	18.87	5.99	18.4	50.2	26.5	5.0	1.89
59-2-115	859.75	1.71	3.42	4.95	1.76	100.00	17.55	13.32	17.7	48.1	23.6	10.6	2.04
60-1-13	866.93	1.27	3.16	3.28	0.00	100.00	11.92	0.65	18.3	60.8	20.3	0.7	3.00
60-4-116	872.46	1.45	2.98	3.71	0.00	100.00	13.70	4.96	17.3	56.5	21.7	4.6	2.61
61-2-22	878.23	1.98	3.43	3.61	1.32	100.00	14.94	4.25	18.9	54.5	22.8	3.8	2.39
61-2-115	879.15	1.26	3.00	3.78	1.07	100.00	14.21	1.20	17.6	58.1	23.1	1.2	2.51
62-3-4	889.14	1.14	2.89	4.25	1.18	100.00	15.26	2.42	17.1	56.5	24.1	2.3	2.34
62-3-5	889.15	1.37	2.80	3.94	1.30	100.00	16.92	2.75	16.4	55.0	26.1	2.5	2.11
62-3-150	890.60	1.88	4.94	4.27	1.16	100.00	13.67	0.00	24.5	54.6	20.9	0.0	2.61
63-1-5	895.85	1.35	3.21	3.21	1.31	100.00	15.97	0.00	17.4	57.1	25.5	0.0	2.24
63-1-56	896.36	1.47	3.24	4.05	1.51	100.00	15.82	1.20	18.4	55.8	24.7	1.1	2.26
64-1-114	906.64	0.49	2.90	3.17	1.06	100.00	11.08	1.00	16.4	63.0	19.6	1.0	3.22
64-1-115	906.65	1.25	2.64	2.97	1.52	100.00	13.77	1.95	16.1	59.2	22.8	1.9	2.59
64-3-36	908.86	0.92	3.58	3.52	0.00	100.00	14.06	2.67	18.3	56.8	22.4	2.5	2.54
65-1-111	916.21	1.30	4.09	4.64	1.34	100.00	11.07	2.50	22.3	57.5	17.8	2.4	3.23
65-2-0	916.60	1.70	3.68	4.92	1.39	100.00	17.85	1.35	20.1	52.5	26.2	1.2	2.00
65-2-37	916.97	1.22	3.10	3.94	1.18	100.00	14.97	3.42	17.4	56.0	23.5	3.2	2.39
66-1-23	925.03	1.45	4.20	4.20	1.30	100.00	13.99	1.87	21.5	55.2	21.6	1.7	2.55
66-2-112	927.42	1.41	4.48	5.12	1.38	100.00	12.26	0.00	24.1	56.5	19.4	0.0	2.91
66-2-114	927.44	1.07	2.92	3.50	1.44	100.00	15.02	0.00	16.8	58.6	24.6	0.0	2.38

Table 7 (continued).

Core, section interval (cm)	Depth (mbsf)	I-Smec	I-Illite	I-(K + C)	I-Chlorite	I-Quartz	I-Plag	I-Calcite	%-Clay	%-Quartz	%-Plag	%-Calcite	Qtz/Plag
66-2-115	927.45	1.83	5.36	5.29	1.59	100.00	13.12	0.57	26.5	53.4	19.6	0.5	2.72
66-3-23	928.04	1.20	4.03	4.47	1.49	100.00	15.83	2.49	20.3	53.7	23.8	2.2	2.26
66-4-71	930.01	0.95	4.37	4.70	1.38	100.00	11.49	0.83	22.9	57.7	18.6	0.8	3.11
67-1-146	935.96	1.32	3.18	3.97	1.14	100.00	18.87	5.68	16.5	51.5	27.2	4.8	1.89
67-2-4	936.04	0.00	4.01	3.30	1.36	100.00	10.43	0.00	19.6	62.2	18.2	0.0	3.42
68-1-5	944.25	2.25	3.96	4.48	1.51	100.00	15.26	5.27	21.1	52.1	22.3	4.5	2.34
68-1-43	944.64	1.37	4.87	4.36	0.99	100.00	12.43	0.00	24.2	56.2	19.6	0.0	2.87
68-1-89	945.10	1.15	3.79	4.19	1.12	100.00	14.40	4.39	19.4	54.6	22.0	4.0	2.48
69-1-0	953.80	1.64	3.05	4.52	0.00	100.00	15.57	7.40	17.6	52.9	23.0	6.5	2.29
69-1-5	953.85	1.86	2.53	2.94	0.00	100.00	11.38	30.91	13.0	47.6	15.2	24.3	3.14
69-1-145	955.25	2.09	3.26	4.77	0.00	100.00	14.76	1.77	20.2	55.3	22.9	1.6	2.42
69-2-110	956.41	1.55	3.09	3.99	1.33	100.00	14.65	18.52	15.8	49.1	20.1	15.0	2.44
69-4-66	958.96	1.41	3.26	5.20	1.36	100.00	14.27	1.73	19.9	56.1	22.4	1.6	2.50
69-5-52	960.32	0.00	3.03	3.38	0.00	100.00	12.83	51.02	10.5	40.7	14.6	34.2	2.78
70-1-31	963.71	1.82	3.50	4.68	1.41	100.00	14.11	18.15	17.9	48.4	19.1	14.5	2.53
70-1-33	963.73	1.52	2.69	4.32	0.00	100.00	11.62	13.70	16.4	53.9	17.5	12.2	3.07
70-1-35	963.75	1.08	3.99	4.33	1.23	100.00	13.38	16.08	18.4	49.8	18.6	13.2	2.67
70-1-113	964.53	1.33	2.69	4.61	0.00	100.00	12.43	7.41	17.2	56.3	19.6	6.9	2.87
70-2-140	966.30	1.15	2.90	3.51	0.00	100.00	11.61	10.26	16.1	56.1	18.2	9.5	3.08
70-3-10	966.50	1.48	4.08	4.42	0.00	100.00	12.23	1.17	22.2	57.1	1.1	2.9	
70-4-0	967.90	1.45	3.18	4.58	1.33	100.00	13.82	6.57	18.4	54.6	21.1	5.9	2.58
70-4-39	968.29	1.57	3.29	4.98	1.23	100.00	12.02	0.00	21.1	59.1	19.9	0.0	2.97
71-1-31	973.41	1.69	3.56	4.33	0.00	100.00	13.57	25.54	16.7	46.2	17.6	19.5	2.63
71-2-112	975.72	1.33	3.29	3.93	1.10	100.00	12.79	13.28	17.1	52.5	18.8	11.5	2.79
71-2-120	975.80	1.45	3.30	3.78	1.13	100.00	13.55	24.68	15.5	47.3	18.0	19.3	2.64
71-3-91	977.01	1.26	2.75	3.81	1.06	100.00	10.11	4.24	17.6	60.9	17.2	4.3	3.53
71-3-105	977.15	1.30	2.16	3.64	0.00	100.00	11.54	30.24	12.1	48.2	15.6	24.1	3.09
71-4-58	978.18	1.08	2.22	3.27	0.00	100.00	10.78	16.78	13.2	55.0	16.6	15.2	3.31
72-1-42	983.22	1.82	3.11	4.04	1.32	100.00	16.90	0.00	18.4	55.4	26.2	0.0	2.11
72-2-44	984.74	1.00	2.47	3.35	0.00	100.00	13.41	13.03	13.8	54.2	20.4	11.7	2.66
72-3-0	985.80	1.46	2.91	3.69	0.00	100.00	15.01	8.39	16.2	53.8	22.6	7.4	2.38
72-3-124	987.04	1.23	2.94	3.14	0.00	100.00	16.74	0.00	16.2	57.1	26.7	0.0	2.13
72-4-60	987.87	1.14	3.72	3.54	1.64	100.00	15.69	0.00	19.0	56.2	24.7	0.0	2.28
73-2-43	994.03	1.05	2.45	3.37	0.00	100.00	13.62	7.20	14.5	57.0	21.7	6.8	2.62
73-5-115	999.25	1.89	3.46	4.56	1.55	100.00	14.34	5.06	19.8	54.0	21.7	4.5	2.49
74-2-13	1003.43	1.10	3.19	3.81	1.10	100.00	13.24	0.00	18.5	59.5	22.1	0.0	2.70
74-2-77	1004.07	1.25	2.24	3.28	0.00	100.00	12.56	2.53	15.0	61.0	21.5	2.5	2.84
75-1-116	1012.46	1.38	2.61	4.21	0.00	100.00	12.93	0.00	17.7	60.4	21.9	0.0	2.76
75-1-117	1012.47	1.54	2.90	3.62	1.12	100.00	13.10	0.00	18.1	59.9	22.0	0.0	2.73
75-2-60	1013.35	1.22	3.28	4.00	1.26	100.00	13.49	0.00	19.0	58.8	22.2	0.0	2.65
75-2-115	1013.90	1.00	2.55	3.77	0.97	100.00	11.64	0.00	16.8	62.7	20.4	0.0	3.07
76-2-115	1023.15	0.99	2.25	3.76	0.95	100.00	14.28	0.00	15.1	60.6	24.2	0.0	2.50
76-5-143	1027.93	0.85	3.31	3.42	0.00	100.00	12.89	0.00	18.1	60.2	21.7	0.0	2.77
77-3-6	1032.96	0.92	3.32	3.61	0.00	100.00	15.69	0.00	17.6	57.2	25.1	0.0	2.28
77-4-0	1034.40	1.26	1.89	4.04	1.33	100.00	13.24	0.00	15.0	62.0	23.0	0.0	2.70
77-4-1	1034.41	0.98	2.15	3.25	0.95	100.00	11.01	0.00	15.0	64.9	20.0	0.0	3.24
78-4-92	1044.52	1.64	3.44	3.61	1.11	100.00	16.10	1.53	18.6	55.2	24.9	1.4	2.22
78-2-115	1041.75	1.39	3.01	4.05	1.31	100.00	11.48	0.00	19.2	61.2	19.7	0.0	3.11
79-1-20	1048.50	0.87	3.73	4.05	0.00	100.00	15.29	0.00	19.3	56.5	24.2	0.0	2.34
79-2-0	1049.80	0.96	3.07	4.47	0.00	100.00	16.44	0.00	17.7	56.4	25.9	0.0	2.17
79-2-47	1050.27	1.25	2.87	4.03	0.00	100.00	13.45	0.00	17.9	59.6	22.5	0.0	2.66
80-2-76	1060.06	1.03	3.72	3.72	0.00	100.00	16.08	18.62	16.1	47.7	21.5	14.7	2.22
80-2-125	1060.55	1.67	2.10	4.31	1.10	100.00	14.61	0.00	16.2	59.4	24.3	0.0	2.44
81-2-67	1069.27	1.14	2.68	3.16	0.00	100.00	11.99	0.00	16.6	62.4	21.0	0.0	2.98
82-1-106	1077.56	1.23	3.13	3.47	0.00	100.00	11.56	0.00	18.6	61.5	19.9	0.0	3.09
82-2-0	1078.00	1.56	3.25	5.02	0.00	100.00	13.58	0.00	20.4	57.6	21.9	0.0	2.63
83-1-57	1086.37	0.55	2.94	3.56	0.00	100.00	11.25	0.00	17.2	63.0	19.8	0.0	3.17
84-1-120	1093.20	1.39	2.99	4.41	0.00	100.00	12.06	0.00	19.3	60.3	20.4	0.0	2.96
84-2-49	1093.99	0.85	3.63	3.69	0.00	100.00	11.11	0.00	19.9	61.1	19.0	0.0	3.21
85-2-26	1100.06	0.98	3.28	3.53	0.00	100.00	11.86	0.00	18.7	61.1	20.3	0.0	3.01
85-2-120	1100.10	1.35	3.68	4.13	0.94	100.00	12.36	0.00	20.8	58.8	20.4	0.0	2.89
85-2-121	1100.11	0.00	1.93	4.01	0.99	100.00	11.86	0.28	13.4	64.8	21.5	0.3	3.01
86-2-115	1110.65	1.09	2.58	3.75	0.00	100.00	11.86	4.42	16.2	59.6	19.8	4.3	3.01
86-2-150	1110.99	1.80	1.56	2.95	0.00	100.00	10.85	92.61	7.0	32.8	10.0	50.2	3.29
86-3-7	1111.07	1.06	2.89	3.26	0.00	100.00	11.04	0.24	17.5	62.8	19.4	0.2	3.23
87-1-18	1117.38	0.59	3.81	3.62	1.21	100.00	12.08	0.00	19.7	60.0	20.3	0.0	2.96
88-1-5	1126.95	1.22	1.82	4.36	0.00	100.00	13.06	0.00	15.2	62.1	22.7	0.0	2.73
88-1-41	1127.31	1.26	2.90	4.21	0.00	100.00	10.76	2.72	18.5	60.5	18.2	2.7	3.32
88-2-19	1128.59	2.00	2.44	3.37	0.00	100.00	10.25	87.05	9.4	33.3	9.5	47.8	3.48
89-1-98	1137.58	1.31	2.71	4.23	0.00	100.00	10.83	27.47	14.5	48.7	14.8	22.1	3.30
89-2-16	1138.26	0.98	2.38	3.39	0.00	100.00	10.83	13.01	14.1	56.6	17.2	12.2	3.30
90-1-0	1146.30	1.55	2.98	4.51	0.00	100.00	11.00	11.46	17.9	54.8	16.9	10.4	3.25
90-1-54	1146.84	1.09	3.53	4.23	0.00	100.00	11.83	5.39	19.3	56.8	18.8	5.1	3.02
90-2-27	1148.07	1.42	3.28	4.11	0.00	100.00	11.81	5.61	18.9	57.0	18.8	5.3	3.02
91-1-0	1155.90	1.25	2.92	3.82	0.00	100.00	9.94	9.03	17.3	57.9	16.1	8.6	3.59
91-1-58	1156.48	1.39	3.31	4.25	0.00	100.00	13.12	2.02	19.3	57.6	21.2	1.9	2.72
91-2-41	1157.81	1.25	3.61	3.90	0.00	100.00	10.99	22.90	16.9	49.3	15.2	18.6	3.25

Table 7 (continued).

Core, section interval (cm)	Depth (mbsf)	I-Smec	I-Illite	I-(K + C)	I-Chlorite	I-Quartz	I-Plag	I-Calcite	%-Clay	%-Quartz	%-Plag	%-Calcite	Qtz/Plag
92-1-129	1166.89	1.38	2.96	3.75	1.09	100.00	10.86	5.00	18.0	59.2	18.0	4.9	3.29
93-1-0	1175.30	1.70	1.85	3.50	0.00	100.00	10.09	5.58	14.9	61.9	17.5	5.7	3.54
93-1-21	1175.51	1.19	2.82	4.33	0.00	100.00	11.26	4.05	17.9	59.4	18.7	4.0	3.17
94-1-0	1194.60	0.96	2.88	4.36	0.00	100.00	9.31	2.01	18.8	62.8	16.4	2.1	3.84
94-1-1	1194.61	1.02	2.10	3.39	0.00	100.00	10.31	0.00	15.3	65.7	19.0	0.0	3.46
94-2-45	1186.85	0.95	4.07	4.00	0.00	100.00	13.06	10.96	19.0	52.4	19.2	9.5	2.73
95-1-13	1194.73	0.95	3.60	3.85	0.00	100.00	10.17	2.49	20.0	60.4	17.2	2.5	3.51
96-1-0	1204.30	1.33	3.11	4.49	0.00	100.00	10.92	0.97	19.9	60.6	18.5	1.0	3.27
96-2-32	1206.12	1.14	4.16	4.49	0.00	100.00	10.47	2.46	22.4	58.2	17.1	2.4	3.41
97-1-24	1214.24	0.93	3.72	3.92	0.00	100.00	11.11	0.00	20.6	60.6	18.8	0.0	3.21
98-1-10	1223.80	1.59	4.59	4.51	0.00	100.00	11.70	0.00	24.2	57.1	18.7	0.0	3.05
99-1-0	1233.40	1.46	2.62	3.58	0.00	100.00	11.49	0.00	17.6	62.4	20.1	0.0	3.11
99-1-1	1233.41	1.27	3.41	3.54	0.00	100.00	11.27	0.00	19.7	61.1	19.3	0.0	3.17
99-1-39	1233.79	1.04	4.22	4.22	0.00	100.00	11.65	0.00	22.2	58.6	19.1	0.0	3.07

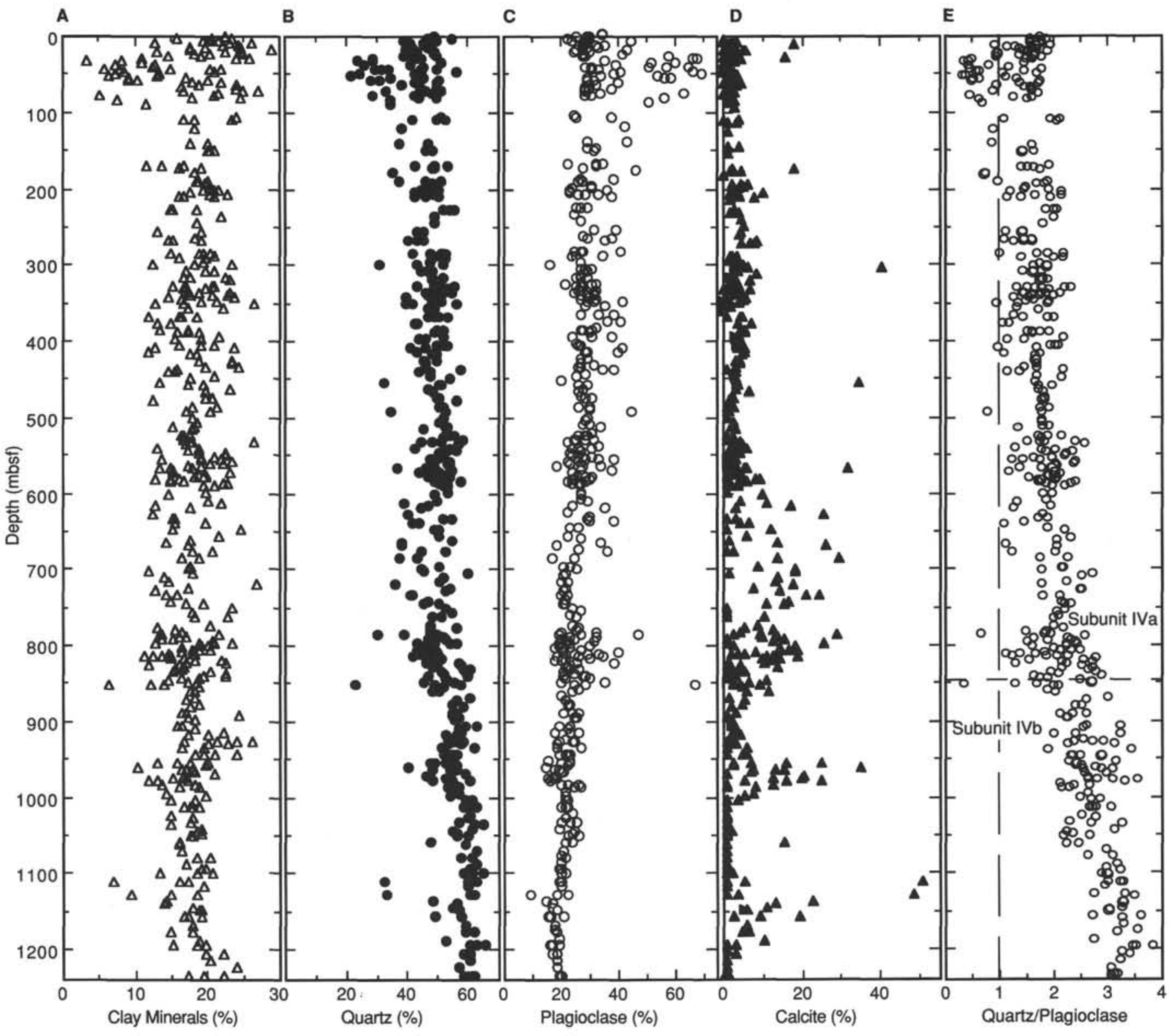

Figure 32. Summary of depth-dependent variations in major minerals at Site 808. Relative percentages of total clay minerals (**A**), quartz (**B**), plagioclase (**C**), and calcite (**D**), are based on weighted XRD peak intensities and have been normalized to 100% (see Explanatory Notes chapter). Weighting factors for peak intensities are from Cook et al. (1976). The steady increase in the quartz/plagioclase ratio (**E**) is probably a function of decreasing mean grain size.

Table 8. X-ray mineralogy data for bulk powders of volcanic-ash layers and vitric mudstone cored at ODP Site 808. Units of measure are uncorrected peak intensities. The approximate peak positions of the measured minerals (from left to right in the column headings) are as follows: smectite (6.2°2θ); illite (8.9°2θ); undifferentiated chlorite + kaolinite (12.5°2θ); chlorite (18.8°2θ); quartz (26.65°2θ); plagioclase (27.9°2θ); calcite (29.4°2θ); undifferentiated clinoptilolite/heulandite (9.9°2θ); amphibole (10.4°2θ); analcite (15.8°2θ); smectite and/or mixed-layer illite:smectite (19.7°2θ); cristobalite (21.9°2θ); pyroxene (29.8°2θ); and siderite (32.1°2θ).

Core, section interval (cm)	Depth (mbsf)	Smec.	Illite	C+K	Chlor.	Quartz	Plag.	Calcite	Zeol.	Amph.	Analc.	Ill:Sm	Crist.	Pyrox.	Sider.
131-808B-															
10-3-52	200.92	0.00	1.82	2.85	0.00	77.02	100.00	7.07	0.00	0.00	0.00	0.00	18.52	0.00	0.00
131-808C-															
15-3-62	437.32	2.14	4.40	4.55	1.05	100.00	14.65	0.00	0.00	0.00	0.00	5.02	0.00	2.81	15.19
30-4-103	583.83	19.27	0.00	0.00	0.00	57.17	42.30	0.00	0.00	0.00	0.00	0.00	68.77	0.00	0.00
30-5-119	585.49	0.00	0.00	0.00	0.00	84.38	100.00	2.87	0.00	8.22	0.00	33.24	18.21	0.00	0.00
37-1-30	645.80	0.00	4.04	0.00	0.00	90.42	100.00	0.00	2.04	0.00	0.00	68.21	8.95	66.74	0.00
38-6-76	663.16	6.68	0.00	0.00	0.00	15.82	34.58	0.00	0.00	0.00	0.00	18.65	8.07	0.00	0.00
45-3-55	725.55	0.00	5.49	0.00	0.00	36.98	100.00	0.00	2.08	0.00	0.00	71.71	0.00	16.80	0.00
45-3-58	725.58	0.00	0.00	0.00	0.00	11.78	100.00	0.00	0.82	0.45	0.00	9.84	0.00	3.92	0.00
54-1-66	809.76	8.89	0.93	0.00	0.00	47.58	100.00	0.00	17.03	0.00	0.00	35.21	0.00	7.03	9.07
57-4-142	844.02	2.36	1.38	4.40	0.00	100.00	18.21	1.18	0.00	0.00	0.00	9.97	0.00	0.33	0.00
73-1-11	992.21	1.44	2.58	3.99	0.00	100.00	14.68	1.60	0.00	0.00	0.00	7.62	0.00	0.00	0.00
100-1-72	1243.72	0.64	2.00	1.81	0.99	100.00	8.90	0.00	0.00	0.00	0.00	5.15	0.00	0.20	0.00
100-CC-2	1245.18	0.71	0.15	0.80	0.00	100.00	2.78	0.00	0.00	0.00	7.96	1.65	0.00	0.64	2.43
101-1-20	1252.40	0.49	0.16	0.86	0.00	100.00	3.66	0.00	0.00	0.00	10.04	0.00	0.00	1.80	1.67
101-2-20	1253.90	0.00	0.55	0.55	0.00	100.00	5.17	0.00	0.00	0.00	14.07	1.21	0.45	1.09	2.43
101-2-115	1254.86	1.76	1.25	0.73	0.00	100.00	10.90	0.00	1.51	0.00	22.71	3.27	0.00	2.84	4.95
101-4-13	1256.73	0.00	0.72	0.74	0.00	100.00	4.29	0.00	0.00	0.00	0.00	2.91	0.00	0.93	0.00
101-4-122	1257.90	0.00	1.05	0.67	0.00	100.00	4.67	0.00	0.00	0.00	0.00	3.05	0.00	1.10	0.00
102-1-11	1261.61	0.00	7.07	1.62	0.00	100.00	89.23	6.78	0.00	0.00	0.00	18.20	0.00	7.07	0.00
102-1-29	1261.79	0.00	1.97	0.72	0.00	100.00	6.12	0.00	0.00	0.00	0.00	4.15	0.00	0.75	0.00
102-2-10	1263.10	0.00	1.44	0.72	0.00	100.00	7.35	0.00	0.00	0.00	0.00	4.08	0.00	3.69	0.00
102-2-30	1263.30	12.49	0.00	0.00	0.00	100.00	21.75	18.31	15.17	0.00	10.22	12.15	0.00	23.11	17.10
102-3-21	1264.71	1.48	0.00	0.00	0.00	100.00	8.58	0.00	8.19	0.00	4.40	6.74	0.00	8.77	0.00
103-1-98	1271.88	0.70	3.07	2.01	0.00	100.00	9.75	0.00	0.00	0.00	0.00	6.70	0.00	4.64	0.00
103-1-130	1272.22	1.01	3.35	2.04	0.00	100.00	11.23	0.00	0.00	0.00	0.00	8.06	0.00	6.11	0.00
103-2-41	1272.81	1.06	3.31	2.33	0.00	100.00	7.40	51.92	0.00	0.00	0.00	6.16	0.00	5.71	0.00
103-2-82	1273.22	1.01	2.94	2.28	0.00	100.00	10.26	0.00	0.00	0.00	0.00	8.33	0.00	4.59	0.00
103-3-48	1274.38	0.00	0.00	0.00	0.00	100.00	16.68	0.00	8.80	0.00	7.41	7.50	0.00	6.56	5.00
104-1-90	1281.30	0.00	2.51	1.91	0.00	100.00	8.80	45.61	0.00	0.00	0.00	6.06	0.00	0.00	0.00
104-2-10	1282.10	1.25	3.55	3.14	0.00	100.00	8.80	40.24	0.00	0.00	0.00	6.44	0.00	4.85	0.00
104-2-123	1283.15	0.97	3.47	2.85	0.00	100.00	9.90	11.39	0.00	0.00	0.00	8.61	0.00	2.91	0.00

49). The last occurrence of *Discoaster tamalis* occurs within the upper part of Zone NN16 (2.65 Ma), and was observed between Samples 131-808C-56R-1, 80–81 cm, and -56R-3, 136–137 cm (830.98 ± 1.78 mbsf). The last occurrence of *Sphenolithus* spp. which occurs within the lower part of Zone NN16 (3.45 Ma), was observed between Samples 131-808C-60R-3, 123–124 cm, and -60R-5, 51–52 cm (872.18 ± 1.14 mbsf). The top of Zone NN15 (3.56 Ma), as marked by the last occurrence of *Reticulofenestra pseudoumbilica*, was placed between Samples 131-808C-60R-5, 51–52 cm, and -60R-CC (Fig. 49, 874.91 ± 1.59 mbsf). *Amaurolithus tricorniculatus* was not observed in Hole 808C, therefore the NN14/NN15 Boundary (3.7 Ma) could not be determined. The first occurrence of *D. asymmetricus* (4.10 Ma) was used to mark the NN14/NN13 Boundary between Samples 131-808C-62R-CC, and -63R-1, 41–42 cm, at 895.06 ± 1.16 mbsf (Fig. 49). *Ceratolithus rugosus* was rarely observed in Samples 131-808C-62R-CC, and -64R-CC, hence the top of Zone NN12, marked by the first occurrence of *C. rugosus* (4.6 Ma), is tentatively set between Samples 131-808C-64R-CC, and -65R-CC (Fig. 49, 918.59 ± 6.21 mbsf). The total absence of *Ceratolithus acutus* and the sporadically and rarely observed *Triquetrorhabdulus rugosus* cause the Miocene/Pliocene boundary (4.9 Ma) to be difficult to determine. The last occurrence of *T. rugosus* was observed between Samples 131-808C-69R-1, 62–63 cm, and -69R-3, 61–62 cm (955.92 ± 1.50 mbsf), and the Miocene/Pliocene Boundary is tentatively placed at this level (Fig. 49), coinciding with the last occurrence of *Discoaster quinqueramus*.

Miocene

The preservation observed in the upper Miocene assemblages is poorer than in the sediments above and below, and the abundance diminishes down toward the basalt. Zone NN11 is defined by the range of *D. quinqueramus*. Its last occurrence (5.0 Ma), which marks the top of Zone NN11 (Fig. 49), was placed between Samples 131-808C-69R-1, 62–63 cm, and -69R-3, 61–62 cm (955.92 ± 1.50 mbsf), and its first occurrence (7.5 Ma) between Samples 131-808-73R-5, 63–65 cm, and -74R-CC (Fig. 49, 1005.02 ± 6.28 mbsf), marks the base of Zone NN11. *Discoaster hamatus* was not observed in Hole 808C, therefore neither the NN10/NN9 nor the NN9/NN8 Boundaries could be determined. Despite the low abundance of *Catinaster coalitus,* its first occurrence (11.1 Ma) could be used to determine the top of Zone NN7 between-Samples 131-808C-83R-CC, and -84R-3, 47–48 cm (Fig. 49, 1092.54 ± 2.95 mbsf). Because of the sporadic occurrence and low abundances of *Discoaster kugleri* the NN7/NN6 Boundary (12.2 Ma) could not be determined precisely. It is tentatively placed between Samples 131-808C-92R-CC, and -93R-1, 104 cm (Fig. 49, 1171.99 ± 4.36 mbsf). The last occurrence of *Cyclicargolithus floridanus* (13.1 Ma) occurs within the lower part of Zone NN6 and was observed between Samples 131-808C-94R-CC, and -95R-CC (1195.79 ± 8.52 mbsf). The lowermost zonal boundary that could be assessed in Hole 808C was the last occurrence of *Sphenolithus heteromorphus* (13.6 Ma) between Samples 131-808C-97R-1, 80–81 cm, and -97R-CC (1219.25 ± 4.45 mbsf). This event marks the top of

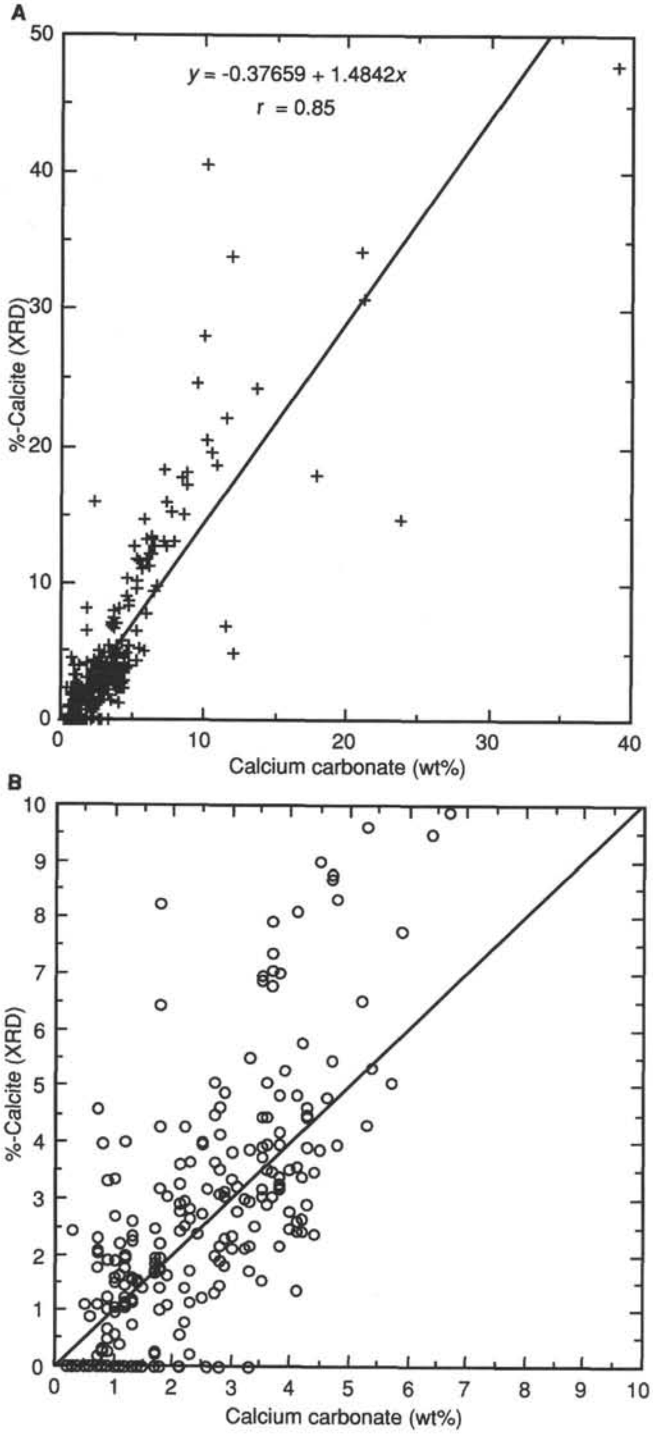

Figure 33. **A.** Linear regression plot of $CaCO_3$ content (in absolute wt%) as measured with the coulometric analyzer vs. relative values of percent calcite calculated from XRD measurements of bulk-sediment powders. Correlation coefficient for the entire linear regression is 0.85. **B.** Data in more detail over a range of 0%–10% calcium carbonate, where the agreement is even better between the two analytical techniques.

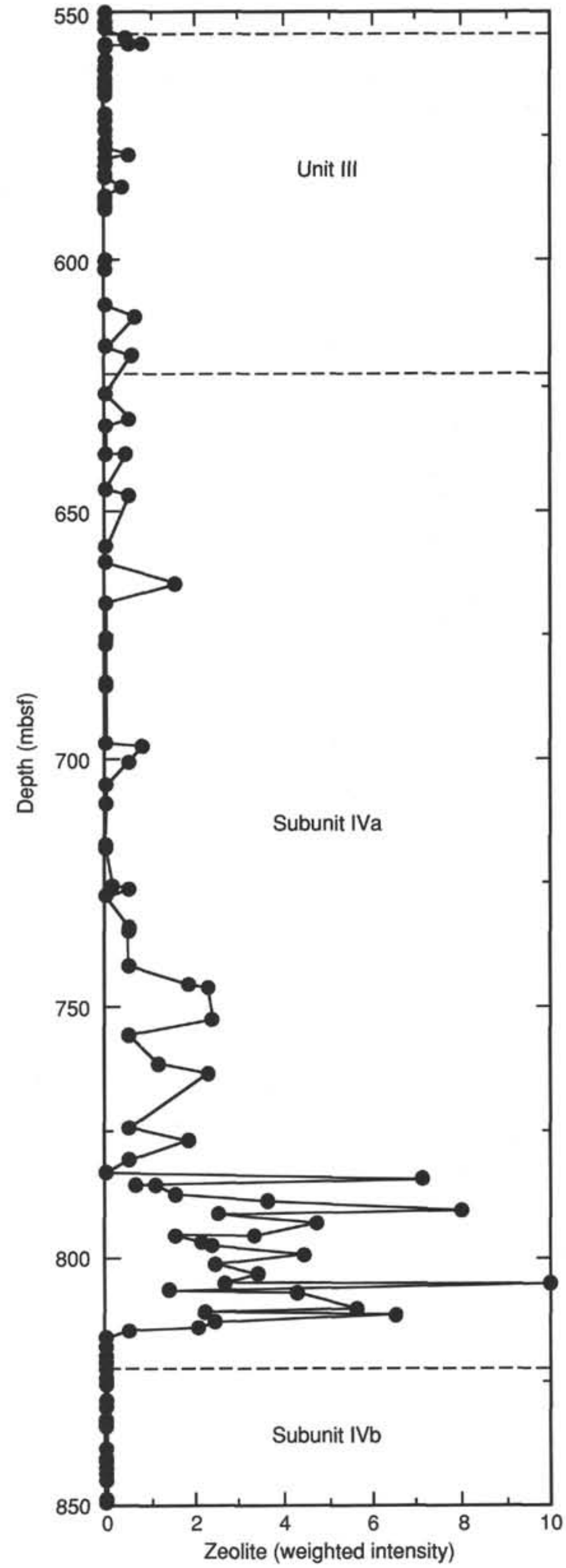

Figure 34. Depth distribution and weighted peak intensities of zeolites (undifferentiated clinoptilolite/heulandite) in facies Unit III and Subunit IVa. Weighted intensities (relative to the principal quartz peak at 26.65°2θ) are based on the diagnostic XRD peak at approximately 9.85°2θ; a weighting factor of 1.56× was adopted from Cook et al. (1976).

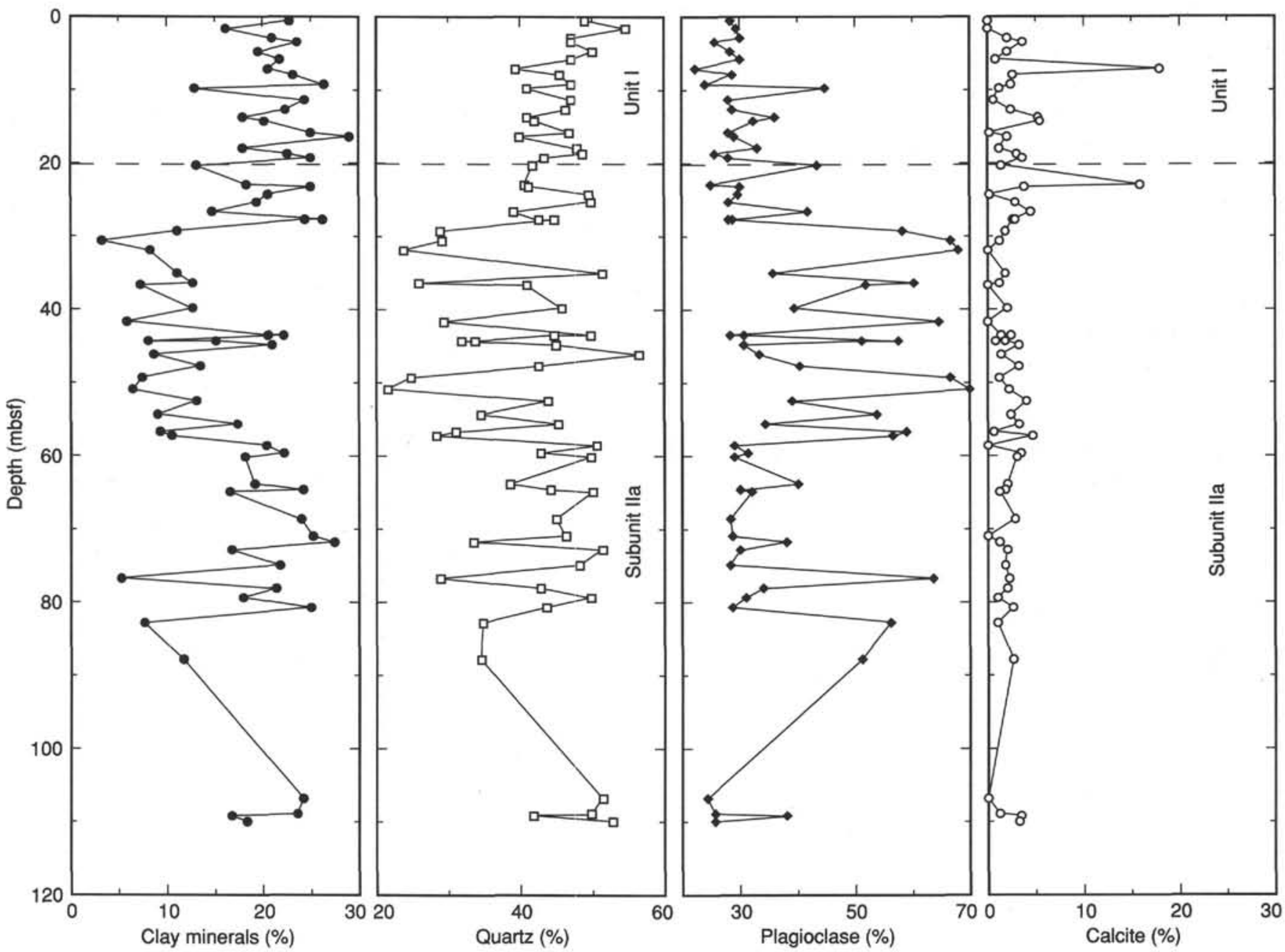

Figure 35. Depth trends in bulk-powder XRD mineralogy for Hole 808A. Values of total clay minerals, quartz, plagioclase, and calcite are based on weighted peak intensities and have been normalized to 100%.

Zone NN5 (Fig. 49) and the remaining sediments down to basement could thus be assigned to Zone NN5 of the middle Miocene. The lowermost sample of the sedimentary sequence that was examined (131-808C-104R-CC) contained abundant moderately well-preserved nannofossils. *Helicosphaera ampliaperta*, which last occurrence marks the top of Zone NN4, was absent in that sample. One sample from within the basalt (131-808C-106R-2, Piece 9) contained common moderately well-preserved nannofossils. *Sphenolithus heteromorphus*, *C. floridanus*, and *Discoaster deflandrei* were the most common species observed. No *H. ampliaperta* was observed; this and one poorly preserved specimen of *C. macintyrei* place this sample within Zone NN5.

Hole 808G

Core 131-808G-8X contains *E. Huxlei* and is assigned to Pleistocene Zone NN21.

Radiolarians

Hole 808A

Radiolarian recovery from Hole 808A was generally poor and sporadic. The radiolarian fauna from Sample 131-808A-1H-CC, is sparse but it contains *Lamprocyrtis nigrinae*, indicative of a middle to late Quaternary age (uppermost *Anthocyrtidium angulare* to *Buccinosphaera invaginata* Zone). Samples 131-808A-2H-CC, and -3H-CC, are barren of radiolarians. Sample 131-808A-4H-CC, contains a sparse middle to late Quaternary fauna which contains taxa indicating the uppermost *Anthocyrtidium angulare* Zone or younger. Samples 131-808A-5H-CC, through -13H-CC, are barren.

Hole 808B

Core-catcher samples from Hole 808B are barren of radiolarians except Sample 131-808B-2X-CC. It contains few and long-ranging Neogene radiolarian species such as *Botryostrobus auritus auritus*, which indicates a middle Miocene to Holocene age.

Hole 808C

Core-catcher samples from Hole 808C are barren of radiolarians except Samples 131-808C-14R-CC, and -19R-CC, that contain sparse and poorly preserved *Tetrapyle octacantha* and *Stylodictya multispira*, which are both long-ranging species.

STRUCTURAL GEOLOGY

Summary

The main objectives of the structural geologists on Leg 131 were to analyze the style, geometry and kinematics of tectonic structures in the toe region of the Nankai accretionary prism. These goals were successfully achieved at Site 808, which

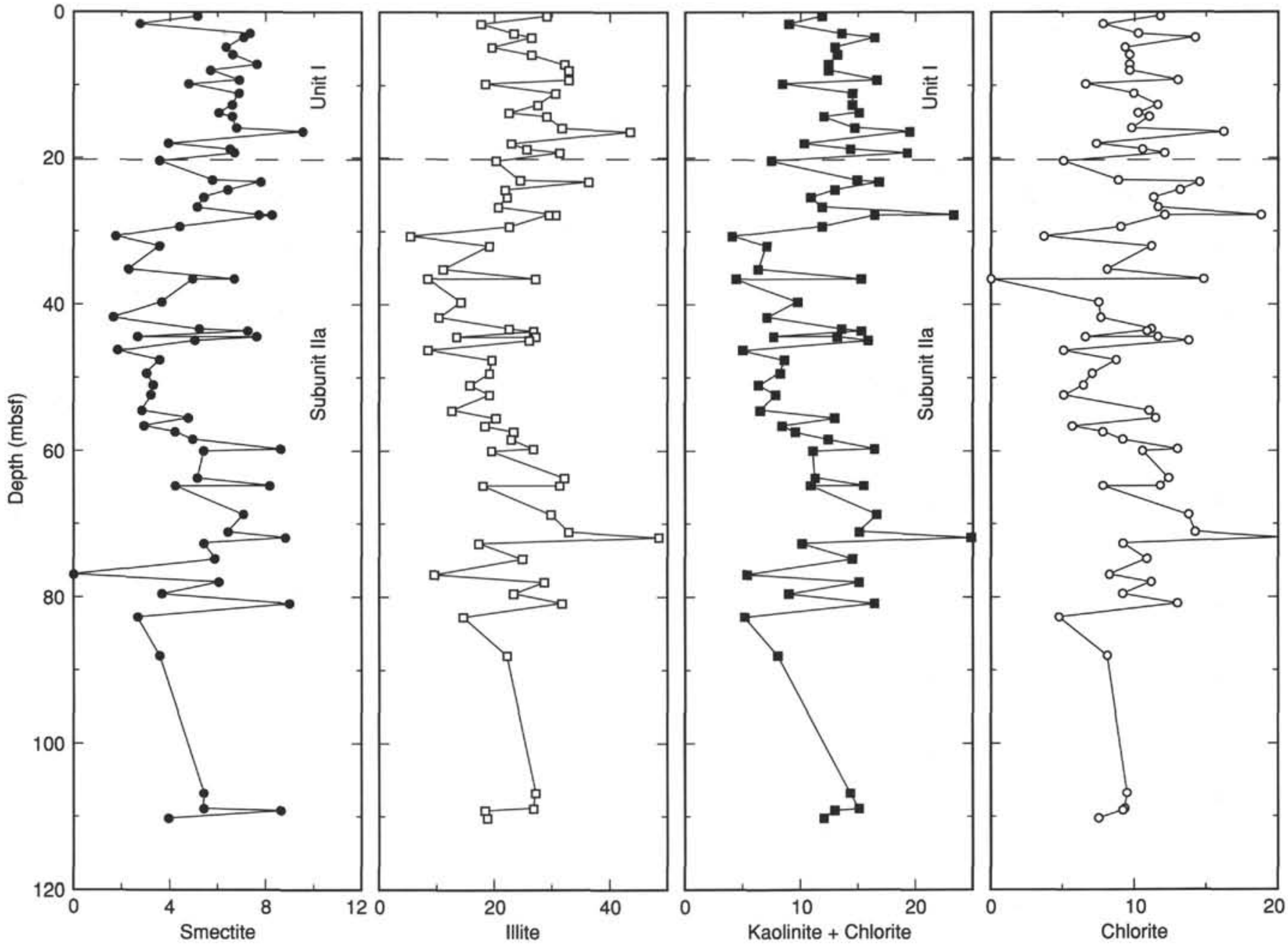

Figure 36. Weighted XRD peak intensities for individual clay minerals detected at Hole 808A. Values are relative to the highest intensity peak (usually quartz), which is equal to 100. Weighting factors were adopted from Cook et al. (1976).

penetrated the entire toe of the prism, including the frontal thrust, the basal décollement, the underthrust sediments, and part of the oceanic basement. Relatively good core recovery allowed detailed structural observations to be made almost continuously from just below the seafloor down to the oceanic crust, and the operations scheme on Leg 131 led to sufficient shipboard time being available for reasonably detailed structural analysis. As a result, over 3000 structural measurements were collected and processed, and over 70% of these measurements were corrected to true geographic coordinates by using approximately 450 paleomagnetic poles (see Explanatory Notes chapter). These orientation data are presented here in microfiche form (in backpocket). This may well represent the most complete structural geological inventory anywhere in the world's oceans.

In the following paragraphs we first briefly summarize the three main conclusions suggested by the structural data and then discuss in some detail the types of structures recognized at Site 808. This discussion is followed by a description of the distribution and geometry of these features, from shallow to deep levels within the prism.

The three main conclusions are:

1. Site 808 can be divided into six structural domains (Fig. 50). Four of these represent the frontal region of the Nankai prism; the other two consist of the underplated sediments and oceanic basement, respectively. The structural and lithologic characteristics of these domains are summarized below.

Domain 1 represents the shallowest structural level and occurs in the interval between the sea floor and the frontal thrust. In the area of Site 808 this domain is composed of slope and trench sediments (lithologic Units I and II, Sedimentology section, this chapter) that have undergone submarine slumping but relatively little tectonic deformation. In effect, this domain constitutes the hanging wall of the frontal thrust.

Domain 2 includes the interval of relatively intense deformation that constitutes the frontal thrust. The zone is defined by steepened and overturned bedding dips, faulting and the development of fine breccias and scaly fabrics. In the area of Site 808 this domain is about 30 m thick and composed of trench sediments (lithologic Unit II).

Domain 3 occurs between the frontal thrust and the décollement and is composed of moderately to intensely deformed trench (lithologic Unit II) and trench-to-basin transitional (lithologic Unit III) sediments, the hemipelagic muds of the upper Shikoku Basin and the upper sediments of the Lower Shikoku Basin (lithologic Unit IV). The deformation is characterized by an array of minor structures, referred to here as small faults, shear bands, and minor zones of breccia and scaly fabric. The distribution of these structures within this domain is markedly inhomogeneous.

Domain 4 includes the basal décollement and the interval of intense faulting and brecciation associated with it. This inter-

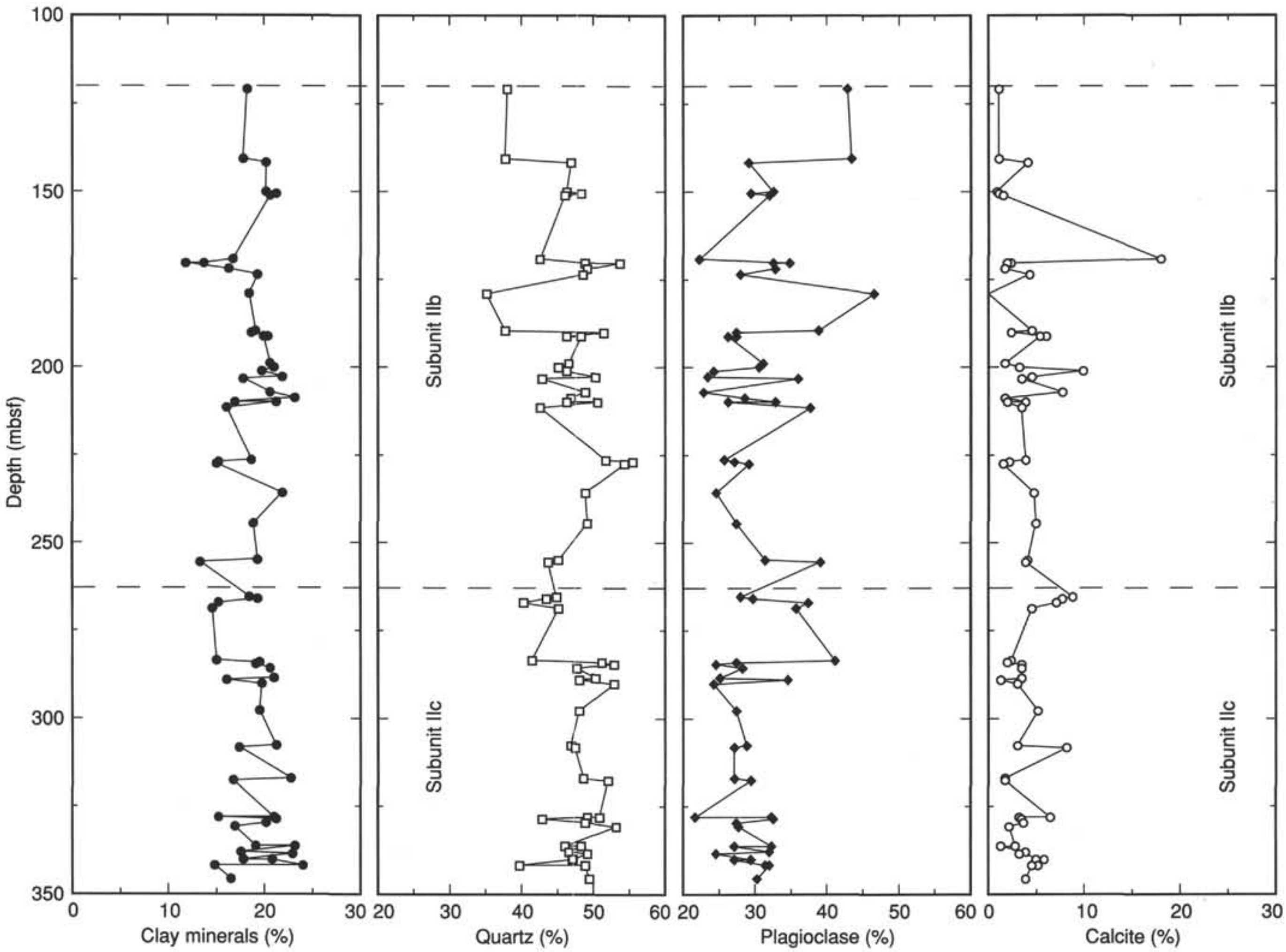

Figure 37. Depth trends in bulk-powder mineralogy for Hole 808B based upon XRD analyses. Relative values for each mineral are based on weighted peak intensities and have been normalized to 100%.

val lies completely within the hemipelagic sediments of the Lower Shikoku Basin (lithologic Unit IV) and is about 19 m thick.

Domain 5 represents the interval of relatively undeformed hemipelagic sediments of the Lower Shikoku Basin (lithologic Unit IV) and acidic volcanic deposits (lithologic Unit V) that is being thrust beneath the décollement and the Nankai accretionary prism.

Domain 6 comprises the fractured and veined basalts of the oceanic basement (lithologic Unit VI).

2. The four dominant structural features at Site 808, namely steepened bedding, faults, shear bands, and zones of breccia/scaly fabric, show a distinctly inhomogeneous distribution. The shear bands are particularly well developed at a relatively shallow structural level and appear to be spatially associated with the frontal thrust. The bands are also conspicuously absent below about 560 mbsf. In contrast, the faults occur throughout the prism and are especially concentrated near the frontal thrust, the décollement and in four intervals between 550 and 900 mbsf. The distribution of strain in the prism toe therefore appears to be markedly heterogeneous.

3. In general, most of the structures trend northeast-southwest, parallel to the Nankai trench, when paleomagnetically corrected for rotations due to drilling. Rotated slickenlines and conjugate shear bands and faults also suggest that the shortening direction associated with these structures trends northwest, parallel to the inferred plate convergence vector. A few exceptions to this generalization occur locally. Normal faults, for example, have slickenlines that trend in a variety of orientations and slickenlines associated with thrust faults near the décollement can trend either northeast-southwest or northwest-southeast.

Types of Structures Observed

Deformation at Site 808 is recorded dominantly by four types of structural features: small faults, shear bands, zones of breccia and scaly fabrics, and steepened bedding. The first two groups include complex variations in type, and, as emphasized in the Explanatory Notes chapter, it is important to note that the nomenclature of these structures and their separation into different categories is at present somewhat arbitrary. The nature and interaction of some of these structures will not be clear until shore-based microstructural analysis has been conducted. It seems likely that there is considerable overlap between types, and it is not always straightforward to distinguish the different types of structures at the macroscopic scale. For example, in some locations the small faults are very well developed and highly concentrated, resulting in the zone approaching a breccia. Some shear bands change thickness along their length and have both gradational and sharp boundaries, suggesting similarities with the small faults. Certain kinds of faults may in some circumstances

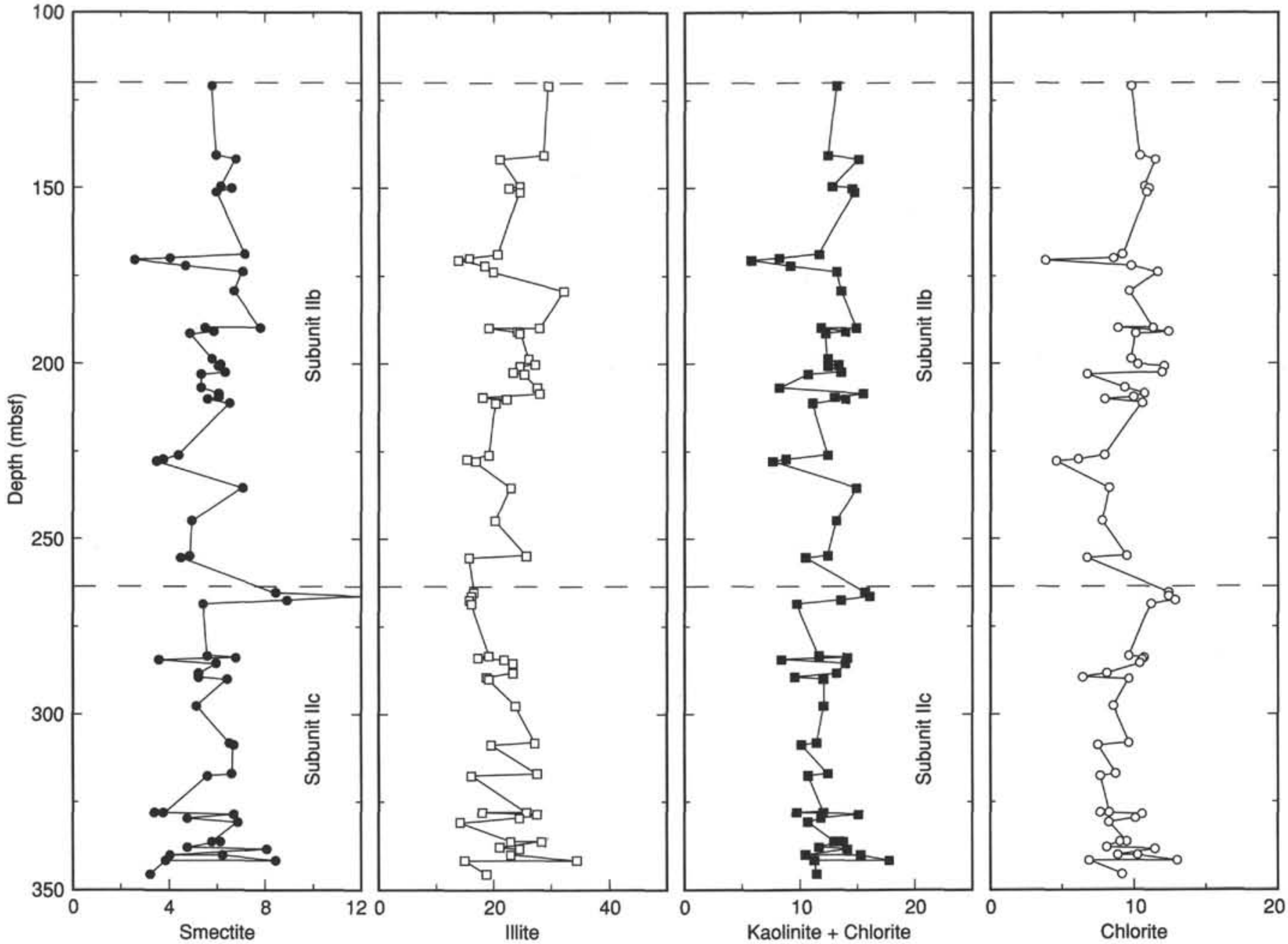

Figure 38. Weighted XRD peak intensities for individual clay minerals detected at Hole 808B. All intensity values are relative to the highest intensity peak (usually quartz), which is set at 100. Weighting factors were adopted from Cook et al. (1976).

initiate independently but elsewhere may evolve from a preexisting structure. The divisions are therefore generalizations that represent end members of a wide range of structures, with characteristics that will only be understood after more detailed studies. At present, however, the division of the deformation structures employed here provides a useful and generally accurate representation of the macroscopic observations at Site 808.

In general, the shear bands and faults appear to record contractional displacements relative to bedding (e.g., Fig. 51)., although faults with extensional and strike-slip displacements are also locally present. Shear bands with strike-slip or normal displacements, however, have not been recognized. The general characteristics of the main types of structures are provided below.

Small Faults

The small faults typically occur as narrow (<1 mm), sharply bounded zones of displacement that appear much darker than the surrounding sediments (Fig. 52). As seen in the cores, the faults commonly extend for several centimeters and record displacements of millimeters up to a few centimeters. The fault surface itself is commonly coated with dark gray to black material, which XRD-analysis suggests may be greigite and/or pyrite. At deep structural levels (more than 600 mbsf) the fault zones are much narrower and material within the fault zone is limited to a very thin coating of black, commonly shiney, coating. The fault surfaces show a polished appearance to various degrees, and are commonly lineated. The lineations consist of fine grooves or slightly broader undulations in the dark material that occurs along the fault surface (Fig. 53). They are referred to here as slickenlines.

Where the faults can be observed in three dimensions they are seen in some cases to have complex geometries. In most examples the faults have a low dip but a wide variation in strike, resulting in a generally low-dipping fabric composed of a web of intersecting faults. In other cases the faults dip moderately and form conjugate arrays about bedding. In detail the faults can be composed of either a single, relatively narrow strand or they can consist of a number of smaller faults that anastomose and intersect at very low angles (Figs. 51C, 52B, and 52D).

In general, the small faults appear to be younger than the shear bands. Cross-cutting relations were observed at a number of depths at Site 808 and in virtually all cases the faults clearly cross-cut the shear bands. The relation of the shear bands to bedding also suggests that they formed relatively early. For example, where the beds dip steeply within the frontal thrust zone, the shear bands preserve their conjugate arrangement around bedding, suggesting that the bands formed before the bedding was rotated. In contrast, the faults form more complex geometries relative to bedding and appear to have formed at several stages of the deformation history.

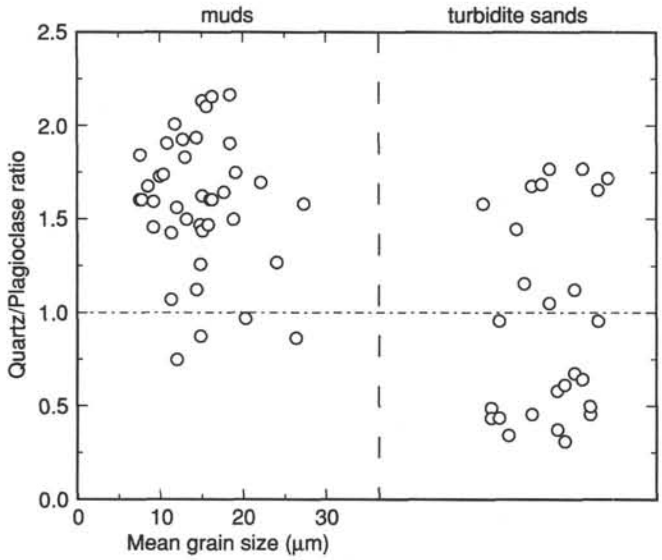

Figure 39. Variations in the ratio of quartz/plagioclase as a function of grain size in Holes 808A and 808B. Note that the sandy turbidites of Subunit IIa display a wide range of values and include the highest percentages of detrital plagioclase. Arbitrary grain-size values were assigned to the sandy deposits simply to separate data points on the diagram; mean grain-size data for muddy deposits were generated using the Lasentec Analyzer (see Sedimentology section of Explanatory Notes chapter).

Shear Bands

Shear bands represent the second most abundant structure recognized at Site 808. They appear macroscopically as diffusely bounded zones that are slightly darker than the surrounding material (Fig. 54; see also Figs. 16, 23A, Sedimentology section, this chapter). The color rarely reaches the dark gray to black typical of the small faults (e.g., compare Figs. 51 and 52). The bands are commonly 1–2 mm across, but some examples reach a width of 1 cm. Where the bands have adjacent marker features, they normally show some displacement, indicating that they are acting as zones of shear. However, the displacements, where observed, are relatively small (less than a few mm) even when the bands are very wide and appear well developed (Figs. 55 and 56). The surfaces of the shear bands typically show very fine grooves and some polish, but these features are not developed to the same extent as in the faults.

In three dimensions the bands appear to form relatively simple conjugate sets that are centered on bedding (Figs. 54, 55, and 57); see also Fig. 23A, Sedimentology section). When corrected with paleomagnetic data for rotations due to drilling, the shear bands show a consistent northeast-southwest strike and a dip either to the northwest or the southeast. We therefore have inferred that the shortening direction associated with the shear bands trends northwest which is approximately parallel to the vector of plate convergence.

In general the shear bands appear to have accommodated a relatively small amount of displacement (often only a few mm) and do not cut bedding (or other markers) with the sharp discontinuity seen in faults. Instead, bedding is commonly gently folded or warped by the displacement associated with the shear band (Figs. 54, 55, and 56). Many examples of the bands occur where no faults are seen.

In some cases, however, the shear bands appear to be associated with faults. The faults are very narrow, discrete structures that cross-cut the shear bands at either a moderate (approximate 30° to 45°) (Figs. 54 and 55) or very low (<20°) angle, relative to the shear band boundaries (Fig. 56). These discrete faults are texturally very similar to the small faults recognized elsewhere. While it is possible that their origin is independent of the shear bands, several observations suggest that the two structures are related. First, the low-angle faults consistently dip in the direction of movement indicated by the shear bands and have displacements consistent with those inferred for the shear bands. These small faults are therefore geometrically and kinematically similar to Riedel shears (Morgenstern and Tchalenko, 1967) and may have a synthetic relation with the shear bands. These observations suggest a possible progressive evolution from shear bands to small faults. A similar conclusion was suggested by Karig and Lundberg (1990) for samples retrieved from Legs 31 and 87A.

Second, in areas where the high-angle faults form an en echelon set (e.g., Fig. 54A), the displacement associated with the faults appears to be transferred through the development of several shear bands that span the distance between the tips of the en echelon faults. These observations therefore suggest that at least some of the small faults may have formed at about the same time as the shear bands. In general, however, observations from Site 808 indicate that the shear bands predate the small faults. Note the angles between shear bands and bedding (Fig. 57).

Structures similar to the shear bands we have described have also been observed in cores from Legs 31 and 87A, and described as kinks by Lundberg and Karig (1986) and Lundberg and Moore (1986). More recently, Karig and Lundberg (1990) have carefully described these structures (which they called deformation bands) at both macroscopic and microscopic scales and have emphasized the geometric and textural complexities present at these scales. Specifically, these authors emphasized that the bands do not consistently display the characteristics of kink bands because individual bands are often composed of irregular to anastomosing sets of sub-bands and small faults. Karig and Lundberg (1990) interpreted these sub-bands and small faults to be sets of Riedel shears and observations from Site 808 are consistent with this interpretation. It is therefore likely that the shear bands reported here have much in common with the deformation bands documented on Leg 87.

Breccia and Scaly Fabric

The zones of breccia and scaly fabrics are marked by a relatively high concentration of small (typically less than 1 to 2 cm in maximum dimension) trapezoidal and lens-shaped fragments of clayey silt that have highly polished and/or slickenlined surfaces (Fig. 58). They range in width from a few centimeters to over 1 m and occur sporadically throughout domains 2, 3, and 4. However, the zones are chiefly developed (i.e. greater than 0.5 m in thickness) in the frontal thrust (domain 2), the décollement (domain 4) and in the lowest structural levels of domain 3.

Steepened Bedding

In much of Site 808 the observed bedding dips reflect the regional orientation expected from the seismic record. However, at several horizons beds are significantly steeper. In the uppermost levels of the prism the steep dips are thought to be the result of gravitational slumping, but elsewhere they are accompanied by an increase in development of the other deformation structures and indicate zones of high tectonic strain. In the frontal thrust zone, for example, the beds pass through vertical to become markedly overturned.

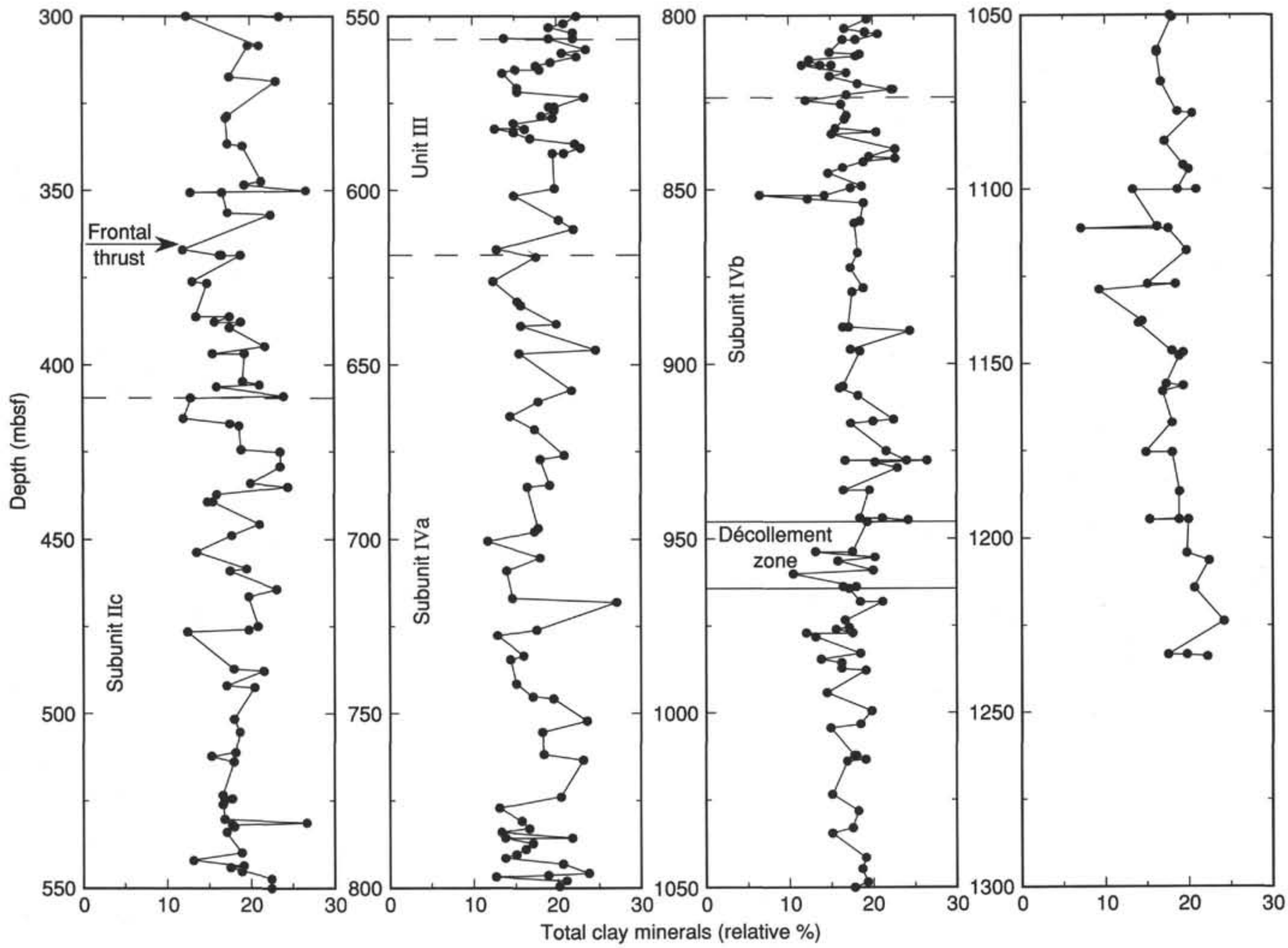

Figure 40. Relative values of percent-clay-minerals for Hole 808C, based on the sum of the weighted XRD-peak intensities of individual clay minerals (smectite, illite, chlorite, and kaolinite).

Distribution of Structures with Depth

To document the distribution of structures at Site 808 the number of faults and shear bands were counted and normalized to the number of structures/meter (Fig. 59). When reading these frequency diagrams allowance has to be made for the intervals where core recovery was poor. The magnitude of bedding dip throughout Site 808 was also plotted versus depth (Figs. 59 and 60).

Important general conclusions of these data are: (1) The uppermost intervals show the effects of gravity-induced slump folding; (2) the onset of tectonic deformation is first recorded at about 260 m depth; (3) the shear bands are clearly concentrated around the frontal thrust and are only feebly present below about 550 mbsf; (4) the increase in abundance of faults at several locations correlates with an increase in bedding dip, and in the upper parts with an increase in shear zone development, suggesting that the distribution of structures/meter accurately reflects the intensity of deformation at this site; (5) deformation around the décollement is highly asymmetric, with essentially no deformation occurring in the underthrust material. A more detailed discussion of the distribution of structures at Site 808 is given in the following paragraphs, starting at the shallowest structural levels.

Domain 1 - Slope Deposits and the Prism above the Frontal Thrust

The shallowest parts of the Nankai accretionary prism contain no tectonic structures and are dominated by subhorizontal sedimentary horizons. However, there are zones where steep and irregular bedding is common, especially at 10–20 mbsf, just above the contact between the slope apron and trench wedge sediments. Numerous tight to isoclinal folds occur, even within a single section (see Figs. 10, 11, 12, 15, Sedimentology section, this chapter) and overturned bedding has been observed locally (Fig. 54). The location of these effects at the base of the slope apron sediments, together with the highly ductile appearance of the folds and the absence of evidence of a major structure in this area on seismic reflection profiles, suggest that they are related to downslope movement of the slope apron sediments. The occasional steep dips that occur down to around 200 mbsf are also thought to be the result of gravity-induced slumping.

At 260 mbsf the first indications of tectonic deformation of the sediments are seen. The materials are unlithified (e.g. 50% porosity, >30% water content, see Physical Properties section, and are easily cut with a wire) but apparently have been able to transmit tectonic stresses. In Hole 808B small faults and shear bands occur at 260 mbsf (Core 131-808B-17X), 280

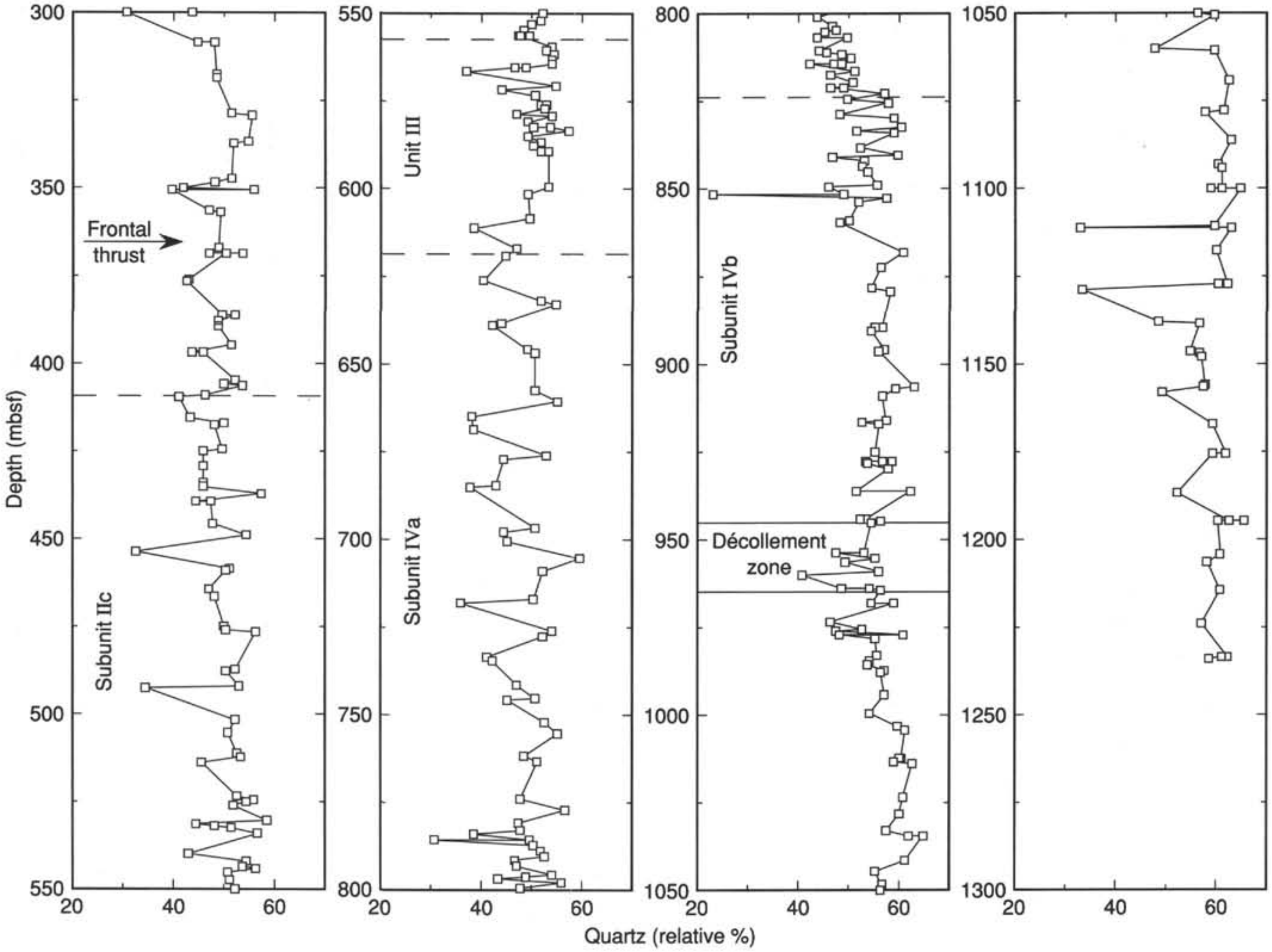

Figure 41. Relative values of percent-quartz for Hole 808C, based on the XRD intensity of the primary quartz peak at 26.65°2θ.

mbsf (Core 131-808B-19X), and 330 mbsf (Core 131-808B-24X) and appear to record tectonically induced layer-parallel shortening (Fig. 61). Similar structures occur in Hole 808C, but at slightly deeper structural levels. For example, shear bands and small faults are present at 300 mbsf (Core 131-808C-1R), 340 mbsf (Core 131-808C-5R), and at 356 mbsf (Core 131-808C-7R).

The intensity of development of these tectonic structures increases downward as the frontal thrust zone is approached (Fig. 53). The transition to domain 2 occurs in Hole 808C between 357 and 366 mbsf and in Hole 808B at about 335 mbsf, and is marked by an abrupt increase in the dip of bedding.

Domain 2 - The Frontal Thrust Zone

Domain 2 represents the frontal thrust of the Nankai accretionary prism. It contains the highest concentration of steeply dipping beds at Site 808, a significantly higher number of shear bands and small faults per meter (Fig. 59), and zones of breccia/scaly fabrics. This domain therefore represents one of the most intensely deformed zones recognized at Site 808. An example of a highly deformed portion of Core 131-808C-8R is shown in Figure 62.

Within this domain bedding increases in dip to up to 90° and becomes overturned (Figs. 63 and 64). The observed bedding orientations closely constrain the style and orientation of the overall structure within the thrust zone, even though the core recovery was relatively poor in the upper part of this domain. When corrected paleomagnetically for rotations due to drilling, some bedding planes young towards the southeast, suggesting the presence of inclined folds, with axial surfaces dipping towards the northwest (Figs. 63 and 64).

The shear bands and faults vary in abundance between 5 and 10 per meter, with localized zones having 20 faults/shear bands per meter. They form relatively complex geometric arrays within this domain, although conjugate sets are also suggested locally. In general, however, both types of structures generally strike to the northeast-southwest, when corrected with paleomagnetic data. The breccia/scaly fabrics are best developed in the uppermost 60 cm of Core 131-808C-8R (366 mbsf) (Fig. 58). In parts of this domain two highly oblique fracture sets produce trapezoidal fragments less than a centimeter across, but many of the fractures are irregular and very closely spaced, reducing the material to a finely broken state. Elongate, flaky pieces resemble those found in some scaly clays, although the surfaces are only feebly shiny. Further, unobserved, highly fragmented zones may account for the poor core recovery within this domain, as speculated in Figure 63 for Cores 131-808C-8R, 131-808C-9R and 131-808C-10R.

The frontal thrust of the prism is therefore regarded not as a discrete fracture but as a zone, which on the basis of steepened bedding dips, brecciation, and fault intensity, extends in Hole 808C from about 357–365 mbsf down to about 390–395 mbsf, a vertical thickness of roughly 30 m. Hole 808B shows similar features beginning in Core 131-808B-25X, 336

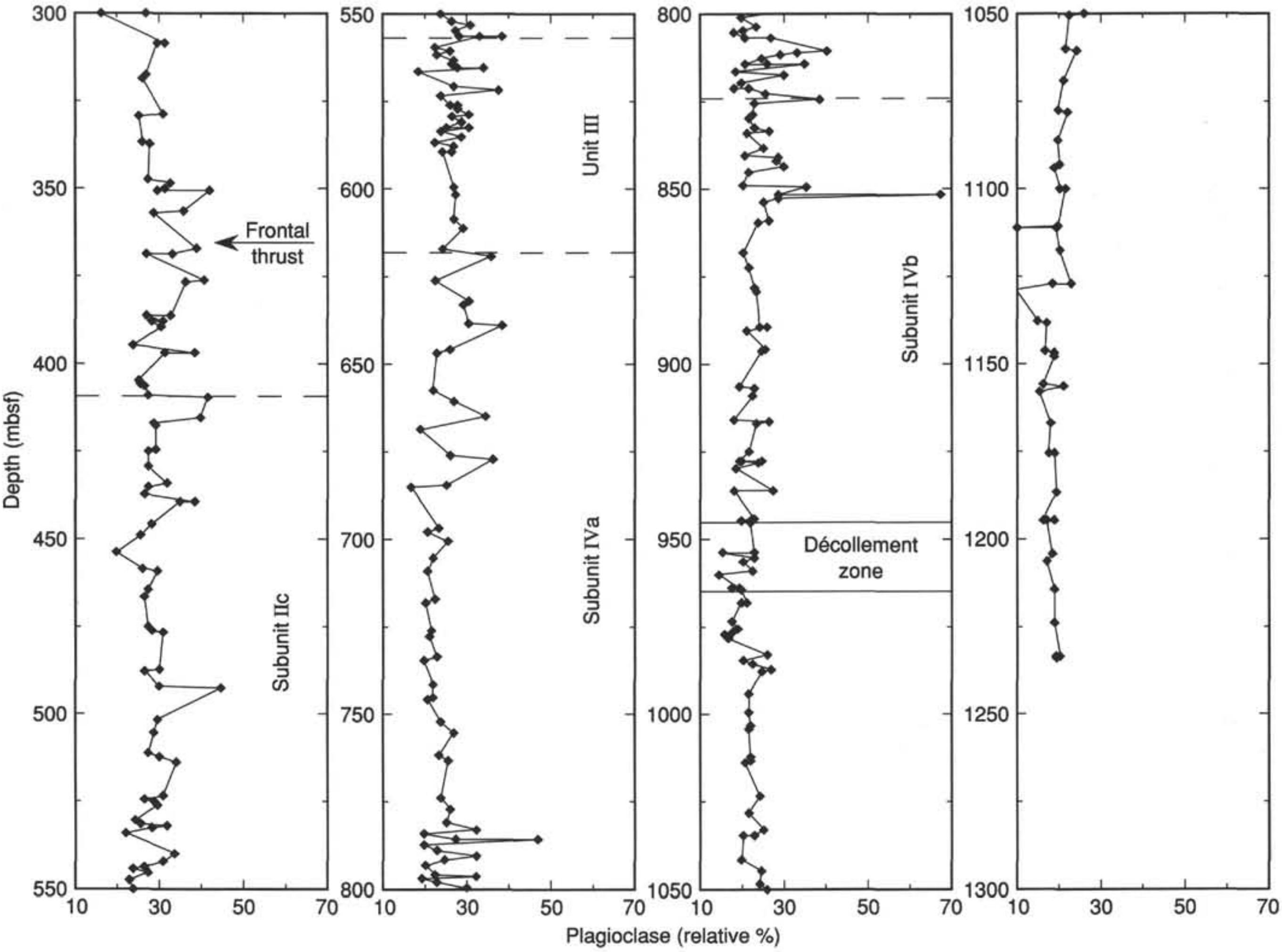

Figure 42. Relative values of percent-plagioclase for Hole 808C, based on the weighted XRD peak intensity at approximately 27.9°2θ. A weighting factor of 2.80 was used to normalize the peak intensity to that of quartz at 26.65°2θ.

mbsf, below which recovery was very poor. Because Hole 808B was discontinued at 359 mbsf, it seems that this hole failed to penetrate the entire thickness of the thrust zone.

Calculations from the depths at which the thrust was first encountered in Holes 808B and 808C and the distance apart of the two holes give a dip for the structure of 25° to the northwest, assuming a roughly trench-parallel strike of 045°. Based on the depths at which a fractured zone was perceived from the drilling characteristics of Holes 808C, 808D, and 808E and their relative locations (T. Pettigrew, pers. comm.), the thrust has an orientation of 040/17°. This dip value seems low, but it could be indicating a local shallowing of the thrust, and we would regard the 30° dip cited from the seismic data as a maximum value for the inclination of the thrust at this site.

On the basis of a 30° dip, the true thickness (thrust-perpendicular) of the thrust zone is 26 meters. The displacement associated with the thrust zone is best marked by the mudstone pebble conglomerate horizon recognized at both 263.4 mbsf in Hole 808B and at 409.1 mbsf in Hole 808C. The observed vertical difference between these two levels, the stratigraphic throw of the thrust, is therefore 145.7 m, and, taking a 30° dip for the structure, the fault-parallel separation is 309 m. This last value also represents the true total movement within the thrust zone (i.e., the fault slip), assuming that the motion is dip-slip, as suggested by slickenline orientations, and that the strikes of the conglomerate horizon and the thrust are parallel. An interpretation of the overall structure within domain 2 is given in Figure 63.

Domain 3 - The Lower Prism above the Décollement

This domain occupies the major portion of the accretionary prism and contains the protothrust and other incipient deformation structures. It is characterized structurally by an overall decrease in the development of shear bands with depth, a generally low bedding dip (<10°), and the presence of faults throughout the zone that also show intervals of marked concentrations.

The shear bands are concentrated in the 200-m interval between just above the frontal thrust (about 300–350 mbsf) and 550 mbsf where on average over 10 bands occur per meter (Fig. 59). Below about 560 mbsf the shear bands are very rare and the few shear bands between 600 and 800 mbsf (Fig. 59) are atypical varieties that may have been better classified as faults. Therefore, the distribution of shear bands in this domain (between 350–550 mbsf) correlates reasonably well with both the frontal thrust and the distribution of the sediments of the outer trench wedge (or lithologic Subunit IIc).

There are probably several factors involved in this restriction of shear band formation, but an appropriate balance between the magnitude of tectonic strain and the intensity of sedimentary fabric appears to be important. The strains associated with development of the frontal thrust provided the

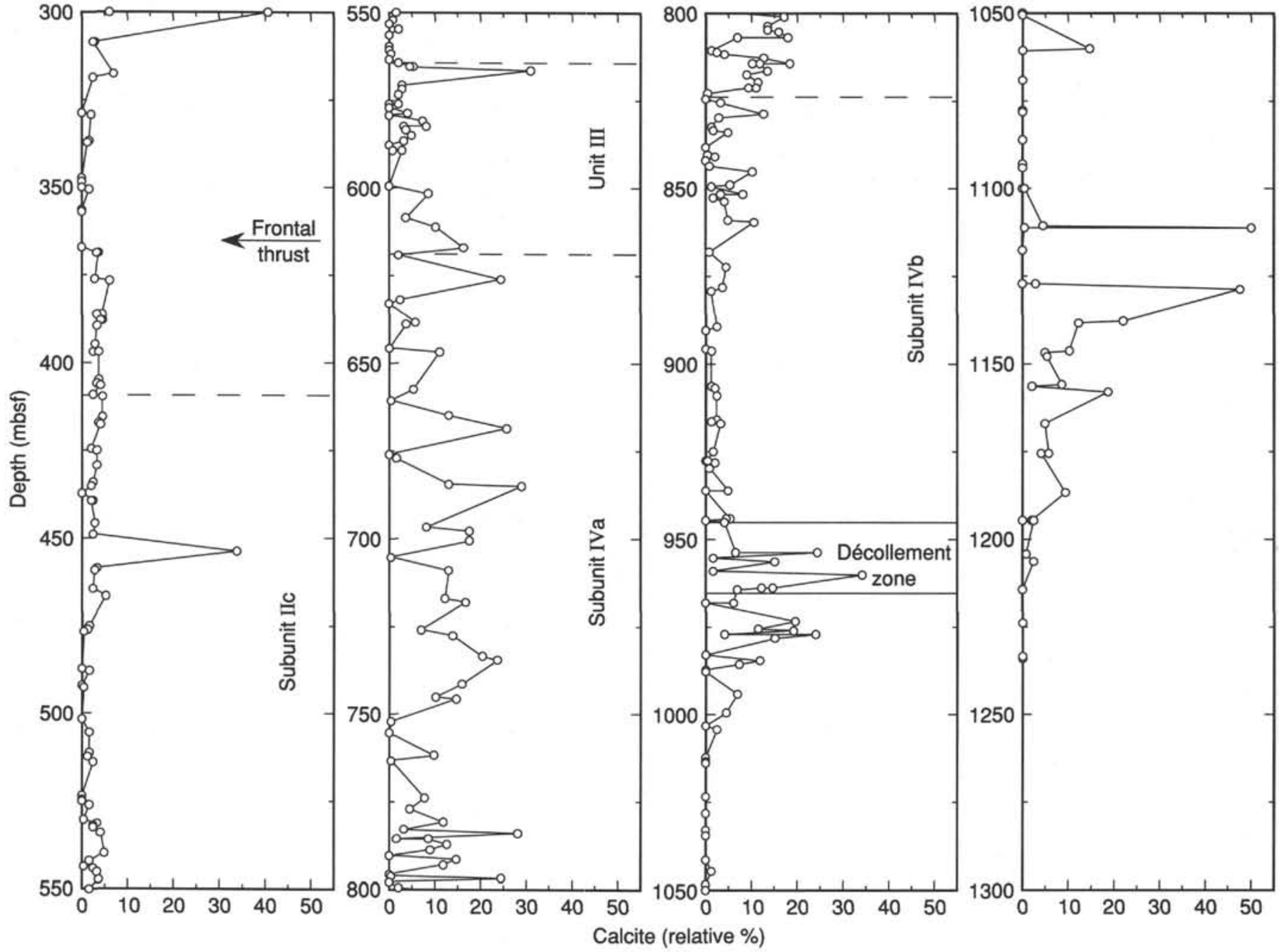

Figure 43. Relative values of percent-calcite for Hole 808C, based on the weighted intensity of the XRD peak at approximately 29.4°2θ. A weighting factor of 1.65 was used to normalize the peak intensity to that of quartz at 26.65°2θ.

necessary deformation, whereas the fine silts and muds of the outer trench wedge may have provided the necessary fissility (either as a primary sedimentary fabric or as a sedimentary fabric enhanced by compaction). Perhaps above 300 m the amount of consolidation was insufficient to produce the required bedding-parallel fabric and below 550 m the dominance of clay-rich hemipelagic sediments and ashes in the Shikoku Basin sediments inhibited the development of sedimentary or compaction fabrics. The important role of primary sedimentary fabric is also suggested by the change in development of the shear bands in sediments with different ichnogenera (e.g., Fig. 23A, Sedimentology section, this chapter).

In contrast to this restricted distribution of shear bands, the small faults have formed throughout these changes in sedimentary facies. Their distribution is heterogeneous, however, with concentrations in five relatively narrow intervals (Fig. 59). Between these zones, deformation is weak. Bedding dips rarely exceed 5° or 6°, brecciated zones are sparse and narrow, and there are typically no more than 5 faults/meter. The five intervals mentioned above appear to represent zones where the deformation of this domain has been concentrated, and so their characteristics are described in turn.

Interval 1: 530–578.3 mbsf (Cores 131-808C-25R through -29R)

This interval contains the largest number of faults per meter recognized at Site 808 and an increase in bedding dip from less than 10 degrees to up to 40 degrees. Two examples of the style of deformation in this interval are shown in Figure 65. Core 131-808C-25R contains both well-developed faults and shear bands, both of which appear to form conjugate geometries about bedding. Both sets of structures and their associated slickenlines indicate a northwest-directed shortening direction. At deeper levels in this interval, e.g., Core 131-808C-29R (Fig. 65), faults are the dominant structural feature and conjugate geometries are no longer present. Instead, the faults generally dip moderately to gently to the southeast, although the associated slickenlines still trend northwest-southeast.

Interval 2: 654.9–664.5 mbsf (Core 131-808C-38R)

This interval is characterized by an increase in the number of faults per meter, ranging up to 10 per meter, and relatively low bedding dips. When considered as a whole, the faults in this interval form complex three dimensional networks, even when the rotations due to drilling are corrected with paleomagnetic data (Fig. 66). However, most of the faults are subhorizontal and have slickenlines that trend northwest, perpendicular to the trend of the Nankai trench. In detail, the faults show more consistent patterns. For example, Figure 66B shows that this interval contains a well developed set of low-angle reverse faults with northwest-trending slickenlines, several northeast-trending reverse faults with northeast-

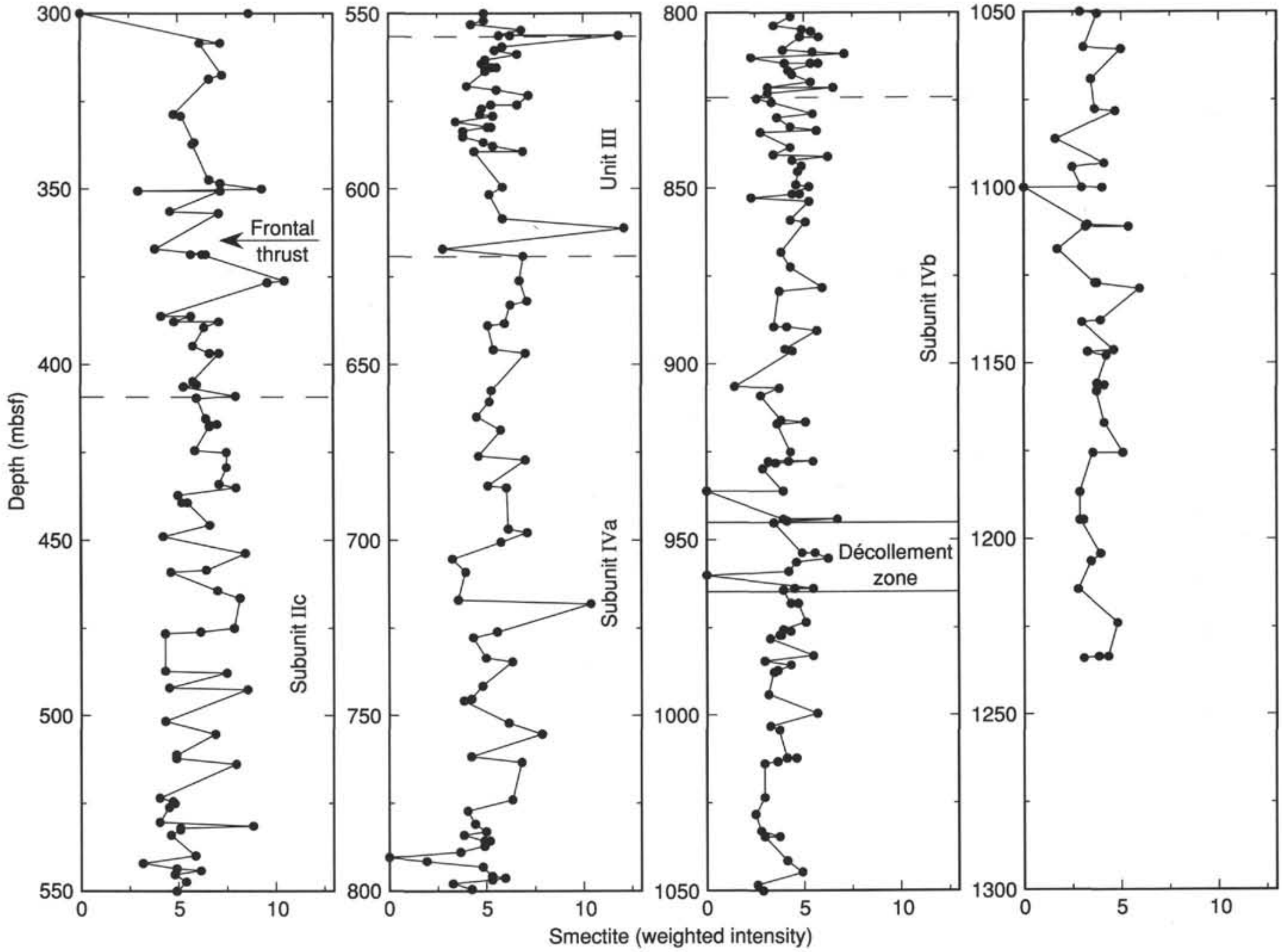

Figure 44. Weighted XRD intensity values for the diagnostic smectite peak (located at approximately 6.2°2θ), Hole 808C. A weighting factor of 3.00 was used to normalize the peak intensity to that of quartz at 26.65°2θ.

trending slickenlines (Fig. 66C), as well as several north-south-trending normal faults (Fig. 66D).

Interval 3: 703.2–710.7 mbsf (Core 131-808C-43R)

This interval shows an increase in number of faults per meter similar to the one recorded in interval 2 together with a slight increase in bedding dip. These dips steepen from a background of 5° to 10° to up to 18°. Although this increase is relatively minor compared to changes preserved in domain 2 and in interval 1, the correlation of increased bedding dip and the concentration of faults suggest that this interval represents a significant zone of tectonic deformation. Similar to interval 2, the faults in this interval are generally subhorizontal and have slickenlines that trend northwest when the rotations due to drilling are corrected with paleomagnetic data. Several east- to northeast-trending normal faults are also present.

Interval 4: 770–820 mbsf (Cores 131-808C-50R to -54R)

This interval is distinguished by an increase in concentration of faults per meter over a relatively wide range of depth, and by a local increase in bedding dip (Fig. 59). Bedding typically dips only about 10° in this interval but increases to 35° at 787.8 mbsf. Faults within this interval dip gently northwest or southeast and are associated with slickenlines that consistently trend to the northwest (Fig. 67).

An isolated, centimeter-wide clastic dike occurs at 813 mbsf in this interval. The dike is composed of medium-grained, gray quartz sand injected into a dark gray silty clay host. The dike dips moderately to the northwest (when corrected with paleomagnetic data) approximately parallel to several faults that are also present in this area (Fig. 67). This apparently isolated feature represents the only evidence observed in the cores for overpressuring anywhere within the prism.

An unusual set of faults are sporadically developed in the lower structural levels of this interval (Fig. 68). These faults have a relatively steep orientation (70° to 90°) and, as a result, can be followed downcore for several tens of centimeters. The dip angle varies down dip, giving a profile much more irregular than the kinds of faults observed elsewhere at this site. The faults also commonly braid and anastomose down dip, with wispy, minor faults splaying away from the main surface. In all cases where displacement was observed, the sense was normal and separation, as observed on the core face, was between 1 and 8 mm. The few observed slickenlines associated with these faults indicated either down-dip or strike-parallel displacements. The faults are considered to be relatively early structures because they rarely occur as open fractures, they appeared to be annealed, and because they are consistently crosscut by low-angle thrust faults.

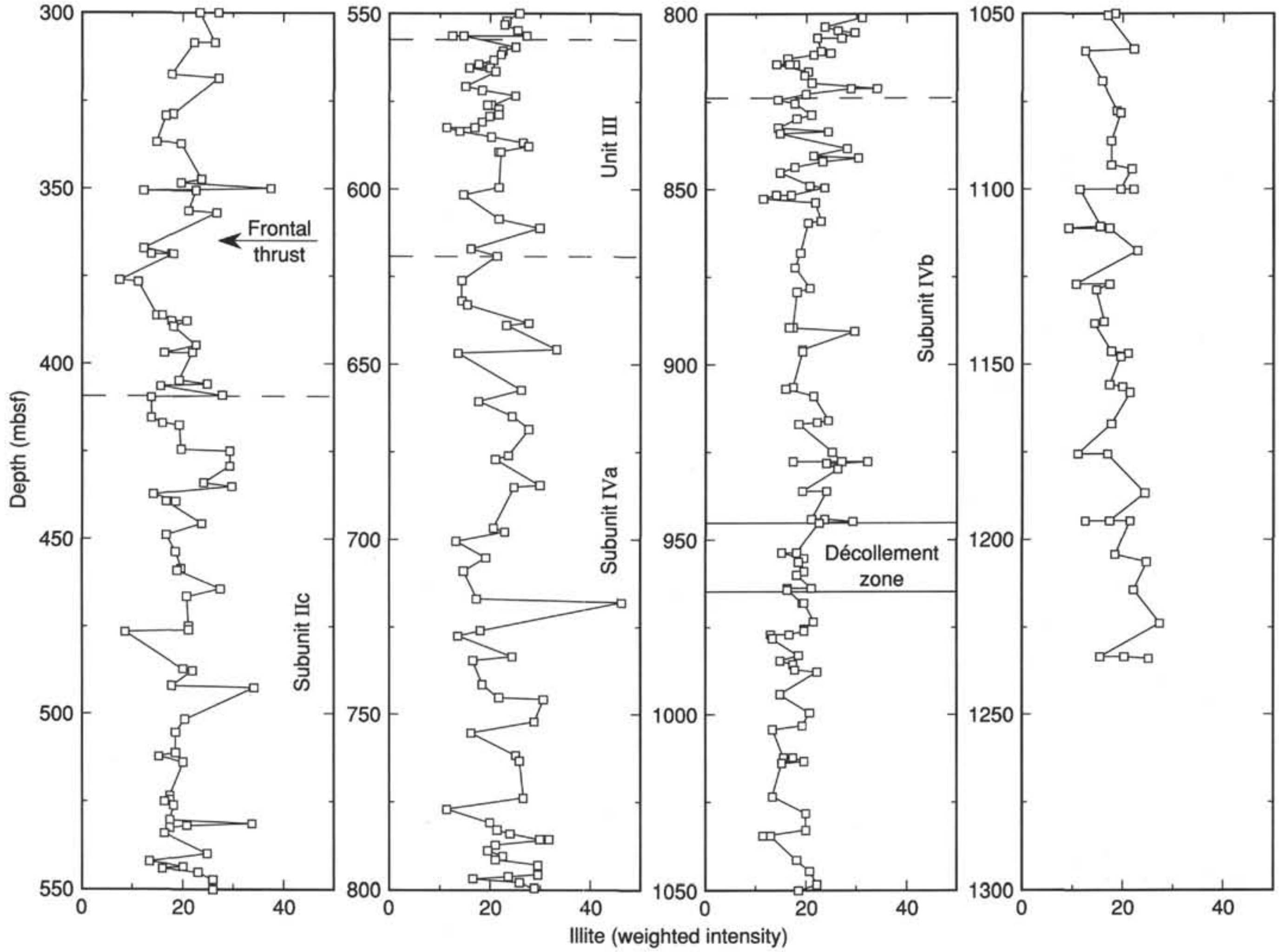

Figure 45. Weighted XRD intensity values for the diagnostic illite peak (located at approximately 8.9°2θ), Hole 808C. A weighting factor of 6.00 was used to normalize the peak intensity to that of quartz at 26.65°2θ.

Interval 5: 880.2–927.3 mbsf (Cores 131-808C-61R to -66R)

This interval contains largely subhorizontal bedding, but shows the highest concentration of small faults (Fig. 59) together with a zone of breccia/scaly fabric development. The fault planes throughout this domain are generally subhorizontal, although strikes range from 90° to 360° when rotations due to drilling are corrected with paleomagnetic data (Fig. 69). The zone of breccia/scaly fabric occurs between 880.2 and 881.5 mbsf and, with a thickness of 1.3 m, represents the most intense brecciation outside the frontal thrust and décollement.

Below this zone of brecciation and down to 924.8 m, the slickenlines associated with the faults trend consistently to the northwest, similar to the results obtained at shallower structural levels. At deeper levels (e.g., between 924.8 to 934.5 mbsf), however, the slickenlines form a tight cluster that trends east-northeast (Fig. 69), parallel to the Nankai trench and 90° to the shortening direction inferred for the accreted sediments at higher structural levels. The reason for this change in orientation of the slickenlines at this depth is at present unclear. Three relatively locally developed low-angle normal faults also occur in this zone below the breccia (Fig. 69).

Domain 4 - The Décollement

Domain 4 represents the basal décollement of the Nankai accretionary prism. It contains marked brecciation, a relatively high concentration of faults per meter and a local increase in bedding dip. The domain appears to be sharply bounded. The top is marked by the abrupt onset of a well-developed, 1.5-m-thick, breccia/scaly fabric zone at about 945 mbsf (Fig. 70), and is accompanied by a sharp increase in the number of faults per meter. The bottom of the domain at 964.3 mbsf is also very sharp and is marked by both an abrupt decrease in brecciation and by a rapid drop in the number of faults per meter (Fig. 59). We therefore consider this domain to have a vertical thickness at Site 808 of 19.2 m.

Within this interval of intense faulting and brecciation we were able to locate a 1–2-m section that was both magnetically and structurally coherent. This zone was carefully dissected for fault orientations and kinematic indicators in order to compare it with the sections above and below the décollement. The faults in this interval generally dip to the northwest and have slickenlines that trend northwest-southeast (Fig. 71), consistent with the direction of plate convergence direction in this area.

Domain 5 - The Underthrust Sequence

Domain 5 shows a marked structural contrast with the prism materials, as tectonic structures are relatively rare throughout. The domain is characterized by essentially subhorizontal bedding and a paucity of structures. Although there are some minor faults, the number per metre is very low.

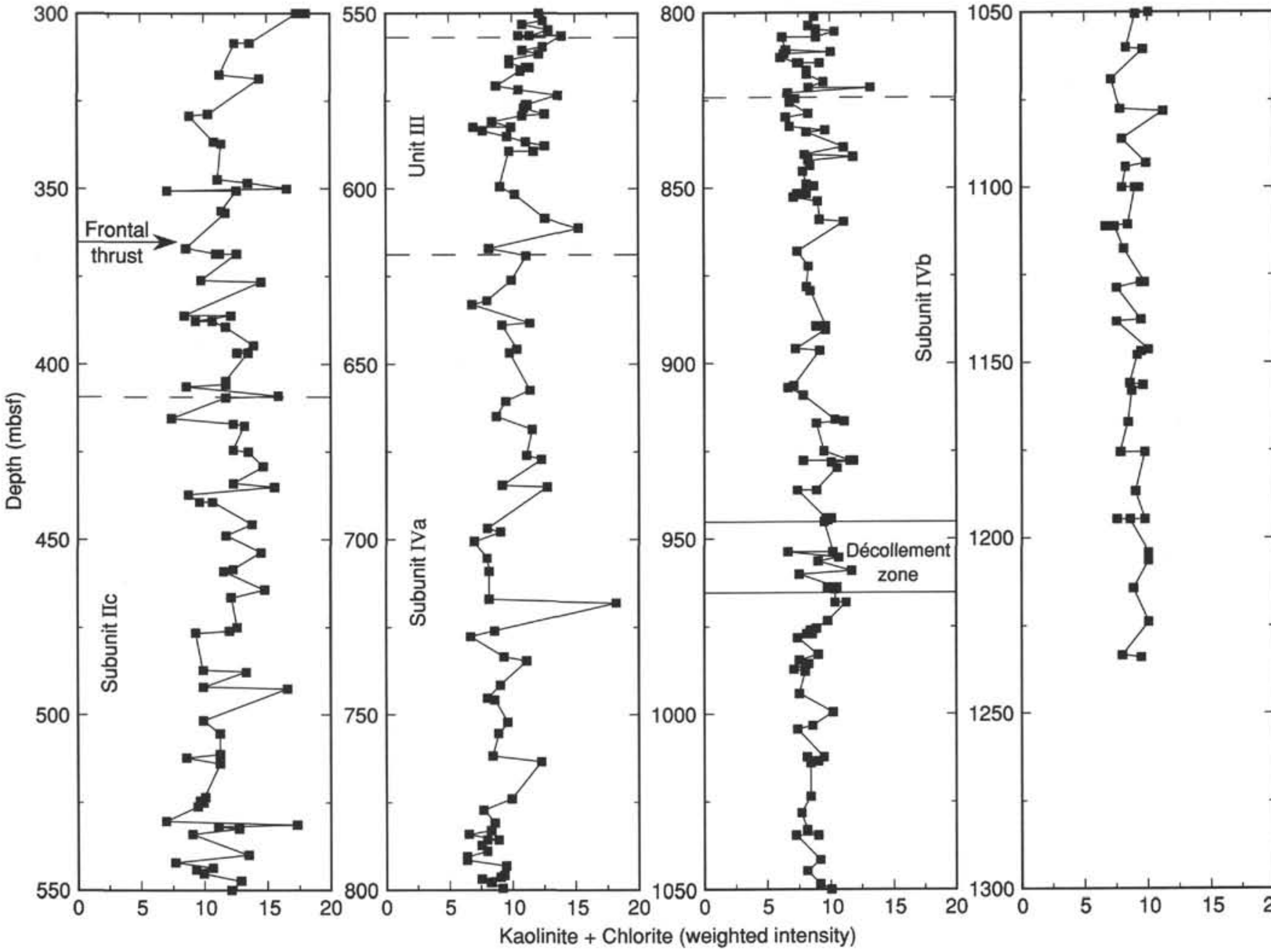

Figure 46. Weighted XRD intensity values for the [chlorite + kaolinite] peak (located at approximately 12.5°2θ), Hole 808C. A weighting factor of 2.25 was used to normalize the peak intensity to that of quartz at 26.65°2θ.

The faults preserve both normal and reverse displacements and occur in a variety of orientations, although most are gently dipping (Fig. 72). Slickenlines associated with these faults generally trend to the east. Some of the normal faults lack any dark material, and are considered to be very early, possibly syn-sedimentary, in origin. One example was observed to be cross-cut by an ash layer, another appeared to pre-date carbonate diagenesis, and another is associated with a slump fold. Other normal faults are texturally very similar to the thrust faults observed at higher structural levels and may be tectonic in origin.

The stresses that generated the wealth of deformation structures within the prism appear to have had little effect in this domain, even though its lithology is not substantially different. The simplest explanation of the structural contrasts between this domain and those above it is that significant tectonic decoupling was achieved along the décollement zone.

Domain 6 - The Oceanic Crust

Extensional veins and locally developed zones of brecciation represent the dominant structural feature observed in the recovered pieces of the oceanic crust, although they probably owe more to fluids circulating within the basalt than to tectonism. The veins are typically 2 to 3 mm wide and are composed dominantly of calcite and chlorite with minor amounts of other materials (e.g., clays, Fe-sulfides). The zones of brecciation are commonly associated with the veins and are composed of the same types of materials as well as fragments and pieces of the surrounding wall rock. They show no systematic internal organization but, like the veins, are commonly associated with yellowish brown to red oxidation halos that may be up to 2 to 3 cm wide.

These structures are discussed more fully in the Igneous Petrology section, this chapter. The disorganization of the structures, and the complete absence of faults and slickensided surfaces, suggests that these structures are not of tectonic origin.

Summary

In summary, the structural geology of the Nankai accretionary prism at Site 808 is dominated by two zones of concentrated deformation: the frontal thrust and the décollement. Structural characteristics of the frontal thrust include vertical and overturned bedding, suggesting an inclined fold-pair, abundant cross-cutting shear bands and faults, and the development of zones of brecciation/scaly fabrics. The décollement also shows an increase in the number of faults per metre but is characterized by a relatively thick zone of breccia/scaly fabric.

Shear bands are restricted to the upper half of the prism, but small faults and narrow breccia zones occur throughout. However, their distribution is heterogeneous, and localized concentrations disclose zones of higher strain, perhaps incip-

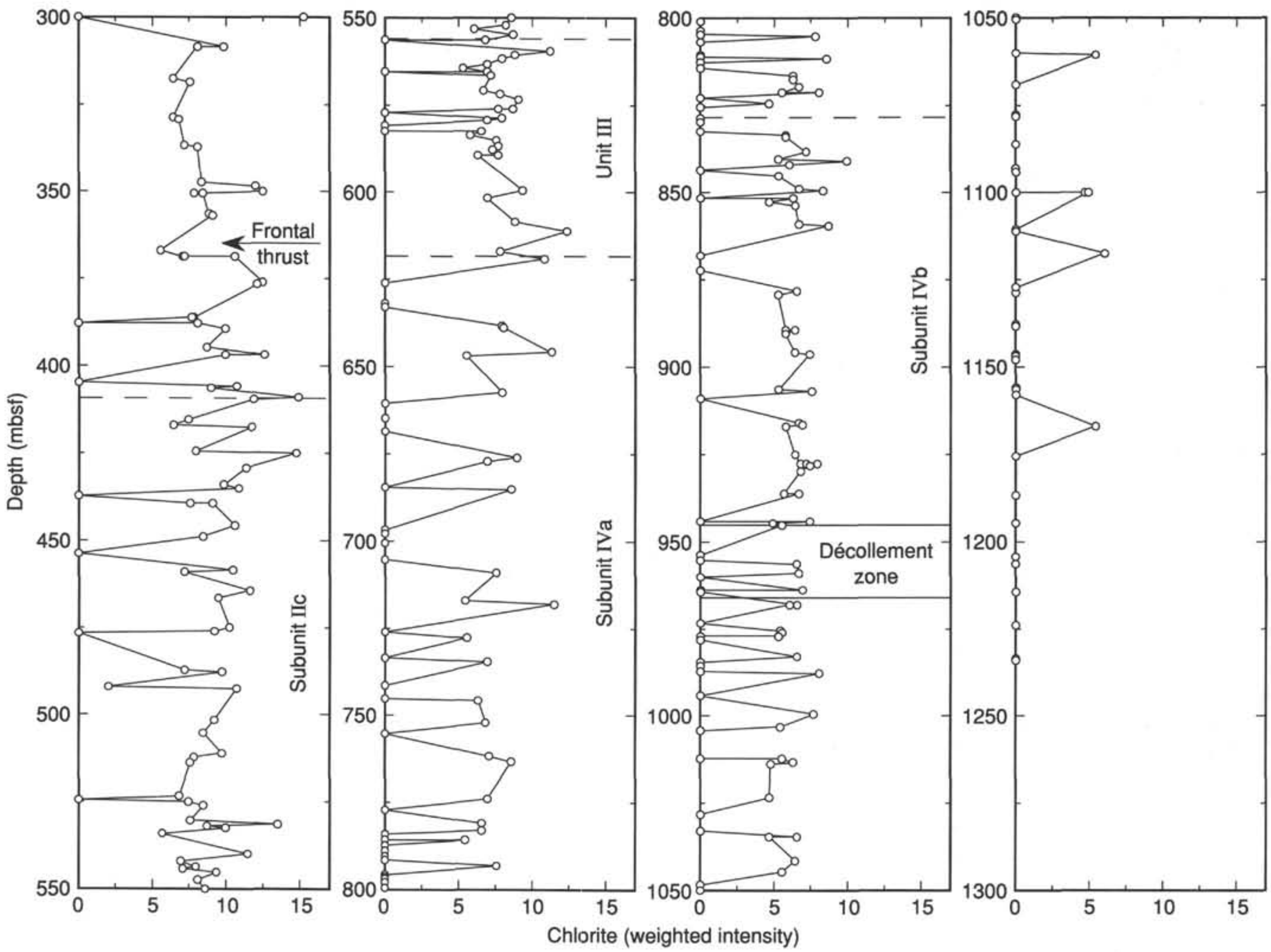

Figure 47. Weighted XRD intensity values for the chlorite peak (located at approximately 18.8°2θ), Hole 808C. A weighting factor of 4.95 was used to normalize the peak intensity to that of quartz at 26.65°2θ.

ient or failed major structures. Deformation is very weak in the underplated material.

A single clastic dike is the only observed evidence for overpressuring or fluid flow within the prism. The complete absence of veins and other mineralized faults or fractures suggests that fluid flow is likely to be distributed throughout the prism rather than channeled along the major tectonic structures observed at Site 808.

PALEOMAGNETICS

Introduction

For three holes at Site 808, remanence measurements were made on archive-half sections of core using the shipboard cryogenic magnetometer. A few sections were not measured, on the grounds of excessive drilling disturbance; otherwise, within the limits of core recovery, a continuous record of remanence variation was obtained.

The primary goal of the paleomagnetic measurements at Site 808 was to establish a magnetostratigraphy. Secondary, but of considerable importance, was the use made by structural geologists and sedimentologists of the remanence to provide core orientation data. For both these purposes it is important to assess the stability of remanence. Measurements were made, at 5- or 10-cm intervals, of natural remanent magnetization (NRM) and after demagnetization in alternating fields of 5, 10, and 15 mT. In many cases the remanence changed little between the two higher steps. The first sections in each core were demagnetized at all steps; some later sections were measured only for NRM and after demagnetization in a field of 10 or 15 mT. The effects of a magnetization acquired during drilling were apparent, and were clearly associated more strongly with one of two core barrels, used alternately (e.g., Fig. 73, for Hole 808C, between 575 and 675 mbsf). This remanence was soft and easily removed.

To obtain declination, inclination, and intensity values the data from the magnetometer were processed under the assumption that the core section is uniformly magnetized. This is adequate if the magnetization is uniform over the sensing distance of the magnetometer sensors (i.e., within about 15 cm of the measuring point), but produces distorted results where the magnetization changes rapidly, as a result either of natural causes or of artifacts (such as voids, or segments rotated differentially within the core-liner). Across a rotated break inclination magnitudes are overestimated and intensities underestimated (see Explanatory Notes chapter, this volume), introducing an artificial scatter in these data. This should be borne in mind when examining the data presented here.

Table 9. Modal data for turbidite sands of facies Subunit IIa, Hole 808A. Symbols for all detrital categories are defined in the Explanatory Notes.

Hole	808A	808A	808A	808A	808A	808A	808A	808A	808A	808A	808A	808H	808A
Core	3H	3H	4H	4H	4H	6H	6H	7H	8H	10H	10H	11H	13H
Section	4	5	4	6	4	4	4	2	1	5	6	2	3
Interval	80–81	25–27	86–88	100–102	50–52	54–55	70–72	80–82	34–36	50–52	100–102	100–102	90–91
Q_m	61	50	40	49	39	58	53	46	56	40	62	53	32
Q_p	25	19	16	9	9	25	22	19	20	23	18	17	18
F	44	57	63	70	68	42	69	58	65	52	57	69	54
V_g	6	6	4	4	8	1	5	4	2	6	11	4	7
V_r	66	93	94	93	82	84	48	73	79	77	64	68	110
L_s	81	64	75	65	83	78	93	90	72	88	82	81	74
L_m	17	11	8	10	11	12	10	10	6	14	6	8	5
H	15	16	17	24	18	12	17	15	18	4	15	22	9
M	3	2	0	0	0	0	0	5	0	2	1	1	0
C	3	1	1	1	1	1	1	3	1	2	3	3	0
O	9	8	2	4	4	5	7	3	0	3	2	5	3
Total	330	327	320	329	323	318	325	326	319	311	321	331	313
Quartz	86	69	56	58	48	83	75	65	76	63	80	70	50
Lithic	170	174	181	172	184	175	156	177	159	185	163	161	196
All Modes	300	300	300	300	300	300	300	300	300	300	300	300	300
Q	28.7	23.0	18.7	19.3	16.0	27.7	25.0	21.7	25.3	21.0	26.7	23.3	16.7
F	14.7	19.0	21.0	23.3	22.7	14.0	23.0	19.3	21.7	17.3	19.0	23.0	18.0
L	56.7	58.0	60.3	57.3	61.3	58.3	52.0	59.0	53.0	61.7	54.3	53.7	65.3
Poly Modes	195	193	197	181	193	200	178	196	179	208	181	178	214
Q_p	12.8	9.8	8.1	5.0	4.7	12.5	12.4	9.7	11.2	11.1	9.9	9.6	8.4
L_v	36.9	51.3	49.7	53.6	46.6	42.5	29.8	39.3	45.3	39.9	41.4	40.4	54.7
L_{sm}	50.3	38.9	42.1	41.4	48.7	45.0	57.9	51.0	43.5	49.0	48.6	50.0	36.9

Measurements of discrete samples were attempted on the ship with the fluxgate spinner magnetometer, but were discontinued when it was realized that some samples were acquiring a significant anhysteretic remanence, associated, we believe, with the presence of higher harmonics in the drive current to the alternating field demagnetizer. Measurements subsequently made onshore using a fluxgate spinner magnetometer and a demagnetizer incorporating a two-axis tumbler are included in this report.

Three holes were drilled at Site 808, using respectively, the advanced piston corer, the extended core barrel system and the rotary core barrel. The results obtained from each are reviewed below.

Hole 808A

This hole penetrated, to a depth of 111 mbsf, the thin turbidites, slumps, and hemipelagic mud of the slope apron, and the thick-bedded sand turbidites of the axial trench wedge. The latter, recovered mainly as fluidized sands, were not measured. The former were much disturbed by gas expansion structures and by coring deformation. Remanence measurements showed a wide scatter of inclination values but, despite evidence of overturned beds in the slump sequences, these were almost exclusively positive. Similarly, relative declinations within a core were consistent. The results suggest that post-depositional remagnetization has occurred.

Hole 808B

The extended core barrel system was used to core from 111 to 359 mbsf. Recovery was poor in the continuing sandy turbidites, but improved as the turbidite units thinned. Coring deformation was apparent in the bowing of planar features in the upper part of the hole and in "biscuiting" at greater depths. The declinations observed are widely scattered, suggesting short, rotated fragments. Inclinations fall between about 40° and 90°; the bias to high values is interpreted as a reflection of the frequency of occurrence of rotated breaks (Fig. 74).

Hole 808C

The depth achieved in this hole (1327 mbsf) far exceeds that at the two preceding holes and in consequence the magnetic record extends back sufficiently far in time for the standard approach to establishing a magnetostratigraphy, of delineating depth intervals as Normally or Reversely magnetized on the basis of positive or negative remanence inclinations, to become applicable. Coring was started at about 300 mbsf in the sediments of the outer marginal trench deposits (lithologic Subunit IIc; see Sedimentology section, this chapter). The hole penetrated the tectonically disturbed zone associated with the frontal thrust (which repeats about 145 m of the succession: see Sedimentology section, this chapter), and it continued through the long sequence of Shikoku Basin sediments before terminating at 1327 mbsf in the basaltic basement.

Cryogenic Magnetometer Results

Figure 73 records the variation, with depth, in inclination before demagnetization and in inclination and intensity after demagnetization at the highest field (10 or 15 mT) to which the archive-half sections were subjected in the cryogenic magnetometer. It is immediately apparent that there are, in terms of inclination, two broadly different styles of behavior on demagnetization.

In the first, taken to characterize Normally magnetized rocks, the inclinations tend to cluster in the range 30° to 60°, on demagnetization. In relatively young, tectonically undisturbed rocks of Normal polarity it can be difficult to distinguish whether the magnetization seen is one acquired originally (i.e., at the time of the rock's formation) in a direction close to that of the present Earth's field, or whether the magnetization is merely a recently acquired overprint. For most of the sediments encountered in the hole bedding-dips are small (of the order of 10° or less), but steeper dips are encountered in the region of the thrust (360–400 mbsf) and at about 535 mbsf, and provide a "fold test," which suggests that

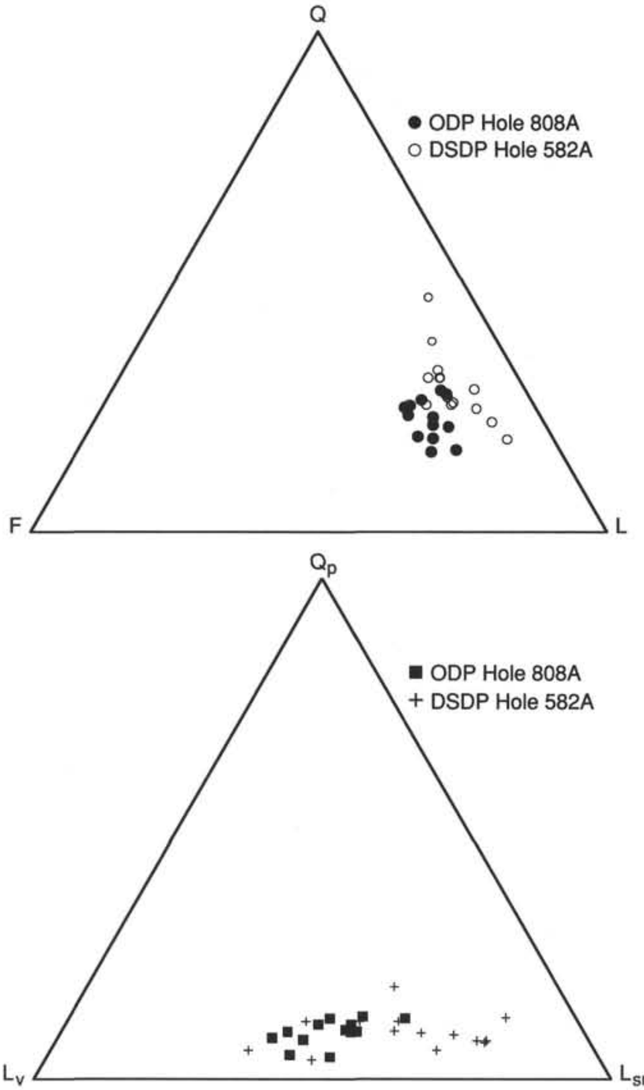

Figure 48. Modal data for turbidite sands from ODP Hole 808A compared to previous results from DSDP Hole 582A (Taira and Niitsuma, 1986). Q = total quartz; F = total feldspar; L = total aphanitic lithic fragments; Q_p = polycrystalline quartz; L_v = volcanic rock fragments and glass shards; L_{sm} = fine-grained sedimentary and metasedimentary rock fragments.

the remanence is, in fact, stable. The fold test is discussed in a subsequent section.

The second style of behavior is characterized by a dispersal of inclinations, and a spread to negative values, on demagnetization. If this pattern of behavior is interpreted as resulting from a conflict between an initial Reversed magnetization and subsequent exposure to the present Normal field, it may be plausible to extend (with discretion) the identification of intervals having an original Reversed magnetization to those in which the inclinations show a tendency to move to low values, even if they do not actually become negative.

On the basis of these characteristics a tentative identification of Normal and Reversed polarity intervals was made (Fig. 75).

Measurements on Discrete Samples

Discrete samples were measured to assess the correctness of the assumptions made in the shipboard applications of paleomagnetic results. These applications were twofold: first magnetostratigraphic and second in the provision of a means of sample orientation. For these essentially confirmatory purposes, measurements were made on minicores at a sampling rate of approximately one sample per two cores over the depth range 350 to 650 mbsf and one sample per core over the depth range 650 to 1100 mbsf.

Results are summarized in Table 11. They are quoted as natural remanent magnetization, and where alternating-field demagnetization indicated a stable remanence, the direction of that remanence (estimated from linear fits to Zijderveld plots), together with an approximate value of the demagnetizing field at which it could first be identified, and its corresponding intensity. For comparative purposes the polarity previously inferred from the continuous-core, cryogenic magnetometer measurements is recorded. Magnetic susceptibility values (in SI units) are included for completeness (and comparison with Fig. 126, Physical Properties section, this chapter). For samples with intensities of the order of 0.1 A/m a sense of polarity may be inferred, but little reliance should be placed on the precise directions quoted.

Magnetostratigraphy

Figure 75 shows how the reversal sequence drawn up from Figure 73 has been matched to the established polarity time scale (Berggren et al, 1985). Details of the age/depth relationship are given in Table 12.

Ages inferred from nannofossil observations (see Biostratigraphy section, this chapter) have been used to provide a firm constraint in matching the present measurements to the polarity time scale: age vs. depth plots derived from biostratigraphy and paleomagnetism are related in Figure 76. Nevertheless, on a finer scale the detailed mapping between the polarity/depth and polarity/time scales is, in general, satisfactory and has not required undue forcing. Attention should, however, be drawn to the interval between 656 and 803 mbsf. The base of the Brunhes Chron is clear at about 656 mbsf, and the Gauss Chron, with its characteristic dominantly Normal signature, has been associated with the depth interval 803 to 865 mbsf. However, many of the details within the depth range 656–803 mbsf, which must, by implication, be assigned to the Matuyama Chron, are difficult to reconcile with the established pattern of reversals. Less material of obviously Reversed polarity is seen than expected. In this depth interval the remanence intensity drops and there is a reduction in values of bulk magnetic susceptibility (see Physical Properties section, this chapter, Fig. 126); both may be associated with the influx of ash and tuff noted in the sedimentary record (see Sedimentology section, this chapter). It is possible that these changes might be accompanied by a change in the general stability of remanence. The reversal sequence can be followed to about 1070 mbsf. Beyond this depth, however, the limited core recovery precludes any confident extension of the correlation, although the dominance of negative inclinations observed in the interval between 1069 and 1220 mbsf would suggest that the base of Chron 11 is correctly identified at about 1069 mbsf. It is noteworthy that the remanence intensity, having climbed slowly through the preceding sediments, again falls sharply by an order of magnitude at about 1070 mbsf. This correlates with a sharp decrease in core recovery, but without any obvious change in lithology. Neither Sedimentology nor Physical Properties (sections, this chapter) record a boundary at this depth. A very tentative association of an age of about 14 m.y. with a depth of 1250 mbsf would appear to satisfy the observed reversal sequence, and would not be greatly at variance with the paleontologically predicted age for this depth.

Measurements on discrete samples (Table 11) have, in general, confirmed the picture pieced together from the cryo-

Table 10. Biostratigraphic events that were observed at Site 808 and their respective age estimates. The depth uncertainty is predominantly caused by barren samples and the sample intervals used. Thrust-corrected depths refer to depths below 400 mbsf that have been reduced by 145 m to correct for the displacement by the thrust. References for the age estimates are presented in the Explanatory Notes chapter.

Event	Zone (Top)	Core, section interval (cm)	Depth interval (mbsf)	Depth (mbsf)	Thrust corr. depths (mbsf)	Error (meters)	Age (Ma)	Sed. rate
		131-808A-		0.00	0.00	0.00	0	
1 OA *E. huxleyi*		9H-5, 5 cm/10H-CC	74.35–87.40	80.88	80.88	6.82	0.09	898.7
		131-808B-						
2 FO *E. huxleyi*	NN20	13X-1, 42 cm/13X-CC	226.22–235.10	230.66	230.66	4.44	0.28	788.3
		131-808C-						
3 LO *P. lacunosa*	NN19	34R-4, 134 cm/34R-CC	622.34–626.20	624.27	479.27	1.93	0.46	1353.4
4 LO *R. asanoi*		37R-CC/38R-CC	647.88–664.72	656.30	511.30	8.42	0.83	86.6
5 FO *R. asanoi*		41R-CC/42R-CC	686.28–703.20	694.74	549.74	8.46	1.06	167.1
6 LO large *Gephyrocapsa*		41R-CC/42R-CC	686.28–703.20	694.74	549.74	8.46	1.10	0.0
7 FO large *Gephyrocapsa*		46R-CC/47R/CC	739.28–751.10	745.19	600.19	10.99	1.36	194.0
8 LO *C. macintyrei*		47R-CC/48R-CC	750.63–760.90	755.77	610.77	5.16	1.45	117.5
9 FO *G. oceanica*		49R-CC/50-2, 63–64 cm	767.53–772.54	770.04	625.04	2.51	1.57	118.9
10 FO *G. caribbeanica*	Pli/Plei	50R-4, 59–60 cm/50R-6, 72–73 cm	775.5–778.62	777.06	632.06	1.56	1.66	78.1
11 LO *D. brouweri*	NN18	51R-3, 85–86 cm/51R-5, 77–78 cm	783.96–786.88	785.42	640.42	1.46	1.89	36.3
12 LO *D. tamalis*		56R-1, 80–81 cm/56R-3, 136–137 cm	829.2–832.76	830.98	685.98	1.78	2.65	59.9
13 LO *Sphenolithus* spp.		60R-3, 123–124 cm/60R-5, 51–52 cm	871.04–873.32	872.18	727.18	1.14	3.45	51.5
14 LO *R. pseudoumbilica*	NN15	60R-5, 51–52 cm/60R-CC	873.32–876.50	874.91	729.91	1.59	3.56	24.8
15 FO *D. asymmetricus*	NN13	62R-CC/63R-1, 41–42 cm	893.9–896.22	895.06	750.06	1.16	4.1	37.3
16 FO *C. rugosus*	NN12	64R-CC/65R-CC	912.38–924.80	918.59	773.59	6.21	4.6	47.1
17 LO *T. rugosus*	Mio./Plio.	69R-1, 62–63 cm/69R-3, 61–62 cm	954.42–957.42	955.92	810.92	1.50	4.9	124.4
18 LO *D. quinqueramus*	NN11	69R-1, 62–63 cm/69R-3, 61–62 cm	954.42–957.42	955.92	810.92	1.50	5.0	0.0
19 FO *D. quinqueramus*	NN10	73R-5, 63–65 cm/74R-CC	998.74–1011.30	1005.02	860.02	6.28	7.5	19.6
20 FO *C. coalitus*	NN7	83R-CC/84R-3, 47–48 cm	1089.59–1095.48	1092.54	947.53	2.95	11.1	24.3
21 FO *D. kugleri*	NN6	92R-CC/93-1, 104 cm	1167.63–1176.34	1171.99	1026.99	4.36	12.2	72.2
22 LO *C. floridanus*		94R-CC/95R-CC	1187.27–1204.30	1195.79	1050.79	8.52	13.1	26.4
23 LO *S. heteromorphus*	NN5	97R-1, 80 –81 cm/97R-CC	1214.8–1223.70	1219.25	1074.25	4.45	13.6	46.9

genic magnetometer readings. Normally magnetized samples (particularly in the Brunhes Chron) show little directional movement on demagnetization, whereas Reversely magnetized samples often show an overprint, the removal of which may require a demagnetizing field in excess of the 15-mT maximum applied to the archive half-core. Zones of very low intensity are again observed and intensities correlate broadly with susceptibilities. The only disagreement of possible significance occurs at 750–760 mbsf, where an interval previously identified as Normal now appears (though on the basis of only weakly magnetized samples) as Reversed. If this is upheld, it might prompt a revision in matching to the polarity time-scale (Fig. 75) such that the Gauss Chron is set to 765–865 mbsf. This would restore the balance of Normal and Reversed intervals and smooth the age/depth curve (Fig. 76), but at the expense of a small discrepancy with biostratigraphic evidence and the presence of three (rather than two) well-established Reversed intervals within the Gauss Chron.

Beginning with Core 131-808C-105R, at 1290 mbsf, basalt samples were recovered, for the most part only in short fragments. Discrete sections that were not thought to have become inverted in the core liner were measured with the cryogenic magnetometer. Median destructive fields for the samples were low (less than 5 mT in Cores 131-808C-105R through -107R; about 5 mT in -108R) and directions of inclination, though consistent and apparently stable within a core, were scattered between cores (thus inclinations were shallow and positive in Core 131-808C-105R, steep and positive in -106R and -108R, and shallow and negative in -107R). In magnetostratigraphic terms the evidence they provide is inconclusive.

Fold Testing

Figure 73 shows that, above 650 mbsf in Hole 808C, the inclination of remanence after demagnetization is generally scattered about a value close to that expected (52°) for a magnetization acquired in an axial dipolar field. Clear departures from this pattern are observed between about 360 and 400 mbsf, and again at about 535 mbsf. In both zones structural observations indicate that the beds are dipping.

A very idealized model of folding in the Nankai Trough area would set fold axes horizontal, and parallel to the

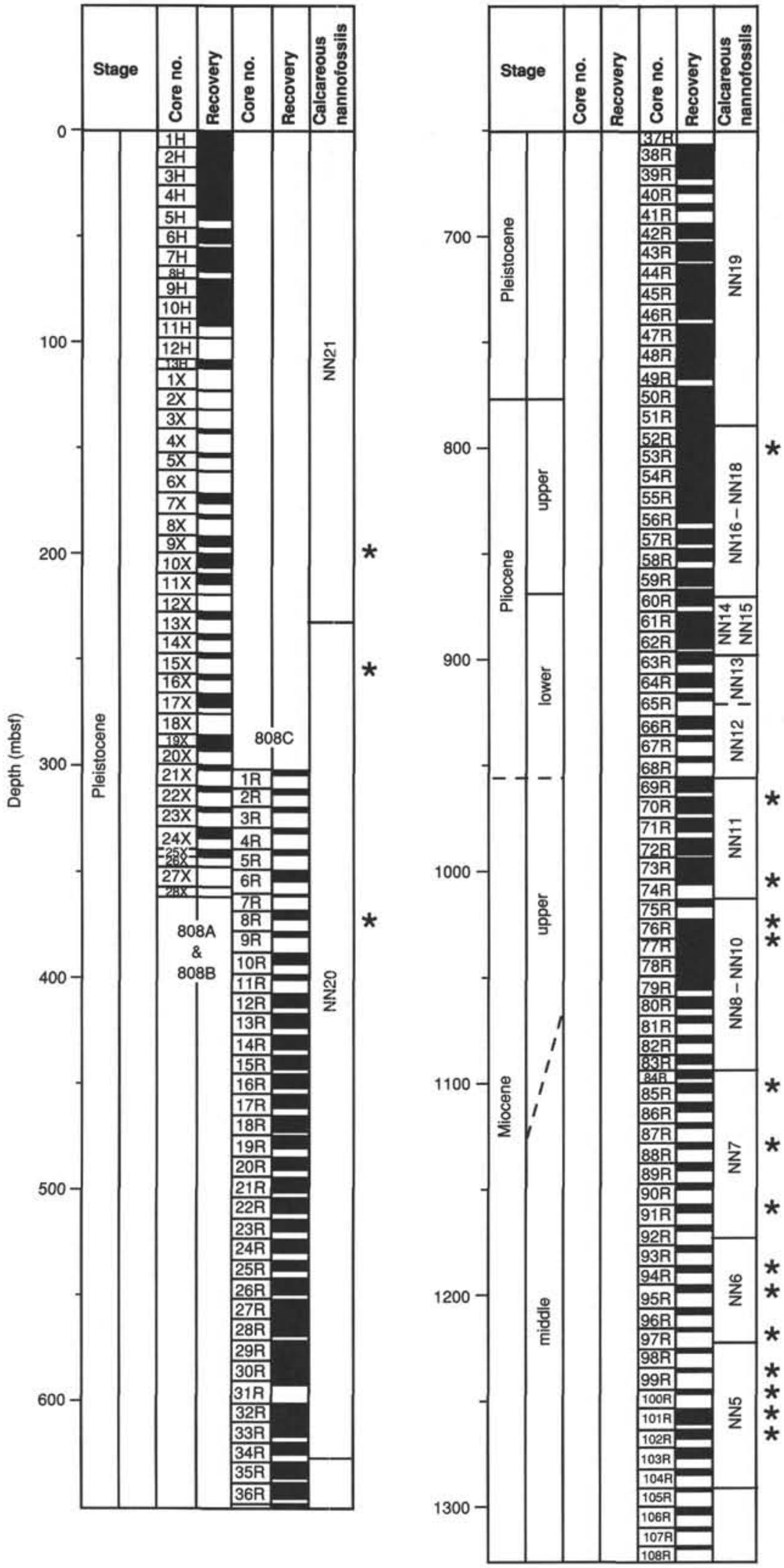

Figure 49. Core recovery at ODP Site 808 together with calcareous nannofossil zonal assignments. Asterisks mark samples that are barren of calcareous nannofossils.

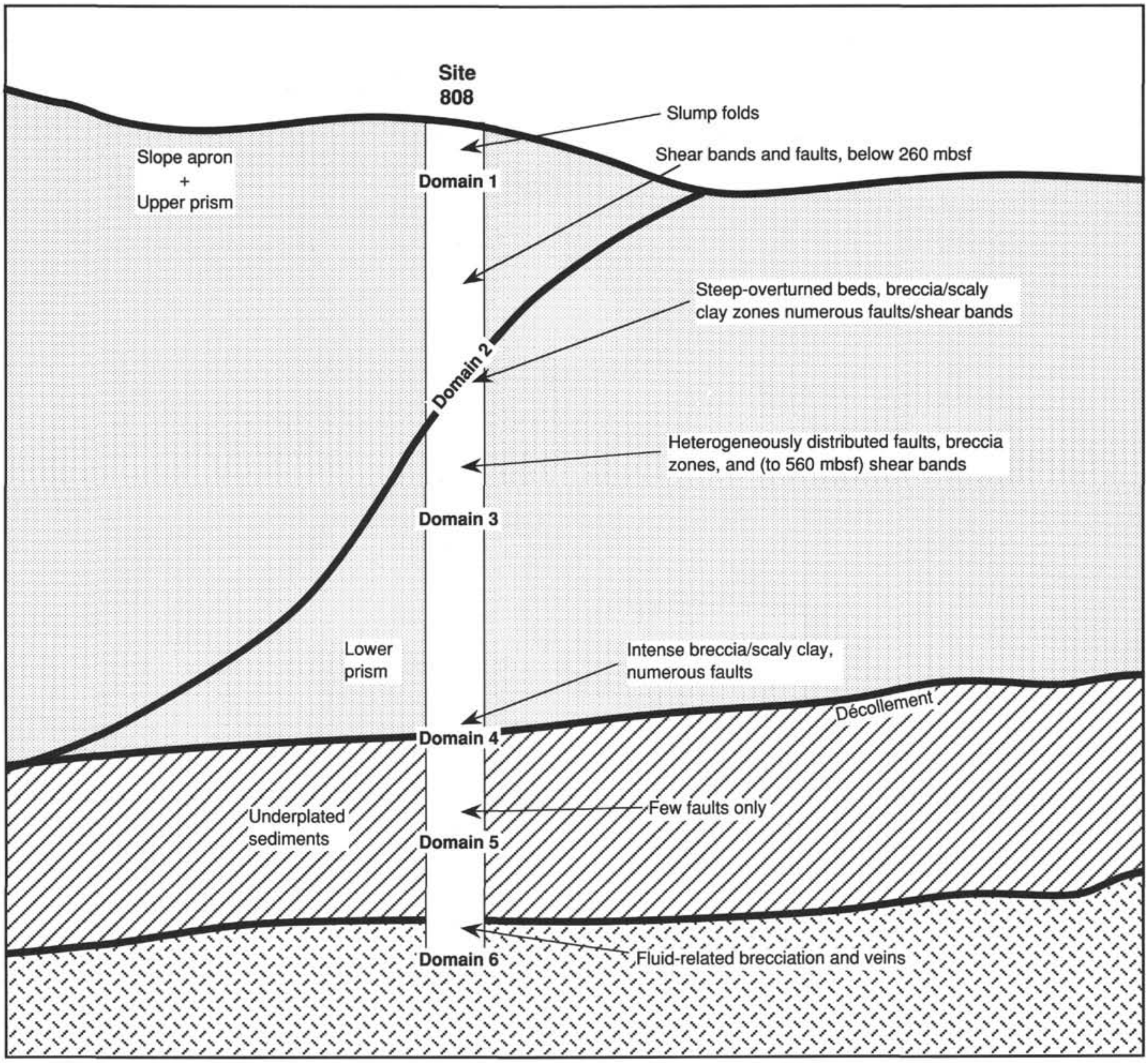

Figure 50. Annotated diagram, about 2× vertical scale, showing the distribution of the structural domains described in the text.

predominant northeast-southwest regional strike. Figure 77 plots the predicted inclinations that result when a horizontal bed containing a "recent Normal" remanence (declination = 0°, inclination = 50°) is rigidly rotated about a horizontal northeast-southwest axis to give southeast dips (see also Fig. 78). Observed bedding dips and magnetization inclinations are also plotted. The agreement between the observations and the model is good in all cases except that of the overturned beds that occur close to the thrust in Core 131-808C-8R. The results provide a strong indication that the remanence is stable. They may additionally suggest that, while a rigid rotation of bedding is in general an adequate model, there may be penetrative deformation, affecting the remanence, in the region of the thrust.

The Use of Remanence for Core Orientation

In the absence of other means of orientating cores, the use of remanence is an attractive possibility, and the technique has been applied enthusiastically to Hole 808C by both structural geologists and sedimentologists. It is, nevertheless, an indirect procedure, and its correct application rests on a number of assumptions. One of the aims in measuring discrete samples was providing a background against which the validity of the technique could be assessed.

The principal assumptions made are: (1) that the samples contain a measurable and stable component of remanence, the acquisition of which can be associated with the magnetic field acting at a known period in the Earth's history. It is assumed that the magnetization was acquired parallel to the direction of the field, but the argument can withstand some shallowing of remanence inclination, as might occur for example, with depositional remanence; (2) that correction has been made for any tectonic modification (due to a bedding dip, for example, in the simplest case) of the remanence direction subsequent to remanence acquisition; (3) that the direction of the paleofield in which the remanence was acquired is known. In practice,

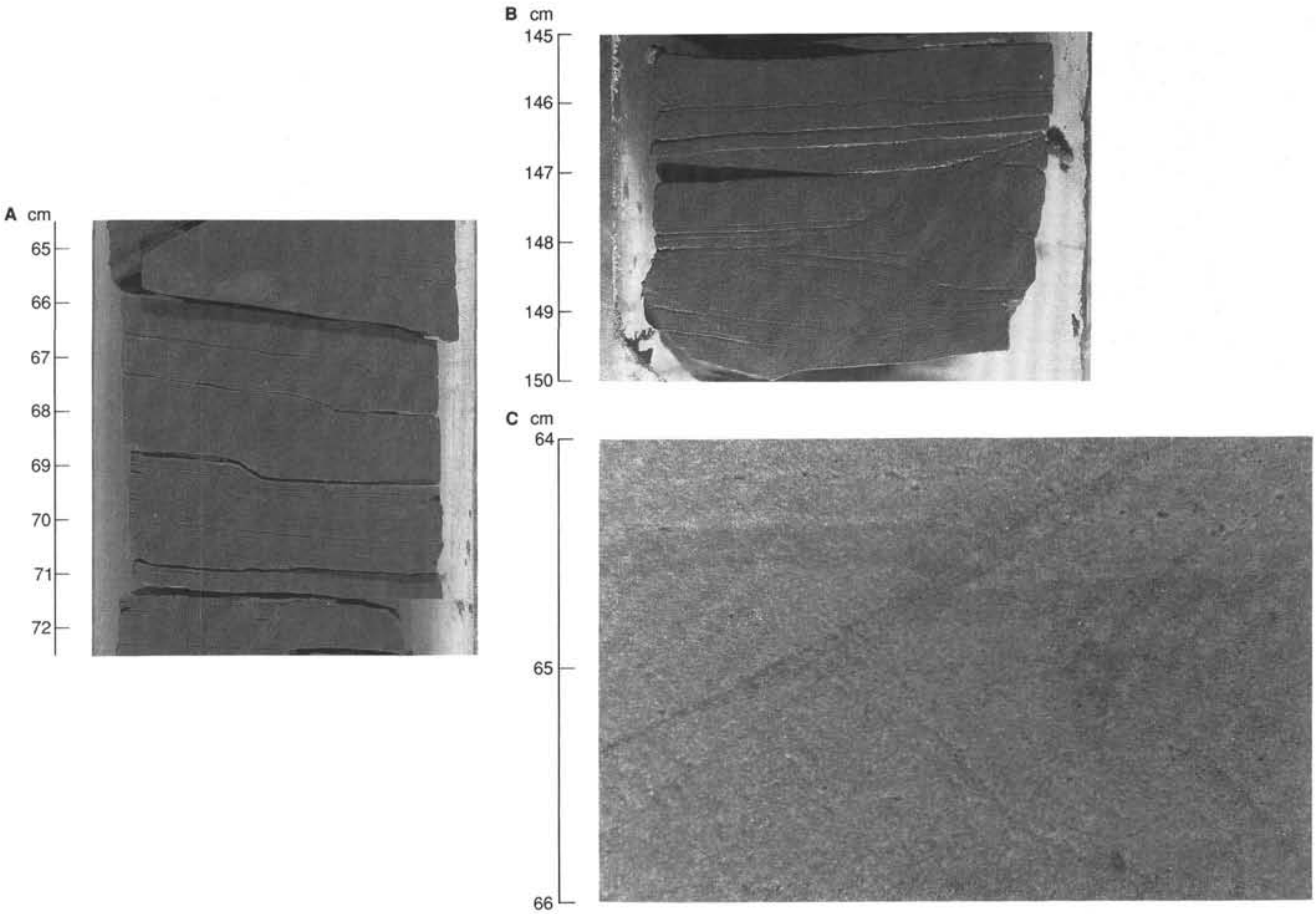

Figure 51. Examples from core photographs of shear bands and faults that record contractional displacements. **A.** shows a shear band from Interval 131-808C-16, 64.5–72.5 cm. **B.** shows a small fault from interval 131-808C-18, 145–150 cm. **C.** shows a fault from interval 131-808B-17X-4, 64–66 cm.

this requires an appeal to an axial geocentric dipolar model of the Earth's field with a known virtual pole position, and an assumption that the time interval represented by a sample is sufficiently long for secular variation to be averaged out.

These assumptions can be examined in turn for the specific context of Hole 808C: (1) Precision of measurement decreases as the noise level of the magnetometer is approached. The noise levels of the fluxgate spinner for minicores and the cryogenic magnetometer for small sections of half-core are roughly comparable and set a lower limit on useful intensities of about 0.3 A/m. Some of the weakest magnetizations encountered in Hole 808C were at or below this level (see Fig. 73 and Table 11).

Spot measurements at a single demagnetizing field (< 15 mT) such as were made on samples from the archive half-core cannot indicate the stability of remanence. Appeal must be made, therefore, to the behavior of nearby discrete samples from the working half for an indirect assessment of stability. In many cases, such measurements demonstrate (Table 11) that a stable primary magnetization component can be isolated at demagnetizing fields below those applied to the archive half-core, though in some instances, particularly for Reversely magnetized rocks, higher demagnetizing fields are required. (2) The effects of bedding dip in modifying remanence direction has been discussed in the preceding section. In the simple model introduced there, the remanence direction rotates around a small circle as the bedding dip increases (see Fig. 78) and therefore introduces a systematic shift in declination. The model provides a means of making an approximate correction, but in the case considered, this error does not exceed 20° unless the beds are steeply overturned (and the model inappropriate anyway). (3) The rocks encountered in Hole 808C are young enough for the Earth's field to be modeled satisfactorily by a central dipole parallel to the geographic N-S axis, although at the highest sedimentation rates encountered (>1 km/m.y.), or with episodic turbidite deposition, secular variation may not be averaged out. The rocks encountered are old enough, however, to have recorded field reversals. When the field is of settled polarity, a dipole model is adequate, but it provides no description of field behavior during polarity transitions. Pointers to the appropriateness of the model for sample orientation purposes in a particular case are provided by the remanence inclination and the sample's position relative to the record of polarity transitions (Fig. 75). Table 11 suggests that for the Brunhes Chron, remanence inclinations, at about 40°, systematically underestimate the inclination (52°) expected for the present latitude of Nankai, but the value is consistent. Remanence directions in which the inclinations are markedly shallower or steeper than this, or those from samples taken close to reversal boundaries, are unlikely to be reliable.

In summary, assessment of the usefulness of a remanence direction for sample orientation must take account of the strength and stability of the remanence, of the remanence inclination, of the sample's tectonic setting and of its position

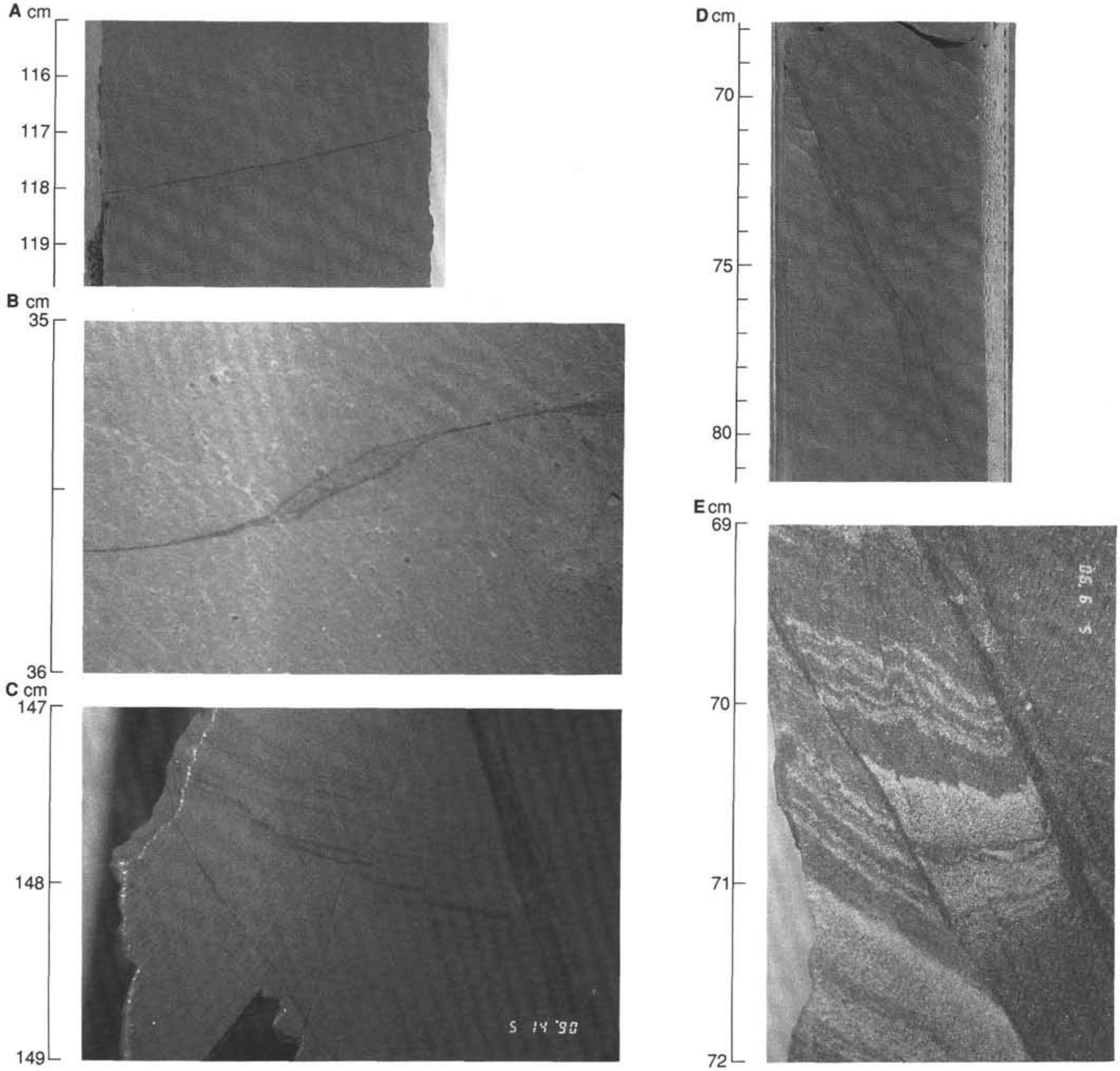

Figure 52. Core photographs showing typical small faults. **A.** shows a typical planar fault consisting of a thin layer of black material (from interval 131-808C-12R-2, 115–120 cm). **B.** shows a close-up photograph of a typical fault (from interval 131-808B-17X-1, 35–36 cm. **C.** shows a set of small faults with a well-developed zone of back material in the fault zone on the right (from interval 131-808C-8R-1, 147–149 cm). **D.** Core-scale photograph of a thrust fault. Bedding can be seen just below the fault in upper left corner; bedding dips approximately 25° (from interval 131-808C-25R-1, 68–81.5 cm). **E.** Close-up photograph of offset bedding (from interval 131-808C-25R-1, 69–72 cm).

with respect to the reversal sequence. Only if the criteria outlined above are satisfied can one use the remanence declination to align the sample with respect to present north. Table 11 suggests that (with due allowance for drilling-induced deformation at shallow depth) the technique is likely to be reliable for the Brunhes Chron (to a depth of about 650 mbsf), but should be treated with caution where intensities are low (650–770 mbsf and 1060–1250 mbsf) or where there are indications of rapid polarity variation.

INORGANIC GEOCHEMISTRY

Interstitial Water Chemistry

Introduction

At Site 808 a large number of closely spaced samples were collected for the study of the composition of the interstitial waters of Holes 808A, 808B, and 808C. The main purpose of these studies was to determine from depth changes in the

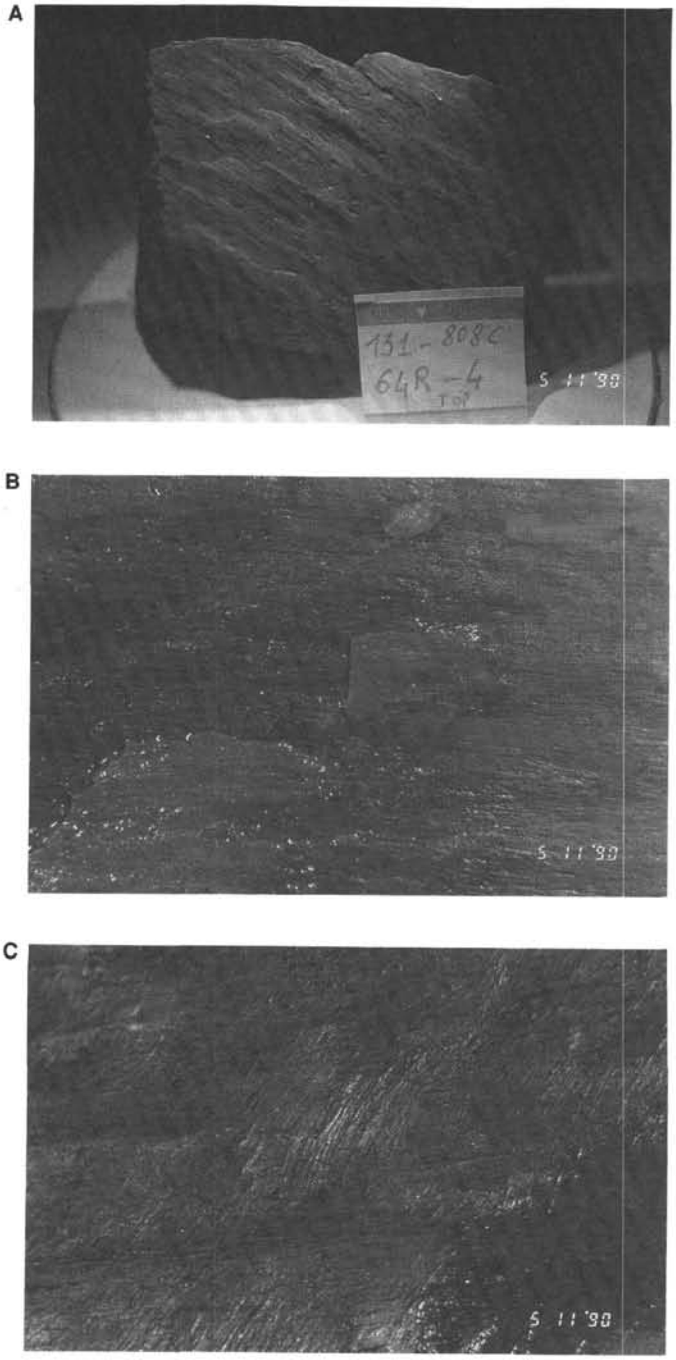

Figure 53. Examples from core photographs of slickensided surfaces from two faults. **A**. shows a polished and well-lineated fault surface from just above the décollement (interval 131-808C-64R-4, 0 cm; width of field of view is about 3 cm). **B**. Close-up photograph of the slickenlined surface shown in **A** (left center). **C**. shows two sets of oblique slickenlines on one slickensided surface (from interval 131-808C-64R-4, 80–81 cm).

interstitial water chemistry whether evidence exists for past and/or present movement of fluids through the sediments of the Nankai accretionary complex. In addition these studies serve as sensitive detectors of potential diagenetic processes occurring in the sediment column, which in turn influence the physical properties of the sediments. Both major interstitial water constituents (chloride, sodium, sulfate, calcium, magnesium, and potassium) as well as minor constituents (silica, lithium, and strontium) and constituents originating from the degradation of organic material (alkalinity, ammonium, and phosphate) have been used for this purpose.

Methods

Sample Retrieval

To obtain acceptable quality in the interstitial water data it is often necessary to retrieve relatively small quantities of "pristine" material from the disturbed whole round cores. In particular, the low porosity sediments near fault zones were characterized by drilling disturbance and the appearance of "biscuits" of undisturbed sediments. At greater depths low porosities did not allow enough material (less than a few cm^3) of pore fluid to be retrieved from the traditional 10-cm whole-round core, thus necessitating taking much longer whole-round samples, sometimes as much as 35 cm. This problem is well demonstrated in Figure 79, in which interstitial water yields per centimeter of whole-round core are plotted vs. depth. Especially at greater depths (Hole 808C), even these longer whole-round samples yielded barely sufficient amounts of interstitial water (less than 2 cm^3). In all whole-round cores any potentially contaminated material must be removed to reduce contamination with drilling fluid (surface seawater with various admixtures of drilling mud). Nonetheless, as is evident in particular from scattered variations in sulfate concentration (usually less than 5%, but sometimes exceeding 10%), some contamination is virtually unavoidable, particularly in the deeper section of Hole 808C. In general, however, the data are relatively unaffected by contamination, so that any major or even minor trends in the data are not obscured. All the interstitial water data obtained in Site 808 are presented in Tables 13 (Hole 808A), 14 (Hole 808B), and 15 (Hole 808C).

Overview of the Results

Cores were recovered from three separate holes at Site 808. Nevertheless, it is appropriate to present first an overview of the database in the form of a composite profile of all three holes. In Figures 80 and 81 the data for Holes 808A and 808B are presented by means of filled circles and those of 808C as open circles. The observations can be categorized in the following order of importance:

1. Low chloride concentrations characterize the zone of the décollement;
2. Major changes in concentration gradients of most constituents occur at the boundary between the trench-fill turbidites and the trench-basin transitional zone (ca. 560 mbsf);
3. Changes in concentration occur in many of the constituents around the major thrust at approximately 366 mbsf;
4. Subtle but distinct changes are observed in silica, calcium, magnesium, potassium, and lithium at about 195 mbsf, possibly related to a diagenetic front in the sediment column or to the base of the hydrate stability field;
5. Changes in some of the constituents occur at the lithologic boundary at 820 mbsf, particularly noticeable in dissolved silica, but also in calcium, magnesium, and sulfate;
6. Large changes occur in biogenic constituents (alkalinity, sulfate, ammonium, phosphate) as well as possibly related changes in chloride, sodium, calcium, and magnesium, in the upper sediment sequence (0–150 mbsf);
7. Effects of exchange with the underlying volcanogenic sediments are noticed in the lowermost part of the hole. This

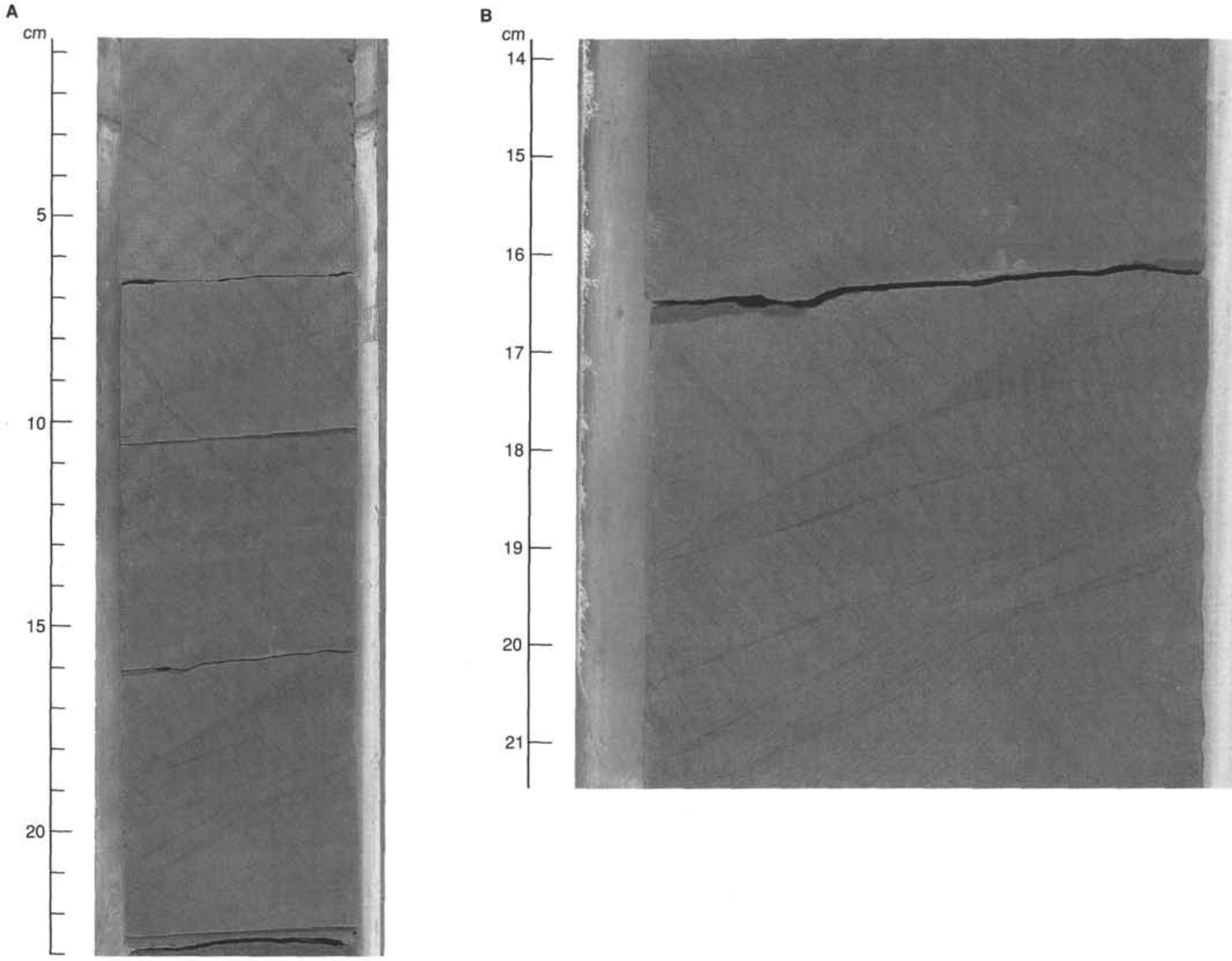

Figure 54. Core photographs of well-developed shear bands. **A.** Interval 131-808C-15R-2, 1–23 cm. **B.** Closer view: interval 131-808C-15R-2, 14–21.5 cm. Bedding dips gently to the left, and the central part of **A** shows it to be only slightly affected by the shear bands.

is particularly evident from the very distinct increases in calcium and strontium and the large decrease in the Na/Cl ratio;

8. Distributions of lithium, strontium, and calcium in the volcanic ash-rich zone between 560 mbsf and 820 mbsf suggest that, perhaps, observed extremes in the concentration depth profiles are related to reactions involving volcanic ash alteration.

In the following sections these various features will be discussed in somewhat greater detail.

Processes Associated with the Décollement

In Figure 82 the concentration-depth profiles of chloride, silica, and calcium are presented to emphasize processes that potentially are associated with the décollement at about 960 mbsf. The data for calcium have been plotted with an upper limit of 30 mM to accentuate the profile in and above the décollement. Some of the noise in the deeper part of the profile of dissolved chloride is the result of contamination with drilling fluid, which has considerably higher contents of chloride (about 550 mM). Below about 560 mbsf a large decrease in dissolved chloride becomes evident, with concentrations rapidly diminishing to a depth of 850 mbsf. From this depth only a slight further decrease occurs, with a broad minimum extending from about 1000 to 1150 mbsf. Below 1150 mbsf the influence of hydration reactions in the volcanic sediments above basaltic basement leads to a sharp increase in dissolved chloride.

The observations of low chloride concentrations are of great importance. In other areas of active margin sediment accretion and subduction similar decreases in chloride concentrations have been observed: in the Barbados Accretionary Prism (Gieskes et al., 1989); in the area of the Peru Trench (Elderfield et al., 1990; Kastner et al., 1990); in Site 438 on the inland slope of the Japan Trench (Moore and Gieskes, 1980), as well as in other areas. Various attempts have been made to explain these chloride decreases: (1) Decomposition of gas hydrates in the accretionary wedge; (2) meteoric water flow from the continent; (3) clay mineral and other hydrous mineral dehydration; (4) ion filtration through clay membranes. In the case of Site 808 the first two hypotheses are improbable, especially because the chloride decreases are noticed well below the zone of the bottom- simulating reflector, and also because of the distance from a land source with enough head.

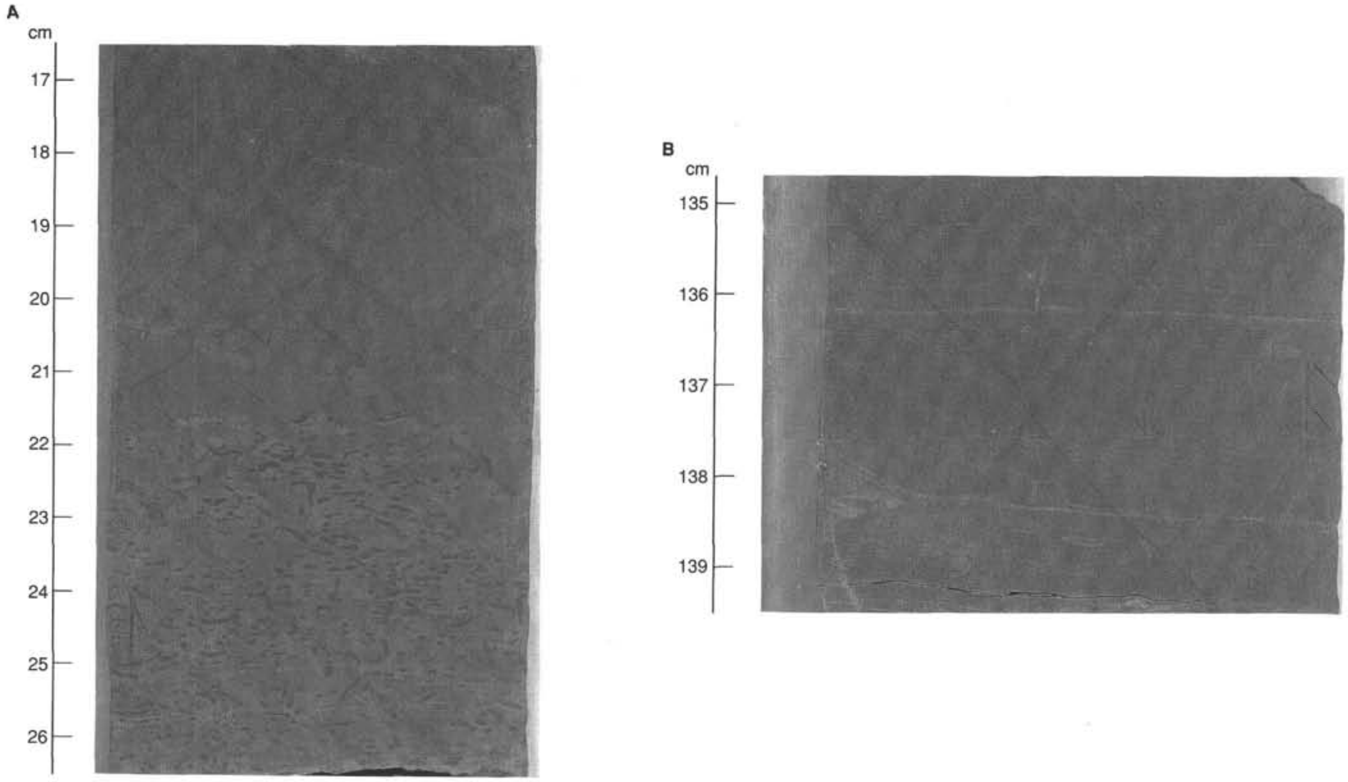

Figure 55. Examples from core photographs of shear bands forming well-developed conjugate sets. **A.** is from interval 131-808C-16R-2, 17–26 cm, and **B.** is from interval 131-808C-16R-3, 135–139.5 cm. Note the different dihedral angles in the two examples and the almost imperceptible offset of bedding in **B**. Note also the much poorer development of the shear bands in the highly bioturbated zone between 22 and 26 cm in **A**.

For the contribution of clay mineral dehydration the sedimentary conditions are ideal in that temperatures of about 60°C prevail at about 650 mbsf and temperatures of about 120°C at 1150 mbsf (Heat Flow section, this chapter), which constitutes the window for the process of clay mineral dehydration (e.g., Burst, 1969; Powers, 1967; Perry and Hower, 1970). Whereas clay mineral dehydration was postulated as a potential process leading to at least some of the dilution of the pore fluids both in the Barbados Transect and off Peru (Gieskes et al., 1989; Elderfield et al., 1990), that process was postulated to occur at some distance into the accretionary wedge or at greater depth, where temperature conditions would be more favorable for such a process. At Site 808, however, this process may be occurring *in-situ* in the sediment column. Even if not all of the dilution can occur within the site, there will be little need to invoke a large-scale, long-range advection as the source of the diluted pore fluids. Additional dilution may occur as a result of the potential process of membrane filtration further down into the prism.

The above discussion does not *per se* rule out the possibility of an advective input of low-chloride fluids along the décollement. Although lower chloride concentrations occur below the décollement, this does not in itself mean that an advective component would be from greater depths, but rather that the minimum that once may have existed in the zone of décollement has migrated downward as a result of diffusive resupply of chloride mainly from the overlying sediments. If an advective input of low chloride fluids indeed has occurred, it is of interest to inquire into the timing and magnitude of this low chloride input. Physical observations of the cores do not seem to support a major advective input of fluids at this time. It is, however, probable that an input of low-chloride fluids has occurred at some time in the past and that this pulse of low chloride was propagated through the sediment column in an upward direction, about 200 m, i.e., to the present level of about 750 mbsf. Similarly, if the input of low-chloride fluids is associated with slight overpressures, some of this fluid could have been pushed to deeper levels, thus contributing to the occurrence of a minimum below the décollement. After this input occurred, diffusive processes would attempt to eradicate the low- chloride concentrations. With an estimated bulk diffusion coefficient of $1x10^{-5}$ cm^2/s in the sediments overlying the décollement, diffusive communication could have been established over a distance of approximately 200 m in about 300 k.y. to a depth level of about 550 mbsf. These computations are based on an analogy to an application to surface heating of a semi-infinite region (Carslaw and Jaeger, 1959, 263–265). This would put the timing of the low-chloride input event at a time not too long after the initiation of the rapid deposition of the trench-fill turbidites. If low-chloride fluids have been introduced only along a fairly narrow zone along the décollement, then the profile of low chloride between about 950 and 560 mbsf would imply that the low-chloride input occurred more than 1 m.y. ago, which, in turn, would imply an input well beyond the seaward reach of the décollement. A combination of *in-situ* production of water by clay mineral dehydration and an advective flow of fluid along the décollement cannot be ruled out. Further studies of the isotopic composition of the fluids will be necessary to resolve this problem. The causes of the chloride decrease in the advected fluids would be similar to those discussed above.

Dissolved silica concentrations show a significant change directly below the décollement. In part this may be a reflection

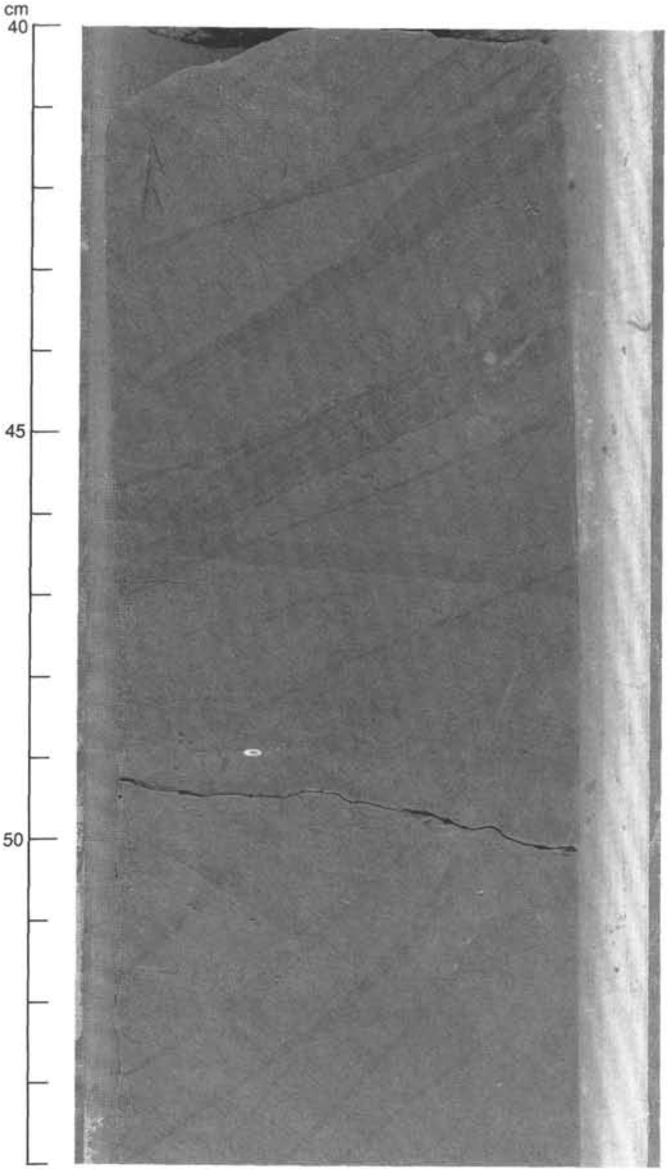

Figure 56. Example from a core photograph of shear bands associated with faults. In the upper half of the photograph, several small faults intersect the shear bands at low angles (from interval 131-808C-16R-4, 40–54 cm). See text for discussion.

of a slightly different sediment composition below the décollement. This difference may have been accentuated by the input of high-silica-containing fluids along the décollement. Toward the base of the sedimentary section, silica concentrations again approach the quartz solubility values observed between 825 and 940 mbsf. High pore-fluid pressures may have retarded clay transformation reactions in the sediments underlying the décollement, thus maintaining the relatively high dissolved silica concentrations.

The concentration-depth profile of dissolved calcium shows little relation to that of either chloride or silica. It should be remembered, however, that calcium is a rather reactive component and its concentration profile is also strongly influenced by diffusive exchange with the underlying volcanic sediments (Fig. 81). A small minimum exists in the zone of décollement, which may be related to advection of fluids. A similar minimum was observed in the zone of décollement in Site 671 (Gieskes et al., 1989).

Lithologic Boundary at 560 mbsf

For the purpose of discussion the concentration-depth profiles of various relevant constituents are plotted in Figures 83 and 84 at a larger scale.

Dissolved silica concentrations (Fig. 83) show an abrupt change at 560 mbsf. This change coincides with the boundary between the trench-fill turbidites and the trench-basin transitional zone. The variability in dissolved silica below this boundary is associated with the occurrence of volcanic ash in the zone from 560–820 mbsf. Above 560 mbsf, dissolved silica values are quite high, though again variable. The impression of a slightly increasing trend with depth toward 560 mbsf may, in part, be a function of increased temperatures.

It is important to note that dissolved chloride and dissolved sodium concentrations appear to increase with depth until the lithologic boundary at 560 mbsf is reached. Thus it appears that downward diffusion of chloride has either not yet started to deplete the chloride concentration above 560 mbsf or that some other process maintains the apparent maximum in chloride at 560 mbsf. This would require an alteration process of significant enough proportion to lead to removal of water by the formation of hydrated clay minerals. One other possible explanation could be in terms of an advective input of high-chloride fluids (originating from overlying sediment?) along the lithologic boundary.

The profiles of calcium, magnesium, and potassium (Fig. 84) indicate large decreases in concentration from about 400 to 560 mbsf. Below this depth the concentration gradients change abruptly. The observations suggest that alteration of volcanic ash in the section between 400 and 560 mbsf plays an important role in establishing the interstitial water gradients. This in turn could explain the maintenance of higher chloride concentrations and the absence of a diffusive gradient in chloride above 560 mbsf.

The Major Thrust at about 366 mbsf

One of the more important tectonic features of the drilled section of Site 808 is the occurrence of a major thrust, which is located in Hole 808C at about 366 mbsf (see Structural Geology, section, this chapter). In the detailed concentration-depth profiles of the interstitial waters presented in Figures 84 and 85 one observes reversals in the concentrations of calcium, magnesium, and lithium, which can be understood in terms of an original discontinuity created by the fault.

Whereas from the structural geology perspective it is argued that the total vertical displacement of the fault is about 145 m, matching of the profiles in Figure 85 suggests a displacement of about 100 m. This argument, of course, assumes that the vertical gradient in any of the properties given in Figure 85 shows no change in the lateral direction. If they did, boundary conditions would change and thus the apparent displacement would be 140 m rather than 100 m. The effect of folding (about 360 to 390 mbsf) can, in principle, also have some effect on the shape of the gradients. Finally, diffusive processes will also be of importance, as they will tend to eliminate the concentration changes instituted by the faulting process. Future modeling efforts will help to set constraints on the various potential physico-chemical processes involved in the creation of the nonsteady state concentration-depth distributions. Effects of recent folding were also noticed in Site 671 of the Barbados Accretionary Prism transect (Gieskes et al., 1989; 1990).

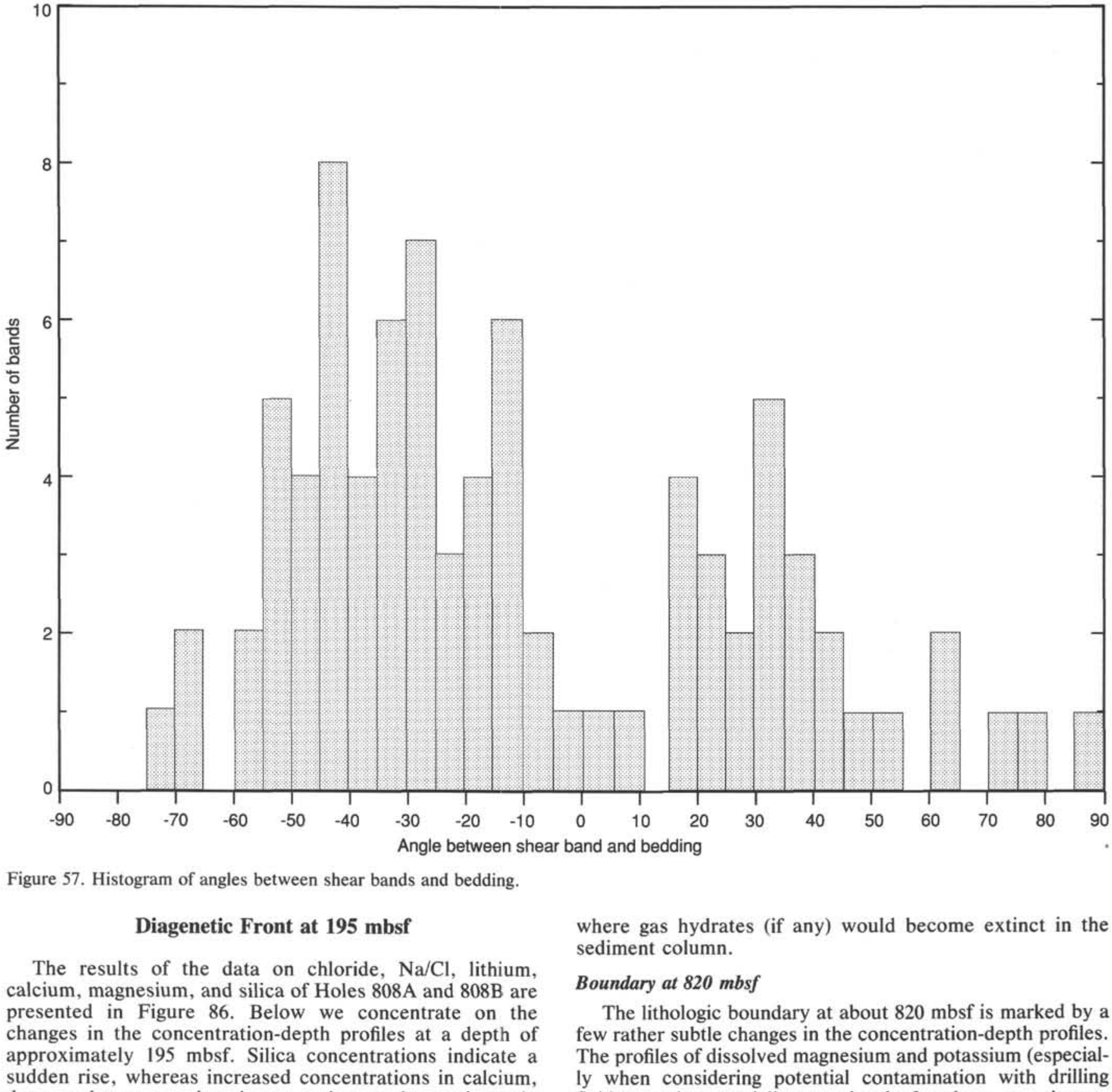

Figure 57. Histogram of angles between shear bands and bedding.

Diagenetic Front at 195 mbsf

The results of the data on chloride, Na/Cl, lithium, calcium, magnesium, and silica of Holes 808A and 808B are presented in Figure 86. Below we concentrate on the changes in the concentration-depth profiles at a depth of approximately 195 mbsf. Silica concentrations indicate a sudden rise, whereas increased concentrations in calcium, decreased concentrations in magnesium, and a maximum in lithium coincide with the horizon of silica increase. These observations can be interpreted in terms of diagenetic reactions, perhaps involving diagenetic changes in silica and, perhaps, also involving volcanic matter. This type of profile has been noticed previously in several sites, e.g., Site 323 (Kastner and Gieskes, 1976), Site 474 (Gieskes et al., 1982), and Site 482 (Gieskes et al., 1983). In each of these cases this phenomenon was explained in terms of a silicification front associated with alteration of volcanic debris. We argue that, however small the concentration effects in the case of Site 808, a diagenetic front may occur in this site at about 195 mbsf. Whether this diagenetic front is actually related to the alteration of volcanic matter in this horizon needs further study, particularly through strontium isotope studies. Interestingly this depth does coincide with the approximate depth where gas hydrates (if any) would become extinct in the sediment column.

Boundary at 820 mbsf

The lithologic boundary at about 820 mbsf is marked by a few rather subtle changes in the concentration-depth profiles. The profiles of dissolved magnesium and potassium (especially when considering potential contamination with drilling fluids) reach essentially zero levels for these constituents below 820 mbsf. On the other hand, increases in sulfate concentration become noticeable below this depth (Fig. 80). Similarly, a small, albeit distinct, decrease in silica occurs below 820 mbsf, accompanied by a reduction in noise in the profile, mostly as a result of the decrease in volcanic ash below this boundary. As noted above in the discussion of the input of low-chloride fluids along the décollement, the chloride concentration depth profile shows relatively little change below 820 mbsf, but a diffusive profile above this depth. Although lithium (Fig. 81) shows a local minimum at 820 mbsf, we argue below that this minimum is mostly the result of the creation of maxima above this boundary, probably as a result of ash alteration reactions.

In general, we cannot argue strongly for major changes associated with the lithologic boundary at 820 mbsf. In par-

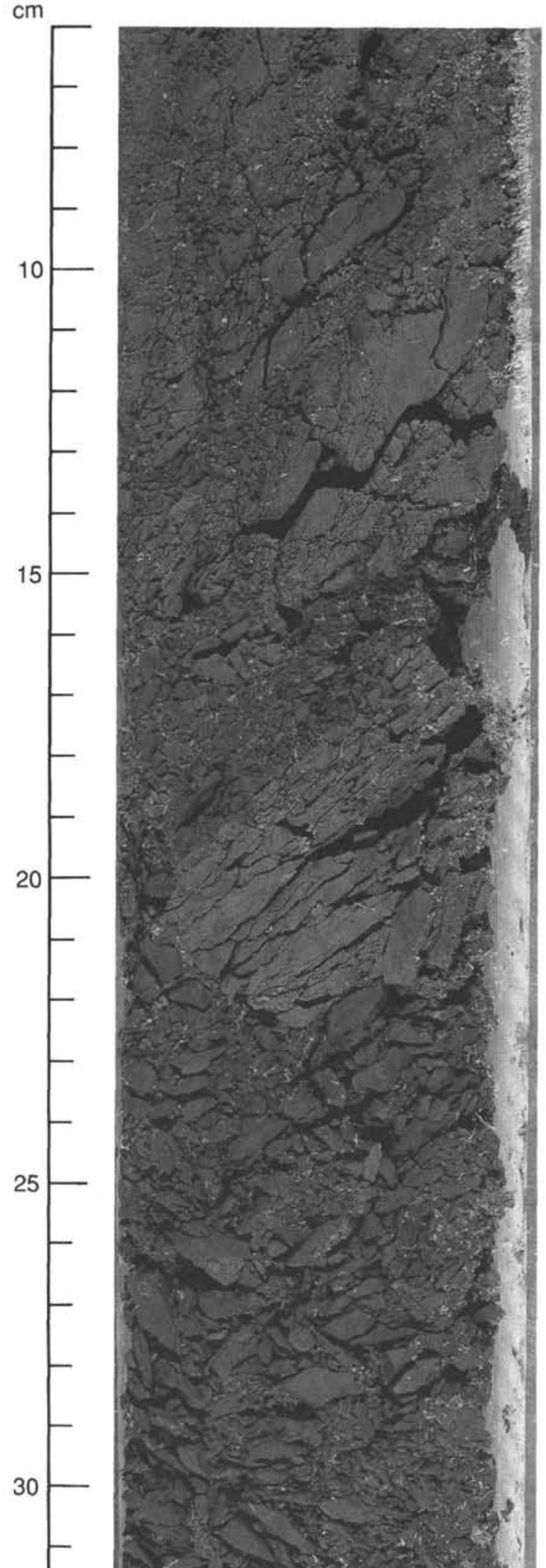

Figure 58. Core photograph of a breccia/scaly fabric zone from the frontal thrust (interval 131-808-8R-1, 6–32 cm). Note that, although the pieces are highly broken and faulted, in places they still form a tight, interlocking network that dips moderately to the left.

ticular the geochemical data do not suggest any important recent fluid input along this boundary.

Biogenic Constituents in Upper Sediment Column

Changes in dissolved sulfate, alkalinity, ammonia, and phosphate in the upper part of the sediment column are presented in Figure 87. Depletions in dissolved sulfate occur within Core 131-808A-1H, and indeed only in the first two samples was the distinct smell of hydrogen sulfide noticed. Alkalinities show a rapid increase in the upper 10–20 m, below which a small minimum occurs followed by a second maximum just below 50 mbsf. Below this a steady decrease occurs to a depth of about 195 mbsf. The large production of alkalinity is caused not only by the sulfate reduction process but also by the process of methane generation in the methane production zone. Clearly, a maximum in dissolved ammonium occurs at about 150 mbsf. Phosphate is rapidly generated in the upper part of the sediment column, but is also rapidly removed as a result of phosphate adsorption or precipitation reactions. It is important to note the rapid increase in chloride in the upper 25 m of the sediment column. This increase of about 4 % can, in part, be understood in terms of a signal associated with Pleistocene sea water salinity increases during periods of ice formation (McDuff, 1985). On the other hand, one observes also a rapid increase in sodium concentrations over and above that expected from the chloride increase. This must be understood in terms of the release of sodium as a result of the alteration of sodium-glass.

In the upper part of the sediment section, rapid decreases are also observed in dissolved calcium and magnesium. These decreases are in part due to carbonate precipitation reactions, and the high ratio of Mg/Ca (Table 13) suggests the possibility of dolomite formation (Baker and Kastner, 1981). An additional process that may lead to the removal of magnesium can be the formation of clay minerals, probably associated with the reactions responsible for the release of sodium. This would be in agreement with the observations of the strong correlation between decreases in magnesium and $\delta^{18}O(H_2O)$ observed in Site 583 (Matsuhisa and Matsumoto, 1985).

"Basement" Effect

Near the bottom of the hole, rapid changes in calcium, strontium, and also in the Na/Cl ratio attest to a signal presumably associated with alteration reactions occurring in the volcanogenic sediments overlying basaltic basement. Associated with these concentration changes is an observed increase in dissolved chloride (Fig. 81). Formation factors in this section are quite large, so that steep gradients are observed in the interstitial water constituents, but mass transport will be minimal as a result of sharply diminished diffusion coefficients.

Ash Alteration in the Volcanic Ash Zone - 560–820 mbsf

As noted above, dissolved silica concentrations in the zone from 560–820 mbsf are characterized by an intense variability, which can be understood best in terms of higher silica solubilities in the layers characterized by the presence of volcanic ash. In Figure 88 data are presented for silica, calcium, lithium, and strontium. A very pronounced maximum occurs in dissolved lithium at about 750 mbsf. This maximum is accompanied by a small maximum in dissolved calcium and a minimum in dissolved strontium. Similar, less pronounced extremes occur at a depth level of 630 mbsf. We suggest that these extremes in the various constituents, particularly those of lithium and strontium, are the result of reactions in the sediment column, perhaps involving the alteration of volcanic ash at higher temperatures. This interpretation is still very speculative in nature and requires work on strontium isotopes as well as on the ashes.

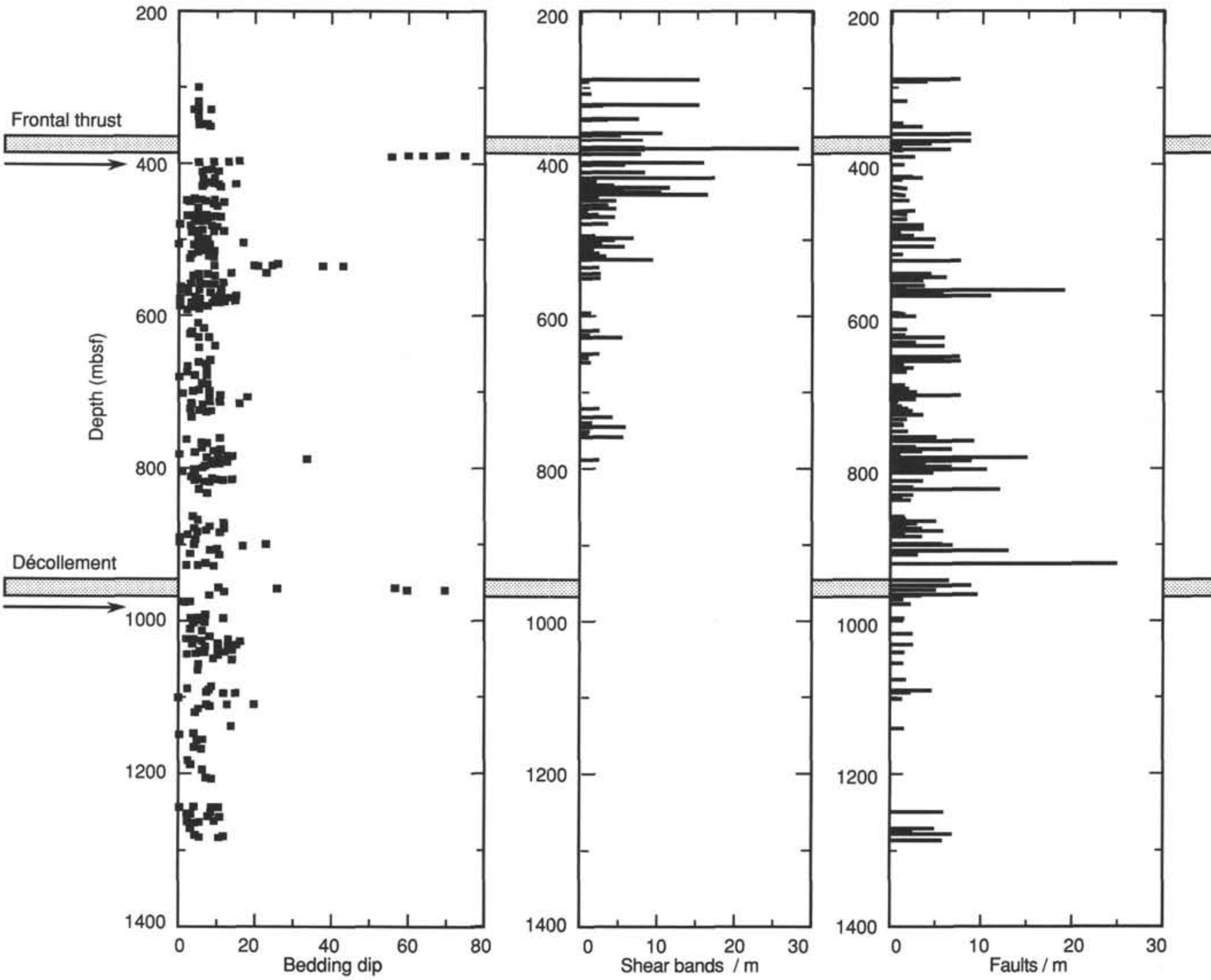

Figure 59. Histograms of the magnitude of bedding dip vs. depth, the number of shear bands/meter vs. depth, and the number of small faults/meter vs. depth. All data are from Hole 808C.

Evidence for Fluid Flow?

One of the major objectives of the interstitial water studies at Site 808 was to establish whether there is any geochemical evidence for fluid flow as a result of fluid expulsion from the Nankai accretionary prism in the area of incipient accretion of the sediment column above the décollement. Although low chloride concentrations in the décollement are reminiscent of the low-chloride fluids in the décollement zone of the Barbados accretionary complex transect of ODP Leg 110 (Gieskes et al., 1989; 1990), where fluid flow was implied, some of the low chloride concentrations could be generated *in-situ* at Site 808. This could be the result of clay dehydration reactions in the temperature range of 60°–120°C prevailing in the sediment section below 560 mbsf. If anywhere in the sediment column flow of low-chloride fluids might have occurred, it would be along the zone of décollement, in which and below which chloride concentrations are at their minimum. This flow, however, would necessarily have had a major influence in the past. The possibility of a leaky décollement cannot be entirely excluded. Such a leakage could, in part, maintain the chloride profile between the décollement and 560 mbsf. Evidence for fluid flow in other zones of lithologic boundaries is weak or nonexistent, even along the recent fault at 366 mbsf, which extends downward almost to the zone of décollement.

Chemistry and Mineralogy of Ashes

As stated above, interstitial water analyses showed that vertical profiles of some elements (such as Li, Sr, and Ca) may be affected by *in-situ* ash alteration, particularly in the ash-rich facies of the Shikoku Basin transitional and hemipelagic sediments between 560 and 820 mbsf. As a preliminary approach to solve this question, 12 samples were selected from various layers between 200 and 1260 mbsf at Site 808 (Table 16), and analyzed for their bulk chemical composition and XRD mineralogical features.

About 1-g fragments of each sample were freeze-dried and powdered onboard for routine XRD analysis. The same powders were utilized for chemical analyses of Si, Ti, Fe, Al, Ca, Mg, Na, K, P, and inorganic C. The latter analyses utilized a wet chemical analytical method similar to that of Donnelly (1980) developed for shipboard use during Leg 131 (Gieskes and Gamo, in press).

Table 16 shows the list of the samples together with the bulk chemical compositions in terms of oxide percentage.

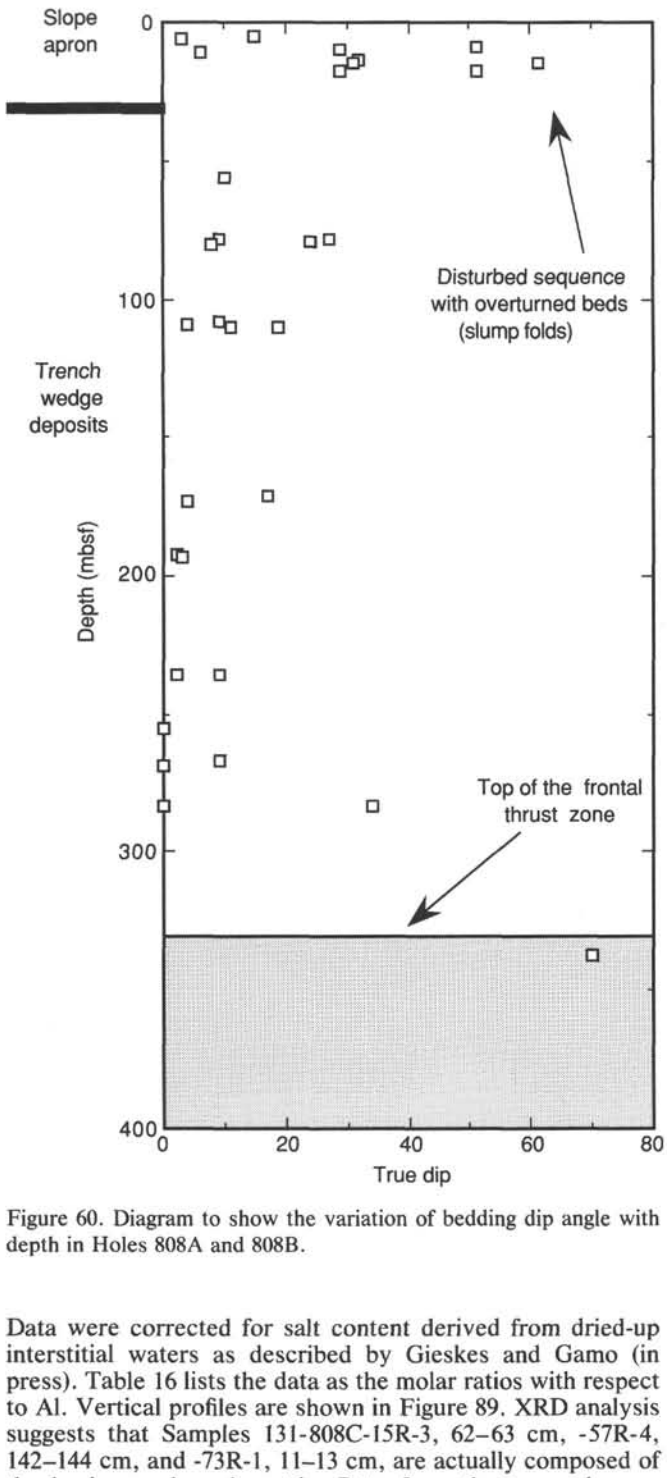

Figure 60. Diagram to show the variation of bedding dip angle with depth in Holes 808A and 808B.

Data were corrected for salt content derived from dried-up interstitial waters as described by Gieskes and Gamo (in press). Table 16 lists the data as the molar ratios with respect to Al. Vertical profiles are shown in Figure 89. XRD analysis suggests that Samples 131-808C-15R-3, 62–63 cm, -57R-4, 142–144 cm, and -73R-1, 11–13 cm, are actually composed of the background mud matrix. Data from these samples are indicated by full circles in Figure 89.

Figures 90 to 101 present the XRD patterns for each sample, and the relative intensities of the most diagnostic peaks for each mineral are summarized in Table 17. Chemical characteristics of each ash sample are briefly described in the following. In this report S/I indicates mixed-layered smectite-illite, and clinoptilolite represents the two zeolites clinoptilolite and heulandite. The bulk X-ray work carried out on board does not permit differentiation between these two zeolites, or between pure smectite and mixed-layer S/I.

Sample 131-808B-10X-3, 52–54 cm (201 mbsf); Figure 90

This sample is characterized by some detectable smectite, but mostly by a large and broad glass peak. Little alteration to clay minerals has occurred. Quartz peaks are less intense than feldspar peaks. The peaks at about 31.7° and 45.5° are those of halite from the pore water.

Sample 131-808C-15R-3, 62–63 cm (437 mbsf); Figure 91

This XRD pattern is not characteristic of ash and/or altered glass. This sample is mineralogically similar to most matrix (background) sediment. High carbonate and Fe contents (relatively low in Ca) suggest the existence of an authigenic Fe-carbonate such as ankerite or siderite. The XRD pattern also shows siderite peaks.

Sample 131-808C-30R-4-103–105 cm (584 mbsf); Figure 92

This sample consists of slightly altered ash; it is less altered and more glassy (less quartz and feldspar) than the shallower Sample 131-808B-10X-3, 52–54 cm, even though the *in-situ* temperature is higher by about 30°C. The large difference in extent of alteration is most probably related to the rhyolitic nature of this ash (higher SiO_2 and lower TiO_2 content). Compared with Sample 131-808B-10X-3, 52–54 cm, the Fe/Al and Mg/Al ratios are also lower. Thus, there are at least two different types of volcanic ash in the sediment column, based on chemical composition.

Sample 131-808C-30R-5, 119–120 cm (585 mbsf); Figure 93

Although only 1 m deeper than the previous sample, considerable alteration can be seen from significant peaks of smectite and/or of mixed-layer clay S/I. Other alteration products are zeolite, calcite, and traces of cristobalite. Ti/Al, Fe/Al, and Mg/Al ratios are significantly higher, and the K/Al ratio is lower than those of sample 131-808C-30R-4, 103–105 cm.

Sample 131-808C-37R-1, 30–32 cm (646 mbsf); Figure 94

This sample is more extensively altered than Sample 131-808C-30R-5, 119–120 cm. Both smectite and/or S/I and clinoptilolite produce higher intensity peaks. Some cristobalite is also present.

Sample 131-808C-38R-6, 76–78 cm (663 mbsf); Figure 95

This ash is mostly altered to cristobalite: Smectite and/or mixed layer S/I is also present. The sudden appearance of the stronger peaks of cristobalite relative to those of quartz and feldspar suggests a temperature-dependent phase change of silica is occurring at this depth interval.

Sample 131-808C-45R-3, 55–57 cm (726 mbsf); Figure 96

Strong alteration to smectite and S/I, zeolite (clinoptilolite) and some cristobalite is evident in this sample. General XRD features are similar to those of Sample 131-808C-37R-1, 30–32 cm.

Sample 131-808C-54R-1, 65–67 cm (810 mbsf); Figure 97

This sample is highly altered to zeolites (mainly clinoptilolite) with less smectite and S/I (but better crystallinity) than in Sample 131-808C-45R-3, 55–57 cm. SiO_2 content is also higher. Mg/Al and Fe/Al ratios are significantly lower and the Na/Al ratio is higher than in Sample 131-808C-45R-3, 55–57 cm, which may reflect alteration primarily to zeolite instead of to smectite.

Sample 131-808C-57R-4, 142–144 cm (844 mbsf); Figure 98

The XRD pattern indicates that this sample is representative of the sediment matrix.

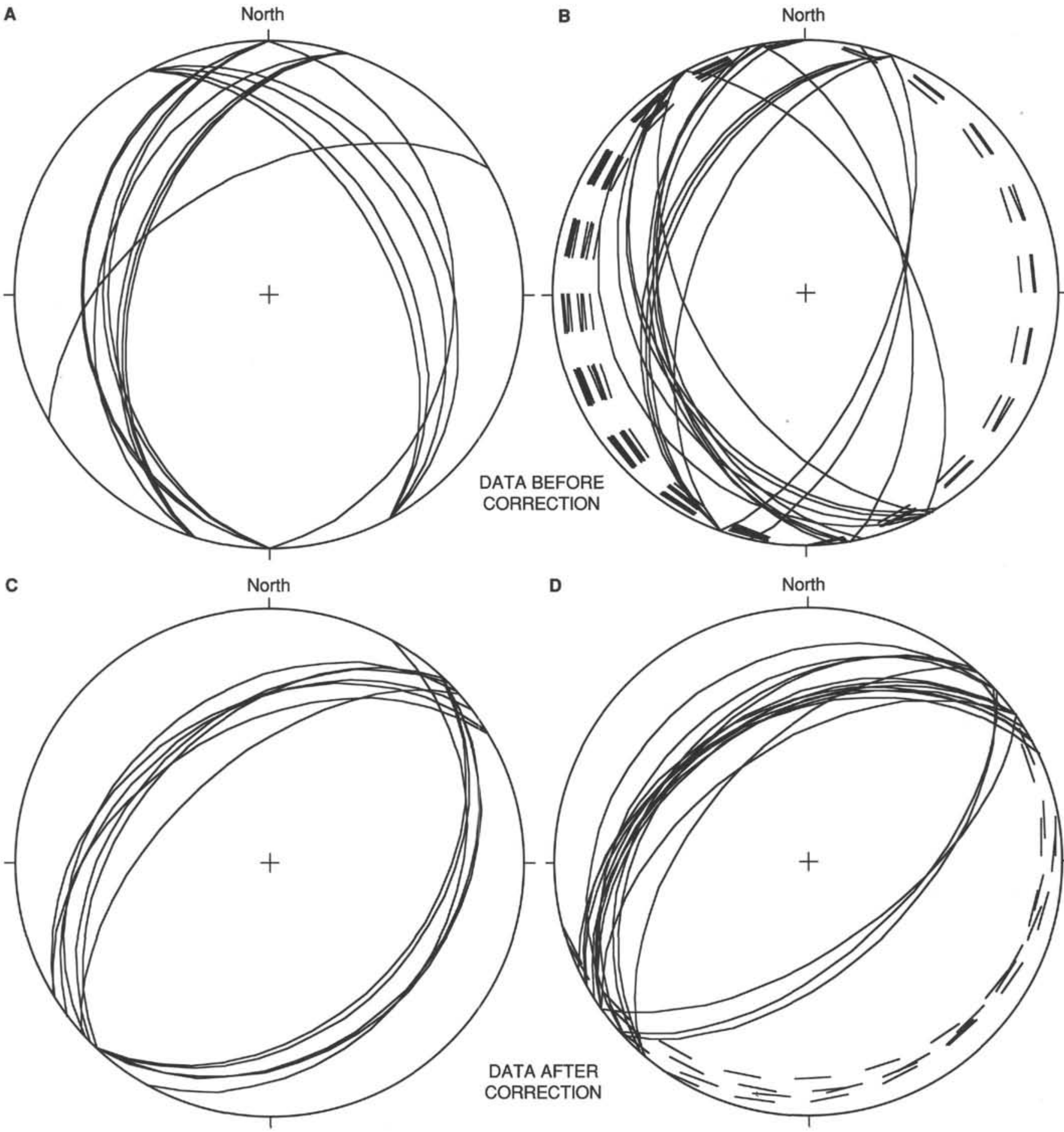

Figure 61. Stereonet projections showing the orientations of shear bands in structural domain 1 (see text). **A.** Core 131-808B-19X before correction. **B.** Core 131-808B-24X before correction. **C** and **D** are the same cores after correction with paleomagnetic data for rotations due to drilling. The dashed lines in **B** and **D** represent bedding. These are equal-area lower hemisphere projections.

Sample 131-808C-73R-1, 11–13 cm (992 mbsf); Figure 99

This sample is also matrix sediment. XRD patterns for Samples 131-808C-15R-3, 62–63 cm; -57R-4, 142–144 cm; and -73R-1, 11–13 cm are very similar to each other.

Sample 131-808C-100R-CC, 20–22 cm (1245 mbsf); Figure 100

This sample contains analcite (zeolite) and quartz with some clay, either smectite or S/I, suggesting strong alteration at elevated temperature. The SiO_2 content of this ash sample is high. Ti/Al, Fe/Al, and Mg/Al ratios are lower than those for the ash samples from the upper Shikoku Basin hemipelagic sediments (131-808C-30R-5, 119–120 cm; -37R-1, 30–32 cm; -38R-6, 76–78 cm, -45R-3 55–57 cm; and -54R-1, 65–67 cm). The low Ti/Al ratio (0.02) suggests a rhyolitic source for this ash.

Sample 131-808C-102-2, 30–32 cm (1263 mbsf); Figure 101

This highly altered ash sample contains mainly smectite, clinoptilolite, and also some analcite. The well-developed smectite peak suggests a higher degree of crystallinity than in

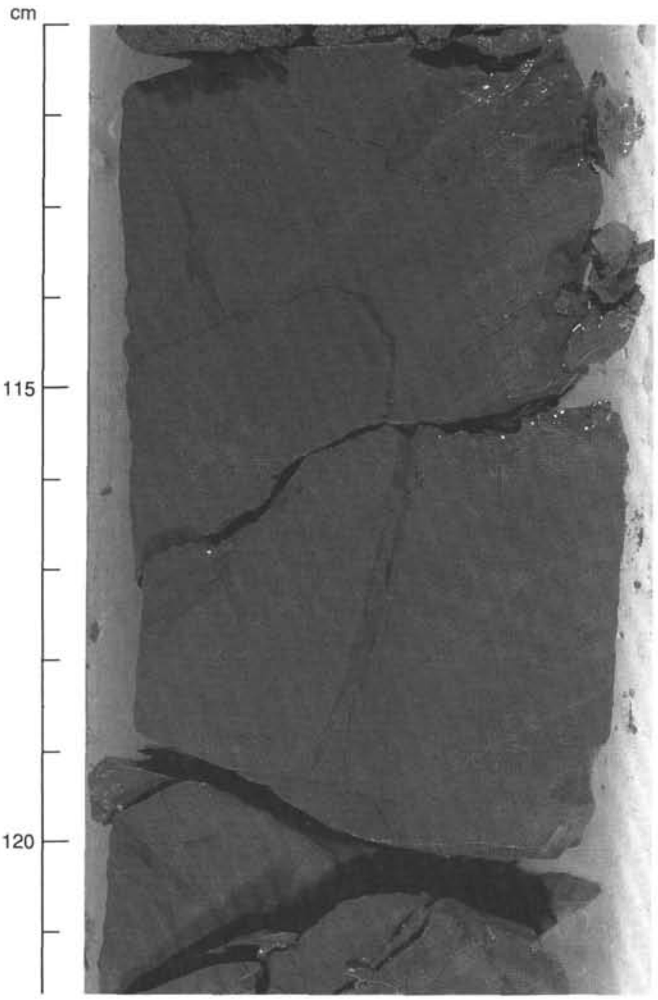

Figure 62. Example from a core photograph of deformation associated with the frontal thrust (from interval 131-808C-8R-1, 111–122 cm). Note particularly the well-developed thick zone of black material that fills the fault zone in the center of the photograph. Bedding in this interval, although not discernible in this photograph, has a moderate dip and is overturned.

the shallower samples. SiO_2 content is significantly lower than in Sample 131-808C-100-CC, 20–22 cm; this is reflected by the difference in the altered mineral species and extent of alteration relative to Sample 131-808C-100R-CC, 20–22 cm.

Discussion

Overall, ash alteration becomes more pronounced with increasing depth. This is probably a result of increased time for reactions and higher *in-situ* temperatures. The two principal parameters that seem to control the degree (or extent) of ash alteration in this section appear to be temperature and the original composition of the ash. The nine ash samples analyzed in this study can be classified into the following three groups: mildly altered ashes (Samples 131-808B-10X-3, 52–54 cm and 131-808C-30R-4, 103–105 cm), moderately altered ashes (131-808C-30R-5, 119–120 cm; 37R-1, 30–32 cm; -38R-6, 76–78 cm; and -45R-3, 55–57 cm), and strongly altered ashes (131-808C-54R-1, 65–67 cm; -100R-CC, 20–22 cm; and -102R-2, 30–32 cm).

The moderately altered ashes are characterized mainly by poorly crystalline smectite and/or mixed-layer S/I, with zeolite and cristobalite as less-abundant constituents. It is worth noting that the moderately altered ashes have higher Fe/Al and Mg/Al ratios, and lower K/Al and Si/Al ratios than the other ashes (Fig. 79). It is probable that these are primary characteristics of the ashes deposited between 560 and 820 mbsf at Site 808.

The strongly altered ashes show higher contents of quartz and zeolite (analcite and clinoptilolite) as well as smectite with improved crystallinity. This mineral assemblage, together with different origins of these ashes, may correspond to lower Ti/Al, Fe/Al, and Mg/Al, and higher K/Al ratios than those of the moderately altered ashes.

Chemical compositions of bulk sediment were measured at Site 582 in the Nankai Trough (Kawahata et al., 1986) and at Site 297 near the Nankai Trough (Donnelly, 1980). Data from the three background sediments at Site 808 (Samples 131-808C-15R-3, 62–63 cm; -57R-4, 142–144 cm; and -73R-1, 11–13 cm) show good agreement with the Sites 582 and 297 data. The ranges (± sigma) of the Site 582 data are shown by two arrows for each profile in Figure 89. The high Fe value for Sample 131-808C-15R-3, 62–63 cm, is due to the existence of siderite as indicated by the XRD pattern (Fig. 91). The slightly higher Na/Al ratio for the Site 582 data may be due to a salt effect, because the Site 297 data (excluding ash samples) show lower Na/Al averaged values (0.196 ± 0.059), similar to our data, than those at Site 582 (0.306 ± 0.030).

This preliminary study demonstrates that bulk chemical compositions, together with XRD characteristics, offer a valuable guide towards the elucidation of various ash alteration reactions under *in situ* temperature and pressure conditions. The framework of this study will form the basis for further shore-based intensive studies on the ash alteration at the Nankai Trough accretionary prism.

ORGANIC GEOCHEMISTRY

Besides monitoring of hydrocarbon generation, performed for safety considerations, the shipboard organic geochemistry studies had two main purposes during Leg 131. One was the assessment of the amount, type, and maturity of the organic matter preserved in the sediments of the Nankai accretionary wedge. The second was the genetic characterization of light hydrocarbons that can be generated by biogenic or thermogenic decay of organic matter and the relation of gas geochemical processes to the accretionary process. Because of the strong temperature dependence of the formation reactions of light hydrocarbons, their analysis represents a sensitive indicator for the thermal hydrocarbon generation process and, therefore, may provide information on the thermal history of the accretionary wedge.

Samples

A total of 130 sediment samples were collected from Site 808 in 10-m intervals over the depth range from 3 to 1280 mbsf. Of these, 11 samples were obtained from Hole 808A, 17 from Hole 808B, and 103 from Hole 808C. All sediments were analyzed for their composition of light hydrocarbons using headspace analysis. In addition to the headspace gas analyses, 18 gas samples collected by Vacutainers from gas pockets of Holes 808A and 808B were also analyzed for their molecular composition. Total organic carbon content (TOC), nitrogen content, and the carbon/nitrogen ratios were determined on all sediments used for headspace analyses.

Details of analytical methods are given in the Explanatory Notes chapter (this volume).

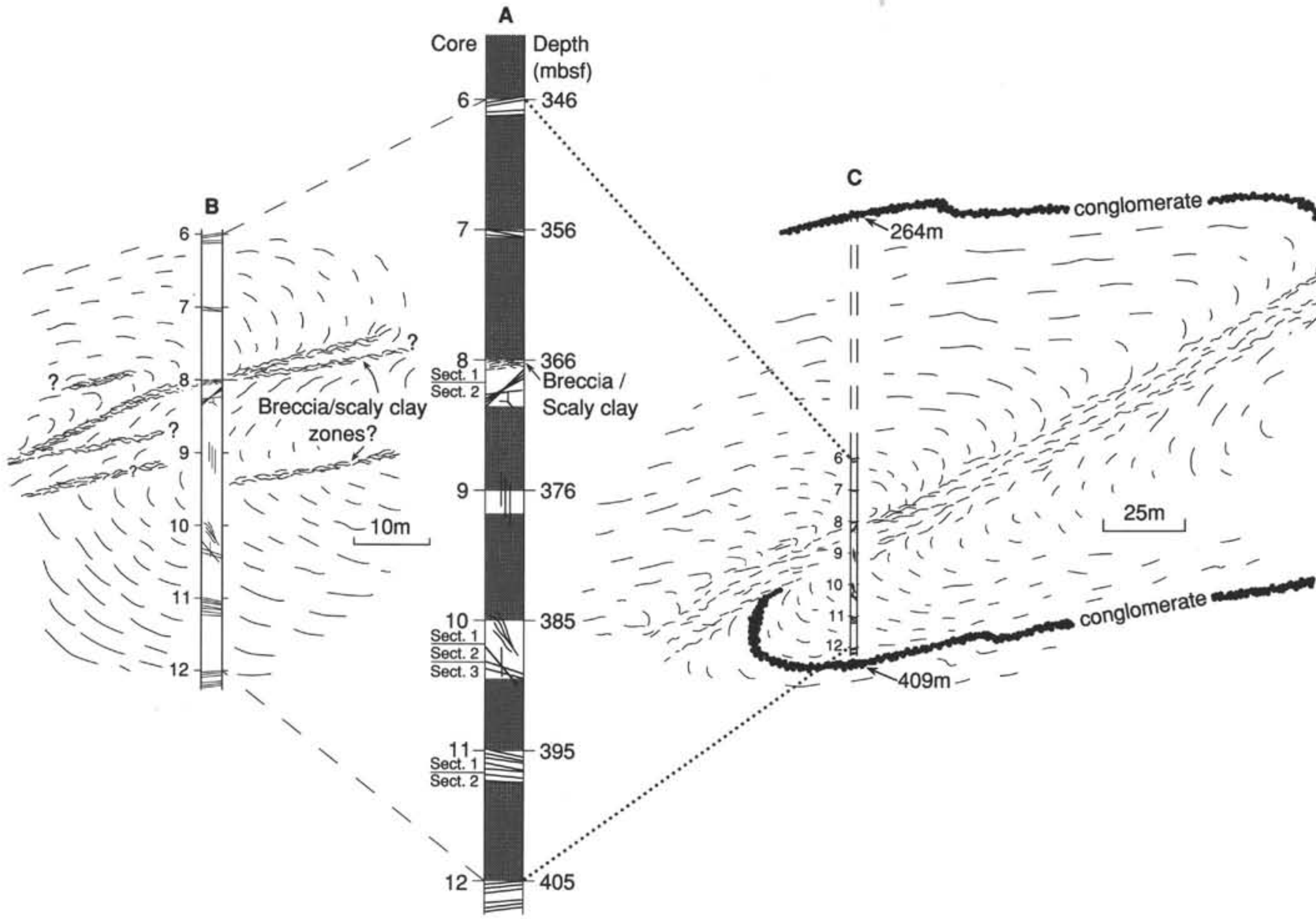

Figure 63. Schematic cross section of the frontal thrust and associated fold as suggested by true dip data and younging directions.

Results and Discussion

Amount, Type, and Maturity of Organic Matter

The amount of organic carbon at Site 808 is low and does not exceed 0.9% TOC (Table 18, Fig. 102). A general decrease of the amount of organic matter with increasing depth is reflected by the decrease of the TOC from 0.75% to 0.1% (average values) from top to bottom of the sediment section. In the sediments from 0 to 824 mbsf (lithologic Units I to IVa, where turbidites or ashes are interbedded with hemipelagic muds, the changes in the organic carbon content show relatively high amplitudes of up to 0.6% which might reflect the sampled sediment types. Below 824 mbsf (lithologic Subunit IVb, only minor changes in the organic carbon contents are observed where sediments consist predominantly of hemipelagic muds. In the Lower Shikoku Basin sediments the amount of organic carbon decreases drastically at 1200 mbsf to values below 0.2%. Similar values are also found in the volcaniclastic sediments (lithologic Unit V, above the basaltic basement.

The nitrogen content of the sediments, which is generally below 0.13% at Site 808, follows the trend of the organic carbon (Table 18, Fig. 102). On the basis of the carbon/nitrogen ratios, marine organic matter is abundant in all samples (compare Romankevich, 1984; Rashid, 1985). In the Upper Shikoku Basin sediments (lithologic Subunit IVa, between 660 and 720 mbsf, a slight change in the carbon/nitrogen ratio to higher values is observed. This may be interpreted as an effect caused by a higher content of terrestrial organic matter in these sediment samples. Below the décollement the organic matter of the sediments shows values that are lower (<5) than those normally observed for marine organic matter (cf. Romankevich, 1984; Rashid, 1985). One possible explanation for this deviation could be a carbon loss due to thermogenic hydrocarbon generation that has been observed in these sediments (see "Hydrocarbon Gases," below), but this has to be confirmed by further shore-based investigations.

The temperature profile (using the present-day heat flow of 130 mW/m^2, Heat Flow section, this volume) shows (Fig. 103) that temperatures below 400 mbsf are high enough (>50°C) to maintain a generation of thermogenic hydrocarbons (Hunt, 1979; Tissot and Welte, 1984) provided that the maturity of the organic matter has reached an appropriate stage. During the cruise no measured maturity data (T_{max} of Rock-Eval) were available and estimates of the maturity of the organic matter were made from the present-day heat flow applying different maturity models (Hood et al., 1975; Waples, 1980; Price, 1983; Barker and Pawlewicz, 1986; Barker, 1988). The time-temperature-dependent model of Waples (1980), assuming a constant heat flow of 130 mW/m^2 during 15 m.y. (Biostratigraphy section, this volume), predicts mature kerogens (0.5% R_E; vitrinite reflectance equivalent) only for the sediments directly overlaying the basalt (Fig. 103A). This stage of maturity corresponds to the onset of

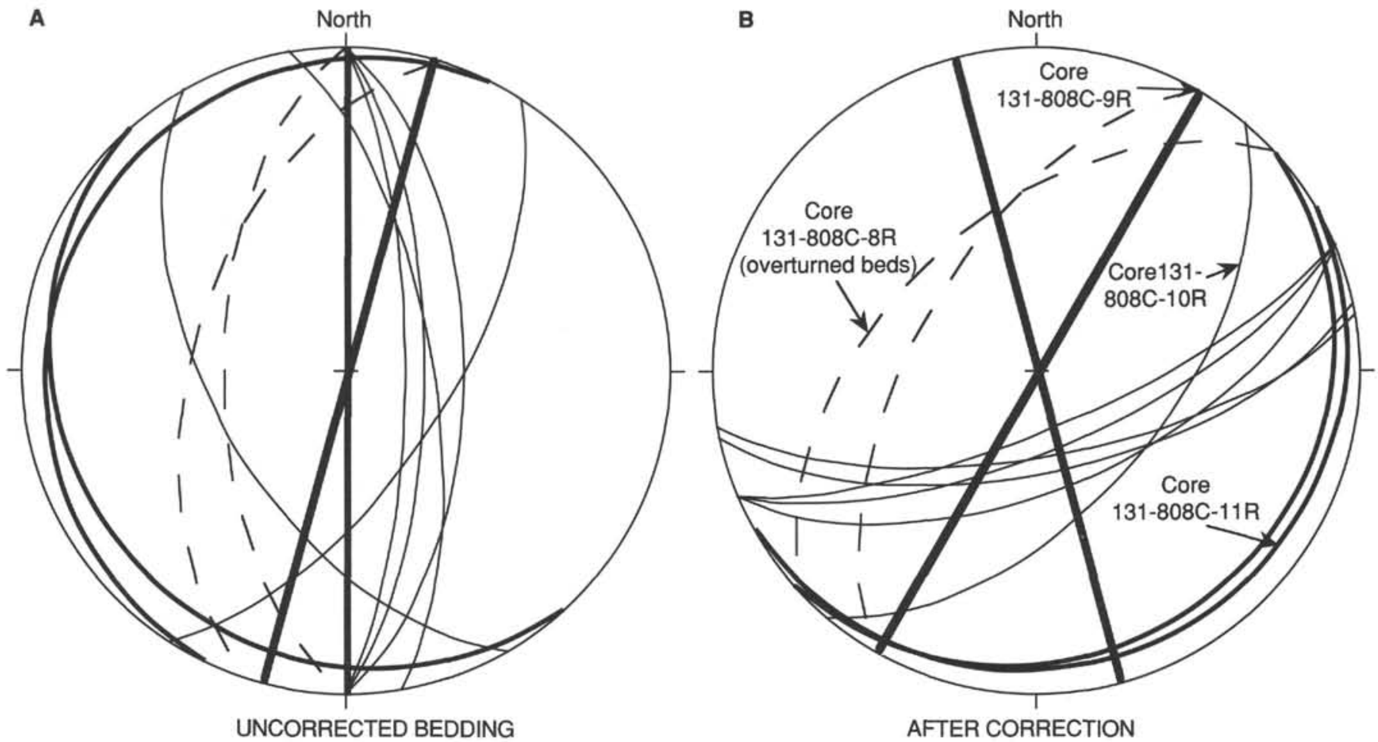

Figure 64. Stereonet projections of bedding planes from the frontal thrust zone. Data shown are from Cores 131-808C-8R (dashed line), 131-808C-9R (very thick line), 131-808C-10R (normal line), and 131-808C-11R (bold line). Note that the beds in Core 131-808-8R are overturned. (**A**) shows data before correction, and (**B**) shows data after paleomagnetic correction for rotations due to drilling. These are equal-area lower hemisphere projections.

thermogenic hydrocarbon generation (cf. Fig. 103B). Identical results are derived by applying the model of Hood et al. (1975). The level of organic maturity (LOM, Hood et al., 1975) reaches only stage 7 for the same sediments if these sediments stayed 0.25 m.y. at the temperature interval 100 to 110°C (Fig. 103A). The maturity of LOM 7 is equivalent to 0.5% vitrinite reflectance (see Tissot and Welte, 1984). Using time-independent models of Price (1983), Barker and Pawlewicz (1986) and Barker (1988) the present-day temperature distribution would lead to maturity values that represent immature to early mature (0.4% to 0.6% R_E; cf. Tissot and Welte, 1984) stages between 580 and 840 mbsf (Fig. 103B). Using the time-independent models, higher maturities, but still below "peak oil window" (0.5% to 0.7% R_E; also cf. Tissot and Welte, 1984), would result for the sediments between 1200 mbsf and the basalt (Fig. 103B).

The application of the time-dependent models of Waples (1980) and Hood et al. (1975) to rapidly subsiding sediments associated with high heat flow seems questionable as both models were set up for slowly subsiding sedimentary basins with low heating rates. The investigations of Price (1983), Barker and Pawlewicz (1986), and Barker (1988) point to a more useful application of the time-independent models in geological settings with high heating rates such as, for instance, occur in the Nankai accretionary wedge (cf. Fig. 103A). In the absence of a knowledge of the time history of heat flow as well as of maximum temperatures, both modeling approaches may lead to an underestimation of the degree of maturity of the organic matter. The modeled maturities, therefore, cannot substitute for careful measurements of the maturity of the organic matter employing vitrinite reflectance, maceral fluorescence, and maceral colors. These needed investigations will be carried out on shore after the cruise.

Hydrocarbon Gases

Headspace gas concentrations of methane are low (14 μL/kg) in Sample 131-808A-1H-2, 145–150 cm, from the sulfate reduction zone (Inorganic Geochemistry chapter, this volume). But significant hydrocarbon concentrations (up to 11646 μL/kg) were recognized below the sulfate zone (depth >4 mbsf) where methane is the only component to a depth of approximately 300 mbsf (this is also supported by the analyses of Vacutainer gases; Table 19). The observed coincidence between low sulfate concentrations and significant amounts of methane in the sediments suggests a bacterial origin of methane (Claypool and Kvenvolden, 1983) in the sulfate-free section of the sediments at Site 808. The methane concentration (14 μL/kg) in the sulfate reduction zone exceeds the level of background methane. This might indicate that either small amounts of methane are generated in the sulfate zone or that methane of the bacterial methane zone migrates upward into the sulfate reduction zone and is partly consumed by sulfate-reducing bacteria. This assumption has to be verified by shore-based stable isotope analyses on the dissolved CO_2 of the interstitial waters in comparison with the carbon isotopes of methanes and kerogens.

The possibility of gas hydrates at Site 808 was considered because sediments down to approximately 190 mbsf are within the pressure-temperature field (Heat Flow section, this chapter) that ensures stability of gas hydrates (Katz et al., 1959). In addition, the methane headspace gas concentrations observed below 4 mbsf are within the same range that Kvenvolden (1985) has reported to be associated with gas hydrates. How-

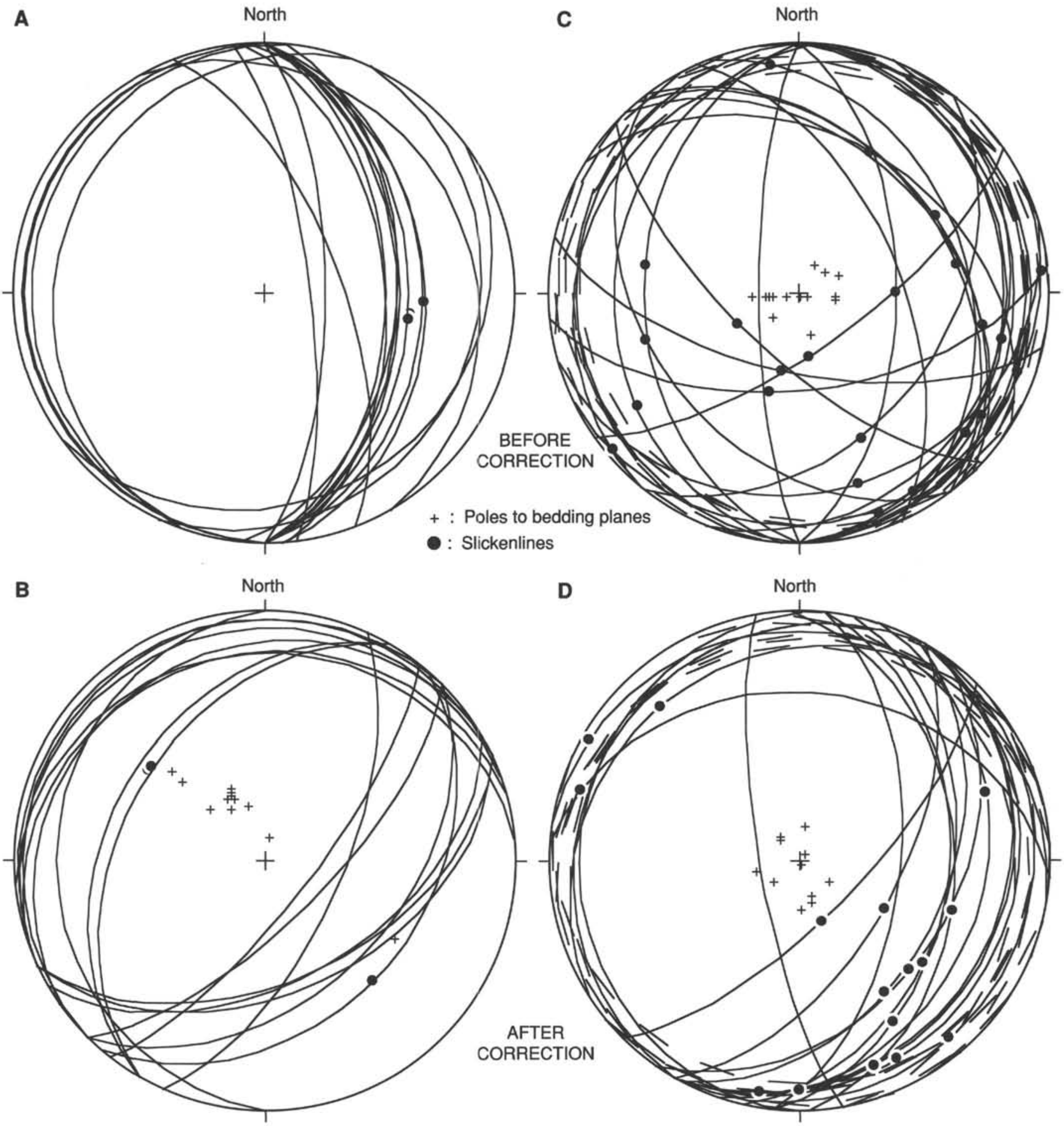

Figure 65. Stereonet projections of typical structures from structural domain 3, interval 1 (see text). (**A**) shows the uncorrected orientations of shear bands and slickenlines from Core 131-808C-25R. (**B**) shows the same structures and poles to bedding planes after correction with paleomagnetic data for rotations due to drilling. (**C**) shows small faults, slickenlines, bedding (dashed lines), poles to bedding planes from Core 131-808C-29R before correction, and (**D**) shows the same structures after paleomagnetic correction. These are equal-area lower hemisphere projections.

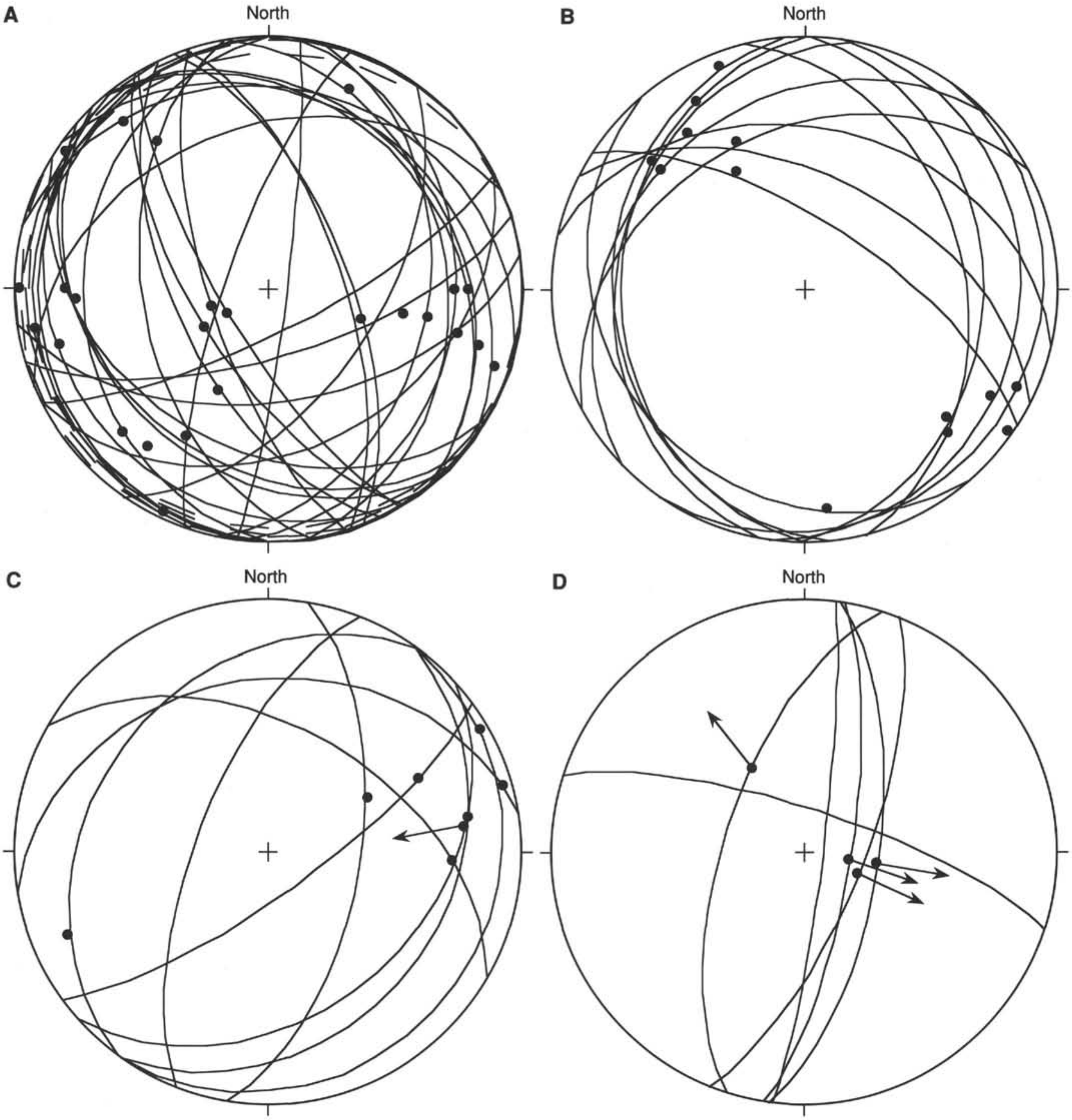

Figure 66. Stereonet projections of typical features from structural domain 3, interval 2. Data shown are from Core 131-808C-38R. (**A**) shows bedding (dashed lines), faults (solid lines), and slickenlines, before correction for drilling rotations. (**B**), (**C**), and (**D**) show slickenlines and the three geometries of faults mentioned in the text, after being corrected for rotations due to drilling. The faults shown in (**B**) are reverse faults, those in (**C**) are also reverse faults, and those in (**D**) are normal faults. The arrows in (**C**) and (**D**) are slip vectors for the motion of the hanging wall, for faults where displacement is known. These are equal-area lower hemisphere projections.

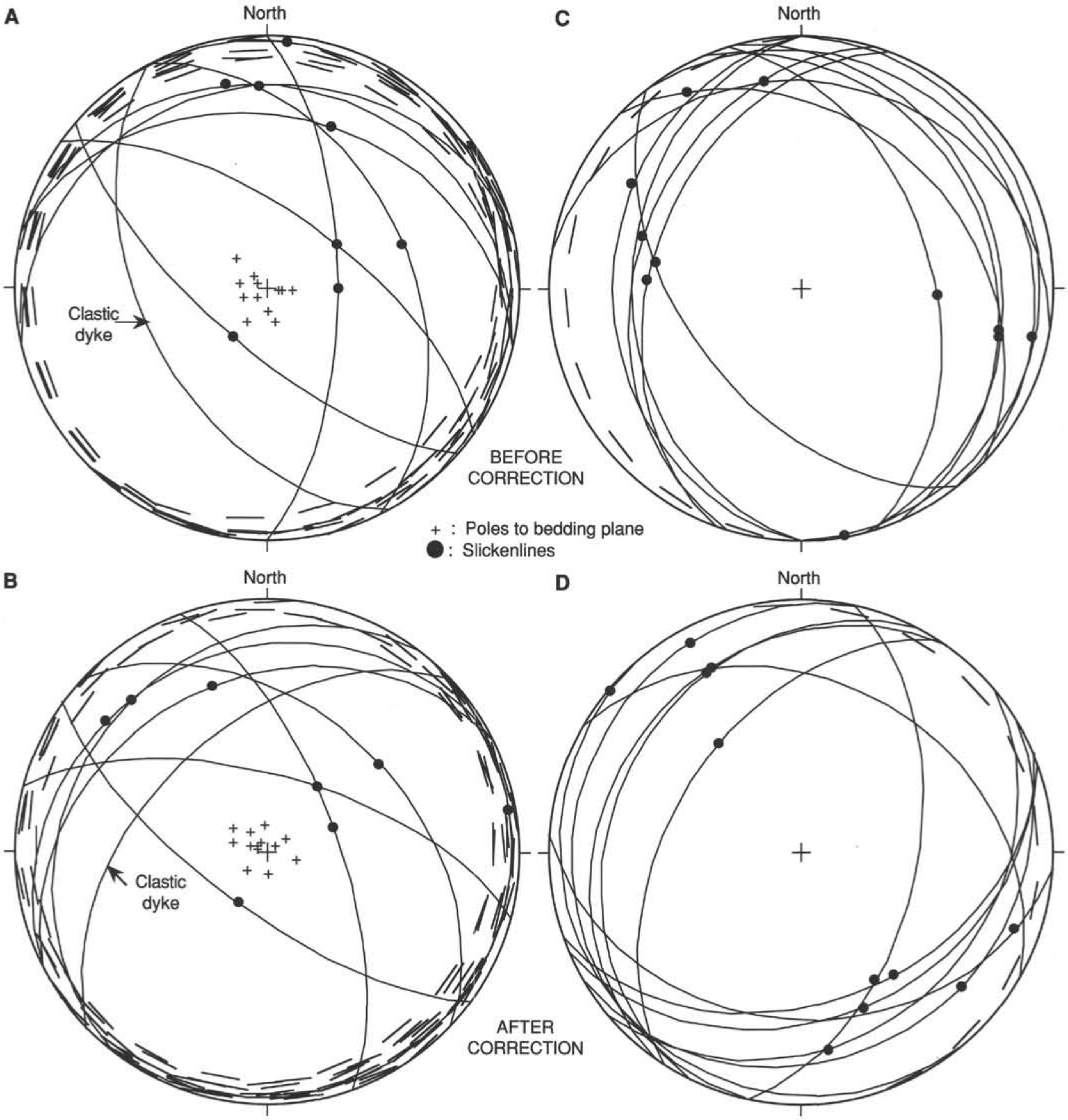

Figure 67. Stereonet projections of typical features from structural domain 3, interval 4. Bedding planes are shown as dashed lines and faults as solid lines. (**A**) shows structures from Core 131-808C-54R before correction. (**B**) shows the same structures after correction, with paleomagnetic data for rotations due to drilling. (**C**) and (**D**) show structures from Core 131-808C-56R before and after paleomagnetic correction. These are equal-area lower hemisphere projections.

ever, only in wash Core 131-808F-4W (90–140 mbsf) was hydrate recovered in association with some plant debris. Decreases in chloride concentrations (Inorganic Geochemistry section, this chapter) around 110 mbsf, however, could point to a more pervasive, diffuse presence of hydrates, which may have been decomposed during core retrieval.

Although methane is still the dominant component, ethane also was detected (Fig. 104, Table 18) below 300 mbsf and from 380 mbsf downward propane is present. Iso-butane first appears between 380 and 920 mbsf and then again between 1060 and 1280 mbsf. *N*-butane is present between 680 and 720 mbsf and again between 1060 and 1280 mbsf. Iso-pentane was

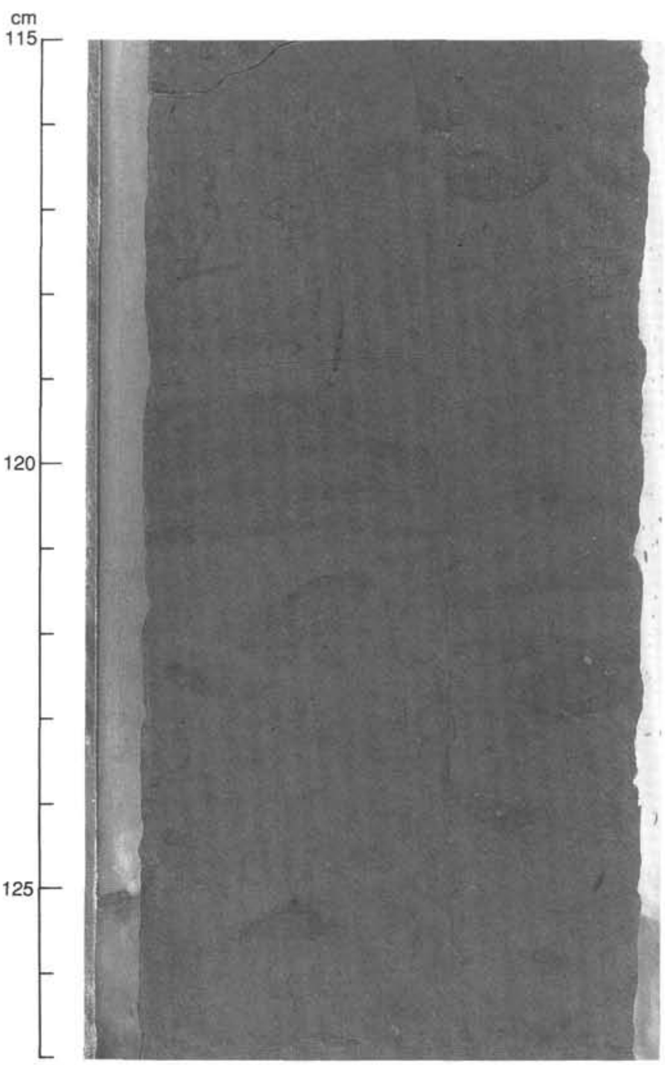

Figure 68. Core photograph showing a typical high-angle fault from structural domain 3, interval 4 (Core 131-808C-59R-3, 115–127 cm).

detected between 680 and 850 mbsf and between 1060 and 1220 mbsf, whereas *n*-pentane is only present between 1110 and 1220 mbsf. The presence of gas components ethane to pentane (Fig. 104, Table 18) indicates that thermogenic hydrocarbons (Evans and Staplin, 1971; Hunt, 1979; Tissot and Welte, 1984; Rashid, 1985) are present in the sediments at Site 808. The gas ratio $C_1/(C_2+C_3)$ (Bernard, 1979; Berner, 1989) shows that the gases above 1020 mbsf are mixtures between biogenic and thermogenic hydrocarbons (Fig. 105). It seems as if below 1020 mbsf at temperatures above 90°C (using the temperature model discussed in the Heat Flow section, this volume) the activity of the methane-producing archae bacteria has stopped and that only thermogenic hydrocarbons are present at higher temperatures. This is in agreement with recent investigations on methanogenic bacteria (H. Koenig, pers. comm., 1990). In addition, the increasing amount of sulfate below 800 mbsf (Inorganic Geochemistry section, this chapter) could also have reduced the bacterial activity (see Claypool and Kvenvolden, 1983) as evident from a steady decrease of the methane concentrations (Fig. 104) noticed below 800 mbsf.

Two major zones of thermogenic hydrocarbons are observed. Peak concentrations are found between 600 to 800 mbsf and 1060 to 1280 mbsf (Fig. 104). The hydrocarbon compositions are different within the two zones. From the gas composition and the gas ratios (Fig. 104 and 106) it seems likely that the hydrocarbons observed between 600 and 800 mbsf are generated from less- mature kerogens than those between 1060 and 1280 mbsf, as the ratio i-C_4/n-C_4 decreases and the C_4/C_5 ratio increases when comparing the shallow to the deep zone. Also in the upper zone (600 to 800 mbsf), only minor amounts of *n*-butane and no *n*-pentane were observed, whereas in the lower zone both components are present. This can be explained by the observation that iso-alkanes, linked to the kerogens by weak bonds, are released at lower temperatures than normal alkanes (compare Tissot and Welte, 1984). The obvious increase of the $C_1/(C_2+C_3)$ and C_3/C_{4+} ratios, as well as the decrease of the i-C_4/n-C_4 ratio below 1170 mbsf (Fig. 105 and 106) in the deep zone indicate that below this depth cracking of longer chain and thermally less stable hydrocarbons occurs rather than a generation of these components. Methane, as the most stable hydrocarbon, increases below 1170 mbsf with increasing depth and temperature relative to the less stable higher hydrocarbons (Fig. 105). From the above comparison of the gas variations it is likely that the gases from the upper zone were generated from kerogens that have reached a maturity stage at the onset of the so called "oil window" (0.5% vitrinite reflectance; also see Tissot and Welte, 1984) and that the gases below the décollement were generated from kerogens that have at least reached peak "oil window" or higher maturities (>0.8% vitrinite reflectance). It is evident that the calculated maturities using the different maturity models (Hood et al., 1975; Waples, 1980; Price, 1983; Barker and Pawlewicz, 1986; Barker, 1988) are lower than those predicted from the gas composition. This could indicate that either the hydrocarbons detected in the two gas-rich zones migrated from sediments of higher maturity into the sediments at Site 808, or that the heat flow used for the temperature/maturity model was higher than measured, or that the models used for the maturity calculations are not appropriate. Clearly further work on the stable isotopic composition of single gas components in comparison with measured maturities of the organic matter is needed and will be done in shore-based studies.

Gas migration leads to an enrichment of the lighter hydrocarbons methane and ethane in the sediments because of their higher mobility (Evans and Staplin, 1971). Migrated gases should, therefore, show a clear predominance of methane and ethane. The high methane concentration in the upper zone, however, can be explained by bacterial generation rather than migration as only small portions of methane are related to the thermal decomposition of the organic matter (see above). Migration should at least be indicated by a strong predominance of ethane in the C_{2+} fraction (cf. Evans and Staplin, 1971) which is not obvious from the data of Site 808, because in the gases from 550 to 870 mbsf propane dominates over ethane. Also the C_3/C_{4+} ratio of the zones at Site 808 shows (Fig. 106) a similar variation pattern as observed by Leythaeuser et al. (1979) and Schaefer and Leythaeuser (1983) for *in-situ* gas generation with increasing maturity. Furthermore, the gas concentrations of the C_{2+} components normalized to the amounts of organic matter should correspond only to the increase of temperature and maturity if the hydrocarbons were generated in the sediments itself (Leythaeuser et al., 1979; Schaefer and Leythaeuser, 1983). This is indeed the case for the gases of the zones (Fig. 104) as lower concentrations are observed in the upper zone than in the lower zone, where temperatures and also maturities are expected to be higher (cf. Fig. 103). Based on the gas concentration and composition, especially in com-

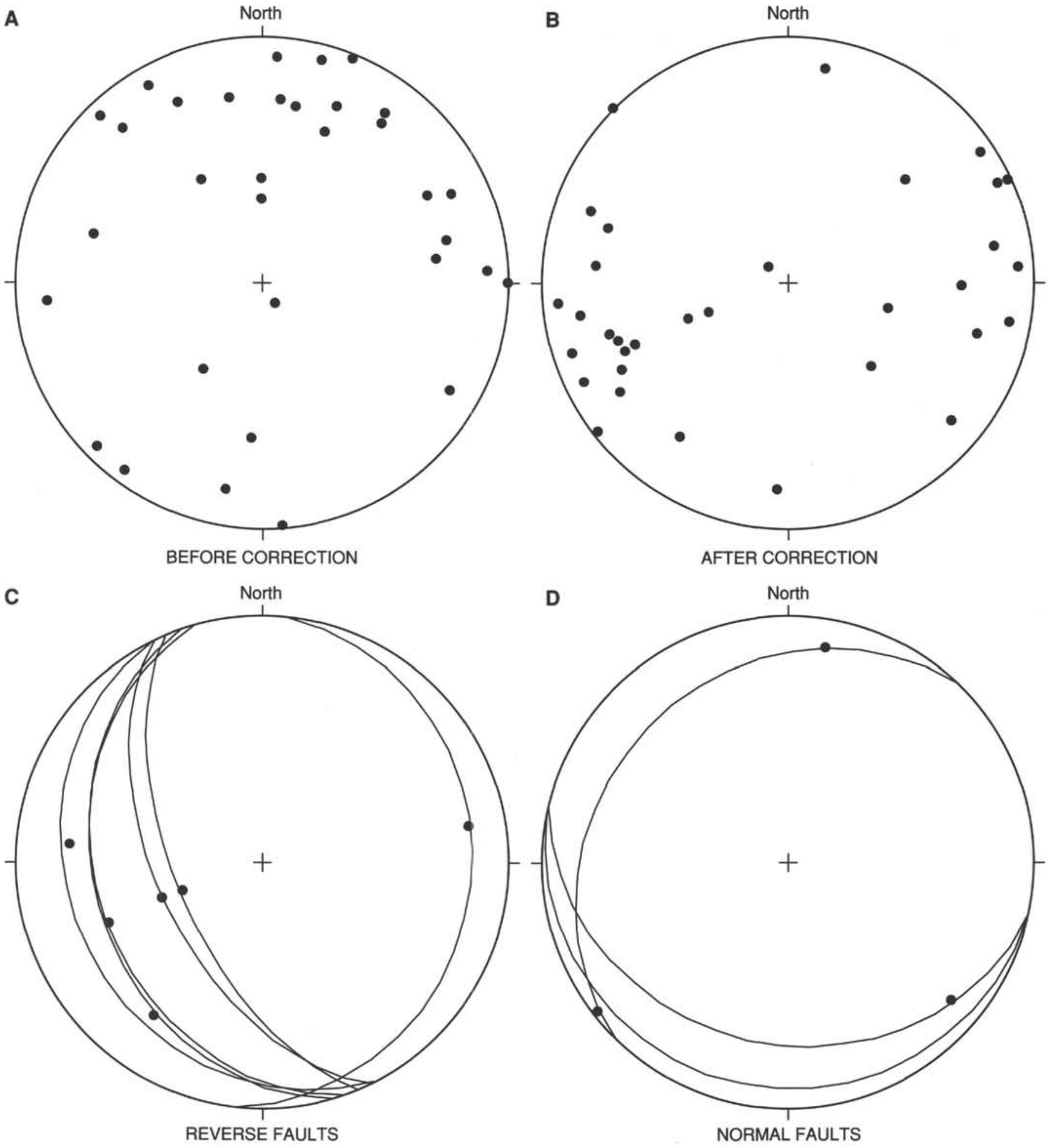

Figure 69. Stereonet projections of features from structural domain 3 interval 5. Data shown are from Core 131-808C-66R. (**A**) and (**B**) show the orientations of all slickenlines in the core before and after correction with paleomagnetic data for rotations due to drilling. (**C**) shows reverse faults and associated slickenlines after paleomagnetic correction. Note the dominance of the northwest-striking faults and west-southwest-trending slickenlines. (**D**) shows low-angle, oblique-slip normal faults and their associated slickenlines, after paleomagnetic correction. These are equal-area lower hemisphere projections.

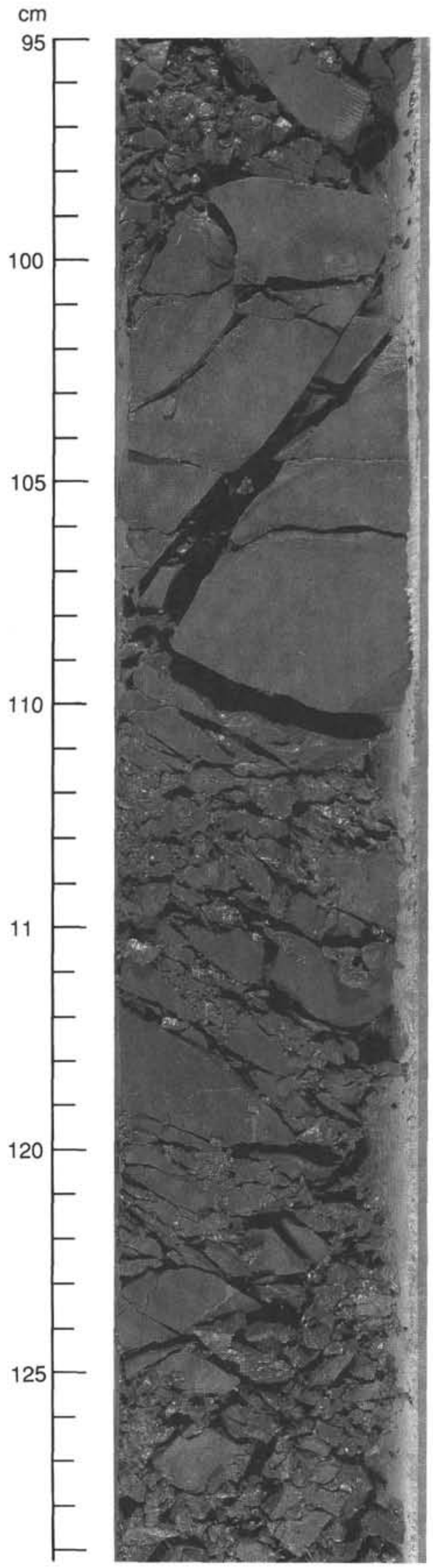

Figure 70. Core photograph of breccia from the décollement, structural domain 4. Example is from Interval 131-808C-69R-4, 95–129 cm.

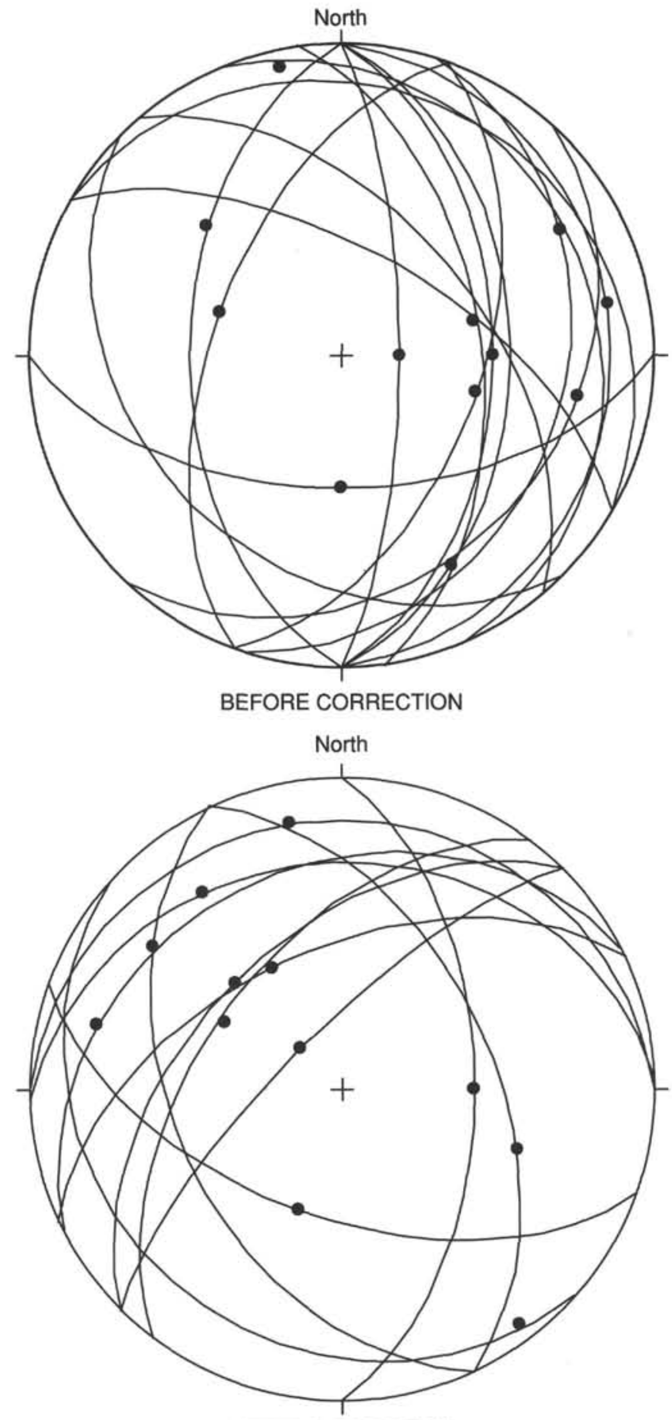

Figure 71. Stereonet projections of faults and associated slickenlines from the décollement, structural domain 4. Data shown are from Core 131-808C-69R. Note the dominance of northwest-southeast trending slickenlines. Data shown "after correction" have been corrected with paleomagnetic data for rotations due to drilling. These are equal-area lower hemisphere projections.

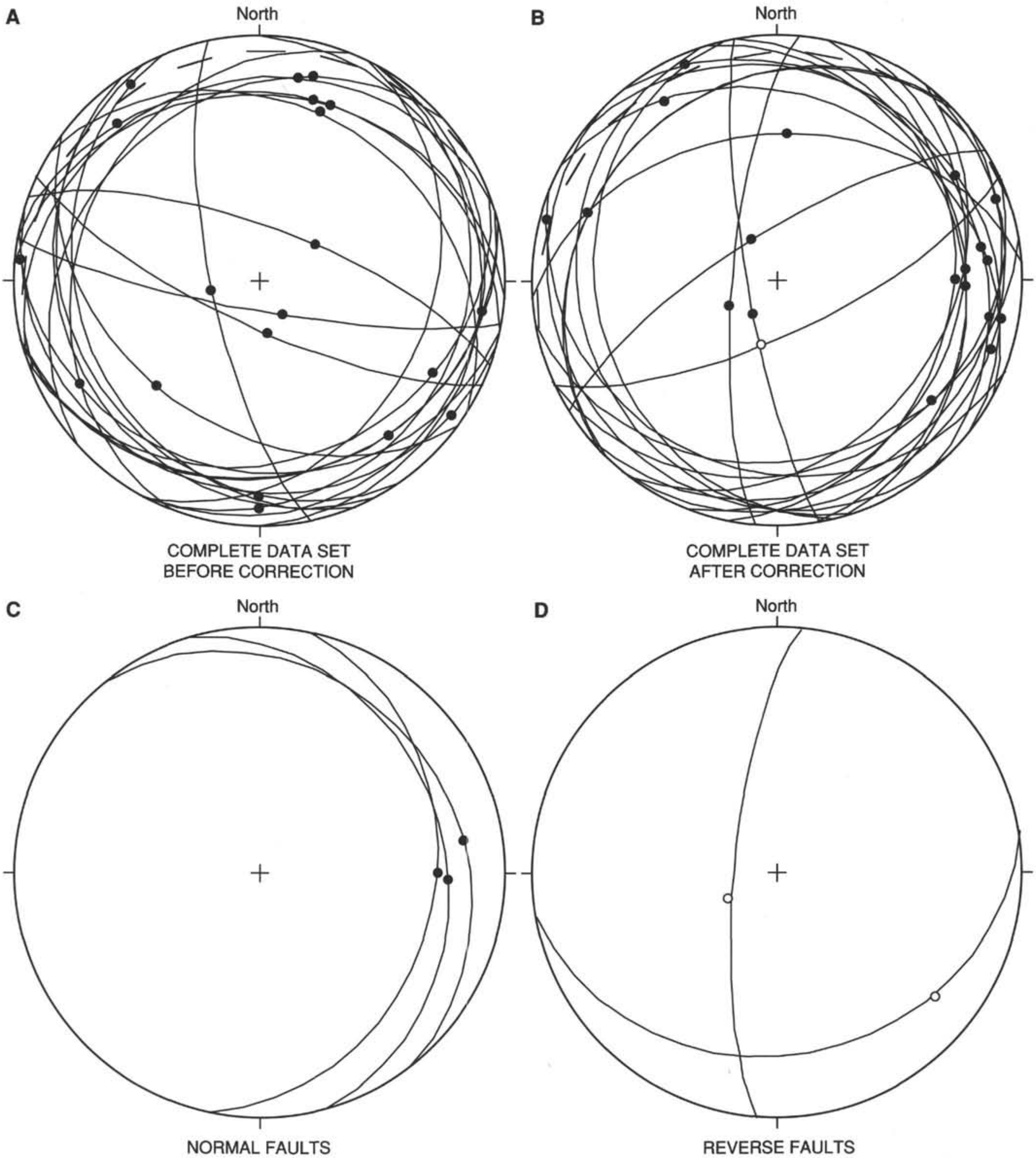

Figure 72. Stereonet projections from domain 5, the underthrust sequence, structural domain 5. Data shown are from Core 131-808C-70R. Bedding is shown as a dashed line, and faults as solid lines. (**A**) shows faults and associated slickenlines before correction with paleomagnetic data for rotations due to drilling. (**B**) shows the orientations after paleomagnetic correction. (**C**) shows the corrected orientations of those faults for which a normal sense of displacement could be distinguished, and (**D**) shows the corrected orientations of reverse faults. These are equal-area lower hemisphere projections.

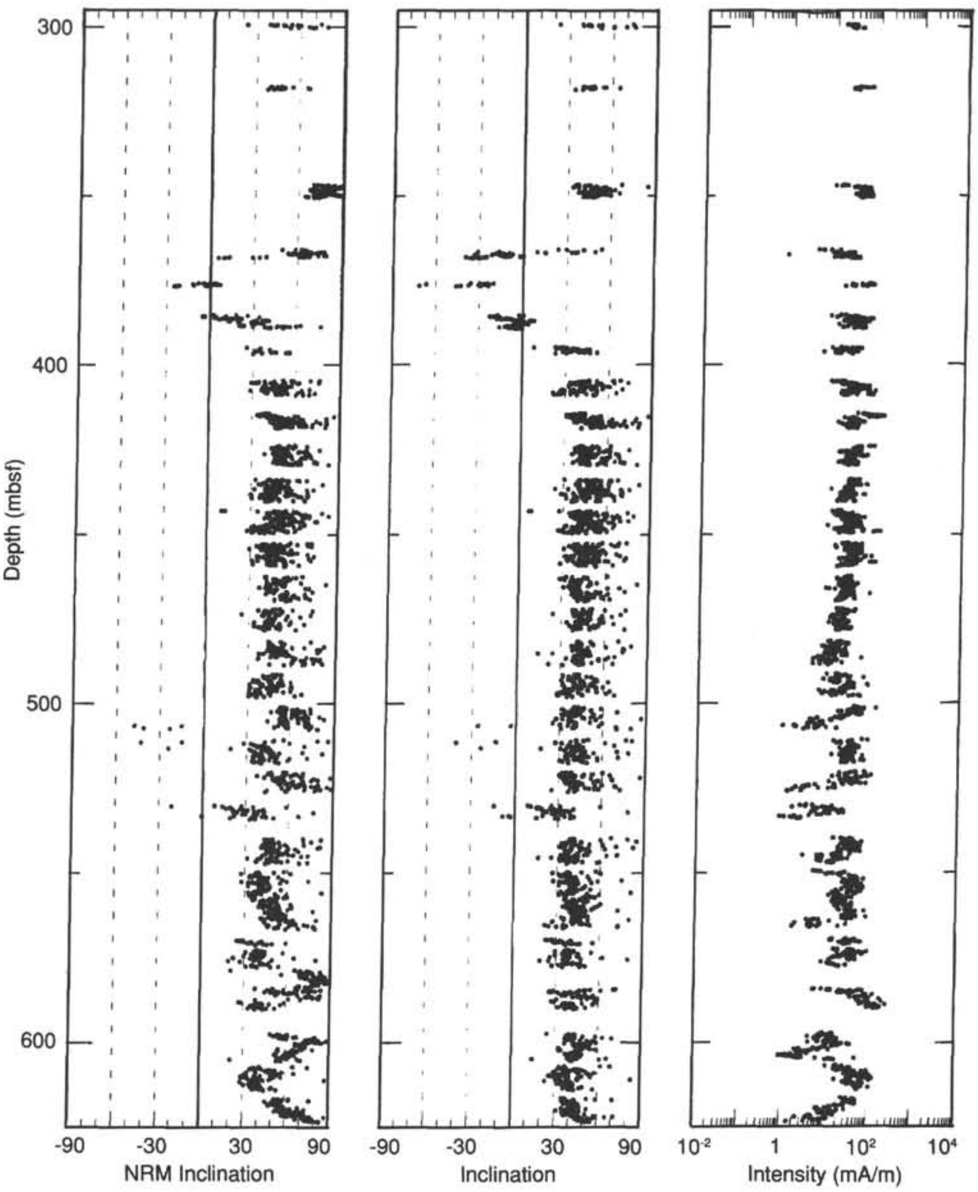

Figure 73. Inclination of NRM, and inclination and intensity after demagnetization at the highest alternating field used (10 or 15 mT), vs. depth for Hole 808C.

parison with the results of Evans and Staplin (1971), Leythaeuser et al. (1979), and Schaefer et al. (1983), it is likely that the hydrocarbons of the zones at Site 808 were generated from the organic matter in the sediment itself rather than laterally migrated from deeper sections of the accretion. Vertical migration of gases from the zone between 1060 and 1280 mbsf to the zone between 600 and 800 mbsf is highly unlikely if we assume steady-state migration, as butanes and pentanes are missing in the sediment section between both gas-rich zones.

The C_{2+} gas concentrations detected between 380 and 600 mbsf, where iso-butane is present only in small amounts but *n*-butane and pentanes are missing, deviate from those detected in the above-mentioned deeper zones (Fig. 104). This also applies to the gases of the sediments between 920 and 1060 mbsf as butanes and pentanes are absent (Fig. 104). The C_{2+} gases between 380 and 600 mbsf could be explained by low-temperature alteration of organic matter (Hunt, 1979). Also, diffusion of gases from the upper zone into the overlaying sediments cannot be excluded. However, it is difficult to explain the nature of the gases detected between 920 and 1060 mbsf. It is still an open question if hot fluids moving along the décollement could have caused extensive heating and cracking of the kerogens. There is some evidence for fluid movement (in the past) along the décollement as has been discussed on the basis of diminished interstitial water chloride concentrations (Inorganic Geochemistry section, this chapter). Maturity measurements of the organic matter could help solve this problem.

Based on the gas data obtained at Site 808 it is evident that no presently active advection of light hydrocarbons occurs along the frontal thrust or the décollement.

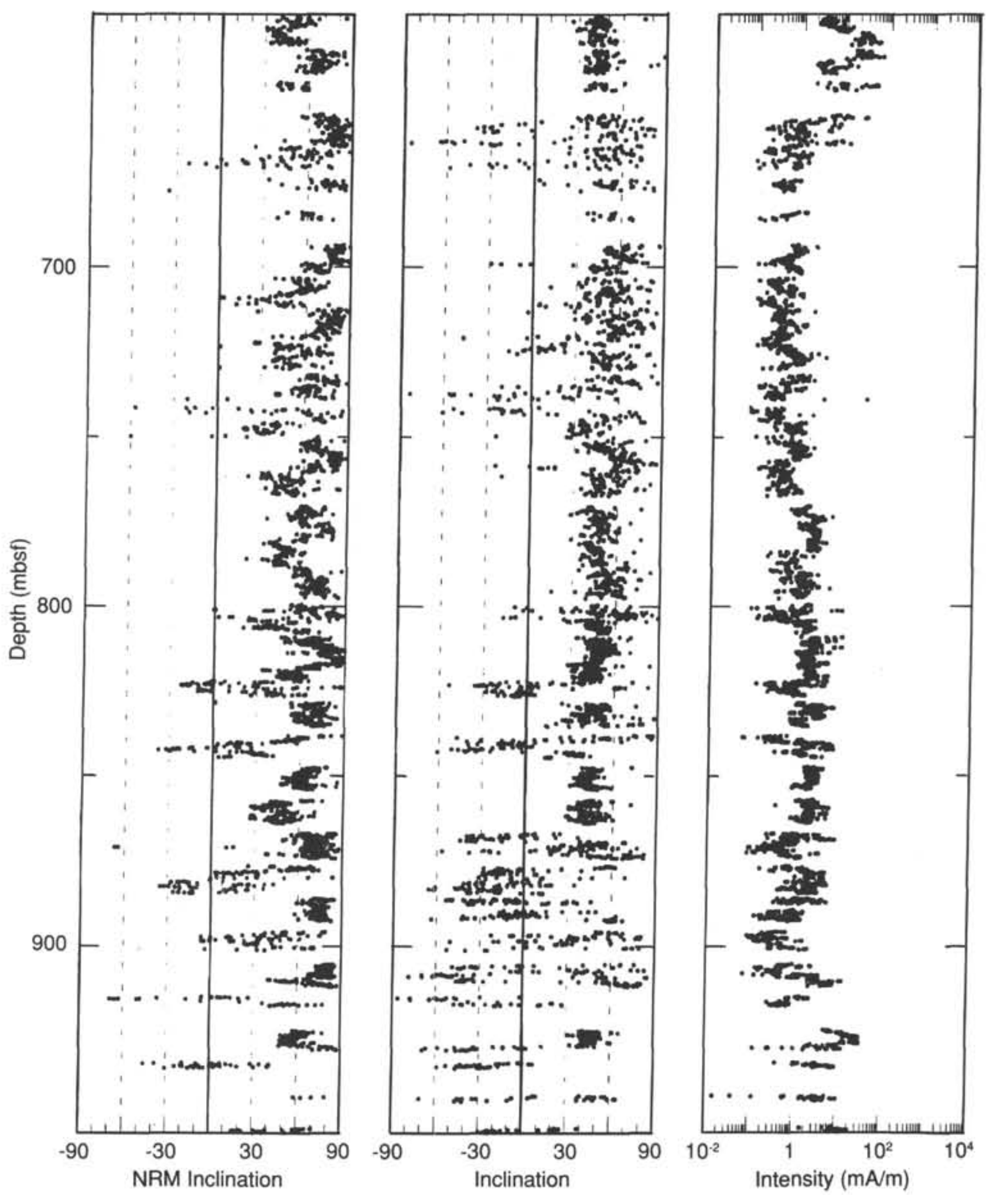

Figure 73 (continued).

Conclusions

1. A general decrease of the amount of organic matter with increasing depth is reflected by the decrease of the TOC from 0.75% to 0.1% (average values) from top to bottom of the sediment section at Site 808.

2. On the basis of the carbon/nitrogen ratios, marine organic matter is abundant in all samples.

3. The observed coincidence between low sulfate concentrations and significant amounts of methane in the sediments suggests a bacterial origin of methane in the sulfate-free section of the sediments at Site 808.

4. The gas components ethane to pentane indicate that thermogenic hydrocarbons are present in the sediments at Site 808 below a sediment depth of 380 mbsf.

5. Gases above 1020 mbsf are mixtures between biogenic and thermogenic hydrocarbons.

6. Below 1020 mbsf at temperatures above 90°C and with elevated sulfate concentrations the activity of the methane-producing archae bacteria has stopped and only thermogenic hydrocarbons are present.

7. Based on the gas composition it is likely that the hydrocarbons from 600 to 800 mbsf and 1060 to 1280 mbsf at Site 808 were generated *in situ* from the organic matter in the sediments of the site rather than migrated from deeper sections of the accretion.

8. The maturity of the organic matter (estimated from the gas geochemistry) cannot be explained by the present-day heat flow.

9. The cause for the low gas concentrations associated with the décollement cannot be explained using shipboard measurements only.

10. No active gas migration along the frontal thrust and the décollement is observed.

The conclusions are necessarily speculative and future work on the isotopic composition of hydrocarbon gases and the maturity of the organic matter will provide additional information that could solve these questions.

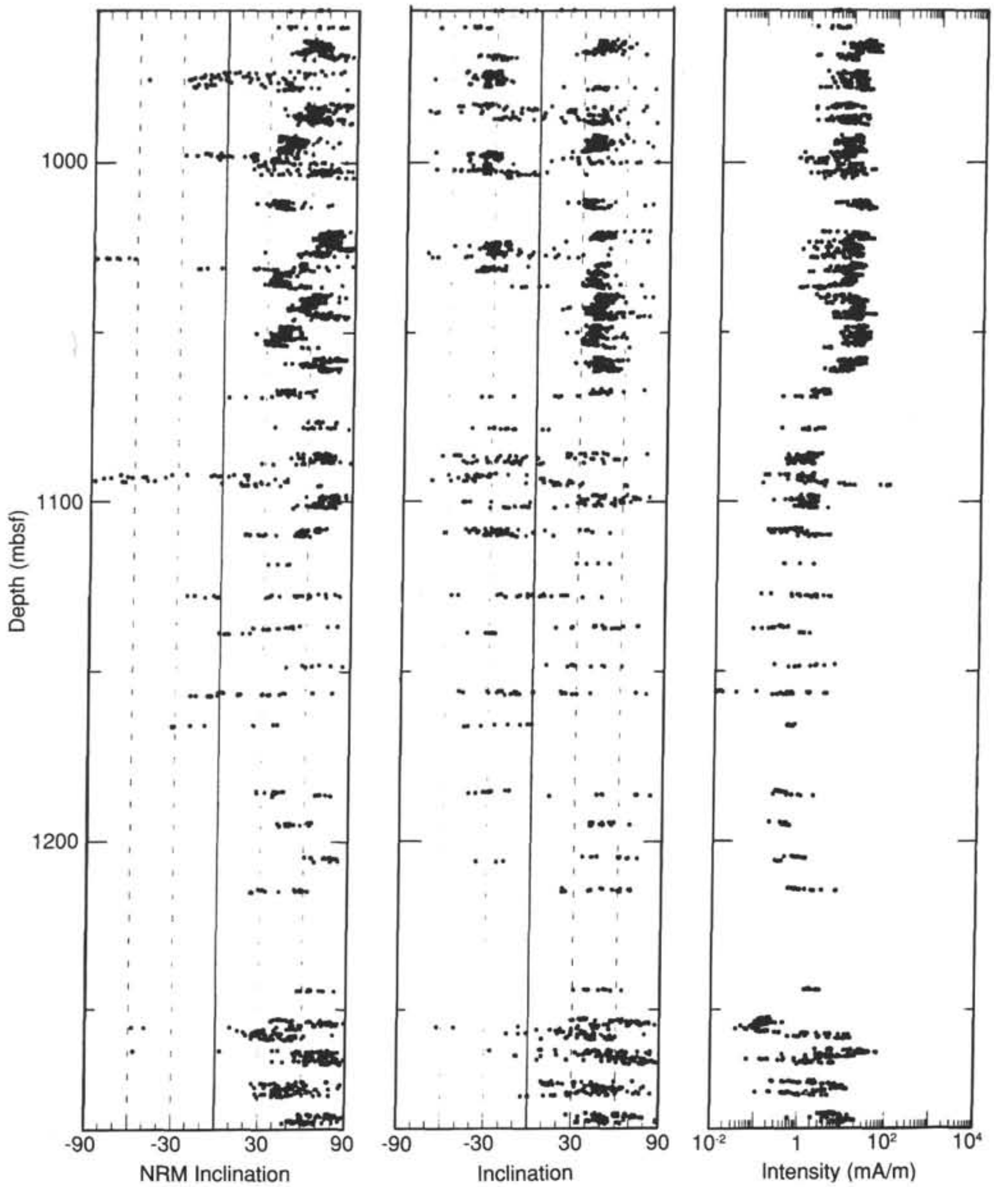

Figure 73 (continued).

BASEMENT LITHOLOGY AND GEOCHEMISTRY

Introduction

Igneous rocks in Hole 808C were encountered at a depth of 1289.9 mbsf (Core 131-808C-105R); coring continued until drilling was stopped at 1327.0 mbsf in Core 131-808C-108R. A total of 37.1 m of igneous rocks was penetrated: total recovery averaged 15.5%, ranging in individual cores from a low of 10.4% in Core 131-808C-108R to a high of 26.1% in Core 131-808C-106R.

The lithostratigraphy, depth, and recovery data of igneous rocks from Hole 808C are summarized in Figure 107.

The age of the lowest hemipelagic layer is between 13.6 and (?)16 Ma, on the basis of calcareous nannofossils (Biostratigraphy section, this chapter). The same age is recorded by the nannofossils found in red tuffaceous mudstone in Section 131-808C-106R-2.

Definitions and interpretations of the lithologic units and of some subunits were complicated by the gaps in recovery, especially because the location of voids in the cores are not known and, by convention, the recovered material is placed at the top of the cored interval. Two main lithologic units were distinguished on the basis of mineralogy, texture, and presence of a brecciated top. It is very important to point out, however, that whereas the two units were identified based on actual observations, critical contacts confirming the mode of their emplacement were not recovered. Available data suggest that Unit 1 consists of sill-like rocks and Unit 2 represents a pillow lava unit.

The database for petrographic descriptions includes 15 thin sections: 1 for lithologic Subunit 1B (Section 131-808C-105R-1), 2 for 1D (Section 131-808C-106R-1), 3 for 1E (Section 131-808C-106R-1), 2 for 1F (Section 131-808C-106R-2), 2 for 1G (Section 131-808C-107R-1), and 4 for lithologic Unit 2 (Section 131-808C-108R-1).

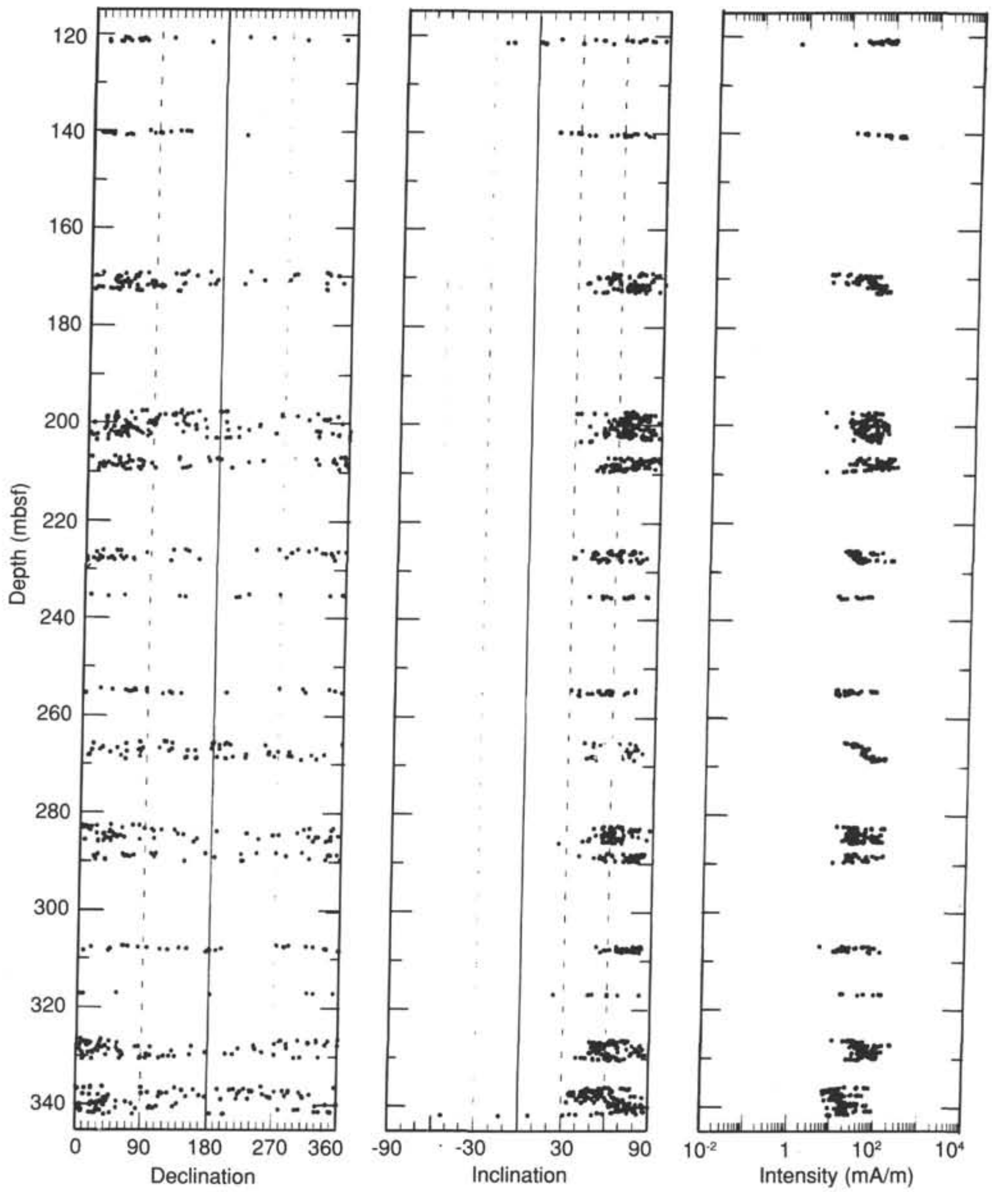

Figure 74. Declination, inclination and intensity vs. depth for Hole 808B.

Although the basalts of Unit 1 are macroscopically similar throughout the recovered sections, and actual contacts were not visible, they were divided into seven subunits using the criteria of changing grain size, occurrence of glassy margins, and changes in texture, primary mineralogy, and phenocryst abundance. Unit 2, representing a single lithologic unit, was not further subdivided.

Lithologic units and subunits were named according to their dominant lithologies. The results are summarized in Figure 107 and Table 20. More complete details can be obtained from the visual core descriptions and thin section descriptions that are printed in the back of this volume.

Lithology and Petrography

Basalts are predominantly nonvesicular, hypocrystalline, fine- to medium-grained, aphyric to (olivine-) plagioclase phyric. Rare, large phenocrysts of plagioclase up to 0.5 cm across were observed in only one instance (Interval 131-808C-106R-1, 74–76 cm). Olivine generally occurs in microphenocryst assemblage. A noteworthy petrographic aspect of these rocks, however, is the scarcity of phenocryst phases. Because of relatively little alteration, textures are well preserved; they are mainly intersertal (locally up to hyalopilitic) and intergranular and, subordinately, subophitic to ophitic.

A detailed description of the most important features of units and subunits is presented below.

Subunit 1A: Plagioclase Phyric Basalt

Subunit 1A is defined as Interval 131-808C-105R-1, 0–8 cm. Neither top nor bottom contacts were observed. The light greenish gray basalt is massive with very scarce (1%–2%), uniformly distributed plagioclase phenocrysts, which occur as 0.2–0.3-mm subhedral tabular, slightly altered crystals. The fine-grained intersertal to subophitic groundmass is composed of altered plagioclase laths, anhedral interstitial clinopyroxene, and altered brownish glassy mesostasis.

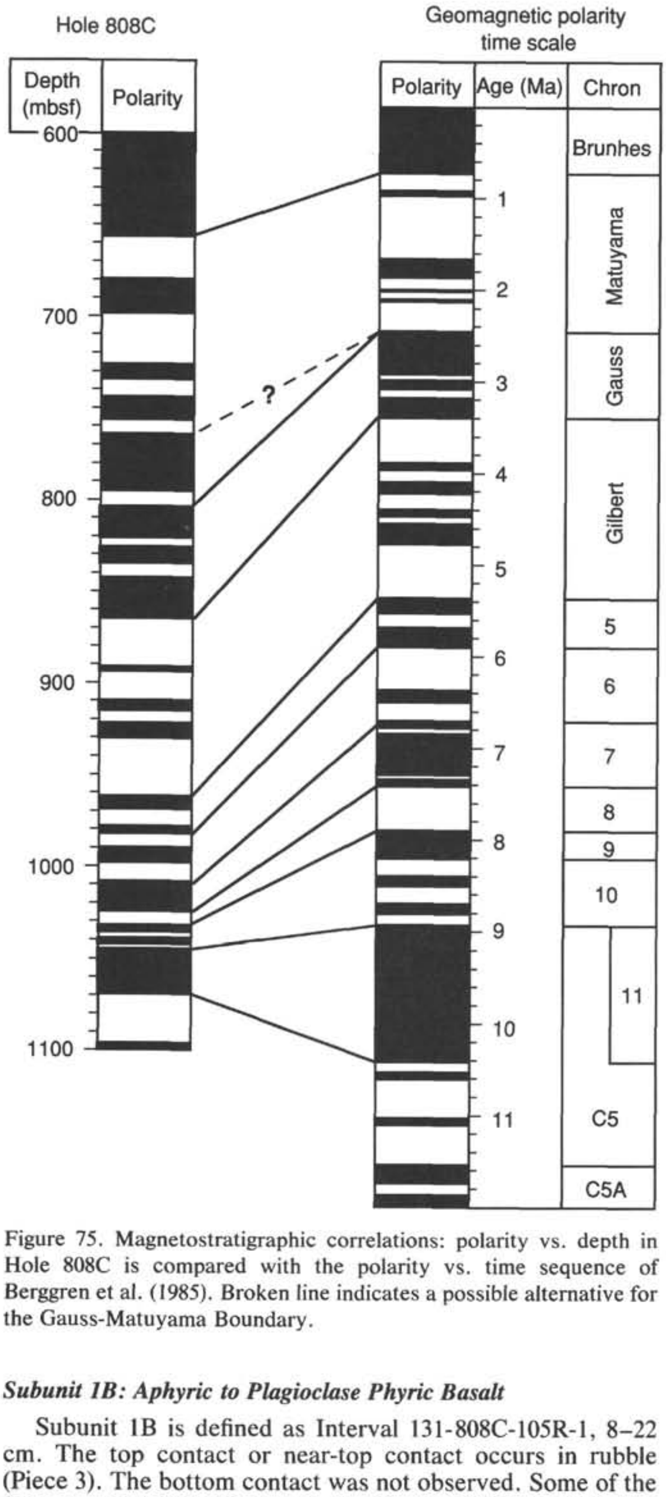

Figure 75. Magnetostratigraphic correlations: polarity vs. depth in Hole 808C is compared with the polarity vs. time sequence of Berggren et al. (1985). Broken line indicates a possible alternative for the Gauss-Matuyama Boundary.

Subunit 1B: Aphyric to Plagioclase Phyric Basalt

Subunit 1B is defined as Interval 131-808C-105R-1, 8–22 cm. The top contact or near-top contact occurs in rubble (Piece 3). The bottom contact was not observed. Some of the fragments of Piece 3 show narrow glassy margins 0.5 mm wide. The rocks are light gray to greenish gray in color with frequent reddish oxidation haloes. In the top part of the subunit, vesicles are common and constitute up to 5% of rock in volume; they occur in patchy distribution or in trails. At greater depth vesicles become rare or absent. They are 0.2–0.4 mm in diameter and are filled with smectite, calcite, and more rarely with altered devitrified glass.

This subunit is characterized by rare (1%) large tabular plagioclase crystals sometimes in glomeroporphyritic and seriate aggregates, or more commonly as discrete phenocrysts, almost totally replaced by clay minerals. A very narrow, fresh rim could be interpreted as an overgrowth. Less than 1% olivine subhedral phenocrysts, totally pseudomorphed by iddingsite, chlorite, and Fe-oxide have also been found.

The fine-grained groundmass is intersertal to hyalopilitic textured. In Piece 3 the two textural types are separated by a reddish-brown oxidation zone. The intersertal texture is characterized by fresh or slightly altered subhedral to euhedral plagioclase laths, subhedral to anhedral prismatic or subequant clinopyroxene and olivine, and glass, which occupies the wedge-shaped interstices between the crystals. When patches of glass are sufficiently large and continuous to enclose a number of plagioclase laths, the texture becomes hyalopilitic. Glassy mesostasis may be fresh or, more commonly, devitrified and altered to smectite and/or chlorite; perlitic and spherulitic textures have also been observed.

Subunit 1C: Aphyric Basalt

Subunit 1C is defined as Interval 131-808C-105R-1, 102–119 cm. Neither top nor bottom contacts were observed, except a brownish glassy margin with variolitic texture in Piece 15. In the glassy mesostasis of this piece, ovoidal or spherical varioles are present, randomly distributed or in patches surrounded by a narrow smectite rim.

The rocks are massive and dark gray to light greenish gray in color. Texture is mainly intersertal, locally grading to intergranular, with the spaces between plagioclase laths occupied by one or more grains of clinopyroxene, olivine, and minor magnetite; plagioclase laths may be in diverse, subradial, or subparallel arrangements.

The fine-grained groundmass consists of 30%–40% plagioclase laths up to 0.5 mm in size, 10%–20% subhedral clinopyroxene, about 15% small subhedral olivine crystals totally pseudomorphed by serpentine, chlorite, and iron oxide. Glassy mesostasis, constituting about 15% of the rock, is partly altered to reddish smectite and partly devitrified.

Vesicles are present only in the top piece of the subunit; they are randomly distributed, spherical, and filled with smectite and minor microcrystalline calcite.

Subunit 1D: Olivine-Plagioclase Phyric to Aphyric Basalt

Subunit 1D is defined as Interval 131-808C-106R-1, 0–64 cm. Piece 1 is a reddish brown fine-grained tuffaceous mudstone, which could be a baked fragment of altered volcaniclastic deposit. No contacts were observed, but in Piece 2, a variolitic and vesicular 1–2-mm thick dark green glassy margin was observed. Grain size coarsens from Piece 2 to 5 and the entire subunit is in general coarser grained and better crystallized than the overlying ones.

The basalt is medium to dark gray, massive and generally fine grained. Intergranular texture predominates, though locally it may grade to subophitic texture, where plagioclase laths are embedded in clinopyroxene subhedral to anhedral crystals. Glassy mesostasis is very scarce (1%–3%), partly devitrified and partly altered to smectite. Vesicles are rare and concentrated in the top part of Piece 2; they are spherical or lobate in shape, 0.1–0.3 mm in size and partly filled with carbonate and/or clay minerals.

Subunit 1D is predominantly aphyric. Phenocrysts, when present, are rare and sparsely distributed. Olivine (0%–5%) microphenocrysts up to 0.3 mm in size, sometimes enclosed in plagioclase, have subhedral morphology and are totally pseudomorphed by chlorite and Fe-oxide. Plagioclase phenocrysts never exceed 3% in volume of the rock and are almost totally replaced by clay minerals except a very narrow fresh rim; their size range is from 0.5 to 0.8 mm.

Subunit 1E: Plagioclase Phyric Basalt

Subunit 1E is defined as Interval 131-808C-106R-1, 64–138 cm. No contacts are present, although Piece 9A has a 2-mm-thick dark green fresh glassy margin with variolitic texture. This subunit is dark gray to greenish-gray in color, with yellowish to reddish irregular patches and haloes. Rocks are fine- to medium-grained with intersertal to intergranular or subophitic texture. The three textural types may coexist even in the same piece, yet in the bottom part of the subunit rocks tend to be finer grained and more glass-rich with a predominance of the intersertal texture.

Vesicles are heterogeneously distributed, being mainly concentrated in the top part of Piece 9; they are generally spherical in shape, about 1 mm in diameter, and filled with greenish smectite and whitish calcite. Plagioclase phenocrysts (1%–5%) are up to 5 mm in size and their abundance decreases downward. They are subhedral to euhedral, tabular, and almost totally replaced by clay minerals. Irregularly shaped patches of groundmass inclusions consisting of devitrified glass give them a sponge-like appearance. Sometimes plagioclase phenocrysts exhibit a narrow, fresh rim that may represent an overgrowth as well as the outermost part of extremely zoned crystals.

Groundmass mainly consists of 30%–40% elongate plagioclase laths, subhedral, with variable degrees of alteration, 30%–40% prismatic to subequant clinopyroxene grains sometimes intergrown with plagioclase, and 10% subhedral olivine, totally replaced by alteration minerals such as chlorite, iddingsite, and Fe-oxide. Glassy mesostasis, almost totally devitrified and altered to green smectite and chlorite, occupies the interstices and increases in amount toward the bottom of the subunit, suggesting a near-contact zone.

Subunit 1F: Clinopyroxene-Plagioclase Phyric to Aphyric Basalt

Subunit 1F is defined as Interval 131-808C-106R-1, 0–35 cm. Neither top contact was found nor substantial variations in grain size were observed. The rocks are gray to dark gray in color, massive, nonvesicular. They are the coarsest grained among the total recovered basalts. Plagioclase and minor clinopyroxene phenocrysts occur only in the top pieces: they are subhedral to euhedral in morphology and generally fresh. The rest of the subunit is aphyric but there is no change in grain size, which is constantly medium.

Texture is holocrystalline, intergranular to subophitic and locally ophitic, due to large clinopyroxene anhedral crystals embedding plagioclase laths.

Groundmass is medium grained and its primary mineralogy consists of about 40% subhedral fresh plagioclase laths, often exhibiting normal compositional zoning, about 49% subhedral clinopyroxene prisms, light pinkish color in plane-polarized light. Very often elongate columnar clinopyroxene crystals form composite radiating or branching groups intergrown with similarly shaped and developed plagioclases, suggesting contemporaneous crystallization. Individual columnar crystals can be seen to consist of straight portions offset slightly from one another and having very slightly different optical orientation. Olivine occurs as subhedral crystals 0.4–0.5 mm in size, totally pseudomorphed by chlorite and iddingsite and surrounded by a film of Fe-oxide. Glassy mesostasis is absent and only minor microcrystalline altered phases occupy the small wedge-shaped interstices between well-crystallized primary minerals. Rubble of Piece 3 shows thin variolitic glassy margins that would suggest a contact to another subunit, but neither texture nor substantial grain size changes support this subdivision. Pieces 9 and 10 consist of a great number of small rounded fragments of reddish brown very fine-grained tuffaceous mudstone. They are followed by the basaltic rubble of Piece 11, which could represent the top of a different unrecovered subunit.

Subunit 1G: Aphyric Basalt

Subunit 1G is defined as Interval 131-808C-107R-1, 0–128 cm. Top and bottom contacts were not found. This subunit is gray to yellowish-gray in color with reddish oxidation haloes, massive and very fine grained. The rocks contain rare (maximum 2%) unevenly distributed spherical, lobate, or irregularly shaped vesicles up to 0.3 mm filled with calcite (sometimes spherulitic textured) and minor smectite and chlorite.

Rocks are generally hypocrystalline, having intersertal divergent to hyalopilitic texture. The groundmass consists of 20%–30% subhedral needle-like, skeletal H-shaped, often radiating plagioclase laths, 15%–40% anhedral skeletal or subequant clinopyroxene, minor amounts of small subhedral, totally pseudomorphed olivine, and abundant (40%) glassy mesostasis often transformed to cryptocrystalline patches of turbid devitrified glass full of tiny grains of iron oxide.

Top contact was not found; bottom contact may be represented by the narrow oxidized and devitrified glassy margins observed in rubble of Piece 6.

Unit 2: Aphyric to Plagioclase Phyric Basalt

Unit 2 is defined as Interval 131-808C-108R-1, 0–132 cm. No actual contacts were found; however, the auto-brecciated Pieces 1 to 10 suggest the upper part is pillow basalt. Angular fragments from one to several centimeters across are healed together by calcite and green fine-variolitic glass with minor smectite (Fig. 108). From Piece 10 downward, matrix amount decreases and fragment size increases until the rock becomes massive and almost totally crystallized, bottom pieces being representative of the well-crystallized interior pillow.

Matrix composition indicates that fragmentation occurred both during cooling (fragments healed together by variolitic glass) and under subsolidus condition (secondary minerals, as calcite veining variolitic glass). In the top pieces basaltic fragments are aphyric and characterized by hyalopilitic very fine grained texture, where tiny needle-like often skeletal plagioclase microlites, radiating or branching are embedded, together with small subequant mafic minerals in brown partly devitrified glass altered to smectite and minor chlorite (Fig. 109). Mafic minerals are almost totally pseudomorphed by calcite, and subordinately by chlorite and iron oxide, losing any original habits. It is possible to recognize olivine and clinopyroxene from only very few small portions unaffected by alteration.

Sometimes small, quenched plagioclase microlites may act as nucleation sites for variolites in glassy mesostasis, where large oxidized patches were frequently observed.

Vesicles are frequent (up to 5%) in the upper pieces, becoming rare or absent downward in the unit. They are spherical or ovoid or have arcuate outlines, but many are highly irregular; they may be partly filled with deuteric or secondary minerals such as calcite, chalcedony(?), chlorite, and zeolite. Zeolite-filling (natrolite?) is often in radiate acicular arrangement. Sometimes vesicles are surrounded by a 0.05-mm rim of brownish smectite and minor green chlorite.

Basalt fragments of the upper brecciated portion of the unit and massive rocks of the middle-lower portion are greenish dark gray to reddish dark gray in color, while the matrix is white to light green.

Alteration

Alteration in basement rocks of Hole 808C ranges from slight to high (generally 10%–30%, locally up to 50%) and it is

Table 11. Remanence measurements on discrete samples.

Sample	Depth (mbsf)	Field (mT)	Declination (relative to core liner)	Inclination (relative to core liner)	Intensity mA/m	Inferred cryomagnetic polarity	Susc. (10^{-6} SI)
131-808C-							
7R-1, 44–46	356.6	NRM	252	23	85		1340
		5	252	27	74	N	
10R-1, 14–16	385.3	NRM	150	15	8.4		282
		10	144	4	7.6	N	
14R-3, 59–61	427.6	NRM	222	37	24		172
		10	230	38	22	N	
17R-1, 112–114	453.8	NRM	094	49	8.7		319
		5	096	41	7.5	N	
19R-1, 131–133	473.3	NRM	214	50	21		348
		0	213	50	21	N	
21R-1, 48–50	491.8	NRM	167	42	9.8		529
		5	165	40	10.5	N	
22R-5, 42–44	507.4	NRM	336	63	14		661
		10	333	42	6.9	N	
25R-1, 44–46	530.4	NRM	135	3	54		277
		10	131	3	48	N	
27R-1, 27–29	549.6	NRM	020	39	8.0		252
		5	022	38	8.0	N	
29R-3, 109–111	572.2	NRM	107	23	22		997
		5	110	27	20	N	
32R-1, 75–77	598.1	NRM	035	50	28		901
		10	025	39	17	N	
33R-1, 124–126	608.1	NRM	135	49	14		417
		10	138	45	11		
35R-1, 66–68	626.9	NRM	031	42	4.6		346
		15	046	43	2.9	N	
37R-2, 14–16	647.1	NRM	341	50	21		669
		5	000	51	14	N	
38R-3, 121–123	659.1	NRM	116	71	3.5		335
		10	112	49	1.0	N	
39R-1, 61–63	665.1	NRM	305	−39	0.7		202
		10	141	−34	0.5	?	
40R-1, 53–55	674.7	NRM	145	66	0.8		207
		Too weak				R?	
42R-5, 11–13	699.6	NRM	107	43	0.4		219
		Too weak				?	
43R-5, 73–75	709.9	NRM	115	28	0.6		203
		Too weak				R	
46R-5, 85–87	738.6	NRM	139	68	<0.1		201
		30	025	−65	0.4	R	
47R-7, 67–69	750.0	NRM	237	−31	0.6		208
		10	242	−7	0.4	N	
48R-5, 56–58	757.7	NRM	330	74	1.6		198
		>15	?	R?	≈0.1	N?	
50R-3, 125–127	773.9	NRM	311	55	4.6		—
		10	315	50	2.7	N	
51R-2, 114–116	782.7	NRM	342	49	2.7		122
		10	341	41	1.8	N	
53R-1, 98–100	800.4	NRM	240	51	0.2		201
		20	333	−42	0.3	R?	
54R-5, 88–90	816.0	NRM	222	49	7.6		347
		5	221	46	4.1	N	
55R-5, 120–122	825.9	NRM	247	−18	0.4		377
		15	018	−20	0.5	R	
56R-3, 69–71	825.9	NRM	019	43	3.4		—
		15	024	27	2.1	N	
57R-1, 31–33	838.4	NRM	116	36	0.3		383
		20	344	−22	0.2	R	
59R-1, 109–111	858.2	NRM	285	54	3.1		377
		10	300	41	1.6	N	
62R-5, 34–36	892.4	NRM	188	81	8.7		466
		0	188	81	8.7	N	
64R-2, 67–69	907.7	NRM	172	69	2.4		442
		15	136	−22	0.8	R	
64R-4, 95–97	911.0	NRM	041	81	8.8		511
		5	318	78	6.4	N	
65R-1, 109–111	916.2	NRM	124	−82	0.6		—
		10	151	−68	0.7	R	
66R-2, 57–59	925.4	NRM	290	51	45		766
		15	301	44	27	N	
67R-1, 76-78	935.3	NRM	012	−21	4.6		571
		15	013	−33	4.7	R	
69R-1, 138–140	955.2	NRM	160	−20	13		1299
			No obvious stable direction			R	
70R-2, 50–52	965.4	NRM	171	52	65		1358
		10	170	40	33	N	

Table 11 (continued).

Sample	Depth (mbsf)	Field (mT)	Declination (relative to core liner)	Inclination (relative to core liner)	Intensity mA/m	Inferred cryomagnetic polarity	Susc. (10^{-6} SI)
71R-2, 73–75	975.3	NRM	191	−43	5.2		1412
		15	152	−49	14	R	
72R-2, 77–79	985.1	NRM	312	60	29		663
		5	310	41	15	R?	
73R-2, 47–49	994.1	NRM	302	44	10		516
		10	304	31	7.2	N	
74R-2, 16–18	1003.5	NRM	316	−21	15		952
		10	306	−33	24	R	
75R-1, 96–98	1012.3	NRM	039	35	35		806
		0	040	34	35	N	
76R-3, 124–126	1024.7	NRM	173	23	8.2		692
		10	150	−51	14	R	
77R-3, 97–99	1033.9	NRM	312	42	18		521
		20	323	38	7.4	N	
78R-2, 27–29	1040.9	NRM	058	53	42		775
		5	058	43	28	N	
79R-1, 82–84	1049.1	NRM	281	40	35		607
		20	291	41	13	N	
80R-1, 38–40	1058.2	NRM	209	47	24		485
		10	317	35	17	N	
81R-2, 41–43	1069.0	NRM	021	47	1.4		495
		10	041	39	0.7	N/R	
83R-1, 130–132	1087.1	NRM	104	70	6.3		433
		20	074	12	1.4	R	
84R-1, 65–67	1092.7	NRM	277	14	1.4		708
			No obvious stable direction			R?	
85R-1, 70–72	1099.0	NRM	216	62	5.2		428
		10	230	42	2.1	?	

due mainly to variable degrees of oxidation, clay development, chlorite, carbonate, and other secondary minerals in minor proportions. The main variation in degree of alteration is related to the presence and amount of veins and fractures, which are loci of entry of fluids and therefore oxidation and alteration processes. On both sides of veins and fractures, especially of the thickest ones, yellowish and reddish brown haloes are commonly observed, characterized by development of smectite and Fe-oxide and hydroxide phases. It is to be pointed out that generally oxidation processes are more intense at the top of the subunits and main units and decrease slightly towards their interior. This is consistent with oxidation due to downward percolation of oxygenated seawater, probably soon after complete consolidation of the rocks.

The main alteration features include the following:

1. Abundant brownish to greenish smectitic clays replacing glassy mesostasis;
2. Opaque clay minerals and minor calcite replacing plagioclase;
3. Pale to dark green chlorite invariably present and replacing clinopyroxene, olivine, and glass;
4. Serpentine (and/or chlorite), iddingsite, and Fe-oxide pseudomorphing olivine;
5. Calcite sometimes replacing mafic phases and, to a lesser extent, plagioclase;
6. Red hematite replacing magnetite; and
7. Actinolite (and minor epidote) replacing clinopyroxene.

The most obvious sign of alteration in these rocks is the almost constant presence of smectite after glassy mesostasis and glassy quench margins. Clinopyroxene may be both fresh and totally pseudomorphed, whereas olivine is invariably totally pseudomorphed. Plagioclase alteration is extremely variable and in several pieces (e.g., Section 131-808C-108R-1). Despite complete alteration of olivine and clinopyroxene, plagioclase phenocrysts and skeletal laths with delicate swallow-tailed shape are surprisingly well preserved.

The development of the bulk of these secondary minerals probably occurred during a low-grade submarine alteration event in the zeolite facies. Calcite most probably was formed together with the other secondary minerals during such an alteration stage, but its presence as filling of several generations of veins suggests that calcite was introduced into these rocks in several stages.

Development of secondary actinolite (and epidote) in some rocks implies a slightly higher grade of alteration, referable to the lower part of the greenschist facies.

Veins and Fractures

All the recovered basaltic rocks are cut to different degrees (0%– 10%) by small, ramifying, and often cross-cutting veins and fractures of widely varying width (0.2–5 mm). The highest concentration of veins was recorded in Subunits 1D and 1E (Section 131-808C-106R-1) and 1G (Section 131-808C-107R-1). As far as Unit 2 (Section 131-808C-108R-1) is concerned the great amount of veins (up to 20%) is related to the brecciated texture of upper part pillow: they are filled with the same material (variolitic glass and calcite) that heals together the basaltic rock fragments.

The majority of veins are oblique (from 40° to 70° dip) or subhorizontal, but the subvertical ones are not uncommon. In general, they have irregular shapes and especially the thinnest ones may be braided and branching. The very common cross-cutting suggest several stages of vein formation. Yellowish to reddish brown oxidation haloes up to 6 mm wide were commonly observed on both sides of the veins.

Veins are infilled with calcite, chlorite, smectite, Fe-oxide, actinolite(?), zeolite, and pyrite in decreasing order of abundance. The widest veins are very often filled with two secondary mineral phases: calcite and chlorite or, more rarely, fibrous actinolite. In such cases calcite is the later mineral and occupies the central part of the veins. Such a multiple or zoned deposit suggests a number of stages of fracturing and infilling. Medium- sized veins are mainly filled with fibrous

Table 12. Depths at which reversal events listed by Berggren et al. (1985) have been identified in Hole 808C. The depth error quoted is the distance by which the depth could *increase*, as estimated from the record of core recovery.

Chron	Age of normal interval (Ma) Top	Base	Depth (mbsf)	Depth error (m)
BRUNHES	0.00		0	
MATUYAMA		0.73	657	<1
Jaramillo	0.91		677	13
		0.98	698	1
Olduvai	1.66			
		1.88	797	3
	2.02			
		2.04		
	2.12			
		2.14		
GAUSS	2.47		804	1
		2.92	822	2
	2.99		826	4
		3.08	834	3
	3.18		843	2
GILBERT		3.40	864	5
	3.88		892	2
		3.97		
	4.10			
		4.24		
	4.40			
		4.47		
	4.57			
		4.77	930	3
5	5.35		962	5
		5.53	968	3
	5.68		978	4
6		5.89		
	6.37			
		6.50	997	1
7	6.70		1004	13
		6.78		
	6.85			
		7.28		
	7.35			
8		7.41	1024	1
9	7.90		1028	3
10		8.21	1031	1
	8.41			
		8.50		
	8.71			
		8.80		
C5	8.92		1046	1
		10.42	1069	7

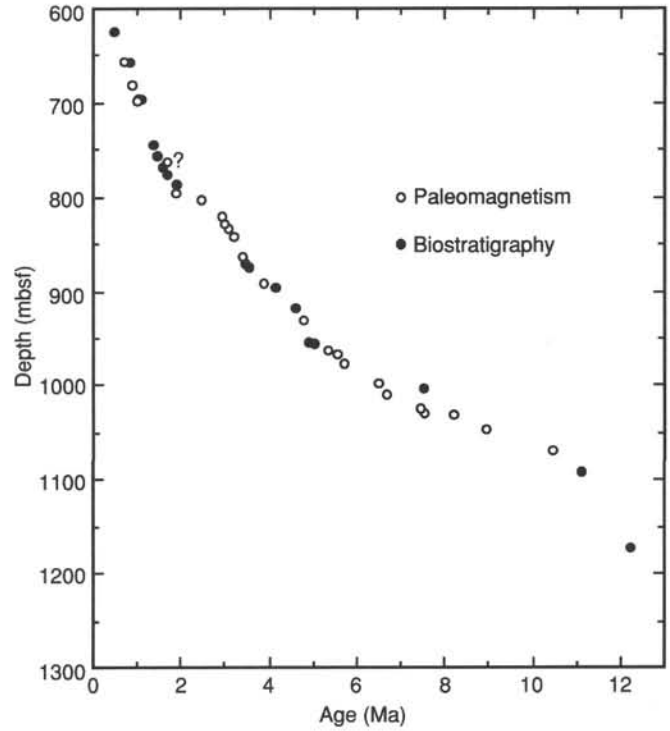

Figure 76. Inferred age of sediment is plotted against depth, to demonstrate the nannofossil control used in establishing the magnetostratigraphy.

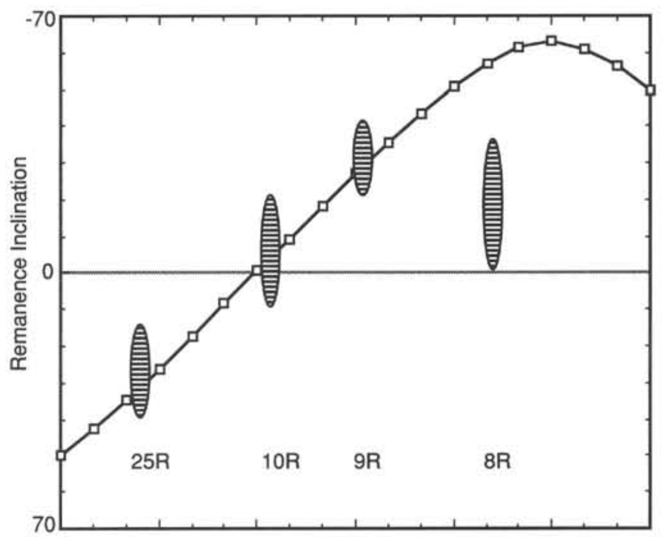

Figure 77. Predicted remanence inclination is plotted against bedding dip. In the model a remanence, of initial declination 0° and inclination 50°, is fixed in the bedding, which is rotated about a northeast-southwest axis to give southeast dips.

calcite. Pyrite is a minor phase that sometimes lines the walls of veins or fractures filled with smectite, calcite, or other materials. The thinnest veins are predominantly filled with microcrystalline calcite (Fig. 110) or, more rarely, with zeolite.

Geochemistry

Major and trace elements of representative samples of Units 1 and 2 were carried out by XRF spectroscopy (Basement Lithology and Geochemistry, in Explanatory Notes chapter, this volume). Data are reported in Table 21 together with loss on ignition (LOI), mg numbers, CIPW norms, and some significant incompatible element ratios. All samples have suffered variable, but generally rather low, degrees ofalteration due to rock/sea water interaction. Nevertheless, alteration could have significantly affected the abundance of at least some elements, and therefore interpretation of their magmatic affinities should be made with care. The misleading effects of vein filling by secondary minerals have been minimized by manually cutting off the veins (Explanatory Notes chapter, this volume).

LOI varies from 1.0 to 2.0 in the least-altered and most crystalline samples, and has values up to 3.7 in the most altered ones (pillow lavas of Unit 2: 131-808C-108R-1, 63–66 cm and 131-808C-108R-1, 118–121 cm; lavas of Subunit 1F:

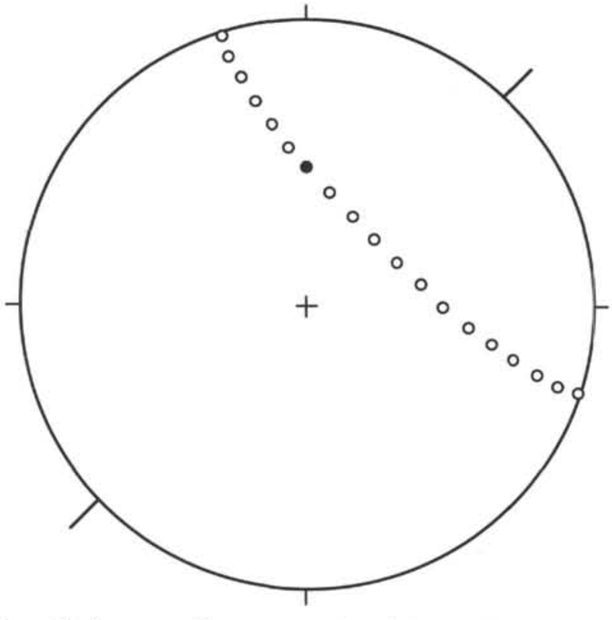

Figure 78. Stereographic representation of the model of Figure 77. The initial remanence direction (solid circle) traces a small circle about the rotation axis. This is an equal-area projection.

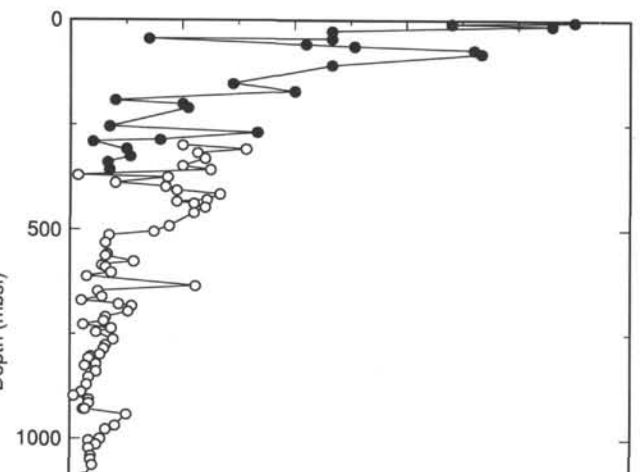

Figure 79. Interstitial water yield per unit length of whole-core sample for Holes 808A and 808B (solid circles) and Hole 808C (open circles).

131-808C-106R-2, 17–22 cm, and 131-808C-106R-2, 60–64 cm).

Comparison between the least-altered and most highly altered samples suggests that secondary chemical changes also involved alkalies (particularly K and Rb) and, to a lesser extent, alkaline-earth elements. In particular, Samples 131-808C-108R-1, 63–66 cm, -108R-1, 118–121 cm, and -107R-1, 104–128 cm, show anomalously high K_2O and Rb contents (and, accordingly, the K/Nb ratio) with respect to the others. MgO removal due to halmyrolysis may also be suspected for Samples 131-808C-108R-1, 63–66 cm, and -108R-1, 118–121 cm, as suggested by their relatively high Ni/MgO ratios (Fig. 111). The high CaO content of samples of Unit 2 appears to be dependent on the amount of calcite replacing primary phases and filling veins and vesicles. Therefore pillow lavas from Unit 2 appear to have suffered the most intense secondary chemical mobilization, which is also reflected in the appearance of as much as 3.7% of nepheline in their norms.

To assess the magmatic affinities of the different units we preferably rely on elements such as Cr, Nb, Y, Zr, Ti, and Rb, which are considered virtually immobile or very slightly mobile during seafloor weathering and low- grade metamorphism (Hart et al., 1974; Bienvenu et al., 1990). In terms of the Ti vs Zr diagram (Fig. 112), the analyzed samples plot in the MORB field. An analogous indication is given by the Ce/Nb vs. K/Nb plot, where only the most altered samples fall outside the MORB field (Fig. 113). This fact indicates that K_2O contents of most samples are close to those of the original magmas, inspite of the high chemical mobility of this element.

The MORB normalized patterns shown in Figure 114 provide us with a comprehensive view of incompatible element distribution. Most elements define a flat pattern between one and three, further supporting the affinity of the studied rocks with MORB. The most highly scattered values are observed for K and Rb, clearly related to the presence of altered samples. Moreover, chondrite-normalized La/Y and Ce/Y ratios suggest a close affinity with normal MORB type (Table 21). Analogous indication is given by the Zr/Y vs Zr/Nb plot of Figure 115. Provided that some rocks show variable degrees of alteration, which also involved some changes in MgO contents, most of the basaltic rocks of Hole 808C appear fairly evolved (mg values of 66–56). The highest mg values (71–68) coupled with high contents of Cr (270–222 ppm) and Ni (126–107 ppm) correspond to Samples 131-808C-106R-1, 90–93 cm, -106R-2, 17–22 cm, and -106R-2, 60–64 cm, whose composition is compatible with nearly primary basaltic magmas.

Comparison with Previous Drilling

Previous DSDP legs in the Nankai Trough region drilled three sites in the trough and on the slope (Sites 298, 582, and 583), never reaching the basement. The Shikoku Basin basement was reached during Leg 58 (Sites 442, 443, and 444; Nisterenko, 1980; Marsh et al., 1980).

Site 442 is the only site from which pillow basalts typical of oceanic Layer 2 were recovered. Two lithologic units have been recognized: Unit 1, comprising mainly massive flows or sills and Unit 2, the underlying pillow lava sequence. High vesicularity, intensive oxidation, and abundance of calcite, filling veins and vesicles characterize these rocks.

Basaltic rocks recovered at Site 443 are represented by massive flows or sills, generally fine to medium grained, aphyric to plagioclase (An 70) phyric and characterized by relatively low vesicularity. Site 444 penetrated a sill 12 m thick, aphyric to plagioclase phyric, medium grained with intersertal to intergranular texture underlain by (mineralogically and texturally similar) basalts.

Petrographically, basalts recovered at Site 808 do not appear significantly different from the other basaltic rocks recovered from the Shikoku Basin basement. The main difference is a generally lower degree of vesicularity, which may be related to different local water contents in the magma. Common petrographic features are the scarcity of phenocrysts, the composition of plagioclase (high anorthite content), the presence of magnetite, and the high degree of oxidation. Site 442

Table 13. Interstitial water data, Hole 808A.

Sample	Depth (mbsf)	pH	Alkalinity (mM)	S	Cl (mM)	SO_4 (mM)	NH_4 (mM)	HPO_4 (μM)	Li (μM)	K (mM)	Ca (mM)	Mg (mM)	Mg/Ca (mM)	H_4SiO_4 (μM)	Na (mM)	Na/Cl	Sr (μM)
131-808A-																	
1H-3, 0–10	3		24.06	34	560	10.63	1	70	18	12.4	6.91	47.62	6.89	453	484	0.86	77
1H-4, 140–150	6	8.18	39.92	34.2	567	0.54	2	197	8	12.2	3.58	41.7	11.65	517	504	0.89	64
2H-3, 0–10	9.3	8.08	47.72	35	561	0.19	4.8	462	5	12	2.41	36.48	15.14	506	516	0.92	
2H-5, 140–150	13.8	7.94	48.11	36	567	0	5.6	465	6	11.2	2.42	35.65	14.73	550	523	0.92	
3H-3, 0–10	18.8	8.01	46.55	34.8	575	0	6	315	7	10.7	2.2	33.01	15.00	534	536	0.93	59
3H-5, 140–150	23.3	7.94	45.95	35	572	0	6.3	290	6		1.98	32.25	16.29	541	533	0.93	
4H-1, 135–150	26.8	7.93	44.96	35.6	575	0.2	6.9	270	6	12	1.53	32.94	21.53	547	534	0.93	73
5H-6, 120–135	43.6	7.91	48.74	35.4	576	0.44	7.5	360	9	11.8	2.64	36.58	13.86	532	529	0.92	95
6H-1, 0–10	44.3	8.1	52.77		577	0.45	8	245		12.2	3.3	37.89	11.48		529	0.92	
7H-4, 135–150	59.7	7.95	55.14	36.2	572	0	8.2	157	9	11.4	5	37.91	7.58	585	523	0.91	110
8H-1, 135–150	64.7	7.9	54.67	35.5	569	0.26	8.3	190	9	11	5.44	37.55	6.90	508	520	0.91	112
9H-3, 140–150	72.8	7.94	53.88		568	0.14	8.8	157	10	11.3	6.19	38.45	6.21	602	514	0.90	110
10H-3, 0–15	80.8	7.88	51.72	35.5	569	0	9.4	100	11	11.2	6.05	36.77	6.08	547	515	0.91	105
13H-2, 122–137	109	7.91	40.63		565	0.13	10.6	52	14	10.4	5.39	30.64	5.68	552	514	0.91	82
Bottom H_2O	0		2.45		555	28.9	0	3	27	10.4	10.55	54	5.12	150	476	0.83	85

Table 14. Interstitial water data, Hole 808B.

Sample	Depth (mbsf)	pH	Alkalinity (mM)	S (mM)	Cl (mM)	SO_4 (mM)	NH_4 (mM)	HPO_4 (μM)	Li (μM)	K (mM)	Ca (mM)	Mg (mM)	Mg/ Ca	H_4SiO_4 (μM)	Na (mM)	Na/ Cl	Sr (μM)
131-808B-																	
5X-1, 88–103	151	7.87	24.97	35	576	0	12.6		14	8.5	4.75	26.69	5.62	628	518	0.92	82
7X-1, 130–145	170	8.05	23.49	34.5	579	0.84	11.2		20	7.6	5.86	22.44	3.83	635	530	0.90	103
9X-2, 135–150	191.2			34	582	0.95	10.6		53	8.2	7.23	17.99	2.27	882	535	0.89	
10X-4, 130–150	203	7.91	17.62	34.5	573	0.81	9.7		50	8	7.33	16.99	2.32	785	527	0.92	109
11X-2, 125–145	209.7	7.71	17.6	34	579	0.83	9.6		44	7.6	7.7	17.4	2.26	866	532	0.91	118
13X-1, 125–145	227	7.71	16.15	34	583	0.73	9		27	6.6	7.64	17.09	2.24	823	536	0.87	125
16X-1, 126–136	255				580	0.32	7.8			7.8	8.34	15	1.80		534	0.91	
17X-2, 130–145	266.5	7.73	13.98	33.5	572	1.14	8.1		56	6.8	7.72	19.35	2.51	730	520	0.88	119
19X-1, 135–150	284	7.77	16.75	33.6	580	0.42	8.4		62	7.6	9.17	17.03	1.80	873	530	0.90	103
20X-1, 140–150	289				577	1.44	8.1			6.3	9.55	17.23	1.80		527	0.91	
22X-1, 140–150	308.5	7.87	16.15		581	0.82	8.6		66	8	10.04	17.61	1.75	825	528	0.91	
23X-CC	317				574	0.45	7.7			7.4	11.61	15.41	1.33	1155	522	0.91	
24X-2, 70–85	328	8.04	14.52	34.5	578	3.33	8.4		71	7.1	11.38	17.69	1.55	790	526	0.91	
25X-3, 135–150	340.5			36	578	1.38	7.2			9	14.35	13.82	0.96	1150	523	0.91	
27X-CC	355			36.2	581	2.12	9.7		85	7.6	9.39	20.25	2.16		522	0.90	

seems to be the most similar to Site 808 with respect to both lithostratigraphic sequence and mineralogical assemblages.

In terms of geochemical characteristics, basalts from Hole 808C compare favorably with those of the Shikoku Basin basement (Sites 442 and 443), analogously identified as Normal MORB. In particular, Nankai Trough basement rocks show a closest chemical resemblance to those from Site 443.

Summary and Conclusion

1. The basaltic rocks at Hole 808C were divided in two main units. Critical contacts confirming the mode of their emplacements were not recovered, yet available data suggest that Unit 1 consists of sill-like rocks, and Unit 2 represents a pillow lava unit.

2. Both lithologic units are morphologically and petrographically similar to typical oceanic crust basalts: they were emplaced as sills and pillow lavas with textures typical of basalts erupted in a marine environment.

3. Both units are aphyric to plagioclase phyric and contain predominant plagioclase and clinopyroxene, and varying proportions of olivine; magnetite occurs mainly in the first unit.

4. Alteration is generally slight to moderate and dominated by smectitic clays, chlorite, serpentine, calcite, minor zeolite, and, locally, actinolite. The secondary assemblages are typical of the early stages of a low-grade submarine alteration event in the zeolite facies; local development of actinolite would imply a slightly higher grade of alteration referable to the lower part of greenschist facies. Calcite was most probably introduced into these rocks in several stages. A later extensive oxidative phase, related to downwards percolation of oxygenated seawater, results in haloes and patches with development of Fe-oxide and hydroxide phases.

5. All the recovered basaltic rocks are cut to different degrees (0%–10%) by ramifying and often cross-cutting veins of varying widths. Veins are infilled with calcite, chlorite, smectite, Fe-oxide, actinolite, zeolite, and pyrite.

6. Geochemical features consistently indicate a Normal MORB affinity for all the Nankai Trough basaltic rocks. They do not reveal any evidence of subduction-related chemical components. In terms of degree of differentiation, they vary from nearly primitive to fairly evolved basaltic magmas.

7. Based on stratigraphy, petrographic, and geochemical features as well as the analogy with Shikoku Basin basement rocks drilled during DSDP Leg 58, Site 808 basaltic rocks can be considered to represent the Nankai Trough basement.

PHYSICAL PROPERTIES

Introduction

The objectives of the physical property measurement program at Site 808 (proposed site NKT-2) were: (1) to measure the properties of the accreted sediment for a direct comparison to the pre-accreted equivalent section at proposed drill site NKT-1; (2) to estimate the state of consolidation and the strength of the sediment as an initial evaluation of the tectonic component of compaction; (3) to physically characterize lithologic units for correlation among holes and downhole logs at Site 808; and (4) to measure thermal conductivity for use in heat-flow analyses. The first objective was not realized, as the planned reference site was not drilled during Leg 131.

Sediments recovered at Site 808 comprise fine-grained terrigenous mud and mudstone, coarse-grained turbidites, and hemipelagic mud, mudstone, and ash. Due to low core recovery and the generally poor quality of the samples, a limited data set was collected from 10 to 350 mbsf (Fig. 116). In the upper 61 mbsf, samples of fine-grained sediment were severely disturbed by gas expansion. This disturbance inhibited reliable measurements of shear strength, resistivity, and acoustic velocity, although a limited data set of these parameters was collected in the upper 61 m. The samples disturbed by methane gas expansion were only useful for index property and magnetic susceptibility measurements. In other sections within the upper 112 m, the sediment intervals consisted of coarse-grained turbidites which, when recovered, were severely disturbed. Some of these sand intervals were fluidized and were observed to be mixed in the core liner on deck. Consequently, only grain density could be determined for these intervals.

Between 142 and 235 mbsf, gas expansion disturbance was not visible and fewer intervals of sand were recovered. This section was sampled with the extended core barrel (XCB), which generally produced cores of small biscuits within a soft drill slurry. Selected biscuits in this interval were analyzed for index properties. Below 260 mbsf, the recovered sediment was predominantly mudstone of good quality in the form of large biscuits and whole-core pieces. These samples were analyzed for acoustic velocity, resistivity, thermal conductivity, and index properties.

All cores were run through the multisensor track (MST) for magnetic susceptibility in which data were collected at 3-cm intervals. When sample quality was good (i.e., the core liner was completely filled and biscuiting was minor), GRAPE and *P*-wave sensors were enabled. Thermal conductivity was measured on all but the most disturbed sections. Index properties determined for Site 808 sediments include bulk density, porosity, water content (expressed as a percentage of dry sample weight), and grain density (Explanatory Notes, chapter, this volume).

Laboratory-measured physical properties and logging data could only be correlated on a gross scale because few data were collected in the upper sediment section (Holes 808A and 808B). Good correlation between these data sets requires a large number of laboratory measurements of physical properties at close intervals, a criterion satisfied primarily in Hole 808C at depths greater than 300 mbsf. Logging results from the latter depths, however, are limited mostly to through-the-pipe logs.

As the most disturbed intervals were coarse sand, the evaluation of sediment consolidation, based on index property data for this site is biased toward the finer-fraction sediment intervals. The sandy intervals were only partially recovered and probably represent a significant portion of the upper 300 m of Site 808, as deduced from logging results.

Index Properties

Low core recovery and poor sample quality resulting from gas expansion in the upper 350 m of Holes 808A and 808B, did not diminish the quality of index physical properties data, although their distribution downhole is sparse and scattered. The number and quality of samples increased significantly below 350 mbsf. Seven major physical properties units were defined for Site 808, based on significant downhole changes in index property values or gradients (Table 22 in backpocket microfiche, Fig. 116). The upper and lower boundaries of most of the units are associated with lithologic or structural features, although these features did not serve as definition criteria for physical properties units.

Unit 1 (0–215 mbsf)

Mass index properties of sediments in the uppermost 215 mbsf show substantial variations (Fig. 116), in which porosity ranges from 73.8% to 33.8%, bulk density ranges from 1.51 to 2.3 g/cm^3, and water content ranges from 93% to 15% dry weight. These fluctuations are largely attributed to lithologic variations within this primarily turbiditic interval, and to sample disturbance. Index property data show two distinct clusters in this upper interval; the smaller porosity and larger density values correspond to sandy turbidite horizons, whereas the larger porosity and smaller density values represent fine-grained end members of the turbidite sequence. This pattern is best seen in Hole 808A data (Fig. 116, 0–112 mbsf). Because sandy intervals in the turbiditic sections of Hole 808A and 808B were often fluidized and completely disturbed, data from these intervals are unlikely to represent *in-situ* values. Grain densities, however, are unaffected by sampling disturbance. The average grain density for the sediments in Unit 1 is 2.71 g/cm^3, reflecting their quartz-rich composition. Grain-density decreases markedly below Unit 1.

Sample lithologies, defined from visual core descriptions from Unit 1 were keyed into the physical properties database so that downhole trends for compaction analysis based on sand-, silt-, and clay-dominated lithologies could be evaluated. However, because most of the sand intervals were highly disturbed and consequently not measured, most downhole trends in Unit 1 are biased toward fine-grained sediment behavior. Index property data for fine-grained material delineate, with only little scatter, a clear downhole trend that is in good agreement with general compaction equations for terrigenous material (Hamilton, 1976) and data from DSDP Site 583 (Bray and Karig, 1986). Porosity decreases exponentially from the surface down to about 190 mbsf (Table 23). At 215 mbsf, porosity is offset to a smaller value. This offset coincides with changes in organic and inorganic geochemical parameters and marks a transition from sandier to siltier trench wedge sediments with a greater hemipelagic component.

Unit 2 (215–395 mbsf)

The top of physical property Unit 2 (215 mbsf) reflects the finer grained composition of sediments corresponding to lithologic Subunit IIb, while the base of this unit (400 mbsf) corresponds to the base of a deformation zone associated with a major thrust fault at the site (see Fig. 5). The turbiditic origin of these sediments can also be seen in index property variations, where compositional changes with depth give rise to

Table 15. Interstitial water data, Hole 808C.

Sample	Depth (mbsf)	pH	Alka-linity (mM)	S (mM)	Cl (mM)	SO_4 (mM)	NH_4 (mM)	HPO_4 (μM)	Li (μM)	K (mM)	Ca (mM)	Mg (mM)	Mg/Ca	H_4SiO_4 (μM)	Na (mM)	Na/Cl	Sr (μM)
131-808C-																	
1R-1, 133–150	299.9	7.68	16.04	33.8	571	1.29	7.6		57	7.03	9.51	17.71		875	528	0.92	124
2R-1, 66–73	308.7			34	572	0.68	7.2		57	6.55	9.63	16.77		749	523	0.91	119
3R-1, 109–117	318.7			33.9	574	2.55	6.3		70	7.61	10.76	17.91		918	523	0.91	119
4R-1, 130–145	328.6		13.48	34.2	580	2.43	6.6		72	7.26	11.15	14.92		823	533	0.92	120
5R-CC	346.6	7.95	15.16	38.2	577	2.42	5.7		68	7.24	11.8	13.78		869	524	0.91	121
6R-1, 135–150	348.1				585	2.1	6.1		72	7.43	11.01	10.96		563	548	0.94	121
6R-3, 103–118	350.7	8.06	15.08	34.5		1.6	5.7			6.91	12.22	10.24		732			130
7R-1, 55–59	356.8			34.8	584	2.63	5.3		94	8.84	11.93	15.73		728	536	0.92	136
8R-2, 126–141	368.7				581		6.8			10.4	18.7				530	0.91	
9R-1, 120–127	376.8				578	4.93	6		50	8.43	10.17	23.28		810	523	0.90	113
10R-2, 130–150	388.1				580	2.74	8.1		58	7.32	9.75	19.35		765	529	0.91	128
11R-2, 50–63	396.8	7.9	16.29		581	1.84	8.6		64	7.24	9.74	18.13		773	531	0.91	107
12R-1, 130–150	406	7.77	16.42	34.2	579	3.63	6.8		68	7.43	10.48	20.92		886	527	0.91	115
13R-2, 135–150	417.2	7.73	16.88	34.8	580	2.54	7.3		86	6.91	11.51	17.76		877	530	0.91	113
14R-3, 131–150	428.4	7.81	16.63	35	588	1.86	7.6		115	7.21	11.49	15.4		968	541	0.92	119
15R-1, 130–150	435.1	7.7	15.81	34.2	581	1.9	7.4		109	6.94	11.71	16		925	532	0.92	116
15R-4, 115–150	439.5			34.8		2.31	7.1		101	6.94	11.91	13.65		780			
16R-2, 130–150	445.9	7.69	14.85	34.4	586	1	7.2		110	6.71	12.12	13.29		875	539	0.92	
17R-4, 130–150	458.6	7.74	11.72	34.2	585	0.78	5.8		100	5.71	12.25	14.72		515	534	0.91	123
18R-3, 130–150	466.8	7.72	13.14	34.2	586	0.96	6.8		115	6.91	12.33	12.36		986	545	0.93	118
19R-2, 127–150	474.8			34.5	591	1.74	6.8		122	6.56	12.51	11.5		990	547	0.93	126
20R-4, 132–150	487.6				583	1.71	5.7		117	6.65	14.2	11.38		769	538	0.92	118
21R-1, 120–144	492.6	7.85	13.27	34.5	585	0.74	5.8		131	5.33	14.81	9.78		405	540	0.92	123
22R-3, 130–150	505.4			34.5	587	0.44	5.4		177	6.11	14.42	7.8		1042	545	0.93	129
22R-3, 130–150	505.4					0.15											
23R-1, 130–150	512.1				592	0.13	4.4		201	5.42	14.9	8.22		934	546	0.92	131
24R-4, 0–20	524.9			33.8	582	0.95	4.8		247	5.69	16.34	9.16		1031	533	0.92	135
25R-2, 0–19	531.6			34	591	0.43	4.4		282	5.52	15.6	7.68		992	544	0.92	145
26R-3, 130–150	544.1			34		0.03	3.5		248	4.37	17.48	6.7		912			140
27R-5, 123–150	556.7				588	0.12	2.7		170	2.89	20.16	4.9		535	533	0.91	
28R-2, 124–150	561.7			34.2	592	0.76	2.7		167	2.87	19.23	6.68		125	544	0.92	129
28R-4, 110–150	564.7				589	2.01	2.6			2.77	20.26	8.27		242	545	0.93	120
29R-6, 125–150	577.5	7.97	4.87	34	588	0.91	2.3		230	2.7	20.86	6.85		220	535	0.91	121
30R-3, 125–150	582.6			34.3	588	0.63	2.2		223	2.99	20.34	6.39		766	534	0.91	137
31R-2, 0–22	589.2				588	0.37	2.3		202	2.31	19.42	6.16		123	539	0.92	162
32R-3, 125–150	601.6	7.68	5.39	33.8	574	1.08	1.8		260	3.05	19.39	6.76		843	526	0.92	145
33R-4, 0–26	611.6				577	0.3	2		276	2.26	19.22	4.88		272	532	0.92	171
33R-4, 0–26	611.6					0.47	1.7			2.36	21.22	3.7					
34R-2, 125–150	619.4	7.86	5.61		579	0.55	1.6		329	2.5	20.95	5.2		145	530	0.92	156
35R-4, 132–150	632.1	7.76	5.02		571	0.47	1.6		379	2.36	22.05	5		255	520	0.91	116
36R-2, 125–150	638.7			33	568	0.12	1.6		357	2.36	20.37	3.9		118	522	0.92	138
37R-2, 0–10	647.1					0.77	1.6		335	1.84	21.13	4.71		68			
38R-4, 125–150	660.7			32.3	557	1.4	1.5		330	1.74	20.1	4.17		70	514	0.92	155
39R-3, 130–150	668.9				559		1.6		363	20.17	4.02				516	0.92	
40R-2, 125–150	677			33	561	1.73	1.6		344	1.39	20.78	5.62		81	519	0.93	156
41R-1, 123–150	685.1	8.2	6.09	32.5	568	1.5	1.6		358	1.48	20.54	4.71		68	524	0.92	168
42R-3, 125–150	697.8				557	0.67	1.6		422	0.86	20.83	4.09		543	515	0.92	183
42R-5, 108–150	700.8																
43R-5, 0–25	709.3				550	1.24	1.4		387	1	21.34	4.24		184	509	0.93	184
44R-4, 123–150	718.4				542	0.81	1.4		454	1.56	21.42	3.83		160	509	0.94	168
45R-4, 125–150	728				537	1.16	1.2		515	1.77	21.98	3.02		145	501	0.93	
46R-2, 125–145	734.4				539	1.47	1.3		581	1.36	20.88	3.47		220	502	0.93	137
47R-3, 125–150	745.9				540		1.2		616	1.53	22.35	2.41		420	506	0.94	114
48R-3, 125–150	755.6				530	1.41	1.1		605		22.53	3.79		237	494	0.93	120
49R-2, 125–150	763.7	8.03	15.84	31	530	1.7	1.1		582	1.4	22.67	3.24		388	495	0.93	126
50R-5, 125–150	777.8				512	0.76	1.3		568	0.99	21.98	2.62		229	479	0.94	120
51R-4, 120–150	786.1	8.34	16.08		516	0.84	1.4		538	1.21	21.49	1.96		214	485	0.94	113
52R-5, 120–150	797			31.7	514	0.93	1.1		476	1.14	21.3	1.5		209	485	0.94	102
53R-4, 120–150	805				512	0.96	1.3		433	1.04	20.1	2.54		190	483	0.94	116
54R-2, 120–150	812				505	1.32	1.5		381	1.27	21.2	1.75		282	476	0.94	145
55R-2, 120–150	822				514	0.96	1.1		307	1.06	20.55	2.44		121	485	0.94	202
56R-4, 120–150	831.3				510	3.52	1		304	2.11	21.53	6.34		102	475	0.93	220
57R-2, 120–150	841				483	1.45	1		363	0.91	21.49	3.76		184	450	0.93	216
58R-3, 115–150	851.8				476	1.34	1		410	0.76	22.34	3.57		136	442	0.93	237
59R-2, 115–150	860				476	1.25	1		421	0.78	22.14	2.47		188	444	0.93	246

Table 15 (continued).

Sample	Depth (mbsf)	pH	Alkalinity (mM)	S (mM)	Cl (mM)	SO_4 (mM)	NH_4 (mM)	HPO_4 (μM)	Li (μM)	K (mM)	Ca (mM)	Mg (mM)	Mg/ Ca	H_4SiO_4 (μM)	Na (mM)	Na/ Cl	Sr (μM)
60R-4, 116–150	872.5				475	2.84	0.8		429	0.82	23.53	3.86		141	441	0.93	262
61R-2, 115–150	878.8				474	3.58	0.9		420	0.92	23.54	4.5		182	440	0.93	258
62R-3, 5–40	889.3				466	3.72	0.8		439	0.77	23.78	3.77		194	433	0.93	266
63R-1, 56–90	896.2				481												
64R-1, 115–150	906.9				481	5.82	0.7		432	1.81	25.16	3.12		154	450	0.94	282
65R-2, 0–34	916.8				485	5.15	0.7		443	1.03	26.15	2.6		96	452	0.93	
66R-2, 115–150	927.6				468	5.01	0.6		449	1.09	24.77	2.78		148	438	0.94	284
66R-2, 11-5-150	927.6																
68R-1, 5–10	944				476	7.57	0.6		457	0.94	26	4.99		178	445	0.93	298
70R-4, 0–35	968	7.66	21.45	29	476	4.61	0.5		573	0.9	24.88	3.81		305	443	0.93	302
71R-2, 120–150	976			28	471	4.75	0.5		575	0.94	23.79	3.43		389	441	0.94	277
71R-3, 105–150	977.4					4.3				1.06	24.99	2.56		359	316		
72R-3, 0–35	986			28	465	4.67	0.4		585	0.83	25	4.19		357	431	0.93	298
73R-5R115-150	999.5			28.2	454	4.67	0.4		634	1.44	25.45	3.08		406	421	0.93	264
74R-2, 72–114	1004.5			31	456	4.18	0.3		571	1.7	25.88	3.48		355	420	0.92	247
75R-1, 117–145	1012.6	7.69	21.23		456	5.71	0.4		669	1.08	26.46	4.52		317	420	0.92	300
76R-2, 115–150	1023.1			28.5	463	4.98	0.4		718	1.26	27.79	2.87		296	426	0.92	300
77R-4, 0–35	1034.6			28.2	465	5.28	0.3		758	2.07	27.18	2.99		340	429	0.92	302
78R-2, 115–150	1042				453	5.1	0.2		753	0.91	27.03	3.14		344	418	0.92	268
79R-2, 0–35	1051				453	6.16			769	0.85	28.12	3.2		321	418	0.92	271
80R-2, 125–150	1061				457	6.48			750	0.82	28.27	3.47		298	422	0.92	287
82R-2, 0–25	1078	7.95	16.74		453	8.42			692	1.8	28.21	2.12		237	424	0.94	285
84R-1, 120–150	1093.3				466	9.06			616	1.81	28.97	7.52		273	426	0.91	283
85R-2, 120–150	1101.1				458	7.26			717	1.22	29.32	4.7		292	420	0.92	296
86R-2, 115–150	1110.8				447	7.19			702	1.03	28.74	4.47		304	410	0.92	299
88R-1, 5–24	1127.2	7.85	15.98		477	8.71			686	1.16	31.01	7.04		290	433	0.91	297
90R-1, 0–29	1146.5				457	6.71			734	1.03	31.51	2.92		253	417	0.91	360
91R-1, 0–25	1156				451	6.71			727	0.96	32.02	1.59		206	413	0.92	356
93R-1, 0–15	1175.5				460	7.25			744	2.6	36.23	2.31		210	411	0.89	
94R-1, 0–35	1185				466	6.34			733	1	37.19	2.16		236	415	0.89	372
96R-1, 0–36,67–81	1205				484	6.97			799	1.87	47.58	2.43		194	412	0.85	396
99R-1, 0–30	1233.5				512	8.89			668	62.44	4.78			124	411	0.80	500

excursions from general downhole exponential trends. Some intervals within the unit comprise large percentages of silt to fine-sand, conglomerate, calcareous-rich layers, and ash-rich zones.

Bulk densities in this unit increase gradually from about 1.9 g/cm^3 to 2.1 g/cm^3. Porosity and water content correspondingly decrease throughout Unit 2 over intervals in which silty clays and clayey silts dominate the lithology and range from about 63%–22% and 46%–15%, respectively. The general downhole compaction trend within this unit closely approximates Unit 1 (Tables 22 and 23) and that defined for DSDP Site 583 index properties (Bray and Karig, 1986).

Unit 3 (395–812 mbsf)

The top of physical property Unit 3 is clearly defined (Fig. 116) by an increase in porosity and a decrease in bulk density. This relatively abrupt discontinuity represents a repetition of the sediment package overlying the frontal thrust fault at about 357–395 mbsf. The sediments of Unit 3 are less dense and more porous relative to their equivalents in Unit 2, suggesting an underconsolidated state. The data become less scattered where these sediments are richer in hemipelagic components, particularly below 570 mbsf. Unit 3 is characterized by a gradual decrease in pore volume, concomitant decreases in porosity and water content with depth, and an increase in bulk density. Grain density within this same unit, however, is fairly constant, averaging 2.64 g/cm^3.

In addition to overall changes with depth, smaller scale trends in index properties were used to define three subunits for Unit 3. Boundaries between subunits are located at 535 and 740 mbsf (Table 23).

Subunit 3a (395–535 mbsf)

This subunit is lithologically similar to the overlying Unit 2, composed of fine-grained (distal) turbidites. Downhole index property changes within Subunit 3a are largely controlled by the 145-m-thick stratigraphic repetition below the thrust fault zone at 357–395 mbsf. The amount of data scatter for porosity, bulk density, and water content within Subunit 3a is considerably smaller than its stratigraphic equivalent in the lower part of Unit 2. Porosity in Subunit 3a varies from 59.8% to 29.6%, bulk density increases from 1.84 to 2.15 g/cm^3, and water content ranges from 45.7% to 17.3%. When the porosity-depth profile for this subunit is thrust-corrected by subtracting 145 m from the depth, the values of porosity are comparable to those of Unit 2 (Fig. 117).

Subunit 3b (535–740 mbsf)

This subunit is predominantly hemipelagic mud/mudstone with abundant ash layers. It exhibits considerable data scatter, although the downhole trend of index properties agrees with the general trend of Unit 3. Porosity ranges from 59.8% to 29.6%, bulk density from 1.84 to 2.46 g/cm^3, water content from 46% to 17%, and grain density from 2.2 to 2.8 g/cm^3. These wide ranges reflect the lithologic characteristics of ash layers that occur as fine-grained, clayey sediment to indurated tuff.

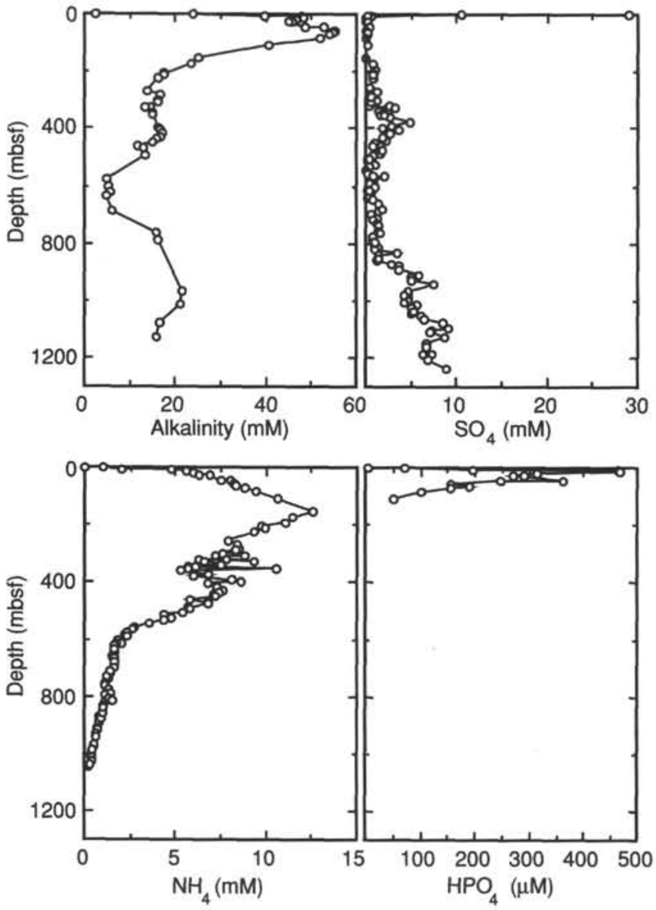

Figure 80. Interstitial water concentrations of alkalinity, sulfate, ammonium, and phosphate, Site 808.

Subunit 3c (740–812 mbsf)

This unit displays a small, but perhaps significant, downhole offset in water content, porosity, acoustic velocity, and impedance. The offset is characteristic of physical property changes across[00a0]thrust faults, where more- consolidated sediment is thrust over less-consolidated material. This unit also corresponds to the depth interval with the highest consistent calcium carbonate content. Correlation among index properties indicates normal changes with depth for Subunit 3c sediments with bulk density increasing from about 1.89 to 2.19 g/cm^3, porosity decreasing from near 50% to 30%, and water content decreasing from 37% to 18%.

Unit 4 (812–965 mbsf)

Unit 4 is characterized by three distinct changes in index property gradients as well as two large offsets. The top of Unit 4 at 812 mbsf is defined by a large change in the bulk density-depth gradient toward greater bulk density, lower porosity, and lower water content coinciding with an offset toward higher grain densities. The bottom of Unit 4 at 965 mbsf is coincident with the uppermost section of the subducted Lower Shikoku Basin sediments that are detached from the accreted sequence above the décollement. Like most other parameters, index properties of sediments within the décollement are strongly offset from general downhole trends, suggesting a tectonically-enhanced consolidation in the deformation zone. Based on these characteristics, physical property Unit 4 was divided into three subunits (4a, 4b, and 4c) with intermediate boundaries at 830 and 950 mbsf. Although most index properties within this unit exhibit very low data scatter, the highly disrupted nature of sediments in the décollement zone produces index properties with a wide range of values. Porosity decreases with increasing depth from 53.8% to 28.5%, bulk density increases from 1.85 to 2.5 g/cm^3, and water content decreases from 40% to 10%.

Subunit 4a (812–830 mbsf)

This subunit shows an irregular behavior with respect to its acoustic properties. Contrary to the normally observed pattern, a large increase in bulk density with depth coincides with a similar decrease in acoustic velocity. This anomalous trend can be attributed to the observed increase in grain density from an average of 2.64 g/cm^3 in Subunit 3c above this interval to an average of 2.69 g/cm^3 in Subunit 4b below this interval.

Subunit 4b (830–950 mbsf)

This subunit is characterized by a normal downhole trend in index properties with very little data scatter. This consistency can be attributed to the homogeneous composition of the hemipelagic Lower Shikoku Basin sediments and the absence of major ash layers. Although sediments in Subunit 4b are lithologically equivalent to Unit 5 (below the décollement), porosity, bulk density, and water content are almost identical to those found 200 m deeper in the section. An exponential porosity-depth function yields an extrapolated surface porosity value of 71% (Table 23), suggesting a normally consolidated state for the sediments of Subunit 4b. Porosity ranges from 21.5% to 53.8% with an average of 34.9%, and bulk density ranges from 2.50 to 2.09 g/cm^3 with an average of 2.19 g/cm^3.

Subunit 4c (950–965 mbsf)

This subunit includes all physical property data sets recovered from the immediate décollement zone. Within this interval all index properties are at variance with respect to normal consolidation with depth. Very low porosity (24.1% to 37.9%) and water content (11.5% to 22.1%) correlates with significantly greater bulk density (2.14 to 2.4 g/cm^3), while constant grain-density indicates the absence of any major lithologic change across the décollement zone. Within the deformation zone, the index properties suggest very great overconsolidation.

Unit 5 (965–1240 mbsf)

The top of Unit 5 is defined by a strong offset in properties relative to the décollement zone sediments of Subunit 4c. Unit 5 comprises the longest and by far most coherent downhole consolidation trend at Site 808. This consistent trend reflects the absence of major structural discontinuities and the generally homogeneous composition of the hemipelagic Lower Shikoku Basin sediments. All index properties show good downhole correlation defining a well-constrained compaction curve with very little scatter (Table 23). Porosity decreases downhole from about 40% to 30%, water content decreases from approximately 22% to 16%, bulk density increases from 2.1 to 2.26 g/cm^3, and grain density exhibits little variation, averaging 2.69 g/cm^3. Extrapolation of an exponential porosity-depth function for this unit yields a surface porosity value of 89%, suggesting under-consolidation, which may in turn be indicative of the presence of excess fluid pressure below the décollement zone.

Unit 6 (1240–1290 mbsf)

The main lithologic constituent of Unit 6 is rhyodacitic ash interbedded with mottled mudstone, yielding a wide data scatter with no apparent downhole trend in index properties. The top of Unit 6 is coincident with the first occurrence of

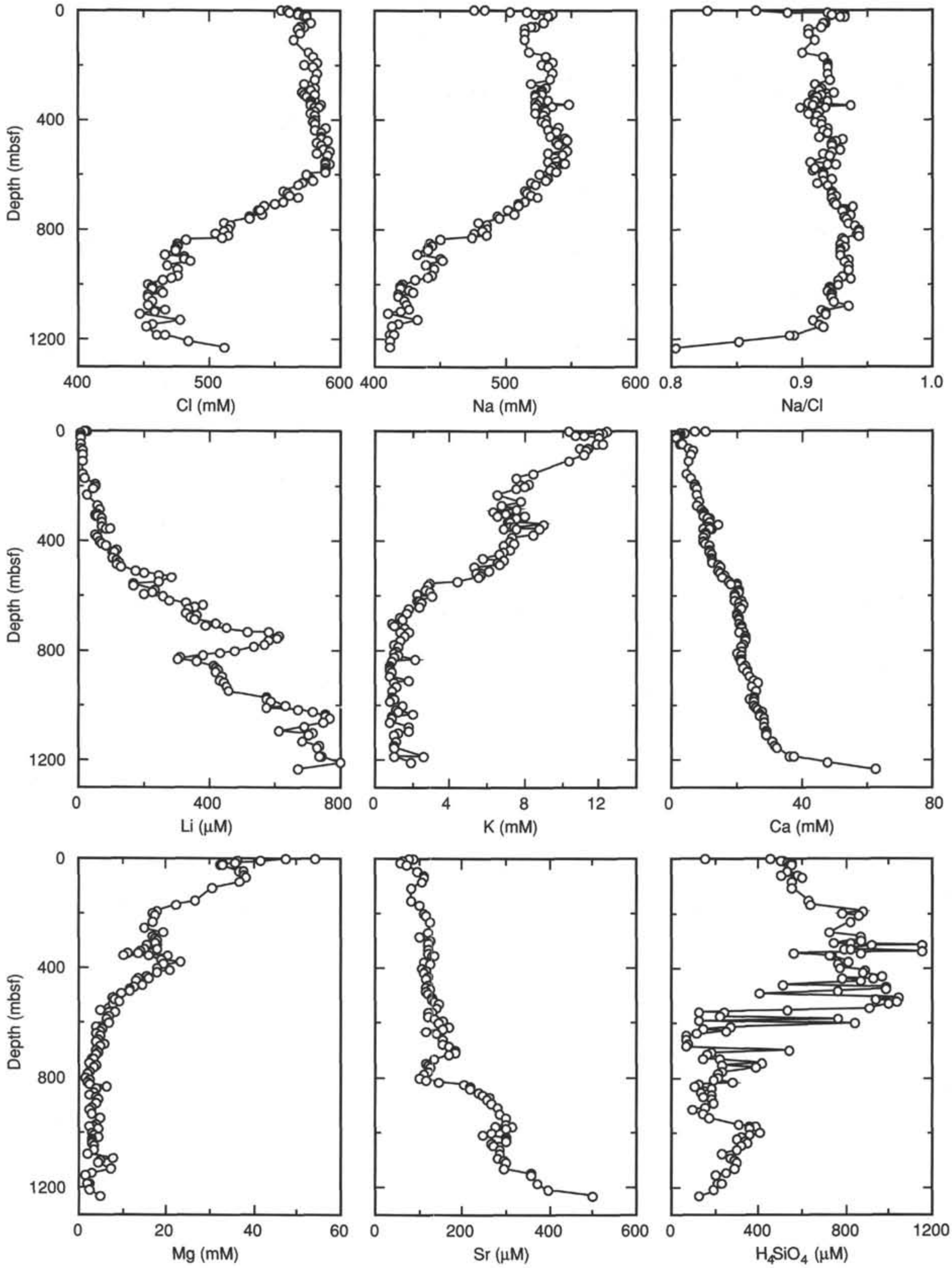

Figure 81. Interstitial water concentrations, Site 808.

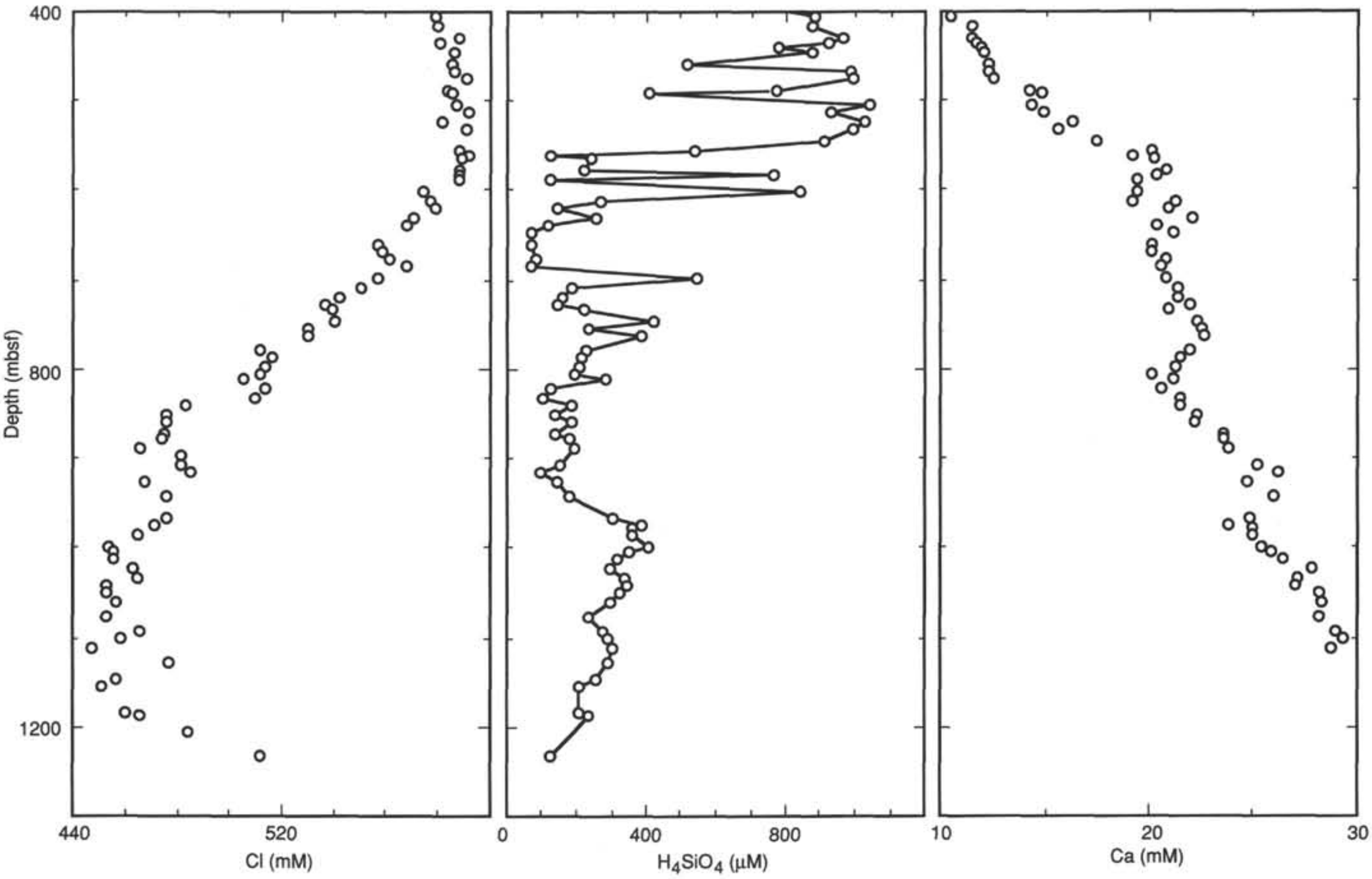

Figure 82. Chloride, silica, and calcium concentrations, Hole 808C, 400–1300 mbsf.

pyroclastic sediments, while the lower boundary defines the base of the sedimentary section at Site 808. Porosity in this unit varies from 34% to 19.1%, bulk density ranges from 2.11 to 2.48 g/cm³, water content ranges from 19.2% to 8.7%, and grain density averages 2.58 g/cm³.

Unit 7 (1290–1327 mbsf)

A strong offset in all index properties defines the top of Unit 7, which encompasses the topmost part of the basaltic basement recovered at Site 808. Standard index property measurements were performed on seven samples collected from this unit. Porosities of the basalts range between 17% and 7%, and the average bulk density closely approaches the average grain density of 2.79 g/cm³.

Shear Strength

Shear-strength measurements were made using a miniature vane in Hole 808A sediments and a pocket penetrometer in Hole 808B material (see Explanatory Notes chapter, this volume). Strengths are reported as undrained values, though in some of the coarser-grained materials this assumption is not valid. Sediment strength increases very little with depth in the upper 50 mbsf, ranging from 5 to 18 kPa, and only increases slightly to about 41 kPa at 73 mbsf (Fig. 118 and Table 24). Sediments recovered from this upper interval were highly disturbed by gas expansion which destroyed the original sediment fabric and strength. Sediment strength increases downhole as indicated by greater induration of sediments in the core liner. At about 140 mbsf, initial biscuiting was observed in the cores. Pocket penetrometer measurements of strength on selected biscuits reveal a range of strengths from 49 to 314 kPa in the 190–230-mbsf interval. The low strength values in this interval are mostly from tests in silty horizons.

A comparison of the range of strengths measured relative to the range of normally consolidated sediments, expressed as the ratio of undrained strength (S_u) to effective overburden stress (P'_o: calculated assuming hydrostatic pressure), suggests the sediments from Site 808 are underconsolidated (Fig. 118). The measurement of low strengths can be attributed to coring disturbance, but underconsolidation due to *in-situ* excess pore pressures cannot be ruled out. Factors which may contribute to excess pore pressure at Site 808 include large sedimentation rates, tectonically induced excess pore pressures, and high methane concentrations in sediments. The downhole trend of increasing strength at Site 808 (about 0.76 kPa/m) is intermediate between that reported for Sites 583 (1 kPa/m) and 582 (0.6 kPa/m) (Bray and Karig, 1986).

Thermal Conductivity

Thermal conductivity was measured using the needle probe method either in the full-space mode for soft sediment or in the half-space mode for consolidated sediment and basalts (Explanatory Notes chapter, this volume). In the full-space mode, measurements were restricted to samples that did not show significant mechanical disturbance. In particular, several depth intervals in Hole 808A where sand is the major constituent were observed to be severely disturbed (fluidized) and were not tested. In addition, in the upper sections of Hole 808A, measurements were limited to the depth intervals where gas expansion cracks were less prominent. After the cores were split, some of the measurement points were found to be disturbed; the data obtained at these core intervals were

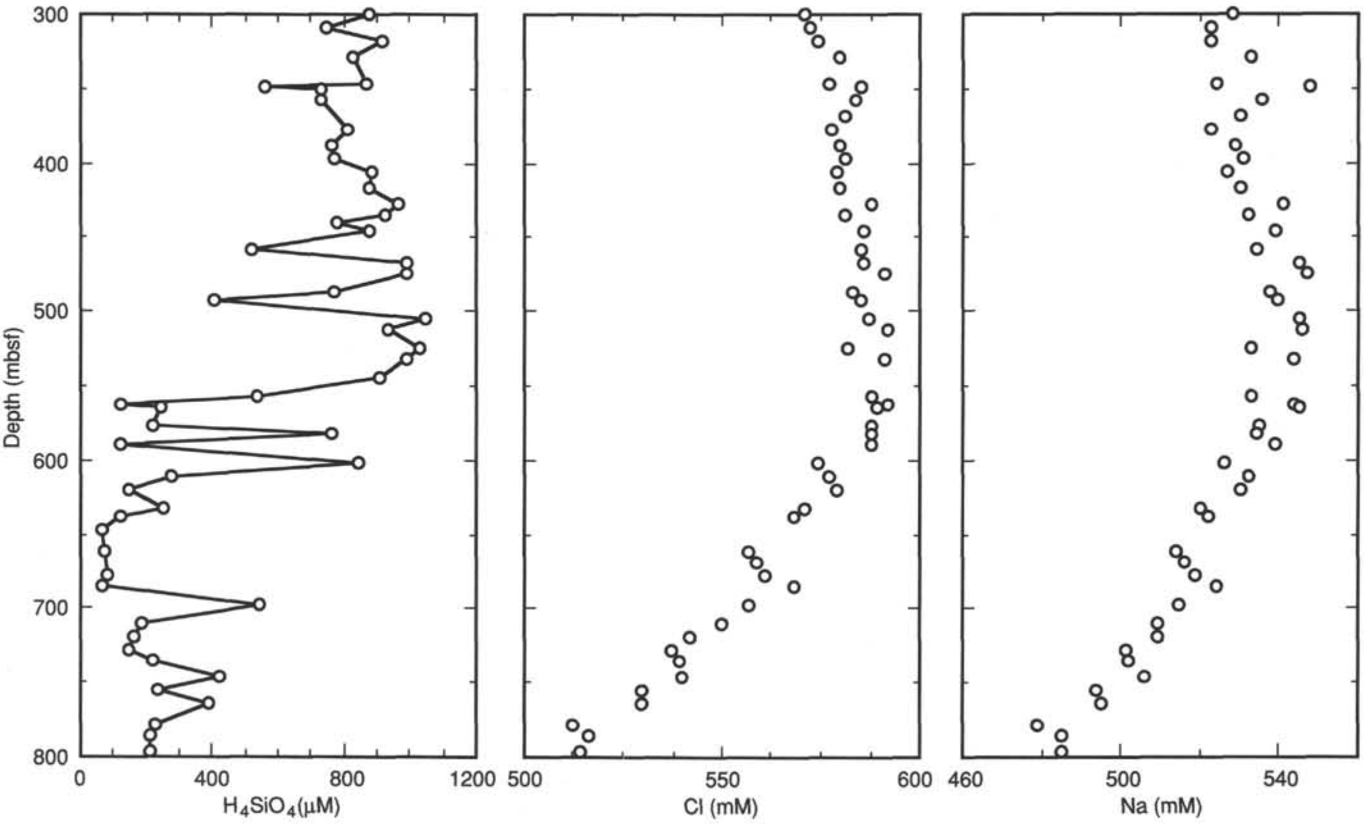

Figure 83. Silica, chloride, and sodium concentrations, Hole 808C, 300–800 mbsf.

discarded. In the half-space mode, whole pieces that had flat surfaces large enough for measurement were selected after splitting the cores. The number of measurements at depths close to and within the décollement are small, and no measurements were made from 1200 to 1240 mbsf, where cores were fractured into small pieces. All thermal conductivity values obtained are listed in Table 25.

Thermal conductivity is highly scattered from 0.7 to 1.3 W/m°C above 75 mbsf in the upper section of physical property Unit 1 (Fig. 119). Larger values are associated with sandy layers, and lower values may result from gas expansion cracks. In Holes 808A and 808B, the average thermal conductivity rapidly increases with depth from about 0.9 W/m°C at the seafloor to about 1.4 W/m°C at 300 mbsf.

Thermal conductivity is greater between 300 and 350 mbsf (Unit 2) in Hole 808C than at the same depths in Hole 808B. Thermal conductivity gradually increases with depth from about 1.55 W/m°C at 400 mbsf to about 1.7 W/m°C at 580 mbsf and is offset to a lower value between 580 and 600 mbsf. Within Unit 3 (from 580 to 820 mbsf), thermal conductivity is almost constant with depth (1.5–1.7 W/m°C). Six measurements were made on ash layers and volcaniclastic sandstones in this unit, and the values are consistently lower than those of the other siltstones or claystones.

Thermal conductivity again increases with depth in Units 4b to 5 from about 1.65 to 1.95 W/m°C. The rate of increase is greater above the décollement than below it. In Unit 6, thermal conductivity is 1.5 to 1.9 W/m°C in tuff layers and 1.9 to 2.2 W/m°C in tuffaceous claystone layers. Thermal conductivity of basalt (Unit 7) in basement ranges from 1.7 to 2.0 W/m°C. These values are typical of samples from the uppermost oceanic crust measured elsewhere (e.g., Karato et al., 1983).

The variations in thermal conductivity with depth at Site 808 are generally consistent with variations in porosity. Thermal conductivity increases as porosity decreases. However, significant offsets in index properties at 400 to 960 mbsf are not apparent in the thermal conductivity profile. The large offset in index properties at the décollement (Core 131-808C-69R) could not be assessed for thermal conductivity because no measurements were made due to lack of whole pieces for half-space tests. Porosity and thermal conductivity measurements are cross-plotted in Figure 120. Siltstone and claystone samples from Hole 808C form a well-defined group (closed circles) and seem to follow a theoretical porosity-thermal conductivity curve for sediment with a 20%–40% quartz content. Samples from Holes 808A and 808B (open circles) have lower thermal conductivity than Hole 808C samples with the same porosity values, which may be due to a variation in mineralogy and tortuosity. For example, most of the samples in the gas-disturbed sections of Hole 808A (triangles) show thermal conductivity lower than the 0% quartz curve. It is probable that gas expansion cracks impede heat conduction more than normally distributed pore spaces and thus result in lower thermal conductivity .

Acoustic Velocity

Acoustic compressional velocity was measured with the DSV and Hamilton frame systems (Explanatory Notes chapter, this volume). Measurements made with the *P*-wave logger on the MST were only reliable in the first core collected in Hole 808A, where the sediment completely filled the core liner

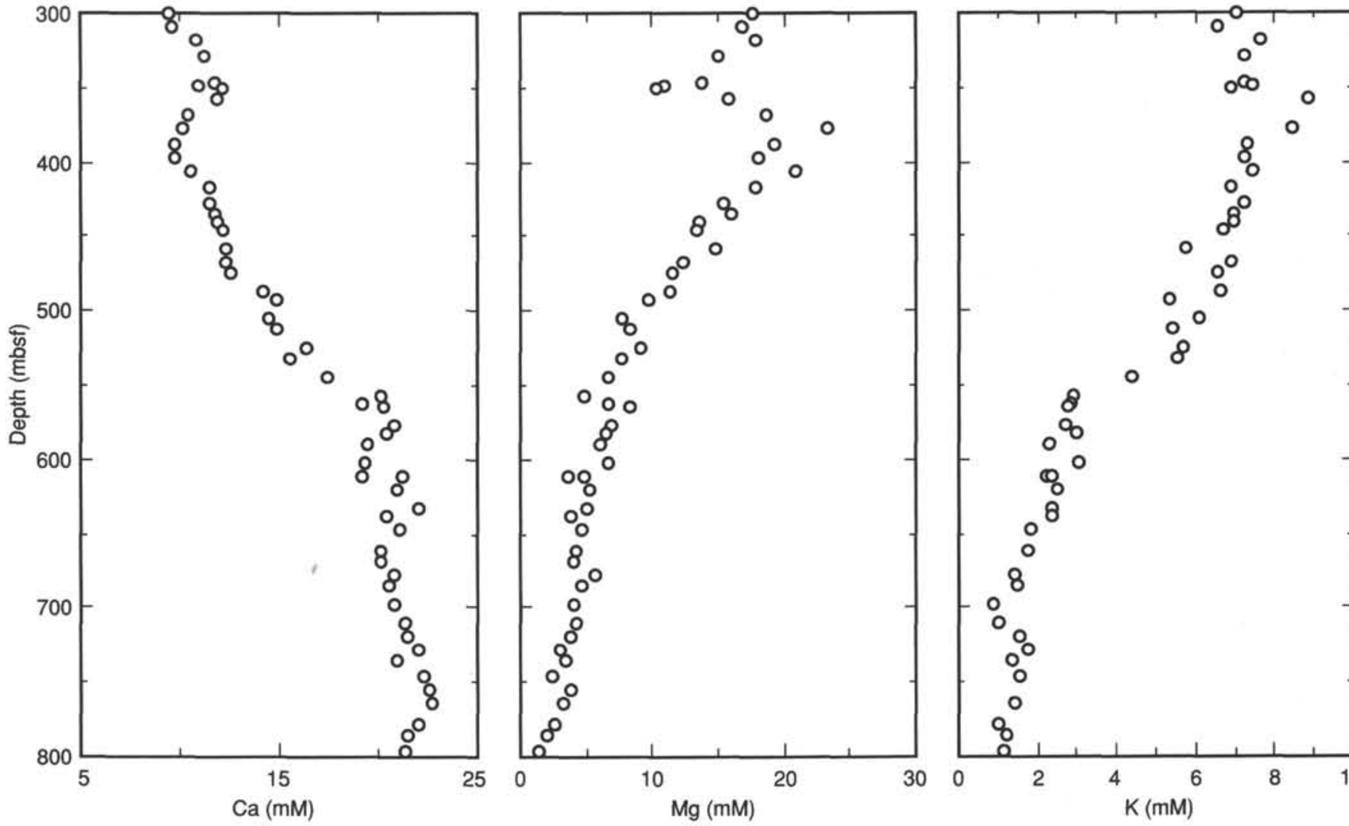

Figure 84. Calcium, magnesium, and potassium concentrations, Hole 808C, 300–800 mbsf.

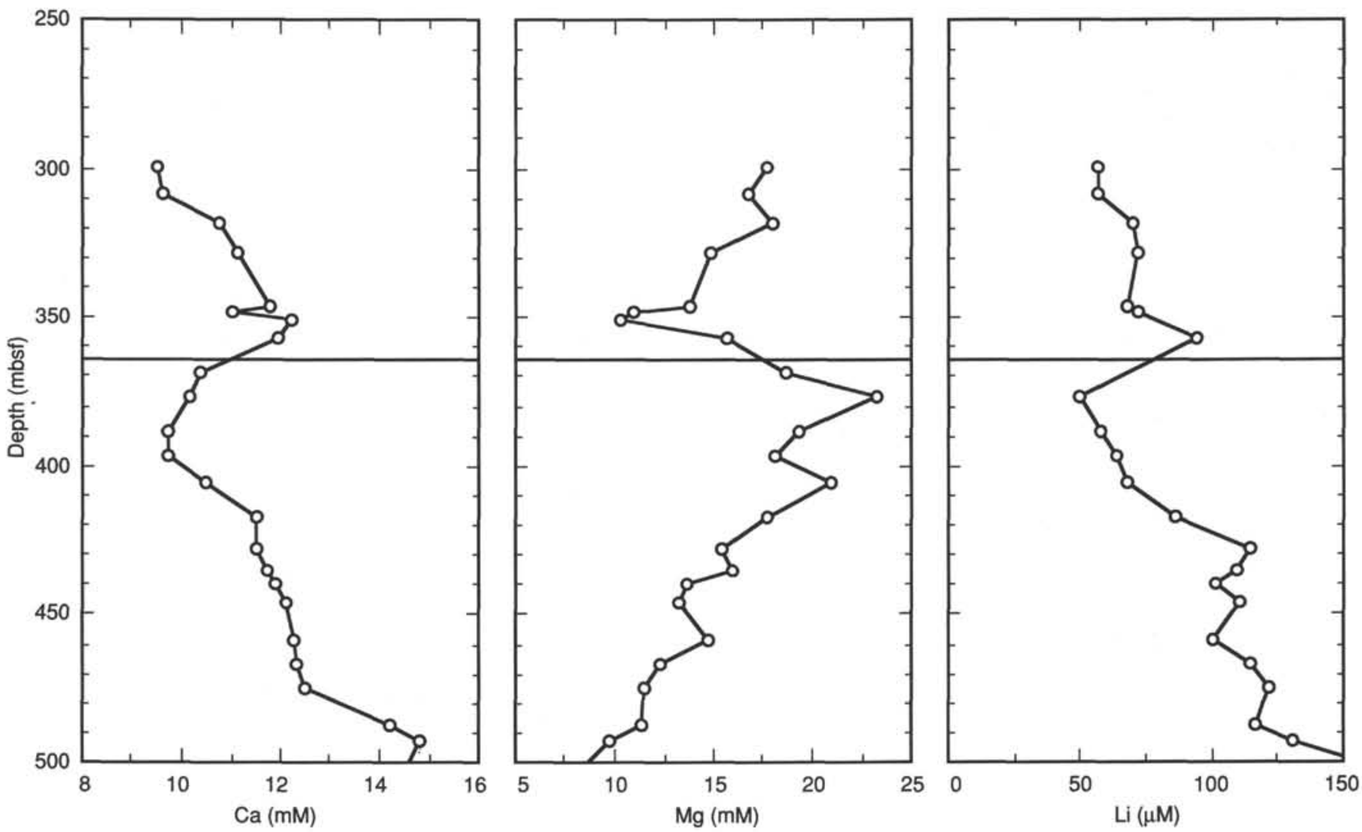

Figure 85. Calcium, magnesium, and lithium concentrations across the thrust of Hole 808C.

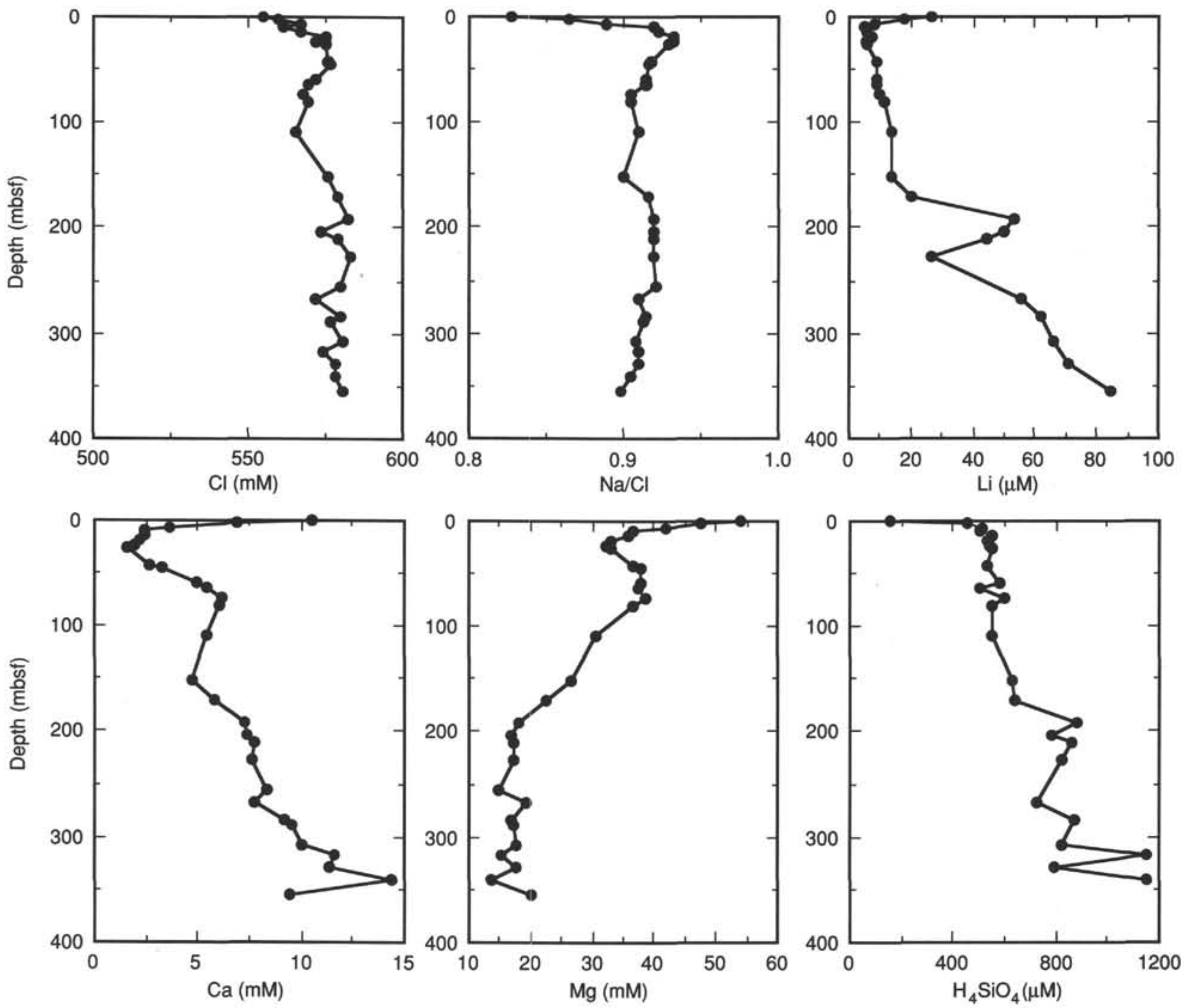

Figure 86. Interstitial water compositions of Cl, Na/Cl, Li, Ca, Mg, and H_4SiO_4 in Holes 808A and 808B.

and little disturbance was visible. Due to large voids in the sand samples and gas-cracked samples, no measurements were made in these materials. The data set in the upper 360 mbsf is consequently limited and biased toward the finer grained lithologies. In Hole 808C reliable measurements were made on samples cut from the core in both the longitudinal (along the core axis) and transverse (perpendicular to the core axis) directions. An index of velocity anisotropy was determined by the following relationship:

$$\text{Anisotropy} = 200/[(V_{pt} - V_{pl})/(V_{pt} + V_{pl})] \quad (1)$$

where V_{pt} is the transverse compressional-wave velocity and V_{pl} the longitudinal velocity (Carlson and Christensen, 1977).

Acoustic velocity increases in the upper 390 mbsf from 1500 m/s near the mudline to 2027 m/s (Fig. 121). A large downhole decrease in velocity occurs at 395 mbsf (Fig. 121). At this depth, the average longitudinal velocity decreases to 1774 m/s, a change of 293 m/s. Below 395 mbsf, the acoustic velocity increases approximately linearly with depth to 743 mbsf. The acoustic velocity increase over this interval (395 to 743 mbsf) also includes higher frequency cycles of increasing and decreasing velocity with depth over a magnitude of 15 to 20 m/s on a scale of 10 to 20 m. These variations in velocity are interpreted to be a result of mineralogical changes associated with ash content. Between 743 and 840 mbsf, the velocity-depth gradient increases to a maximum (peak at 812 mbsf) and then anomalously decreases to a minimum at 840 mbsf (Fig. 121). From 840 mbsf to the décollement, the velocity profile is normal as velocity increases with depth. At the décollement, the velocity sharply increases and then decreases, creating a large impedance contrast over the depth range of Core 131-808C-69R (Fig. 121). Below the décollement, the velocity profile increases normally with depth until 1214 mbsf, where the gradient increases again to basement.

Comparison of the measured velocities to a predicted velocity-depth profile was done by using a porosity-depth function of Brückmann (1989) for a sand-silt-clay mixture and computing the corresponding acoustic velocity using a function for terrigenous sediment (Hamilton, 1979), corrected for the assumed temperature and pressure at Site 808 (Fig. 122). The comparison shows greater measured velocity at Site 808 above the décollement, suggesting either an overconsolidated condition or coarser sediment than the predicted reference; and a good correlation below the décollement, suggesting a normally consolidated state. The Site 808 velocity profile was also compared with Site 582 data (Bray and Karig, 1986). To correlate the two data sets, Site 582 data were corrected for

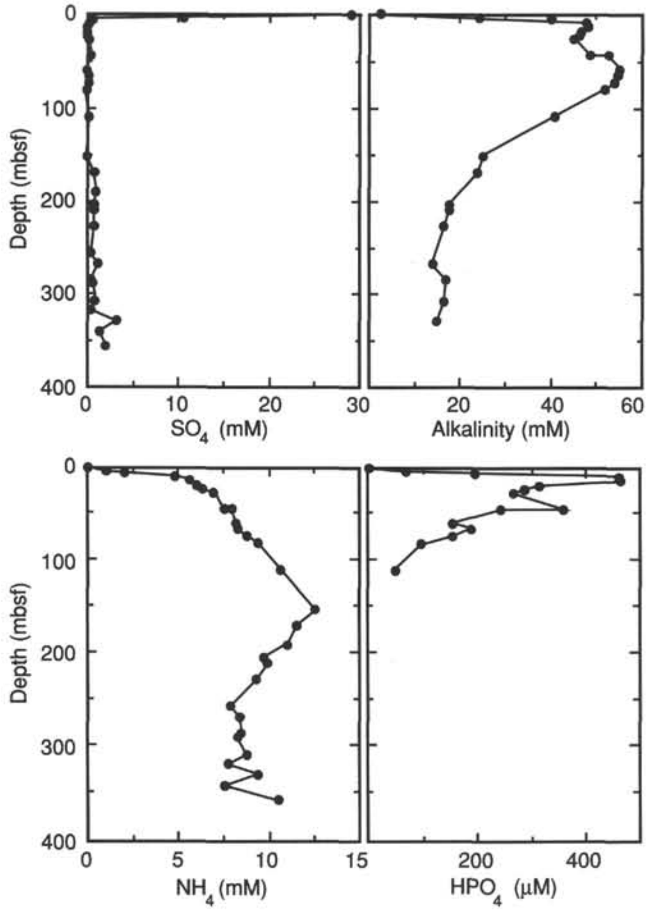

Figure 87. Interstitial water concentrations of SO_4, Alkalinity, NH_4, and HPO_4 in Holes 808A and 808B.

temperature (Kinoshita and Yamano, 1986), and pressure (calculated from Site 582 index property data). A linear regression of Site 582 transverse velocity data with Site 808 data shows lower velocity for the former (Fig. 121). This comparison is consistent with the site comparison of porosity data where porosity is greater for Site 582. Both of these comparisons suggest that Site 808 sediments are either overconsolidated with respect to Site 582 or that the column at Site 808 consists of a generally coarser sediment sequence with greater acoustic velocity and lower porosity. A comparison of Site 808 velocities with those of the equivalent frontal thrust site from Leg 87 could not directly be made because of lack of data from Site 583. However, porosity estimates for the Leg 87 transect, which were based on seismic reflection and refraction velocity and supplemented with sample-measured velocity (Bray and Karig, 1985), are lower than Site 808 by 10% to 20% porosity. This suggests that the interpreted velocity structure for the Leg 87 area is significantly greater than for the Leg 131 study area. This difference could result from a generally coarser grain size at Site 583 relative to Site 808, that the porosity-velocity function used for Site 583 is inappropriate, or that the section at Site 583 is more consolidated than the Site 808 section.

The impedance profile for Site 808 (Fig. 121) follows the same general trends as discussed for acoustic velocity, suggesting that the reflectors observed in seismic records at the site result primarily from changes in sediment velocity, rather than of bulk density. A direct comparison of bulk density with acoustic velocity results in relatively poor correlation (Fig. 123). Large impedance contrasts (>300 Mg/m^2-s) occur at five positions downhole, which indicate depths where seismic reflections can occur. At 395 mbsf the impedance decreases from an average of 4100 to 3700 Mg/m^2-s. At 761 mbsf, the impedance increases from 3547 to 4154 Mg/m^2-s over a 2-m-thick interval. An increase of 750 Mg/m^2-s occurs over the depth range of 810 to 812 mbsf. The largest impedance

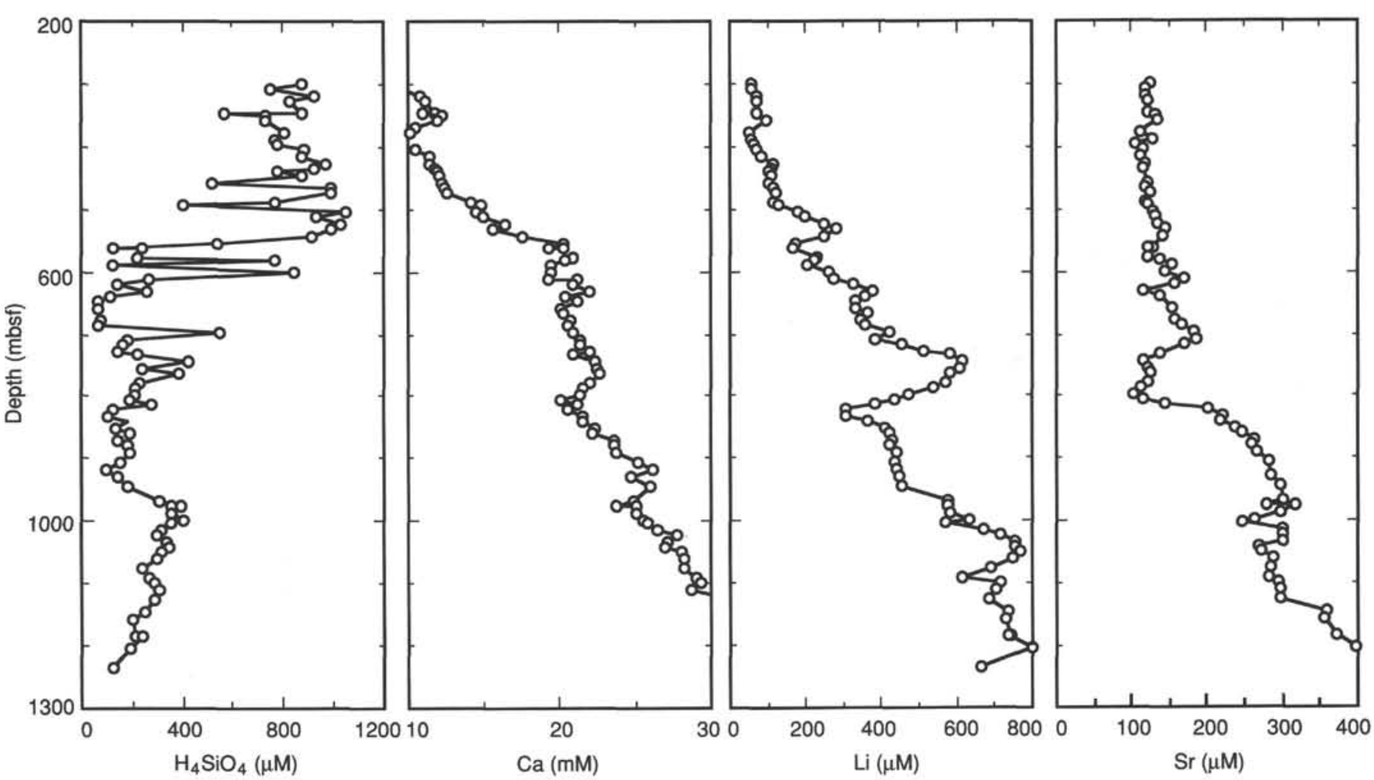

Figure 88. Silica, calcium, lithium, and strontium concentrations, Hole 808C.

contrast occurs at the décollement between 960 and 964 mbsf where it decreases from 5935 to 4215 Mg/m^2-s. The deepest contrast in impedance, measured from Site 808 cores, is at 1129 mbsf, where a positive change of 500 Mg/m^2-s occurs over an 8-m-thick interval.

Acoustic anisotropy is variable with depth at Site 808 (Fig. 121). Anisotropy is generally greater than zero, indicating positive transverse anisotropy. In fine-grained marine sediment under vertical principal stress conditions, anisotropy is expected to increase with depth. At Site 808, however, the acoustic anisotropy shows an anomalous decrease with depth between 400 and 950 mbsf. Below the décollement, the anisotropy trend follows the expected trend for vertically loaded sediments. Within Unit 5, the transverse anisotropy increases from near 0% just below the décollement to about 20% at the base of the unit.

Formation Factor

Resistivity measurements were performed with the four-pin electrode array inserted transverse and longitudinal to the core axis (Explanatory Notes chapter, this volume). The results (Table 22 in backpocket microfiche and Fig. 124) are presented in terms of formation factor (the ratio of the measured resistance of the sediment to the resistance of a seawater standard), which is closely related to porosity and tortuosity. Highly disturbed core sections from the upper 300 m (Holes 808A and 808B) were not tested, resulting in a limited data set from that section. A selected number of indurated sediment samples were measured by making drill holes for inserting the electrode pins. Contact between pins and sample was assured by filling the guide holes with seawater.

The formation factor ranges from 2 to 28 and generally increases with greater depth (Fig. 124). The limited data collected in both longitudinal and transverse directions suggest resistivity anisotropy in the formation is not significant (Figs. 124 and 125). Similar to the other physical properties, an offset occurs in the formation factor at the décollement. Much larger values of the formation factor were measured in two samples from the ash-rich, mottled greenstone of physical properties Unit 6 relative to the overlying section. This large formation factor correlates well with the other physical properties of this basal sediment section. Formation factor and resistivity, expressed as functions of porosity, are shown in Figure 125. The form of the empirical equation used is that described by Kermabon et al. (1969) for modern marine clays and turbidite sands expressed as: $(a/n)^m - b$, where n is the porosity expressed in decimal format. The three curve-fit constants from our formation factor data are somewhat different from those obtained by Kermabon et al. (1969), as these are: $a = 3.80$ (Leg 131), 1.72 (Kermabon); $b = 4.755$ (Leg 131), 0.719 (Kermabon); and $m = 1.14$ (Leg 131), 1.46 (Kermabon).

Magnetic Susceptibility

Volumetric magnetic susceptibilities were measured in all recovered cores from Holes 808A, 808B, and 808C. The quality of these results degraded in XCB and RCB sections, where the core was undersized or disturbed by drilling. The general downhole trends are useful for hole to hole stratigraphic correlation.

Magnetic susceptibility data display a wide range of data scatter that is clearly related to lithologic variation (Fig. 126). Very large average susceptibility values, ranging from 50 to 900 cgs units in the upper 125 mbsf, are correlated with the occurrence of thick-bedded sandy turbidites, while generally small susceptibility values down to the frontal thrust fault zone at about 380 mbsf are associated with thin-bedded sand and silt turbidites. The highly variable susceptibility data of the upper 400 mbsf changes drastically below the thrust fault. Similarities in the susceptibility record above and below the thrust fault corroborate the approximate 145-m stratigraphic repetition deduced from lithostratigraphic evidence.

Silty turbidites and hemipelagic muds between 410 and 660 mbsf are characterized by three cycles of increasing susceptibility between 50 and 200 cgs units. Below 660 mbsf down to 800 mbsf, susceptibility drops sharply to an average of about 30 cgs units, which correlates well with a large increase in carbonate content over the same interval.

Several physical property units that were defined based on index properties, but are clearly related to lithologic boundaries, are identifiable in the magnetic susceptibility data (Fig. 126). Physical properties Subunit 4c, defining the immediate zone of deformation at the décollement, displays a local maximum with susceptibility values around 125 cgs units. Unit 5 is clearly delineated by a steady decline of susceptibility from about 120 cgs units at the top of the unit to 20 cgs units at the bottom. In a similar way, physical properties Units 6 (ashes) and 7 (basalt) are defined by a strong offset in average susceptibility. Unit 6 averages about 100 cgs units with a peak susceptibility of 175 cgs units, and Unit 7 displays an average magnetic susceptibility around 400 cgs units.

Discussion

The distribution of physical properties with depth is a key to understanding the mechanical processes of sediment subduction and frontal accretion. Recovery of the complete thrust package and subducted sediment from the Nankai prism offers a first-time opportunity to document the physical state of the lower prism slope package. Several primary physical units are distinguished from the downhole distribution of physical properties. The boundaries of some of these units are defined through structural control, such as at the décollement (945–965 mbsf) and at the major frontal thrust fault (357–395 mbsf). Other units appear to be linked to lithologic controls, though these are not unambiguously defined.

The topmost 380 m at Site 808 (Units 1 and 2) is the upper thrust package at this site location on the lower slope. The package is dominated by thick-bedded sand-to-silt turbidites. Initial porosity of fine-grained sediments within this unit is less than that described for terrigenous sediments (Hamilton, 1976), although the downhole porosity reduction is similar. The high permeability of these sandy and silty sediments most likely allows this unit to rapidly dewater in response to lateral tectonic and rapid sedimentation loads. The distinctive bimodal character of most physical properties in this upper section corresponds with an equivalent bimodal composition of turbidites. This characteristic is most noted in Unit 1 and is significantly reduced in Unit 2, where the finer-grained sediment dominates the lithology.

A major thrust fault zone at 357–395 mbsf, distinguished in cores by significant fracturing, marks the contact where approximately 145 m of vertical stratigraphic duplication takes place. This contact offsets similar compositional lithologies. The thrust fault marks the depth at which the downhole compaction trend, developed in the overlying section, is reset. The repeated stratigraphic section does not show a large reduction in porosity, suggesting delayed dewatering since thrusting or a very recent thrust event (Fig. 117).

Smaller scale downhole trends of physical properties in the tectonic package between the major thrust fault and décollement define one unit with several subunits. Compositional variations within the mainly hemipelagic section are closely linked to a number of these subunits. An unresolved question is how changes of these properties reflect primary depositional

Table 16. Chemical compositions of the ash samples in terms of (a) oxide percentage, and (b) molar ratio with respect to Al.

Core-section, interval (cm)	Depth (mbsf)	SiO_2 (%)	TiO_2 (%)	Al_2O_3 (%)	Fe_2O_3 (%)	MgO (%)	CaO (%)	Na_2O (%)	K_2O (%)	P_2O_5 (%)	LOI (%)	Total (%)
131-808B-												
10X-3, 52–54	201	63.563	0.722	15.052	4.170	1.383	2.899	3.427	3.682	0.214	6	101.110
131-808C-												
15R-3, 62–63	437	54.594	0.626	14.356	8.796	2.942	3.306	1.719	2.730	1.385	11.7	102.154
30R-4, 103–105	584	70.840	0.283	12.660	2.226	0.486	1.123	3.572	2.591	0.040	8.4	102.223
30R-5, 119–120	585	55.660	0.840	17.153	8.703	2.763	3.016	2.530	0.870	0.213	11.9	103.648
37R-1, 30–32	646	59.170	0.615	15.473	6.754	2.843	1.885	2.893	0.726	0.121	11.7	102.178
38R-6, 76–78	663	58.708	0.876	15.004	6.646	2.679	2.588	3.061	0.957	0.272	12.2	102.991
45R-3, 55–57	725	56.964	0.444	15.059	6.363	3.232	1.555	2.868	0.545	0.162	12	99.193
54R-1, 65–67	810	64.045	0.473	13.584	2.920	1.289	1.933	3.676	0.443	0.211	14	102.576
57R-4, 142–144	844	58.190	0.714	16.964	6.131	2.482	1.528	2.161	2.472	0.070	9.3	100.011
73R-1, 11–13	992	58.592	0.784	16.110	6.030	2.523	0.633	1.628	3.266	0.070	7.2	96.836
100R-CC, 20–22	1245	73.620	0.271	10.963	2.006	0.963	1.284	3.079	1.815	0.702	6.8	101.503
102R-2, 30–32	1263	59.419	0.471	14.639	2.305	1.473	4.108	2.265	2.325	0.110	13	100.114

characteristics of the sediment compared to those properties modified by structural features that may have, in turn, produced a secondary compositional overprint on the original sedimentary section. For instance, physical properties Subunit 3c appears to be tied to a 2compositional increase of calcium carbonate (Sedimentology section, this chapter). Acoustic anisotropy behaves anomalously within this unit (decreasing anisotropy with depth), suggesting that the sediment fabric has been influenced by tectonic loads. Within this same interval, higher molecular weight hydrocarbons (isopentane) occur in the sediments and lithium in pore water displays a sharp peak (see Organic Geochemistry and Inorganic Geochemistry sections, respectively, of this chapter). Arguments have been advanced for explaining these features as original sedimentary properties altered by diagenetic reactions and possibly hydrothermal events, though evidence for either scenario is still inconclusive.

The distinctive changes in acoustic velocity, index properties, and thermal conductivity at about 812 mbsf are also visible in pore-water chemistry shifts downhole. Subunit 4a is also characterized by an anomalous downhole trend of decreasing porosity with increasing velocity. The average grain density of this unit is distinctly greater than the overlying Subunit 3c and appears to increase downhole. These trends are likely associated with compositional changes in Subunit 4a.

The base of physical properties Unit 4 is clearly defined by the contrasting properties of sediments from the décollement zone to subducted sediments within the subducted package. Shear-induced consolidation in the décollement zone results in a very localized compaction zone approximately 20 m thick. The mudstones from Subunit 4c have the greatest densities and smallest porosities of the entire mudstone sequence. This consolidation may have taken place through local dewatering along fractures within the slip plane. However, no clear evidence of significant dewatering through this surface is gleaned from other shipboard results.

The subducted sedimentary sequence may be underconsolidated, as interpreted from extrapolation of the porosity-depth function for Unit 5 and from comparison with the porosity-depth function of Shikoku Basin sediments from Site 582 (Bray and Karig, 1986). Subunit 4b, of similar composition and uncomplicated by intense local deformation, displays a downhole porosity gradient similar to that defined for Unit 5. This comparable rate of consolidation, combined with localized overconsolidation of Subunit 4c, suggests that dewatering of these deeper accreted and subducted sediments occurs only through the lower matrix permeability. The low matrix permeability furthermore provides a mechanism for sustained pore pressures in excess of hydrostatic, which in part supports the offscraped thickening package, although no direct measure of pressure exists in that section. Acoustic anisotropy, however, increases normally with depth below the décollement, suggesting that the sediment has seen a normal consolidation pattern in the past. As yet unresolved is why the décollement developed in the stratigraphic position it now occupies.

The discussion above provides a backdrop to the shore-based studies of physical and mechanical properties of the sediments from Site 808. These physical properties are complemented by the downhole logging results (see Downhole Measurements section, this chapter), which provide a better characterization of formation scale properties not attainable from core samples. Formation porosity and velocity, for instance, may vary significantly from the matrix equivalents obtained in the laboratory. Formation-scale characteristics are most likely to diverge from the matrix properties in zones with significant structural deformation such as the upper thrust fault and at the décollement. A comprehensive understanding of the physical character of subduction/accretion necessitates a merger of these two data sets. Further shore-based analyses will also serve to constrain the correction of lab measurements to *in-situ* conditions.

ANELASTIC STRAIN RECOVERY

Introduction

The measurement of anelastic strain recovery (ASR) is a particularly promising technique for the determination of *in-situ* stress because it is simpler and far less expensive than currently available downhole techniques. At present, however, very few ASR results have been published, and the conditions under which the technique provides useful results are still being investigated. In general it appears that stronger, more uniform lithologies, such as fine-grained igneous rocks (e.g., Wolter and Berkhemer,1989) produce the largest anelastic response.

Comparison of ASR stress measurements with those from wellbore breakouts and from experimental hydrofracturing during the Multiwell Experiment (MWX) in the Piceance Basin of Colorado (Teufel and Warpinski, 1984; Warpinski et al., 1985) demonstrated that the method can be applied to sandstone at depths as shallow as 1.6 km. ASR results from mudstones interbedded with these sandstones were less straightforward, in that the anelastic strains recorded were very low and the differential stresses were ambiguous (Warpinski and Teufel, 1987). Less-consolidated mudstones from the North Sea were reported to produce no useful ASR

Table 16. (continued).

Core-section, interval (cm)	Inorganic C (%)	Si/Al	Ti/Al	Fe/Al	Mg/Al	Ca/Al	Na/Al	K/Al	P/Al
131-808B-									
10X-3, 52–54	0.08	3.586	0.030	0.179	0.117	0.175	0.375	0.265	0.010
131-808C-									
15R-3, 62–63	1.21	3.227	0.028	0.392	0.260	0.210	0.197	0.206	0.069
30R-4, 103–105	0.03	4.747	0.014	0.114	0.049	0.081	0.465	0.222	0.002
30R-5, 119–120	0.09	2.752	0.032	0.322	0.204	0.160	0.243	0.055	0.005
37R-1, 30–32	0.1	3.248	0.025	0.278	0.232	0.111	0.308	0.051	0.006
38R-6, 76–78	0.06	3.318	0.038	0.284	0.226	0.157	0.336	0.069	0.007
45R-3, 55–57	0.09	3.209	0.019	0.268	0.272	0.094	0.314	0.039	0.004
54R-1, 65–67	0.04	3.999	0.022	0.139	0.120	0.130	0.445	0.036	0.011
57R-4, 142–144	0.15	2.909	0.027	0.232	0.185	0.082	0.210	0.158	0.003
73R-1, 11–13	0.15	3.086	0.031	0.240	0.198	0.036	0.167	0.220	0.003
100R-CC, 20–22	0.44	5.704	0.016	0.118	0.111	0.107	0.463	0.180	0.046
102R-2, 30–32	0.03	3.448	0.021	0.103	0.127	0.255	0.255	0.173	0.006

results (L. W. Teufel, 1989, pers. comm.), but the details of these measurements were not given.

Apparently the lower anelastic component of strain in mudstones than in sandstones overwhelms the effect of a lower Young's Modulus (E) in the mudstone. A second consideration reported by Warpinski (1989, pers. comm.) is that weaker rocks are more likely to fail during the coring process, producing no or spurious results. Moreover, the shallower the sample the lower is the stress difference produced by coring and thus the lower the total strain.

The only use of ASR during the ODP to date has been on Leg 123 by R. Brereton (Gradstein, Ludden, at al., 1990), who measured the response of basalt cores. These measurements showed both expansional and contractional components, and were not readily interpretable.

With this meager background, ASR measurements were made on the deeper sediments at Site 808, with the recognition that the chances of success were minimal. Not only were the sediments mud-rich, but the *in-situ* stresses were much less than those of even marginally successful measurements. Nevertheless, testing the limitations of the technique was felt to be a valuable exercise, and the samples were also to be used for post-cruise mechanical analyses.

Procedure

Samples suitable for ASR measurements became available in Hole 808C, with unbroken lengths of consolidated core more than 15 cm long, below 375 mbsf. At this depth the sediment was still quite fissile, with subhorizontal extensional cracks, most likely resulting from mechanical failure during drilling. Nevertheless, the first sample was taken from Core 131-808C-10R at 386 mbsf, primarily to gain experience with the apparatus and to rectify problems before more promising samples became available. Five subsequent samples were taken from Hole 808C, determined by the apparent useful duration of the test then in progress and by the availablility of adequate unfractured core.

ASR samples were selected on the basis of apparent coherence and uniformity as seen through the core liner. As soon as possible after the section was labeled, the sample was removed and some indication of bedding or structural orientation sought. Unfortunately, no such evidence was obtained from these samples, but, had the strain measurements been valid, orientation would have been sought by correlation with paleomagnetic measurements on contiguous pieces of core.

In the shipboard lab, the length and diameter of the sample was recorded, and a notch cut in the edge of the upper surface denoting the best estimate of the plane of structural symmetry (e.g., the azimuth of the bedding dip) as a reference plane. The sample was then coated with wax, as quickly and at as low a temperature as possible, followed by the inking of the reference plane and the pinhole positions for the six linear variable displacement transformers (LVDT's) on the wax coating. Three LVDT's were placed radially at 0°, 45°, and 90° from the reference plane, one placed axially, and two obliquely (45°), one in the reference plane and the other in an axial plane at 90° to it (Fig. 127). A seventh LVDT, at 45° in the reference plane, was to have also been used, but the core samples had significantly smaller diameters than full-size cores, which caused physical interference among the frames. Fortunately, this LVDT was redundant and could be left unused.

Pairs of holes about 2 mm deep were drilled through the wax and into the sample to contain the LVDT pins, using a jig to insure that the two holes for each LVDT were aligned

Table 17. X-ray mineralogy data for bulk powdered samples. See Table 8 (this chapter) for detailed explanation.

Sample Core-section, interval (cm)	Smectite	Illite	Chlorite &	Chlorite Kaolinite	Quartz	Plagioclase	Calcite	Zeolite	Amphibole	Analcite	S/I	Pyroxene	Siderite
131-808B-													
10X-3, 52–54	0	1.82	2.85	0	77.02	100	7.07	0	0	0	0	0	0
131-808C-													
15R-3, 62–64	2.14	4.4	4.55	1.05	100	14.65	0	0	0	0	5.02	2.81	15.19
30R-4, 103–105	19.27	0	0	0	57.17	42.3	0	0	0	0	0	0	0
30R-5, 119–120	0	0	0	0	84.38	100	2.87	0	8.22	0	33.24	0	0
37R-1, 30–32	0	4.04	0	0	90.42	100	0	2.04	0	0	68.21	66.74	0
38R-6, 76–78	6.68	0	0	0	15.82	34.58	0	0	0	0	18.65	0	0
45R-3, 55–57	0	5.49	0	0	36.98	100	0	2.08	0	0	71.71	16.8	0
54R-1, 65–67	8.89	0.93	0	0	47.58	100	0	17.03	0	0	35.21	7.03	9.07
57R-4, 142–144	2.36	1.38	4.4	0	100	18.21	1.18	0	0	0	9.97	0.33	0
73R-1, 11–13	1.44	2.58	3.99	0	100	14.68	1.6	0	0	0	7.62	0	0
100R-CC, 20–22	0.71	0.15	0.8	0	100	2.78	0	0	0	7.96	1.65	0.64	2.43
102R-2, 30–32	12.49	0	0	0	100	21.75	18.31	15.17	0	10.22	12.15	23.11	17.1

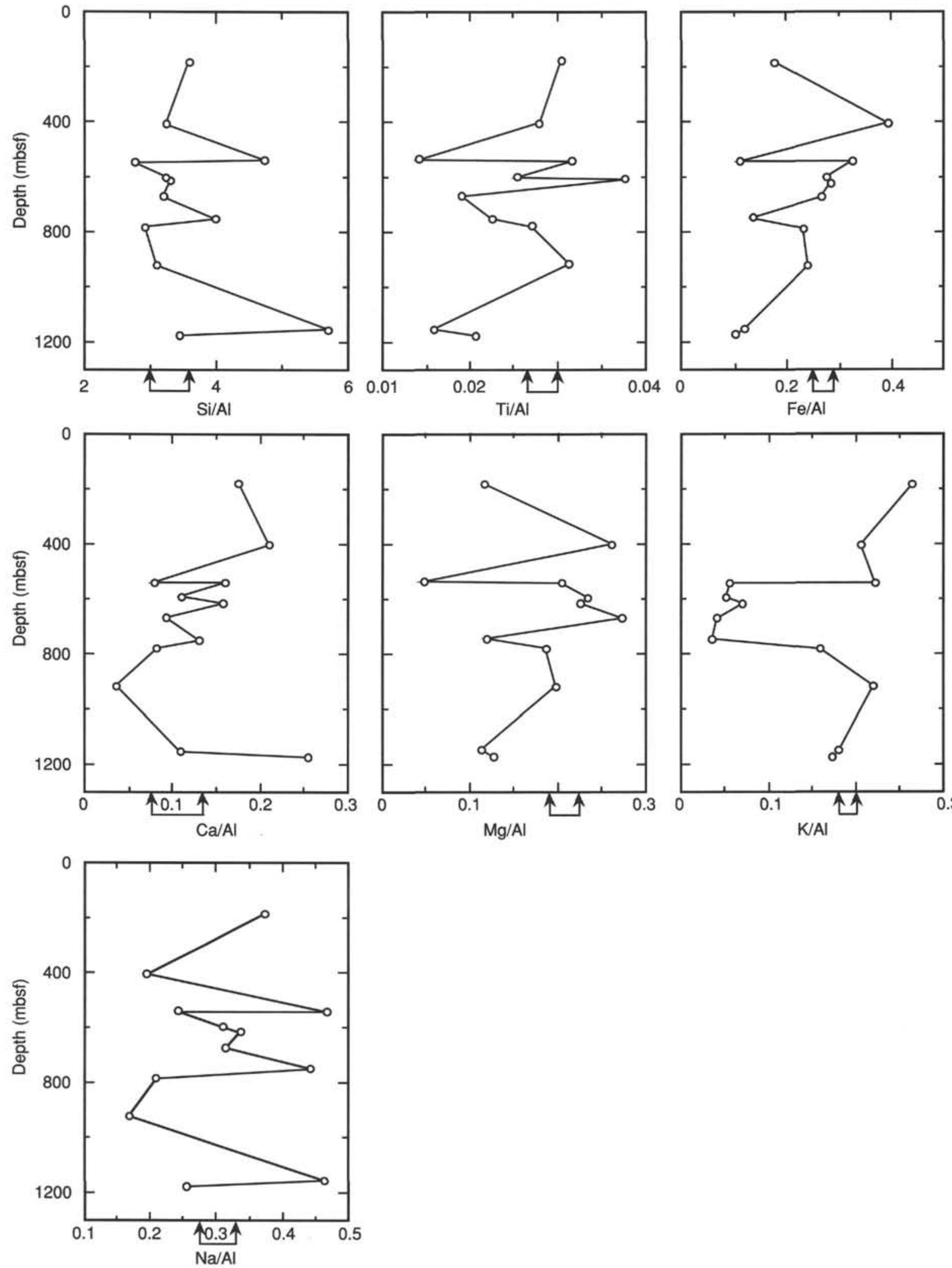

Figure 89. Vertical profiles of Si, Ti, Fe, Ca, Mg, K, and Na (in terms of molar ratios with respect to Al) for the 12 ash samples discussed in this study. Three filled circles stand for the background matrix samples as judged from their XRD patterns. Two arrows indicate the range of Site 582 sediment data (± sigma) between 5 and 590 mbsf (Kawahata et al., 1986).

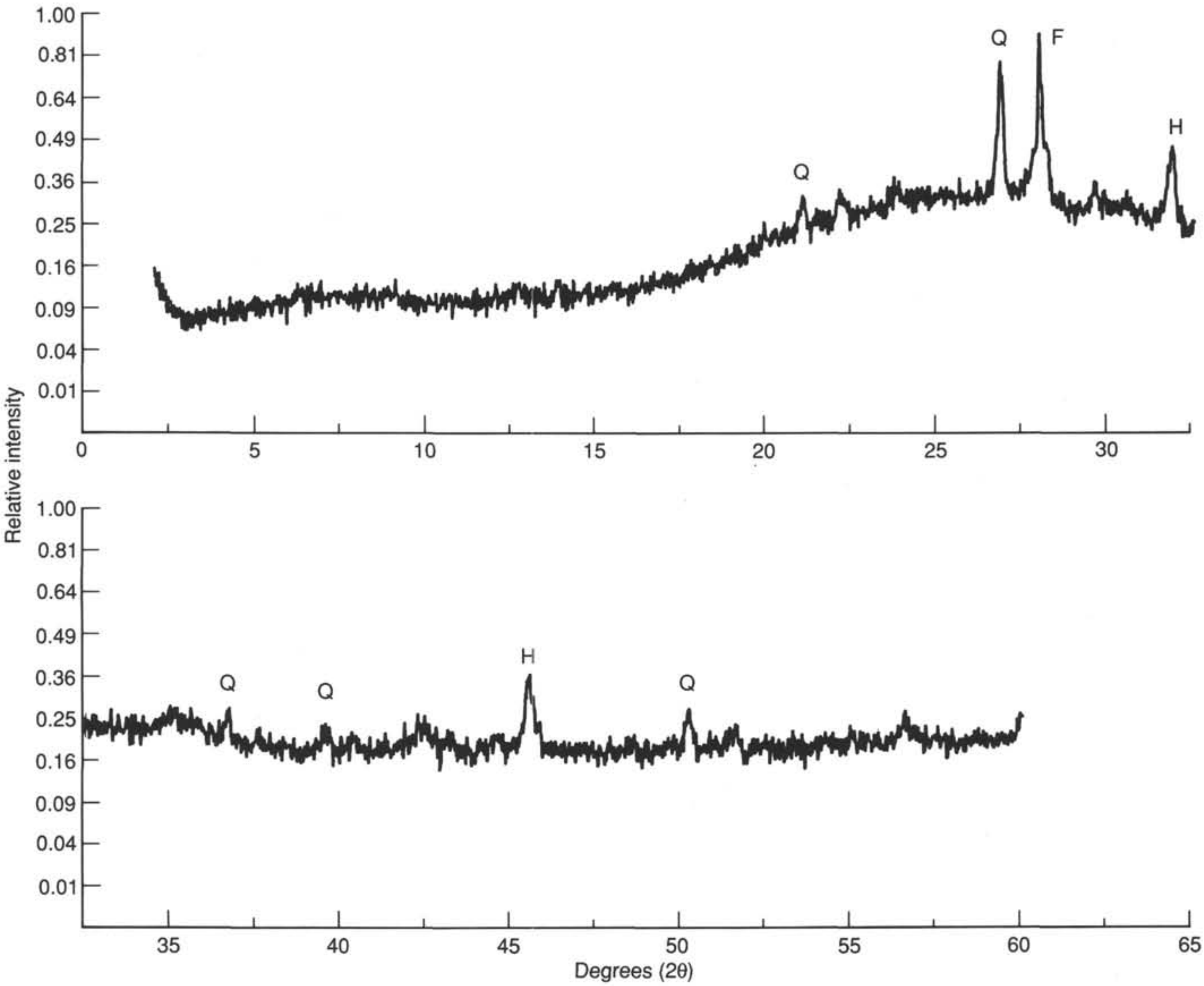

Figure 90. XRD pattern of Sample 131-808B-10X-3, 52–54 cm. The abbreviations are as follows: A = Analcite, Cl = Clinoptilolite, Cr = cristobalite, F = feldspar, H = halite, Q = Quartz, Si = siderite, and S = smectite and/or mixed layer S/I.

correctly and were diametrically opposed. A final hole was drilled from the upper edge of the sample to the center for one of the thermistors, the other being imbedded in the wax coating.

The LVDT frames were then attached and adjusted to insure that only the pins touched the sample, and the edge of the holes were sealed with wax. The final step before beginning the test was insertion of LVDT's into their frames and adjustment to their null position. The time between the cutting of the core and the start of the test varied between 2.8 and 3.5 hr, of which 1.5 hr was absorbed by core retrieval and 0.5 hr by initial core handling. The time for sample preparation was reduced to 0.75 hr with experience.

Results

Background and Calibration

The ASR apparatus used in this study was completed just prior to the leg, requiring that calibration and instrument response tests be made before testing of the samples. In addition to thermistor calibration, these included tests of stability of the signal voltage and of the mechanical stability of the LVDT frames.

Calibration of the two thermistors was done using a Lauda waterbath from the shipboard geochemical laboratory, accurate to better than ±0.1°C. These data were fit with a second-order polynomial and embedded in the computer software. Mechanical and voltage stability were checked together using a plastic cylinder as a sample. This test showed temperature-corrected total variations of less than ±0.001 V (±5 microstrains) over a 40-hr interval for the worst LVDT and less than ±0.0001 V (0.5 microstrains) for most. We demonstrated that the simple foam pad used to isolate the apparatus from shipboard vibration was entirely adequate. In fact, the apparatus was remarkably insensitive to disturbances other than the actual movement of the sample or frames.

Sediment Samples

ASR measurements were made on six samples from Hole 808C, between depths of 386 and 1098 mbsf (Table 26). The two shallowest samples were recognized as being too unconsolidated to provide valid results, and were assumed to be

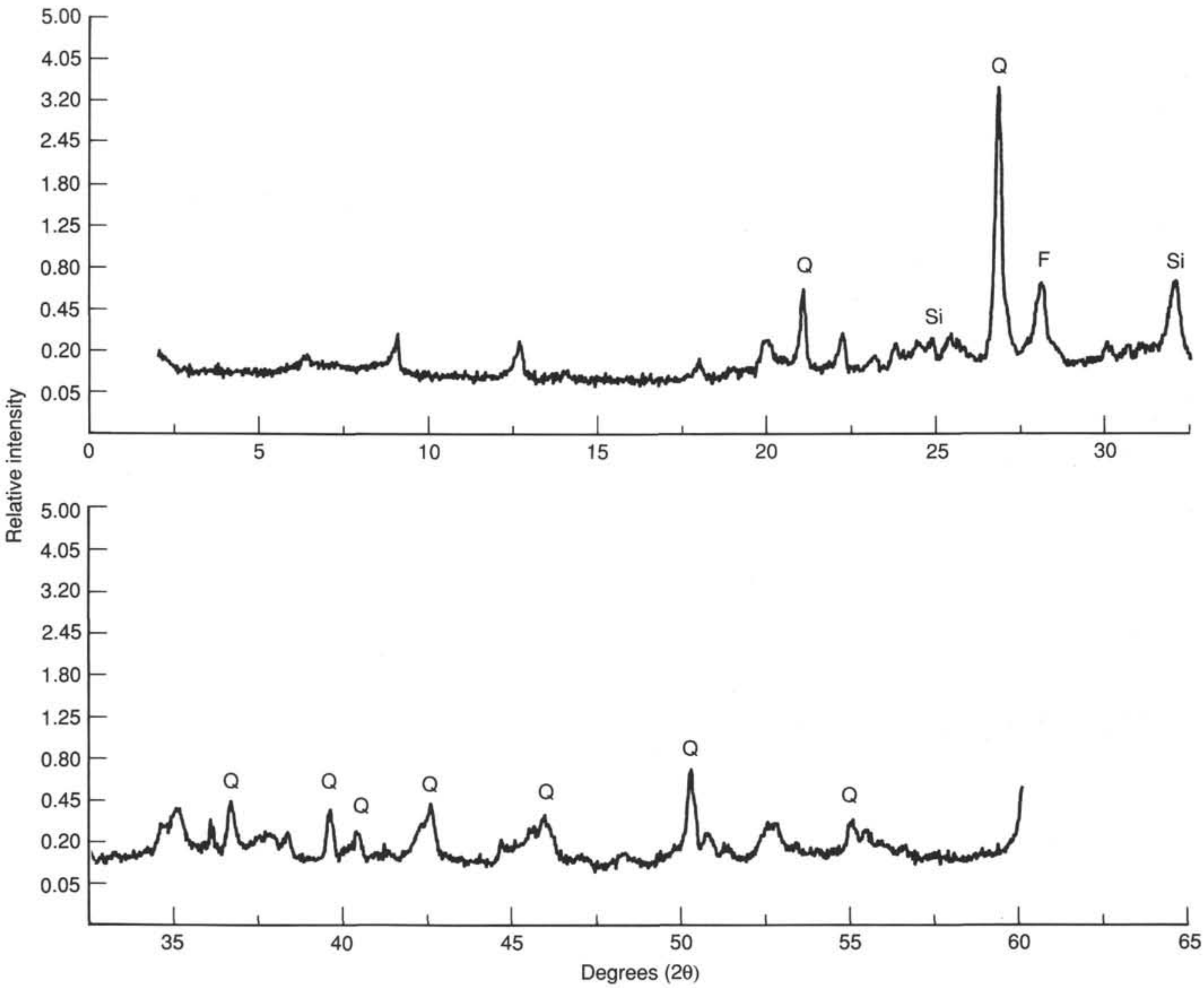

Figure 91. Same as Figure 90 except for Sample 131-808C-15R-3, 62–63 cm.

tests of the technique. Tests ASR-3 and ASR-4 were on samples from the hemipelagic sequence above the décollement, whereas tests ASR-5 and ASR-6 were on samples taken below that boundary, in an attempt to investigate the change in stress across it.

Strains of the test samples were recorded for periods increasing from 25 to 65 hr in subsequent tests, primarily because the strains were not decreasing with increasing time. As expected, the measurements on the first two samples were degraded by errors in technique. Nevertheless, these and subsequent samples were dominated by negative (shortening) strains, which increased with test duration to more than 1500 microstrains.

The general strain response, as shown in test ASR-6 (Fig. 128), was an initial very rapid negative strain on all LVDT's, which decreased approximately exponentially within 5 hr after the start of the tests, to a fairly linear rate, which continued to the end of the tests. Departures from linearity were correlated with changes in room temperature. It should be noted that the samples had come to approximate thermal equilibrium with room conditions at the start of the tests, the largest disturbance being due to surface heating during application of the wax. Comparison of internal and external temperatures showed that the thermal response in the center of the sample to be a muted reflection of external changes with a delay of 1 to 2 hr.

The large quasilinear negative strains on the various LVDT's were not random, although the initial responses were more so. Axial strains were always the largest and radial strains the smallest, with oblique strains intermediate in value (Fig. 128). Axial strains from the six tests, in the time range with linear strain, varied from 17 microstrains/hr in ASR-2 to 24 microstrains/hr in ASR-6, with no clear trend. The ratio of the minimum radial strain rate to axial strain rate for the useful tests was in the range of 0.30 to 0.52.

No estimate of the direction of maximum principal strains in the horizontal direction seems warranted, but during tests ASR-5 and ASR-6, which were the most reliable, all the radial strains were very similar.

Interpretation

The value in analyzing data from these ASR tests is more for an assessment of the technique as applied to the sediments recovered during ODP drilling than in determining the orienta-

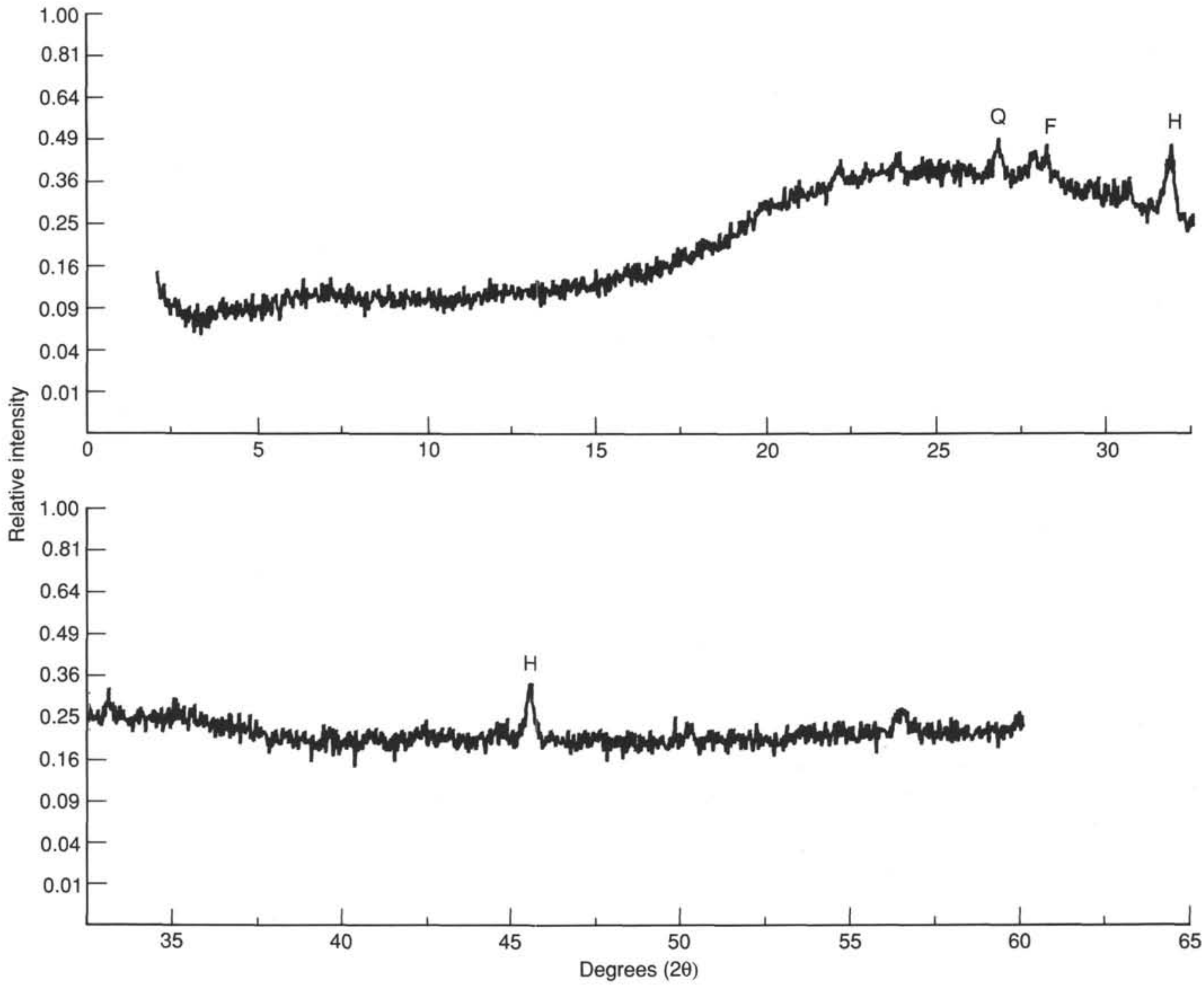

Figure 92. Same as Figure 90 except for Sample 131-808C-30R-4, 103–105 cm.

tion of stress, as it is clear that processes other than anelastic strain recovery dominated the measurements. The principal objective is to explain the negative strains and to modify the testing procedure in such a way as to avoid these, if they mask a useful signal. Possible causes of shrinkage include degassing, some delayed response of thermal stress, and desiccation.

Degassing might be visualized as causing shrinkage if the exsolution of dissolved gas put the sample into a state of tension, which then decayed as the gas escaped. The amount of gas measured in these samples was of the order of magnitude necessary to explain the response, but most of this volume should be in solution. Moreover, this process should produce an exponential decay of the strain, which was not observed.

It is difficult to assess the possible effects of thermal stress that might be caused by the rapid cooling of the core from its *in-situ* temperature to that of the drilling fluid. No such effects have been reported from ASR measurements on samples from higher temperature environments, and no information was available confirming the existence of such effects.

Volume reduction due to desiccation is the most likely cause of the negative strains. This conclusion is supported by a supplementary strain measurement run on sample ASR-6, after allowing that sample to soak in salt water for 6 days, after which it was assumed to be strain relieved and resaturated. This test (ASR-7) showed, after an initial period of mixed small strains, a suite of negative strains very similar to that observed during the initial ASR test (Table 26). Dehydration results in shrinkage through the generation of negative pore pressure, which puts the sample into compression (e.g. Wetzel, 1984). This compression resulted in a radial/axial strain ratio of about 0.4 because of the strongly anisotropic fabric of the sediment.

There is no clear trend with depth in axial strain rate or in strain ratio, as might be anticipated if there were an increase in anisotropy with decrease in porosity. In part this may reflect the different stress regimes above and below the décollement, but the variations do not show such a correlation. Moreover, the strains during the tests are functions of permeability and moisture content, both of which are variable. In particular, permeability is anisotropic and varies significantly with minor differences of lithology. Finally, the systematic distribution of negative strain points to a very small but general permeability of the wax coating rather than local leakage.

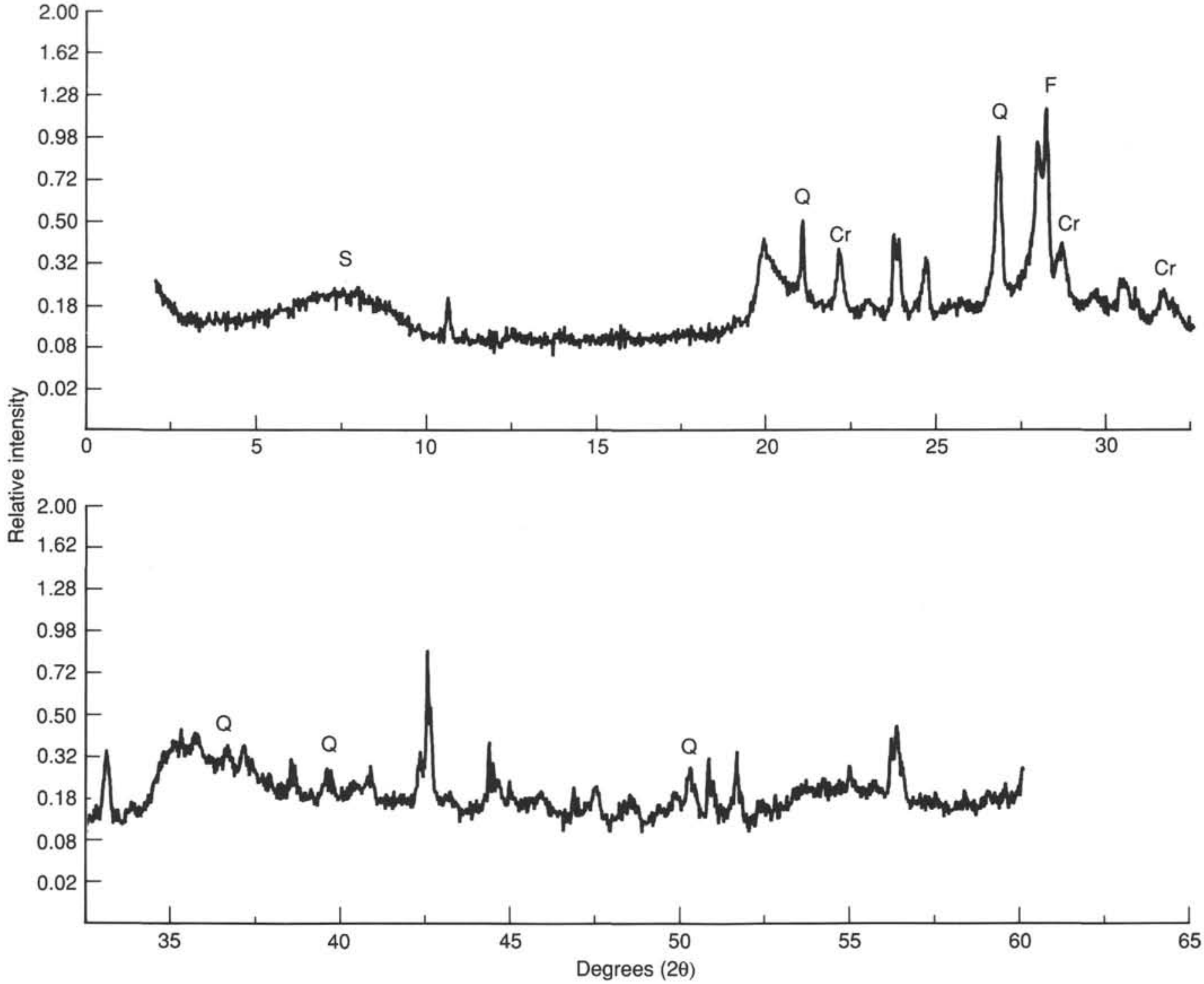

Figure 93. Same as Figure 90 except for Sample 131-808C-30R-5, 119–120 cm. The broad S peak indicates poor crystallinity.

Conclusions

Although the ASR apparatus proved quite capable of measuring anelastic strains of very small magnitude, it is still unclear as to whether poorly cemented, mud-rich sediments at depths likely to be recovered in ODP holes will display measurable anelastic strain. It does seem clear that, before this question can be answered, the problem of desiccation will have to be overcome, either by immersing the sample in a fluid such as silicon oil (Brereton *in* Gradstein, Ludden et al., 1990), or by coating it with a less- permeable material such as latex. Minor tuning of the electronic circuitry would improve the accuracy of all the measurements to better than ±0.5 microstrains, which is probably far less than the "noise" introduced by environmental effects such as errors in temperature corrections or degassing.

DOWNHOLE MEASUREMENTS

Introduction

A large variety of downhole measurements and experiments were attempted at Site 808. This section reports on the downhole logs including log temperature. The hole-bottom WSTP measurements, LAST tool, packer, vertical seismic profile (WST), and ONDO long-term downhole temperature recorder are described in other sections. The primary objectives of the logging program were to accurately define the *in-situ* physical properties in the toe of an accretionary wedge, and thus determine the effect of the tectonic deformation processes. Particularly important is the decrease in porosity and fluid loss associated with sediment accretion in a subduction zone.

A major effort was made to obtain good logs at this site, but with only limited success. Hole stability problems were severe; the upper portion of the section penetrated unconsolidated sands that readily washed out and the deeper portion penetrated clays that were subject to swelling and hole blockage. In addition, there may have been hole deformation induced by tectonic stress.

Two short open hole logs were obtained with the seismic stratigraphy tool string; from 80–180 mbsf and 525–615 mbsf. The lithoporosity and geochemical tool strings obtained data through a variety of combinations of pipe, bottom-hole assembly, and casing from the seafloor to 891 mbsf (Table 27). These

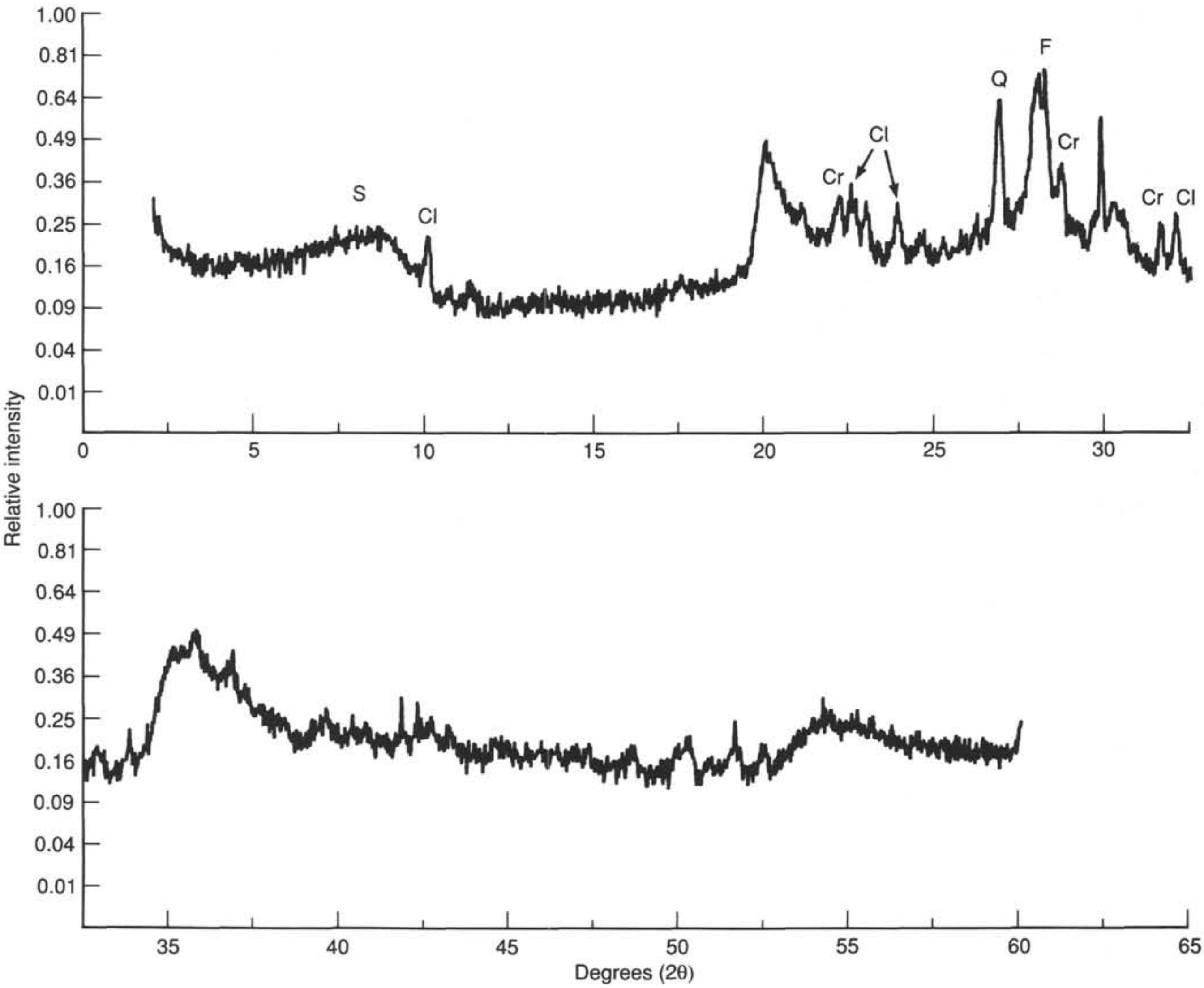

Figure 94. Same as Figure 90 except for Sample 131-808C-37R-1, 30–32 cm.

latter logs will require post-cruise editing and processing to give much useful data.

Hole 808B

Hole 808B was drilled in a water depth of 4676 m and reached a sub-bottom depth of 359 mbsf. The hole was cored with APC/XCB using a 29.5-cm (11 5/8-in.) diameter bit. Due to hole instability, only a single log run was obtained for the interval 80 to 180 mbsf, using the seismic stratigraphy tool string, including the Lamont temperature tool (TLT). Spectral gamma data were also obtained through the pipe and drill collars in the upper part of the hole. Hole instability and washouts precluded running the Formation Microscanner, which requires a diameter of less than 38.1 cm. The hole was too shallow to warrant a vertical seismic profile (VSP) with the well seismic tool (WST).

Logging Operations

Because the upper 100 m of Hole 808B penetrated unstable sandy lithologies, it was necessary to set the end of the pipe near the bottom of this interval, and to use the sidewall entry subassembly (SES). The hole conditioning prior to logging included a cleaning wiper trip and a mud sweep using 1.85% (13.5 ppt) salinity and 1 kg/L (8.8 lbs/gal)-weight mud. The wireline heave compensator was not used on the first run because the sea was calm; the compensator gives erratic responses unless ship motion is substantial. The drill pipe was lowered to 80 mbsf for the first run with the seismic stratigraphy string. The tool would not pass below 180 mbsf, so only the interval above this depth was logged, 180 to 80 mbsf in open hole and 70 mbsf to the surface through the drill collars and drill pipe. Useful data were not obtained during the entry into the pipe at 70 to 80 mbsf.

In light of the bridging (blockage) encountered on the first run, the sidewall entry subassembly (SES) was installed before the lithoporosity run. The rigging and testing of the logging string/SES for the second run proved to be difficult because of the combination of very strong near-surface current (3.0–3.5 knots to a depth of 300 m), which dragged the logging cable horizontally beneath the ship, and worsening weather conditions. The pipe was lowered to the bottom of the hole with little or no resistance from obstructions. The pipe was pulled up by 30 m and the logging tool lowered, but after the tool passed through the end of the pipe, the pipe was

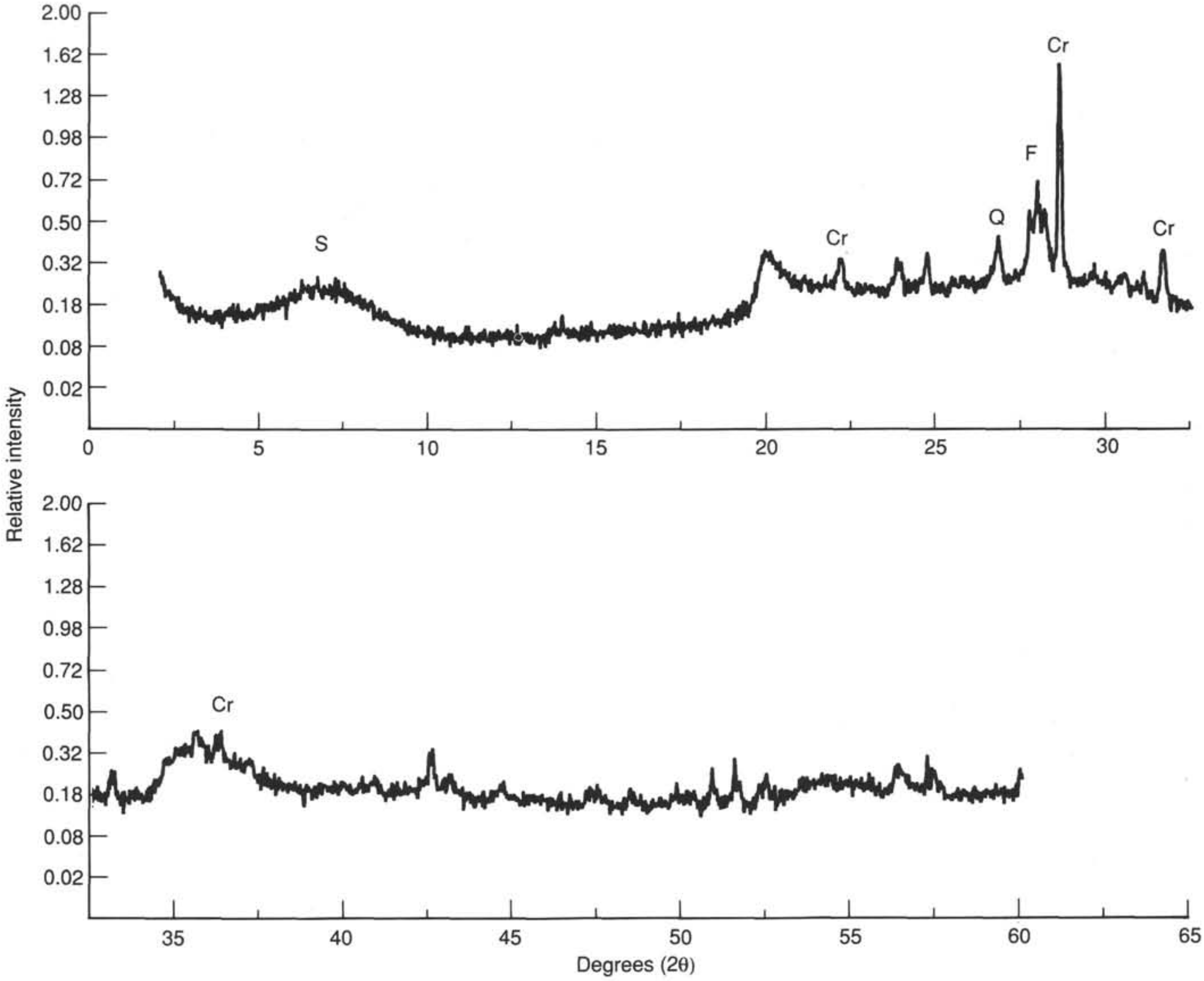

Figure 95. Same as Figure 90 except for Sample 131-808C-38R-6, 76–78 cm.

lowered again and communication to the instrument was lost. Attempts to free and raise the logging tool were unsuccessful, and when the pipe was raised, only the lowermost piece of cable and the top of the swivel were recovered. It appeared that the logging tool had been struck by the bit and severed in the hole. Fishing for the tool was unsuccessful and the hole was cemented and abandoned.

Logs Obtained in Hole 808B

The seismic stratigraphy tool string provided logs over two intervals:

(1) 70–0 mbsf (through pipe): Spectral gamma and temperature, and (2) 180–80 mbsf (open hole): Spectral gamma, resistivity, velocity, and temperature.

Summary velocity, resistivity, total gamma-ray logs are shown in Figure 129. The depth ranges are different for different log parameters because of the length of the tool string. The open-hole data quality appeared good and included three electric logs (SFLU-shallow; ILM-medium; ILD-deep), sonic log (MEDDT), total gamma log, as well as uranium, potassium, and thorium determined from the gamma spectra. The TLT gave good data only on the upward run because the temperatures were disturbed by the irregular motion on the downward run as the tool was moved up and down in the hole while attempting to break through bridges.

Hole enlargement in prominent sand sequences was a problem in this hole. No caliper log was obtained, but limited hole diameter information is available from the sonic log. The sonic caliper employs a seismic refraction interpretation technique for the different-length travel paths. Eight hole radii estimates are obtained from the four processed traveltimes generated by the tool. The radii are calculated from the traveltimes using an *in-situ* fluid velocity estimated for the density and salinity of the mud in the hole. The sonic caliper data show the sections where log-determined parameters should be treated with caution. The data from the lowermost 5 m of the logged section probably reflect a large wash out. Collapse of this formation into the hole may also have been the cause of the hole blockage. In the upper 10 m of the logged section the resistivity logs gave erratic results and are unreliable because of instrument problems.

Short variable depth offsets of up to 1 or 2 m are apparent from the detailed matching of thin layers on the different logs in the string. Even with moderate sea conditions, some ship heave and cable stretch is transmitted to the downhole tools. Thus, care must be taken in very detailed cross-correlation

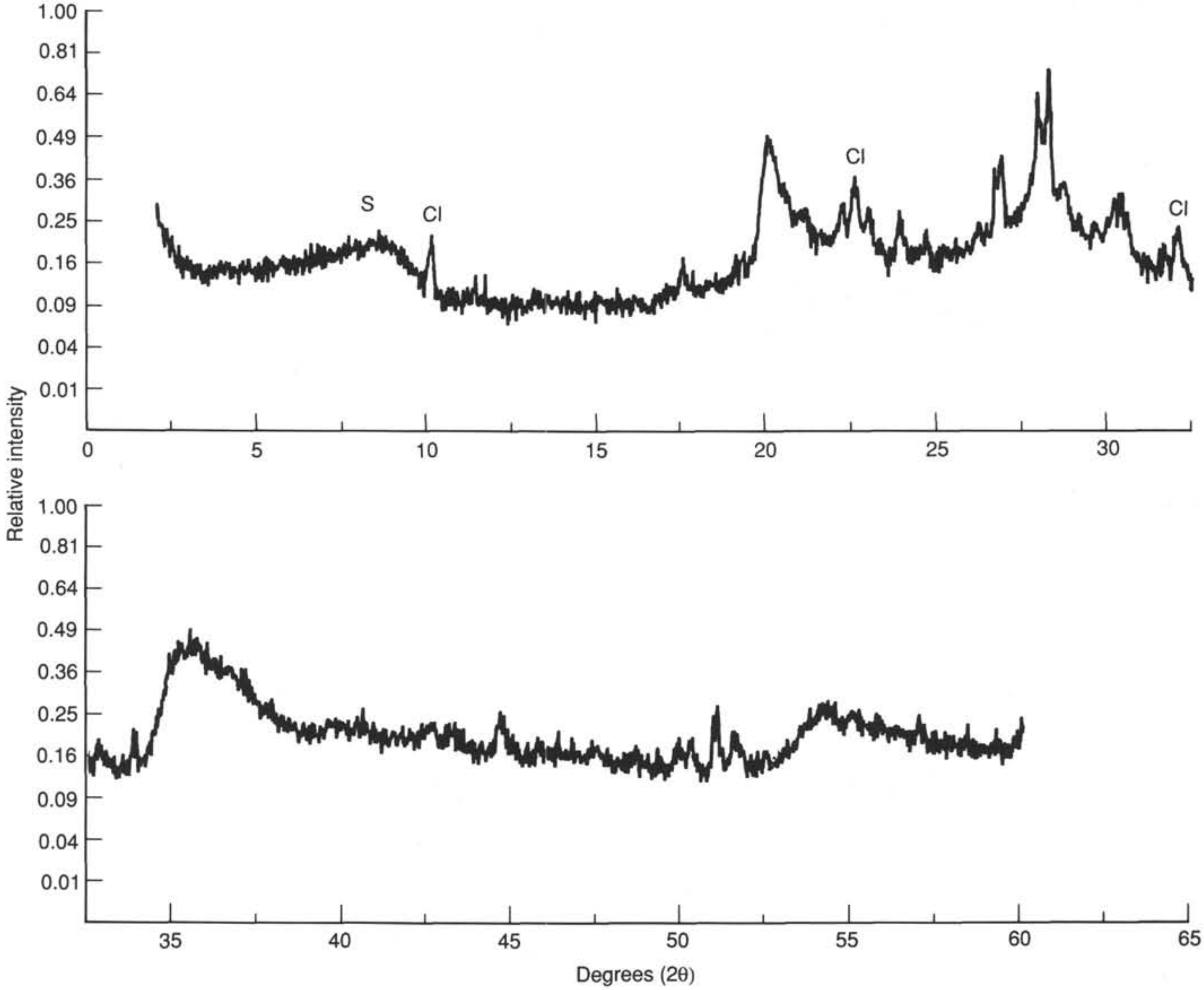

Figure 96. Same as Figure 90 except for Sample 131-808C-45R-3, 55–57 cm.

between the logs in a single string; either depth adjustments must be made or smoothed data used in correlations.

Only very minor differences were evident between the different sonic log outputs. A limited amount of data correction was carried out, consisting of removing unreliable data points exhibiting cycle skipping as detected from anomalously large or small measured traveltimes or differences between pairs of traveltimes. The median slowness (MEDDT) and the derived sonic velocity are calculated from the pairs of processed traveltimes.

The three electrical logs also give very similar records, with the exception that the thin high resistivity zones that correspond to high velocity zones are only resolved in the higher resolution SFLU log (see below). The separation between the three logs is a function of their depth of investigation; they will differ primarily because of the degree of borehole irregularity and the extent of infiltration of drilling fluid that has a different resistivity to the formation fluid.

The logs through pipe show a pronounced and variable attenuation effect. The total gamma, uranium, thorium, and-potassium logs for the complete section of the hole are shown in Figure 130. There is a large difference in log amplitude through the casing and through the thicker drill collars (that extend to the seafloor), which has been roughly compensated by multiplying the amplitudes by a factor of 2 for the casing alone and a factor of 4 for the casing and drill collars (see below). A more accurate estimate of attenuation will be carried out after the cruise.

Temperature

One log was obtained with the TLT temperature tool to 200-mbsf depth in Hole 808B (Fig. 131). Only the up-going log gave useful data. Because of the frequent oscillation of the probe associated with efforts to break through bridges, both the temperature and pressure (depth) records were very irregular on the down-going log. The up-going log suffers from the disturbance associated with the pushing of the borehole fluid ahead of the tool in the within-pipe portion of the log as the tool diameter is close to the pipe internal diameter. The large mass of tool ahead of the sensor that is at the bottom of the string may also be important. The bottom-water temperature was recorded at about 1.6°C, which agrees well with

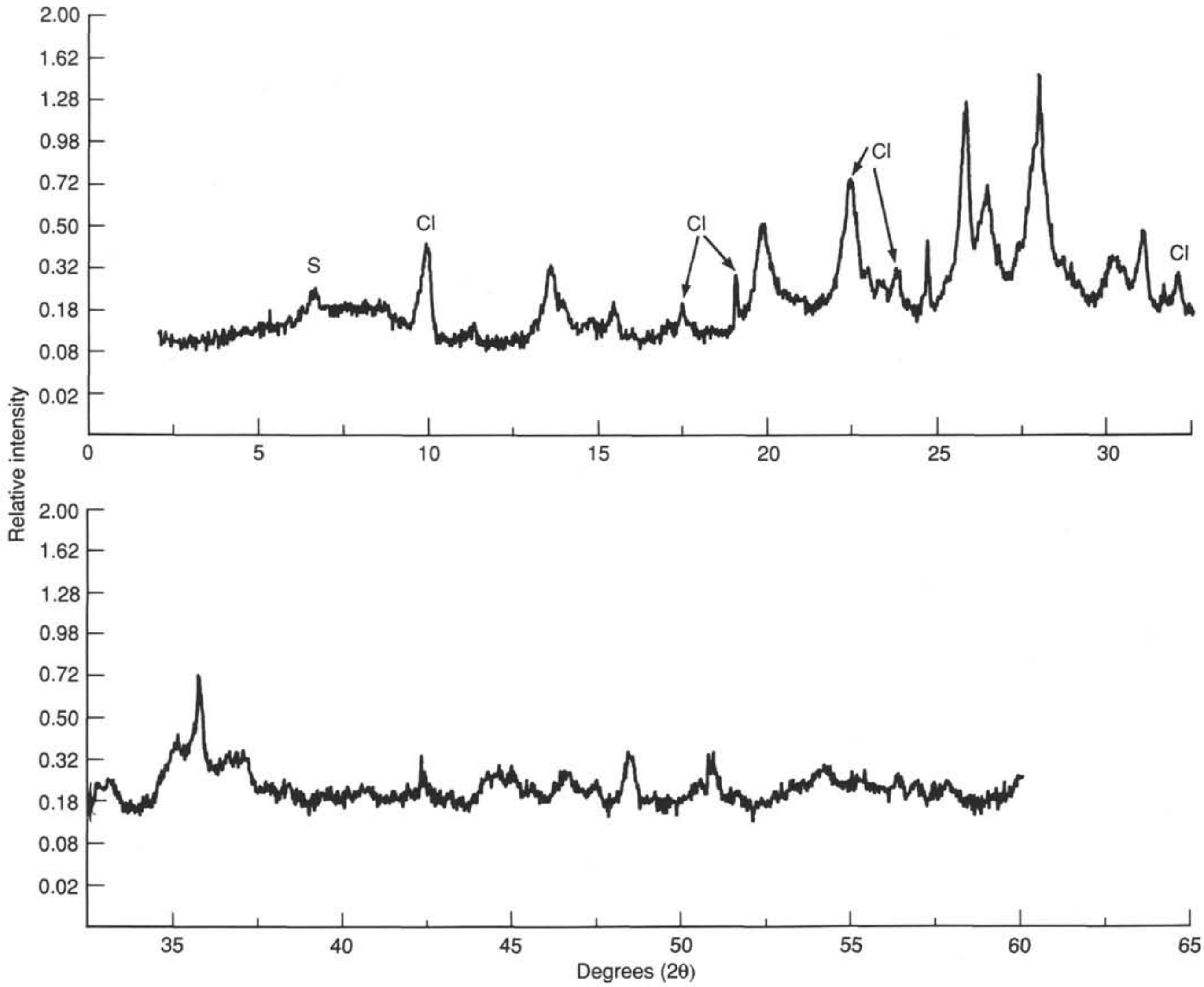

Figure 97. Same as Figure 90 except for Sample 131-808C-54R-1, 65–67 cm. S peak shows better crystallinity than the shallower samples.

oceanographic data, and the temperature increased smoothly with depth to approximately 6°C at 200 mbsf This is much less than the sediment *in-situ* temperature of about 26°C estimated from the WSTP measurements at the site, indicating that only a small part of the drilling disturbance had decayed at the time of the log. The temperature log data are presented and interpreted in the Heat Flow section, this chapter, along with the WSTP and thermal conductivity data.

Hole 808C

Coring at Hole 808C used a 25.1-cm (9-7/8-in.) diameter rotary coring bit to a depth of 1327 mbsf. Three downhole log runs were made within the drill pipe to a depth of 880 mbsf. Temperature data only were obtained on the first run with the seismic-stratigraphy string, as the cable was damaged and the temperature tool has a self-contained recording system. Through-pipe data were obtained from the lithoporosity and geochemical strings on the subsequent two runs.

Logging Operations

The drill-in casing was set from 19–105 mbsf. Based on the core-sample data, the interval from 550 to 840 mbsf with extensive volcanic ash in the hemipelagic muds had particular potential for swelling and blockage of the hole (Clay Instability Tests, this chapter), especially between 550 and 700 mbsf. Two wiper trips to clean the hole were followed by filling the hole with mud: seawater + 4% KCl + lime + prehydrated gel + Pac-R, having a weight of 1 kg/L (8.8 lb/gal) with a salinity of 3.6% (36 ppt). In spite of the addition of the KCl, further wiper trips met with generally steady resistance (see Operations, this chapter) and the décollement was considered too unstable to leave the pipe set across it.

For the seismic stratigraphy run, the pipe was set at 747 mbsf. The tool stopped at a bridge before it was completely out of the pipe. Attempts to break through resulted in temporary tool failure, and cable kinking was suspected, so the tool was recovered. Upon recovery at the rig floor, 1 m of cable just above the tool was found to be kinked. The landing cone of the temperature tool at the base of the string was filled with a plug of dense mud indicating that the tool had encountered a bridge.

After a wiper trip from 748 mbsf to the total drilled depth encountered steady resistance both down and up, especially across the décollement zone, the pipe was positioned at 981

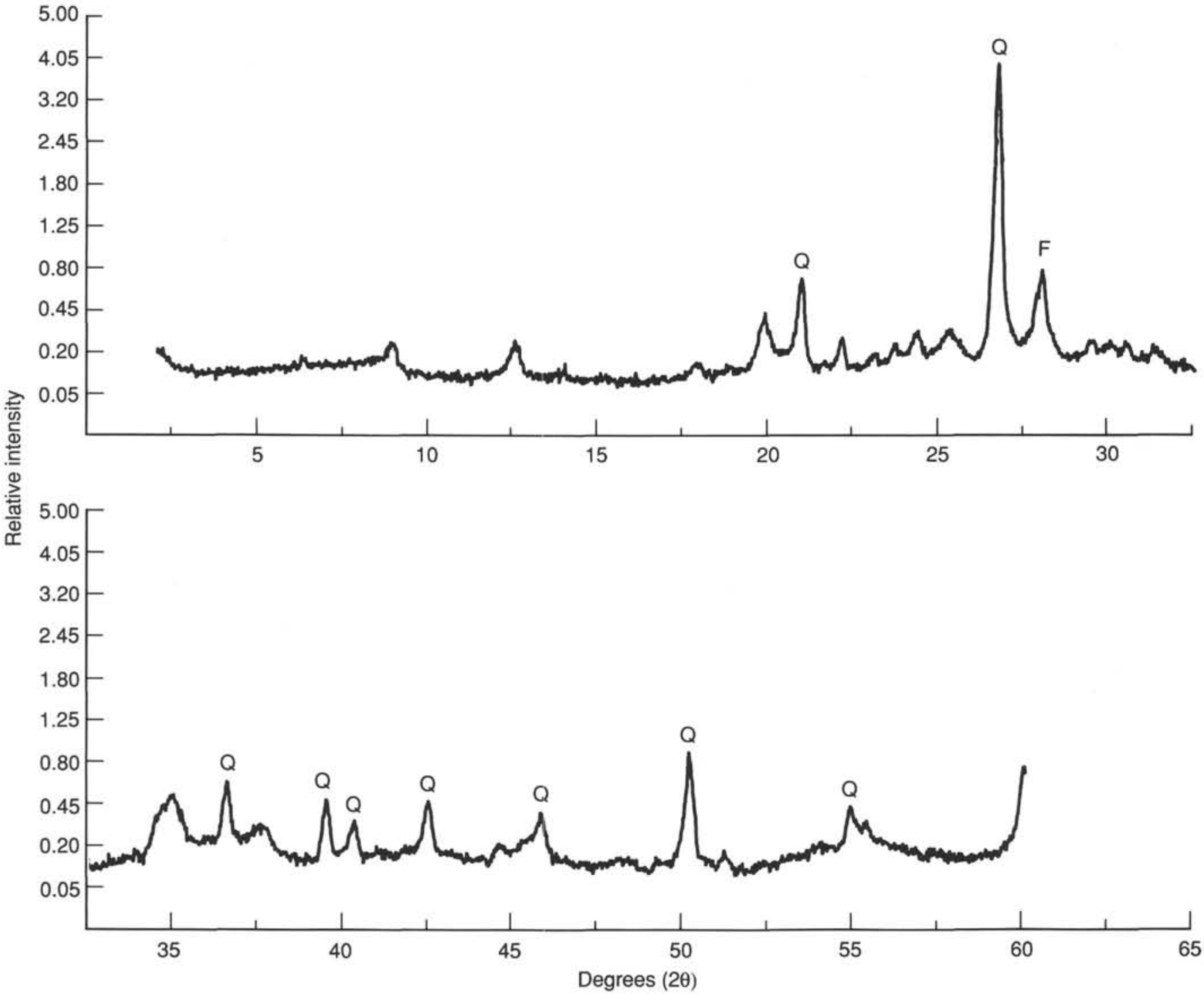

Figure 98. Same as Figure 90 except for Sample 131-808C-57R-4, 142–145 cm.

mbsf, which was the greatest depth considered to be safe. We decided to run the lithoporosity tool string, as a through-pipe log could be obtained even if the tool could not penetrate the open hole. It proved impossible to enter the open hole and through-pipe logs were obtained at 150 m/hr from 891 mbsf to the seafloor.

At this time, mud was pumped at a high rate to attempt to blow out any mud that might be plugging the end of the pipe; no sudden pressure drop was observed to indicate that a plug had been blown out. We thus concluded that no open-hole logs could be obtained. Wiper trips had not improved the hole conditions appreciably and the SES was not considered safe because of the significant resistance met by the drill string on each wiper trip; the SES does not allow pipe rotation. The clay swelling or other source of hole collapse appeared to be distributed down much of the hole. The geochemical tool string was then also run through the pipe at 150 m/hr; it too was unable to penetrate into the open hole.

Logs Obtained in Hole 808C

No open-hole logs were obtained in this hole. The seismic stratigraphy string obtained temperatures only, as that parameter is internally recorded, and cable damage prevented other recording. The two other strings recorded through-pipe logs (Fig. 132).

The through-pipe logs are strongly affected by the presence of the pipe. Not only does the extra thickness of pipe reduce the amplitude of the signal reaching the tool detectors, but the variable thickness of the drill string (joints, bottom-hole assembly) introduces offsets and regular spikes into the data. This problem is discussed briefly in a later section. An initial attempt at filtering the pipe-joint spikes is shown in Figure 133. A Fourier transform filter using a 30-point spectral window was used to remove short spatial wavelength components in the logs (< 10 m). This filter was effective to some degree in removing the sharp spikes, but wavelengths equal to the pipe-joint spacing are still evident.

All of the basic logs exhibit significant variation, at least a factor of two (gamma, porosity, density, some geochemical). Some check on the degree to which the through-pipe logs are responding to the formation rather than to hole conditions is provided by a comparison with the short open-hole log of Hole 808B over 110 to 160 mbsf. A detailed correlation within laterally variable section is not expected because of the offset

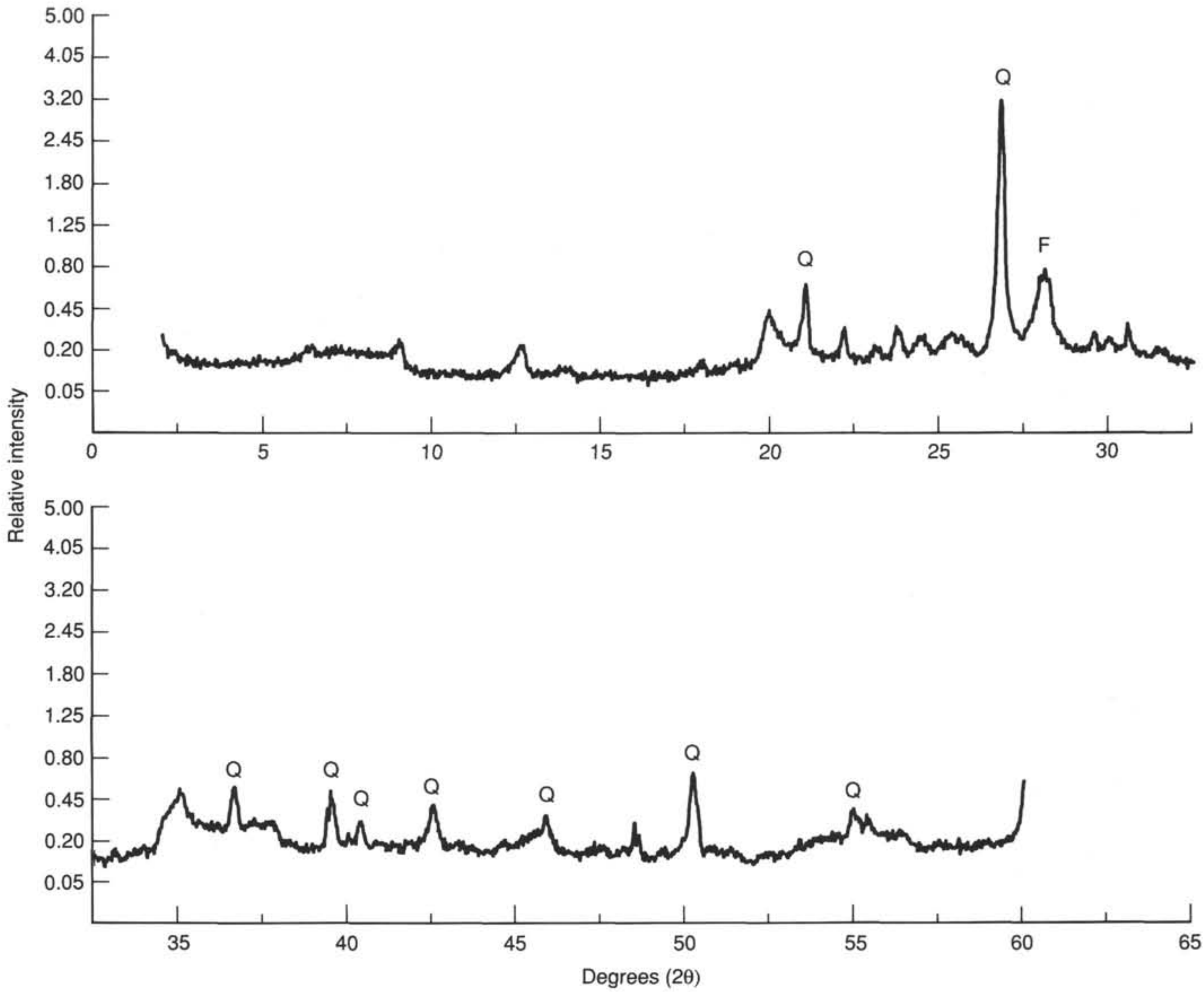

Figure 99. Same as Figure 90 except for Sample 131-808C-73R-1, 11–13 cm.

of the two holes, but the average levels and amplitudes are approximately the same. Some correlations are evident such as the irregular decrease in uranium above 110 mbsf.

Temperatures

One TLT log was obtained on the seismic stratigraphy run in the pipe in Hole 808C. The TLT appears to have recorded good temperatures during the lowering and on part of the upward log (Fig. 134). The seafloor temperature (1.6°C) agrees well with nearby oceanographic data, giving some confirmation of the calibration. The measurement depth was obtained from the instrument pressure record, corrected using the estimated mud density (see Explanatory Notes chapter, this volume). Although the mud may have been partly pumped out of the pipe (into the hole), good agreement with the position of the seafloor and of the bottom of the hole were then obtained. Both the down-going and up-going logs will be affected by the fluid in the pipe being pushed ahead of the tool, but the effect of the tool is undoubtedly most serious on the up-going log. The up-going log gave temperatures 2° to 4°C higher than the down log.

The temperature profile is roughly linear (±3°C variation) with a gradient of about 50 mK/m, about half that of the gradient indicated by the WSTP at this site. This seems a reasonable recovery from the drilling disturbance to equilibrium temperatures (about 50%), assuming the WSTP temperatures reflect equilibrium. Drilling circulation rates and times were recorded and it may be possible to obtain near-equilibrium temperatures by taking these into account.

Of particular interest is the temperature near the top of the hole, which is about 14°C above seafloor temperature. The upper 180 m of the hole also has a low gradient. This high temperature could result from drilling disturbance; drilling fluid that has been warmed at depth in the hole is circulated up the outside of the pipe. However, the offset from seafloor temperature is remarkably large, and there is the possibility that the high temperature reflects an upward water flow in the hole from between 150 to 180 mbsf, to the surface. Such a flow would probably be initiated by the hole connection to the surface from a permeable and overpressured formation. It does not require an upward flow through the formation prior to drilling. This depth corresponds to quite substantial

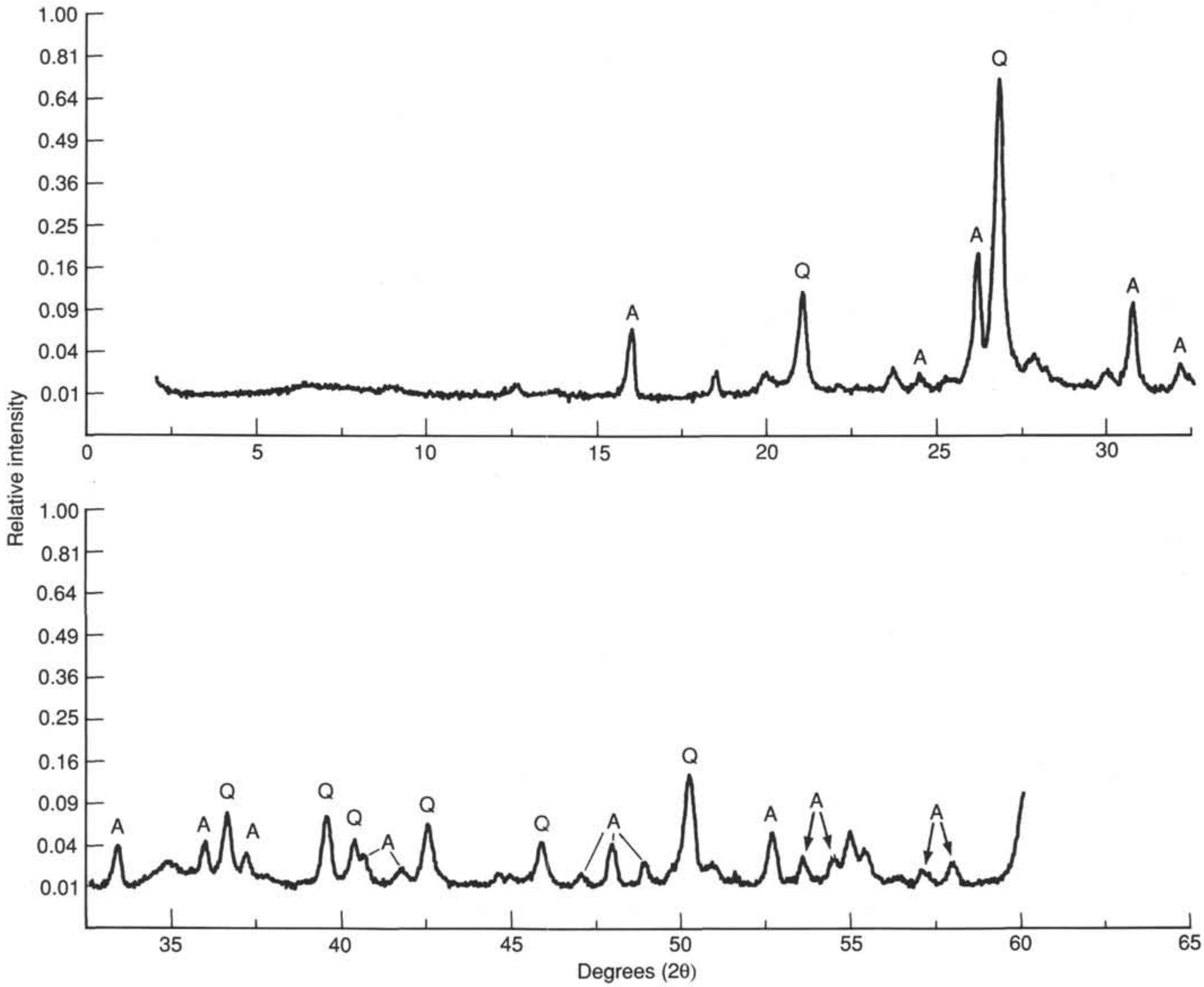

Figure 100. Same as Figure 90 except for Sample 131-808C-100R-CC, 20–22 cm.

changes in core pore-water chemistry (see Inorganic Geochemistry section, this chapter).

Hole 808E

Introduction

Hole 808E was drilled without coring with a 37.5-cm (14-3/4-in.) diameter bit to a depth of 554 mbsf for casing. Casing was set to a depth of 524 mbsf. The remainder of the hole to a total depth of 1200 mbsf was drilled without coring using a 25.1 cm (9-7/8-in.) diameter bit. The primary objective was to obtain logs across the décollement. This proved not to be possible, and due to hole instability only a short open-hole section of log was obtained with the seismic stratigraphy string on two runs, extending from 524–576 and 524–622 mbsf. Through-casing gamma logs were obtained to the seafloor.

Logging Operations

After wiper trips and circulation, the hole was filled with mud of composition: seawater +3% KCl + lime + prehydrated gel + Pac-R; weight 1.2 kg/L (10.5 lb/gal), salinity 2.1% (21 ppt). In spite of the KCl addition, wiper trips met with some limited resistance (see Operations, this chapter) and the décollement zone was considered too unstable to leave the pipe set across it.

For the first logging run of the seismic stratigraphy, the BHC sonic tool was used instead of SDT, as the SDT failed during preparation. The pipe was set in the casing at 54 mbsf. The tool stopped at a bridge at 576 mbsf, and the hole was logged upward from this point.

A short wiper trip was made to again clear the upper portion of the hole for logging, and the pipe was positioned in the casing at 487.5 mbsf. The seismic stratigraphy/temperature string was run again, this time reaching 621.6 mbsf.

Following another wiper trip, the drill string was brought to the surface, the drill-string packer and the landing shoe added to the BHA, and reentry made. The landing shoe is designed to take some of the pipe weight on the cone, thereby steadying the pipe and reducing noise for the VSP. In spite of the use of the landing shoe, the noise level recorded by the WST was very high (see Seismic Stratigraphy and Vertical Seismic Profile sections, this chapter). The drill-string packer was then deployed just inside the casing, but no useful data were obtained (see Packer Experiments, this chapter).

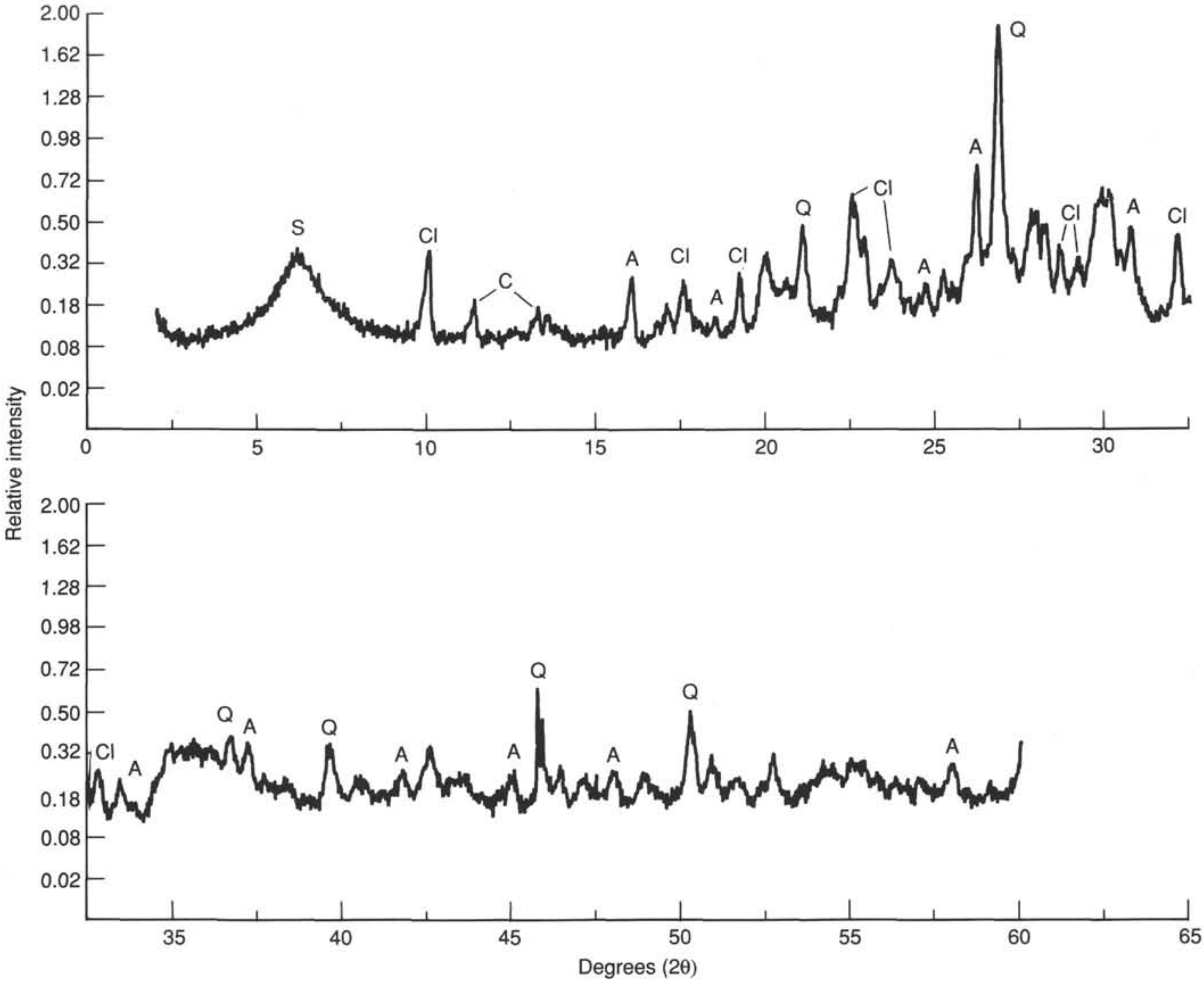

Figure 101. Same as Figure 90 except for Sample 131-808C-102-R-2, 30–32 cm.

Logs Obtained in Hole 808E

A short section of open-hole data with the seismic stratigraphy string was obtained on two runs with some overlap (Fig. 135), and the remainder of the hole was logged through the casing (Fig. 136).

The quality of the open-hole logs appears good. No problems were encountered leaving or reentering pipe or casing. As discussed below, the logs through the casing and casing/pipe need further post-cruise processing. Based on the sonic, resistivity, and gamma-ray logs, a qualitative interpretation of hole diameter was made, and two intervals with suitable packer seats were identified. The large-diameter section below the cased interval is apparent on the logs. Several washouts are also apparent from 533.8–539.9 mbsf, 566.7–570.4 mbsf, and 572.2–574.7 mbsf, as well as the intervals of gauge hole mentioned above. There is a substantial difference among the three electrical logs of different penetrations, not seen in the shallower open-hole section (Fig. 135). This may result from using more conductive mud in comparison to that in Hole 808B. The low resistivity values associated with the high temperature in this borehole should also be noted. No sonic caliper has as yet been computed for this open-hole section, so the influence of hole size is not known. This will be determined during post-cruise processing.

The through-casing logs show apparently good data. There seems to be uniform attenuation without the major effect of joints seen on the through-drill-pipe logs. The hole diameter variation behind the casing is unknown, but may be much smaller than that for the in-pipe logs. As noted below there is reasonable correlation between these logs and the core-defined lithology.

Temperature

Two temperature logs were obtained, one on each seismic stratigraphy run (Fig. 137). As in Hole 808C, only the downgoing logs give good data. For the first run, the pipe was set near the top of the casing so the last short period of mud circulation only disturbed measurements from that point to the seafloor. For the second run, the pipe was set near the bottom of the casing, and the disturbing effect of the short period of mud circulation extending from that depth to the seafloor is evident. In the open-hole section (below 524 mbsf), temperatures are less disturbed by mud circulation and are close to the equilibrium formation temperature estimated from the WSTP data. The down-going runs were at a slow logging speed of 300 m/hr. The second up-going run was at a much higher speed. The finite response time of the probe may explain the high temperatures obtained. Also, there may have been mud plugging the sensor and slowing the response time.

Analysis of Log Data

Open-hole Borehole Diameter Corrections Using Sonic Caliper

Many of the logs run are very sensitive to hole-diameter variations, and as no caliper was run on any of the logs, there is a serious problem with hole-diameter corrections. The sonic log provides a low-accuracy diameter log for the open-hole sections that can be used to correct the other logs. As discussed below, there is no information available on hole diameter for in-pipe logs, and such hole diameter variation may be the source of much of the apparent variation in these logs. The sonic caliper hole-diameter correction has so far only been applied to the open-hole total gamma-ray log for the upper open-hole section from Hole 808B (Fig. 138). A substantial correction of up to 20% for much of the logged section is required. Future processing will need to evaluate the sonic caliper and the need for further hole-diameter corrections to the open-hole logs.

Log Attenuation Through the Pipe and Casing

Much of the depth interval logged at Site 808 was through the drill pipe, BHA or casing. Their presence has a pronounced effect on all of the responses. The pipe joints show up strongly as anomalous values over 1 to 2 m sections at 10-m intervals on all of the basic logs, and the presence of the casing and the BHA are also obvious (e.g., Fig. 132). These effects will need close study and post-cruise processing if really useful information is to be obtained. Only a qualitative assessment is presented here. An indication that at least the gamma log is measuring material outside the pipe is given by the good agreement between the ex-centralized gamma on the lithoporosity tool and the centralized gamma on the geochemical tool. The porosity from the lithodensity neutron tool and that from hydrogen on the geochemical tool are also very similar.

As a test, a qualitative correction for pipe attenuation has been applied to the through-pipe logs of Hole 808B for total gamma, uranium, thorium, and potassium (Fig. 130). There is a large difference in log amplitude through the casing and through the thicker drill collars (that extend to the surface), which has been roughly compensated by multiplying the amplitudes by a factor of two for the casing alone and a factor of four for the casing and drill collars.

An examination of all of the logs shows that the gamma log within the pipe is attenuated by approximately 60% by comparison with the small overlap of the measured open-hole and within-pipe sections. The amplitude of the gamma through the pipe joints is reduced by about 80%, and through the BHA by about 75%. These ratios approximately correspond to the relative thicknesses of the pipe, pipe joints, and casing (pipe 1.85 cm, pipe joints 7.32 cm, casing 2.2 cm, BHA 5.0 cm avg.). Figure 139 shows the estimated attenuation with thickness. There is some indication that the U amplitudes may be attenuated more than the K or Th amplitudes, perhaps associated with the different gamma energy bands used. The attenuation appears to be roughly similar for the other logs such as the density and the porosity.

The filtered version of the through-pipe Hole 808C logs (Fig. 133) shows the long-wavelength trends. However, it is evident that the pipe-joint sections will need to be actually corrected in amplitude or removed. Because they approach delta functions, they contain energy at all wavelengths and cannot effectively be filtered.

The interference of the pipe has been reasonably successfully removed from porosity, density, and geochemical logs during post-cruise processing in the past, so it is hoped that these logs can be processed to give useful data. Probably much more serious than the reasonably predictable attenuation by drill pipe and casing is the inability to determine the hole diameter in this probably enlarged hole.

Problems of Hole Diameter and Washouts for Within-pipe Logs

Unfortunately, much of the observed within-pipe log variations may be associated with variations in hole diameter. Part of the variability could be associated with the position of the pipe with respect to the center of the hole, but the good agreement between the two gamma and two porosity logs suggests that this is not a serious problem. The main problem is the unknown and probably highly variable hole diameter. The effect is probably very large; note that the hole diameter correction to the gamma log in open Hole 808B using the sonic caliper was commonly 20% and in places much more (Fig. 129). There are indications of both highly variable hole diameter and of short washout sections.

Sections in the upper part of the hole with both low gamma and high inferred porosity from resistivity and velocity, are probably enlarged. In unconsolidated terrigenous sediments, the opposite correlation is expected; high porosity is associated with finer grained sediments that should generally have higher gamma response than sandy sections, as seen in the open-hole logs. However, it should be noted that the correlation between porosity and grain size (and probably gamma) is reversed at greater depths; i.e., below about 500 to 1000 mbsf, sands tend to have greater porosity than muds because of the much more rapid consolidation with depth of muds compared to sands (Busch, 1989 and references therein).

Several geochemical logs provide indicators of major hole enlargement. The H/Si ratio appears to be most sensitive. Without hole enlargement, this ratio should approximately follow porosity. It has very high and irregular amplitudes at the restricted intervals that correspond to the high-porosity, low-gamma sections. Hole sections with H/Si ratios higher than about double the general level (above about a factor of two in the pipe sections) are undoubtedly seriously washedout to large hole diameter, and in these sections most of the other logs are unlikely to be reliable.

The larger gamma, porosity, and density variations are associated with large H/Si excursions so may primarily reflect hole-diameter variations. Of course, washouts are also a lithology indicator, probably of uncemented sand. Major washouts are indicated at approximately 270–290 mbsf, 315–415 mbsf, 480–510 mbsf, 550–560 mbsf, and 605–615 mbsf, and minor washouts are present over many other sections.

It is important to note that while the log amplitudes are attenuated through the casing such as in the upper 110 m of Hole 808B, there are no strong washout indications. The formation is probably relatively tight against the outside of the casing. Thus, logs through casing may be more useful than through pipe in a hole of unknown diameter.

Log Trends in Through-Pipe Logs

Although probably strongly affected by the hole-diameter problem, the density log does suggest a small density decrease from near the seafloor to 500 mbsf, then an increase to greater depths. In contrast, there may be a small increase in porosity with depth; again this is barely resolved, with the large

Table 18. Molecular composition of headspace gases, total organic carbon and nitrogen content of sediment samples from Site 808 (n.d.: not determined). Gas concentrations (μL/kg) are mL gas per kg organic carbon of sediment.

Hole	Core	Type	Sect.	Top cm	Bottom cm	Depth mbsf	Methane μL/kg	Ethane μL/kg	Propane μL/kg	*i*-Butane μL/kg	*n*-Butane μL/kg	*i*-Pentane μL/kg	*n*-Pentane μL/kg	C_1/C_2	$\frac{C_1}{C_2+C_3}$	C_2/C_3	C_3/C_{4+}	$i\text{-}C_4/n\text{-}C_4$	C_4/C_5	TOC %	N %	C/N
808A	1	H	2	145	150	2.95	14	0.00	0.00	0.00	0.00	0.00	0.00							0.58	0.08	7.25
808A	2	H	6	0	5	13.80	2421	0.00	0.00	0.00	0.00	0.00	0.00							0.66	0.11	6.00
808A	3	H	6	0	5	23.30	1866	0.00	0.00	0.00	0.00	0.00	0.00							0.73	0.10	7.30
808A	4	H	2	0	5	26.80	1237	0.00	0.00	0.00	0.00	0.00	0.00							0.63	0.11	5.73
808A	5	H	6	130	134	43.60	851	0.00	0.00	0.00	0.00	0.00	0.00							0.66	0.11	6.00
808A	6	H	1	0	5	44.30	1972	0.00	0.00	0.00	0.00	0.00	0.00							0.34	0.06	5.67
808A	7	H	2	5	10	55.35	2056	0.00	0.00	0.00	0.00	0.00	0.00							0.62	0.11	5.64
808A	8	H	1	133	135	64.63	976	0.00	0.00	0.00	0.00	0.00	0.00							0.52	0.09	5.78
808A	9	H	4	0	5	72.80	938	0.00	0.00	0.00	0.00	0.00	0.00							0.63	0.12	5.25
808A	10	H	5	0	5	83.90	2634	0.00	0.00	0.00	0.00	0.00	0.00							0.13	0.04	3.25
808A	13	H	2	118	122	109.08	1010	0.00	0.00	0.00	0.00	0.00	0.00							0.60	0.11	5.45
808B	4	X	1	0	3	139.90	1164	0.00	0.00	0.00	0.00	0.00	0.00							0.74	0.11	6.73
808B	5	X	2	0	3	151.00	1713	0.00	0.00	0.00	0.00	0.00	0.00							0.48	0.08	6.00
808B	7	X	3	0	2	171.80	1236	0.00	0.00	0.00	0.00	0.00	0.00							0.42	0.08	5.25
808B	9	X	3	0	2	191.20	780	0.00	0.00	0.00	0.00	0.00	0.00							0.75	0.12	6.25
808B	10	X	4	0	5	201.90	1262	0.00	0.00	0.00	0.00	0.00	0.00							0.83	0.11	7.55
808B	11	X	1	145	150	208.25	853	0.00	0.00	0.00	0.00	0.00	0.00							0.86	0.10	8.60
808B	13	X	2	0	3	227.30	1951	0.00	0.00	0.00	0.00	0.00	0.00							0.75	0.12	6.25
808B	14	X	1	0	3	235.10	2473	0.00	0.00	0.00	0.00	0.00	0.00							0.84	0.11	7.64
808B	15	X	cc	0	3	245.40	368	0.00	0.00	0.00	0.00	0.00	0.00							0.26	0.06	4.33
808B	16	X	1	118	121	255.38	262	0.00	0.00	0.00	0.00	0.00	0.00							0.65	0.08	8.13
808B	17	X	2	127	130	266.17	1285	0.00	0.00	0.00	0.00	0.00	0.00							0.81	0.12	6.75
808B	19	X	2	147	150	285.47	700	0.00	0.00	0.00	0.00	0.00	0.00							0.62	0.11	5.64
808B	20	X	2	0	3	289.40	570	0.00	0.00	0.00	0.00	0.00	0.00							0.66	0.11	6.00
808B	22	X	1	0	2	307.10	2077	0.00	0.00	0.00	0.00	0.00	0.00							0.59	0.10	5.90
808B	23	X	1	0	2	316.80	3241	0.00	0.00	0.00	0.00	0.00	0.00							0.61	0.10	6.10
808B	24	X	2	62	65	328.52	723	0.00	0.00	0.00	0.00	0.00	0.00							0.51	0.10	5.10
808B	25	X	3	132	135	338.82	298	0.04	0.00	0.00	0.00	0.00	0.00	7102	7102					0.69	0.12	5.75
808C	1	R	1	130	132	299.80	1254	0.24	0.00	0.00	0.00	0.00	0.00	5336	5336					0.75	0.11	6.82
808C	2	R	1	64	66	308.64	341	0.07	0.00	0.00	0.00	0.00	0.00	5223	5223					0.66	0.11	6.00
808C	3	R	1	0	3	317.60	250	0.07	0.00	0.00	0.00	0.00	0.00	3538	3538					0.66	0.10	6.60
808C	4	R	1	0	3	327.20	2725	0.63	0.00	0.00	0.00	0.00	0.00	4317	4317					0.61	0.10	6.10
808C	5	R	cc	0	3	337.40	1056	0.22	0.00	0.00	0.00	0.00	0.00	4737	4737					0.67	0.10	6.70
808C	6	R	1	0	3	346.60	2809	0.52	0.00	0.00	0.00	0.00	0.00	5354	5354					0.61	0.09	6.78
808C	7	R	1	59	60	356.79	2630	0.42	0.00	0.00	0.00	0.00	0.00	6270	6270					0.56	0.10	5.60
808C	8	R	2	124	126	368.64	739	0.23	0.00	0.00	0.00	0.00	0.00	3212	3212					0.65	0.11	5.91
808C	9	R	1	131	132	376.91	1511	0.22	0.06	0.00	0.00	0.00	0.00	6723	5378	4.0				0.65	0.10	6.50
808C	10	R	3	99	100	389.19	1895	0.73	0.24	0.03	0.00	0.00	0.00	2595	1946	3.0	8.0			0.60	0.08	7.50
808C	11	R	1	0	2	394.80	1933	0.62	0.35	0.05	0.00	0.00	0.00	3134	2009	1.8	7.0			0.74	0.10	7.40
808C	12	R	3	0	2	407.60	2477	1.06	0.96	0.20	0.00	0.00	0.00	2344	1228	1.1	4.8			0.57	0.09	6.33
808C	13	R	2	133	135	417.13	4819	1.42	0.86	0.17	0.00	0.00	0.00	3396	2114	1.6	5.0			0.43	0.12	3.58
808C	14	R	3	124	126	428.24	1957	0.80	0.49	0.10	0.00	0.00	0.00	2441	1511	1.6	5.0			0.60	0.09	6.67
808C	15	R	1	133	136	435.03	2277	0.63	0.39	0.05	0.00	0.00	0.00	3638	2252	1.6	8.0			0.61	0.11	5.55
808C	16	R	5	59	60	449.59	1729	0.42	0.09	0.00	0.00	0.00	0.00	4105	3359	4.5				0.54	0.09	6.00
808C	17	R	5	0	3	458.70	648	0.37	0.37	0.06	0.00	0.00	0.00	1747	874	1.0	6.0			0.61	0.09	6.78
808C	18	R	1	0	3	462.40	2144	0.62	0.39	0.09	0.00	0.00	0.00	3462	2116	1.6	4.4			0.67	0.10	6.70
808C	19	R	2	149	150	474.99	1355	0.60	0.30	0.00	0.00	0.00	0.00	2262	1508	2.0				0.40	0.07	5.71
808C	20	R	4	132	135	487.52	3197	0.76	0.57	0.16	0.00	0.00	0.00	4222	2413	1.3	3.5			0.59	0.09	6.56
808C	21	R	1	0	3	491.30	2323	0.74	0.40	0.00	0.00	0.00	0.00	3148	2037	1.8				0.65	0.09	7.22
808C	22	R	5	0	2	507.00	2064	0.80	0.92	0.24	0.00	0.00	0.00	2574	1201	0.9	3.8			0.65	0.08	8.13
808C	23	R	2	0	2	512.20	4392	1.64	1.64	0.48	0.00	0.00	0.00	2670	1335	1.0	3.5			0.43	0.08	5.38
808C	24	R	2	148	150	523.28	11646	2.62	1.45	0.34	0.00	0.00	0.00	4446	2863	1.8	4.2			0.54	0.08	6.75
808C	25	R	1	148	150	531.48	3196	1.01	0.94	0.30	0.00	0.00	0.00	3154	1634	1.1	3.1			0.73	0.10	7.30
808C	26	R	3	123	125	543.93	1005	0.41	0.64	0.15	0.00	0.00	0.00	2461	957	0.6	4.2			0.63	0.08	7.87
808C	27	R	5	122	124	556.52	2286	n.d.	n.d.	n.d.	n.d.	n.d.	n.d.							0.19	0.04	4.75
808C	28	R	1	148	150	560.38	1226	0.62	1.24	0.16	0.00	0.00	0.00	1984	661	0.5	7.8			0.53	0.08	6.63
808C	29	R	4	0	1	573.10	4859	1.34	1.18	0.16	0.00	0.00	0.00	3637	1932	1.1	7.5			0.46	0.08	5.75
808C	30	R	4	0	2	582.80	6696	1.74	1.42	0.00	0.00	0.00	0.00	3858	2122	1.2				0.31	0.06	5.17
808C	31	R	1	148	150	589.08	948	0.34	0.61	0.03	0.00	0.00	0.00	2829	998	0.5	22.0			0.54	0.08	6.75
808C	32	R	3	0	3	600.30	4676	1.69	2.75	0.11	0.00	0.00	0.00	2767	1054	0.6	26.0			0.36	0.07	5.14
808C	33	R	1	0	3	606.90	1899	0.76	2.05	0.21	0.00	0.00	0.00	2494	675	0.4	9.7			0.60	0.07	8.57
808C	35	R	5	0	3	632.20	4650	1.75	5.34	1.03	0.00	0.00	0.00	2663	656	0.3	5.2			0.34	0.06	5.67
808C	36	R	3	0	1	638.90	2276	0.82	4.17	0.82	0.00	0.00	0.00	2781	456	0.2	5.1			0.50	0.07	7.14
808C	37	R	1	0	1	645.50	3293	1.16	3.61	0.42	0.00	0.00	0.00	2829	690	0.3	8.6			0.30	0.06	5.00

Table 18 (continued).

Hole	Core	Type	Sect.	Top cm	Bottom cm	Depth mbsf	Methane μL/kg	Ethane μL/kg	Propane μL/kg	*i*-Butane μL/kg	*n*-Butane μL/kg	*i*-Pentane μL/kg	*n*-Pentane μL/kg	C_1/C_2	$\frac{C_1}{C_2 + C_3}$	C_2/C_3	C_3/C_{4+}	i-C_4/n-C_4	C_4/C_5	TOC %	N %	C/N
808C	38	R	5	0	1	660.90	2153	1.01	3.73	0.34	0.00	0.00	0.00	2134	455	0.3	10.9			0.45	0.06	7.50
808C	39	R	4	0	2	669.00	519	0.36	2.77	0.18	0.00	0.00	0.00	1460	166	0.1	15.6			0.78	0.06	13.00
808C	40	R	1	0	2	674.20	470	0.39	1.39	0.06	0.03	0.00	0.00	1211	265	0.3	16.7	2.0		0.63	0.06	10.50
808C	41	R	1	148	150	685.28	881	0.65	2.73	0.27	0.02	0.18	0.00	1359	261	0.2	9.1	11.0	1.7	0.70	0.07	10.00
808C	42	R	1	0	2	693.50	1461	1.16	5.65	0.61	0.05	0.40	0.00	1255	215	0.2	8.6	12.2	1.6	0.42	0.06	7.00
808C	43	R	1	0	3	703.20	423	0.27	1.67	0.10	0.00	0.00	0.00	1540	217	0.2	17.0			0.89	0.06	14.83
808C	44	R	5	0	1	718.40	1493	1.22	4.62	0.46	0.00	0.28	0.00	1226	256	0.3	10.0		1.7	0.43	0.07	6.14
808C	45	R	1	0	2	722.00	706	0.66	3.18	0.38	0.00	0.32	0.00	1069	184	0.2	8.5		1.2	0.62	0.07	8.86
808C	46	R	1	0	3	731.70	1262	0.98	3.41	0.36	0.00	0.19	0.00	1290	288	0.3	9.4		1.9	0.50	0.06	8.33
808C	47	R	1	0	2	741.40	1051	1.02	3.38	0.45	0.00	0.35	0.00	1032	239	0.3	7.5		1.3	0.48	0.07	6.86
808C	48	R	3	123	125	755.33	1250	1.33	4.63	0.65	0.00	0.46	0.00	939	210	0.3	7.2		1.4	0.43	0.06	7.17
808C	49	R	2	123	125	763.43	2714	2.13	6.19	0.80	0.00	0.46	0.00	1274	326	0.3	7.7		1.7	0.41	0.07	5.86
808C	50	R	5	125	130	777.65	789	0.76	1.97	0.27	0.00	0.21	0.00	1039	289	0.4	7.2		1.3	0.46	0.06	7.67
808C	51	R	1	0	3	780.10	903	0.93	2.83	0.36	0.00	0.34	0.00	975	240	0.3	7.9		1.0	0.49	0.07	7.00
808C	52	R	2	0	2	791.30	679	0.81	1.29	0.16	0.00	0.10	0.00	836	323	0.6	8.0		1.7	0.43	0.06	7.17
808C	53	R	1	141	142	800.81	678	0.94	1.36	0.09	0.00	0.09	0.00	718	294	0.7	14.4		1.0	0.37	0.07	5.29
808C	54	R	1	0	2	809.10	621	n.d.	n.d.	n.d.	n.d.	n.d.	n.d.							0.54	0.05	10.80
808C	55	R	2	0	2	820.20	149	0.47	1.07	0.17	0.00	0.17	0.00	315	97	0.4	6.4		1.0	0.62	0.07	8.86
808C	56	R	1	145	146	829.85	704	1.31	1.57	0.00	0.00	0.00	0.00	538	245	0.8				0.38	0.07	5.43
808C	57	R	1	0	2	838.10	683	1.38	2.07	0.31	0.00	0.26	0.00	495	198	0.7	6.8		1.2	0.44	n.d.	n.d.
808C	58	R	4	0	1	851.90	576	0.86	1.03	0.00	0.00	0.00	0.00	673	306	0.8				0.36	0.06	6.00
808C	59	R	2	115	158	859.75	560	1.24	1.72	0.00	0.00	0.00	0.00	450	189	0.7				0.47	n.d.	n.d.
808C	60	R	3	0	3	869.80	366	1.35	1.16	0.00	0.00	0.00	0.00	271	146	1.2				0.36	0.05	7.20
808C	61	R	2	113	115	879.13	359	1.15	0.82	0.00	0.00	0.00	0.00	313	182	1.4				0.39	0.07	5.57
808C	62	R	2	148	150	889.08	308	1.33	1.00	0.08	0.00	0.00	0.00	232	133	1.3	12.0			0.38	0.07	5.43
808C	63	R	2	0	3	898.30	258	1.23	0.85	0.09	0.00	0.00	0.00	210	124	1.4	9.0			0.33	0.06	5.50
808C	64	R	2	0	3	907.00	229	1.23	0.74	0.00	0.00	0.00	0.00	186	116	1.7				0.37	0.06	6.17
808C	65	R	1	143	145	916.53	222	1.19	0.82	0.04	0.00	0.00	0.00	187	111	1.5	22.0			0.40	0.06	6.67
808C	66	R	1	0	2	924.80	96	0.70	0.46	0.00	0.00	0.00	0.00	137	82	1.5				0.50	0.07	7.14
808C	67	R	1	0	2	934.50	83	0.58	0.42	0.00	0.00	0.00	0.00	142	83	1.4				0.34	0.07	4.86
808C	68	R	1	15	20	944.35	72	0.56	0.19	0.00	0.00	0.00	0.00	129	97	3.0				0.32	0.05	6.40
808C	69	R	5	65	67	960.45	191	1.89	1.62	0.00	0.00	0.00	0.00	101	54	1.2				0.29	0.06	4.83
808C	70	R	2	148	150	966.38	196	2.01	1.41	0.00	0.00	0.00	0.00	97	57	1.4				0.26	n.d.	n.d.
808C	71	R	2	115	120	975.75	144	1.38	1.04	0.00	0.00	0.00	0.00	104	60	1.3				0.35	n.d.	n.d.
808C	72	R	2	0	2	984.30	174	3.14	2.44	0.00	0.00	0.00	0.00	55	31	1.3				0.20	0.06	3.33
808C	73	R	2	0	2	993.60	106	1.62	1.27	0.00	0.00	0.00	0.00	66	37	1.3				0.28	n.d.	n.d.
808C	74	R	1	145	150	1003.25	172	2.76	1.84	0.00	0.00	0.00	0.00	63	38	1.5				0.21	n.d.	n.d.
808C	75	R	2	0	2	1012.80	145	3.20	1.60	0.00	0.00	0.00	0.00	45	30	2.0				0.22	0.08	2.75
808C	76	R	3	0	2	1023.50	131	2.20	1.22	0.00	0.00	0.00	0.00	60	38	1.8				0.26	0.07	3.71
808C	77	R	1	148	150	1031.38	125	2.78	2.27	0.00	0.00	0.00	0.00	45	25	1.2				0.25	0.06	4.17
808C	78	R	1	114	115	1040.24	78	2.51	2.20	0.00	0.00	0.00	0.00	31	17	1.1				0.20	0.07	2.86
808C	79	R	1	0	2	1048.30	93	2.97	2.08	0.00	0.00	0.00	0.00	31	18	1.4				0.21	0.07	3.00
808C	80	R	3	0	2	1060.80	86	n.d.	n.d.	n.d.	n.d.	n.d.	n.d.							0.22	n.d.	n.d.
808C	81	R	2	88	90	1069.48	113	5.01	5.01	0.53	0.67	0.67	0.00	22	11	1.0	4.2	0.8	1.8	0.27	0.06	4.50
808C	82	R	1	148	150	1077.98	66	1.90	1.93	0.25	0.28	0.10	0.00	35	17	1.0	3.6	0.9	5.5	0.27	0.07	3.86
808C	84	R	1	115	120	1093.15	46	2.31	2.00	0.00	0.00	0.00	0.00	20	11	1.2				0.29	0.08	3.63
808C	85	R	1	0	2	1098.30	54	2.09	2.16	0.19	0.27	0.00	0.00	26	13	1.0	4.7	0.7		0.26	0.08	3.25
808C	86	R	1	0	2	1108.00	40	1.68	1.93	0.35	0.26	0.00	0.00	24	11	0.9	3.2	1.4		0.29	0.08	3.63
808C	87	R	1	0	2	1117.60	109	4.66	3.54	0.55	0.52	0.26	0.39	23	13	1.3	3.3	1.1	1.6	0.23	0.08	2.88
808C	88	R	1	0	2	1126.90	111	5.41	4.20	0.75	0.82	0.38	0.49	20	12	1.3	2.7	0.9	1.8	0.27	0.07	3.86
808C	89	R	1	0	2	1136.60	90	3.34	2.21	0.30	0.46	0.00	0.00	27	16	1.5	2.9	0.6		0.23	0.07	3.29
808C	90	R	1	0	2	1146.30	49	2.86	3.29	0.86	0.79	0.37	0.61	17	8	0.9	2.0	1.1	1.7	0.25	0.07	3.57
808C	91	R	1	26	27	1156.16	17	1.15	1.00	0.40	0.00	0.00	0.00	15	8	1.1	2.5			0.28	0.00	n.d.
808C	92	R	1	0	2	1165.60	71	4.12	3.59	1.02	0.72	0.33	0.43	17	9	1.1	2.1	1.4	2.3	0.30	0.08	3.75
808C	93	R	1	4	6	1175.34	65	3.27	2.67	0.79	0.43	0.00	0.00	20	11	1.2	2.2	1.8		0.27	0.08	3.38
808C	94	R	1	0	35	1184.90	87	4.30	2.42	0.69	0.44	0.00	0.00	20	13	1.8	2.1	1.6		0.26	0.08	3.25
808C	95	R	1	7	10	1194.87	112	5.61	4.50	1.00	0.63	0.19	0.41	20	11	1.2	2.8	1.6	2.7	0.21	0.00	n.d.
808C	96	R	2	0	2	1205.80	697	32.43	18.34	2.99	2.93	0.40	2.13	21	14	1.8	3.1	1.0	2.3	0.05	0.00	n.d.
808C	97	R	1	0	2	1214.00	74	5.72	5.15	0.97	0.57	0.00	0.00	13	7	1.1	3.3	1.7		0.05	0.07	0.71
808C	98	R	1	0	2	1223.70	294	12.62	6.64	0.38	0.55	0.00	0.00	23	15	1.9	7.2	0.7		0.12	0.07	1.71
808C	99	R	1	0	2	1233.40	458	26.26	17.77	0.35	1.63	0.00	0.00	17	10	1.5	9.0	0.2		0.04	0.07	0.57
808C	100	R	1	0	2	1243.00	136	4.46	2.52	0.00	0.07	0.00	0.00	31	20	1.8	34.0	0.0		0.19	0.06	3.17
808C	101	R	4	148	150	1258.18	1115	22.85	11.18	0.36	1.65	0.00	0.00	49	33	2.0	5.6	0.2		0.04	0.00	n.d.
808C	102	R	2	0	2	1261.50	345	7.78	4.86	0.00	0.00	0.00	0.00	44	27	1.6				0.06	0.00	n.d.
808C	103	R	2	0	2	1270.90	158	5.43	2.96	0.00	0.00	0.00	0.00	29	19	1.8				0.12	0.00	n.d.
808C	104	R	1	0	2	1280.40	183	6.94	3.36	0.08	0.39	0.00	0.00	26	18	2.1	7.1	0.2		0.18	0.00	n.d.

variation assigned to hole-diameter variations. Unfortunately, although porosity- and velocity-related information is of primary importance for the scientific objectives of this site, it appears that little such information can be obtained.

The salinity indicator Cl/H has very little variation; there may be a very slight decrease with depth, consistent with the laboratory pore-fluid data. However, the log will be strongly influenced by the salinity of the fluid in the pipe and hole, which will be some combination of ocean surface water and mud, particularly in the enlarged sections of the hole.

The uranium log is very scattered; there are probably inadequate signal levels to give useful results. The Ca log has very low amplitudes (<0.02) and is scattered, so probably gives little useful information; similarly, sulfur is probably not resolved.

The element ratios not involving water should be the least affected by hole diameter. Silicon is the largest formation constituent (after water) and it appears reasonably well determined, so it is probably the best reference. However, low-signal levels give scatter at washouts, and there are undoubtedly variations in the attenuation by the pipe and the hole volume with the different energy levels used for different elements. The ratio Al/Si (Fig. 133) may be the best indicator of clay content (although the core lithology does not exhibit substantial variations downhole in total clay content). The K/Si, U/Th, U/K, and Th/K ratios may also be useful lithology indicators.

Lithology Defined by Through-Casing Log in Hole 808E

Logs obtained through the casing in Hole 808E show a good correlation with lithostratigraphic units. Total gamma ray shows a character change from long-period (3–6 m) to short-period (1–2 m) variations at about 127 mbsf. This change probably corresponds to the boundary between lithostratigraphic Subunits IIa (upper axial trench wedge) and IIb (lower axial trench wedge). The upper wedge has thicker sandy intervals that yield the longer period gamma-ray cycles, whereas the lower trench wedge has much thinner sandy units that yield shorter period gamma-ray cycles. The base of the axial trench wedge (263.4 mbsf in Hole 808C) is probably represented by the sharp change in total gamma ray from 45 to about 60 API units at 275–280 mbsf. A similar increase occurs below the frontal thrust at about 425 mbsf, which is probably the location of the Subunit IIb to IIc transition.

Total gamma ray also exhibits character changes at 355 mbsf and 390 mbsf, the interval that corresponds to the frontal thrust zone in Hole 808C. Below the thrust, total gamma-ray character is fairly consistent to the base of the casing.

Open-Hole Interpretation

Two 100-m open-hole intervals were logged with the seismic stratigraphy tool string, and most of the useful interpretation is done with this data. Limited correlations between the through-pipe logs and lithology have been possible. In the next sections, the two open-hole log sections are considered in more detail.

Open Hole 808B; 80–180 mbsf

The log responses between 80 and 180 mbsf reflect large but irregular variations in physical properties. No major lithologic contrasts were encountered in this short section of hole that could be correlated with the core recovered in adjacent Hole 808A (the upper section was not cored in Hole 808B). Correlation between the logs and core was also hampered by the very low core recovery within this interval. However, the logs are characteristic of the interbedded sand-mud sequences sampled in Hole 808A. The large variation in log seismic velocity is also consistent with the strong reflectivity of the upper several hundred meters in the seismic reflection record. Although it is difficult to make specific correlations between the logs and reflection record over the short velocity log depth interval, the low velocity and resistivity zone at the base of the logged section near 180 mbsf may correlate with a particularly strong reflection. The sonic log caliper indicates that the zone is washed out to large diameter, so the log response probably comes from the enlarged hole in an unconsolidated sand section, and the reflection comes from the low-porosity, coarse sand layer.

The log responses between 524 and 622 mbsf exhibit a similar large irregular variation to the shallower open-hole interval. However, for this deeper interval, there is quite good core recovery, and comparisons may be made between the log and core velocities. The laboratory data were collected from subsamples cut from split cores as described in the Explanatory Notes (this volume); only the vertical orientation measurements are used for comparison here. A smaller number of core resistivity measurements are also available, but adjustment for the difference in temperature between lab and log have not yet been undertaken to allow comparison. The downhole log velocities and laboratory core velocities for Hole 808E are compared in Figure 140. There is an excellent agreement in the overall mean values but the detailed correspondence is only moderate. The region of low log velocities between 530 and 540 mbsf undoubtedly reflects a hole washout, and correlation with the core data is not expected. However, the disagreement in data between 510 and 535 mbsf, where there are short intervals with the core data both higher and lower than the logs, is more difficult to explain. Laboratory velocities that fall below log velocities may be explained by sediment rebound following coring, but those that fall above log values are more troublesome. In this case, the two data types track each other closely, but there is a consistent offset over the 15-m interval.

The open-hole logs document the sharp boundary between lithologic Units IIc (outer marginal trench wedge) and III (trench-to-basin transition) at 565 mbsf. Above this boundary, sonic velocity is relatively constant (1.95–2.05 km/s). Just below the boundary, velocity drops to 1.75 km/s and gradually increases to 2.0–2.2 km/s to the bottom of the log. Uranium values are generally lower above the boundary than below. The change in velocity and uranium content reflects the lithologic change from interbedded silts and muds above the boundary to dominantly muds below the boundary (Cores 131-808C-27-28R). Uranium content gradually increases from the base of Subunit IIc (565 mbsf) to the top of the log (525 mbsf), reflecting the overall coarsening-upward nature of the axial trench wedge. Several low-velocity peaks in Unit III are probably correlated with layers of altered volcanic ash reported in the lithologic summary (i.e., 572 and 589 mbsf).

General Characteristics of the Open-Hole Logs

The velocity, resistivity, and gamma logs in the open-hole intervals, particularly in the upper interval (Hole 808B) appear to reflect three clearly definable characteristics of the formation penetrated:

1. There is a general increase in velocity and resistivity with depth that probably reflects a systematic decrease in porosity.
2. There are sections with irregular alternating, upward-decreasing, and upward-increasing velocity and resistivity,

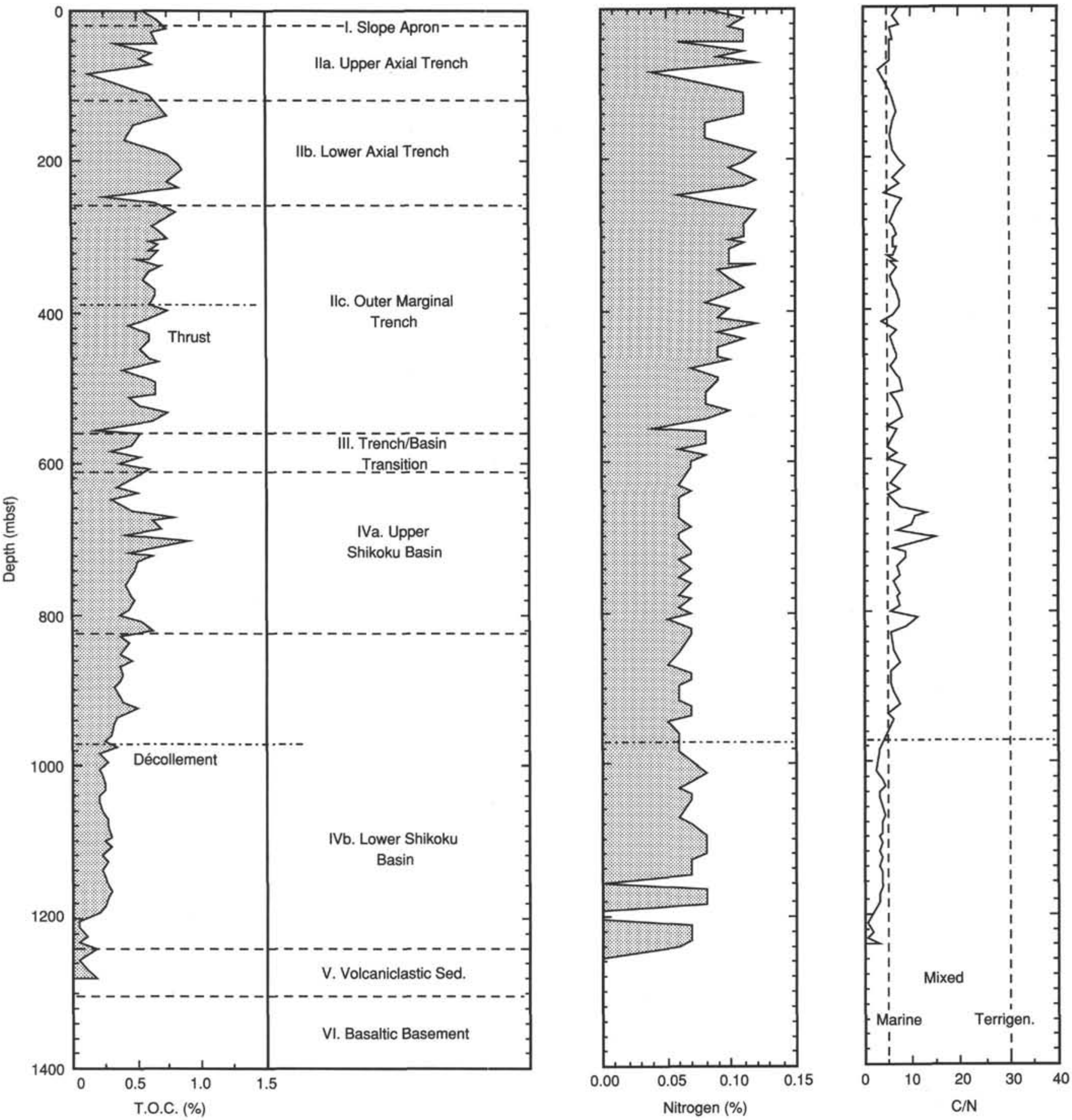

Figure 102. Organic carbon and nitrogen contents in sediments from Site 808.

and the opposite trends in gamma (particularly uranium) response over several depth scales ranging from a few meters to several tens of meters. These trends may reflect turbidite-like upward fining and coarsening sequences. Upward-fining trends may be somewhat more common.

3. There are a number of thin (less than 3-m thick) beds 5 to 10 m apart of very high velocity and high resistivity, particularly in the upper interval. They have no strong gamma signature. These intervals probably represent low-porosity coarse sand layers.

Porosity Decrease With Depth

Through the large, short-wavelength variability there is a clear trend of increasing log resistivity and velocity and inferred decreasing porosity with depth. Figure 141 shows a comparison with the core laboratory measurements (Physical Properties section, this chapter); there is general agreement. In spite of the variation in grain size to a greater proportion of finer clay with depth, the trend is reasonably represented by an exponential decrease in porosity with depth having an

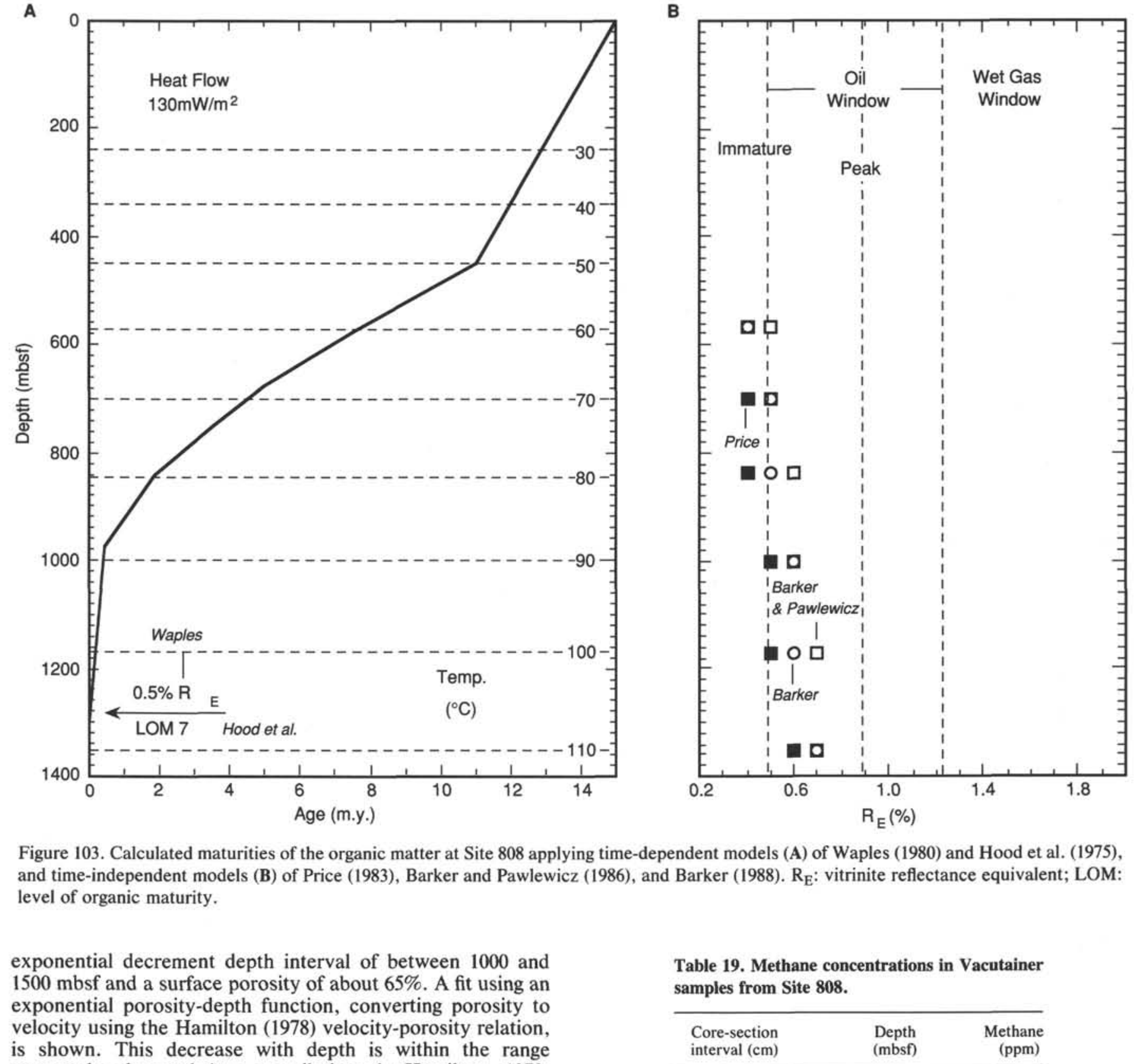

Figure 103. Calculated maturities of the organic matter at Site 808 applying time-dependent models (**A**) of Waples (1980) and Hood et al. (1975), and time-independent models (**B**) of Price (1983), Barker and Pawlewicz (1986), and Barker (1988). R_E: vitrinite reflectance equivalent; LOM: level of organic maturity.

exponential decrement depth interval of between 1000 and 1500 mbsf and a surface porosity of about 65%. A fit using an exponential porosity-depth function, converting porosity to velocity using the Hamilton (1978) velocity-porosity relation, is shown. This decrease with depth is within the range commonly observed (see compilations in Hamilton, 1979; Busch, 1989). Such an ideal function can, of course, be only a rough approximation for the section penetrated because of the change in lithology, particularly the decrease in grain size, downward, and because of the effect of thrusting and tectonic shortening. A more quantitative analysis will require post-cruise integration of laboratory core data and logs with seismic data from the immediate area.

Upward Fining and Coarsening Sequences

Sequences with upward-decreasing resistivity and velocity and increasing gamma response over depth intervals of 10 to 20 m, as well as the opposite trends, are common in the logs from the shallower open-hole section (Fig. 142). The trends between 80 and 180 mbsf are very irregular and are evident at a number of wavelengths, but they are consistent for all three parameters. Low values of resistivity and sonic velocity correlate with zones of high uranium content (high mud

Table 19. Methane concentrations in Vacutainer samples from Site 808.

Core-section interval (cm)	Depth (mbsf)	Methane (ppm)
131-808A-		
2H-5, 31–35	12.61	839326
3H-3, 134–138	20.14	840994
4H-2, 148–150	28.28	652804
6H-1, 40–45	44.75	739750
7H-5, 22–26	60.02	874342
9H-3, 114–115	72.44	835456
10H-2, 130–131	80.60	828439
13H-3, 48–50	109.88	870000
131-808B-		
5X-1, 30–32	149.80	711669
7X-3, 41–42	172.21	1640
9X-4, 51–52	193.21	731652
10X-2, 74–75	199.44	821430
10X-4, 90–91	202.80	10472
11X-2, 82–83	209.12	693563
13X-1, 149–150	227.29	722537
17X-1, 82–83	264.22	802499
19X-1, 114–115	283.64	814199
25X-2, 64–65	338.14	673913

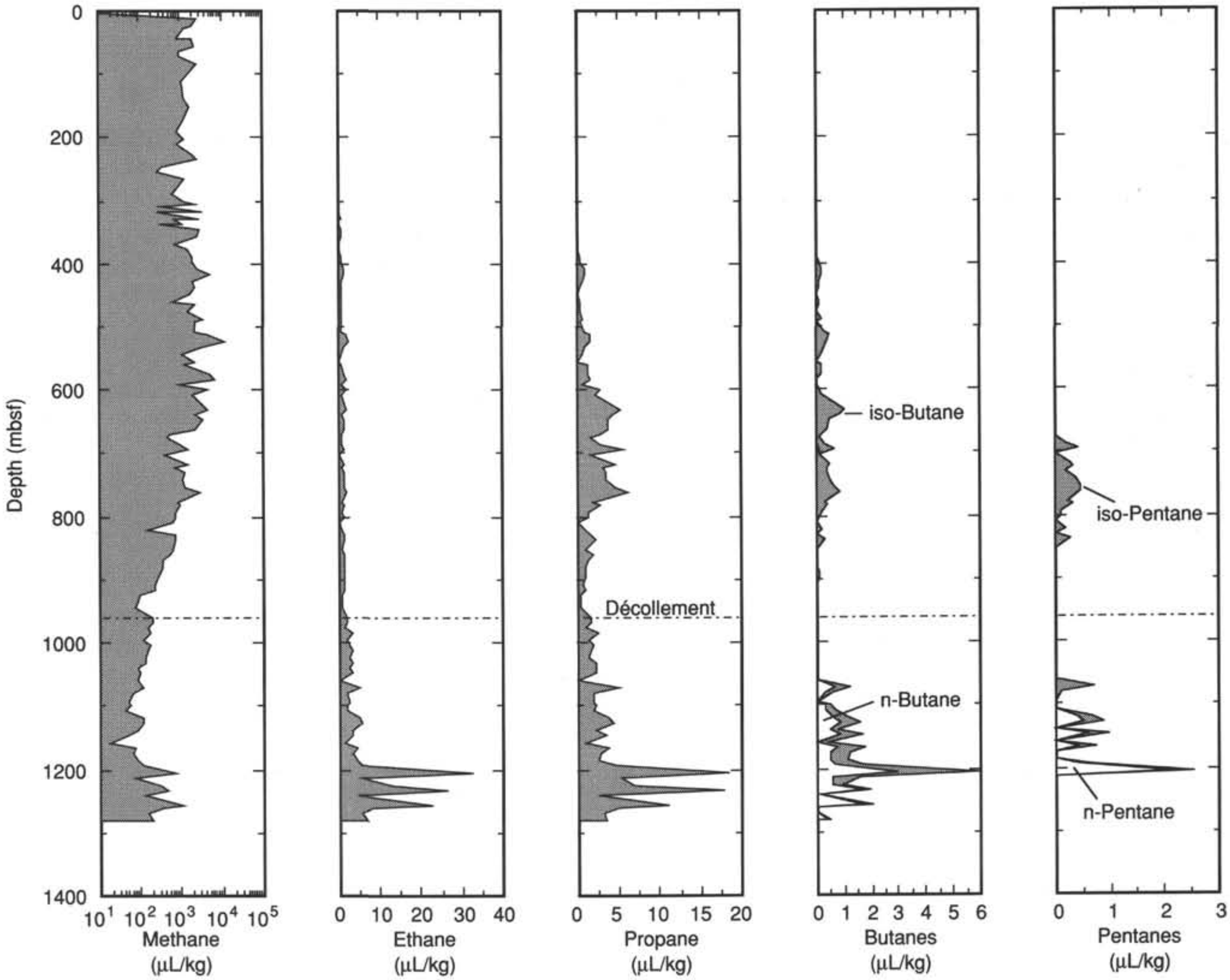

Figure 104. Molecular composition of headspace gases from Site 808. Gas concentrations (μL/kg) are unit of gas per unit organic carbon of sediment.

percent). The trends undoubtedly reflect variations in grain size from mud to sand. A good correlation between grain size and porosity is expected for such a relatively unconsolidated section (e.g., Hamilton, 1974), the sand being low porosity, the mud, high porosity. The uranium content revealed by the downhole logs in Hole 808B should reflect the amount of mud in the section, as uranium is generally concentrated in the more slowly deposited muds compared to the sands. Because core recovery over the logged interval was very poor, a direct comparison between logs and core is possible only over a very short interval.

A limited comparison of the uranium log with the visual core description is available for the one nearly complete core within the logged section (Core 131-808A-10H, 77.8–87.4 mbsf); for this section uranium content in the logs shows a good correlation with core grain size. The uranium values are less than 1.5 ppm from 90 to 88 mbsf. This corresponds to a sandy interval in the core. From 88 to 85 mbsf the uranium values are generally greater than 1.5 ppm, and the cored section fines upward from fine sand to sandy silt to clayey silt. From 85 to 82 mbsf, the uranium values decrease from 1.0 to less than 0.5 ppm and the cored section coarsens upward from medium sand to medium and coarse sand. Sonic velocity also correlates well with the lithology through this section: from 90 to 88 mbsf, velocities are 1800 to 2100 m/s; from 88 to 86 mbsf the velocities drop to approximately 1700 m/s. Resistivity logs are not available for this section. Core recovery was too poor throughout the rest of the logged section to provide further calibration. We also note that the thin, high-resistivity and high-velocity layers discussed below, interpreted as sandy layers, may correlate with zones of interpreted low mud, high sand content on the uranium log.

Assuming that the uranium log is a reliable indicator of sand/mud content for the recorded section, the log facilitates a reasonable interpretation of the sedimentary sequences. The logged open-hole section (80–163 mbsf) is completely within the uplifted trench wedge, dominated by thick sand beds (Sedimentology section, this chapter). It is reasonable to expect that both large- and small-scale sedimentary sequences should be present, due to the migration of channels and associated sediment facies within the trench. Figure 143 shows an interpretation of such sequences on the uranium log. There seems to be at least two orders of fining-upward and coarsening-upward sequences in this section. The thinner sequences are 3–7 m thick, and the thickest sequences observed are 10–25 m thick. These sequences may represent shifts in the turbidity current distribution system in the Nankai Trough.

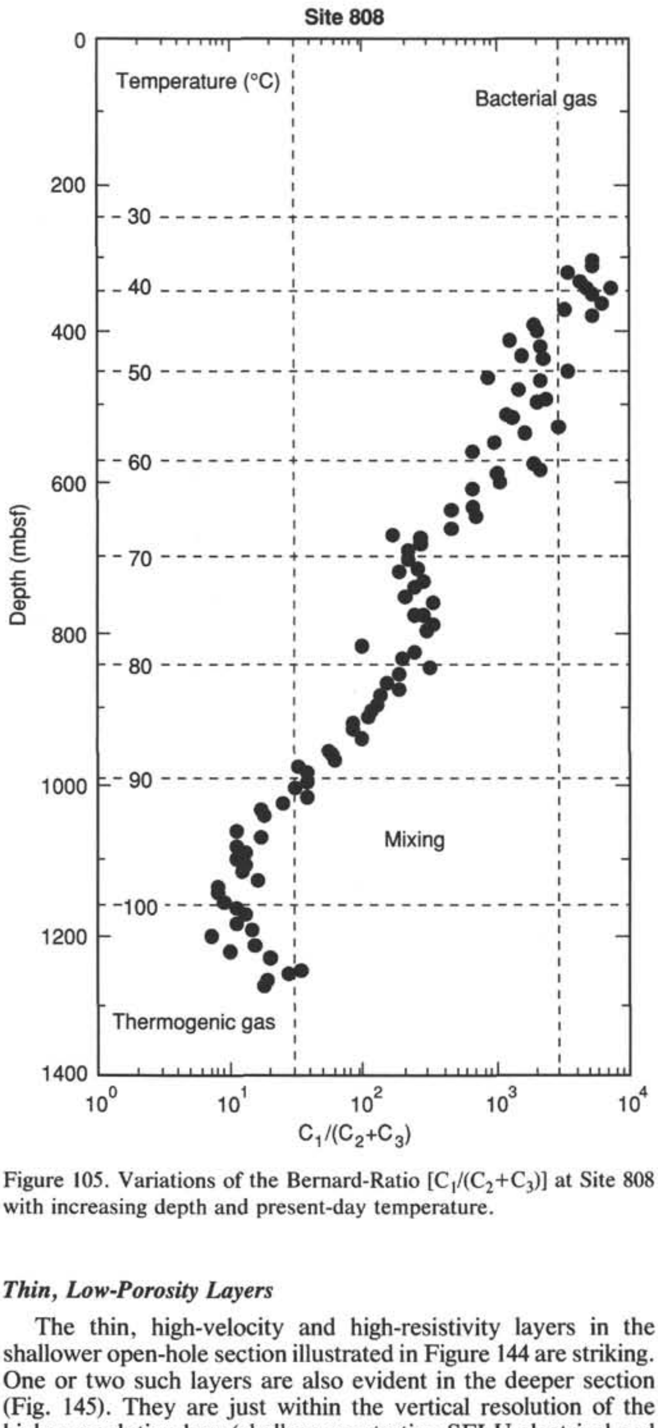

Figure 105. Variations of the Bernard-Ratio $[C_1/(C_2+C_3)]$ at Site 808 with increasing depth and present-day temperature.

Thin, Low-Porosity Layers

The thin, high-velocity and high-resistivity layers in the shallower open-hole section illustrated in Figure 144 are striking. One or two such layers are also evident in the deeper section (Fig. 145). They are just within the vertical resolution of the higher resolution logs (shallow penetration SFLU electrical and MEDDT sonic) so the velocity and resistivity undoubtedly are somewhat smoothed and the peak velocity and resistivity values, 2.15 km/s and 2.25 ohm-m, are a minimum. The inferred porosity in the layers, about 20%–30% for both logs, is thus a maximum. The Hamilton (1979) grain-size-porosity relation gives a minimum mean grain size of about 1 mm. It should be noted that the layers are not resolved by the medium penetration resistivity used in the velocity-resistivity cross plot shown below (seen only in the SFLU higher resolution resistivity) so they appear off the main trend of the velocity-resistivity relation. The thin zones are probably not ash layers as laboratory measurements on ash layers in the core gave low velocities (Physical Properties section, this chapter). Again, it is unknown if these thin layers are of regional distribution or represent deposition within local channels.

Cross Plots and Derivative Logs

An important objective of the logging at this site is the inter-relation of a number of physical properties parameters. Particularly important is determination of the relation between velocity and porosity to interpret landward velocity increases in the accretionary wedge as obtained by seismic reflection and refraction measurements, to quantify changes in porosity and pore-fluid expulsion. No open-hole neutron porosity log was acquired but an approximate porosity can be obtained from the resistivity logs. That both resistivity and velocity are related to a common factor, porosity, is suggested by the correlation of the two logs seen in the upper section in Figure 129. The correlation is much less evident in the deeper open-hole section (Fig. 135). Thus, the following discussion applies primarily to the shallower open-hole interval.

Some of the scatter in the resistivity-velocity cross plot between 80 to 180 mbsf comes from small offsets in the two depth scales, and the correlation was improved somewhat by plotting logs filtered (7 point running average) to reduce the effect of the small depth offsets associated with tool heave (not shown). In any case, the correlation between the short-wavelength variations visually evident in the two logs is not resolved in the cross plot; that would require very accurate depth adjustment.

Velocity-porosity and Resistivity-porosity Relations

A number of relations were attempted to match the cross-plot data in the upper open-hole interval, and future detailed analysis will include application of the core physical properties data, so only a brief discussion is given here. Unfortunately, as both velocity-porosity and resistivity-porosity must be estimated and the data scatter is large, agreement with the data can be obtained with a range of model combinations.

Figure 145 illustrates a number of velocity-porosity relations that have been suggested for terrigenous deep-sea sediments. The Hamilton (1974) relation was derived using primarily seafloor samples. It predicts quite low porosities for particular velocities compared to most of the other relations. Even lower porosities are predicted by the Raymer et al. (1980) relation obtained from petroleum industry log data. In contrast, the Wyllie time average equation predicts unreasonably high porosities for unconsolidated sediments of velocity less than about 3.0 km/s, as has frequently been recognized. An "unconsolidated" correction is sometimes applied to bring this relation into agreement with log data for unconsolidated sediments.

A combination of the two Hamilton (1978) relations for low-porosity and high-porosity sediments was found to give generally good agreement with log and laboratory core data for ODP holes in the Labrador Sea, by Jarrard et al. (1989). A smooth polynomial approximation of the Hamilton (1978) relations is shown in the figure. It deviates slightly from the Hamilton (1978) relations to allow for the Hamilton high-porosity relation giving slightly high porosities for velocities around 1.7 km/s, and slightly low porosities for velocities around 2.0 km/s, compared to the log data of Jarrard et al. (1989). This polynomial is very close to the function involving a combination of the Wood and Wyllie relations that Nobes et al. (1986) derived to fit their compilation of DSDP data. D. Karig (pers. comm., 1990) also found that the Hamilton (1978) relations give a reasonable fit to the sample data for the previous drilling in the Nankai Trough. The

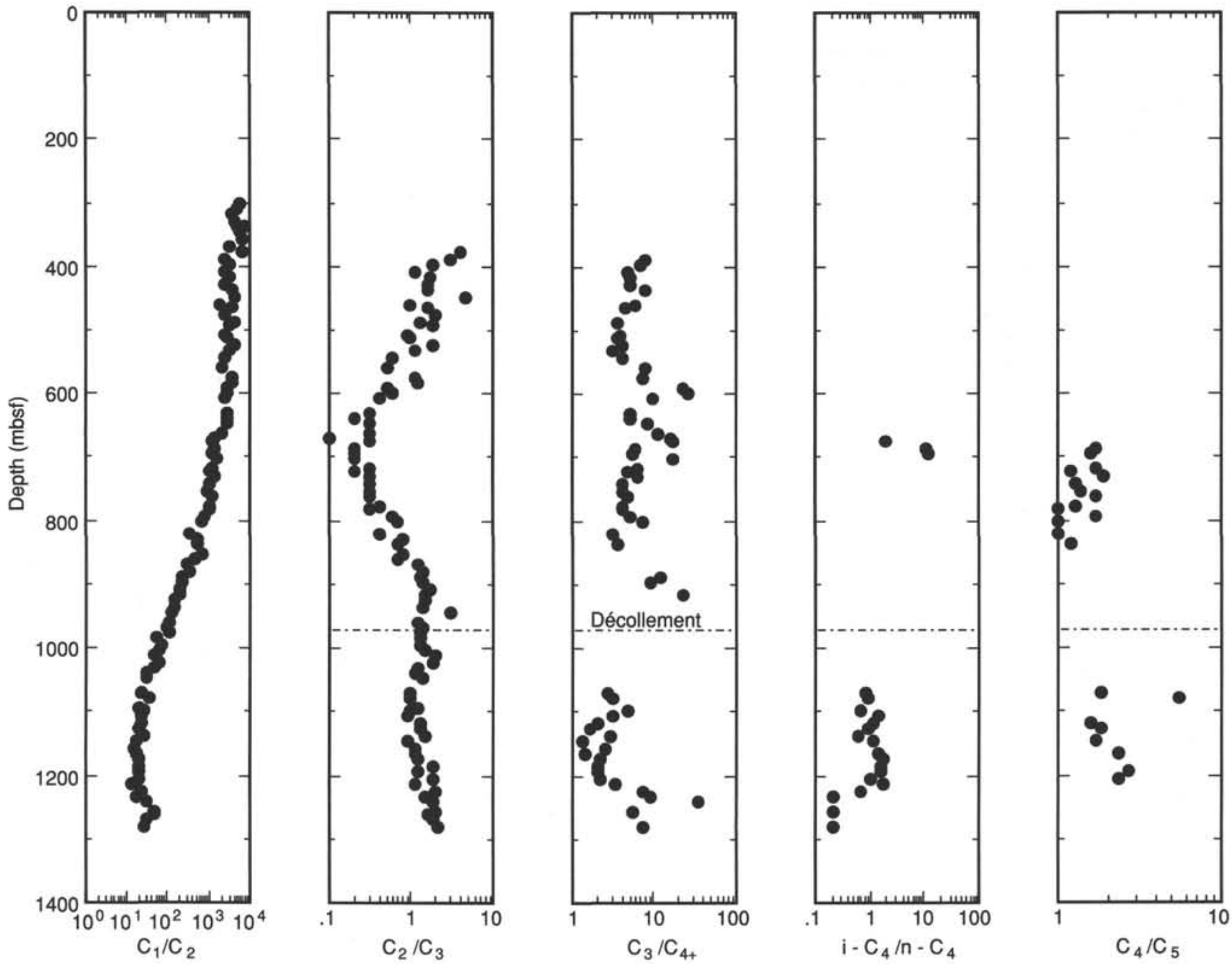

Figure 106. Gas ratios at Site 808.

relations of Hamilton (1974) and the polynomial approximation of the Hamilton (1978) relations have been used to give a reasonable range of porosity-depth profiles from the sonic log.

Less information is available on the relation between resistivity and porosity for deep-sea sediments. The relationship is generally found to be of the form of Archie's law, $R = a\,R_{\text{fluid}}/\varphi^r$ (Archie, 1947). The standard values of $a = 1$ and $r = 2$ fit many crystalline rocks and appear to fit data from some clean sands (e.g., Archie, 1947; Lovell, 1984). The Humble form of the formula is widely used in the petroleum industry, $a = 0.62$, $r = 2.15$ (e.g., Winsauer, 1952). A slightly different form was found by Kermabon et al. (1969) from seafloor measurements: $R = R_{\text{fluid}}\ (1.45/P)^{1.46}$ - 0.719. From core samples from the Atlantic off North Africa (Boyce, 1980) and from the Bering Sea (Boyce, 1968), good fit was obtained with values of $a = 1.30$ and $r = 1.45$. Almost identical values were found by Lovell (1984) for northeast Atlantic samples. These relations are shown in Figure 146, illustrating the range. A seawater pore- fluid (see Inorganic Geochemistry, this chapter) resistivity of 0.22 ohm-m was used, appropriate for a temperature of about 15°C. The appropriate pore-fluid resistivity for the deeper section is about half, 0.11 ohm-m for a temperature of about 58°C (see Heat Flow, this chapter). This resistivity value assumes that there is little cooling of the formation by drilling circulation at the main depths of log penetration. Thus, the same porosity for the deeper section should give about one-half the resistivity of the shallower section.

The relations between resistivity and velocity predicted by this range of velocity-porosity and resistivity-porosity relations are compared with the shallower open-hole section (Hole 808B) log data in Figure 147. A velocity-resistivity cross plot for the deeper open-hole section is shown in Figure 148. As noted above, there is a rather poor correlation exhibited in the latter and it is not discussed further here. In the shallower section, for the velocity-porosity relation by Hamilton (1978), all of the resistivity-porosity relations give resistivities that are much too low or velocities that are much too high. The Hamilton (1974) relation for seafloor sediments however, gives reasonable agreement for all of the resistivity relations, with the Humble and the Boyce (1968) relations giving a slightly better fit.

There are important sedimentological differences among the different sections in these studies. The differences in lithology and diagenesis are well recognized. For example, the Jarrard et al. (1989) Labrador Sea- and Boyce (1968) Bering Sea samples are mainly terrigenous silty clays and clayey silts, similar although somewhat finer, compared to the section of Hole 808B logged. The Boyce (1980) data from the Atlantic is

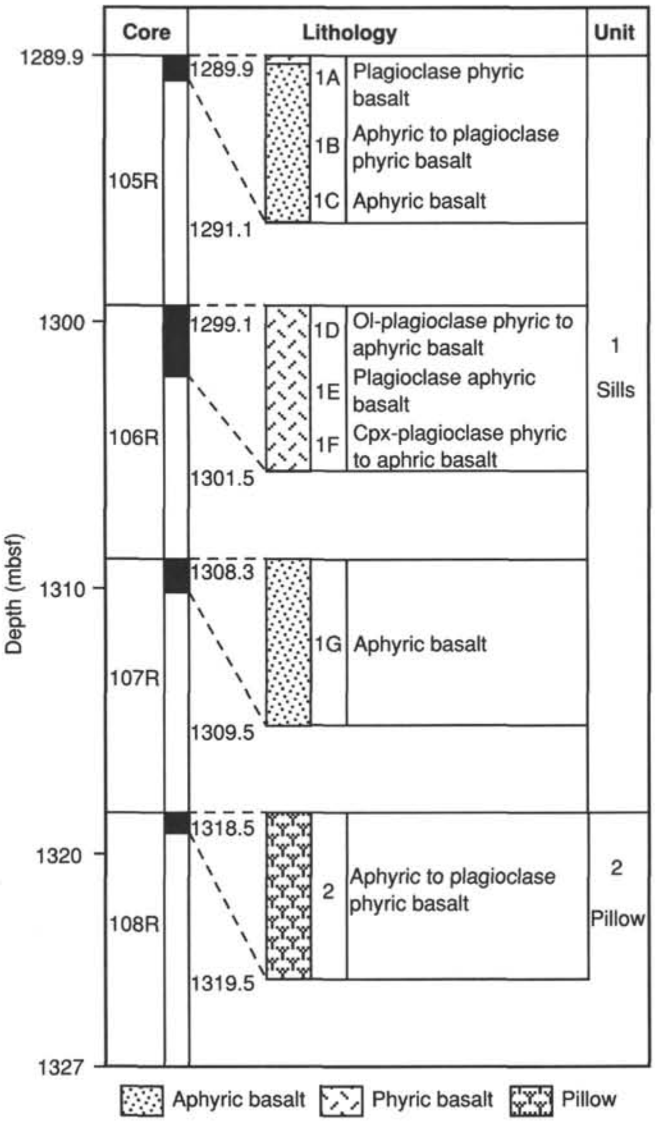

Figure 107. Lithostratigraphy, recovery, lithologic units, and subunits of basement rocks, Hole 808C.

for a very different lithology, nannofossil marl and chert. However, another difference appears to be of greater importance, namely, porosity variation with depth due to mechanical compaction, chemical alteration, and diagenesis, vs. porosity variation due to variations in grain size over a limited depth range. That is, variation with depth in deep holes vs. variation with grain size for near seafloor samples. As expected, the Site 808 data for which there is large short-wavelength porosity variation is consistent with the near-seafloor data of Hamilton (1974). In Hole 808B, the porosity variation is primarily due to variations in grain size over short depth ranges, and to a much smaller change with depth due to consolidation and diagenesis.

A difference between the velocity-porosity relation associated with depth consolidation and that for grain-size variation is to be expected, as consolidation and diagenesis will more strongly increase the grain bonding and thus the shear modulus. The difference in resistivity-porosity behavior between the two types of porosity variation is not readily resolved with the available Site 808 data. Porosity-depth functions for the upper open-hole section using a variety of velocity-porosity and resistivity-porosity functions is shown in Figure 149.

Conclusions

On ODP Leg 131 a major attempt was made to obtain good logs through the toe of the accretionary wedge at Site 808. While one hole was successfully drilled to basement and a second to near basement, and a substantial amount of time was applied to logging, there was only limited success. A particular disappointment was that no logs could be obtained through the main subduction décollement. As discussed in the log operations outlined here and in Operations (this section), hole stability problems were severe.

Two short open-hole logs were obtained with the seismic stratigraphy tool string that gave generally good data: 80–180 mbsf and 525–615 mbsf.

The lithoporosity and geochemical tool strings obtained data through a variety of combinations of pipe, bottom-hole assembly, and casing from the seafloor to 891 mbsf. While attenuation by the pipe may be corrected, there are probably substantial hole enlargement effects that will be very difficult to determine.

In the one section where there is open-hole log data and good core recovery, 524 to 622 mbsf, the log- and laboratory core-velocity averages are very close, but the detailed correlation is only fair. The reason for this difference is not known. In the upper open-hole log section very little core was obtained, and what was obtained was seriously biased to muds vs. sands so that little useful log-core correlation could be made.

The main lithologic variations in the section drilled as seen in the core are also evident in the logs. These are the pronounced irregular alterations of sand and mud, characteristic of turbidite sequences, particularly in the upper trench wedge part of the section. This is seen both in the gamma log and in the resistivity and velocity logs that are sensitive to porosity. The main lithologic units of the trench wedge turbidites and the deeper finer grained sections are resolved in the logs. Grain size generally decreases downward, and there is some evidence of slightly more quartz in the mud and with depth as indicated in the core data. The compositional variations indicated by the logs (as in the core) are minor except where ash layers may be resolved.

A number of velocity-porosity and resistivity-porosity relations were tried to fit the log data in the upper open-hole section, 80–180 mbsf, to obtain porosity data, and a velocity-porosity relation for use in interpreting seismic data. There are two dominant factors affecting the relation for terrigenous deep-sea sequences that give different relations. The velocity-porosity relation is substantially different for data sets obtained from relatively unconsolidated sediments for which the porosity variation is associated with grain size (sand to mud), compared to the relation for porosity variation with depth associated with sediment consolidation and diagenesis. The Hamilton (1974) relation appears to fit the former, and the Hamilton (1978) relations (also Jarrard et al., 1989; Nobes, 1986) appear to fit the latter. We conclude that the latter relations are appropriate for use in converting regional velocities from seismic data to porosity.

Other features of the sediment section resolved in the log data, mainly the data from the open-hole sections, include: (1) some definition of the function describing the porosity decrease with depth, and an approximate velocity-porosity calibration that can be applied to regional seismic velocity data; (2) in the upper open-hole section, strong, irregular, upward-fining and

Table 20. Modal proportions (%) of major phases (including plagioclase composition) and secondary minerals (including vesicle and vein filling) of basaltic rocks, Hole 808C. Abbreviations: plag = plagioclase; ol = olivine; cpx = clinopyroxene; mt = magnetite; meso = mesostasis; ves = vesicles.

Sample	Location	Phenocrysts				Groundmass								Secondary
Core-section	interval	Plag	An	Ol	Cpx	Plag	An	Ol	Cpx	Mt/oxide	meso	ves	veins	minerals
				Subunit	1B			Aphyric	To	Plagioclase	Phyric	Basalt		
105R-1	8–19	1		–	–	40	52–54	10	10	–	30	5	–	42.8
				Subunit	1C			Aphyric	Basalt					
105R-1	102–105	–		–	–	40	54–56	15	20	5	15	5	–	36
				Subunit	1D			Olivine	Plagioclase	Phyric	Basalt			
106R-1	5–9	3		5	0,5	40	64	–	44	3	3	–	2	27
106R-1	28–31	–		–	–	50	70	6	35	4	1	–	4	26
				Subunit	1E			Plagioclase	Phyric	Basalt				
106R-1	74–75	5		–	–	35	65–70	12	35	–	4	1	1	26
106R-1	90–93	1		–	–	30		14	20	6	5	–	24	45
106R-1	122–125	1	70	–	–	40	60	10	30	6	10	–	4	44
				Subunit	1F			CPX	Plagioclase	Phyric	Basalt			
106R-2	17–22	3	70	–	1	40	64	10	38	–	2	–	–	23
106R-2	60–64	2	65	–	–	48	60	10	30	6	<1	–	5	18
				Subunit	1G			Aphyric	Basalt					
107R-1	28–31	–		–	–	30	68–70	10	36	–	10	2	10	23
107R-1	104–128	2	70	–	–	20		2	18	3	40	1	7	13
				Unit	2			Aphyric	To	Plagioclase	Phyric	Basalt		
108R-1	6–12	–		–	–	25	>54	10	10	–	50	5	–	85
108R-1	12–15	1		1	–	50	60	5	5	–	30	–	–	36
108R-1	63–66	–		–	–	45	68	10	25	5	5	–	10	36
108R-1	108–121	6	80	–	–	30	57	10	30	3	7	–	–	37

upward-coarsening depositional cycles up to 25 m thick that are associated with variations in the trench turbidite sediment distribution regime; and (3) primarily in the upper open-hole section, definition of very distinct thin (1- to 2-m maximum) layers of high resistivity and high velocity, and with low inferred porosity that probably represents coarse sand layers.

PACKER EXPERIMENTS

Objectives

The packer experiments were intended to determine bulk permeability and give some indication of formation pore pressure. Conditions in Hole 808E prevented deploying the packer directly above the décollement, as was originally planned. Instead, we hoped to deploy the packer first near the base of the cased section, to measure pressure and determine the permeability of the entire open section, and then to place the instrument as far down the hole as possible for a second test. After inflating the packer for the first time, we intended to leave it in place in the casing without pressurizing the formation for at least 1 hr to see if the isolated zone would become "overpressured."

Operations

The packer experiment began following the completion of vertical seismic profiling (VSP) operations. The rotary shifting tool was lowered into the drill pipe to unlatch the pipe from the 16-in. landing subassembly used to hold the pipe steady for the VSP, and the packer was lowered into position at a depth of 5200 mbsf. With the packer at this depth, the end of the bottom- hole assembly protruded about 22 m past the end of the casing shoe and into the open hole. Two Kuster gages with 6-hr clocks were prepared and attached to the bottom of the go-devil, inside stainless-steel cages and an inner core barrel, which was then dropped into the end of the pipe to free fall into position in the packer. The circulating head and ball-drop sub were attached and the pipe was picked up with the blocks. The go-devil was pumped down the pipe for about 15 min with the mud pump at 50 strokes/min (spm; 1 spm is about 0.32 L/s). The pump was then turned off to allow the go-devil to land under only its own weight. We waited an

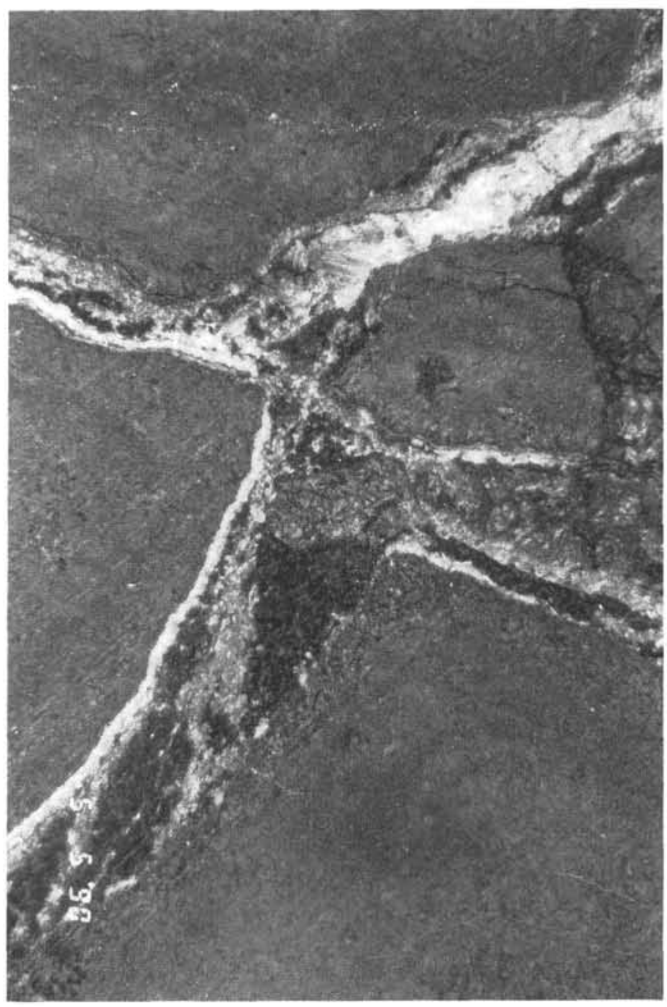

Figure 108. Photomicrograph (scale not available) of auto-brecciated structure in the top part of Unit 2. Angular fragments are healed by calcite and fine variolitic glass. Section 131-808C-108R-1, Piece 1A.

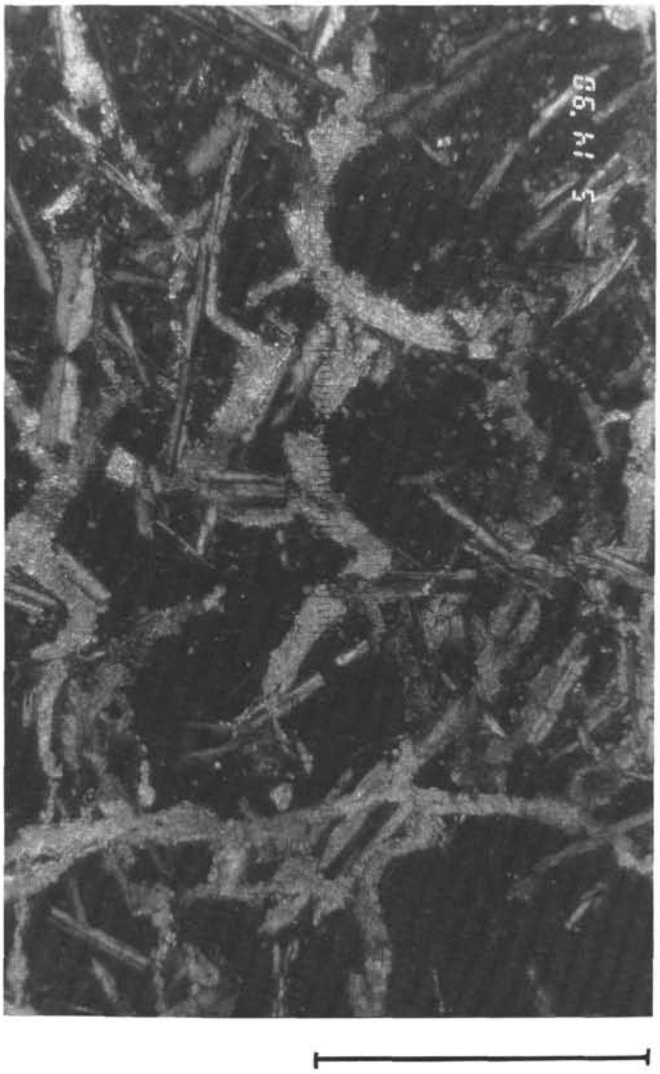

Figure 109. Photomicrograph of hyalopilitic texture in basaltic fragments of top part of Unit 2. Crossed polarizers were used. Bar scale is 0.5 mm. Section 131-808C-108R1-1, Piece 1A.

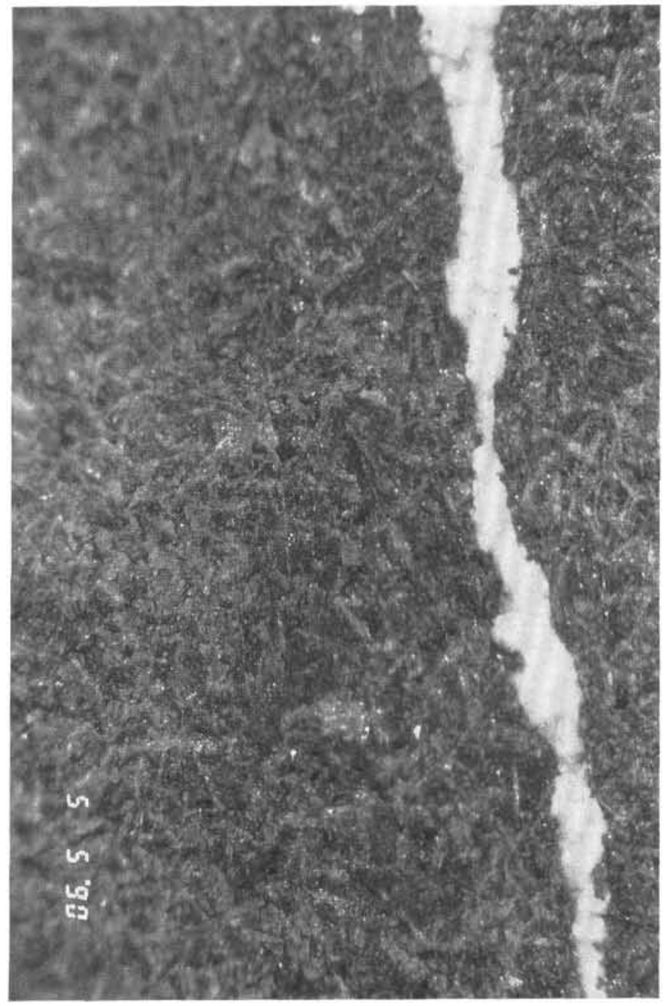

Figure 110. Photomicrograph (scale not available) of thin irregular vein, filled with microcrystalline calcite. The texture of the rock is intersertal-to-intergranular. Section 131-808C-108R-1, Piece 12A.

additional 35 min for the go-devil to land and for the pressure gages to record a hydrostatic baseline.

We started pumping at about 20 spm to bring pressure up to 1000 psi and set the packer element firmly against the wall of the casing. When the pressure reached 1000 psi we stopped pumping and shut in at the standpipe. Over the next 10 min, pressure dropped slowly to about 900 psi, according to the gages in the driller's shack. A pressure record generated by a separate Gould 5000-psi pressure transducer attached to the standpipe suggests that the pressure had actually dropped to about 750 psi after the first 10 min. We slacked off on the heave compensator to put 15,000 lb on the packer, and it supported the weight. We then brought the pressure up to 2000 psi to shear three pins, shift a sleeve in the go-devil, and lock pressure in the inflated packer element. When we then bled off pressure at the stand pipe, to allow the sleeve to shift back and open a passage through the go-devil for testing, the packer stopped supporting weight. Repeated pumping would not reinflate the packer element, as there was now no way to block off the hydraulic connection between the pipe and the open hole. We know that the packer was not completely deflated because, although it would not support significant weight, it did provide several thousand pounds of resistance when the driller moved the pipe. We dropped the deflation ball to allow the element to deflate completely so that we could retrieve the go-devil and try again.

The go-devil was finally recovered with a standard Otis RS overshot on the fourth attempt, following two lowerings of the overshot and one of a core barrel and "hard-formation" core catcher. The polypack and O-ring seals on the outside of the go-devil were gone; if the seals were compromised while the go-devil was free-falling, we might never have had a tight hydraulic seal inside the packer during the first experiment. With the new go-devil, a good seal is required to maintain pressure in the packer element. The go-devil and gages were redressed for a second deployment, but the packer continued to drag along the inside of the casing, suggesting that the tool was still only partially deflated. In addition, attempts to circulate fluid through the pipe caused pressure to build in the drill string, indicating that there was either a plug in the pipe or at least a partial seal between the packer and the wall of the casing.

As we could not pump the redressed go-devil and gages down the pipe, we lowered them by wireline for the second

Table 21. Major (wt%) and trace-element (ppm) analyses, Mg values, CIPW norms, and some incompatible element ratios of igneous rocks from Hole 808C. Mg values and normative minerals based on $Fe_2O_3/FeO = 0.15$. La_N, Ce_N, and Y_N represent chondrite-normalized values according to Henderson, 1984.

Core-section interval (cm)	105R-1 8–19	105R-1 102–105	106R-1 5–9	106R-1 28–31	106R-1 90–93	106R-1 122–125	106R-2 17–22	106R-2 60–64	107R-1 28–31	107R-1 104–128	108R-1 63–66	108R-1 118–121
SiO_2	47.52	49.71	47.74	48.37	49.14	47.65	46.35	47.04	46.93	47.28	45.39	47.16
TiO_2	1.58	1.69	1.56	1.56	1.66	1.56	1.56	1.30	1.64	1.83	2.14	2.00
Al_2O_3	16.43	16.54	15.65	16.42	15.88	16.26	16.33	14.37	14.59	14.78	15.31	14.87
Fe_2O_3	11.00	8.63	11.10	10.41	9.34	10.15	10.11	10.42	11.90	12.28	12.58	11.66
MnO	0.30	0.17	0.18	0.13	0.14	0.15	0.13	0.13	0.18	0.16	0.17	0.18
MgO	6.57	7.32	7.12	8.90	9.14	7.78	9.45	11.00	8.31	6.77	4.46	5.40
CaO	11.88	10.78	11.39	10.22	9.66	11.28	10.17	9.61	11.06	11.70	13.05	12.18
Na_2O	3.17	3.42	3.00	2.65	2.71	2.81	2.65	2.16	2.90	2.64	3.05	3.02
K_2O	0.07	0.09	0.08	0.08	0.08	0.09	0.08	0.09	0.15	0.44	0.29	0.43
P_2O_5	0.20	0.23	0.22	0.24	0.24	0.24	0.24	0.21	0.25	0.26	0.30	0.28
LOI	1.28	1.41	1.96	1.01	2.00	2.03	2.92	3.68	2.09	1.86	3.26	2.82
mg	57.6	65.9	59.4	66.1	69.0	63.6	68.1	70.6	61.4	55.7	44.7	51.3
V	254	242	229	227	238	219	222	196	280	314	311	311
Cr	295	290	262	255	270	250	244	222	279	333	284	267
Ni	121	102	124	131	126	121	127	107	88	87	81	99
Co	52	45	32.5	44	42	41	42.5	37	38	41	34	22
Rb	2	1	2	1	1	1	1	2	3	13	6	12
Ba	24	26	23	31	26	27	21	24	35	35	42	40
Sr	226	219	226	213	212	214	200	181	192	208	260	251
Zr	116	119	108	112	116	112	110	98	107	113	151	148
Nb	2	3	2	2	3	2	2	2	5	5	6	5
Y	34	36	33	34	34	34	33	30	35	39	44	43
La	5	5	6	4	4	5	6	4	6	4	8	7
Ce	15	15	17	12	14	15	16	11	17	16	23	22
Or	0.41	0.53	0.47	0.47	0.47	0.53	0.47	0.53	0.89	2.60	1.71	2.54
Ab	24.28	28.94	25.39	22.42	22.93	23.78	22.42	18.28	24.54	22.34	18.98	24.05
An	30.40	29.52	29.00	32.67	30.93	31.49	32.43	29.25	26.53	27.18	27.23	25.75
Ne	1.06	0.00	0.00	0.00	0.00	0.00	0.00	0.00	0.00	0.00	3.70	0.81
Di	22.34	18.18	21.32	13.34	12.44	18.62	13.30	13.75	21.94	23.96	29.60	27.12
Hy	0.00	7.08	3.21	14.39	20.34	5.85	6.24	18.23	0.54	3.43	0.00	0.00
Ol	13.15	8.21	12.12	9.29	4.59	11.39	15.90	10.45	16.68	11.16	7.30	9.24
Mt	2.07	1.64	2.10	1.97	1.77	1.91	1.91	1.97	2.25	2.32	2.38	2.20
Il	3.00	3.21	2.96	2.96	3.15	2.96	2.96	2.47	3.11	3.48	4.06	3.80
Ap	0.47	0.55	0.52	0.57	0.57	0.57	0.57	0.50	0.59	0.62	0.72	0.66
Ti/Zr	82	85	87	84	86	83	85	80	92	97	85	81
Zr/Nb	58	40	54	56	39	56	55	49	21	23	25	30
Zr/Y	3.4	3.3	3.3	3.3	3.4	3.3	3.3	3.3	3.1	2.9	3.4	3.4
Ce/Nb	7.5	5.0	8.5	6.0	4.7	7.5	8.0	5.5	3.4	3.2	3.8	4.4
Ba/Nb	12	8.7	12	16	8.7	14	11	12	7.0	7.0	7.0	8.0
Ba/Sr	0.1	0.1	0.1	0.1	0.1	0.1	0.1	0.1	0.2	0.2	0.2	0.2
Ba/Zr	0.2	0.2	0.2	0.3	0.2	0.2	0.2	0.2	0.3	0.3	0.3	0.3
K/Nb	276	242	324	334	226	380	339	373	249	736	401	709
La_N/Y_N	0.9	0.9	1.2	0.8	0.8	0.9	1.2	0.9	1.1	0.7	1.2	1.1
Ce_N/Y_N	1.0	0.9	1.2	0.8	0.9	1.0	1.1	0.8	1.1	0.9	1.2	1.2

test, using a standard coring head. Once in position in the packer, the go-devil was repeatedly raised and lowered 20–100 m at a high speed to shear a pin in the coring head and separate the wire from the tool. It was necessary to repeat this operation several times because it was not possible to determine from the weight on the wire whether or not the go-devil was still attached. The coring head was then retrieved, without the go-devil, and the circulation head was installed. After top-filling the pipe and bleeding off air from the system, we turned on the pumps at 30 spm and pressurized to 1000–1200 psi. Continued pumping at 6–7 spm was required to maintain this pressure, indicating once again that we probably did not have a good seal between the packer and the go-devil. After 10 min., we increased the pump rate to 40–50 spm to bring the pressure up to 2500 psi and shear the pins in the control sleeve in the go-devil, locking inflation pressure in the packer. We then shut in the pressure and slacked off on the heave compensator to put weight down on the packer, but it would not support any weight. Surprisingly, the pressure in the system still held near 2500 psi. We also tried pulling the packer up the hole, but it offered no resistance, suggesting that the element was not fully inflated, despite the high pressure held by the system. Finally, we bled the pressure off, allowing the spring in the go-devil to shift the sleeve back, opening the hydraulic connection to the hole below the packer. As the packer would still not support any weight, we pumped down the deflation ball and ended the test.

As the pipe needed to be tripped in preparation for the deployment of the ONDO tool, we elected to leave the go-devil and gages in the packer so that we could examine the condition of the seals and the position of the go-devil after the assembly was returned to the surface. When the packer was removed from the BHA we found that the inner barrel and the connector between the two gage cages had both backed off, presumably because of vibration in the drill string resulting from the strong current, and both complete gage assemblies were lost. Examination of the go-devil revealed that three of four main seals had been stripped off the tool during the trip down the pipe on the wireline at the start of the second test. Without these seals, we never had a chance of holding pressure in the packer element. In addition, the packer element was partially filled with a mixture of formation and logging mud, probably pumped in during the first inflation, which explains why the element would not deflate completely after we dropped the deflation ball. Apparently the collapse of a significant portion of the open

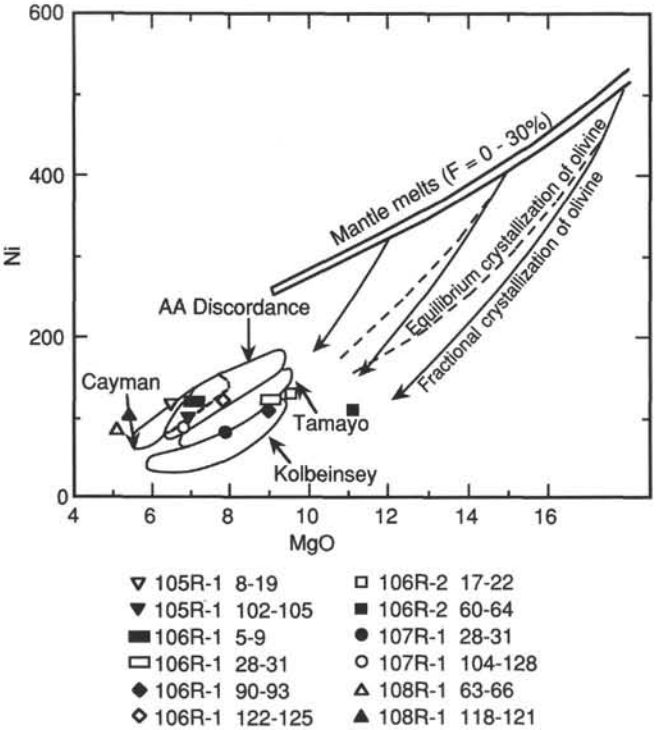

Figure 111. Ni vs. MgO discrimination diagram of Hole 808C basalts. Fields for rocks from mid-Cayman Rise, East Pacific Rise southward of Tamayo transform, Australia-Antarctic (AA) discordance, and Kolbeinsey ridge are also shown (after Klein and Langmuir, 1987).

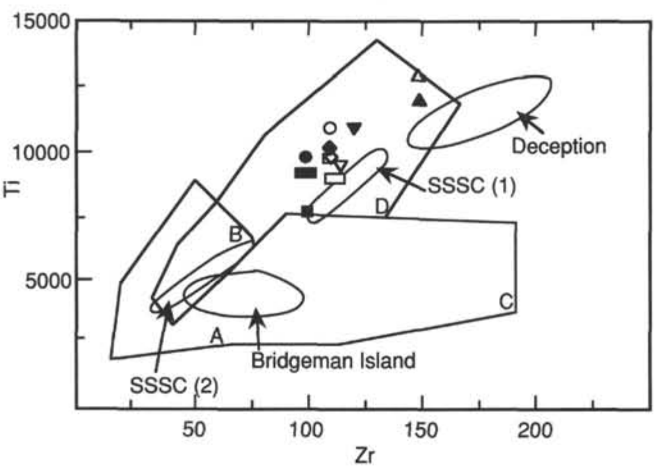

Figure 112. Ti vs. Zr discrimination diagram for basaltic rocks from Hole 808C. Fields **A**, **B**, island-arc tholeiites; **B**, **D**, ocean ridge basalts; **B**, **C**, calc-alkaline basalts (after Pearce and Cann, 1973). Backarc basalts are reported for comparison: SSSC(1) and SSSC(2), South Sandwich Spreading Centre dredges 20-23 and 22-24 respectively (East Scotia Sea); Deception and Bridgeman islands, Branfield strait (Antarctica) (after Saunders et al., 1980). Symbols as in Figure 111.

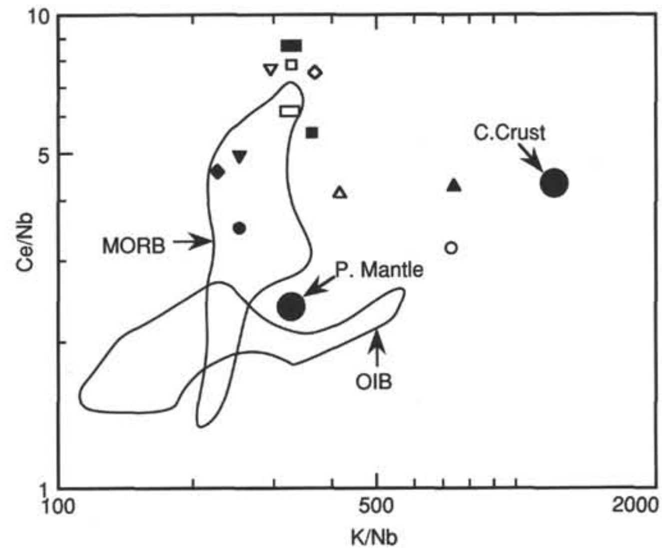

Figure 113. Ce/Nb vs. K/Nb discrimination diagram for Hole 808C basaltic rocks. Fields of MORB and OIB (Ocean Island Basalts) are reported for comparison (after Saunders et al., 1988). Averages for bulk continental crust (Weaver and Tarney, 1984) and primordial mantle estimate (Sun, 1980) are also indicated. Symbols as in Figure 111.

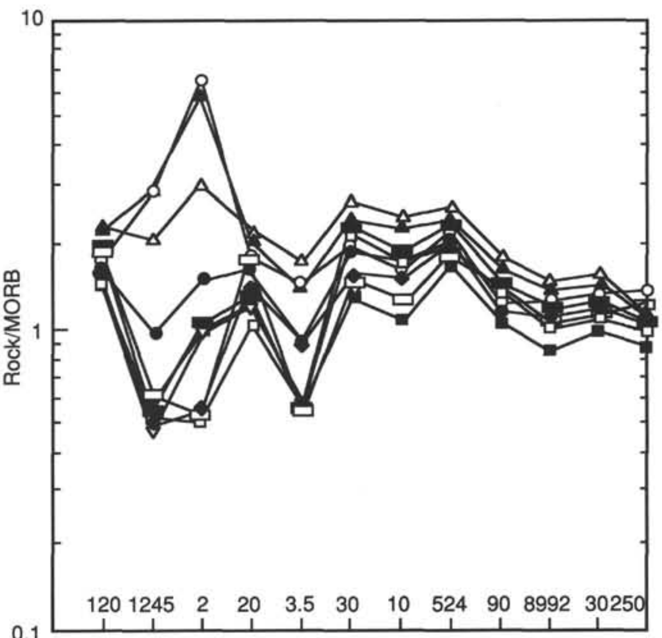

Figure 114. Normal-MORB normalized trace-element patterns for Hole 808C basaltic rocks. Normalizing values after Pearce (1982) except for La and Cr. Symbols as in Figure 111.

hole below the casing displaced mud up inside the casing, as well as the BHA and packer assembly, making repeated sets impossible.

LAST-I

The lateral stress tool (LAST-I) was run at Site 808. This tool is designed to measure *in-situ* lateral effective stress and pore pressure (see Explanatory Notes, this volume). In addition, the tool is equipped with a temperature sensor so that the strain gages used to measure effective stress can be temperature corrected for determination of *in-situ* stress. The deployment and measurements at Site 808 mark the first time that *in-situ* stress measurements were obtained in an active margin setting.

LAST-I was deployed in Holes 808F and 808G (Table 28). The deployments in Hole 808F did not result in measurements of stress or pore pressure in the seabed due to operational

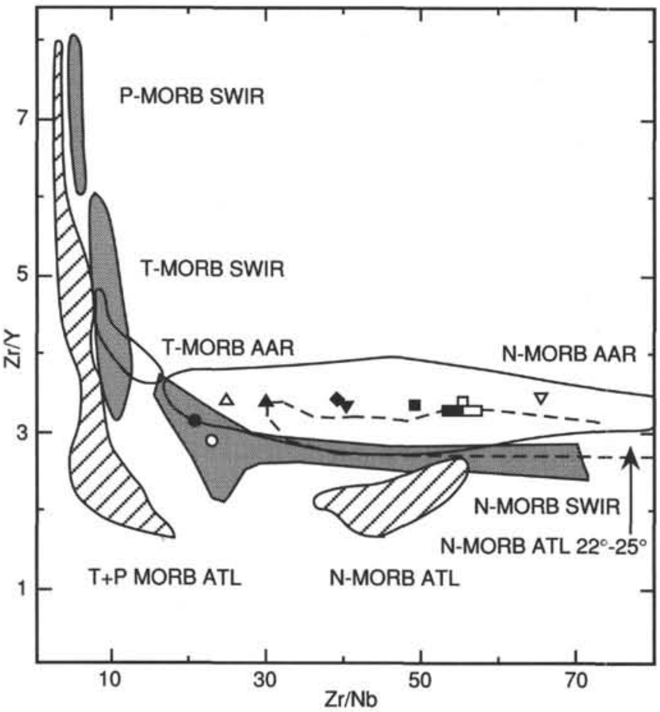

Figure 115. Zr/Y vs. Zr/Nb discrimination diagram for Hole 808C basaltic rocks. Field for P-, T-, and N-MORB form South West Indian Ridge (SWIR), American Antarctic Ridge (AAR), and Atlantic Ridge (ATL) are also reported for comparison. Symbols as in Figure 111.

problems with the LAST-I software. Deployments 808G1, 808G3, and 808G4 in Hole 808G were successful. This first ODP test of LAST-I showed the tool to be very rugged, withstanding the high vibration of the drill string at this Site 808 (see Operations section, this chapter). Although the tool was subjected to excessive vibrations, it was deployed and recovered seven times with only minor damage to the tool. On the second deployment, one of the lateral stress sensors was damaged. This was most likely due to sand infiltration within the pore-fluid pressure chamber. On the final two deployments, the tool was recovered under very low power so that only the binary data could be transferred from the tools. Shore-based decoding of these files showed that the strain sensors were overstressed and require re-calibration to interpret the results. These calibrations will be completed for the *Scientific Results* volume of ODP Leg 131.

Deployment 808G1 shows a complete pore-pressure response over the tool deployment period (Fig. 150). The pore-pressure decay curve (Fig. 151) shows the maximum possible excess pore pressure at the time of pullout of the tool. At a depth equivalent to full penetration of the tool below the bottom of the hole (191 mbsf), the hydrostatic pressure is 49,030 kPa, which is shown as a heavy line on Figure 151. The pore pressure decayed to a minimum of 49,520 kPa prior to tool pullout. The combination of very rapid decay of the high pore pressure response and the shape of the decay curve suggest that the pore pressure was close to equilibrium prior to tool pullout. However, this can only be substantiated by measurement of consolidation test parameters that will be completed for the Leg 131 *Scientific Results* volume. This initial interpretation of the pore-pressure data, however, suggests excess fluid pressure at 186 mbsf.

Lateral stress measurements for deployment 808G3 show that equilibrium measurements were reached for the two working sensors (Fig. 152). These sensors are located 120° apart in the horizontal plane. Sensor 3 measured a higher effective lateral stress (3540 kPa) than sensor 2 (2400 kPa). Three lateral measurements are required to resolve principal stresses in one plane. However, if the sensor 3 measurement is assumed to be the maximum stress in the horizontal plane, then the minimum stress in this plane is 2210 kPa. The vertical effective stress (1878 kPa), which is shown as a dark line on Figure 152, is less than the measured horizontal stresses. The K-ratios (σ_H/σ_r) resulting from these measured values range from 1.2 to 1.9.

The equilibrium temperature measurement for deployment 808G-1 was 22°C. Figure 153 shows the temperature response of the tool, which shows unusually high temperature measurements within the drill string with the tool 20 m above the bottom of the hole.

In summary, the first deployments of LAST-1 proved the tool to be rugged in very harsh environments. Measurements indicate that high lateral stresses exist even within the shallow sediment section. Also, pore pressure response indicates excess fluid pressure at shallow depths below seafloor within the prism.

ONDO

Introduction

It is likely that significant movement of interstitial water is occurring in accretionary prisms, driven by subduction and accretion processes. As the fluid flows carry not only materials but also heat, the flow patterns are reflected in the subsurface temperature structure. At ODP Sites 674 and 676 in the Barbados Ridge area, changes in downhole temperature gradients were observed at fault zones, indicating the existence of warm fluid flow along the faults (Shipboard Scientific Party, 1988). Such pore-water flows may vary with time, associated with tectonic processes such as earthquakes, and the variation can be detected through monitoring the temperature structure.

Up to the present, monitoring of the temperature below the seafloor has been done only in the surface sediment, down to several meters. The ONDO experiment is the first attempt to monitor the temperature profile in a deep hole on the seafloor, and a new long-term temperature recording system, the ONDO tool, was developed for this purpose (see ONDO section, Special Tools chapter, this volume). The system originally had an 800-m-long temperature cable with 19 thermistor sensors at intervals of 40 m and one pressure gage at each end (cf. Fig. 5, Special Tools chapter, this volume). Temperature and pressure are recorded once a day, and the data can be retrieved at any time by a surface ship using acoustic telemetry signals. The system is expected to work for at least 3 yr, and has an estimated battery life of 5 yr.

Objectives

One of the main objectives of the ONDO experiment is to monitor temporal variations in the fluid flows at Site 808. Possible patterns of fluid movement are diffuse flow throughout the sediment layers and localized flow along particular zones (e.g., the first major thrust at about 366 mbsf and the décollement at about 950 mbsf). Although the thermistor cable does not reach the décollement, the effect of the fluid movement along it might be propagated through the hole and detected. If the top of the hole can be sealed when the appropriate technology is available, the pressure sensors will provide information on the variation in pore pressure of the surrounding layers.

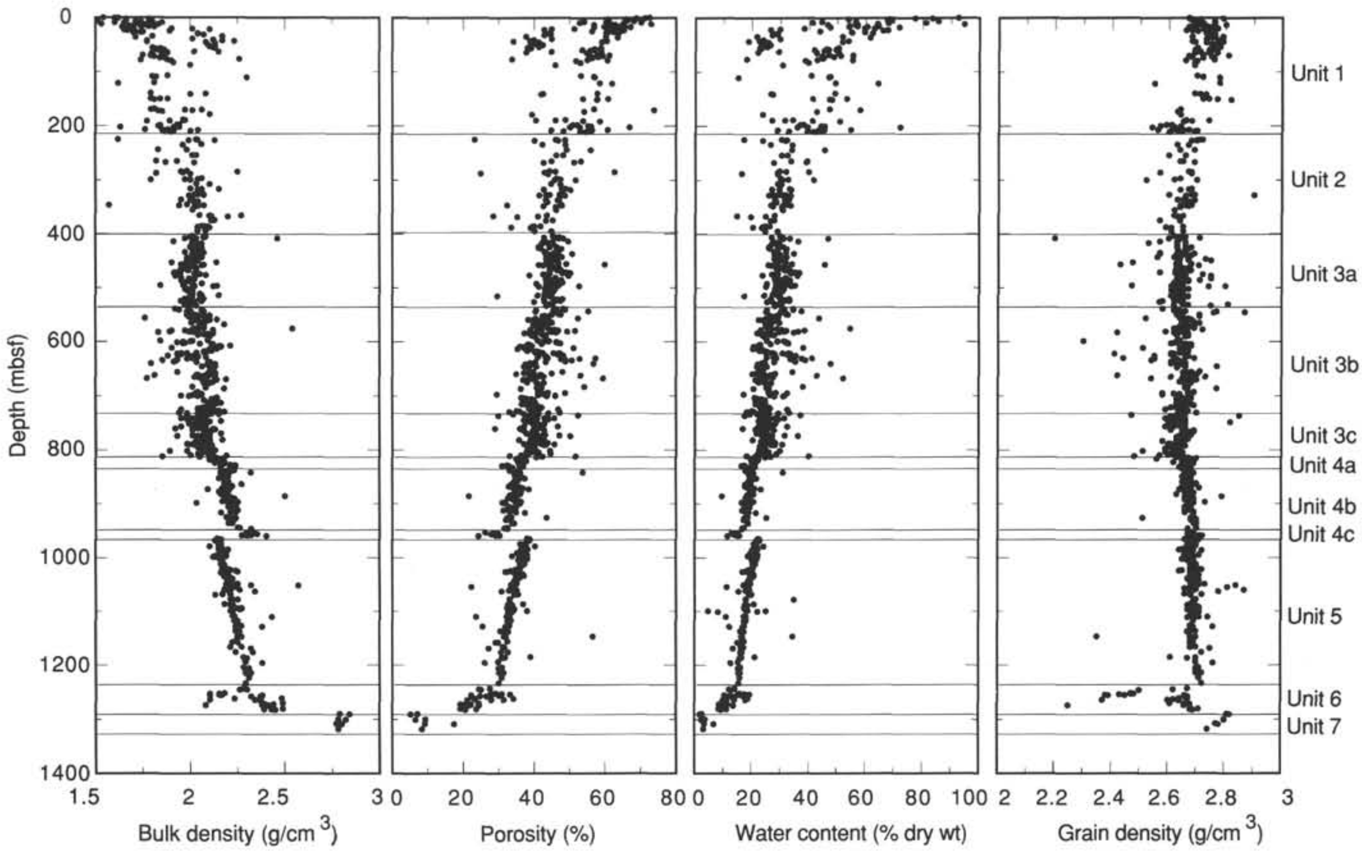

Figure 116. Composite plots of Site 808 index properties vs. depth subdivided into physical property units.

Another main objective is to determine the temperature profile at this site accurately, which is very important for investigating the heat-transfer regime and the origin of the large surface heat flow (see Heat Flow section, this chapter). Temperature data in ODP drill holes are usually obtained either by pushing sensors into the undisturbed sediments below the bottom of the hole or by logging the temperature in the hole after drilling. However, the push-in tools cannot be used for well-consolidated sediments below a certain depth, and it is often difficult to extrapolate the wireline temperature logs to equilibrium with enough accuracy. The ONDO system will provide not only the equilibrium temperature structure but also record the variations in the temperature profile while approaching the equilibrium, data that will constrain models for extrapolating the temperature disturbed by drilling circulation.

Operations

Deployment of the ONDO system was attempted in Hole 808E, which was 1200 m deep and cased down to 520 mbsf. During downhole logging it was proved that the hole conditions were too unstable to deploy the 800-m-long cable. The bottom 280 m of the cable carrying six temperature sensors was cut off before deployment, and the bottom end of the cable was expected to be only about 10 m below the casing shoe when the system was set in the hole.

First, the thermistor cable and recording package were lowered into the drill pipe and a test of acoustic data transmission was made in the air, keeping the acoustic transducer above the rig floor. As the system did not respond to any acoustic command, the recording package was recovered on the deck and examined. It was found that strong vibration of the pipe excited by the Kuroshio current had loosened and rotated connections between pressure housings of the recording package while they were hanging inside the drill pipe, resulting in breaks of some electric wires in the recording package.

After the electronics was repaired and the connections were strengthened, the system was lowered down through the drill pipe with the logging cable. However, the tool became stuck about 3830 m below the rig floor and was retrieved to the surface. During the round trip to 3830 m, physical connections of several parts of the system were unscrewed and sheared.As a result, the acoustic transducer was severely damaged, a zinc anode fell off, and the electronics stopped responding to acoustic commands. The lost zinc anode was thought to be causing the jamming of the tool in the drill pipe. The acoustic transducer and electronics were repaired, and the mechanical strength of the system was enhanced as far as possible.

When the third lowering attempt was made, the tool stopped at the same depth. The whole system, including the thermistor cable, was brought up on the rig floor to examine the drill pipe. The weight at the bottom end of the cable, consisting of five 60-cm long rods, was found to be missing due to unscrewing of the connection. It was suspected that these rods were jammed inside of the drill pipe and prevented the tool from going down. A core barrel with a sinker bar was run down to the bottom end of the drill pipe to clear any obstructions, but none were found.

On the fourth trial, the system was lowered with a new weight. This time it jammed inside the bottom-hole assembly. The wire tension suddenly decreased when the top of the tool reached about 4660 m below the rig floor with the landing pads

Table 23. Index property-based unit divisions and exponential regression equations for porosity-depth and bulk density-depth.

Unit/ Subunit	Interval (mbsf)	
1	0–215	Slope apron/axial trench wedge
2	215–395	Axial trench wedge/ trench to basin transition
3a	395–535	Trench to basin transition
3b	535–740	Ash/Tuff, hemipelagic mud—Upper Shikoku Basin
3c	740–812	Ash/Tuff, hemipelagic mud—Upper Shikoku Basin
4a	812–830	Hemipelagic mud—Lower Shikoku Basin
4b	830–950	Hemipelagic mud—Lower Shikoku Basin
4c	950–965	Hemipelagic mud—décollement zone
5	965–1240	Hemipelagic mud—Lower Shikoku Basin
6	1240–1290	Ash
7	1290–1327	Basalt
Exponential regression porosity vs. depth		R
Unit 1	porosity = 56.225 $e^{(-0.00045\ z)}$	0.216
Unit 2	porosity = 53.206 $e^{(-0.00062\ z)}$	0.244
Unit 3	porosity = 54.519 $e^{(-0.00018\ z)}$	0.471
Subunit 3.a	porosity = 50.373 $e^{(-0.00024\ z)}$	0.125
Subunit 3.b	porosity = 62.185 $e^{(-0.00025\ z)}$	0.325
Subunit 3.c	porosity = 56.668 $e^{(-0.00045\ z)}$	0.121
Subunit 4.b	porosity = 70.930 $e^{(-0.00082\ z)}$	0.300
Unit 5	porosity = 89.200 $e^{(-0.00090\ z)}$	0.576
Exponential regression bulk density vs. depth		R
Unit 1	bulk density = 1.80 $e^{(0.00034\ z)}$	0.25
Unit 2	bulk density = 1.76 $e^{(0.00042\ z)}$	0.36
Unit 3	bulk density = 1.94 $e^{(0.00009\ z)}$	0.265
Subunit 3.a	bulk density = 2.15 $e^{(0.00015\ z)}$	0.182
Subunit 3.b	bulk density = 1.88 $e^{(0.00014\ z)}$	0.19
Subunit 3.c	bulk density = 1.69 $e^{(0.00025\ z)}$	0.199
Subunit 4.b	bulk density = 1.85 $e^{(0.00020\ z)}$	0.281
Unit 5	bulk density = 1.63 $e^{(0.00029\ z)}$	0.692

z = depth (mbsf)

about 60 m above the re-entry bit. The collar locator installed just above the acoustic transducer indicated that the tool kept going down farther and stopped when the landing pads came somewhere between 10 and 20 m above the bit. The whole system was retrieved again, and it was found that the lower part of the weight was lost. A core barrel was then lowered to 20 m below the casing shoe, and it was shown that the drill pipe and the casing were clean.

Attaching a new sinker to the bottom end of the thermistor cable, the system was lowered once more. It stopped at the same place as in the previous attempt. As it was suspected that friction from the spring-loaded landing pads was too large inside the bottom-hole assembly, which has a smaller diameter than the drill pipe, the landing pads were replaced by thinner ones with weaker springs.

The final attempt with the new landing pads, however, failed again. The tool jammed at the same depth and could not pass through the bit. Operations were terminated at this stage because of a shortage of available time.

The most probable cause of the failure was that the thermistor cable was stretched by its own weight plus the weight of the sinker much more than expected, and the sinker landed on a bridge more than 20 m below the casing shoe. The large friction between the landing pads and the bottom-hole assembly may also have contributed. In the last four trips through the drill pipe, the tool itself suffered no significant damage.

Leg 132

The ONDO system was successfully deployed in Hole 808E during the following engineering leg, Leg 132 (Fig. 154). After the operations on Leg 131, the thermistor cable was shortened by 80 m, and the strength of the landing pads was further reduced. The tool, as finally deployed, contained 11 temperature sensors.

The tool passed through the pipe, landed on the landing subassembly, and was released with the electric release system. After pulling up the drill pipe, a test of acoustic telemetry was conducted with all of the thrusters of the ship shut down. No data were obtained, but this was probably due to the high level of ship's noise.

SEISMIC STRATIGRAPHY AND VSP

General Setting

Site 808 is located on the first anticline at the base of the Nankai Trough accretionary prism, approximately 665 m landward of the frontal thrust and 2900 m landward of the deformation front. The bulk of the core data came from Hole 808C, which is located at approximately CDP 950 on the depth-migrated seismic section. A prominent structural feature on the seismic section is the frontal thrust at 366 mbsf. The thrust dips landward at approximately 40°, and distinctive seismic horizons are displaced approximately 200 m. A second prominent structural feature on the seismic line is the décollement at 945–965 mbsf, which is imaged as two strong positive reflections separated by a strong negative reflection (note that for the 40-Hz peak frequency content of the seismic data, the limit of resolution, one-quarter wavelength, is 12.5 m, so the upper and lower boundaries of a 20-m thick unit should be resolvable).

Correlation between Seismic Stratigraphy and Lithostratigraphy

Depth migration of seismic line NT62-8 provided an excellent image in depth because of velocity control pro-

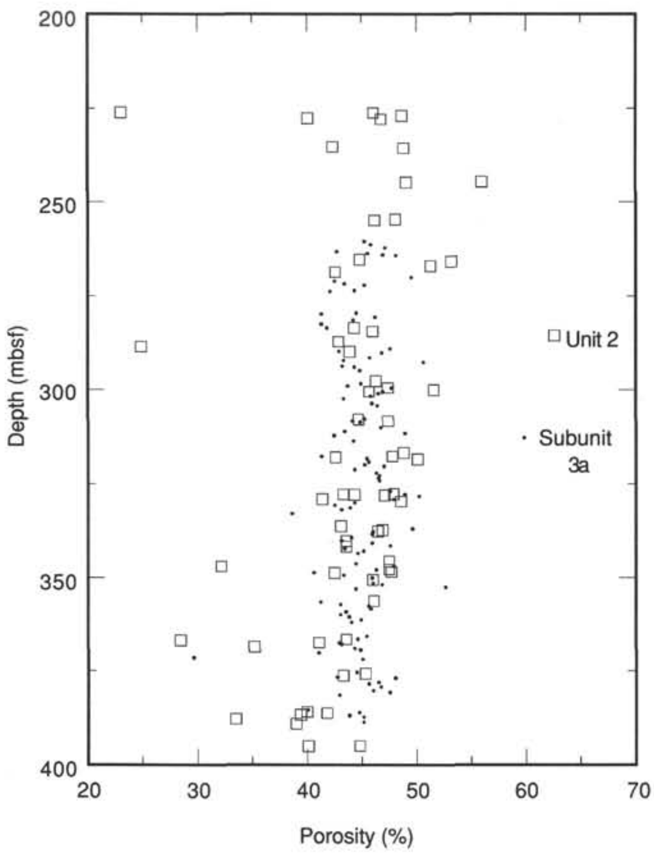

Figure 117. Porosity vs. depth for Unit 2 (open squares) and thrust-corrected Subunit 3a (filled points) sediments illustrates the lack of noticeable additional compaction for the deeper section.

vided by a predrilling two-ship experiment (Stoffa et al., in press). Thus, many of the lithostratigraphic units defined by the shipboard sedimentologists correlate well with seismic reflections (backpocket Fig. 155). The axial trench wedge (lithologic Subunits IIa and IIb, Sedimentology section, this chapter) is imaged as a series of laterally continuous, medium-amplitude reflections. The outer marginal trench wedge (lithologic Subunit IIc) is a zone of low- amplitude reflections imaged above and below the frontal thrust fault. The frontal thrust places the middle of Subunit IIc over the bottom of Subunit IIb at a depth of 366 mbsf. The trench-to-basin transition (Unit III) is a series of four moderate- to high-amplitude reflections that are continuous laterally to the southeast, below the trench wedge. The upper 60 m of the upper Shikoku Basin hemipelagites (lithologic Subunit IVa) are acoustically nonreflective; the lower part of Subunit IVa is a series of three moderate-amplitude, laterally continuous reflections. The upper part (above the décollement) of the lower Shikoku Basin hemipelagites (Subunit IVb) is characterized by low-amplitude, discontinuous reflections. Below the décollement, Subunit IVb is almost acoustically nonreflective; this zone has several very low-amplitude, highly continuous reflections. The acidic volcaniclastic deposits (Unit V) are represented by a single moderate-amplitude reflection overlying the very high-amplitude, laterally continuous, low-frequency basement reflection.

Correlation between Seismic Section and Physical Properties Data

Acoustic impedance (Mg/m^2-s) is the product of velocity (m/s) and bulk density (Mg/m^3). Seismic reflections occur at interfaces that exhibit changes in acoustic impedance. Accordingly, downcore acoustic impedance calculations allow correlation of the sampled lithostratigraphy with the seismic stratigraphy. Physical properties measurements were hampered in the upper 260 mbsf due to low core recovery and sample disturbance due to gas expansion. Below 260 mbsf, the recovered sediment was of sufficient quality to obtain good velocity and density measurements (see Physical Properties section, this chapter).

Figure 121 includes a plot of variation in acoustic impedance with depth. Reflections on the seismic section (backpocket Fig. 155) that correlate with major changes in acoustic impedance occur at 395 mbsf (frontal thrust zone), 761 mbsf (reflection within the upper Shikoku Basin hemipelagites), 810 mbsf (base of upper Shikoku Basin section), 960 and 965 mbsf (top and bottom of the décollement), 1243 mbsf (at the top of the volcaniclastic section) and at 1290 mbsf (the top of volcanic basement). The impedance change at 1129 does not correspond to a reflection. Acoustic impedance increases sharply at the top of the décollement and then drops sharply at the base of the décollement. This correlates very well with the décollement reflections, which are a strong positive reflection followed by a strong negative reflection. The top of the volcaniclastics and the top of basement also correspond to sharp increases in acoustic impedance and strong positive reflections. An increase in density at the boundary between the upper and lower Shikoku Basin hemipelagites yields a positive change in acoustic impedance and a positive seismic reflection.

VSP

Introduction

A vertical seismic profile (VSP) experiment was conducted to determine the detailed velocity-depth structure and reflection seismogram for the sedimentary sequence penetrated at Site 808. Because of excessive banging of the drill pipe due to drag by the strong Kuroshio Current, the VSP was very noisy and extensive processing will be necessary before final results can be obtained.

Methods

The energy source for the VSP experiment was a 400-in^3 (6.6 L) water gun that was deployed 5 mbsl suspended from the aft port side crane (Fig. 156). The horizontal offset of the water gun from the vertical center-line of the hole was 48 m. The zero time, frequency, and wave shape of the sound signal of the water gun was measured using a hydrophone suspended 4.75 m below the source.

Downgoing and reflected seismic waves produced by the water gun were measured by the Schlumberger well seismic tool (WST) within the cased section of the hole (76–524 mbsf) and in the upper 64 m of the open hole below the casing (524–588 mbsf). The WST consists of four vertically oriented 10-Hz geophones wired in series and a single-step preamplifier (60 dB). It was pressed against the borehole wall by two extendable arms. Seismic signals were recorded in analog form by the WST and transmitted up the logging cable to the Schlumberger-CSU logging data acquisition system, where they were digitized and recorded in LIS format on digital tape. The data tape was then converted to SEG-Y format on the shipboard VAX for shore-based processing.

After we locked the drill pipe into the re-entry cone and engaged the heave compensator, the experiment proceeded as follows: the WST was first deployed to the deepest depth possible in the open hole (approx. 588 mbsf) and clamped to the borehole wall. The logging cable was slacked about 15 ft (3 m). The water gun was then fired 15–20 times. Data were

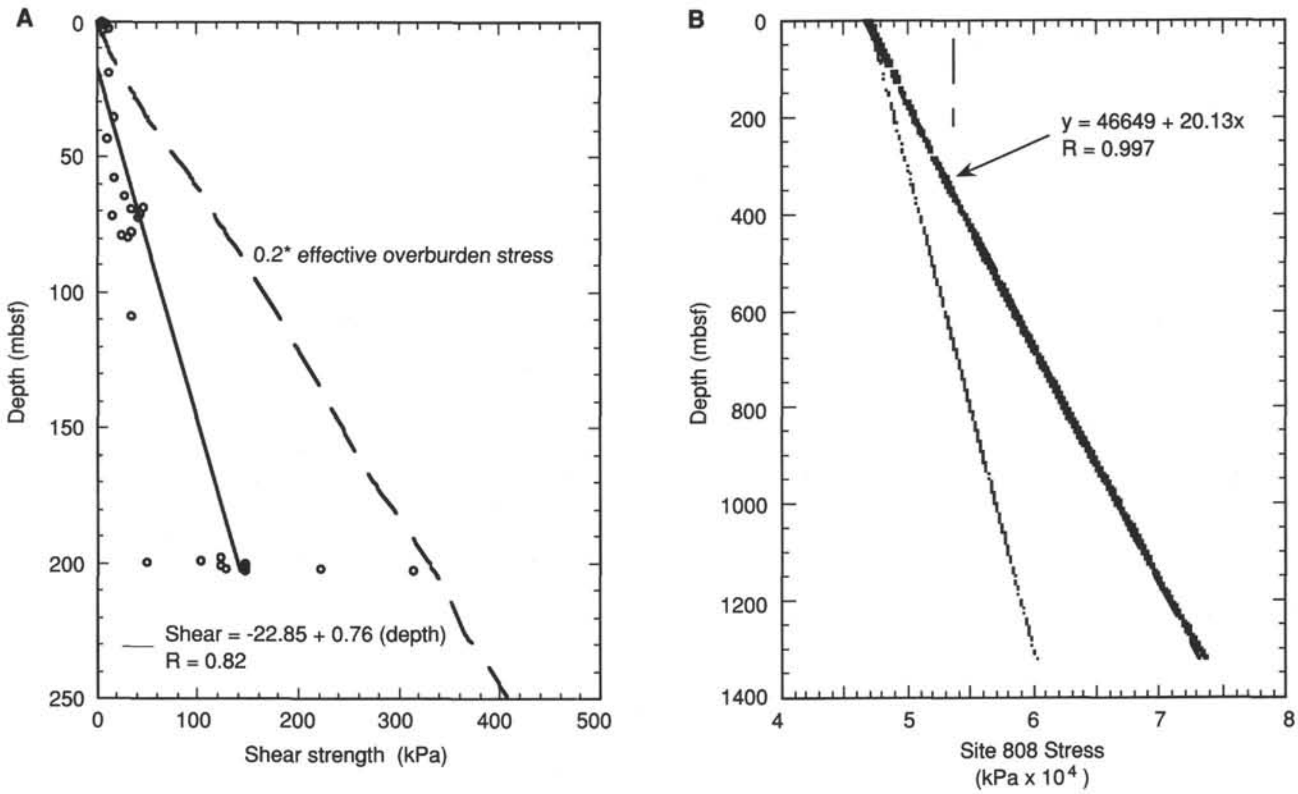

Figure 118. **A.** Shear strength vs. sub-bottom depth for Site 808 sediments. Tests in the upper 110 m were done using a vane and the remainder with a penetrometer. The curve shown for $0.2*p'_0$ marks the lower limit of what are generally considered normally consolidated sediments. **B.** Hydrostatic and lithostatic stress distributions calculated assuming zero excess pore-fluid pressure for Site 808.

recorded at seven levels at 30-ft (9.1-m) intervals within the open hole. At the base of the casing (524 mbsf), the clamp interval was increased to 40 ft (12.2 m), and 38 levels were recorded, ending at 76 mbsf. Approximately 15 shots were fired and stacked at each level. Each individual shot was also recorded. Signals were recorded for 3.0 s at 1 ms sample interval. The WST was then unclamped and moved up to the next level (30 or 40 ft), and the procedure was repeated.

Results

The VSP experiment took approximately 15 hr to complete. During this time, seas were relatively calm, but the Kuroshio Current was very strong. A total of 45 seismometer clamp positions were occupied. Approximately 5 min per level was required.

Preliminary processing of the VSP was carried out post-cruise at the University of Hawaii (Fig. 157). Processing consisted of resampling 2 ms, filtering (18-24-80-100 Hz), editing of obvious bad traces, median stacking, muting to first arrival, scaling (AGC), and plotting. The preliminary VSP record is very noisy, but a distinct first arrival is detected at most recording levels, so time-depth correlations and interval velocity calculations will be possible. A band of up-going (reflected) arrivals can also be seen dipping from about 4.1–4.2 s at the deepest recording level to 4.3–4.4 s on the shallowest level. Other indistinct up-going and down-going arrivals can also be seen. Future processing (including dip filtering) will be necessary before final interpretation can be undertaken.

HEAT FLOW

Introduction

The main goal of the heat-flow program at Site 808 was to determine the thermal regime of the toe of the Nankai accretionary prism. Of particular importance was the relationship between heat loss and fluid flow during sediment accretion.

Previous studies of the Nankai accretionary prism and adjacent Nankai Trough (Kinoshita and Yamano, 1986) have found high heat flow at the toe of the prism. Site 808 is located within this high heat-flow zone, which encompasses the trench and the lowermost part of the prism and extends along it over more than 200 km between 134°E and 136°E (Fig. 158). The surface heat flow values in this region consistently exceed 100 mW/m². Heat flow gradually decreases upslope on the prism to about 50 mW/m². In the Shikoku Basin, the heat flow values show a large scatter, with the most reliable measurements averaging 82 mW/m² (Yamano and Uyeda, 1988).

The landward decrease in heat flow can be explained by low temperatures at depths associated with subduction, the tectonic thickening of the prism, and high sedimentation rates, but the origin of the high heat flow at the toe of the prism remains poorly understood (Kinoshita and Yamano, 1986). One interpretation is that the high heat flow results from conductive cooling of the young, still hot, Philippine Sea lithospheric plate that is being subducted beneath the Nankai prism. The Shikoku Basin is generally believed to have formed by oceanic spreading between 25 and 15 m.y. ago (e.g., Shih, 1980). The predicted conductive heat flow for an

Table 24. Undrained shear strength of Site 808 sediments. In the lithology column, clayey silts and silty clays are not distinguished.

Sample Core-section interval (cm)	Comment	Lithology*	Depth (mbsf)	Strength kPa)
131-808A-				
1H-1, 95			0.95	9.40
1H-1, 60			0.60	5.00
1H-2, 100			2.50	12.30
1H-2, 20			1.70	8.00
1H-3, 42		sand	3.42	6.80
3H-3, 50	gassy	silt	19.30	12.50
5H-1, 50			35.30	17.80
5H-6, 95			43.25	10.00
7H-3, 115	gas cracked		57.95	16.70
8H-1, 125	small cracks		64.55	26.70
9H-1, 30	small cracks		68.60	45.70
9H-1, 125	small cracks		69.55	33.40
9H-2, 125	small cracks		71.05	42.30
9H-3, 42	Torvane		71.72	14.70
9H-3, 125	small cracks		72.55	41.20
10H-1, 20			78.00	33.40
10H-1, 115			78.95	23.40
10H-2, 15		sandy silty clay	79.45	30.10
13H-2, 100	clay		108.90	33.40
131-808B-				
10X-1, 57	biscuit		197.97	123.00
10X-1, 135	biscuit		198.75	103.00
10X-2, 20	p. penetrometer		199.10	103.00
10X-2, 73	p. penetrometer	silt	199.63	49.00
10X-2, 125	p. penetrometer		200.15	147.00
10X-3, 28	p. penetrometer		200.68	123.00
10X-3, 110	p. penetrometer		201.50	147.00
10X-3, 125	p. penetrometer		201.65	147.00
10X-4, 10	p. penetrometer	sand	202.00	128.00
10X-4, 27	p. penetrometer		202.17	221.00
10X-4, 83	dark color	sand	202.73	147.00
10X-4, 89	below color change		202.79	314.00

*Lithology is silty clay except where noted; silty clay and clayey silts are not distinguished.

oceanic plate of 15 m.y. age is about 130 mW/m^2 (Lister, 1977), close to the high heat flow measured in the Nankai Trough. If this interpretation is correct, the lower heat flow measured in the Shikoku Basin implies that a large amount of heat flowing in this basin from the cooling Philippine Sea Plate is dissipated to the seafloor through convective heat transfer, and not measured. The heat flow regime would then evolve from mixed conductive and convective in the Shikoku Basin to largely conductive in the Nankai prism, possibly because the increasing sediment thickness seals fluid conduits between the permeable crust and the seafloor. Although this interpretation may well account for the high heat flow at the toe of the Nankai prism, thermal effects of fluid outflow associated with sediment accretion remain undocumented. The thermal effects of fluid circulation can dominate the thermal regime at the toe of accretionary prisms, as observed for the Barbados prism (Langseth et al., 1990), and this might also be true for the Nankai prism.

Specific objectives of the geothermal measurements program at Site 808 were:

1. To determine the advective vs. conductive nature of heat transfer. Simple upward pore-water advection may generate a curved temperature profile while localized flows may produce discontinuities in temperature-depth profiles.
2. To identify thermal anomalies associated with channelized fluid flow, possibly along the décollement or the main frontal thrusts.
3. To use thermal data to assist in modeling accretion and fluid flow through pores and along fractures.
4. To provide a reference and calibration for studies of the location and stability field of methane hydrate bottom-simulating reflectors (BSRs) in this and other areas.
5. To provide control for geochemical studies and models, for studies of vitrinite reflectance, palynomorph color thermal alteration, and other thermal indicators.
6. To obtain a measurement of deep conductive heat flow (below fluid flow levels) from the Philippine Sea Plate for regional tectonic interpretation.

To meet these objectives, eleven downhole temperature measurements were attempted at Site 808 using the WSTP tool (Explanatory Notes chapter, this volume). Six deployments were successful, five in Hole 808B between 217 and 347 mbsf and one in Hole 808F at 91 mbsf. Four temperature logs using the TLT probe (Explanatory Notes chapter, this volume) were also recorded, a short one in Hole 808B from 0 to 215 mbsf, a longer one in Hole 808C between 0 and 770 mbsf, and the two others in Hole 808E, the first one between 0 and 600 mbsf and the second one between 0 and 650 mbsf.

In addition, extensive thermal conductivity measurements were made on the recovered cores (see Physical Properties section, this chapter), allowing thermal gradients to be reliably converted to heat flow.

WSTP Measurements and Results

Hole 808A

A single deployment of the WSTP tool was attempted in Hole 808A, following Core 131-808A-12H at 96.9 mbsf. The hole penetrated largely unconsolidated sand and was extremely unstable, and we were unable to wash past 3 m of fill in the bottom of the hole to push the probe into undisturbed sediment. When circulation was stopped following deployment of the probe, sand was apparently forced up inside the pipe and the tool was jammed. The tool was later recovered with a standard overshot on the sandline. No temperature record was obtained from this deployment.

Hole 808B

Five of six deployments of the WSTP tool in Hole 808B were successful, as summarized in Table 29. Significant frictional heating occurred on all penetrations, with the temperature vs. time records exhibiting the characteristic probe-penetration heating pulse and subsequent decay. For most measurements the probe was kept in the bottom for 10 to 12 min, allowing accurate extrapolation to equilibrium formation temperature. The 1/time approximation was used for extrapolation from the temperature record over a time interval of approximately 4–12 min. The effective origin time of the thermal pulse was estimated by varying the assumed origin time until the thermal pulse decay followed the theoretical curve. A delay of 35 to 140 s from the time of initial penetration heating was found to be required to give a linear 1/t plot. All of the measurements reported appear to be reliable, exhibiting good penetration heating and initial decay curves.

The first deployment took place following Core 131-808B-10X with a probe depth of 198.3 mbsf (Fig. 159A). This run used the Uyeda recording package with a sampling interval of 1 min. The sea state was moderate (2-m swell) but the hole was unstable. During the first penetration attempt, 2 m of fill prevented the bit from reaching total drilled depth (TD). The probe was then unlatched from the bit and circulation and rotation of the pipe commenced to clean out the hole. The probe was then relatched at the bit and pushed in past TD, resulting in a good penetration record. The equilibrium temperature determined from this run is 25.6 (±0.1) °C (Fig.

159B). A 10-min pause at near the seafloor following collection of sediment temperatures revealed an apparent bottom-water temperature of about 2.5°C, which was later shown to be about 0.8°C too high, probably due to circulation during the measurement and positioning of the probe slightly below the seafloor.

The next deployment took place after Core 131-808B-11X to a depth of 217.4 mbsf and produced an excellent record (Fig. 160A). We used the new WSTP recording package that sampled at 4.98-s intervals. The sea state was still moderate and the hole was kept clear of fill by continuous circulation. The final temperature from this run was estimated to be 28.7 (± 0.1) °C (Fig. 160B). An unusually high near-bottom temperature measurement led us to assume initially that the recording package was faulty; all remaining runs in Hole 808B were completed using the Uyeda electronics. We now believe that these higher than bottom water temperatures resulted from positioning the probe just below the seafloor, where the hole temperature was affected by drilling circulation disturbance.

The third deployment of the WSTP tool took place following Core 131-808B-15X at a probe depth of 255.3 mbsf (Fig. 161A). The probe apparently moved about 8 min after penetration, allowing cold bottom water to reach and cool the thermistor. The earlier portion of the decay curve did provide enough information, however, for us to estimate a well-constrained final sediment temperature of 30.2 (±0.1) °C (Fig. 161B).

A fourth measurement following Core 131-808B-20X at a probe depth of 298.6 mbsf took place in calm seas and good hole conditions. The resulting temperature profile yielded a good decay curve (Fig. 162A) and an extrapolated temperature of 31.4 (±0.2) °C (Fig. 162B). The estimated error associated with this measurement is somewhat larger than in previous measurements because of a small-amplitude oscillation of unknown origin affecting the temperature record.

The fifth and final successful temperature measurement in Hole 808B followed Core 131-808B-26X at a probe depth of 346.7 mbsf. Despite the formation as recovered in the core being both hard and friable, allowing extremely poor recovery with the XCB coring system, the probe apparently penetrated well into the sediment, yielding an excellent thermal decay curve and an extrapolated equilibrium sediment temperature of 39.7 (±0.1) °C (Fig. 163).

A sixth temperature measurement was attempted following Core 131-808B-28X but hole conditions had deteriorated so that it was not possible to keep the hole clean to TD to allow penetration of the probe into undisturbed formation. An irregular and low-temperature record was obtained. During the fifth and sixth deployments of the WSTP tool in Hole 808B, accurate bottom- water temperature measurements were finally made by holding the tool approximately 50 m above seafloor for 10 min with the circulation pumps off, immediately prior to lowering the tool to the bit. This procedure yielded consistent temperatures of 1.6°C for the bottom water.

Hole 808C

A single WSTP deployment was attempted in Hole 808C immediately prior to collecting Core 131-808C-1X at a depth of 298.5 mbsf. Unfortunately it was not possible to keep the hole clear to TD and we were unable to push the tool into the undisturbed sediment. No useful data were collected during this run.

Hole 808F

Two measurements were attempted in Hole 808F, with the first following Core 131-808F-1M at a depth of 56.1 mbsf. Although the tool functioned properly, the temperature record from this run suggests that the core barrel behind the tool did not unlatch from the bit, so that the tool was pulled out of the sediment before the probe had a chance to equilibrate. We used this first run in Hole 808F to make a confidence test with the new electronics package, by running both recorders at the same time. The old (Uyeda) electronics package was used to monitor the main-probe thermistor, while the new package monitored a thermistor taped to the side of the metal shell which surrounds the electronics and plumbing of the WSTP tool. The results of this experiment established that the new electronics package was working properly.

The second WSTP run in Hole 808F followed Core 131-808F-3M at a depth of 91.1 mbsf. This run was successful and yielded an equilibrium temperature of 12.1 (± 0.2) °C (Fig. 164).

Hole 808G

Two measurements were attempted in Hole 808G, the first following Core 131-808G-4X at a depth of 140.1 mbsf. When the tool was returned to the surface and separated from the core barrel, it was found to have flooded. Inspection of the tool suggested that the flooding occurred when the valve opened to sample pore fluid, after the tool had been inserted into the sediment, because one of the fittings between the rear bulkhead of the tool and the fluid overflow chamber was loose. This fitting was tightened prior to tool deployment but must have backed off because of pipe vibration. When the valve opened, the hydraulic connection between the inside of the tool, which was at approximately atmospheric pressure, and the fluid in the borehole, at hydrostatic pressure near 500 bars, was made complete, and the tool must have filled rapidly. The seawater in the tool shorted out the electronics packages controlling temperature recording and fluid sampling so that nothing useful was obtained.

A second run in Hole 808G was attempted following Core 131-808G-7M and a run of the WSTP tool in pore-pressure configuration, at a depth of 192.0 mbsf. Because the WSTP temperature tool was flooded on the previous deployment, we rigged the old Uyeda probe, which has no water-sampling capability and requires the use of the narrower, original electronics package. We used the same front bulkhead as was used in the previous WSTP deployment, after plugging the water inlet lines and replacing the electronic connector. When the Uyeda tool was returned to the surface it was found to be flooded, and to be holding seawater under great pressure as well. Inspection of the front bulkhead revealed that the electrical pass-through connector had ruptured from the inside out. These connectors are designed to hold pressure from the outside only, and the rupture most likely occurred while the tool was being raised to the surface, because the fluid trapped inside under pressure could not escape as quickly as the external pressure dropped. As this was a new connector, it is unlikely to have been flawed prior to deployment. The source of the leak into the pressure case remains unresolved.

Preliminary Results of WSTP Temperature Tests

The two shallowest measurements in Hole 808B and the one in Hole 808F are consistent with a thermal gradient in the upper 217 mbsf of 122°C/km (constrained to pass through the bottom-water temperature of 1.6°C). The third and fourth measurements in Hole 808B at 255 and 298 mbsf deviated substantially below this gradient, the gradient between 217.4 and 298.6 mbsf being 30°C/km. The final measurement in Hole 808B suggests a higher gradient between 298.6 and 346.7 mbsf of 173°C/km. Taking all six sediment temperatures together, the least-squares gradient constrained to pass through the bottom-water temperature is 111°C/km (Fig. 165).

Table 25. Thermal conductivity of Site 808 samples. Values shown have been corrected to estimated *in-situ* temperature and pressure conditions.

Core, section interval (cm)	Lithology*	Depth (mbsf)	Thermal Conduct. (corr.)(W/m °C)
131-808A-			
1H-1, 55	T8	0.55	1.07
1H-1, 105	T8	1.05	1.06
1H-2, 55	T8	2.05	1.09
1H-2, 105	T4	2.55	1.08
1H-3, 50	T8	3.50	1.21
1H-3, 100	T8	4.00	1.00
1H-4, 50	T6	5.00	1.27
1H-4, 100	T8	5.50	0.98
2H-1, 122	T8	7.52	0.91
2H-3, 107	T4	10.37	0.83
2H-5, 21	T4	12.51	1.03
2H-6, 86	T4	14.66	0.93
2H-7, 44	T8	15.74	0.87
3H-1, 50	T8	16.30	0.92
3H-1, 100	T8	16.80	0.88
3H-2, 50	T6?	17.70	0.82
3H-3, 50	T5	19.20	0.96
3H-3, 100	T8	19.70	0.77
3H-4, 15	T8	20.35	0.86
3H-5, 90	T4	22.60	0.87
3H-6, 50	T6?	23.70	0.97
4H-1, 25	T8	25.55	0.95
4H-1, 95	T8	26.25	0.88
4H-2, 30	T8	27.10	0.95
4H-2, 90	T8	27.70	0.94
4H-3, 50	T8	28.33	0.86
5H-6, 100	T6	40.72	1.02
6H-1, 24	T6	44.54	1.14
6H-1, 90	T8	45.20	0.90
7H-1, 50	T6	54.30	1.24
7H-1, 90	T6	54.70	1.08
7H-2, 25	T8	55.55	0.88
7H-3, 113	T8	57.88	1.05
7H-4, 10	T8	58.35	0.85
7H-4, 90	T8	59.15	0.74
7H-5, 18	T8	59.93	0.77
7H-6, 20	T6	61.28	1.22
9H-2, 110	T8	70.90	1.07
9H-3, 109	T8	72.39	1.15
9H-4, 35	T8	73.15	1.00
13H-1, 12	T8	106.52	0.95
13H-2, 65	T8	107.89	0.91
131-808B-			
2X-1, 25	T8	120.85	0.99
2X-1, 65	T8	121.25	0.94
4X-1, 20	T8	140.10	1.08
4X-1, 70	T5	140.60	1.32
5X-1, 23	T8	149.73	1.12
5X-2, 25	T8	150.78	1.09
7X-1, 90	T5	169.70	1.13
7X-2, 105	T5	171.35	1.19
7X-3, 30	T5	172.10	1.09
7X-4, 15	T5	173.35	1.34
7X-4, 60	T8	173.80	1.12
9X-2, 15	T5	189.85	1.14
9X-2, 65	T5	190.35	1.16
9X-4, 40	T5	193.10	1.28
10X-1, 35	T8	197.75	1.17
10X-1, 95	T6	198.35	1.12
10X-2, 10	T5	199.00	1.43
10X-2, 130	T8	200.20	1.10
10X-3, 25	T8	200.65	1.10
10X-3, 125	T8	201.65	1.08
10X-4, 35	T8	202.25	1.22
10X-4, 105	T8	202.95	1.25
11X-1, 48	T8	207.28	1.12
11X-2, 42	T8-T6	208.72	1.14
11X-2, 86	T8	209.16	1.08
11X-3, 16	T6	209.96	0.99
13X-1, 48	T8	226.28	1.27
13X-1, 91	T8	226.71	1.23
13X-2, 40	T5	227.70	1.44
13X-2, 82	T8	228.12	1.13
16X-1, 45	T5	254.85	1.41
17X-1, 70	T5	264.10	1.51
17X-2, 86	T8	265.76	1.36
17X-2, 106	T8	265.96	1.39
17X-3, 10	T8	266.50	1.41
17X-3, 52	T8	266.92	1.41
17X-4, 4	T8	267.94	1.44
17X-4, 55	T8	268.45	1.50
19X-1, 105	T8	283.55	1.30
19X-1, 127	T8	283.77	1.54
19X-2, 56	T8	284.56	1.22
19X-2, 101	T8	285.01	1.22
19X-2, 124	T8	285.24	1.48
19X-3, 27	T8	285.77	1.22
20X-1, 21	T8	288.11	1.53
20X-1, 123	T8	289.13	1.62
20X-CC, 30	T8	290.00	1.53
130-808C-			
1R-1, 76	T4	299.26	1.53
1R-1, 100	T4	299.50	1.58
1R-2, 40	T4	300.40	1.70
130-808B-			
22X-1, 136	T8	308.46	1.56
130-808C-			
3R-1, 75	T8	318.35	1.64
130-808B-			
24X-1, 22	T8	326.62	1.53
130-808C-			
4R-1, 45	T8	327.65	1.65
4R-1, 65	T8	327.85	1.69
130-808B-			
24X-2, 45	T8	328.35	1.36
24X-2, 105	T8	328.95	1.30
24X-3, 75	T8-T5	330.15	1.16
24X-3, 85	T8-T5	330.25	1.43
130-808C-			
5R-1, 16	T5	337.06	1.60
130-808B-			
25X-4, 50	T8	341.00	1.45
25X-4, 95	T8	341.45	1.42
130-808C-			
6R-1, 23	T8	346.83	1.67
6R-2, 115	T8	349.25	1.47
6R-3, 72	T8	350.32	1.54
130-808B-			
28X-CC, 11	T6	355.31	1.36
28X-CC, 20	T8-T6	355.40	1.38
130-808C-			
7R-1, 41	T8	356.61	1.66
8R-2, 11	T8	367.51	1.57
9R-1, 101	T8	376.61	1.37
10R-1, 14	T8	385.34	1.54
10R-2, 107	T8	387.77	1.64
11R-1, 95	T8	395.75	1.59
11R-2, 15	T8	396.45	1.57
12R-1, 120	T8	405.80	1.49
12R-2, 150	T8	407.60	1.60
12R-3, 93	T8	408.53	1.55
12R-4, 35	SR2	409.45	1.60
13R-1, 145	T8	415.75	1.53
13R-2, 122	T8	417.02	1.57
13R-3, 105	T8	418.35	1.72
13R-CC, 4	T8	419.34	1.68
14R-1, 113	T8	425.13	1.60
14R-2, 5	T8	425.55	1.46

Table 25 (continued).

Core, section interval (cm)	Lithology*	Depth (mbsf)	Thermal Conduct. (corr.)(W/m °C)
14R-3, 36	T8	427.36	1.61
14R-4, 23	T8	428.73	1.62
15R-1, 10	T8	433.80	1.56
15R-2, 3	T8	435.23	1.70
15R-2, 107	T8	436.27	1.74
15R-3, 123	T8	437.93	1.73
15R-4, 54	T8	438.74	1.58
15R-5, 13	T8	439.83	1.64
16R-1, 91	T8	443.91	1.54
16R-2, 35	T8	444.85	1.69
16R-3, 15	T8	446.15	1.61
16R-4, 3	T8	447.53	1.66
16R-5, 48	T8	449.48	1.46
17R-1, 19	T8	452.89	1.72
17R-2, 28	T8	454.48	1.67
17R-3, 44	T8	456.14	1.59
17R-4, 64	T8	457.80	1.73
17R-5, 9	T8	458.75	1.65
18R-1, 44	T8	462.84	1.69
18R-2, 121	T8	465.11	1.68
18R-3, 94	T8	466.34	1.71
18R-4, 95	T8	467.85	1.53
18R-5, 90	T8	469.30	1.60
19R-1, 10	T8	472.10	1.42
19R-2, 5	T8	473.55	1.63
19R-3, 85	T8	475.85	1.65
19R-4, 59	T8	477.09	1.66
19R-5, 7	T8	478.07	1.49
20R-1, 36	T8	482.06	1.70
20R-2, 19	T8	483.39	1.64
20R-3, 46	T8	485.16	1.64
20R-4, 118	T8	487.38	1.62
20R-5, 90	T8	488.60	1.77
21R-1, 83	T8	492.13	1.60
21R-2, 20	T8	493.00	1.79
21R-4, 72	T8	496.52	1.56
21R-5, 52	T8	497.82	1.45
22R-1, 10	T8	501.10	1.51
22R-2, 12	T8	502.62	1.42
22R-3, 37	T8	504.37	1.49
22R-4, 110	T8	506.60	1.51
22R-5, 28	T8	507.28	1.62
23R-1, 102	T8	511.72	1.59
23R-2, 86	T8	513.06	1.66
23R-3, 50	T8	514.20	1.61
23R-4, 12	T8	515.32	1.79
23R-5, 16	T5-T8	516.86	1.62
24R-1, 73	T8	521.03	1.64
24R-2, 40	T8	522.20	1.68
24R-3, 40	T8	523.70	1.58
24R-4, 45	T8-T5	525.25	1.60
25R-1, 118	T8	531.18	1.60
25R-2, 90	T8	532.40	1.70
25R-3, 75	T8	533.75	1.61
26R-1, 10	T8	539.80	1.57
26R-2, 13	T8	541.33	1.58
26R-3, 86	T8	543.56	1.67
26R-4, 25	T8	544.45	1.59
26R-5, 23	T8	545.93	1.63
27R-1, 26	T8	549.56	1.58
27R-2, 19	T8	550.99	1.68
27R-3, 29	T8	552.59	1.71
27R-4, 9	T8	553.89	1.65
27R-5, 8	T8	555.38	1.63
27R-6, 92	T8	557.72	1.74
28R-1, 46	T8	559.36	1.65
28R-2, 13	T8	560.53	1.78
28R-3, 24	T8	562.14	1.79
28R-4, 100	T8	564.40	1.63
28R-5, 16	T8	565.06	1.68
29R-2, 55	T8	570.10	1.71
29R-3, 28	T8	571.33	1.63
29R-4, 42	T8	572.97	1.84
29R-5, 40	T8	573.53	1.64
29R-6, 116	T8	575.79	1.68
29R-7, 4	T8	576.17	1.73
30R-1, 110	T8	579.40	1.58

Table 25 (continued).

Core, section interval (cm)	Lithology*	Depth (mbsf)	Thermal Conduct. (corr.)(W/m °C)
30R-2, 5	T8	579.85	1.60
30R-3, 27	T8	581.57	1.76
30R-4, 48	T8	583.28	1.69
30R-5, 92	T8	585.22	1.92
31R-1, 30	T8	587.90	1.73
31R-2, 26	T8	589.36	1.77
32R-1, 116	T8	598.46	1.78
32R-2, 12	T8	598.92	1.45
32R-3, 5	T8	600.35	1.57
32R-4, 112	T8	602.92	1.51
32R-5, 28	T8	603.58	1.72
32R-6, 50	T8	605.30	1.78
33R-1, 16	T8	607.06	1.69
33R-2, 1	T8	608.41	1.80
33R-3, 106	T8	610.96	1.70
33R-4, 26	V1	611.66	1.24
34R-1, 144	T8	617.94	1.68
34R-2, 1	T8	618.01	1.64
34R-4, 26	V1	622.26	1.28
34R-5, 70	T8	623.20	1.84
35R-1, 63	T8-V1	626.83	1.52
35R-2, 118	T8	628.88	1.71
35R-3, 1	T8	629.21	1.62
35R-5, 86	T8	633.06	1.48
36R-3, 5	T8	638.95	1.58
36R-5, 1	T8	641.91	1.71
37R-1, 124	T8	646.74	1.55
37R-2, 75	T8	647.75	1.77
38R-1, 15	T8	655.05	1.75
38R-2, 16	T8	656.56	1.49
38R-3, 116	T8	659.06	1.70
38R-4, 16	T8	659.56	1.75
38R-5, 4	T8	660.94	1.58
38R-6, 52	V1	662.92	1.26
39R-1, 38	T8	664.88	1.63
39R-2, 3	T8	666.03	1.59
39R-3, 120	T8	668.70	1.69
39R-4, 44	T8	669.44	1.86
39R-5, 34	T8	670.84	1.55
40R-1, 103	T8	675.23	1.76
40R-2, 6	T8	675.76	1.65
41R-1, 23	T8	684.03	1.67
41R-2, 1	T8	685.31	1.58
42R-1, 20	T8	693.70	1.71
42R-2, 17	T8	695.17	1.55
42R-3, 106	T8	697.56	1.65
42R-4, 26	T8	698.26	1.49
42R-5, 1	T8	699.51	1.58
42R-6, 4	T8	701.04	1.49
43R-1, 90	T8	704.10	1.66
43R-2, 67	T8	705.37	1.92
43R-3, 98	T8	707.18	1.66
43R-4, 122	T8	708.92	1.73
43R-5, 128	T8	710.48	1.67
43R-6, 83	T8	711.53	1.77
44R-1, 9	T8	712.49	1.58
44R-2, 27	T8	714.17	1.74
44R-4, 112	T8	718.02	1.60
44R-6, 23	T8	720.13	1.60
45R-1, 140	T8	723.40	1.67
45R-2, 137	T8	724.87	1.60
45R-4, 18	T8	726.68	1.61
45R-5, 76	T8	728.76	1.76
46R-2, 117	T8	734.37	1.67
46R-4, 123	T8	737.43	1.70
46R-5, 129	V1	738.99	1.31
47R-1, 33	T8	741.73	1.47
47R-2, 32	T8	743.00	1.54
47R-3, 100	T8	745.18	1.56
47R-5, 75	T8	747.93	1.67
47R-6, 20	T8	748.88	1.58
47R-7, 48	T8	749.86	1.73
48R-1, 41	T8	751.51	1.51
48R-2, 1	T8	752.61	1.59
48R-3, 61	T8	754.71	1.66
48R-4, 44	T8	756.04	1.63
48R-5, 72	T8	757.82	1.56

Table 25 (continued).

Core, section interval (cm)	Lithology*	Depth (mbsf)	Thermal Conduct. (corr.)(W/m °C)
49R-1, 97	T8	761.67	1.60
49R-2, 115	T8	763.35	1.67
49R-3, 141	T8	765.11	1.72
49R-5, 59	T8	767.29	1.72
50R-1, 3	T8	770.43	1.73
50R-2, 1	T8	771.13	1.74
50R-3, 122	T8	773.84	1.54
50R-4, 1	T8	774.13	1.63
50R-5, 99	T8	776.61	1.52
50R-7, 81	T8	779.43	1.72
51R-1, 40	T8	780.50	1.57
51R-2, 114	T8	782.74	1.70
51R-3, 50	T8	783.60	1.46
51R-4, 87	T8	785.47	1.60
51R-5, 49	T8	786.59	1.61
51R-6, 5	T8	787.65	1.59
52R-1, 52	T8	790.32	1.48
52R-2, 1	T8	791.31	1.57
52R-3, 22	T8	793.02	1.60
52R-4, 29	T8	794.59	1.61
52R-5, 114	T8	796.94	1.59
52R-6, 25	T8	797.55	1.77
53R-1, 110	T8	800.50	1.74
53R-2, 27	T8	801.17	1.62
53R-3, 18	V1	802.58	1.37
53R-4, 13	T8	804.03	1.56
53R-5, 25	T8	805.65	1.64
54R-1, 140	T8	810.50	1.57
54R-2, 27	T8	810.87	1.68
54R-3, 3	V1	812.13	1.34
54R-4, 1	T8	813.61	1.51
54R-5, 32	T8	815.42	1.64
54R-6, 136	T8	817.96	1.78
55R-1, 35	T8	819.05	1.71
55R-4, 6	T8	823.26	1.78
56R-1, 9	T8	828.49	1.79
56R-2, 60	T8	830.50	1.74
56R-3, 6	T8	831.46	1.71
56R-4, 42	T8	833.32	1.68
56R-5, 3	T8	834.43	1.93
57R-1, 23	T8	838.33	1.78
57R-2, 27	T8	839.87	1.82
57R-4, 97	T8	843.57	1.60
57R-5, 17	T8	844.27	1.85
58R-1, 122	T8	848.62	1.78
58R-3, 49	T8	850.89	1.80
59R-1, 76	T8	857.86	1.75
59R-2, 47	T8	859.07	1.80
59R-3, 8	T8	860.18	1.80
59R-4, 18	T8	861.78	1.78
60R-1, 37	T8	867.17	1.70
60R-2, 130	T8	869.60	1.80
60R-3, 10	T8	869.90	1.64
60R-5, 5	T8	872.85	1.75
61R-1, 9	T8	876.59	1.68
61R-2, 19	T8	878.19	1.81
61R-4, 15	T8	881.07	1.75
61R-5, 106	T8	883.48	2.04
62R-1, 130	T8	887.40	1.76
62R-2, 127	T8	888.87	1.76
62R-3, 47	T8	889.57	1.82
62R-4, 102	T8	891.62	1.84
62R-5, 28	T8	892.38	1.83
63R-1, 99	T8	896.79	1.76
63R-2, 84	T8	898.14	1.79
63R-3, 42	T8	899.22	1.94
64R-1, 6	T8	905.56	1.73
64R-2, 89	T8	907.89	1.84
64R-3, 81	T8	909.31	1.72
64R-4, 109	T8	911.09	1.73
65R-1, 8	T8	915.18	1.77
65R-1, 132	T8	916.42	1.90
66R-1, 130	T8	926.10	1.82
66R-2, 10	T8	926.40	1.91
66R-3, 93	T8	928.73	1.82
66R-4, 63	T8	929.93	1.94
68R-1, 24	T8	944.44	1.75

Table 25 (continued).

Core, section interval (cm)	Lithology*	Depth (mbsf)	Thermal Conduct. (corr.)(W/m °C)
70R-1, 143	T8	964.83	1.79
70R-2, 60	T8	965.50	1.75
70R-4, 46	T8	968.36	1.69
70R-5, 1	T8	969.41	1.89
71R-1, 141	T8	974.51	1.76
71R-3, 12	T8	976.22	1.84
72R-1, 33	T8	983.13	1.72
72R-2, 1	T8	984.31	1.84
72R-3, 139	T8	987.19	1.97
72R-CC, 1	T8	989.08	1.90
73R-1, 9,	T8	993.00	1.79
73R-2, 43	T8	994.03	1.85
73R-3, 25	T8	995.35	1.74
73R-4, 77	T8	997.37	1.95
73R-5, 7	T8	998.17	1.86
73R-6, 1	T8	999.61	1.86
74R-1, 139	T8	1003.19	1.81
74R-2, 136	T8	1004.66	1.85
75R-1, 9	T8	1011.39	1.77
75R-2, 5	T8	1013.10	1.85
76R-1, 134	T8	1021.84	1.73
76R-2, 10	T8	1022.10	1.89
76R-3, 16	T8	1023.66	1.89
76R-4, 13	T8	1025.13	1.99
76R-5, 25	T8	1026.75	1.85
76R-6, 1	T8	1028.01	1.92
77R-1, 133	T8	1031.23	1.85
77R-2, 36	T8	1031.76	1.89
77R-3, 31	T8	1033.21	1.67
77R-4, 64	T8	1035.04	1.95
77R-5, 4	T8	1035.94	1.81
78R-1, 40	T8	1039.50	1.88
78R-2, 29	T8	1040.89	1.92
78R-3, 2	T8	1042.12	1.82
78R-4, 85	T8	1044.45	1.92
78R-5, 135	T8	1046.45	1.84
79R-1, 14	T8	1048.44	1.83
79R-2, 51	T8	1050.31	1.88
79R-3, 25	T8	1051.55	1.85
79R-4, 60	T8	1053.40	1.83
80R-1, 37	T8	1058.17	1.87
80R-2, 89	T8	1060.19	2.00
80R-3, 5	T8	1060.85	1.86
81R-1, 39	T8	1067.49	1.77
81R-2, 90	T8	1069.50	1.82
82R-1, 33	T8	1076.83	1.85
82R-1, 40	T8	1076.90	1.85
83R-1, 16	T8	1085.96	1.81
83R-3, 31	T8	1089.11	1.92
84R-1, 1	T8	1092.01	1.89
84R-2, 132	T8	1094.82	1.98
85R-1, 4	T8	1098.34	1.76
85R-1, 66	T8	1098.96	1.86
86R-1, 5	T8	1108.05	1.67
86R-CC, 1	T8	1111.39	1.93
89R-1, 43	T8	1137.03	1.76
89R-2, 74	T8	1138.84	2.06
90R-1, 53	T8	1146.83	2.01
91R-1, 90	T8	1156.80	1.90
91R-1, 139	T8	1157.29	1.96
92R-1, 9	T8	1165.69	1.98
92R-CC, 1	T8	1167.41	1.98
93R-1, 104	T8	1176.34	1.83
94R-1, 41	T8	1185.31	1.94
94R-2, 18	T8	1186.58	1.94
95R-1, 58	T8	1195.18	1.85
95R-1, 135	T8	1195.95	1.95
100R-1, 85	V1/T8	1243.85	1.95
100R-2, 23	V1/T8	1244.73	2.09
101R-1, 101	V1	1253.21	1.78
101R-2, 98	V1	1254.68	1.88
101R-3, 16	V1	1255.36	1.51
101R-4, 56	V1	1257.26	2.05
101R-5, 1	V1	1258.21	1.88
102R-1, 128	V1	1262.78	2.11
102R-2, 1	VT8	1263.01	2.22
102R-3, 34	V1	1264.84	1.63

Table 25 (continued).

Core, section interval (cm)	Lithology*	Depth (mbsf)	Thermal Conduct. (corr.)(W/m °C)
102R-3, 50	V1	1265.00	1.66
103R-1, 72	VT8	1271.62	1.93
103R-2, 48	VT8	1272.88	2.19
103R-3, 92	V1	1274.82	1.62
103R-CC, 1	VT8	1275.58	2.16
104R-1, 1	VT8	1280.41	2.04
104R-2, 129	VT8	1283.19	2.20
105R-1, 113	basalt	1291.03	1.78
105R-1, 121	basalt	1291.11	1.91
106R-1, 68	basalt	1299.78	1.75
106R-1, 108	basalt	1300.18	2.00
106R-2, 1	basalt	1300.49	1.80
106R-2, 83	basalt	1301.31	1.85
107R-1, 33	basalt	1308.63	1.85
107R-1, 56	basalt	1308.86	1.73
107R-1, 86	basalt	1309.16	1.88

*Lithotypes
T4 sand, silt, clay
T5 silt/siltstone
T6 sand/sandstone
T8 silty clay/clayey silt
SR2 conglomerate
V1 volcanic ash/tuff
VT8 volcanic mudstone

Results of TLT Logs

Hole 808B

A short TLT temperature log was obtained in Hole 808B between 0 and 200 mbsf (Downhole Measurements, section, this chapter). The measurement took place 10 hr after fluid circulation had ceased. A total disturbance time of 91.5 hr was estimated from the drilling log for the upper part of the hole near seafloor. The downward temperature log from 139 to 189 mbsf (Fig. 166) exhibits a roughly uniform temperature of 5.0°C. There is no apparent change in the temperature gradient pointing to water flowing into or out of the formations. A comparison of the measured 5.0°C at 189 mbsf with the 23.1°C interpolated from the WSTP gradient indicates a thermal recovery from drilling disturbance of only 17%, assuming that such disturbance is the origin of the low temperatures measured.

Hole 808C

A TLT temperature log was obtained in Hole 808C through the drill pipe between 0 and 770 mbsf (Downhole Measurements section, this chapter). The operation took place about 6 hr after fluid circulation had ceased. The duration of the drilling disturbance was 13 days 4 hr in the top part of the hole and 8 days 2 hr at 800 mbsf. The up-going log gave temperatures 2° to 4°C higher than the down-going log. The difference is explained by the fluid in the pipe being pushed ahead of the tool. Both the up-going and down-going logs should be affected but the up-going log is expected to be most seriously disturbed because of the position of the temperature probe at the lower end of the logging string. Only the down-going data are used in the interpretation (Fig. 166).

The TLT temperature profile is roughly linear, with an average gradient of 48°C/km. Starting near the base of the casing (110 mbsf), the upper 180 m of the hole has a significantly lower gradient of approximately 15°C/km. The temperature near the seafloor is remarkably 14°C higher than the bottom-water temperature. This high temperature could represent remaining drilling circulation disturbance or, in principal, upward fluid flow from the formation entering the hole below the base of the casing, between 150 and 200 mbsf. This last possibility seems unlikely.

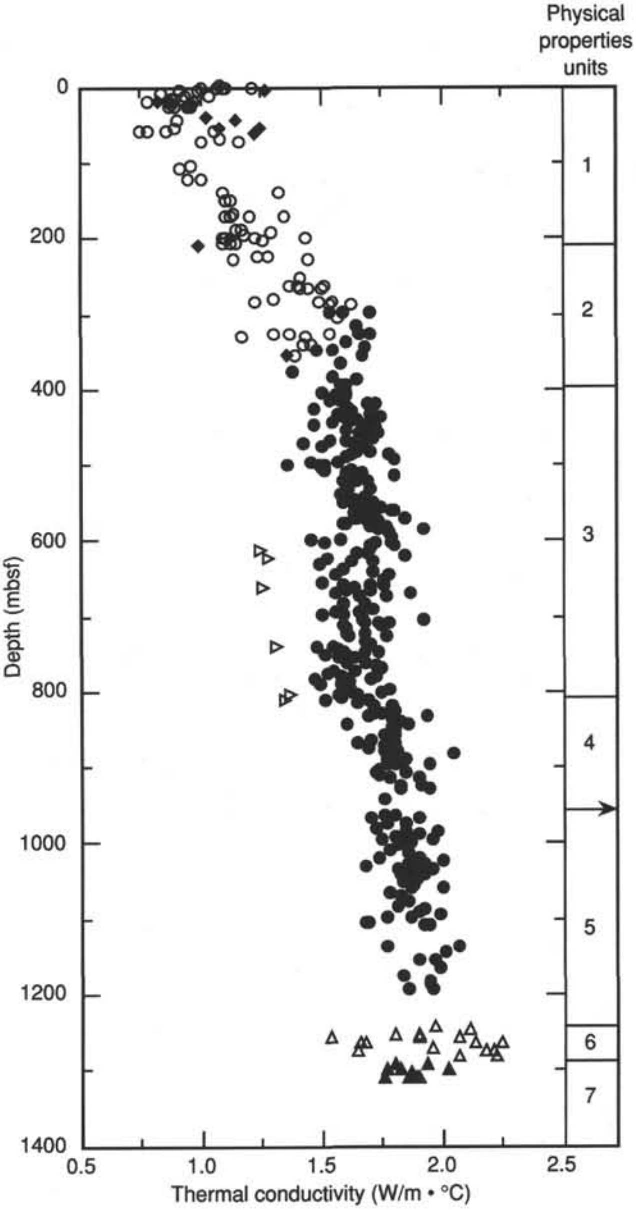

Figure 119. Thermal conductivity vs. depth below seafloor, Site 808. Open circles are the data measured on silt and clay samples from Holes 808A and 808B, and closed circles are those from Hole 808C. Filled diamonds, open triangles, and filled triangles represent the measurements in sandy layers (>50% sand), volcanic layers including tuffaceous claystone, and basalts, respectively.

Hole 808E

Two TLT temperature logs were run in Hole 808E approximately 6 and 3 hr respectively after circulation had ceased (Downhole Measurements section, this chapter). The first log, shown as 808E-1 in Figure 166, was run through the drill pipe and casing from seafloor to 54 mbsf, then through the casing to 524 mbsf, and finally in the open hole to 595 mbsf. The second log, shown as 808E-2 in Figure 166, was run through the drill pipe and casing from seafloor to 488

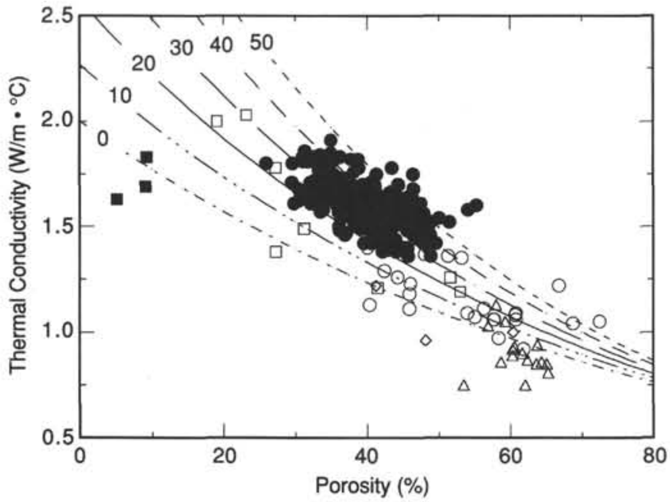

Figure 120. Thermal conductivity (uncorrected for temperature and pressure) vs. porosity (uncorrected for elastic rebound) for Site 808. Open circles are silt and clay samples from Holes 808A and 808B, and filled circles are those from Hole 808C. Triangles represent the data measured in gas-expanded sections of Hole 808A. diamonds, open squares, and filled squares are the data in sandy layers (>50% sand), volcanic layers including tuffaceous claystone, and basalts, respectively. Curves are theoretical porosity-thermal conductivity relationships for sediments containing 0, 10, 20, 30, 40, and 50% (dry volume) quartz, assuming a mean geometric model for the bulk conductivity with three components: water, clay minerals, and quartz, with conductivities of 0.6, 2.0, and 7.0 W/m·°C, respectively (Brigaud and Vasseur, 1989).

mbsf, then through the casing to 524 mbsf, and finally in the open hole to 639 mbsf.

Both TLT temperature profiles strongly reflect drilling circulation disturbances. The 808E-1 profile is roughly linear from near the base of the drill pipe (approximately 70 mbsf) to near the total depth reached (540 mbsf), with an average gradient of 69°C/km and a temperature extrapolated to seafloor of 14°C. This extrapolated seafloor temperature is 12°C higher than the sea-bottom temperature, which is similar to the excess temperature of 14°C measured near seafloor in Hole 808C. The 808E-1 profile was obtained after Hole 808E was drilled to a total depth of 1200 mbsf. A possible explanation for the excess temperature measured near seafloor is that the upper part of the hole was warmed by the drilling fluid returning to seafloor from the hole bottom at a temperature significantly higher than the bottom-water temperature. Circulation rates lower than 25 L/s could produce this situation (Burch and Langseth, 1981). Circulation rates in holes of Site 808 were between 15 and 45 L/s. Conducted 12 hours after the 808E-1 profile was obtained, the 808E-2 log measured a lower temperature from seafloor to approximately 500 mbsf, which probably reflects cooling related to rapid fluid circulation in the upper part of the hole between the two logs.

Implications

Heat-Flow Estimates and Thermal Structure

We have calculated a temperature profile with depth, assuming that heat flow is constant and purely conductive, and compared the calculated temperatures to those measured at the WSTP deployment depths. We used:

$$T(z) = T_0 + \frac{q}{\displaystyle\int_0^z \frac{dz}{k(z)}} \tag{1}$$

where T is temperature, q is heat flow, k is thermal conductivity, T_0 is the bottom-water temperature and z is the sub-bottom depth in meters. We approximated the thermal conductivity by $k(z) = 0.91 + 0.0017\,z$, between 0 and 400 mbsf, and $k(z) = 1.40 + 0.00040\,z$, between 400 and 1400 mbsf (Fig. 167), using the best-fitting linear approximations determined from the large set of data collected (Physical Properties section, this chapter).

Over the depth interval of the WSTP measurements, the temperature solution is thus:

$$T(z) = 1.6 + \frac{q}{0.0017} \ln\left(\frac{0.91 + 0.0017 \cdot z}{0.91}\right) \tag{2}$$

The least-squares best fit of the calculated temperature profile to the six WSTP datums and the bottom-water temperature was obtained for heat flow of 126 mW/m^2 (Fig. 168). The measured temperatures deviate from those predicted by less than 1.8°C except for that at 298.6 mbsf where the measured temperature is 3.1°C lower than that calculated. Excluding the measurement at 298.6 mbsf, a good fit was obtained for a heat flow of 129 mW/m^2 (Fig. 168). The calculated temperature profile departs from individual measured WSTP temperatures by less than 1°C at 198.5, 255.3, and 346.7 mbsf. The measured temperature plots 1.4°C below that calculated at 91.1 mbsf and 1.2°C above that calculated at 217.4 mbsf. The excluded measured temperature at 298.6 mbsf falls 3.8°C below that calculated. A constant conductive heat flow of 126–129 mW/m^2 appears therefore to describe the overall thermal structure satisfactorily, but the relatively low measured temperature at 298.6 mbsf may define a large local anomaly. This local anomaly could be related to a fluid flow disturbance or may result from an experimental error, such as an insufficient penetration of the probe into the sediment ahead of the bit, which was not detected.

The WSTP temperature measurements were restricted to the depth interval from the seafloor to 346.7 mbsf, and the discussion above applies only to this interval. Below 346.7 mbsf, the nearly constant slope of the TLT log of Hole 808C from the seafloor to 750 mbsf (Fig. 166) suggests that no drastic change in the temperature profile occurs down to this depth. Assuming that a constant conductive heat flow of 129 mW/m^2 applies also below 346.5 mbsf, the extrapolated temperature is 72°C at 750 mbsf, where the TLT log measured a temperature of 52°C, indicating a surprisingly large recovery from the drilling disturbance. The extrapolated temperature is 88°C at the décollement (950 mbsf) and 112°C at the sediment-basement interface (1290 mbsf).

Heat Flow and Crustal Age

The age of the oceanic basement at Site 808, determined from biostratigraphic dating of the sediment overlying it, is between 13.6 and 16.0 m.y. (Biostratigraphy section, this chapter). The predicted heat flow from conductive cooling of a lithospheric plate of this age is 125 to 136 mW/m^2 (Lister, 1977), which does not differ significantly from the value of 126–129 mW/m^2 determined in the upper sedimentary column. The good agreement between the measured heat flow and that

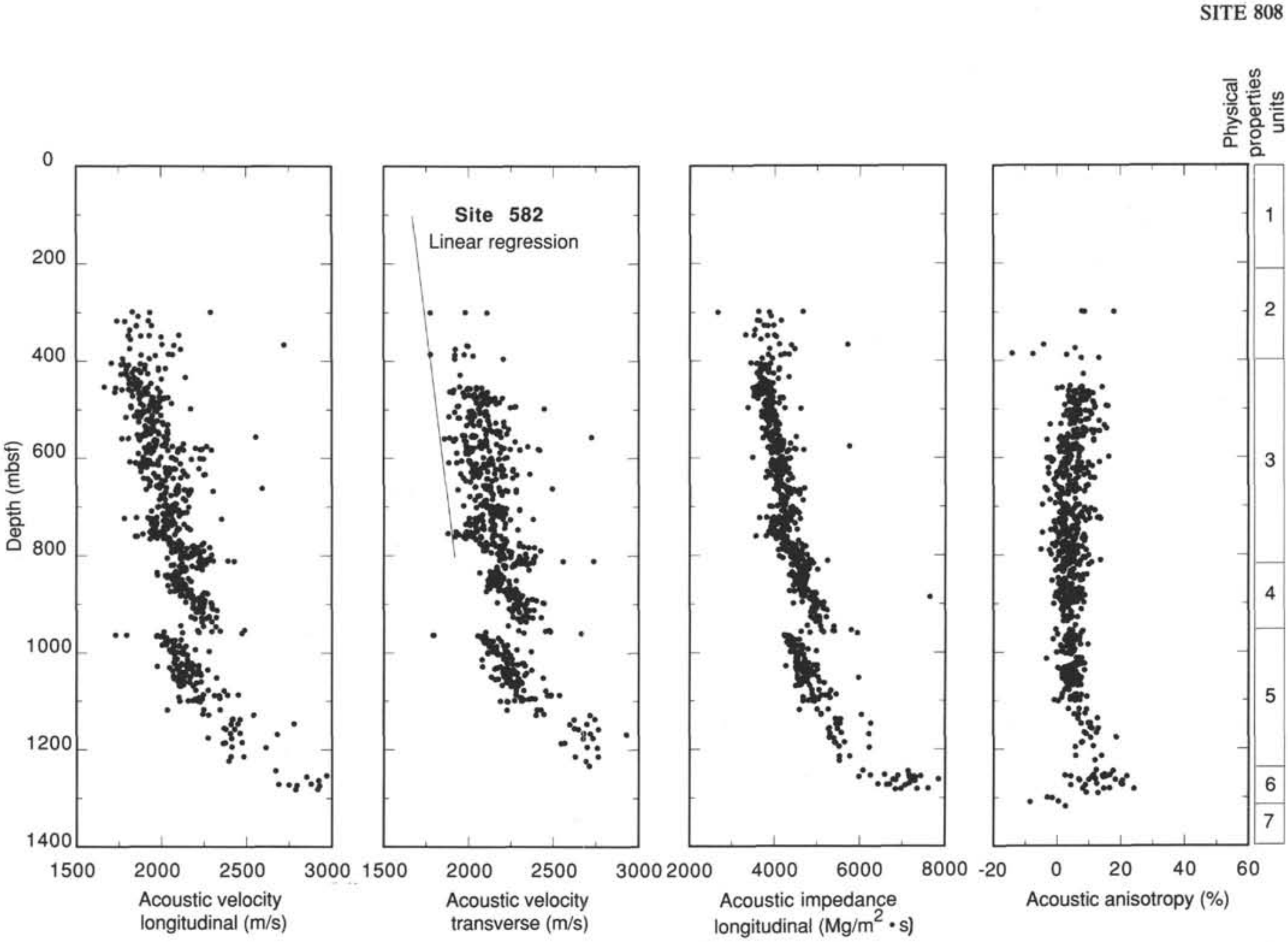

Figure 121. Acoustic velocity, impedance, and anisotropy vs. depth for Site 808. Acoustic anisotropy is defined by equation 1.

predicted from a conductive cooling model of the lithosphere, favors conduction as the most significant heat transfer process through the oceanic crust and its sediment cover at Site 808.

However, a slightly lower (by about 10%) predicted heat flow results from taking into account the cooling effects of the high sedimentation rates at the toe of the prism (Yamano et al., 1984). The measured heat flow would then exceed that predicted, by about the amount of the correction.

Evidence for Fluid Flow

Neither the WSTP nor TLT temperature data provide evidence of present-day fluid flow activity at Site 808. No evidence that formation waters are flowing into the holes or that the borehole water is flowing into the formations was found from the TLT data. However, the high temperatures measured in the upper part of Holes 808C and 808E are surprising and the TLT data must be processed ashore and corrected for the drilling circulation disturbance before fluid flow can be excluded.

Calibration of Heat-Flow Estimates from BSR Depths

A very important source of thermal data in accretionary wedges is obtained from the depth to the commonly observed gas hydrate bottom-simulating reflector (BSR) (e.g., Yamano et al, 1982). This reflector, at a depth of several hundred meters, is taken to mark the base of the temperature-pressure field for hydrate stability. The stability field is relatively weakly dependent on pressure; the primary depth dependence is from temperature. Thus, the BSR provides a temperature reference. Determination of the heat flux from the BSR depth requires estimates of: (1) the reflection time to the BSR from seismic reflection data, (2) the velocity-depth relationship to convert reflection times to depth, (3) the applicable pressure-temperature relationship for hydrate stability to determine the temperature at the BSR, (4) the pressure at the BSR from the water depth, and sediment thickness and density, (5) the seafloor temperature to obtain the temperature gradient, and (6) the thermal conductivity-depth relationship to obtain heat flow. Of these factors, the critical relationship, that has so far been obtained only from laboratory data, is the P-T constraints on hydrate stability. Even if the laboratory data are valid, there is the question of which P-T curve to employ. Is it the relationship for pure methane and seawater salinity, or are other constituents such as CO_2 and higher hydrocarbons that increase the maximum temperature for stability important? Although the new constraints are relatively weak, Site 808 provides an opportunity for a field test of the applicability of the laboratory data. The laboratory stability fields are shown in Figure 169.

There is no clear BSR on the multichannel seismic sections in the area of the Site 808 holes and, although hydrates were recovered in one core, it was well above the BSR depth. There were also no open-hole logs over the expected BSR depth range. Thus, the temperature and velocity data at the site must be combined with BSR depth data from regions just to the landward where a BSR is

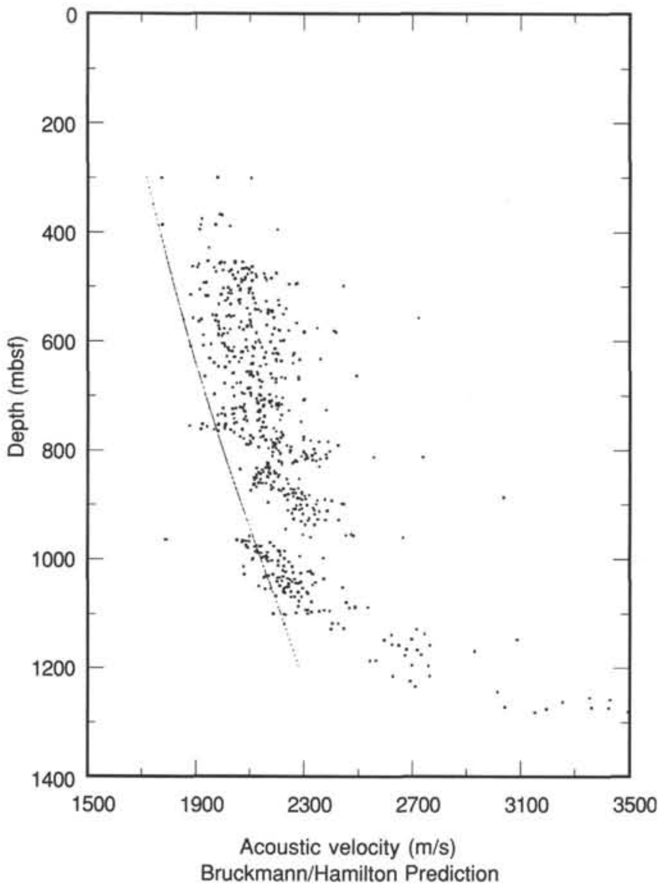

Figure 122. Longitudinal acoustic velocity (squares) for Hole 808C plotted vs. depth and compared with a predicted velocity from Brückmann (1989) and Hamilton (1979) and corrected for the assumed temperature and effective pressure at Site 808.

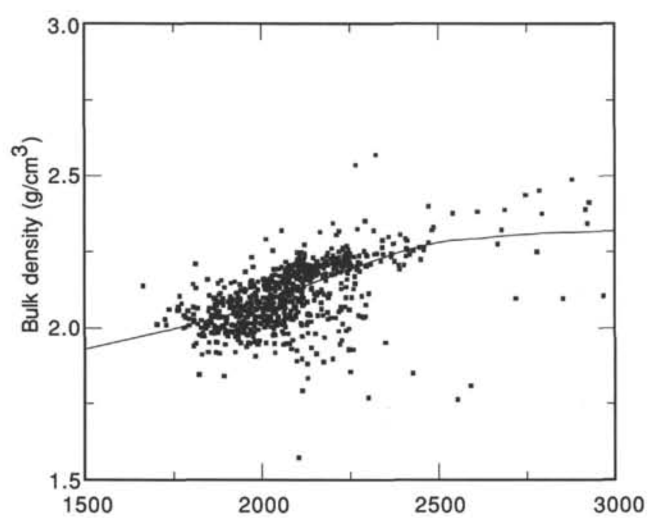

Figure 123. Cross plot of acoustic velocity and bulk density. The correlation is log-linear.

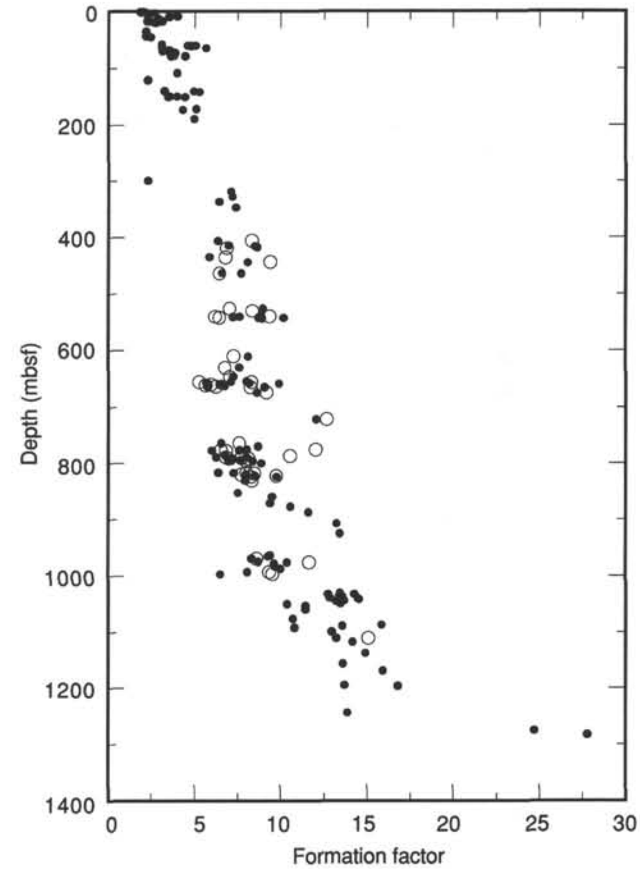

Figure 124. Formation factor vs. depth for Site 808. Solid symbols: transverse; Open symbols: longitudinal.

observed. Figure 170 shows the BSR depth (in seconds) as a function of distance landward from Site 808 on the multichannel seismic line that passes over the site. The BSR depth is seen to decrease toward the trench in a smooth systematic way. This is consistent with the increase in heat flow from about 50 mW/m^2, 50 km landward from the deformation front, to about 150 mW/m^2, 10 km seaward of the deformation front (Preliminary report of the KH 85-6 cruise of the *Hakuho-Maru*, Ocean Research Institute, University of Tokyo). We could extrapolate the velocity and temperature data at the drill site to where a BSR is observed, but we have chosen to use the drill site as a reference and extrapolate the BSR depth to its location. The linearly extrapolated depth (two-way traveltime) at Site 808 is 230±10 ms.

This reflection time must be converted to depth. Two sources of data are available at the site, the downhole velocity log and the laboratory data on core samples. The core recovery for the upper 200 m was very poor and biased to muds rather than sand. Thus, only the log data has so far been used. The log velocity data also are available only from 80 to 160 m depth, so they must be extrapolated to the remaining intervals between the seafloor and the approximately 200-m depth of the BSR (Fig. 171). The extrapolation requires an exponential porosity-depth relation with parameters such that the inferred velocities pass through the mean and have the slope of the velocity log data. The Hamilton (1978) porosity-velocity relation was used to convert porosity to velocity (Downhole Measurements section, this chapter). Based on

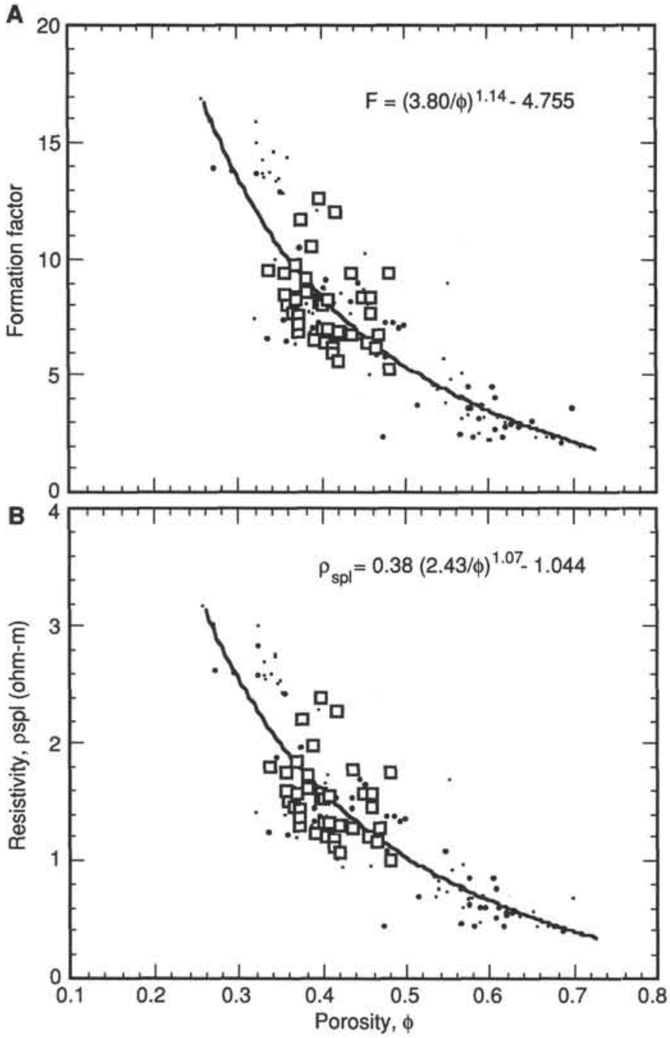

Figure 125. **A.** Formation factor vs. porosity of Site 808 sediments. Solid symbols: transverse; Open symbols: longitudinal. The solid line shows the best-fit equation with a regression coefficient of 0.88 for the transverse data. The form of the empirical equation is that described by Kermabon et al. (1969) for modern marine clays and turbidite sands. **B.** Resistivity-porosity cross plot. Resistivities were obtained from the formation factor assuming a seawater resistivity equal to 0.189 ohm-m (salinity = 35, temp.= 25°C). The solid line shown is a best-fit equation for transverse data that yields a regression coefficient of 0.88.

this relationship, the effective mean velocity from the surface to 200 m is 1.79 km/s. Thus, the BSR extrapolated at the site has a depth of 205±10 m.

The temperature measurements made with the WSTP probe at Site 808 (Fig. 165) could reflect minor thermal disturbance due to lateral fluid flow. The temperature profile gives a temperature of 26.4 ± 0.5°C at the extrapolated depth of the BSR. This temperature corresponds well with the base of the hydrate stability field for pure methane and pure water (Fig. 169). Close-to- seawater salinity pore fluids were measured in the pore, so this explanation is unlikely. More probable is that the BSR corresponds to the base of the field for a combination of fluid of near-seawater salinity and gas that contains some CO_2 with the methane. Approximately 7% CO_2 is required (Fig. 169). Thus, while the estimated BSR temperature has an accuracy of only about± 1°C, this estimate suggests that CO_2 may play an important role and that the pure water, pure methane curve may provide the best estimate of heat flow from BSR depths.

It is also useful to note that the mean thermal conductivity to the BSR from the Site 808 sample data is 1.07 W/m °C, slightly less but within the uncertainty of the value of 1.20 W/m °C used by Yamano et al. (1982). The conductivity is expected to increase landward with ongoing sediment consolidation, and the BSR is at greater depth landward over most of the accretionary prism, so the average value of 1.20 W/m °C they used is probably appropriate for the upper several hundred meters of the accretionary wedge in general.

SEDIMENT ACCUMULATION RATES

Both the calcareous nannofossil and paleomagnetic datums (Biostratigraphy and Paleomagnetics sections, this chapter) from Site 808 were used to construct sedimentation and sediment mass accumulation plots (Table 30, and Figs. 172, 173, 174, and 175). Age vs. depth plots are found in Paleomagnetics section, this chapter. Mostly paleomagnetic datums were used because of their inherent synchroneity and because their depth-in-core error was generally smaller than that of the nannofossil datums. Nannofossil datums were used to fill in gaps in the Pleistocene and in the middle Miocene where no paleomagnetic datums were available. Both paleomagnetic and nannofossil datums tabulated are the mid-point depths within the estimated depth range. The interval across the thrust fault, between nannofossil datums at 230.66 and 624.27 mbsf, was corrected for stratigraphic displacement by subtracting 145 m from the core depth (mbsf). Although datums below the thrust fault were shifted in depth, the interval thicknesses between those datums were unaffected by the correction. Sedimentation rates (m/m.y.) were calculated for each interval, and multiplied by the dry-bulk density (g/cm^3) for that interval (derived from porosity and water content data (Physical Properties section, this chapter) to produce the sediment accumulation rates.

The large accumulation rates in the top 624 m reflects the onset of turbidite deposition (lithologic Units I to III; less than 0.5 Ma). The interval between 624 and 800 m corresponds to the upper hemipelagites with interspersed ash beds of lithologic Subunit IVa. Below this, the lower accumulation rate reflects the deposition of hemipelagites with no interspersed ash. It is noteworthy that there is a zone of reduced accumulation rate about 1010 to 1090 mbsf in this interval.

CLAY INSTABILITY TESTS

Introduction

Gamma-ray logs have shown that bridging is due to clay swelling, indicated by a correlation between high gamma-ray values and small hole diameter on the caliper log. Swelling clays (montmorillonite especially), whether concentrated in distinct horizons (cm-scale) or dispersed throughout an interval (m-scale) can effectively constrict the hole enough to block logging tools. Montmorillonite is the most notorious clay mineral from the standpoint of formation sensitivity to drilling fluids, but it is not the only water-sensitive clay. Montmorillonite (smectite) forms from the alteration of volcanogenic sediments, ash, and basalt. Other common clay minerals such as illite, kaolinite, and chlorite exhibit only minor swelling.

Since Leg 110, the increased focus on logging fluids has led to a dramatic decrease in bridging problems. This is associated with increased hole conditioning, filling the hole with mud prior to logging, and with cutbacks in the use of freshwater muds. As a result, logging productivity has been nearly

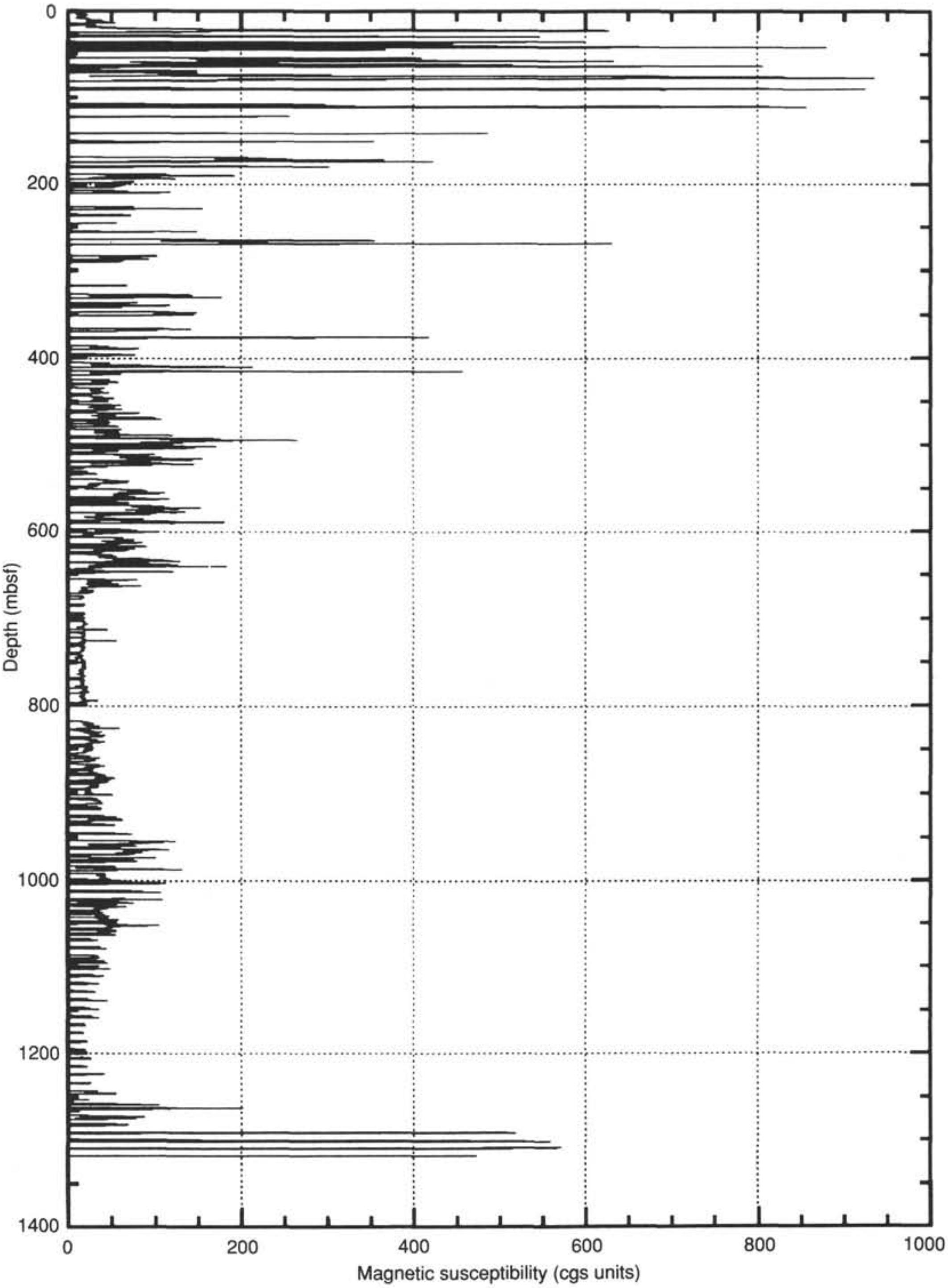

Figure 126. Magnetic susceptibility of Site 808 cores. Data plotted are 25-cm interval averages of original scan measurements made at 3cm spacing on whole-round core sections.

doubled. Freshwater muds were often used in the past because they sweep the hole so well and because they flocculate the drilling mud clays. However, the difference in salinity between the drilling mud and the pore fluids is probably the cause of clay swelling.

Because logging generally is one of the last things to be done in a hole, hole stability is often difficult to preserve. The drill string is usually able to clear all hole obstructions by pushing, pulling, and rotating with great force during wiper trips. The logging tools have only a fraction of the weight and strength of the drill string; pulling too hard can damage the cable, damage the tool, or break the weak point and lose the entire tool in the hole. Attempts to punch through obstructions by dropping down on them with the weight of the tool (bridge-bashing) can result in cable kinking or tool shutdown. While the use of the sidewall entry subassembly (SES) permits raising and lowering the pipe with the logging tools rigged up, its use eliminates the option of rotating the drill string and

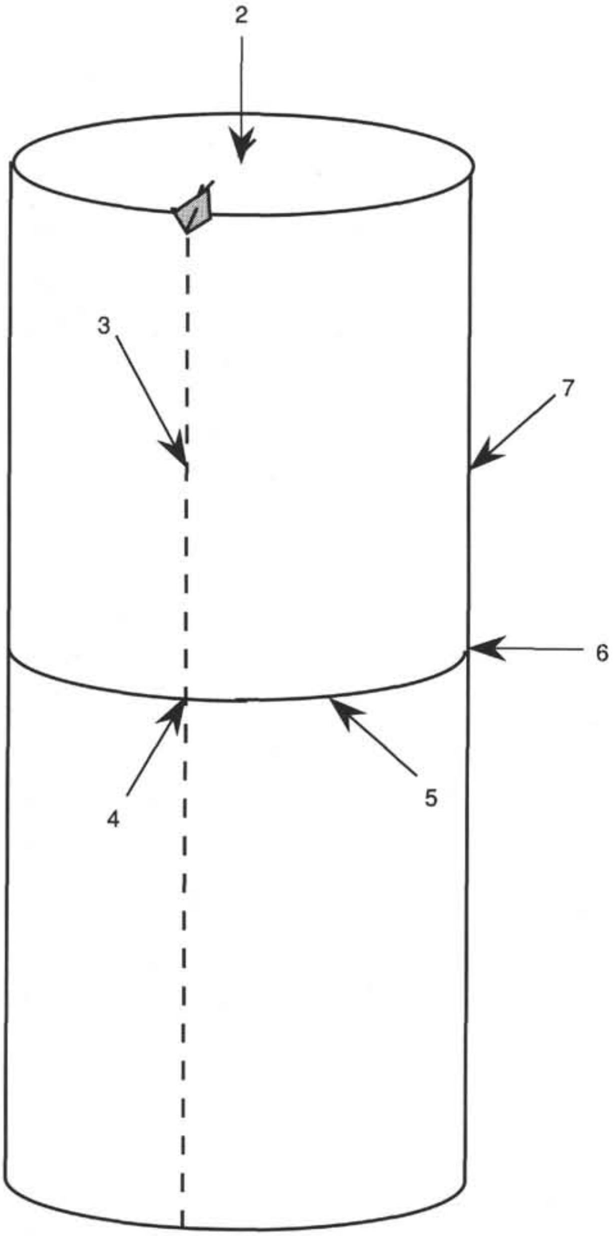

Figure 127. Diagram of LVDT locations on a sample used for an ASR test. LVDT no. 1 was not used because the undersized core diameter restricted the space for the LVDT frames. Measurements from the six LVDT's are adequate to define strains in the three orthogonal planes shown, from which principal strains can be calculated.

Table 26. Summary of data from ASR tests at Site 808.

Test	Sample 131-808C- interval (cm)	Depth (mbsf)	Axial strain rate (s^{-1})	Radial/axial strain ratio
ASR-1	10R-1, 58–67	385.8	N.O.	N.O.
ASR-2	23R-4, 19–34	515.5	17	0.52
ASR-3	41R-2, 9–25	685.5	36	0.30
ASR-4	57R-5, 0–16	844.2	21	0.45
ASR-5	74R-2, 114–130	1004.6	38	0.40
ASR-6	85R-1, 22–38	1098.5	24	0.37
ASR-7	85R-1, 22–38	1098.5	28	0.40

N.O. = not obtained

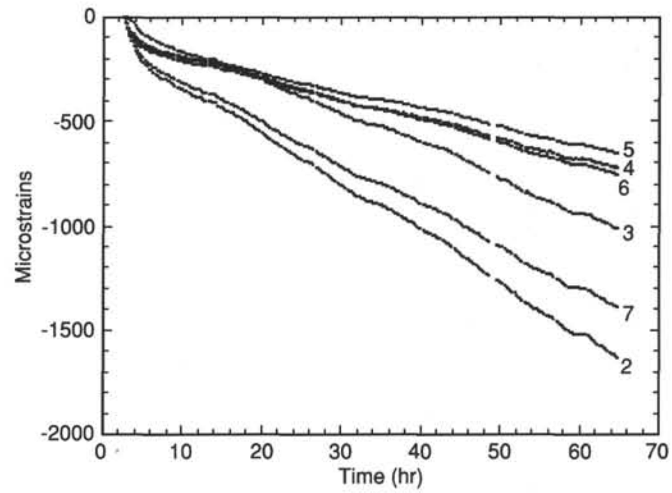

Figure 128. Preliminary strain data from test ASR-6. These results show the quasi-linear negative strains that are attributed to sample dehydration. The departures from linearity are primarily correlatable with changes in room temperature.

Table 27. Site 808. Actual depth summary of the log data obtained for ranges shown vary by up to 10 m for the individual log parameters because of the different positions of the tools in the log string. Data were not obtained over a short interval, near pipe entrance, for some logs. Data marked * was recorded at 300 m/hr logging speed.

Hole	Log Type	Depth Range (mbsf)	Hole Conditions
808B	Seismic Stratigraphy/Temperature	0–44	pipe
		44–80	BHA
		80–180	open hole
808C	Lithoporosity, Geochemical, Temperature	0–000	re-entry core
		20–110	pipe and casing
		110–826	pipe only
		826–891	in BHA
808E	Seismic Stratigraphy Run 1	0–54.2	casing and BHA
		54.2–523.8	casing *
		523.8–578	open hole *
		487.5–523.8	casing *
		523.8–621.6	open hole *

thereby increases the chances of getting the bottom-hole assembly stuck. The SES is time-consuming to rig up and difficult to run successfully, and is further complicated by poor weather, strong currents, or deteriorating hole conditions.

Hole conditions for logging can be predicted to some degree by examining core recovery and lithology (Fig. 176) and by recording the pull exerted on the drill string during wiper trips. One indirect predictor of hole problems is clay instability potential, which can be estimated from lab tests performed on samples from recovered cores. The same tests determine the optimum amount of KCl to inhibit clay swelling. Based upon the results of these tests, the LDGO logging scientist may request the addition of a fixed amount of KCl to the mud used for hole conditioning and logging. While KCl mud is no guarantee of hole stability, this strategy is successful enough that the process has been carried out since Leg 110.

Clay Instability Potential Testing

Clay instability potential is a qualitative estimate derived from one or several quantitative measurements, both in the borehole (gamma vs. caliper, wiper trip resistance vs. time,

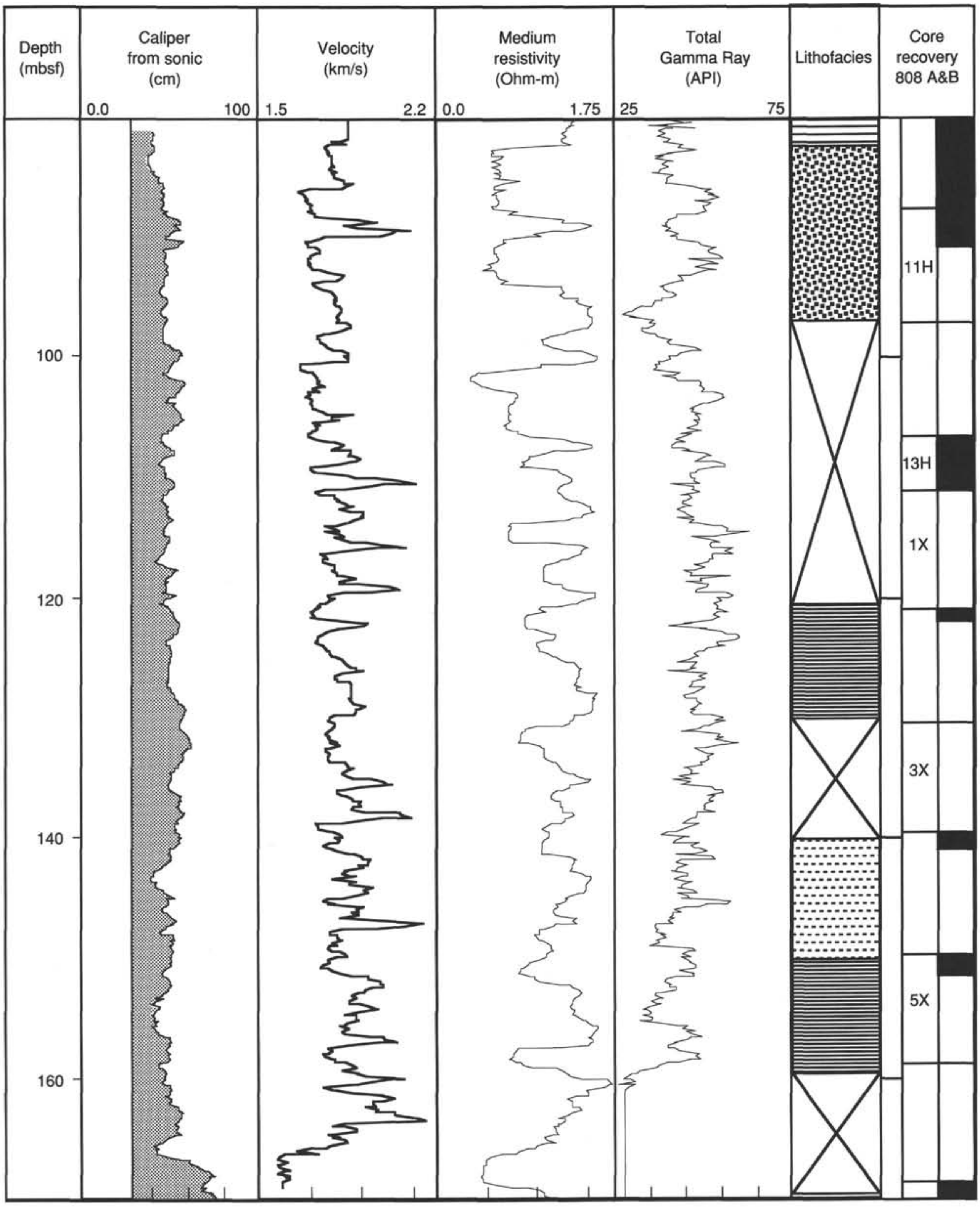

Figure 129. A summary of the open-hole log data obtained from Hole 808B, along with the hole diameter log determined from the sonic log, and a simplified lithologic column from the cores of Holes 808A and 808B. The logs are uncorrected for hole diameter variations.

drilling properties of the formation) and in the lab (capillary suction time, linear expansion). Also, hole stability has been shown to correlate with core recovery to some extent. This is true in general regardless of lithology. While clay instability potential as determined by these relatively simple tests is a function of several variables, it is invaluable as a quick, easily-measured quantity which has proven its usefulness over time.

When clays present in the formation are exposed to water with a different ionic composition than the ambient composition, they may react by either swelling or dispersing. Two clay instability tests are carried out routinely at sea, especially when ash-bearing lithologies are identified: (1) Capillary Suction Test and (2) Linear Expansion Measurement.

Capillary Suction Test (CST)

The principle of the test is that clay dispersibility is a quantitative estimation of the extent of intergranular cohesion and of the resistance to hydration forces and mechanical dispersion. Clay dispersion into the borehole fluid occurs when colloidal clay particles (less than 2 μm) subdivide. Clay dispersion increases the colloidal solids content. The increase in the solids concentration decreases the interparticle distance and increases the van der Waals attractive force. At the same time, the amount of free deionized water decreases, which causes a reduction in the filtrate volume, resulting in increased CST values (see description of procedures, below).

The capillary suction test uses the capillary suction pressure of a special porous filter paper to achieve the filtration of a colloidal suspension, which is formed when the powdered sample is mixed with the fluid. When the mixture is transferred to the CST apparatus (Fig. 177), the fluid begins to move into the filter paper in proportion to the amount of free water. The filtration rate and volume is a reflection of the clay's dispersion tendencies. The results of the CST test depend on clay dispersion potential, solids content of the suspension, particle-size distribution in the suspension, the filtration area, and the filtration pressure (number of papers used). The test has been standardized to exclude each of these factors but the first.

The CST test has been run on many samples and the results have been compared with mineralogic analyses. All of the CST tests that were calibrated with chemical analyses of clay mineralogy show that seawater diminishes clay swelling regardlessof the montmorillonite content, and that KCl reduces it even further.

Linear Expansion Test

The principle of the test is that clays swell by adsorbing water between their platelets. This is often accompanied by a loss of cations (Na, Mg, Ca, and K) from their sites between the plates into solution. If the concentration of cations in the solution is increased, the rate of exchange of cations and water between the clays and the suspension is decreased. This test measures, by means of a digital electronic caliper (see description of procedures, below), the linear expansion of a block sample immersed in fluid. The linear expansion (in the z-direction, i.e., vertical expansion) is recorded as a function of time and as a function of KCl concentration.

Results from Hole 808C, Leg 131

CST tests were performed on three samples from Hole 808C. These results are shown in Figure 178. The CST times are listed in Table 31.

Interpretation of CST Tests

It is often observed that the CST will be on the order of 200–300 s in deionized water, but decreases to 50 s after 2%–4% KCl is added.

CST values are loosely grouped according to the following times, based on a synopsis of tests run on ODP samples:

CST > 500 = very high (some of the highest measured on ODP legs so far)
CST > 300 = high
CST > 150 = must use some KCl above this value
CST < 150 = no problem from clay swelling anticipated

According to these guidelines, all the samples tested from Hole 808C show either high or very high clay instability potential. The CST time of 577 s is one of the highest measured on ODP legs. Each of the CST profiles levels out above 4% KCl concentration. Based on these data, 4%–5% KCl (corresponding to 14.0–17.5 lb/bbl) should be added to the logging and sweep mud.

Logging at Site 808 was severely limited due to the extensive clay swelling encountered there. In Hole 808C, for instance, several wiper trips were performed before and during logging operations. These wiper trips met with steady resistance and were unsuccessful in opening the open-hole portion to logging. KCl mud was used to fill the borehole just before logging began. Even with a high inhibition mud, the clay swelling was not controlled. This can be attributed in part to the age of the hole; more than 13 days passed between the first core and the first logging run.

KCl Logging Muds

Based on the above tests, the optimum amount of KCl to be added is determined. The types of logging mud that are mixed can be divided into three categories:

1. LOW CLAY INHIBITION: To increase the ionic activity level to that of seawater. Normally when formulating mud and mud pills, bentonite is prehydrated in freshwater and then mixed with varying concentrations of seawater and/or polymer. The lower the amount of seawater added, the lower the resulting salt concentration. By adding KCl, this can bring the activity level back to that of seawater.

Dilution

	10%	20%	30%	40%	50%
KCl	8	7	6	5	4.5 (lb/bbl)

The amounts of KCl required (in lb/bbl) for different seawater dilutions of prehydrated gel is as follows:

2. MEDIUM CLAY INHIBITION: 10–15 lb/bbl = 2.8%–4.3% KCl.

3. HIGH CLAY INHIBITION: 15–30 lb/bbl = 4.3%–8.6% KCl.

Description of Apparatus and Procedures

Capillary Suction Test

The CST apparatus has two main components: the timer control box and the test head (Fig. 177). The test head consists of two lucite slabs, one solid and one that bears three

A

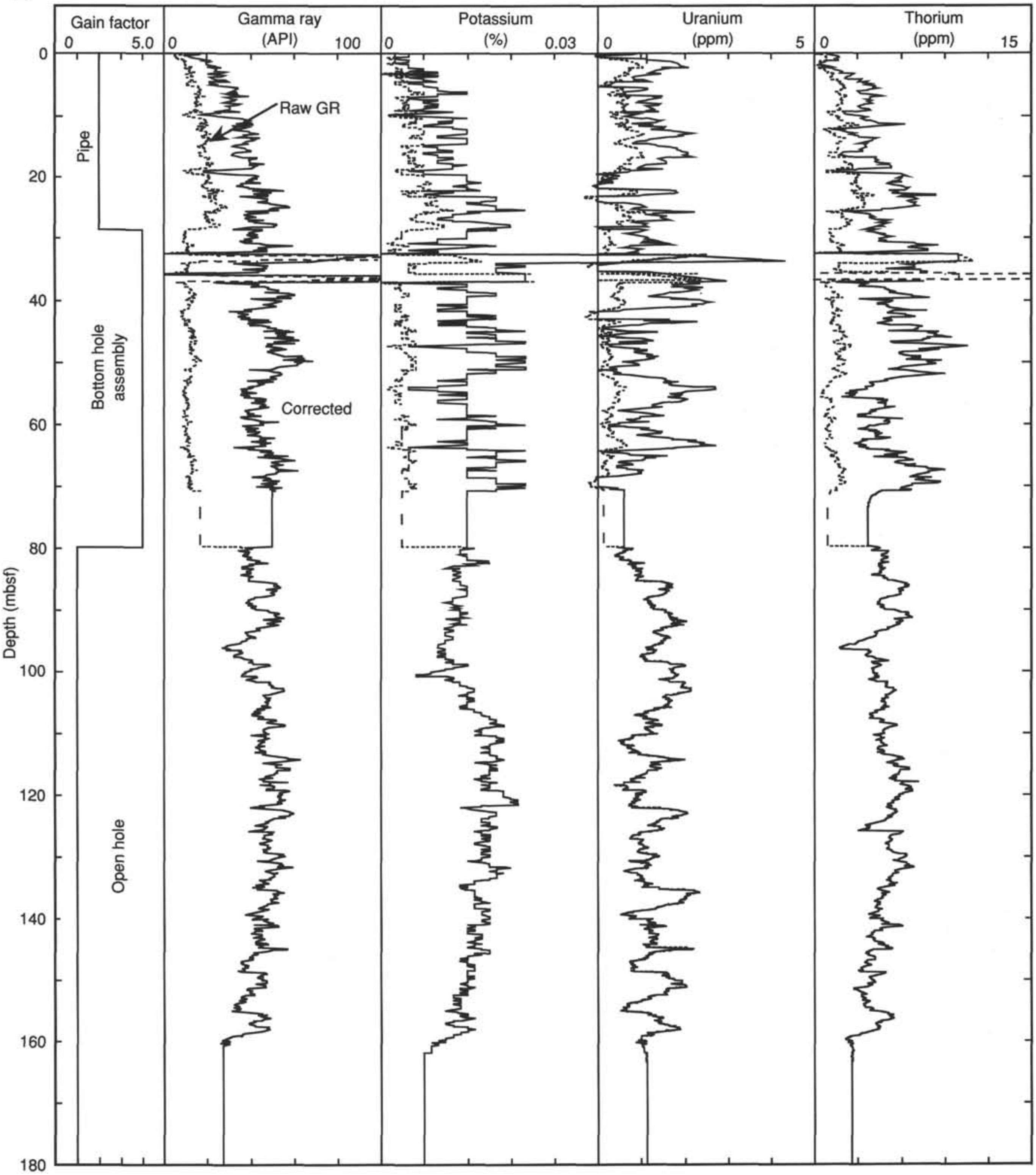

Figure 130. Total gamma, potassium, uranium, and thorium logs for Hole 808B (**A**) open-hole and (**B**) through pipe. Note approximate corrections applied for attenuation by the pipe and BHA. These logs have not been corrected for borehole diameter.

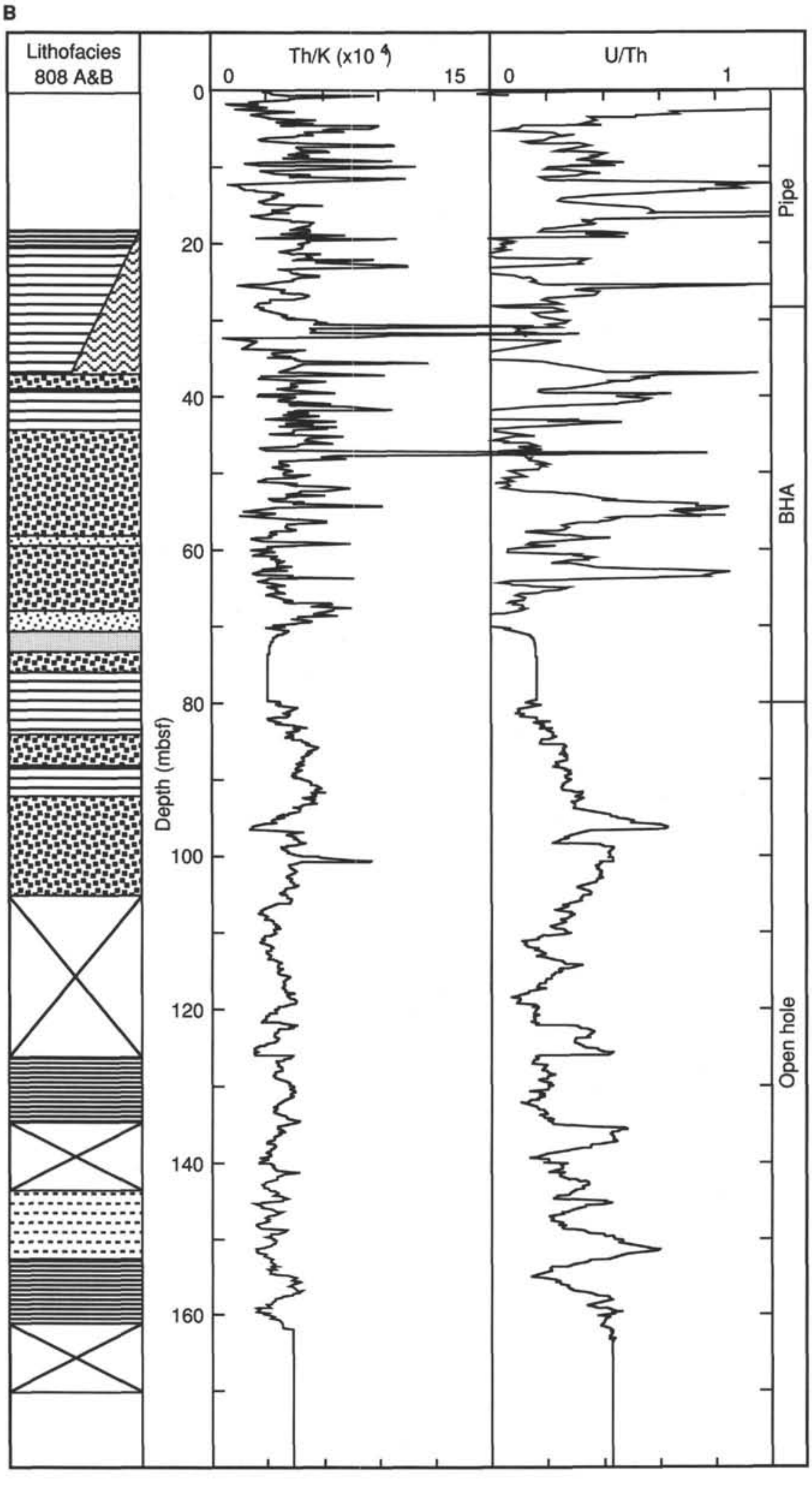

Figure 130 (continued).

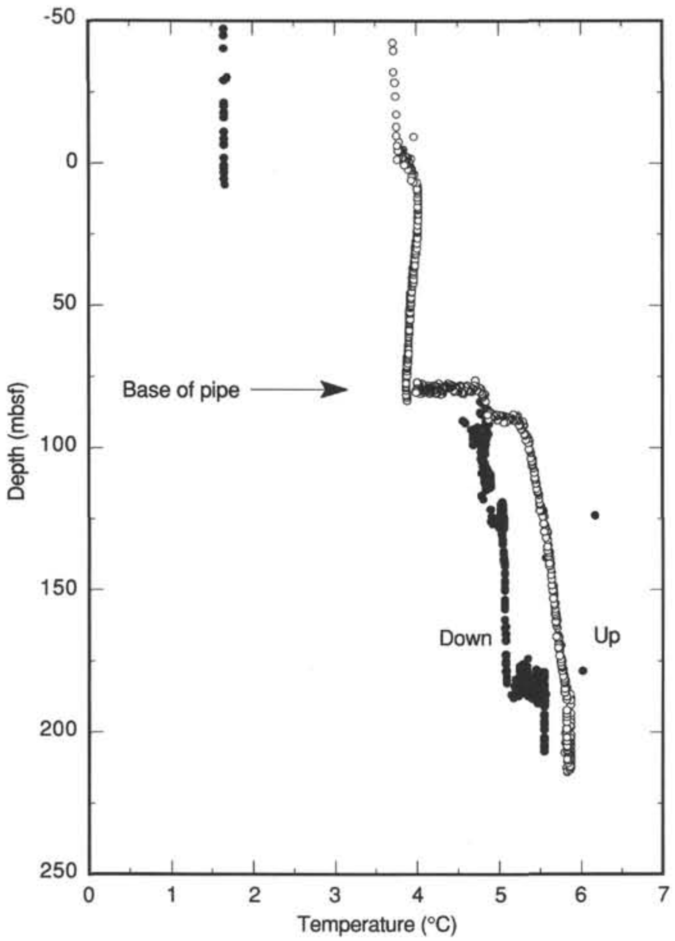

Figure 131. Downhole temperature logs obtained from Hole 808B using the TLT tool.

electrodes arranged around a central opening. The electrodes are positioned on two concentric electrically conducting circles; two electrodes lie on the inner circle, and the other lies on the outer circle. A filter paper (available from the manufacturer) is placed between these two slabs, which lie horizontally. A stainless steel funnel fits snugly into the opening in the upper plastic slab, and rests on the filter paper below this. The timer control box is connected to the electrode array. It bears a power switch and a reset button.

A 10-g sample is dried for 4 hr at 65°C, then crushed and powdered in a paint-shaker type crusher. The powder is sieved through a 170-μm mesh. Then 5 g of the sample is mixed in 100 mL of deionized water. If the mud will be made up with half seawater/half freshwater, 1.65 g of NaCl (equal to 16.5 ppt or half the salinity of seawater) are added and mixed in a blender for 10 min. The blender used has only one speed; for multispeed blenders, one setting should be used consistently.

When the sample has been mixed for 10 min, it is poured into a beaker. Then 10 mL (more than enough to fill the funnel) is drawn into a plastic syringe and quickly placed in the funnel. The suction exerted by the replaceable filter papers is constant, and the sample preparation procedure ensures a relatively narrow range of particle sizes. When the sample suspension is placed into the funnel, free water from the suspension is slowly drawn into the filter paper and is sucked radially outward. When the wetting front reaches the inner electrode pair, the timer starts.

The elapsed time is recorded until the wetting front passes the second electrode, at which point the run is finished. The elapsed time, called the capillary suction time, is read directly from the timer; it is plotted vs. concentration of KCl in the fluid.

Three duplicate runs are performed for each KCl concentration. First, the CST is measured with deionized water; then the sample is stirred with a magnetic stirrer while 2 g of KCl is added. After mixing for 2 min, the next set of three duplicate runs can be made. This is usually repeated for up to 6 g of added KCL, or until the CST has dropped to some constant low level.

Linear Expansion Test

The Digimatic Swelling Indicator is an electronic caliper that records linear strain (swelling of the sample) with a resolution of 1×10^{-4} in. The distance between caliper faces is adjustable, and the caliper can be rezeroed. Readings can be recorded in millimeters or inches.

Three separate samples are required for this test (immersed in freshwater/saltwater, freshwater/saltwater + 2% KCl, and freshwater/saltwater + 4% KCl, respectively) and each must be sufficiently indurated to be clamped firmly between the caliper faces.

While this test is operationally simpler than the capillary suction test, the sample requirements are more stringent. Three fresh $1.5 \times 1 \times 1$-in. (nominal) blocks are required, marked to indicate the vertical direction, and their dimensions carefully measured. Each block is set in a plastic bag, then clamped between the caliper faces with the vertical axis of the sample parallel to the axis of the caliper. The caliper screw is tightened until the faces just touch the sample, and the caliper is zeroed. Then the screw is tightened 0.1 in. further, and the caliper is rezeroed. The saturating fluid is poured into the bag until the sample is covered. The bag is clipped shut to prevent evaporation, and the test begins. The change in length in the vertical direction is measured as a function of time, and later converted to percentage linear expansion.

This test is repeated with varying KCl concentrations, and linear expansion is plotted as a function of KCl concentration.

Displacement is converted to linear percent swelling as follows:

$$\text{Linear \% swelling} = (\text{displacement} \times 100) / \text{sample length}.$$

REFERENCES

Archie, G. E., 1947. Electrical resistivity - an aid in core analysis interpretation. *AAPG Bull.*, 31:350–366.

Baker, P. A., and Kastner, M., 1981. Constraints on the formation of sedimentary dolomites. *Science*, 213:214–216.

Barker, C. E., 1988. Geothermics of petroleum systems: implications of the stabilization of kerogen maturation after a geologically brief heating duration at peak temperature. *In* Magoon, L. (Ed.), *Petroleum Systems of the United States:* USGS Bull., 1870:26–29.

Barker, C. E., and Pawlewicz, M. J., 1986. The correlation of vitrinite reflectance with maximum paleotemperature in humic organic matter. *In* Buntebarth, G., and Stegena, L. (Eds.), *Paleogeothermics:* New York (Springer Verlag), 79–93.

Berggren, W. A., Kent, D. V., Flynn, J. J., and Van Couvering, J. A., 1985. Cenozoic geochronology. *Geol. Soc. Am. Bull.*, 96:1407–1418.

Bernard, B. B., 1979. Light hydrocarbons in marine sediments. [Ph. D. dissert.]. Texas A&M University, College Station, Texas.

Berner, U., 1989. Entwicklung und Anwendung empirischer Modelle fuer die Isotopen-variationen in Mischungen thermogener Erdgase. [Ph.D. dissert.]. Technische Universitaet, Clausthal, Germany.

Bienvenu, P., Bougault, H., Joron, J. L., Treuil, M., and Dmitriev, L., 1990. MORB alteration: rare-earth element/non-rare-earth hygromagmaphile element fractionation. *Chem. Geol.,* 82:1–14.

Boyce, R. E., 1968. Electrical resistivity of modern marine sediments from the Bering Sea. *J. Geophys. Res.,* 73:4759–4766.

_______, 1980. Determination of the relationships of electrical resistivity, sound velocity, and density/porosity of sediment and rock by laboratory techniques and well logs from deep sea drilling project sites 415 and 416 off the coast of Morocco. *In* Lancelot, Y., Winterer, E. L., et al., *Init. Repts. DSDP,* 50: Washington (U.S. Govt. Printing Office), 305–318.

Bray, C. J., and Karig, D. E., 1985. Porosity of sediments in accretionary prisms, and some implications for dewatering processes. *J. Geophys. Res.,* 90:768–778.

_______, 1986. Physical properties of sediments from the Nankai Trough, Deep Sea Drilling Project Leg 87A, Sites 582 and 583. *In* Kagami, H., Karig, D. E., Coulbourn, W. C., et al., *Init. Repts., DSDP,* 87: Washington (U.S. Govt. Printing Office), 827–842.

Brigaud, F., and Vasseur, G., 1989. Mineralogy, porosity and fluid control on thermal conductivity of sedimentary rocks. *Geophys. J.,* 98:525–542.

Brückmann, W., 1989. Typische Kompakationsmuster mariner Sedimente und ihre Modifikation in einem rezenten Akkretionskeil (Barbados Ridge). *Beitr. Geol. Inst. Univ. Tübingen,* Rh. A, 5:1–135.

Burch, T. K., and Langseth, M. G., 1981. Heat flow determinations in three DSDP boreholes near the Japan Trench. *J. Geophys. Res.,* 86:9411–9419.

Burst, J. F., 1969. Diagenesis of Gulf Coast clayey sediments and its possible relation to petroleum migration. *AAPG Bull.,* 53:73–93.

Busch, W. H., 1989. Patterns of sediment compaction at Ocean Drilling Program Sites 645, 646, and 647, Baffin Bay and Labrador Sea. *In* Srivastava, S. P., Arthur, M., Clement, B., et al., *Proc. ODP, Sci. Results,* 105: College Station, Texas (Ocean Drilling Program), 781–790.

Carlson, R. L., and Christensen, N. I., 1977. Velocity anisotropy and physical properties of deep-sea sediments from the western South Atlantic. *In* Perch-Nielsen, K., Supko, P. R., et al., *Init. Repts. DSDP,* 39: Washington (U.S. Govt. Printing Office), 555–559.

Carslaw, H. S., and Jaeger, J. C., 1959. *The Conduction of Heat in Solids:* London (Oxford Univ. Press).

Chamley, H., Cadet, J. P., and Charvet, J., 1986. Nankai Trough and Japan Trench Late Cenozoic paleoenvironments deduced from clay mineralogic data. *In* Kagami, H., Karig, D. E., Coulbourn, W. C., et al., *Init. Repts. DSDP,* 87: Washington (U.S. Govt. Printing Office), 633–642.

Chijiwa, K., 1988. Post-Shimanto sedimentation and organic metamorphism: an example of the Miocene Kumano Group, Kii Peninsula. *Mod. Geol.,* 12:363–388.

Claypool, G. E., and Kvenvolden, K. A., 1983. Methane and other hydrocarbon gases in marine sediment. *Annu. Rev. Earth Planet. Sci.,* 11:299–327.

Cook, H. E., Johnson, P. D., Matti, J. C., and Zemmels, I., 1975. Methods of sample preparation and X-ray diffraction data analysis, X-ray Mineralogy Laboratory, Deep Sea Drilling Project, University of California, Riverside. *In* Hayes, D. E., Frakes, L. A., et al., *Init. Repts. DSDP,* 28: Washington (U.S. Govt. Printing Office), 999–1007.

De Rosa, R., Zuffa, G. G., Taira, A., and Leggett, J. K., 1986. Petrography of trench sands from the Nankai Trough, southwest Japan: implications for long-distance turbidite transportation. *Geol. Mag.,* 5:477–486.

Donnelly, T. W., 1980. Appendix. Chemical composition of deep sea sediments -Sites 9 through 425, Legs 2 through 54, Deep Sea Drilling Project. *In* Rosendahl, B. R., Hekinian, R., et al., *Init. Repts. DSDP,* 54: Washington (U.S. Govt. Printing Office), 899–949.

Elderfield, H., Kastner, M., and Martin, J. B., 1990. Composition and sources of fluids and sediments of the Peru subduction Zone. *J. Geophys. Res.,* 95:8819–8827.

Evans, C. R., and Staplin, F. L., 1971. Regional facies of organic metamorphism in geochemical exploration. *3rd Inter. Geochem. Expl. Symp. Proc.,* Can. Inst. Min. Metal., 11:517–520.

Gieskes, J. M., Blanc, G., Vrolijk, P., et al., 1989. Hydrogeochemistry in the Barbados Accretionary Complex: Leg 110 ODP. *Palaeogeogr., Palaeoclimatol., Palaeoecol.,* 71:83–96.

Gieskes, J. M., Elderfield, H., Lawrence, J. R., Johnson, J., Meyers, B., and Campbell, A., 1982. Geochemistry of interstitial waters and sediments, Leg 64, Gulf of California. *In* Curray, J. R., Moore, D. G., et al., *Init. Repts. DSDP,* 64 (Pt. ?): Washington (U.S. Govt. Printing Office), 675–694.

Gieskes, J. M., Elderfield, H., and Nevsky, B., 1983. Interstitial water studies, Leg 65. *In* Lewis, B.T.R., Robinson, P., et al., *Initial Repts. DSDP,* 65: Washington (U.S. Govt. Printing Office), 441–449.

Gieskes, J. M., and Gamo, T., in press. Wet chemical analysis of sediments for major element composition. *ODP Tech. Note,* 16.

Gieskes, J. M., Vrolijk, P., and Blanc, G., 1990. Hydrogeochemistry of the Northern Barbados Accretionary Complex Transect: ODP Leg 110. *J. Geophys. Res.,* 95:8809–8818.

Gradstein, F. M., Ludden, J. N., et al., 1990. *Proc. ODP, Init. Repts.,* 123: College Station, TX (Ocean Drilling Program).

Hamilton, E. L., 1974. Prediction of deep-sea sediment properties: state of the art. *In* Inderbitzen, A. L. (Ed.), *Deep-Sea Sediments: Physical and Mechanical Properties:* New York (Plenum), 1–44.

_______, 1976. Variations in density and porosity with depth in deep-sea sediments. *J. Sediment. Petrol.,* 46:280–300.

_______, 1978. Sound velocity-density relations in sea-floor sediments and rocks. *J. Acoust. Soc. Am.,* 63:366–377.

_______, 1979. Sound velocity gradients in marine sediments. *J. Acoust. Soc. Am.,* 65:909–922.

Hart, S. R., Erlank, A. J., and Kable, J. D., 1974. Sea floor basalt alteration: some chemical and Sr isotopic effects. *Contrib. Mineral. Petrol.,* 44:219–230.

Henderson, P., 1984. General geochemical properties and abundances of the rare earth elements. *In* Henderson, P. (Ed.), *Rare Earth Element Geochemistry:* New York (Elsevier), 1–29.

Hood, A., Gutjahr, C.C.M., and Heacock, R. L., 1975. Organic metamorphism and the generation of petroleum. *AAPG Bull.,* 59:986–996.

Hunt, J. M., 1979. *Petroleum Geochemistry and Geology:* San Francisco (W. H. Freeman).

Hyndman, R. D., Davies, E. E., and Bornhold, B., in press. A mechanism for the formation of methane hydrate and sea floor bottom simulating reflectors by vertical fluid expulsion. *J. Geophys. Res.*

Jarrard, R. D., Dadey, K. A., and Busch, W. H., 1989. Velocity and density of sediments of Eirik Ridge, Labrador Sea: control by porosity and mineralogy. *In* Srivastava, S. P., Arthur, M. A., Clement, B., et al., *Proc. ODP, Sci. Results,* 105: College Station, TX (Ocean Drilling Program), 811–835.

Kagami, H., Karig, D. E., Coulbourn, W. T., et al., 1986. *Init. Repts. DSDP,* 87: Washington (U.S. Govt. Printing Office).

Karato, S., Wilkens, R. H., and Langseth, M. G., 1983. Shipboard physical-properties measurements of basalts from the Costa Rica Rift, Deep Sea Drilling Project Legs 69 and 70. *In* Cann, J. R., Langseth, M. G., Honnorez, J., Von Herzen, R. P., White, S. M., et al., *Init. Repts. DSDP,* 69: Washington (U.S. Govt. Printing Office), 675–681.

Karig, D. E., Ingle, J. C., Jr., et al., 1975. *Init. Repts. DSDP,* 31: Washington (U.S. Govt. Printing Office).

Karig, D. E., and Lundberg, N., 1990. Deformation bands from the toe of the Nankai accretionary prism. *J. Geophys. Res.,* 95:9099–9109.

Kastner, M., 1979. Zeolites. *In* Burns, R. G. (Ed.), *Marine Minerals.* Min. Soc. Am., Rev. Mineral., 6:111–123.

Kastner, M., Elderfield, H., Martin, J. B., Suess, E., Kvenvolden, K. A., and Garrison, R. E., 1990. Diagenesis and interstitial-water chemistry at the Peruvian continental margin - major constituents and strontium isotopes. *In* Suess, E., von Huene, R., et al., *Proc. ODP, Sci. Results,* 112: College Station, TX (Ocean Drilling Program), 413–440.

Kastner, M., and Gieskes, J. M., 1976. Interstitial water profiles and sites of diagenetic reactions, Leg 35, DSDP, Bellingshausen Abyssal Plain. *Earth Planet. Sci. Lett.,* 33:11–20.

Katz, D. L., Cornell, D., Kobayashi, R., Poettmann, F. H., Vary, J. A., Elenbaas, J. R., and Weinaug, C. F., 1959. Water-hydrocarbon systems. *In* Katz, D. L., et al. (Eds.), *Handbook of Natural Gas Engineering,* New York (McGraw-Hill), 189–221.

Kawahata, H., Fujioka, K., and Ishizuka, T., 1986. Sediments and interstitial water at Sites 582 and 584, the Nankai Trough and the Japan Trench landward slope. *In* Kagami, H., Karig, D. E., Coulbourn, W. C., et al., *Init. Repts. DSDP*, 87: Washington (U.S. Govt. Printing Office), 865–875.

Kermabon, A., Gehin, C., and Blavier, P., 1969. A deep-sea electrical resistivity probe for measuring porosity and density of unconsolidated sediments. *Geophysics*, 34:554–571.

Kinoshita, H., and Yamano, M., 1986. The heat flow anomaly in the Nankai Trough area. *In* Kagami, H., Karig, D. E., Coulbourn, W. C., et al., 1986. *Init. Repts. DSDP, 87:* Washington (U.S. Govt. Printing Office), 737–743.

Klein, E. M., and Langmuir, C. H., 1987. Global correlations of ocean ridge chemistry with axial depth and crustal thickness. *J. Geophys. Res.*, 92:8089–8115.

Klein, G. deV., Kobayashi, K., et al. 1980. *Init. Repts. DSDP,* 58: Washington (U.S. Govt. Printing Office).

Kvenvolden, K. A., 1985. Comparison of marine gas hydrates in sediments of an active and passive continental margin. *Mar. Petrol. Geol.*, 2:65–71.

Langseth, M. G., Westbrook, G. K., and Hobart, M., 1990. Contrasting geothermal regimes of the Barbados Ridge accretionary complex. *J. Geophys. Res.*, 95:8829–8843.

Leythaeuser, D., Altebaeumer, F. J., and Weiner, B., 1979. Generation of low molecular weight hydrocarbons from organic matter in source beds as a function of temperature and facies. *Chem. Geol.*, 25:95–108.

Lister, C.R.B., 1977. Estimates for heat flow and deep rocks properties based on boundary layer theory. *Tectonophysics,* 41:157–171.

Lovell, M. A., 1984. Thermal conductivity and permeability assessment by electrical resistivity measurements in marine sediments. *Mar. Geotechnol.*, 6:205–240.

Lundberg, N., and Karig, D. E., 1986. Structural features from the Nankai Trough lower slope, DSDP Sites 582 and 583. *In* Kagami, H., Karig, D. E., Coulbourn, W. C., et al., *Init. Repts, DSDP,* 87: Washington (U.S. Govt. Printing Office), 797–808.

Lundberg, N., and Moore, J. C., 1986. Macroscopic structural features in Deep Sea Drilling Project cores from forearc regions. *In* Moore, J. C. (Ed.), *Structural Fabrics Preserved in Deep Sea Drilling Project Cores From Forearcs:* Mem. Geol. Soc. Am., 166:13–44.

Marsh, N. G., Saunders, A. D., Tarney, J., and Dick, H.J.B., 1980. Geochemistry of basalts from the Shikoku and Daito Basins, Deep Sea Drilling Project Leg 58. *In* Klein, G. deV., Kobayashi, K., et al., *Init. Repts. DSDP,* 58: Washington (U.S. Govt. Printing Office), 805–842.

Matsuhisa, Y., and Matsumoto, R., 1985. Oxygen isotope ratios of interstitial waters from the Nankai Trough and the Japan Trench, Leg 87. *In* Kagami, H., Karig, D. E., Coulborn, W. C., et al., *Init. Repts. DSDP,* 87: Washington (U.S. Govt. Printing Office), 853–856.

McDuff, R. E., 1985. The chemistry of interstitial waters, Deep Sea Drilling Project, Leg 86. *In* Heath, G. R., Burckle, L. H., et al., *Init. Repts. DSDP,* 86: Washington (U.S. Govt. Printing Office), 675–687.

Moore, D. M., and Reynolds, R. C., Jr., 1989. *X-ray Diffraction and the Identification and Analysis of Clay Minerals.* New York (Oxford Univ. Press).

Moore, G. F., Shipley, T. H., Stoffa, P. L., Karig, D. E., Taira, A., Kuramoto, H., Tokuyama, and Suyehiro, K., 1990. Structure of the Nankai Trough accretionary zone from multichannel seismic reflection data. *J. Geophys. Res.*, 95:8753–8765.

Moore, G. W., and Gieskes, J. M., 1980. Interactions between sediment and interstitial water near the Japan Trench, Leg 57, Deep Sea Drilling Project. *In* von Huene, R., Nasu, N., et al., *Init. Repts. DSDP,* 56/57 (Pt. 2): Washington (U.S. Govt. Printing Office), 1269–1275.

Morgenstern, N. R., and Tchalenko, J. S., 1967. Microscopic structures in Kaolin subjected to direct shear. *Geotechnique,* 13:309–328.

Nishi, H., 1988. Structural analysis of the Shimanto accretionary complex, Kyushu, Japan, based on planktonic foraminiferal zonation. *Mod. Geol.*, 12:47–69.

Nisterenko, G. V., 1980. Petrochemistry and geochemistry of basalts in the Shikoku Basin and Daito Basin, Philippine Sea. *In* Klein, G. deV., Kobayashi, K., et al., *Init. Repts. DSDP,* 58: Washington (U.S. Govt. Printing Office), 791–804.

Nobes, D. C., Villinger, H., Davis, E. E., and Law, L. K., 1986. Estimation of marine sediment bulk physical properties at depth from seafloor geophysical measurements. *J. Geophys. Res.*, 91:14033–14043.

Pearce, J. A., 1982. Trace elements characteristics of lavas from destructive plate boundaries. *In* Thorpe, R. S. (Ed.), *Andesites: Orogenic Andesites and Related Rocks:* New York (Wiley), 525–548.

Pearce, J. A., and Cann, J. R., 1973. Tectonic setting of basic volcanic rocks determined using trace element analyses. *Earth Planet. Sci. Lett.*, 19:290–300.

Perry, E. A., Jr., and Hower, J., 1970. Burial diagenesis of the Gulf Coast pelitic sediments. *Clays Clay Miner.*, 18:167–177.

Powers, M. C., 1967. Fluid-release mechanisms in compacting marine mudrocks and their importance in oil exploration. *AAPG Bull.*, 51:1240–1254.

Price, L. C., 1983. Geologic Time as a parameter in organic metamorphism and vitrinite reflectance as an absolute paleogeothermometer. *J. Pet. Geol.*, 6:5–38.

Rashid, M. A. (Ed.), 1985. *Geochemistry of Marine Humic Compounds:* Berlin (Springer-Verlag).

Raymer, L. L., Hunt, E. R., and Gardner, J. S., 1980. An improved sonic transit time-to-porosity transform. *Trans. SPWLA 21st Annu. Log. Symp.*, Paper P.

Romankevich, E. A., 1984. *Geochemistry of Organic Matter in the Ocean:* New York (Springer-Verlag).

Saunders, A. D., Norry, M. J., and Tarney, J. 1988. Origin of MORB and chemically depleted mantle reservoirs: trace elements constraints. *J. Petrol.* (Spec. Lithospheric Issue), 415–445.

Saunders, A. D., Tarney, J., Marsh, N. G., and Wood, D. A., 1980. Ophiolites as ocean crust or marginal basin crust: a geochemical approach. *Proc. Int. Ophiolite Symp.*, Cyprus, 193–204.

Schaefer, R. G., and Leythaeuser, D., 1983. Generation and migration of low-molecular weight hydrocarbons in sediments from Site 511 of DSDP/IPOD Leg 71, Falkland Plateau, South Atlantic. *In* Bjoroy, M. (Ed.), *Advances in Organic Geochemistry 1981.* New York (Wiley), 164–174.

Shih, T. C., 1980. Magnetic lineations in the Shikoku Basin. *In* Klein, G. deVries, and Kobayashi, K., et al., *Init. Rept. DSDP,* 58: Washington (U.S. Govt. Printing Office), 783–788.

Shipboard Scientific Party, 1988. Synthesis of shipboard results: Leg 110 transect of the northern Barbados Ridge. *In* Mascle, A., Moore, J. C., et al., *Proc. ODP, Init. Repts.*, 110: College Station, TX (Ocean Drilling Program), 577–591.

Stoffa, P. L., Fokkema, J. T., de Luna Freire, R. M., and Kessinger, W. P., 1990. Split-step Fourier migration. *Geophysics,* 55:410–412.

Stoffa, P. L., Wood, W. T., Shipley, T. H., Moore, G. F., Nishiyama, E., Bothelo, M.A.B., Taira, A., Tokuyama, H., and Suyehiro, K., in press. High resolution expanding spread and split-spread marine seismic profiles: acquisition and velocity analysis methods. *J. Geophys. Res.*

Sun, S. S., 1980. Lead isotopic study of young volcanic rocks from mid-ocean ridges, ocean islands and island arcs. *Philos. Trans. R. Soc. London,* A297:409–445.

Taira, A., and Niitsuma, N., 1986. Turbidite sedimentation in the Nankai Trough as interpreted from magnetic fabric, grain size, and detrital modal analyses. *In* Kagami, H., Karig, D. E., Coulbourn, W. C., et al., *Init. Repts. DSDP,* 87: Washington (U.S. Govt. Printing Office), 611–632.

Teufel, L. W., and Warpinsky, N. R., 1984. Determination of *in-situ* stress from anelastic strain recovery measurements of oriented core: comparison to hydraulic fracture stress measurements. *Proc. 25th U.S. Symp. Rock Mechanics,* Northwestern Univ., 176–185.

Tissot, B. P., and Welte, D. H., 1984. *Petroleum Formation and Occurrence* (2nd ed.): Heidelberg (Springer-Verlag).

Waples, D. W., 1980. Time and temperature in petroleum formation: application of Lopatin's method to petroleum exploration. *AAPG Bull.*, 64:916–926.

Warpinski, N. R., Branagan, P. T., and Wilmer, R., 1985. *In-situ* stress measurements at DOE's Multiwell Experiment Site, Mesaverde Group, Rifle, Colorado. *J. Pet. Tech.*, 37:527.

Warpinski, N. R., and Teufel, L. W., 1987. *In-situ* stresses in low-permeability, non-marine rocks. *Soc. Pet. Eng. Ann. Mtg.*, Paper SPE/DOE 16402:125–138.

Weaver, B. L., and Tarney, J., 1984. Estimating the composition of the continental crust: an empirical approach. *Nature,* 310:575–577.

Wetzel, A., 1984. Interrelationships between sediment composition, compaction, pore space, and shrinkage, Leg 75, Hole 532A. *In* Hay, W. W., Sibuet, J.-C., et al. *Init. Repts., DSDP,* 75 (Pt. 2): Washington (U.S. Govt. Printing Office), 1129–1136.

Winsauer, W. O., Shearin, H. M., Jr., Masson, P. H., and Williams, M., 1952. Resistivity of brine saturated sands in relation to pore geometry. *AAPG Bull.*, 36:253–277.

Wolter, K. E., and Berkhemer, H., 1989. Time dependent strain recovery of cores from the KTB-deep drill hole. *Rock Mech. Rock Eng.*, 22:273–287.

Yamano, M., Honda, S., and Uyeda, S., 1984. Nankai Trough: a hot trench? *Mar. Geophys. Res.*, 6:187–203.

Yamano, M., and Uyeda, S., 1988. Heat flow in the ocean basins and margins. *In* Nairn, A.E.M., Stehli, F. G., and Uyeda, S. (Eds.), *The Ocean Basins and Margins* (Vol. 7): New York (Plenum), 523–557.

Yamano, M., Uyeda, S., Aoki, Y., and Shipley, T. H., 1982. Estimates of heat flow derived from gas hydrates. *Geology,* 10:339–343.

Ms 131A-106

NOTE: All core description forms ("barrel sheets") and core photographs have been printed on coated paper and bound as Section 4, near the back of the book, beginning on page 289.

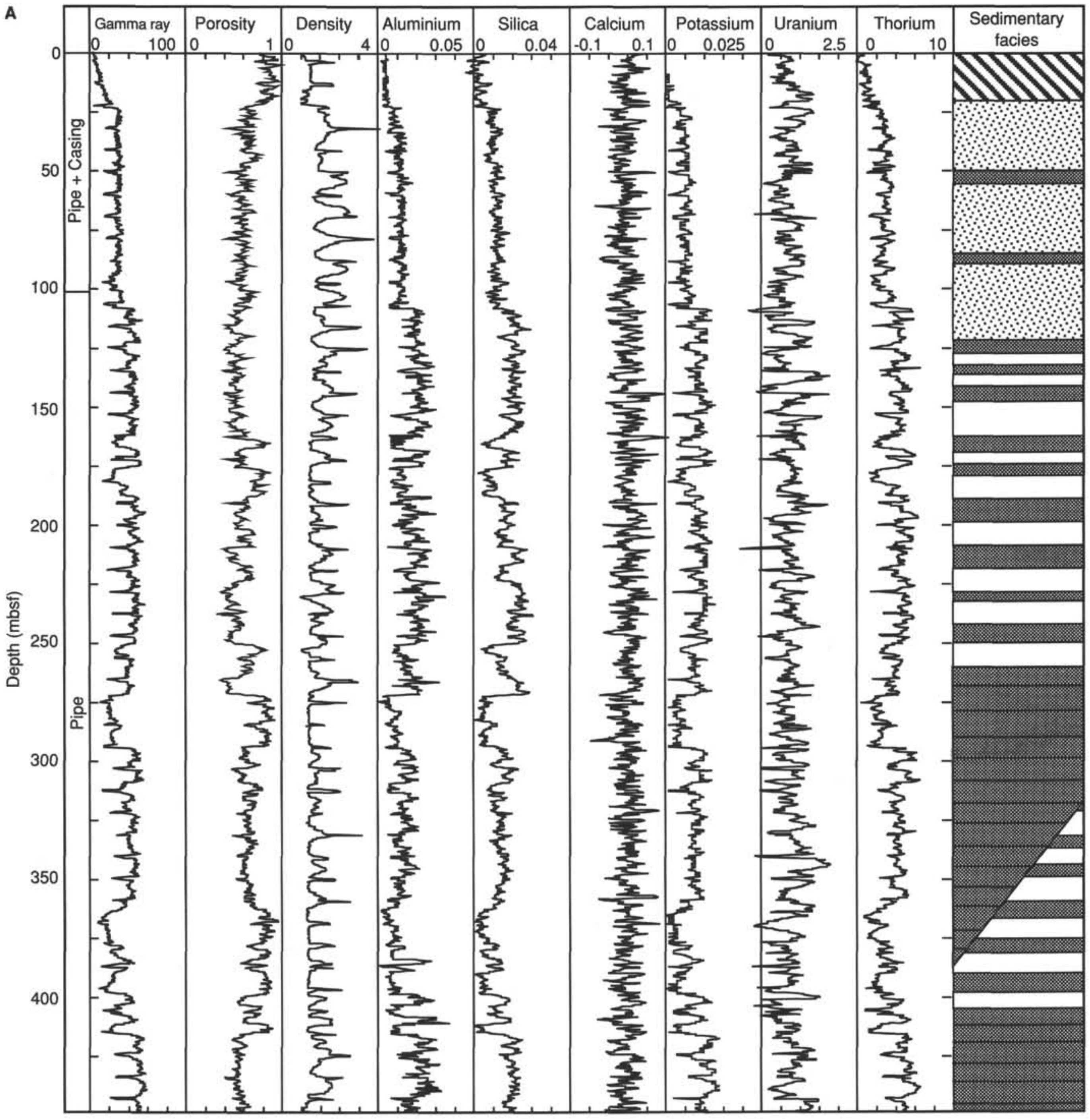

Figure 132. Summary of the logs obtained through the pipe in Hole 808C. A. 0–450 mbsf. B. 450–900 mbsf. Note the variable attenuation due to pipe joints, BHA etc.

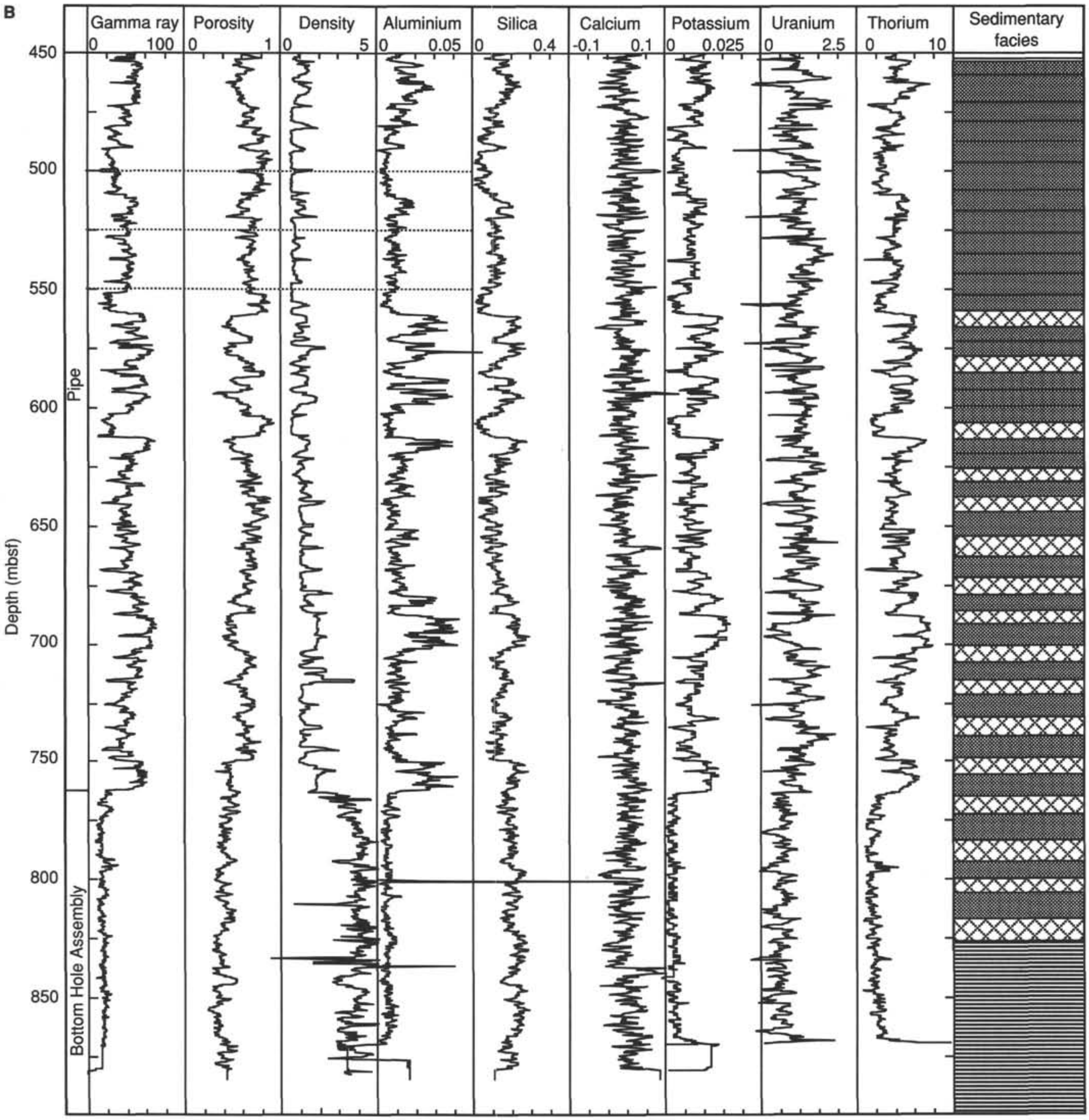

Figure 132 (continued).

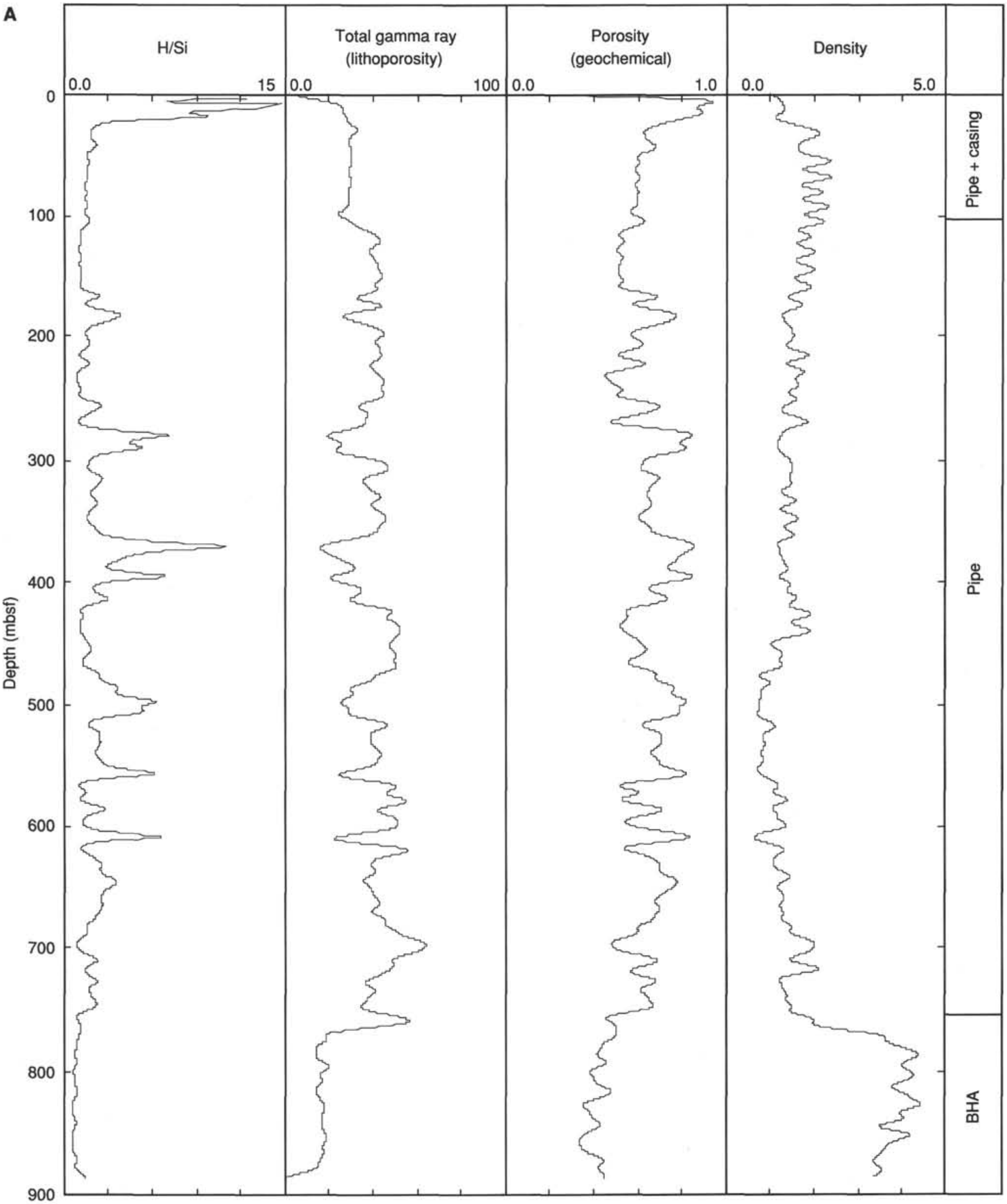

Figure 133. **A**, **B**, and **C** are logs obtained through the pipe in Hole 808C, filtered to reduce the effect of the pipe joints.

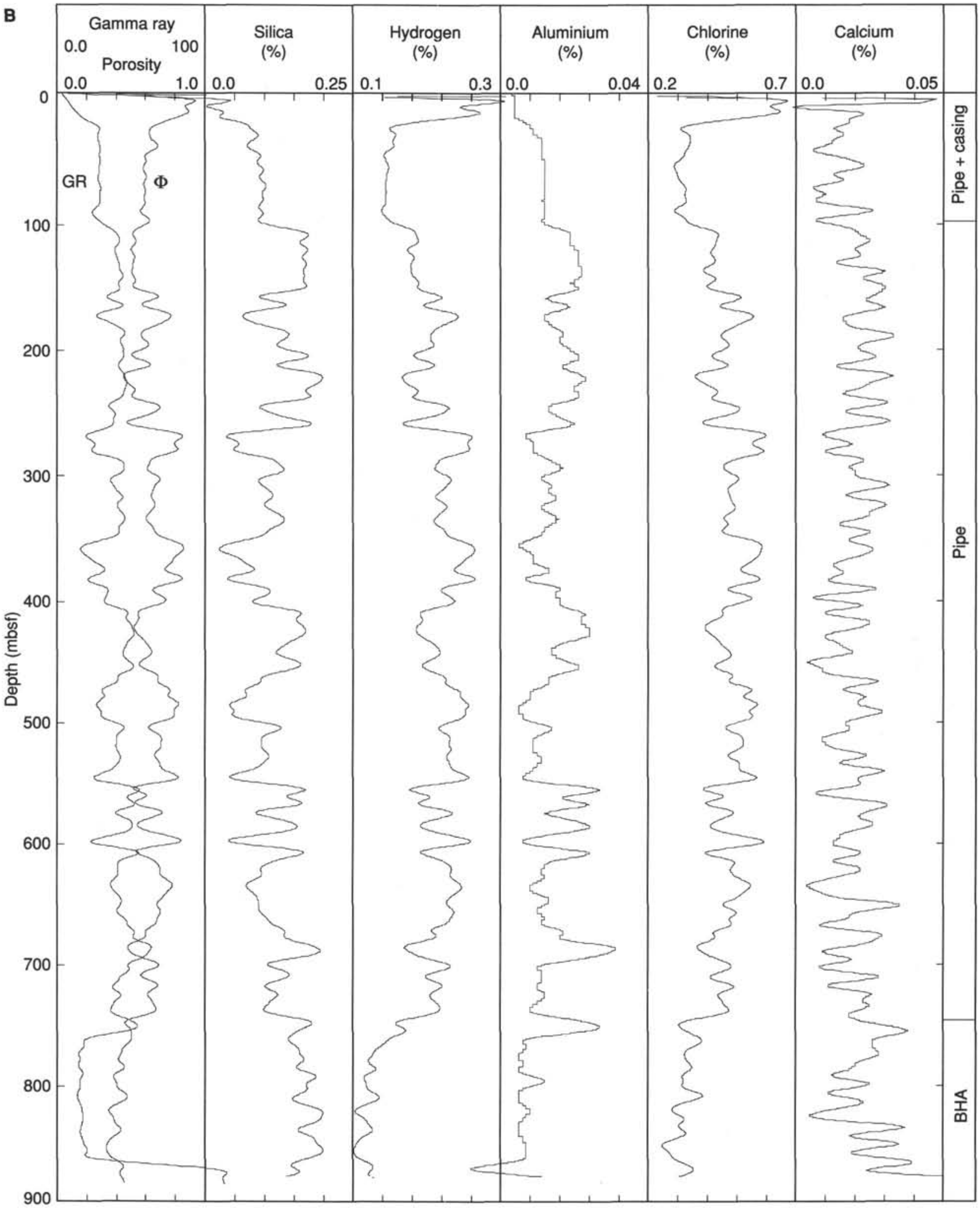

Figure 133 (continued).

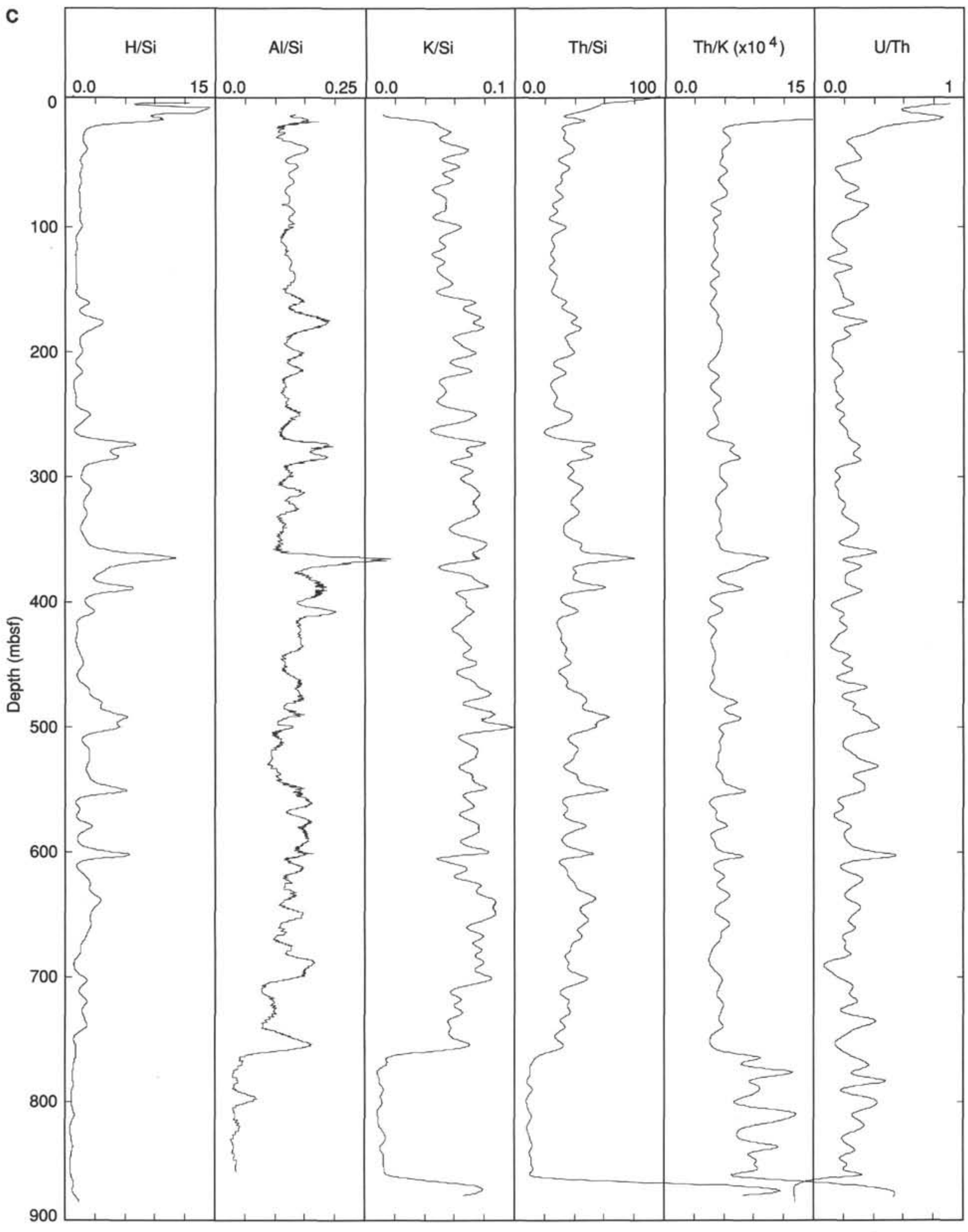

Figure 133 (continued).

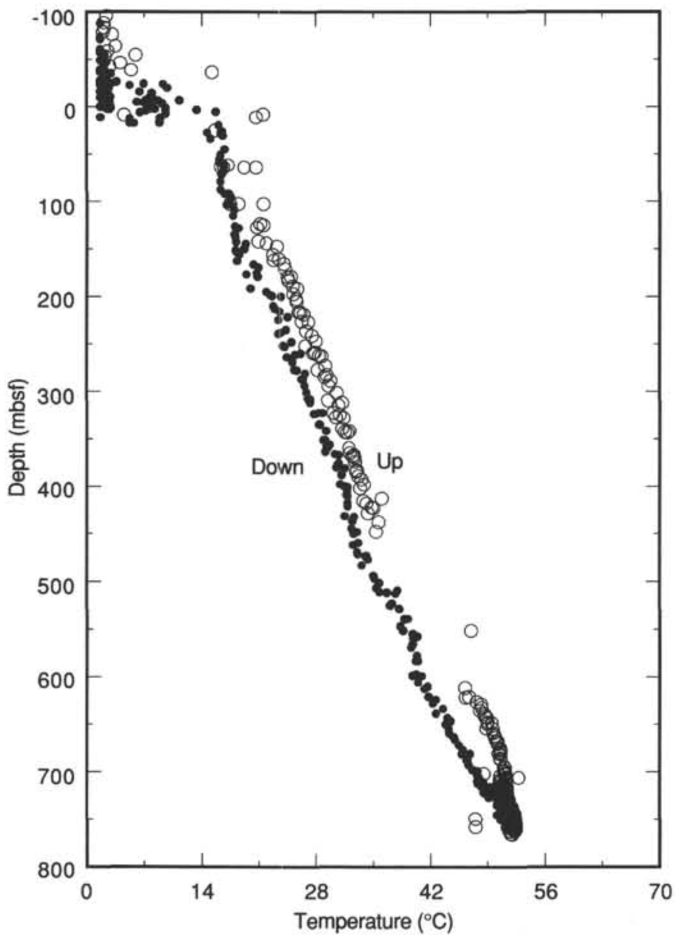

Figure 134. Downhole temperature logs obtained from Hole 808C using the TLT tool through pipe.

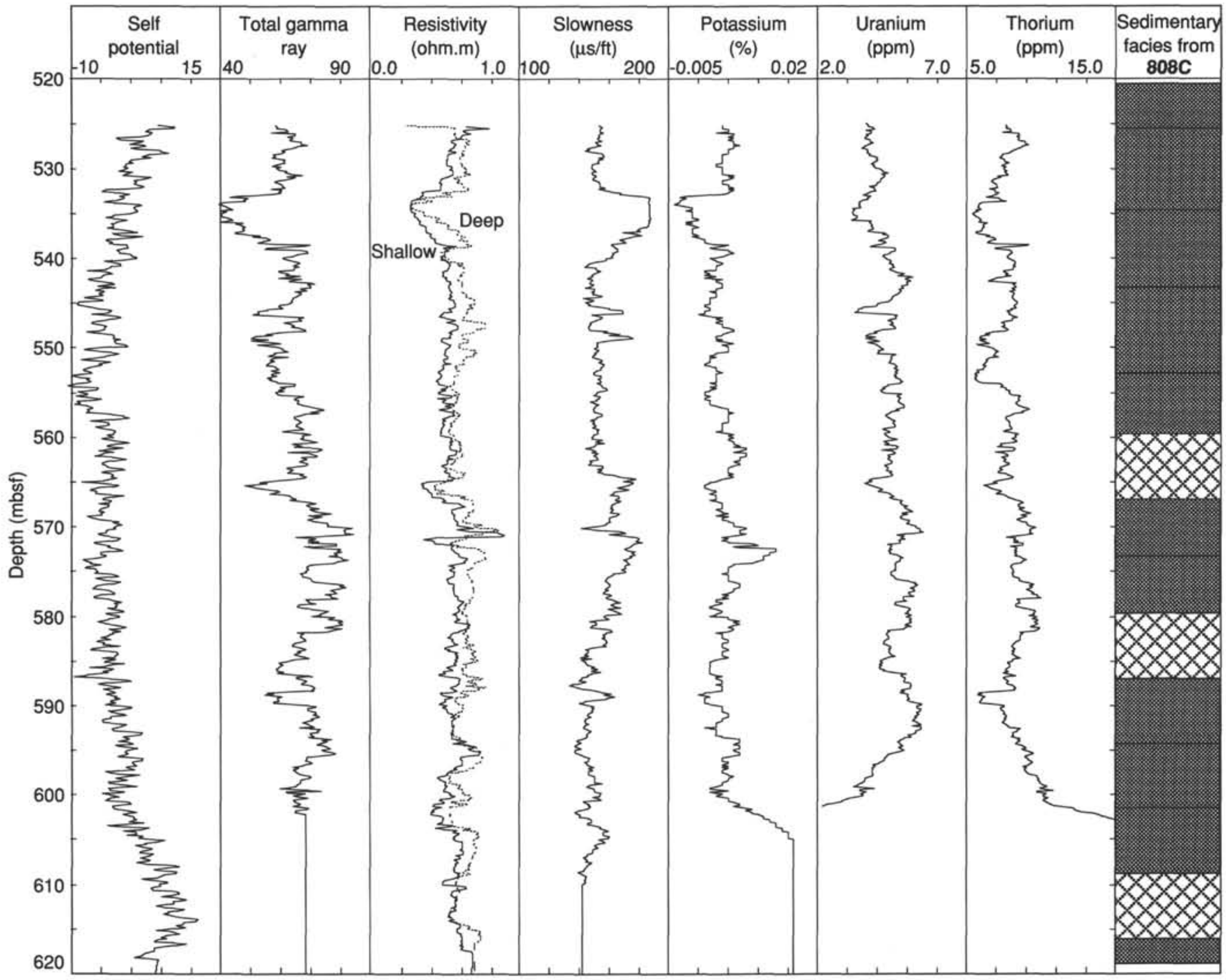

Figure 135. Summary of the open-hole log data obtained from Hole 808E.

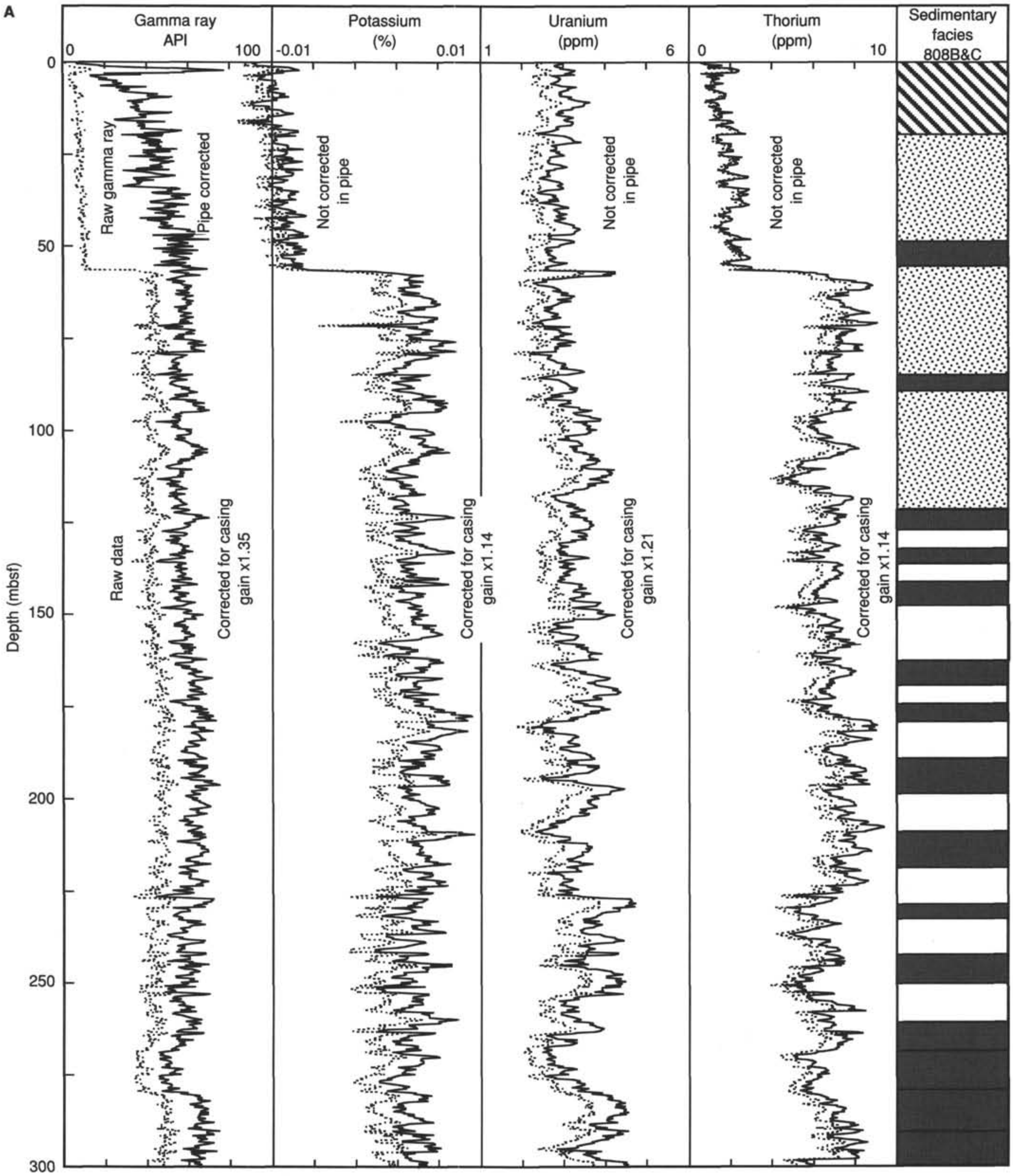

Figure 136. Summary of through-casing total gamma, potassium and thorium log data obtained from Hole 808E. **A.** Depths 0–300 mbsf. **B.** Depths 300–600 mbsf. Note that all of the traces have been approximately corrected for the attenuation of the casing. Only the total gamma has been corrected for the additional attenuation through the BHA in the upper 55 mbsf.

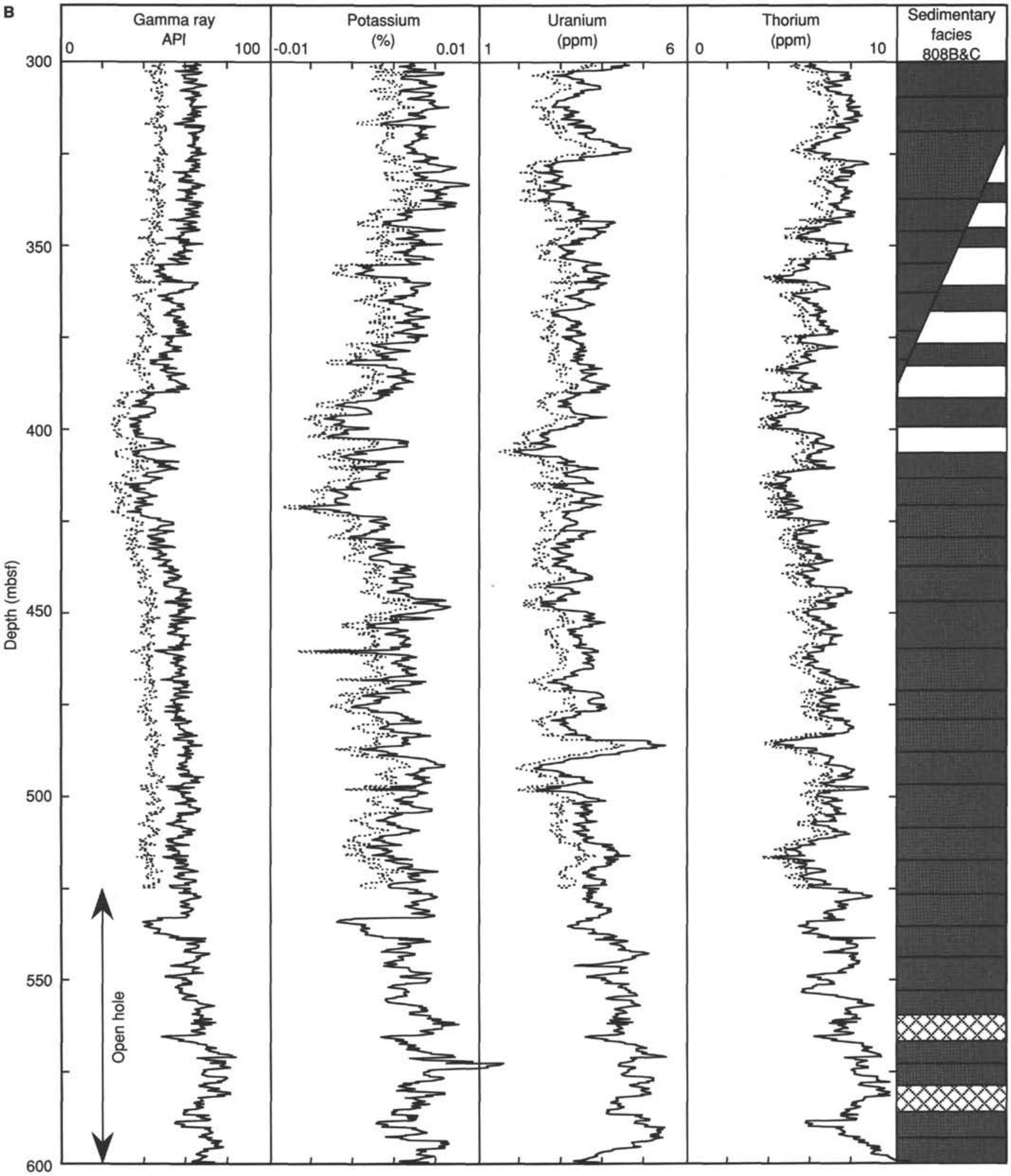

Figure 136 (continued).

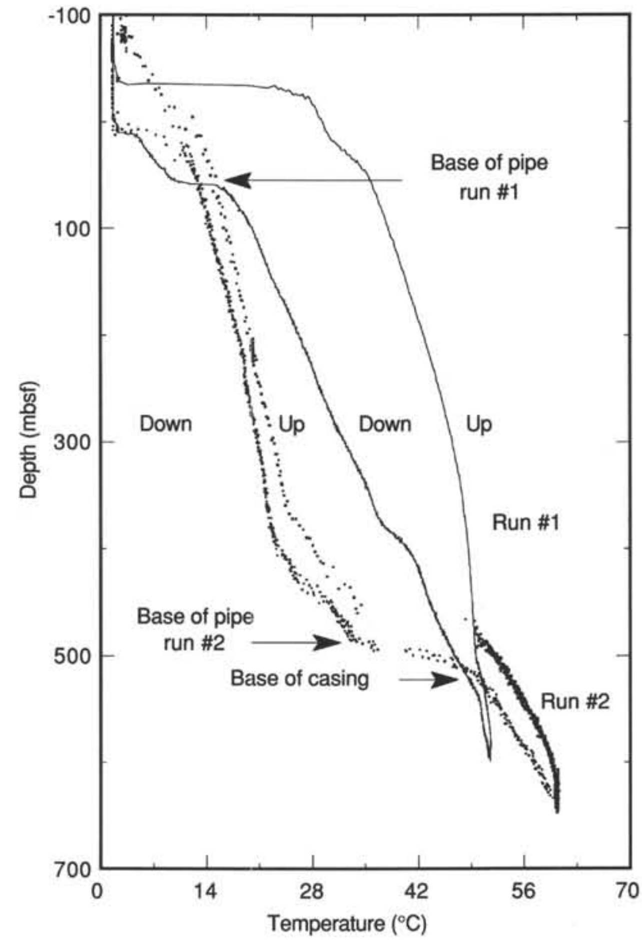

Figure 137. Downhole temperature logs obtained from Hole 808E using the TLT tool.

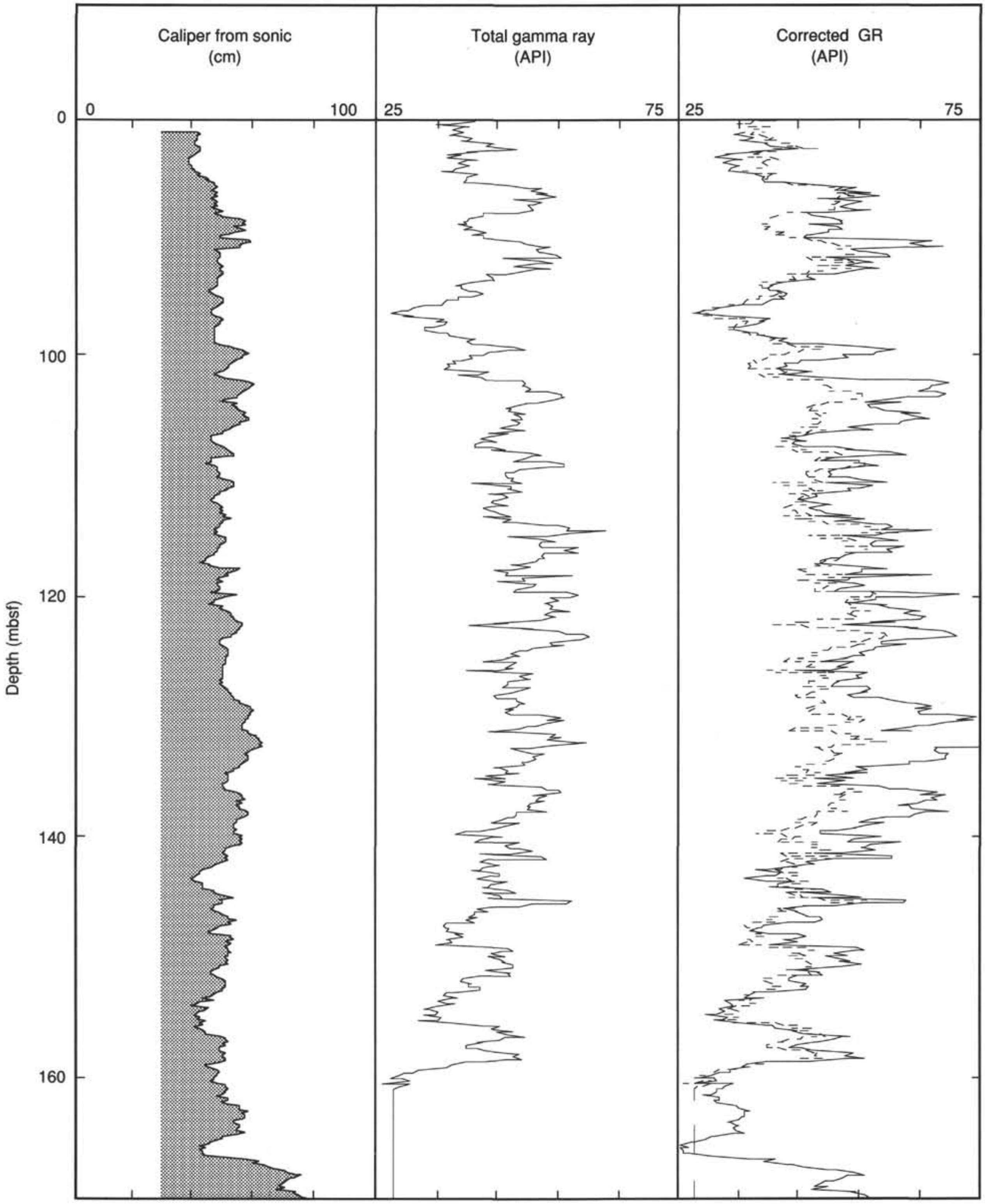

Figure 138. The sonic caliper log and the results of correcting the total gamma-ray log for the hole diameter variations.

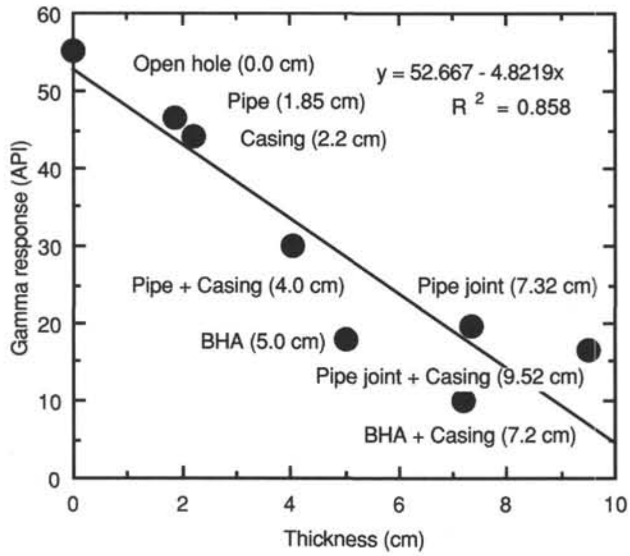

Figure 139. Total gamma attenuation estimated as a function of pipe thickness (pipe, pipe joints, casing, BHA).

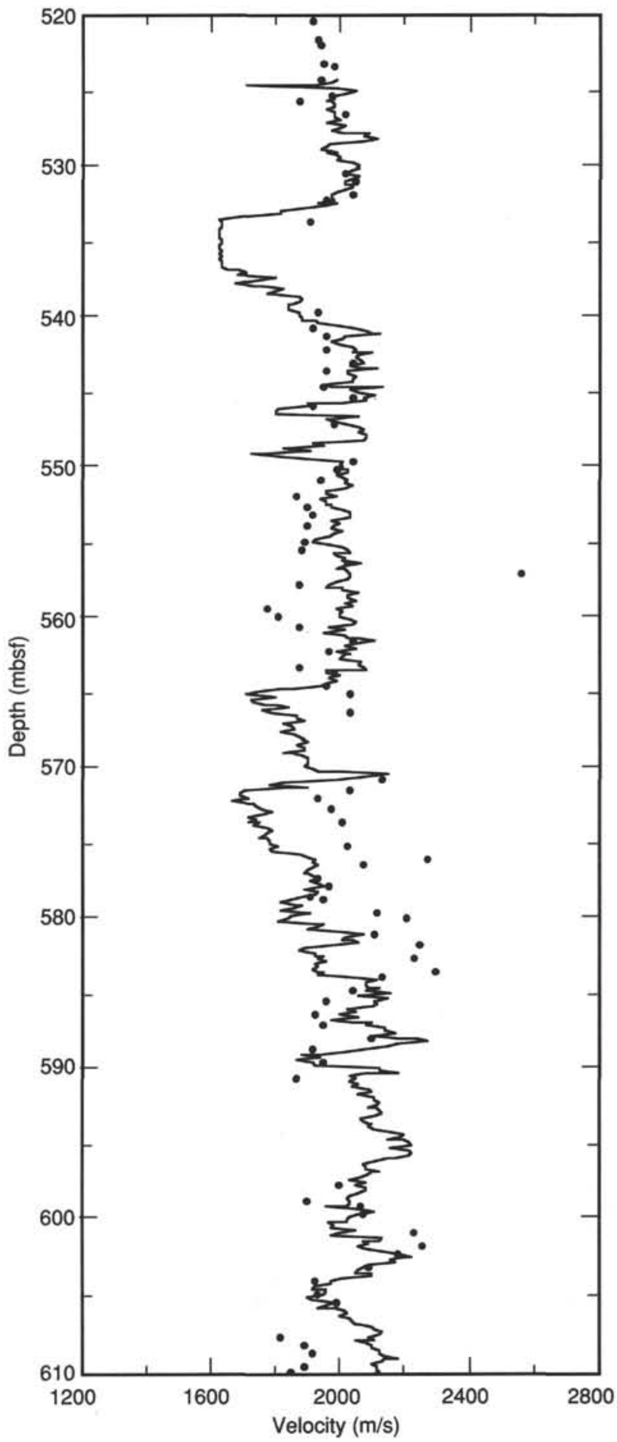

Figure 140. Velocity vs. depth for the deeper open hole interval (Hole 808E, graph) compared to core laboratory measurements (filled circles).

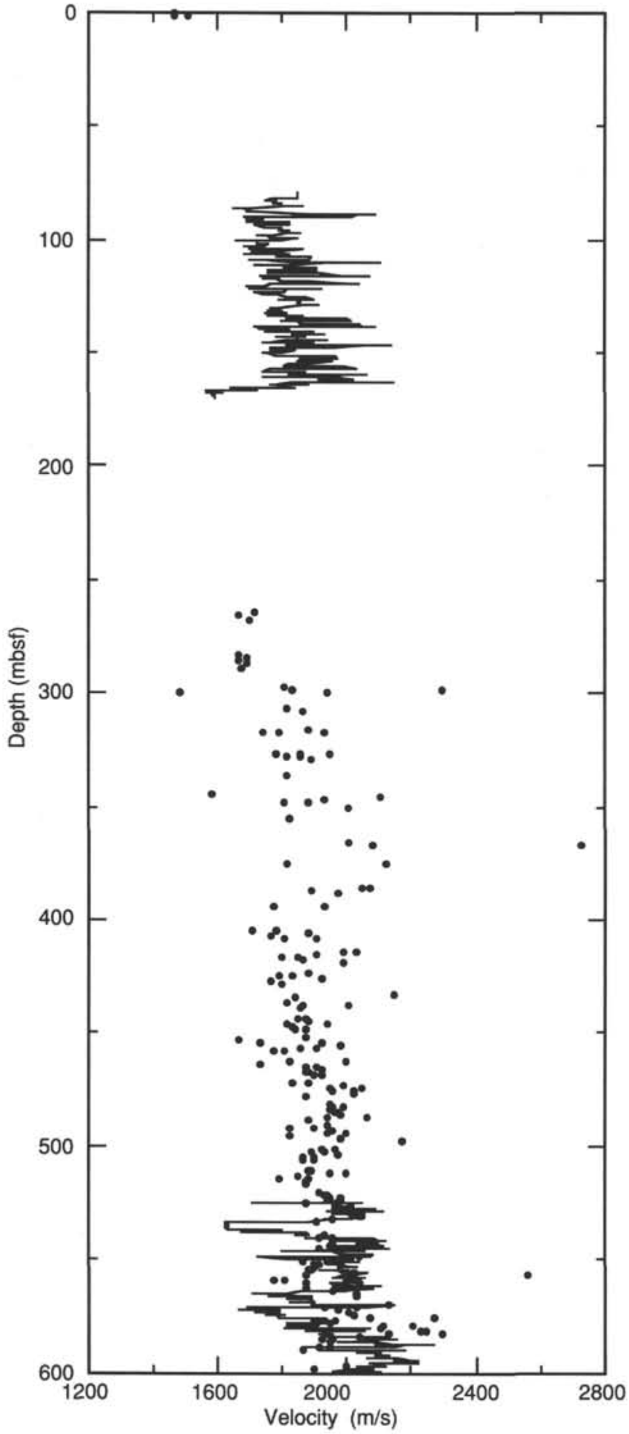

Figure 141. Velocity vs. depth for both open hole intervals (Holes 808B and 808E, graphs) compared to core laboratory measurements (filled circles). A simple porosity-depth function converted to velocity using the Hamilton (1978) velocity-porosity relation is shown.

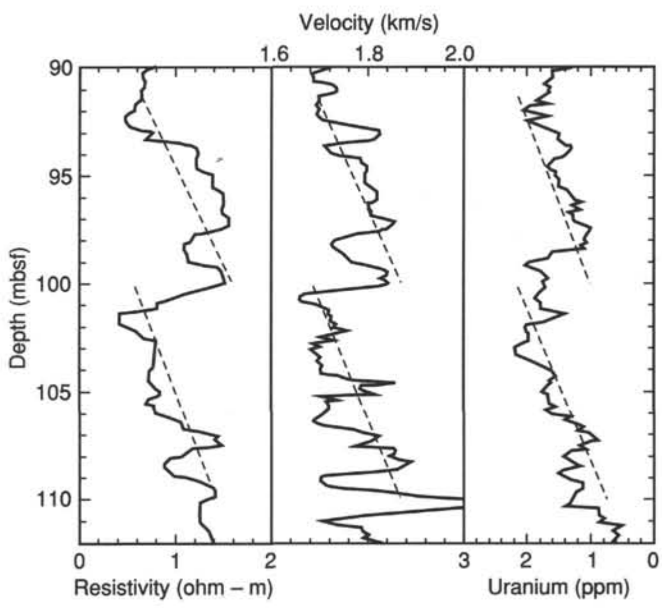

Figure 142. An example of an upward grain-size fining trend expressed in resistivity, velocity, and uranium logs in the upper open-hole section, Hole 808B. The lines follow the general trends.

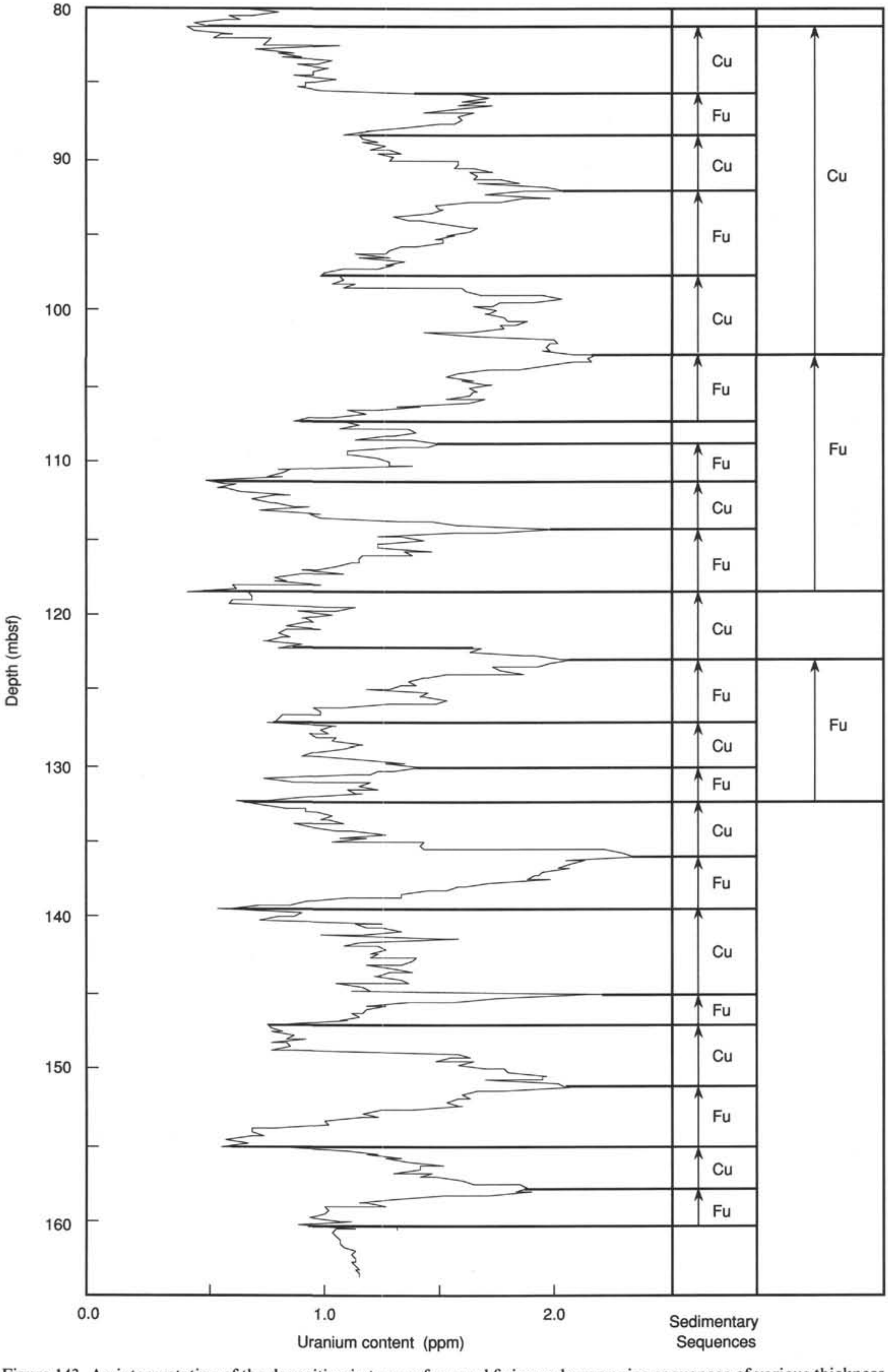

Figure 143. An interpretation of the deposition in terms of upward fining and coarsening sequences of various thickness based on the uranium log for the upper open-hole interval.

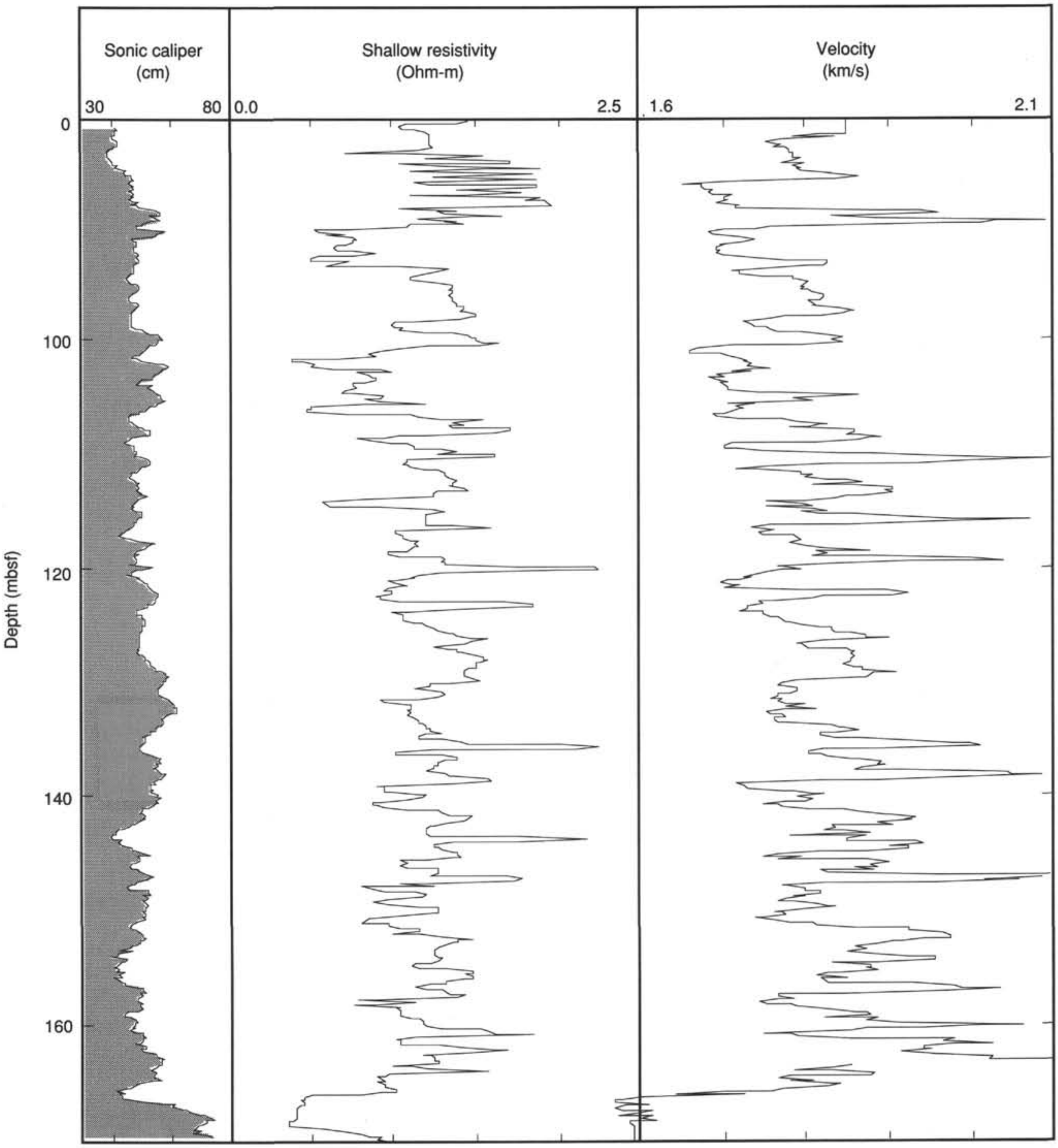

Figure 144. The sonic and shallow penetration resistivity logs illustrating the thin high-velocity and high-resistivity layers 1 to 2 m thick that probably represent coarse sand layers.

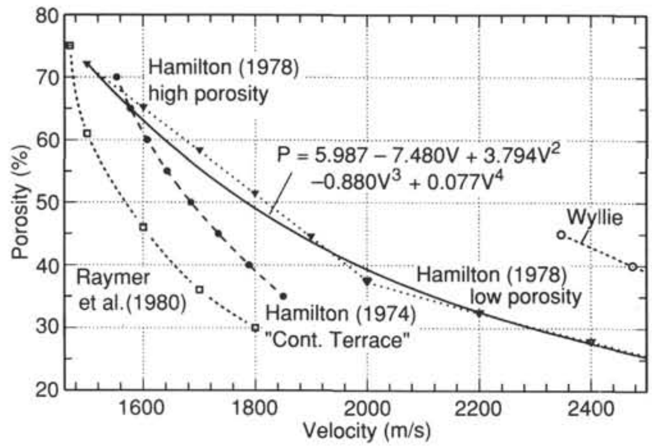

Figure 145. A number of velocity-porosity relations that have been obtained for deep-sea sediments.

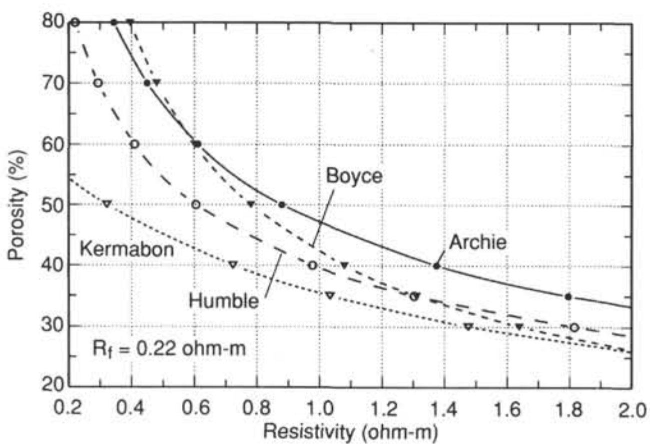

Figure 146. A number of resistivity-porosity relations that have been obtained for deep-sea sediments.

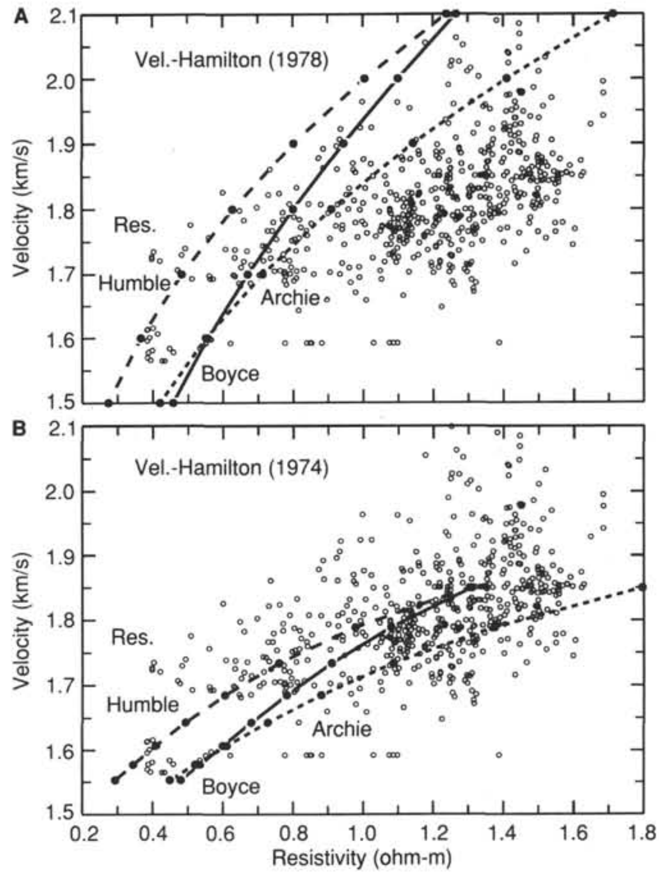

Figure 147. **A, B.** Velocity-resistivity cross plots for the shallower open-hole section (Hole 808B) with several combinations of velocity-porosity and resistivity-porosity relations.

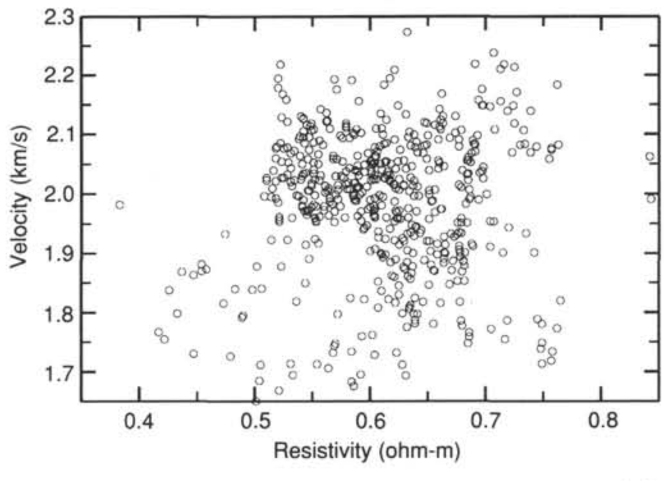

Figure 148. Velocity-resistivity cross plot for the deeper open-hole section (Hole 808E).

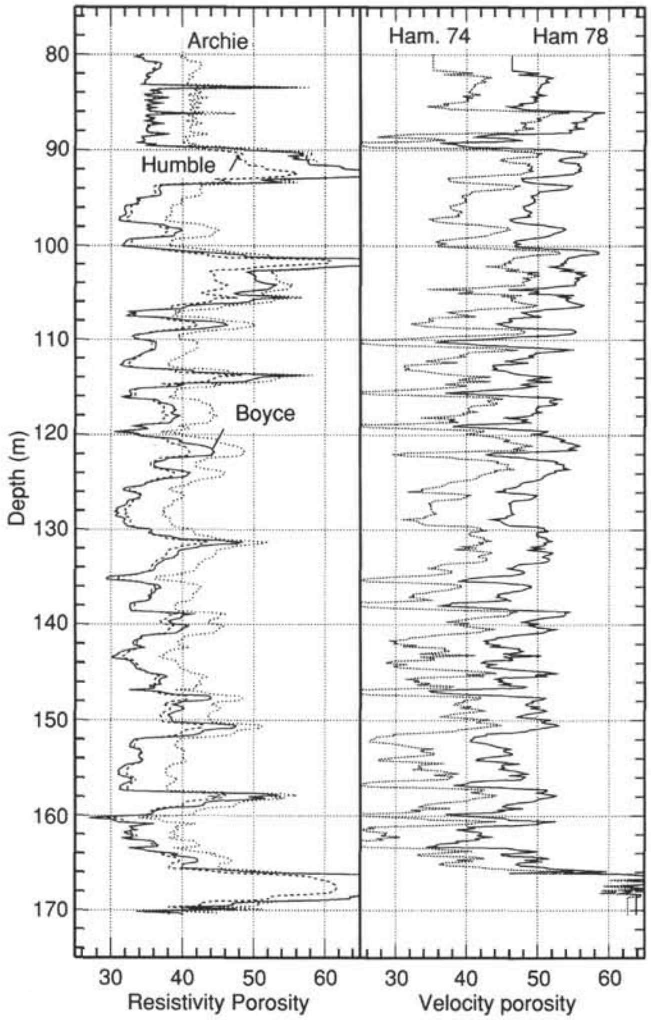

Figure 149. Porosity-depth in upper open-hole section (Hole 808B) using a variety of velocity-porosity and resistivity-porosity relations.

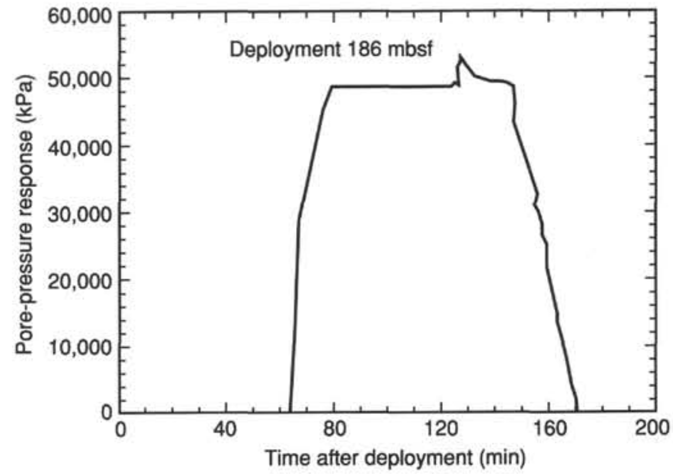

Figure 150. Pore-pressure response over the deployment time interval for the first LAST-I deployment in Hole 808G.

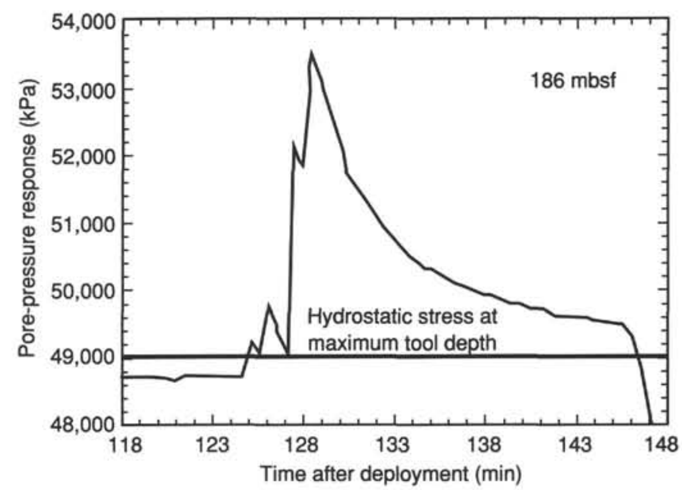

Figure 151. Pore-pressure response for LAST-I deployment 1 in Hole 808G.

Table 28. Record of LAST deployments.

Hole	Deployment	Depth (mbsf)	Tool No.	Comment
F	1	50?	001	Mechanical success; oper. software error
F	2	85	001	Mechanical success; oper. software error
G	1	186	001	Successful deployment (two stress cells)
G	2	203	001	Piston corer did not fire
G	2A	203	002	Mechanical success; no data recovered after penetration
G	3	212	001	Successful deployment (two stress cells)
G	4	213	002	Successful deployment

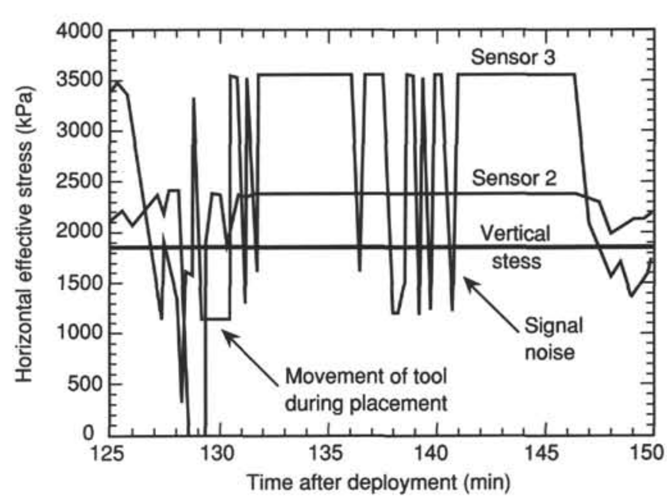

Figure 152. Lateral effective stress vs. time after LAST-I deployment 1 in Hole 808G. Small movements of the tool after placement resulted in large sensor fluctuations.

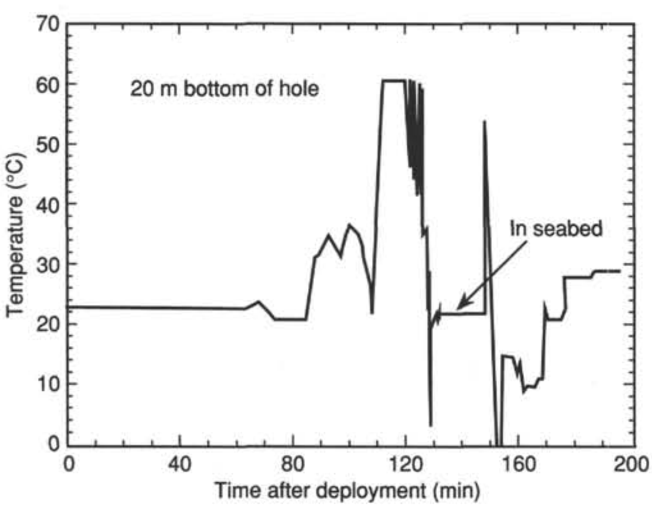

Figure 153. Temperature vs. time for LAST-I deployment 1 in Hole 808G.

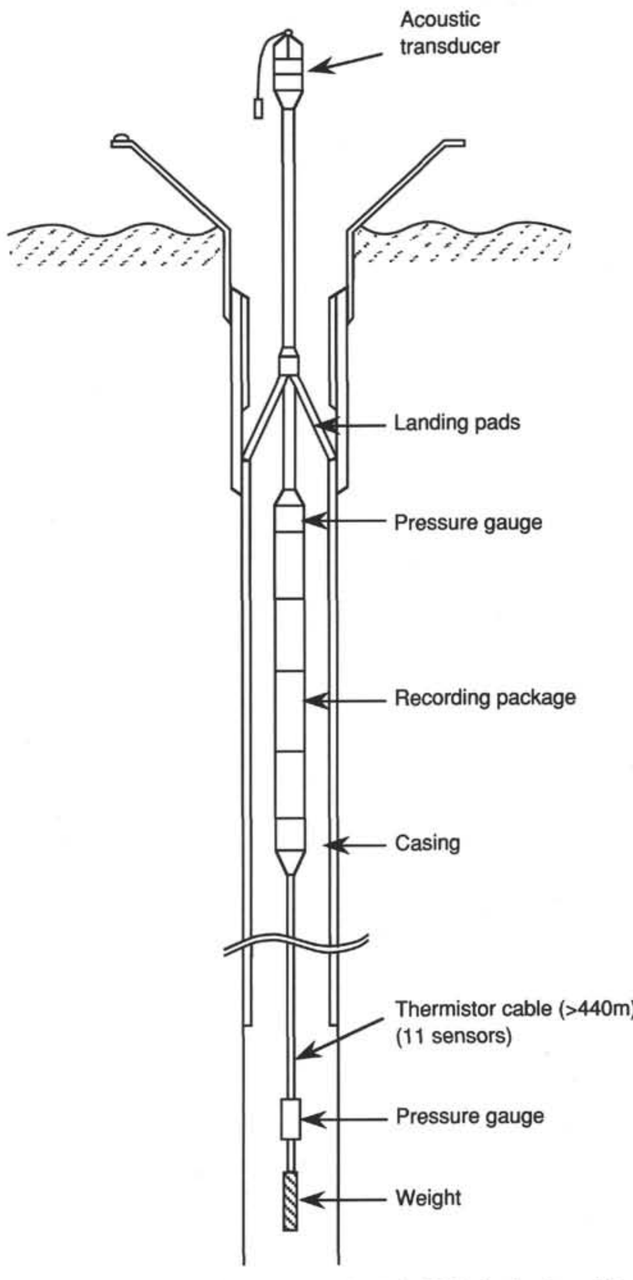

Figure 154. The ONDO system set in Hole 808E during Leg 132.

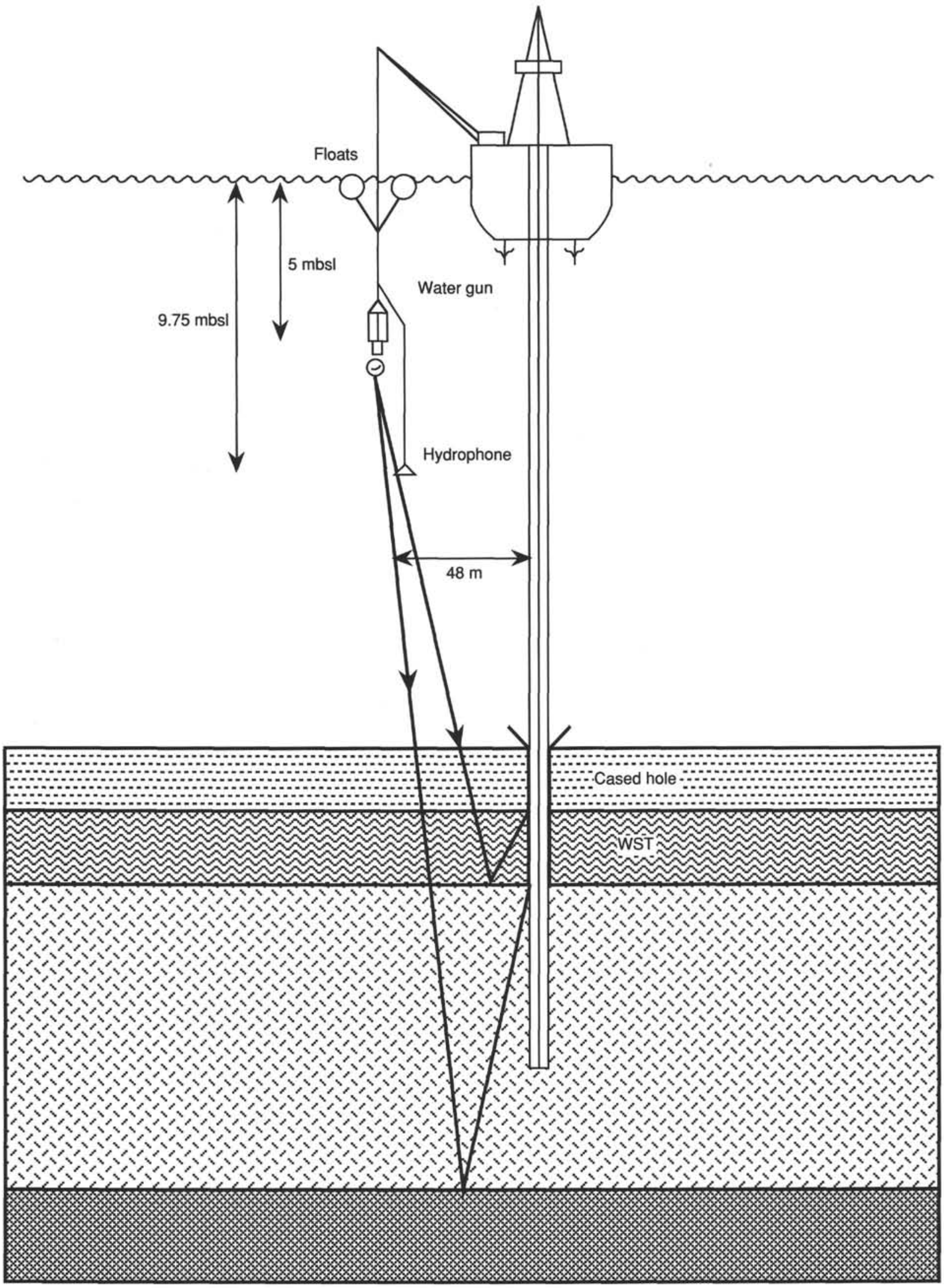

Figure 156. Configuration of vertical seismic profile (VSP) experiment at Hole 808E (from Ingle, Jr., Suyehiro, von Breymann, et al., 1990, p. 370). Downgoing and upgoing reflected waves are shown with dark lines. The location of the water gun and hydrophone in relationship to the ship and borehole are also shown.

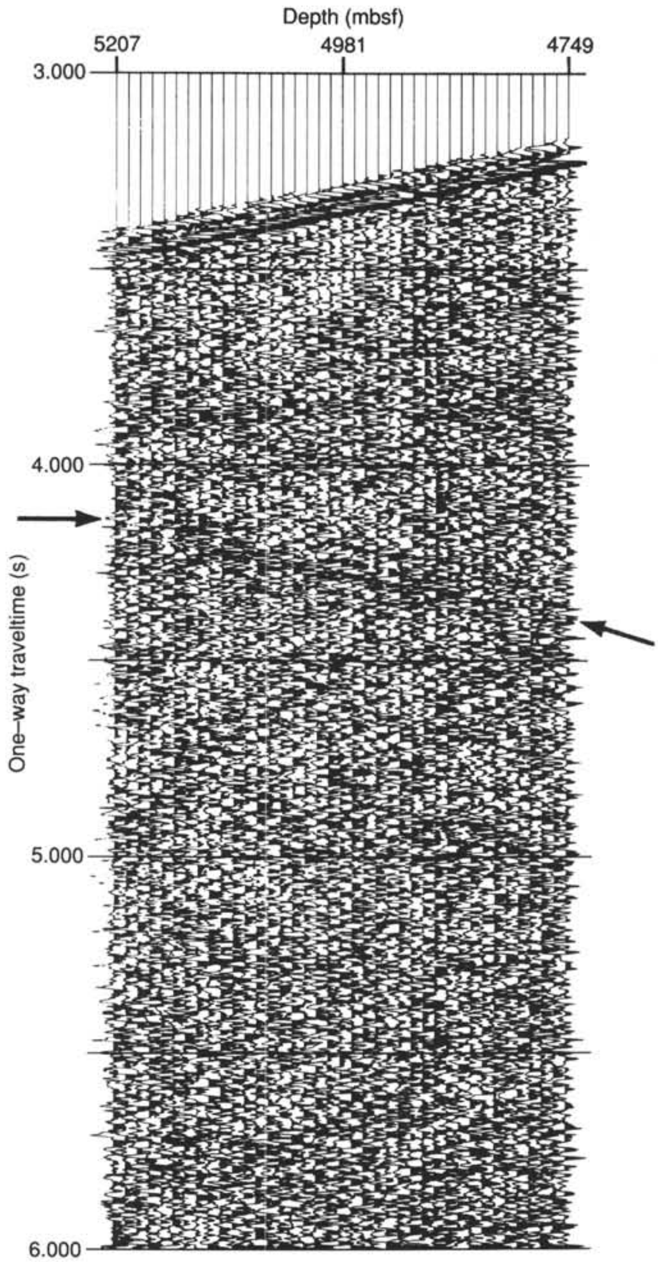

Figure 157. Preliminary plot of VSP collected in Hole 808E. Bold arrows indicate arrivals referred to in text.

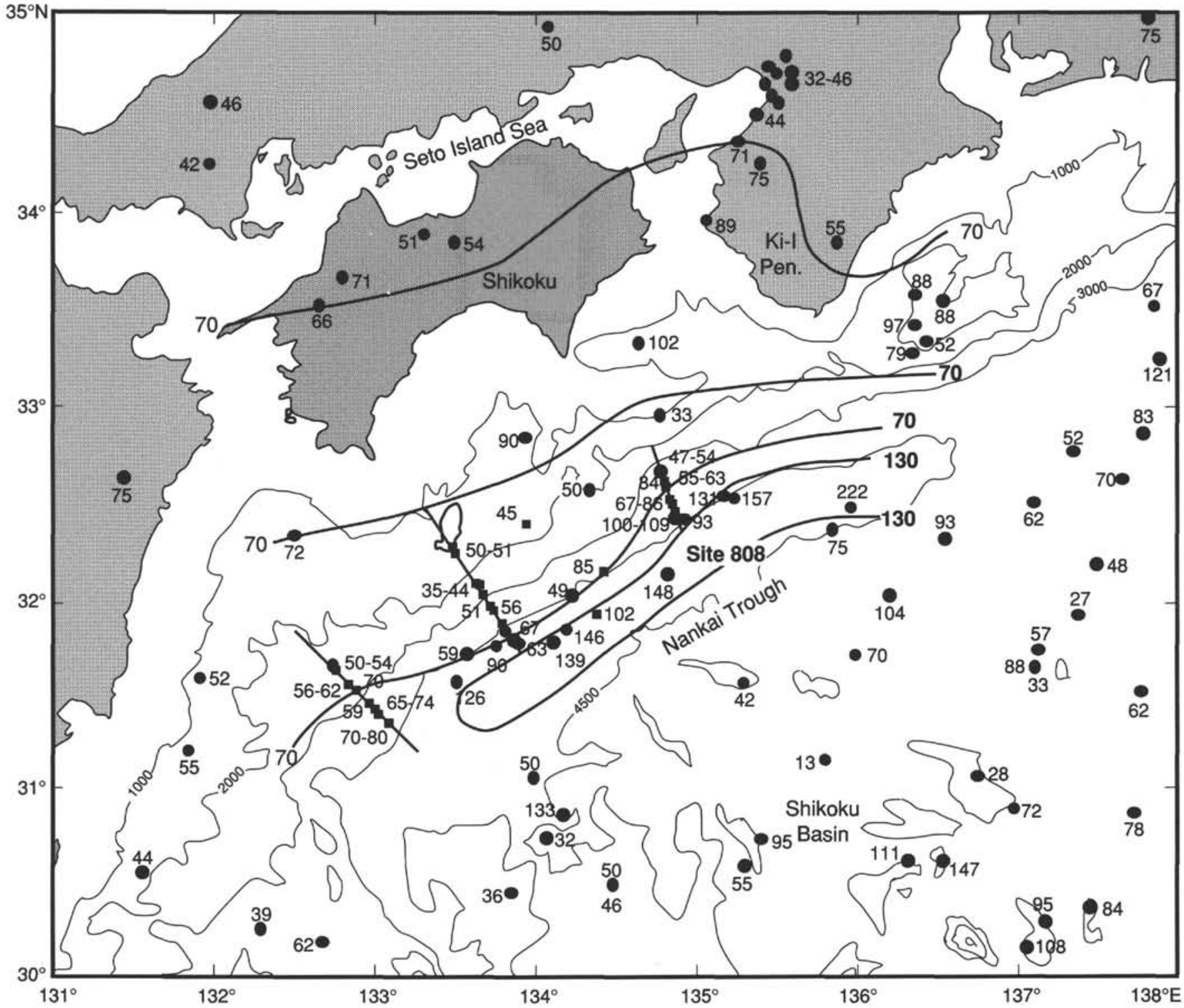

Figure 158. Heat-flow data distribution in the Shikoku basin, Nankai Trough, and on the Nankai prism (after Kinoshita and Yamano, 1986). Heat flow in mW/m^2. Data located by squares along the three seismic lines across the toe of the prism are estimates from BSR depths.

Table 29. Sediment Temperature Summary, Site 808.

Hole	Core	Depth (mbsf)	Temperature (°C)	Recorder*
808F	3M	91.1	12.1 ± 0.2	2
808B	9X	198.5	25.6 ± 0.1	1
808B	11X	217.4	28.7 ± 0.1	2
808B	15X	255.3	30.2 ± 0.1	1
808B	20X	298.6	31.4 ± 0.2	1
808B	26X	346.7	39.7 ± 0.2	1

*1 = Old (Uyeda) electronics, 2 = New electronics

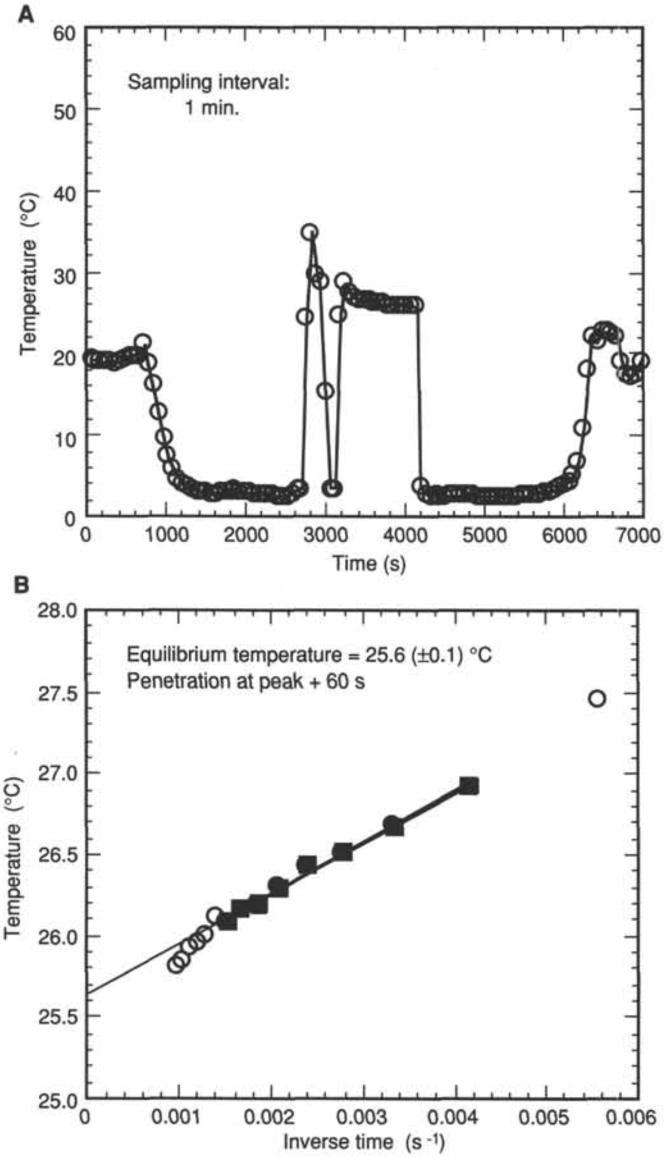

Figure 159. Records from WSTP deployment in Hole 808B at 198.5 mbsf. **A.** Temperature vs. time for entire run. **B.** Temperature vs. 1/time for penetration and extrapolated equilibrium temperature. Data points shown by filled squares were used for extrapolation.

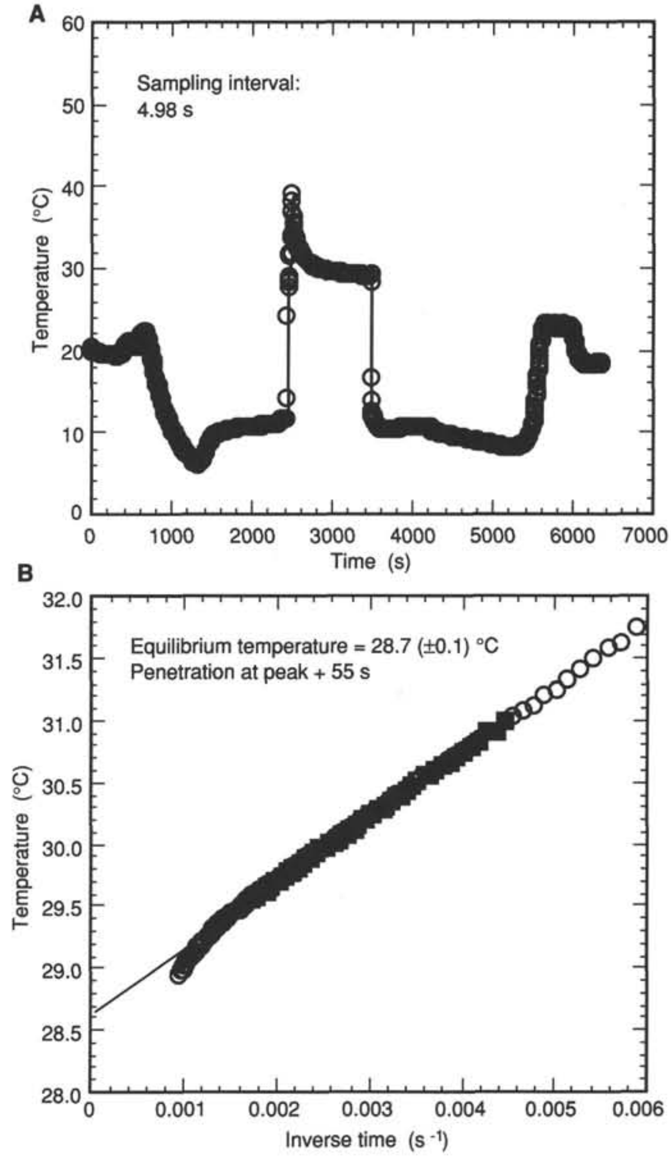

Figure 160. Records from WSTP deployment in Hole 808B at 217.4 mbsf. **A.** Temperature vs. time for entire run. **B.** Temperature vs. 1/time for penetration and extrapolated equilibrium temperature. Data points shown by filled squares were used for extrapolation.

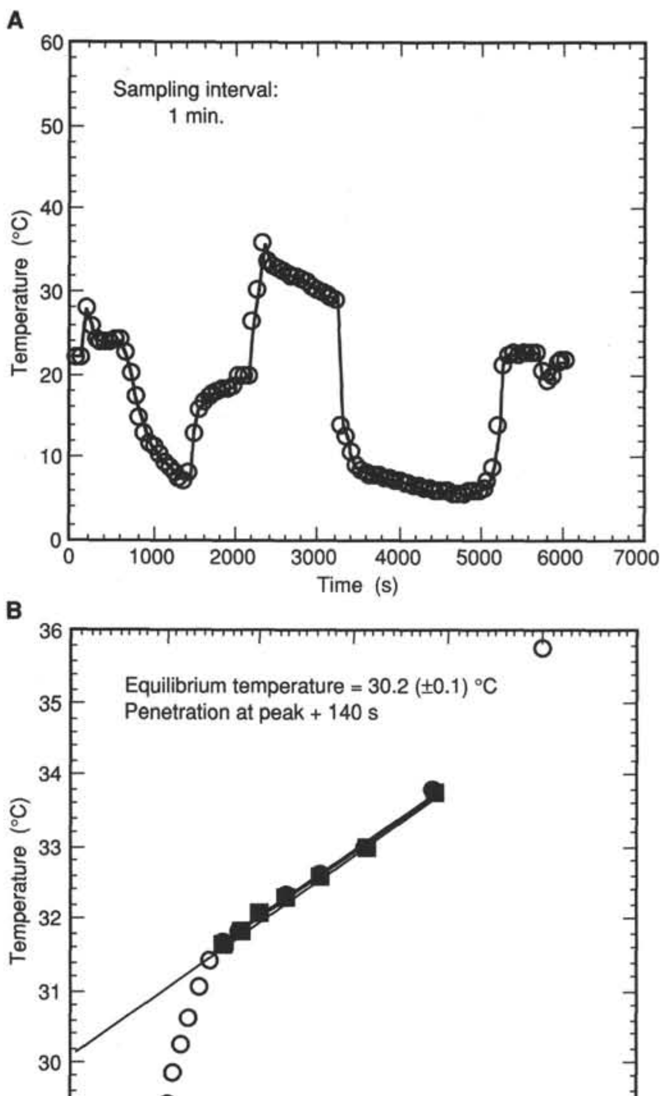

Figure 161. Records from WSTP deployment in Hole 808B at 255.3 mbsf. **A**. Temperature vs. time for entire run. **B**. Temperature vs. 1/time for penetration and extrapolated equilibrium temperature. Data points shown by filled squares were used for extrapolation.

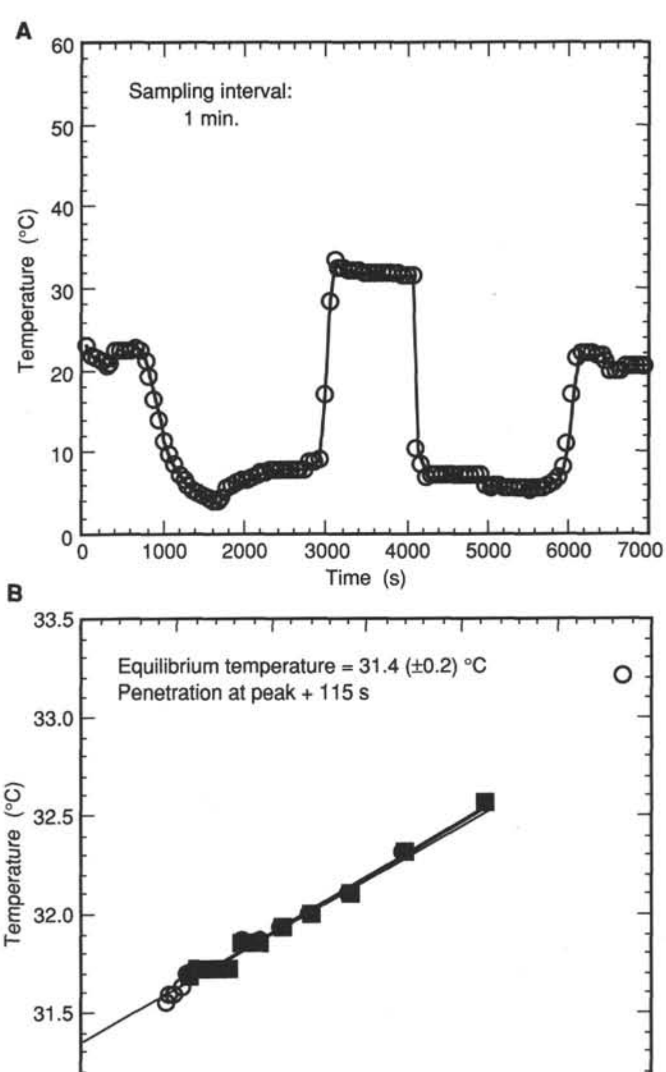

Figure 162. Records from WSTP deployment in Hole 808B at 298.6 mbsf. **A**. Temperature vs. time for entire run. **B**. Temperature vs. 1/time for penetration and extrapolated equilibrium temperature. Data points shown by filled squares were used for extrapolation.

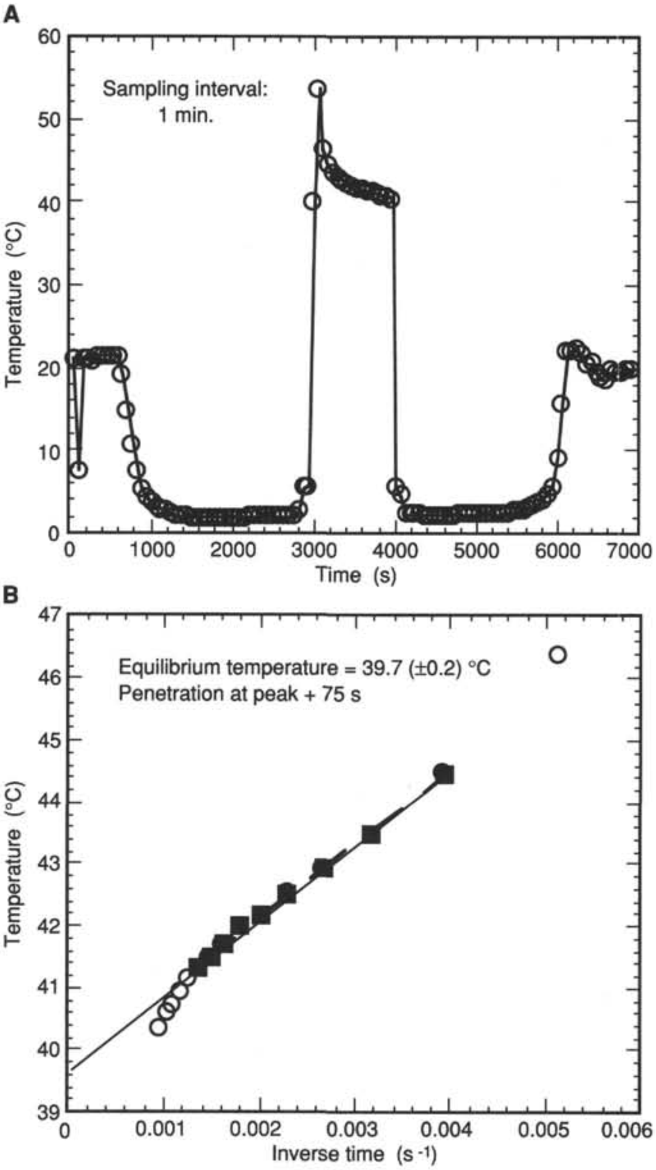

Figure 163. Records from WSTP deployment in Hole 808B at 346.7 mbsf. **A**. Temperature vs. time for entire run. **B**. Temperature vs 1/time for penetration and extrapolated equilibrium temperature. Data points shown by filled squares were used for extrapolation.

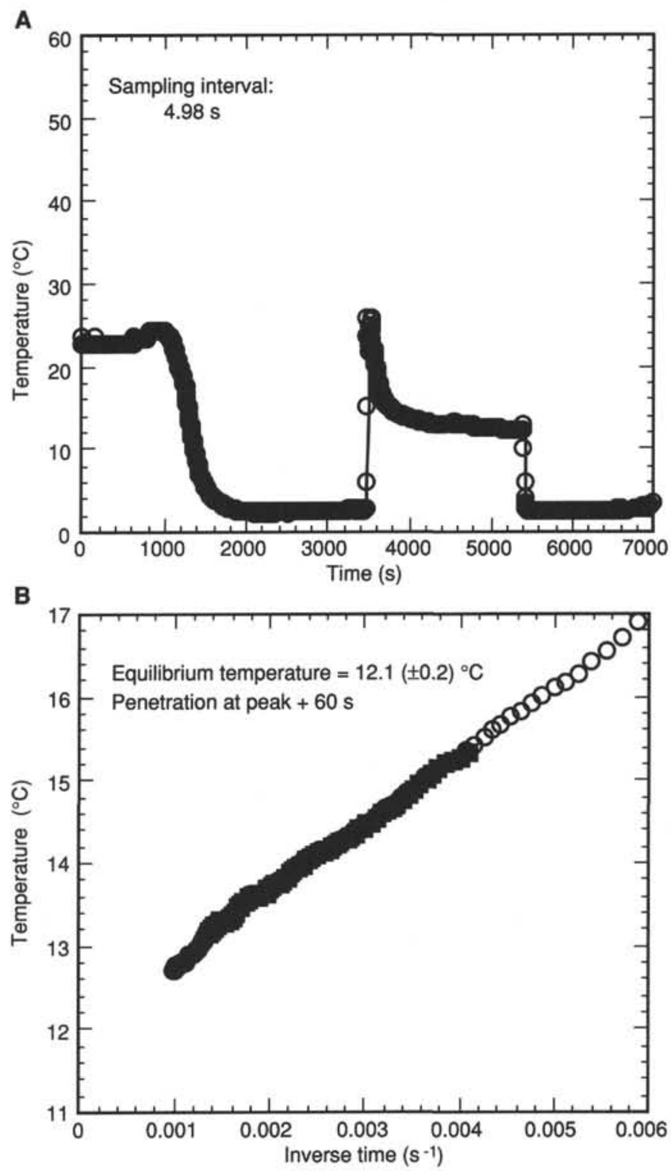

Figure 164. Records from WSTP deployment in Hole 808F at 91.1 mbsf. **A**. Temperature vs. time for entire run. **B**. Temperature vs. 1/time for penetration and extrapolated equilibrium temperature. Data points shown by filled squares were used for extrapolation.

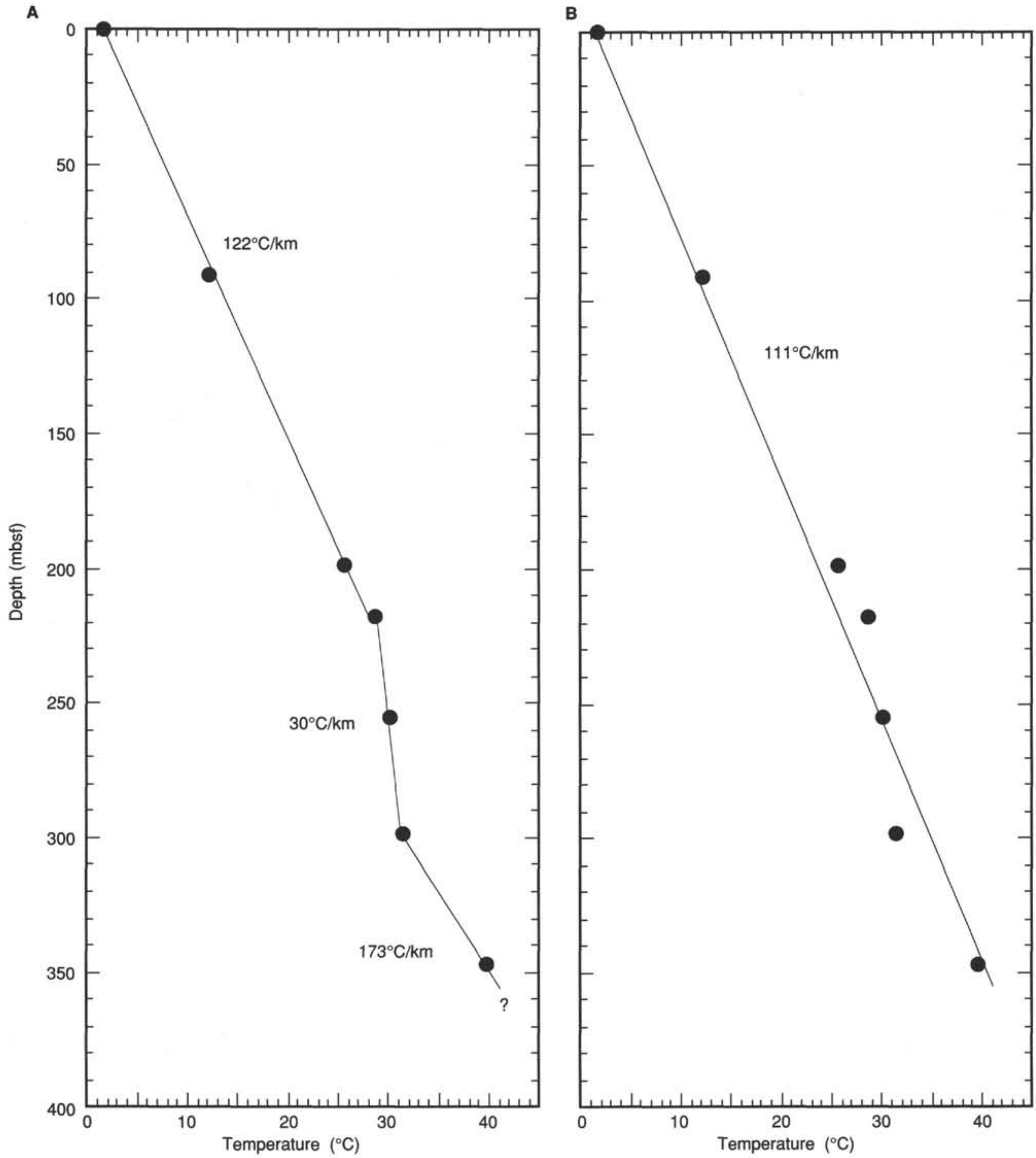

Figure 165. Thermal gradients at Site 808. **A**. Gradients over individual intervals. **B**. Overall gradient using all data. All gradients that include the bottom-water temperature were forced to pass through this point.

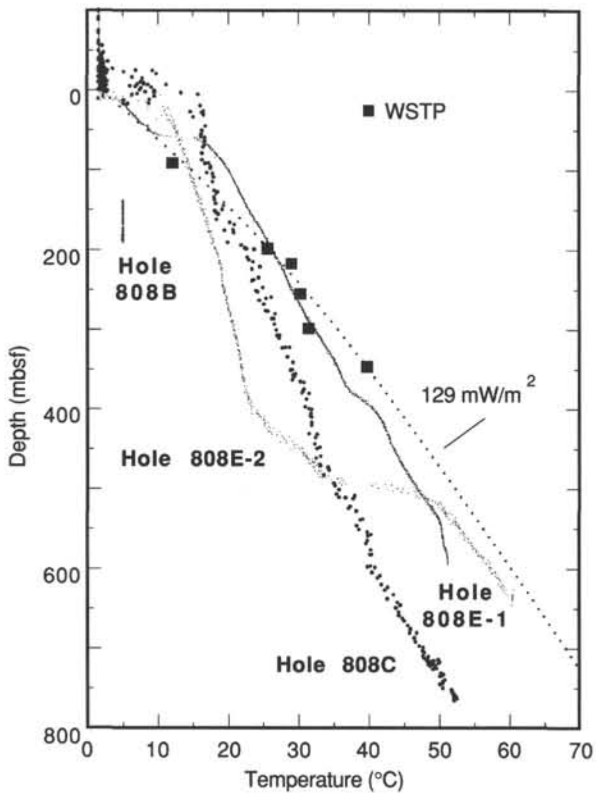

Figure 166. Summary of TLT data from Holes 808B, 808C, and 808E. All WSTP data are shown for reference. Also shown is the temperature profile for a constant conductive heat flow of 129 mW/m^2 (see discussion of heat-flow estimates and thermal structure).

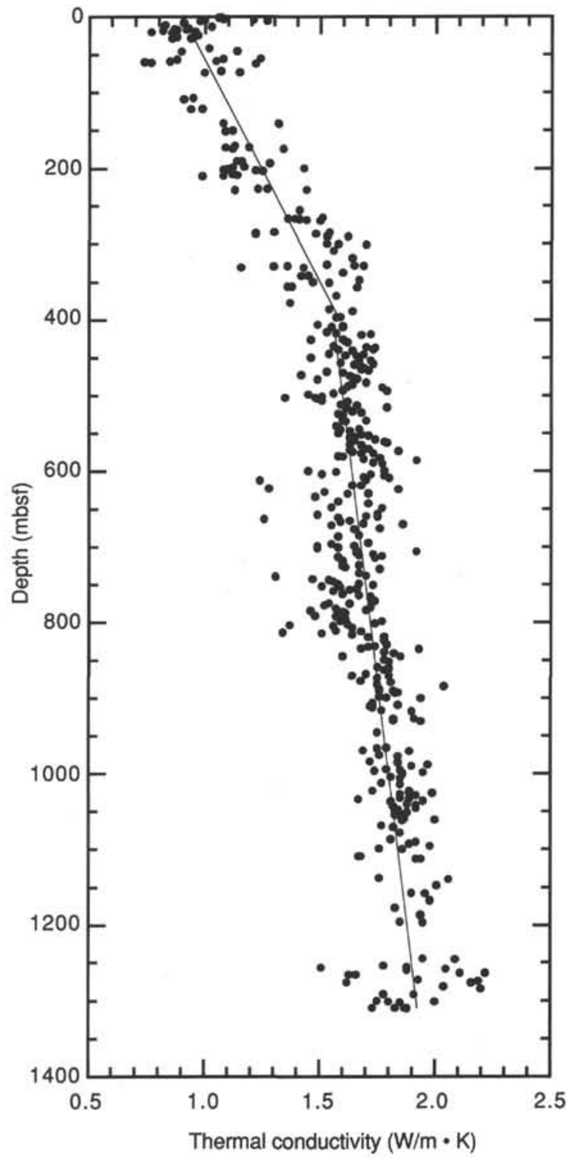

Figure 167. Thermal conductivity vs. depth at Site 808 (Holes 808A, 808B, 808C; Physical Properties section, this chapter). Linear approximations shown by line segments.

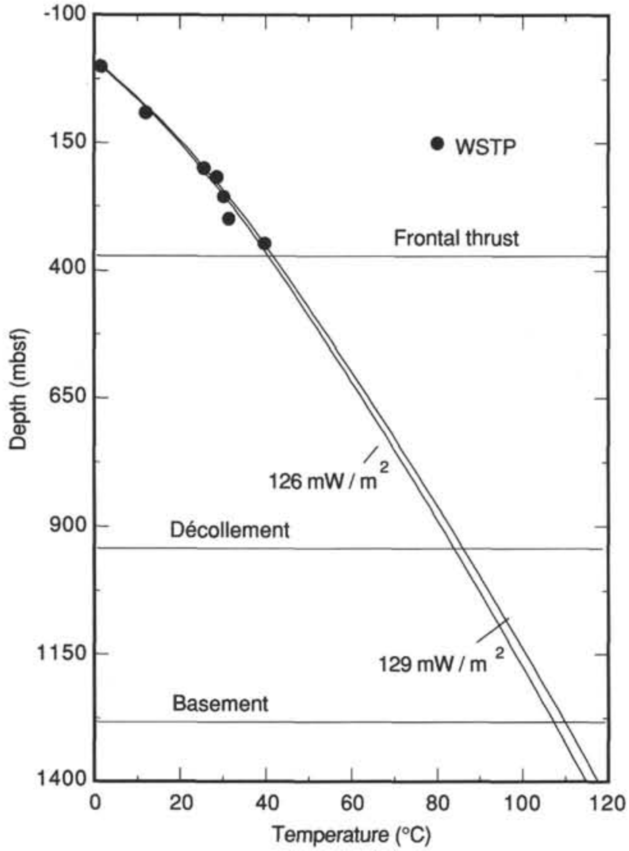

Figure 168. Site 808 temperature profiles calculated for constant conductive heat flows of 126 and 129 mW/m^2. WSTP data shown for reference.

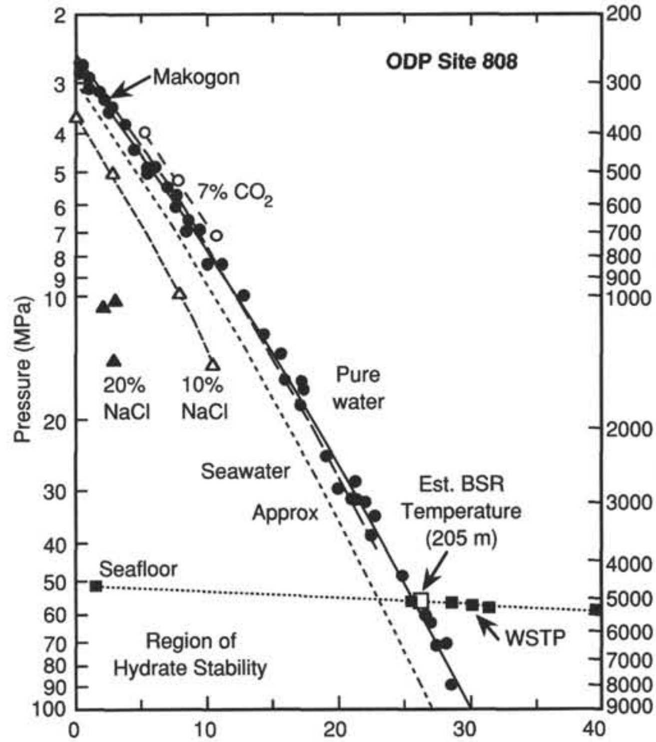

Figure 169. A summary of pressure-temperature stability fields for hydrates determined in the laboratory (Hyndman et al., in press). WSTP data from Site 808 are shown for reference. The estimated depth of the BSR is 205 mbsf.

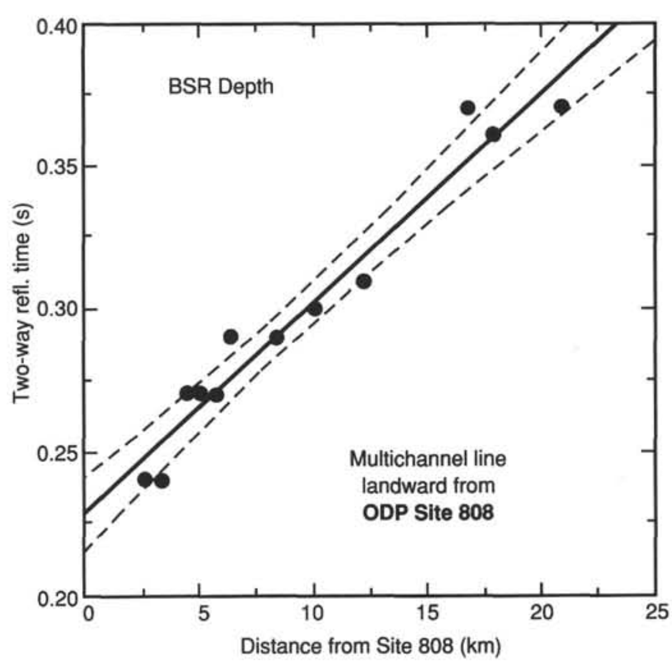

Figure 170. Depth below seafloor (seismic reflection two-way travel-time) to the gas hydrate bottom-simulating reflector (BSR) as a function of distance landward from Site 808. The linear regression and 95% confidence limits are shown.

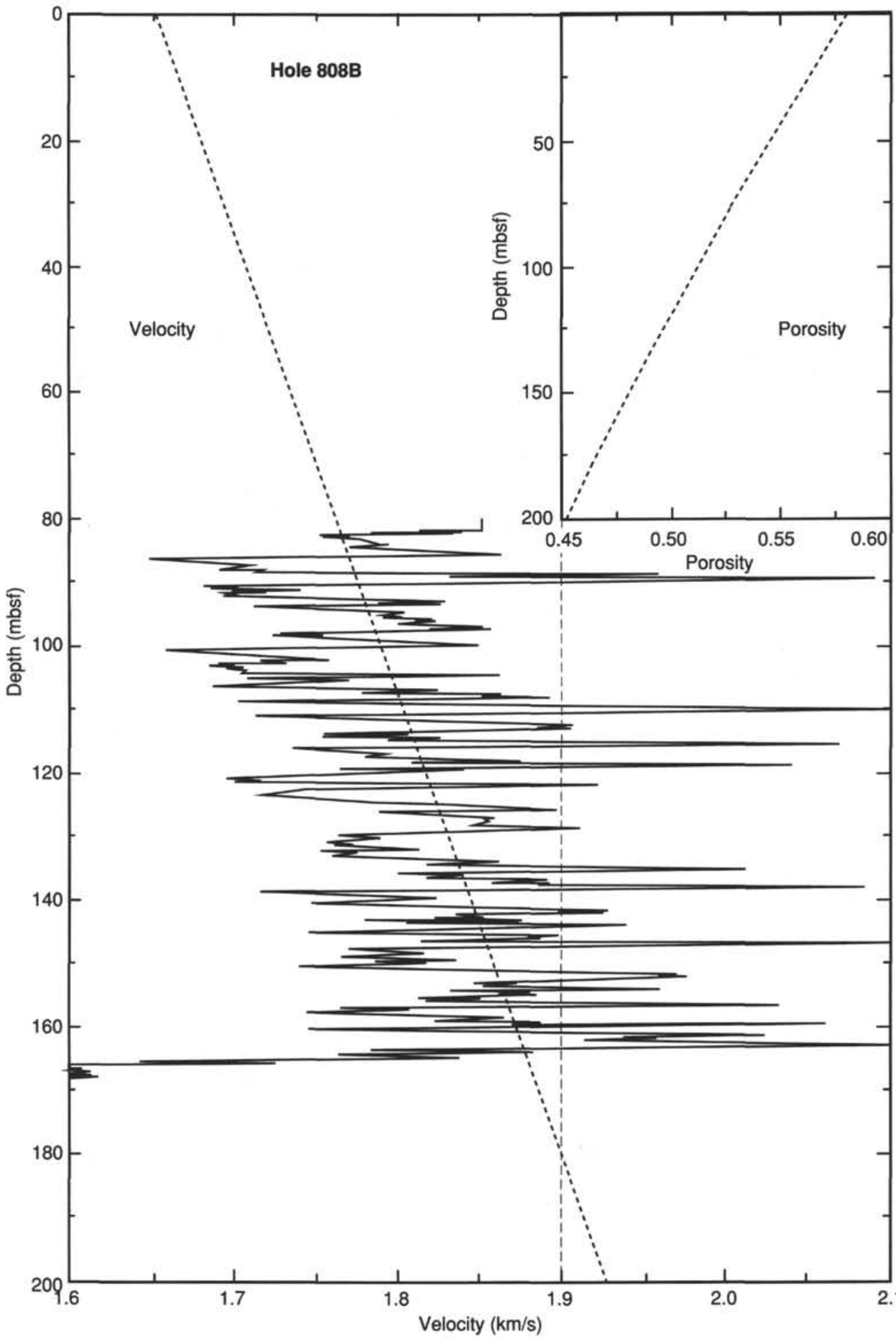

Figure 171. Downhole log velocity-depth data above the BSR at Site 808. The data were extrapolated over the depth intervals with no log data using the exponential porosity-depth function shown and the porosity-velocity relation of Hamilton (1978).

Table 30. List of depths (mbsf), thrust-corrected depths (mbsf), and ages of calcareous nannofossil and paleomagnetic reversal datums, sedimentation rates, dry-bulk densities (* of clay units only), and mass accumulation rates (MAR) for Site 808.

Depth		Depth		Base age		Sed. rate	Dry bulk	MAR
mbsf (top)	mbsf (bot)	Thrust (top)	Thrust (bot)	(ma)	Datum	(m/m.y.)	(g/cm^3)	(mg/m^2·m.y.)
0.00	81.17	0.00	81.17	0.09	Nanno	901.89	1.08	974.04
81.17	230.66	81.17	230.66	0.28	Nanno	786.79	1.44	1132.98
230.66	624.27	230.66	479.27	0.46	Nanno	1381.17	1.49	2057.94
624.27	657.50	479.27	512.50	0.73	Pmag	123.07	1.58	194.46
657.50	683.50	512.50	538.50	0.91	Pmag	144.44	1.68	242.67
683.50	698.50	538.50	553.50	0.98	Pmag	214.29	1.62	347.14
698.50	745.00	553.50	600.00	1.36	Nanno	122.37	1.61	197.01
745.00	756.00	600.00	611.00	1.45	Nanno	122.22	1.65	201.67
756.00	770.00	611.00	625.00	1.57	Nanno	116.67	1.72	200.67
770.00	777.00	625.00	632.00	1.66	Nanno	77.78	1.73	134.56
777.00	798.50	632.00	653.50	1.88	Pmag	97.73	1.66	162.23
798.50	804.50	653.50	659.50	2.47	Pmag	10.17	1.64	16.68
804.50	823.00	659.50	678.00	2.92	Pmag	41.11	1.70	69.89
823.00	828.00	678.00	683.00	2.99	Pmag	71.43	1.79	127.86
828.00	835.50	683.00	690.50	3.08	Pmag	83.33	1.85	154.17
835.50	844.00	690.50	699.00	3.18	Pmag	85.00	1.84	156.40
844.00	866.50	699.00	721.50	3.40	Pmag	102.27	1.86	190.23
866.50	893.00	721.50	748.00	3.88	Pmag	55.21	1.89	104.34
893.00	931.50	748.00	786.50	4.77	Pmag	43.26	1.87	80.89
931.50	964.50	786.50	819.50	5.35	Pmag	56.90	2.03	115.50
964.50	969.60	819.50	824.50	5.53	Pmag	27.78	1.96	54.44
969.50	980.00	824.50	835.00	5.68	Pmag	70.00	1.77	123.90
980.00	997.50	835.00	852.50	6.50	Pmag	21.34	1.78	37.99
997.50	1010.50	852.50	865.50	6.70	Pmag	65.00	1.80	117.00
1010.50	1024.50	865.50	879.50	7.41	Pmag	19.72	1.83	36.08
1024.50	1029.50	879.50	884.50	7.90	Pmag	10.20	1.83	18.67
1029.50	1031.50	884.50	886.50	8.21	Pmag	6.45	1.81	11.68
1031.50	1046.50	886.50	901.50	8.92	Pmag	21.13	1.83	38.66
1046.50	1072.50	901.50	927.50	10.42	Pmag	17.33	1.82	31.55
1072.50	1092.00	927.50	947.00	11.10	Nanno	28.68	1.83	52.48
1092.00	1172.00	947.00	1027.00	12.20	Nanno	72.73	1.96	142.55
1172.00	1196.00	1027.00	1051.00	13.10	Nanno	26.67	2.08	55.47
1196.00	1219.00	1051.00	1074.00	13.60	Nanno	46.00	2.06	94.76

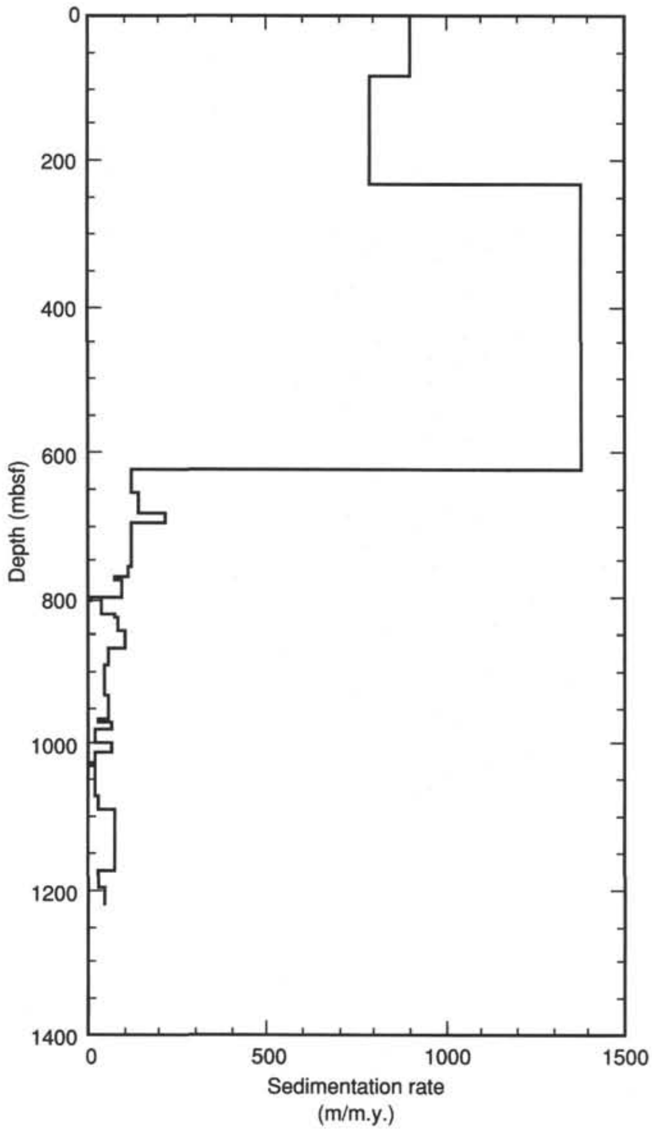

Figure 172. Sedimentation rates vs. depth for Site 808.

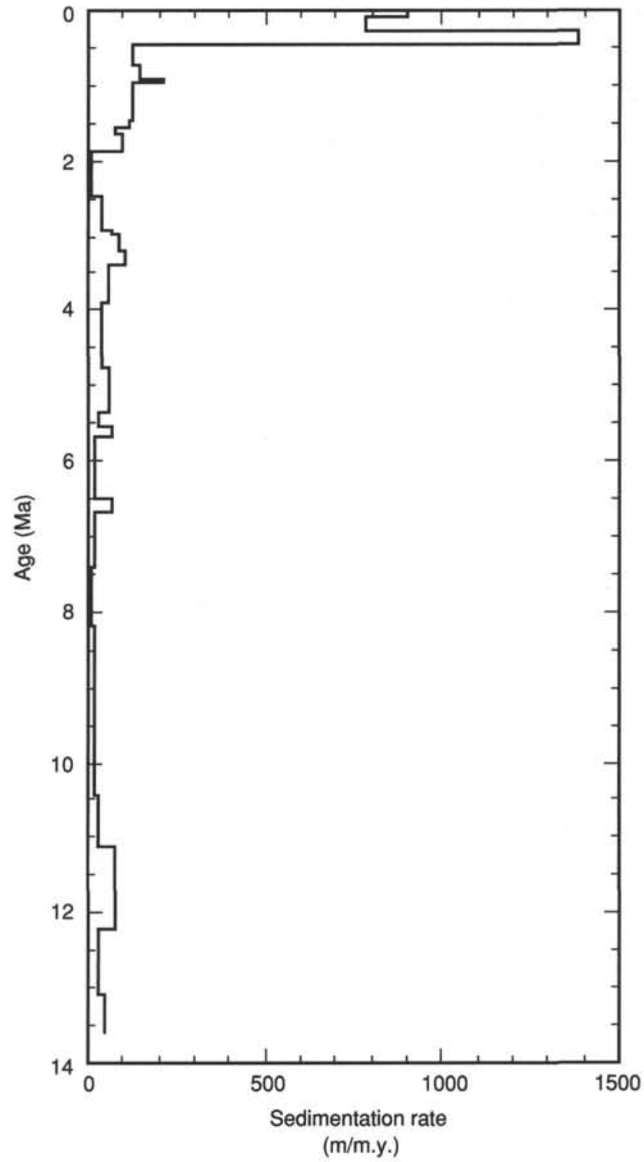

Figure 173. Sedimentation rates vs. age for Site 808.

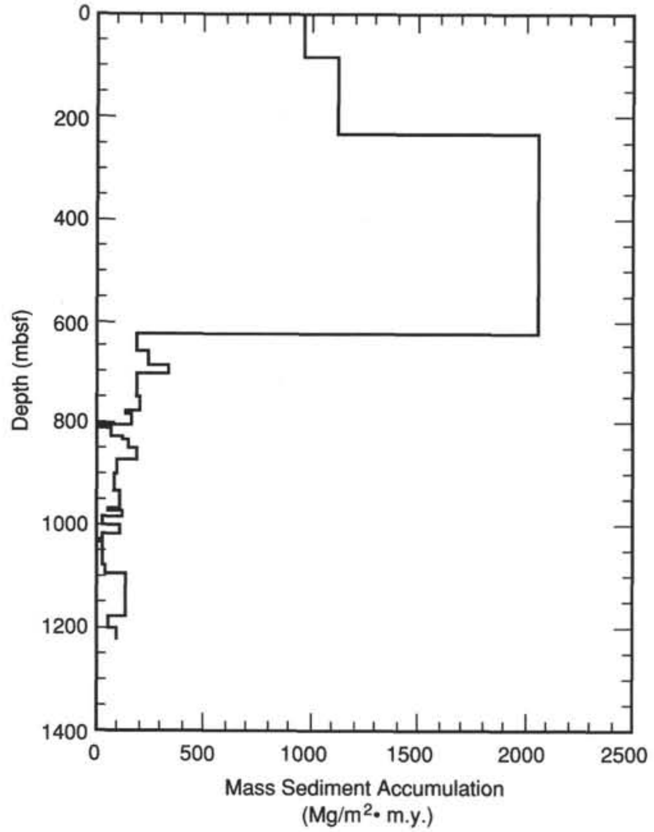

Figure 174. Sediment accumulation rates vs. depth for Site 808.

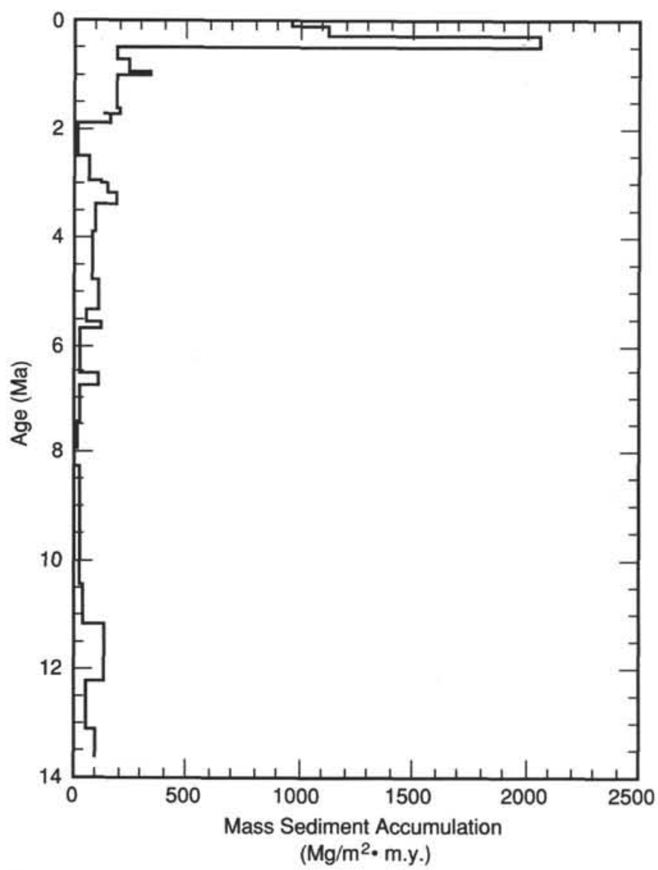

Figure 175. Sediment Accumulation rates vs. time for Site 808.

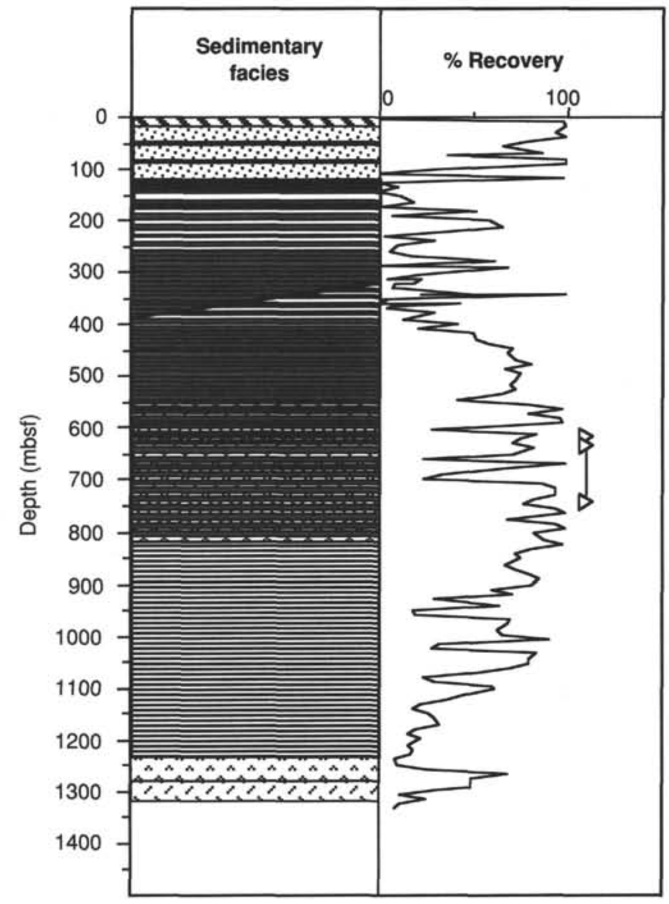

Figure 176. Plot of lithology and core recovery (composite core recovery of Holes 808A, 808B, and 808C). Triangles mark the location of the samples used in the CST test. The ash-bearing interval between 550 mbsf and 830 mbsf was found to have significant clay swelling capacity.

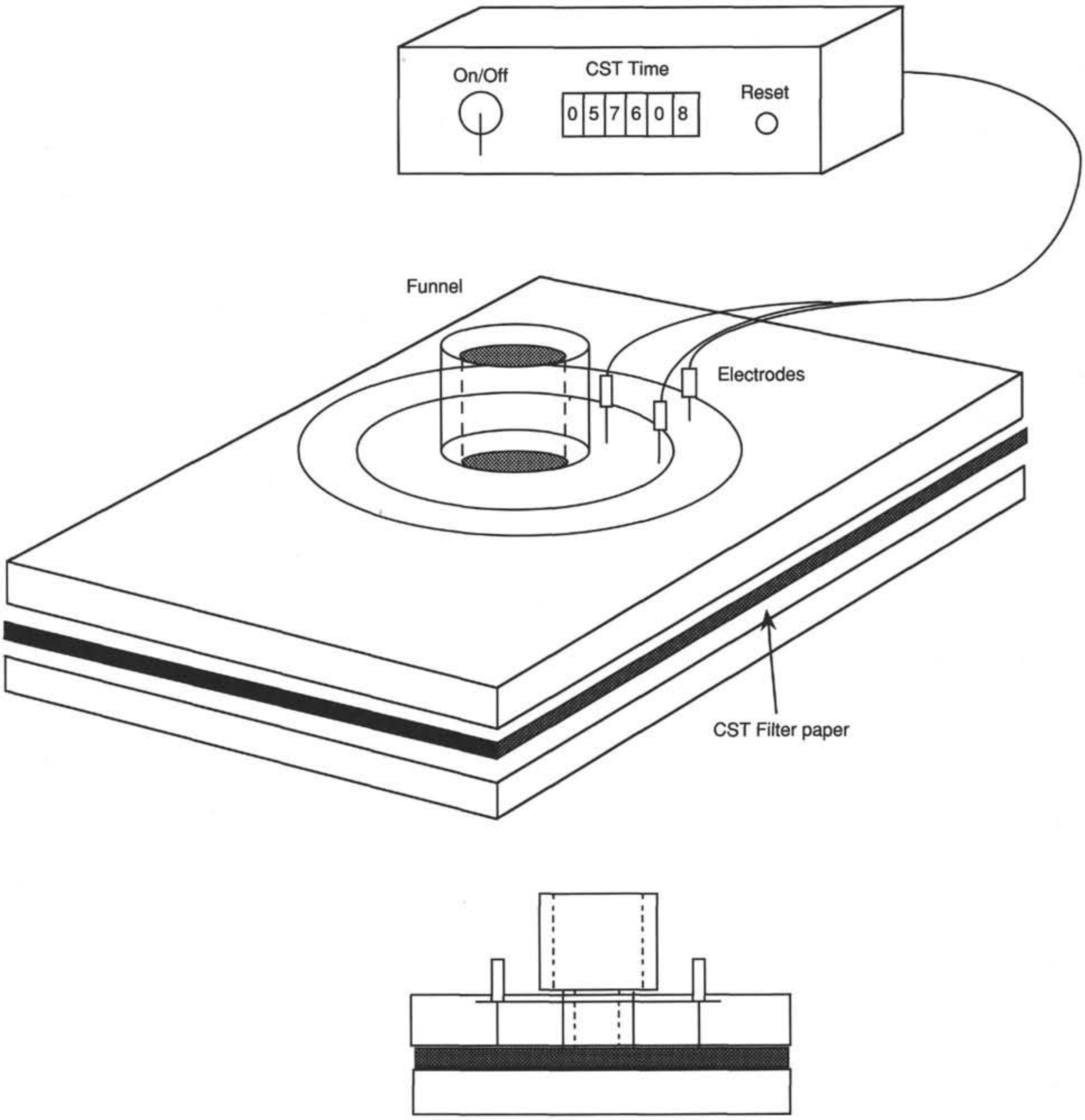

Figure 177. Diagram of capillary suction apparatus, including timer control box (top), test head (middle), and cross section of test head (bottom).

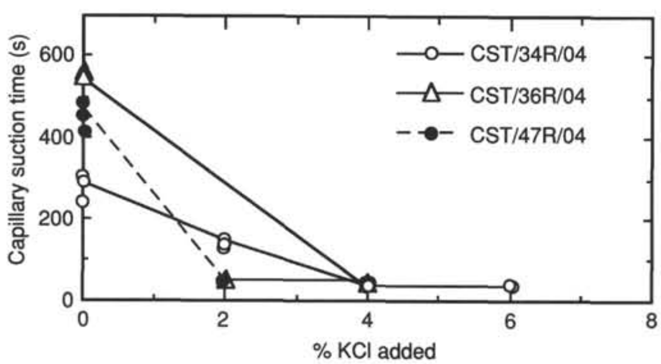

Figure 178. Results of capillary suction tests (CST) at Site 808. Three CST times are plotted for each of the three samples at each KCl concentration.

Table 31. Table listing sample number, percentage KCl in suspension, and capillary suction time for three samples from Hole 808C.

808C-34R-04, 128–130 cm
0% KCl: 237 s, 304 s, 290 s;
2% KCl: 150 s, 140 s, 148 s;
4% KCl: 40 s, 45 s, 41 s;
6% KCl: 41 s, 32 s, 35 s.

808C-36R-04, 124–126 cm
0% KCl: 576 s, 577 s, 550 s;
2% KCl: 55 s, 53 s, 50 s;
4% KCl: 52 s, 53 s, 50 s;

808C-47R-04, 011–013 cm
0% KCl: 412 s, 455 s, 474 s;
2% KCl: 50 s, 55 s, 51 s;
4% KCl: 48 s, 50 s, 52 s;

Hole 808B: Resistivity-Sonic-Gamma Ray Log Summary

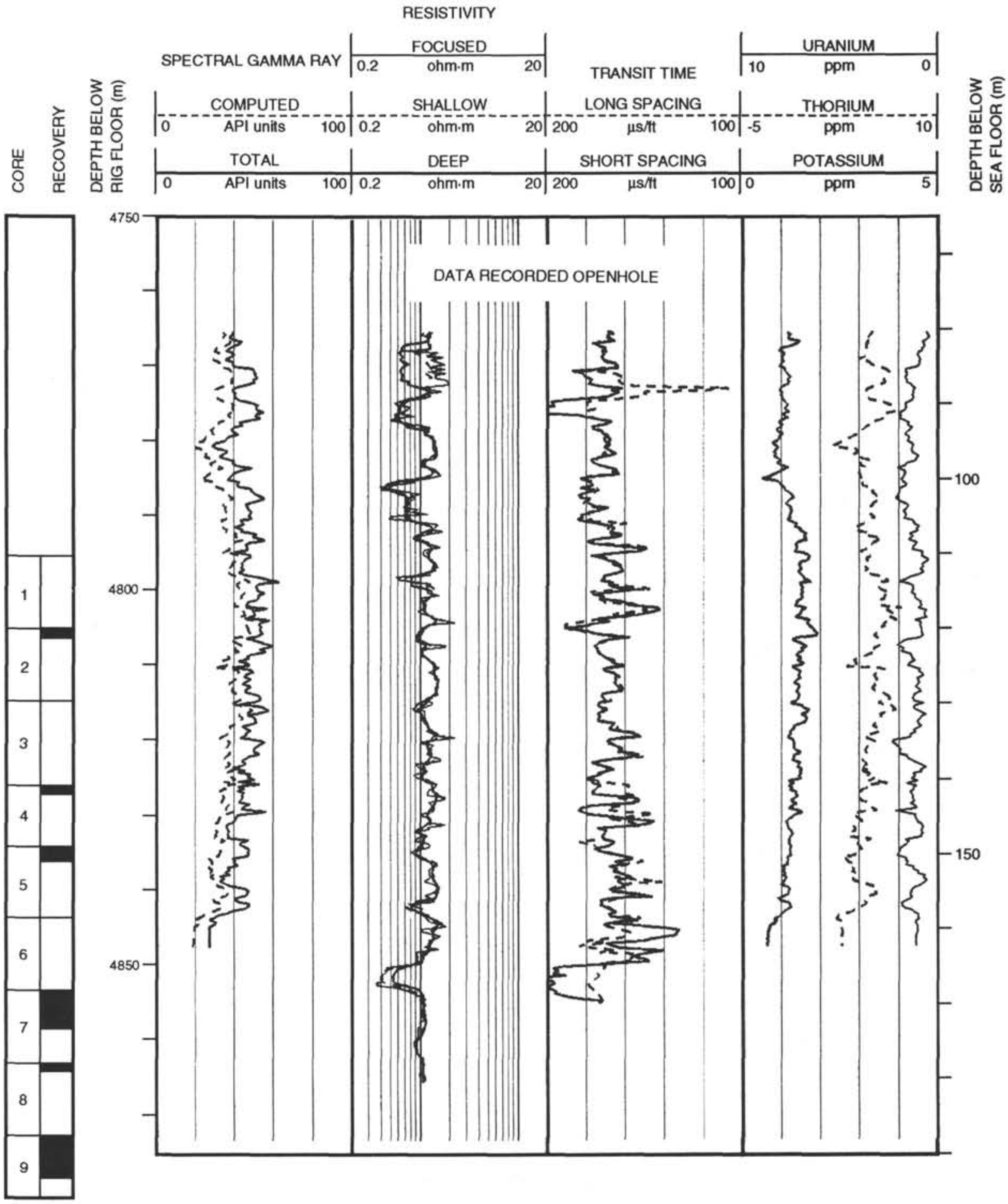

Hole 808C: Natural Gamma Ray Log Summary

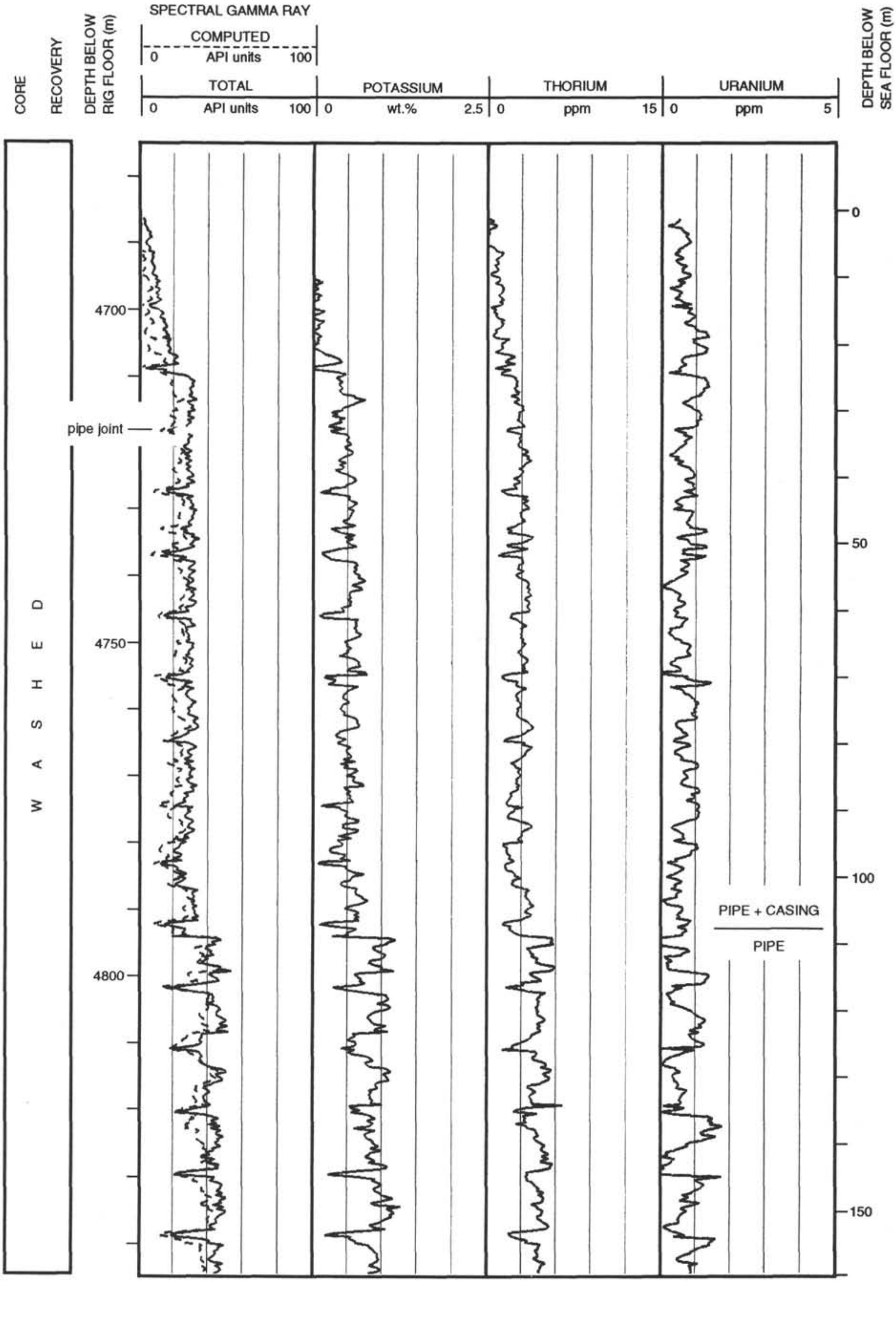

Hole 808C: Natural Gamma Ray Log Summary (continued)

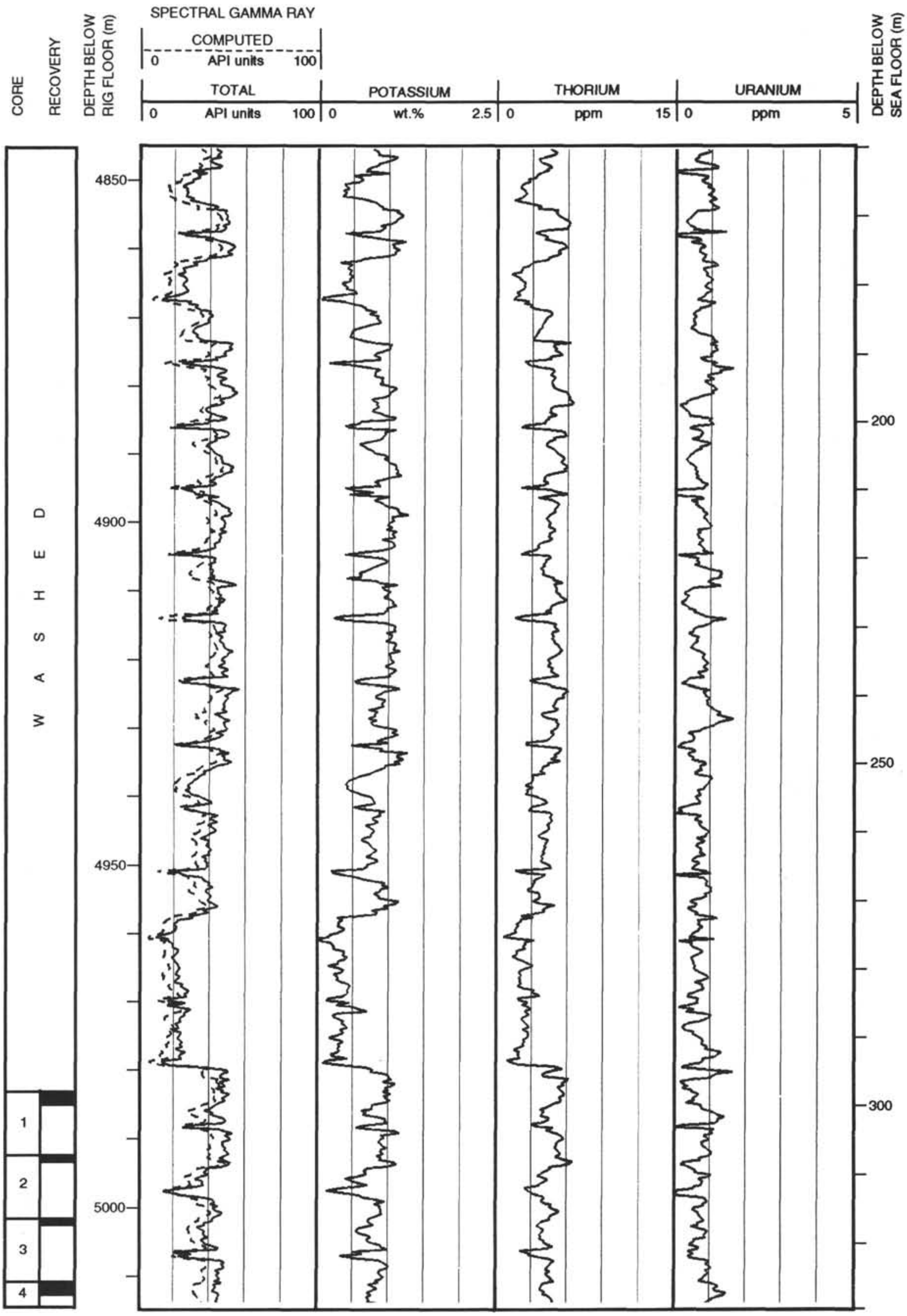

Hole 808C: Natural Gamma Ray Log Summary (continued)

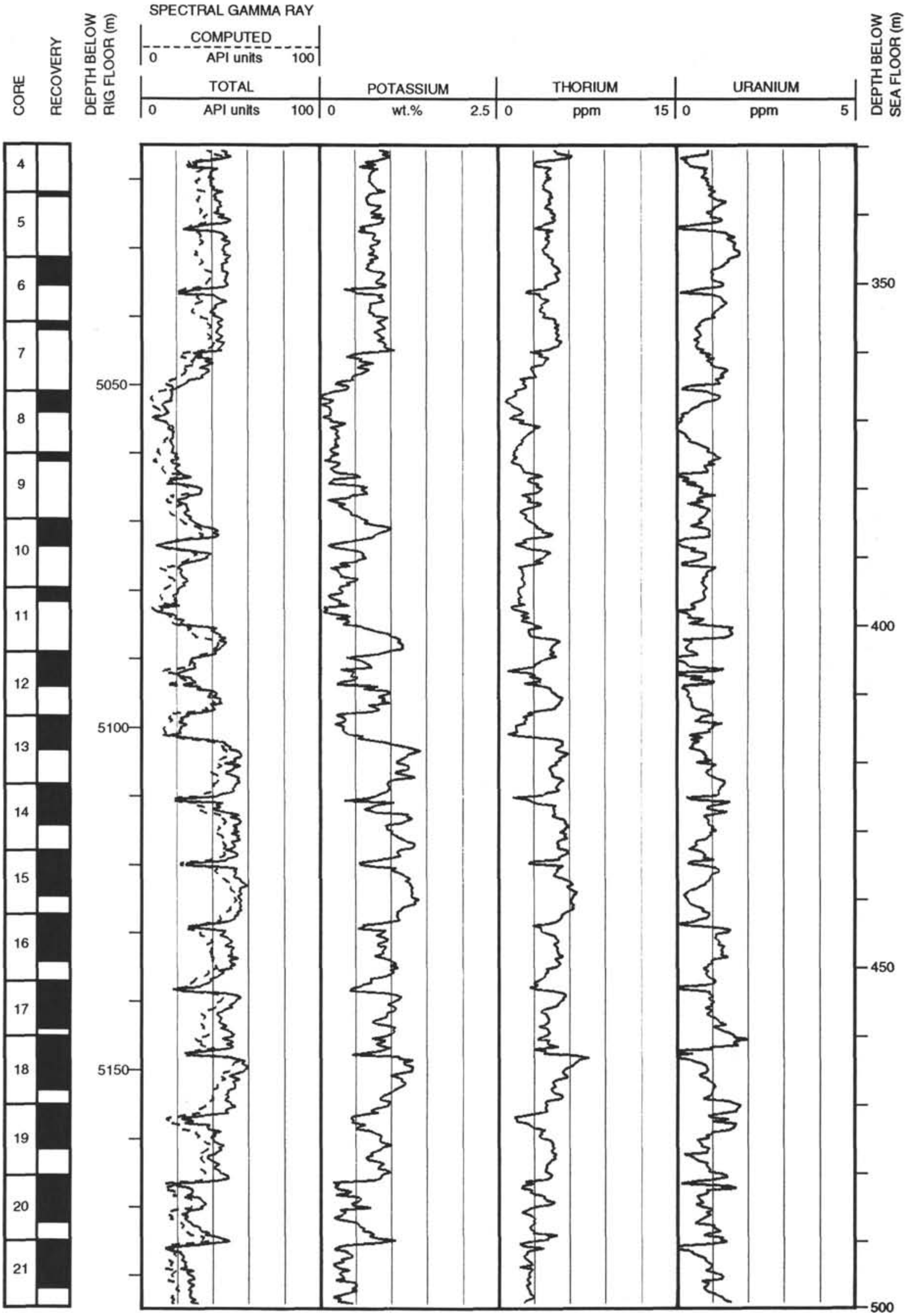

Hole 808C: Natural Gamma Ray Log Summary (continued)

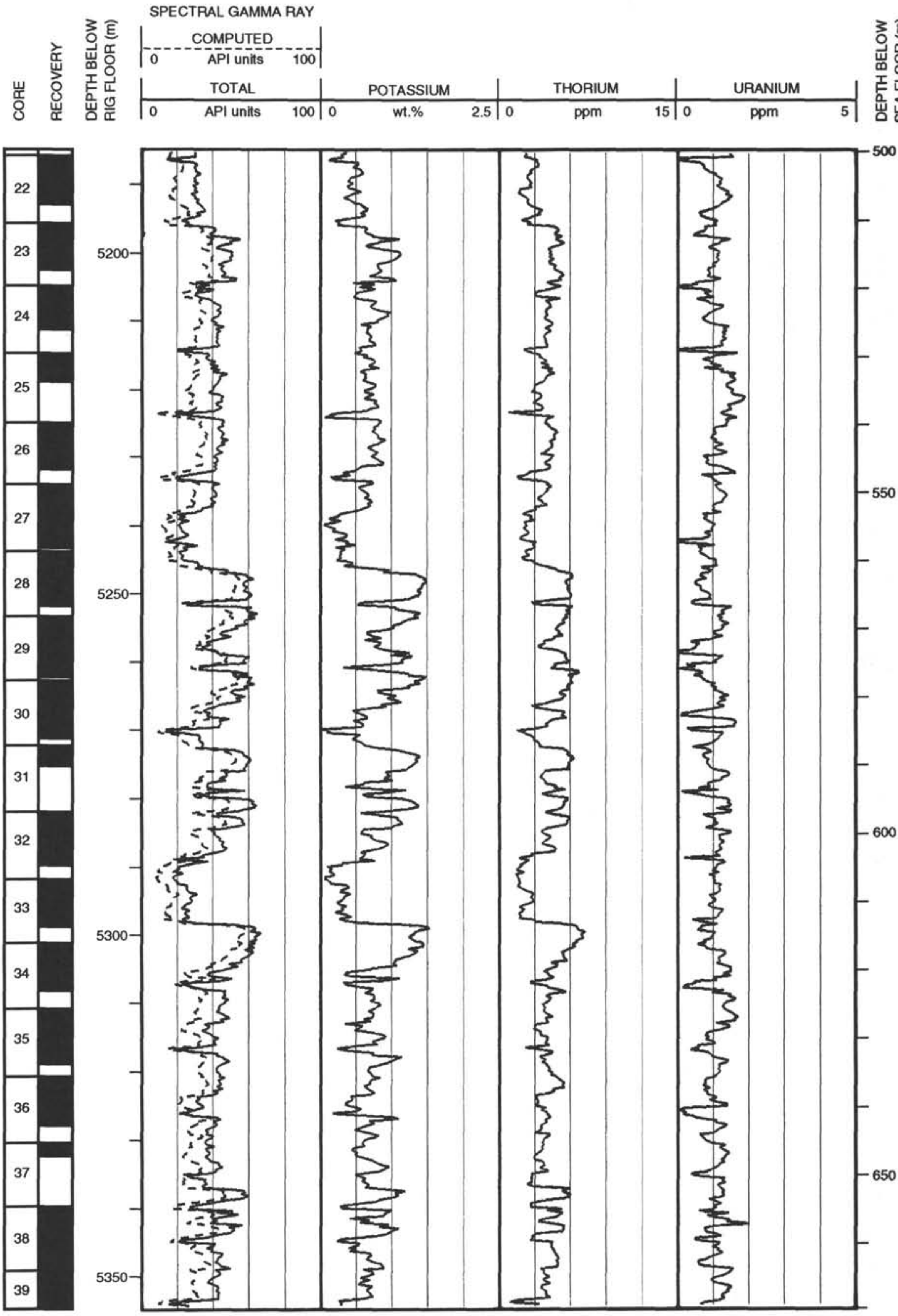

Hole 808C: Natural Gamma Ray Log Summary (continued)

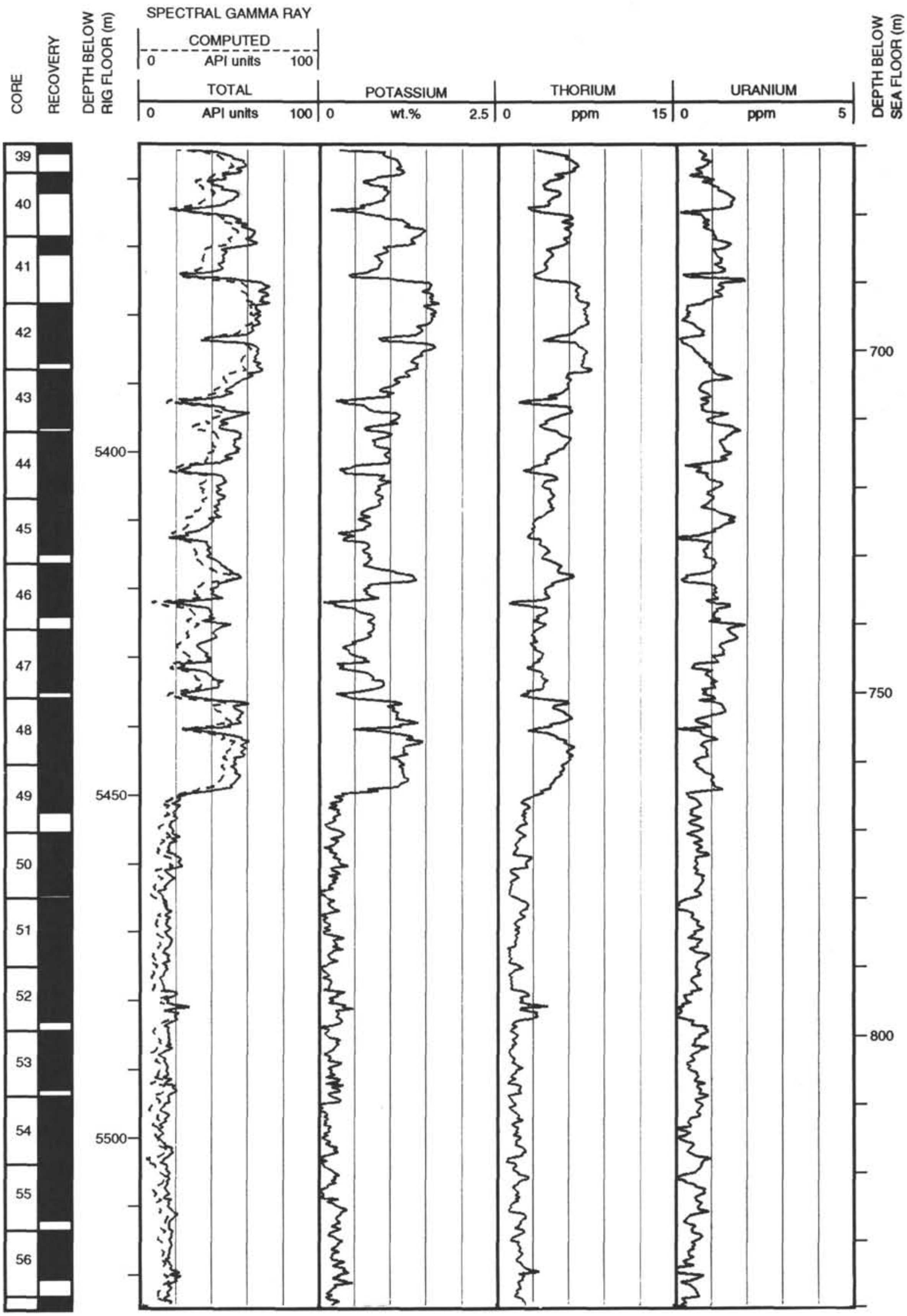

Hole 808C: Natural Gamma Ray Log Summary (continued)

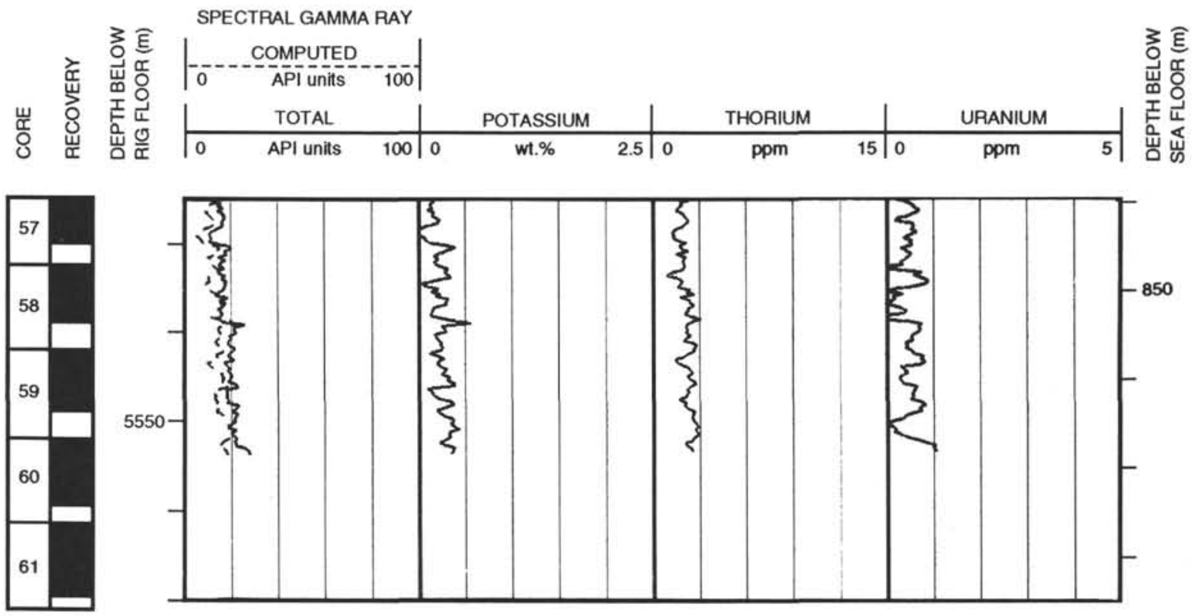

Hole 808C: Geochemical Log Summary

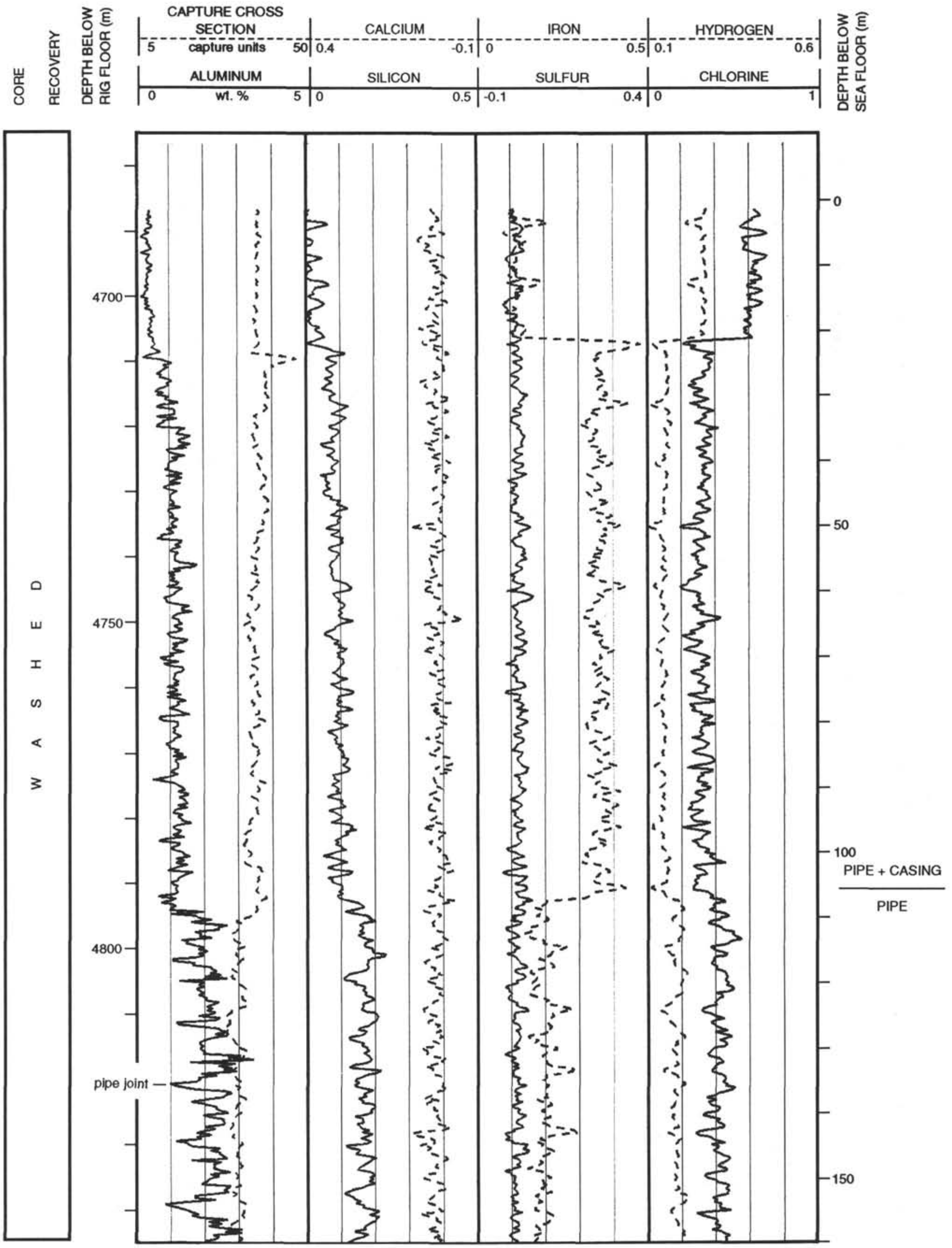

Hole 808C: Geochemical Log Summary (continued)

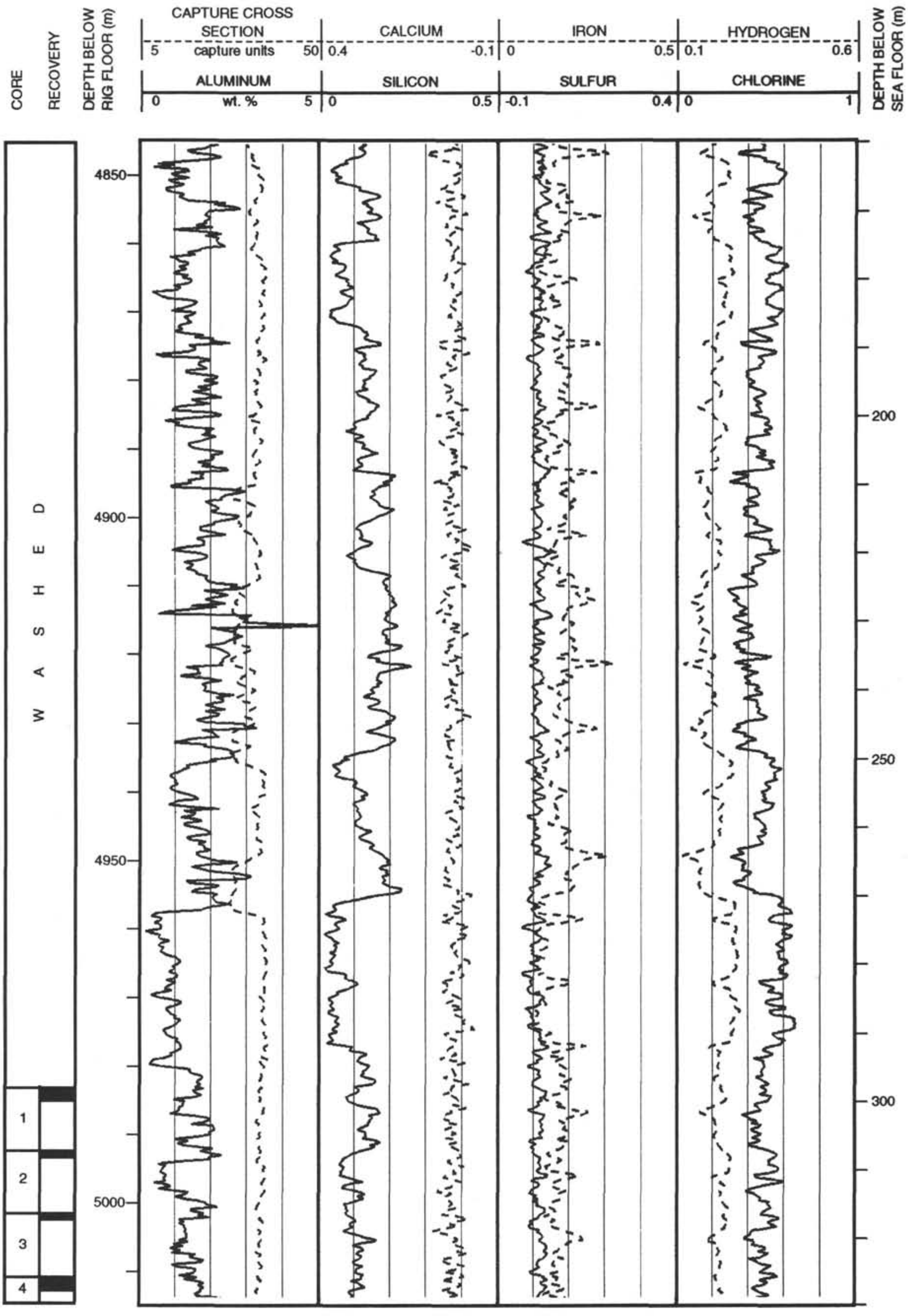

Hole 808C: Geochemical Log Summary

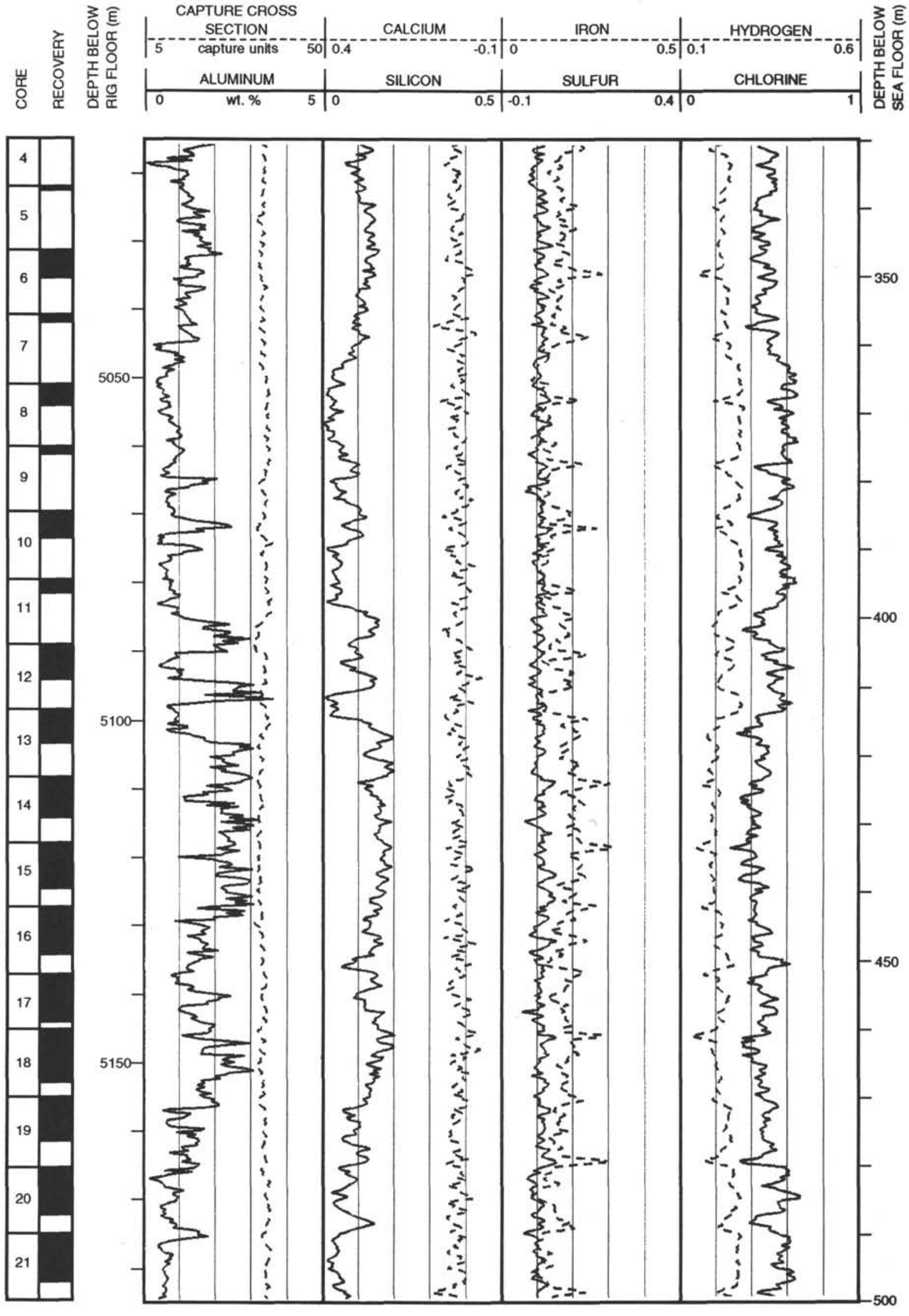

Hole 808C: Geochemical Log Summary (continued)

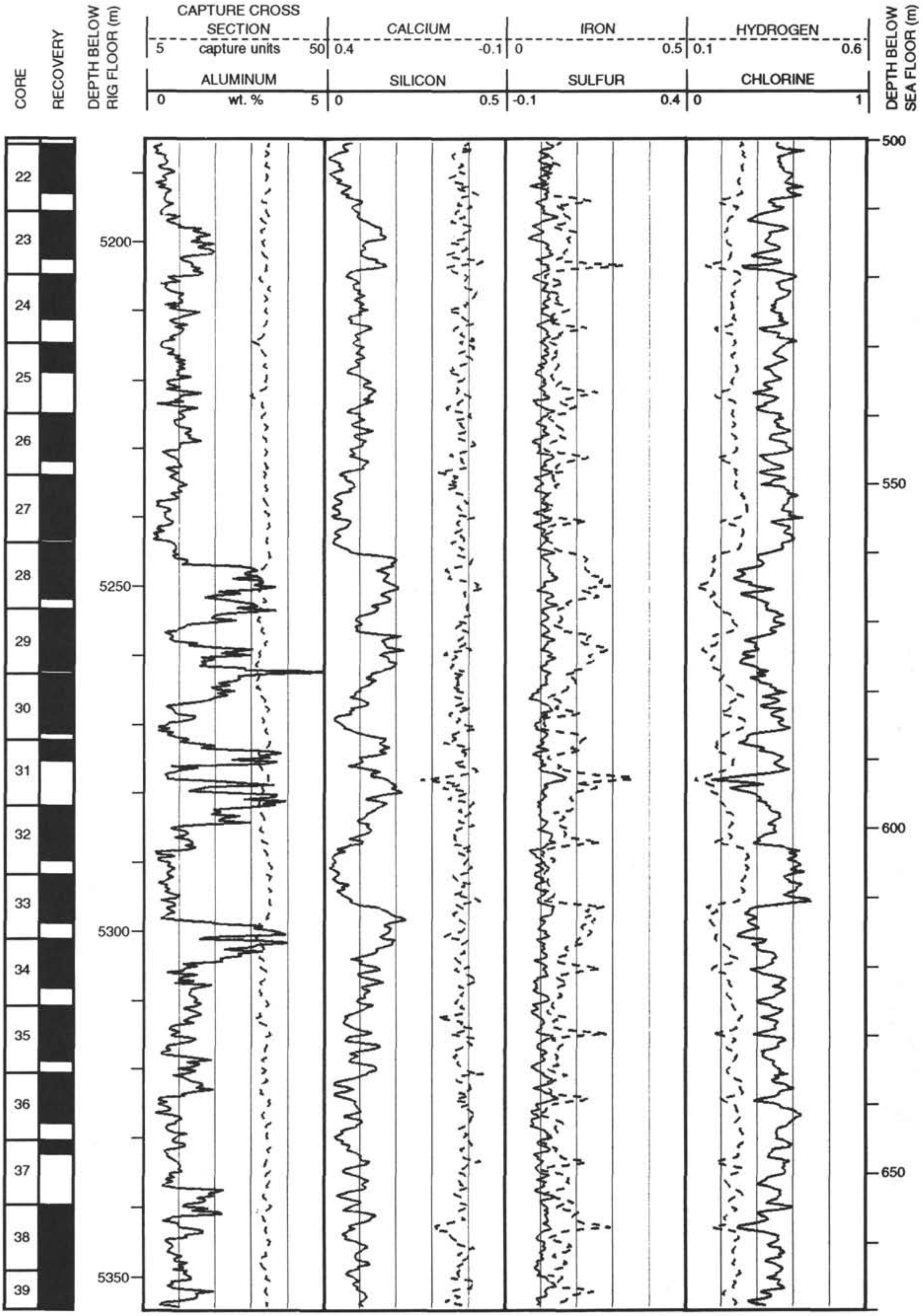

Hole 808C: Geochemical Log Summary (continued)

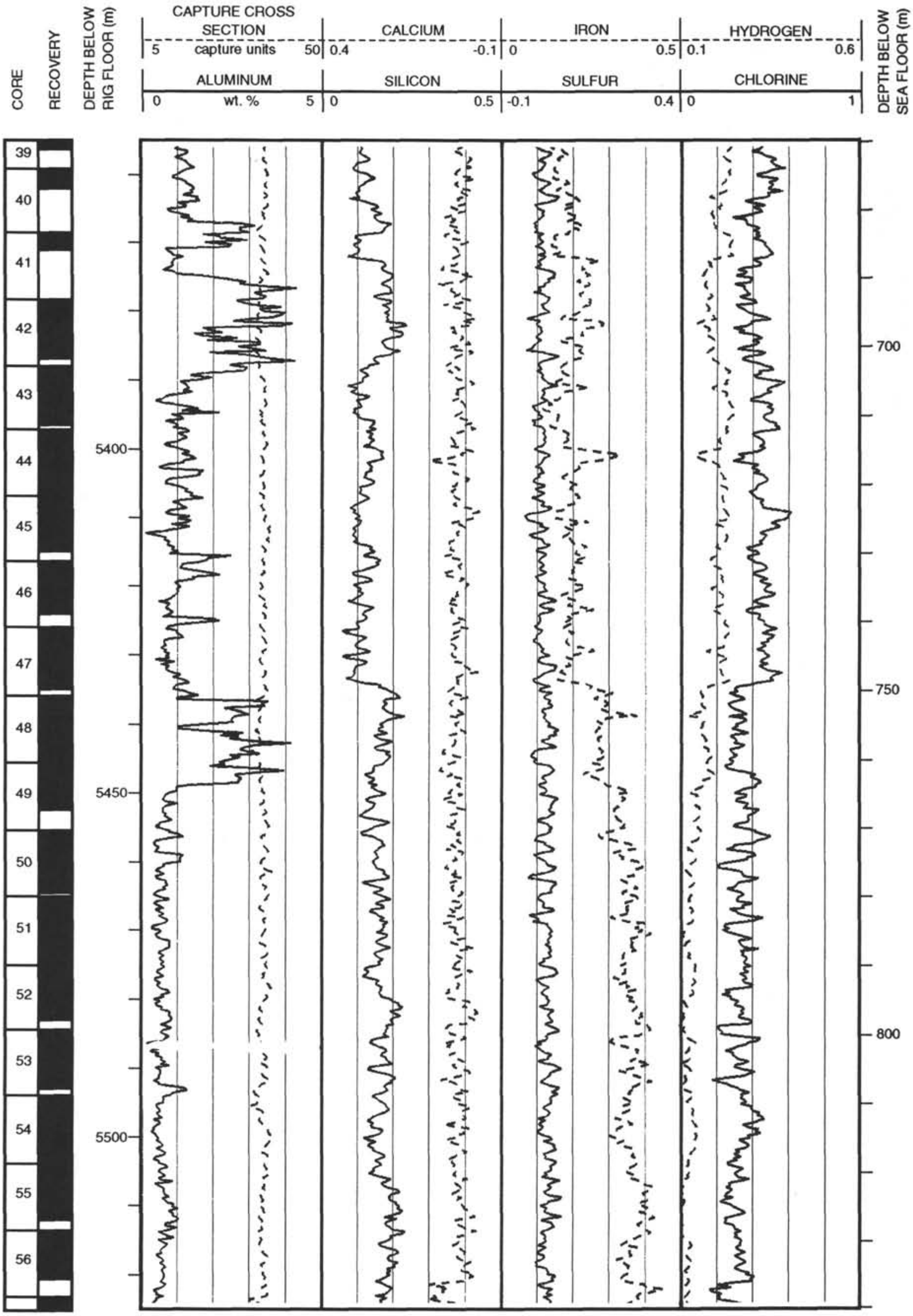

Hole 808C: Geochemical Log Summary (continued)

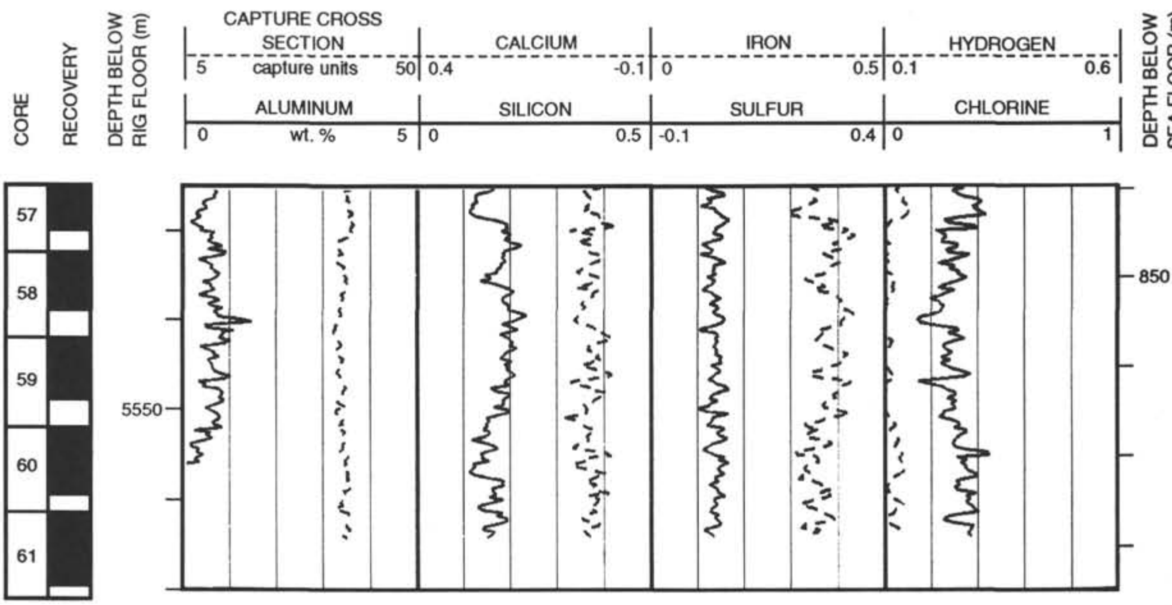

Hole 808E: Resistivity-Sonic-Gamma Ray Log Summary